hep-ph/0410364

Physics Interplay of the LHC and the ILC

The LHC / ILC Study Group

Editors:

G. Weiglein[1], T. Barklow[2], E. Boos[3], A. De Roeck[4], K. Desch[5], F. Gianotti[4], R. Godbole[6], J.F. Gunion[7], H.E. Haber[8], S. Heinemeyer[4], J.L. Hewett[2], K. Kawagoe[9], K. Mönig[10], M.M. Nojiri[11], G. Polesello[12,4], F. Richard[13], S. Riemann[10], W.J. Stirling[1]

Working group members who have contributed to this report:

A.G. Akeroyd[14], B.C. Allanach[15], D. Asner[16], S. Asztalos[17], H. Baer[18], T. Barklow[2], M. Battaglia[19], U. Baur[20], P. Bechtle[5], G. Bélanger[21], A. Belyaev[18], E.L. Berger[22], T. Binoth[23], G.A. Blair[24], S. Boogert[25], E. Boos[3], F. Boudjema[21], D. Bourilkov[26], W. Buchmüller[27] V. Bunichev[3], G. Cerminara[28], M. Chiorboli[29], H. Davoudiasl[30], S. Dawson[31], A. De Roeck[4], S. De Curtis[32], F. Deppisch[23], K. Desch[5], M.A. Díaz[33], M. Dittmar[34], A. Djouadi[35], D. Dominici[32], U. Ellwanger[36], J.L. Feng[37], F. Gianotti[4], I.F. Ginzburg[38], A. Giolo-Nicollerat[34], B.K. Gjelsten[39], R. Godbole[6], S. Godfrey[40], D. Grellscheid[41], J. Gronberg[17], E. Gross[42], J. Guasch[43], J.F. Gunion[7], H.E. Haber[8], K. Hamaguchi[27] T. Han[44], S. Heinemeyer[4], J.L. Hewett[2], J. Hisano[45], W. Hollik[46], C. Hugonie[47], T. Hurth[4,2], J. Jiang[22], A. Juste[48], J. Kalinowski[49], K. Kawagoe[9], W. Kilian[27], R. Kinnunen[50], S. Kraml[4,51], M. Krawczyk[49], A. Krokhotine[52], T. Krupovnickas[18], R. Lafaye[53], S. Lehti[50], H.E. Logan[44], E. Lytken[54], V. Martin[55], H.-U. Martyn[56], D.J. Miller[55,57], K. Mönig[10], S. Moretti[58], F. Moortgat[4], G. Moortgat-Pick[1,4], M. Mühlleitner[43], P. Nieżurawski[59], A. Nikitenko[60,52], M.M. Nojiri[11], L.H. Orr[61], P. Osland[62], A.F. Osorio[63], H. Päs[23], T. Plehn[4], G. Polesello[12,4], W. Porod[64,47], A. Pukhov[3], F. Quevedo[15], D. Rainwater[61], M. Ratz[27], A. Redelbach[23], L. Reina[18], F. Richard[13], S. Riemann[10], T. Rizzo[2], R. Rückl[23], H.J. Schreiber[10], M. Schumacher[41], A. Sherstnev[3], S. Slabospitsky[65], J. Solà[66,67], A. Sopczak[68], M. Spira[43], M. Spiropulu[4], W.J. Stirling[1], Z. Sullivan[48], M. Szleper[69], T.M.P. Tait[48], X. Tata[70], D.R. Tovey[71], A. Tricomi[29], M. Velasco[69], D. Wackeroth[20], C.E.M. Wagner[22,72], G. Weiglein[1], S. Weinzierl[73], P. Wienemann[27], T. Yanagida[74,75], A.F. Żarnecki[59], D. Zerwas[13], P.M. Zerwas[27], L. Živković[42]

[1]*Institute for Particle Physics Phenomenology, University of Durham, Durham DH1 3LE, UK*
[2]*Stanford Linear Accelerator Center, Menlo Park, CA 94025, USA,*
[3]*Skobeltsyn Institute of Nuclear Physics, Moscow State University, 119992 Moscow, Russia*
[4]*CERN, CH-1211 Geneva 23, Switzerland*
[5]*Universität Hamburg, Institut für Experimentalphysik, Luruper Chaussee, D-22761 Hamburg, Germany*
[6]*Centre for Theoretical Studies, Indian Institute of Science, Bangalore, 560012, India*
[7]*Davis Institute for HEP, Univ. of California, Davis, CA 95616, USA*
[8]*Santa Cruz Institute for Particle Physics, UCSC, Santa Cruz CA 95064, USA*
[9]*Kobe University, Japan*
[10]*DESY, Deutsches Elektronen-Synchrotron, D-15738 Zeuthen, Germany*
[11]*YITP, Kyoto University, Japan*
[12]*INFN, Sezione di Pavia, Via Bassi 6, Pavia 27100, Italy*
[13]*LAL-Orsay, France*
[14]*KEK Theory Group, Tsukuba, Japan 305-0801*
[15]*DAMTP, CMS, Wilberforce Road, Cambridge CB3 0WA, UK*
[16]*University of Pittsburgh, Pittsburgh, Pennsylvania, USA*
[17]*LLNL, Livermore, Livermore, California, USA*
[18]*Physics Department, Florida State University, Tallahassee, FL 32306, USA*
[19]*Univ. of California, Berkeley, USA*
[20]*Physics Department, State University of New York, Buffalo, NY 14260, USA*
[21]*LAPTH, 9 Chemin de Bellevue, BP 110, F-74941 Annecy-Le-Vieux, France*
[22]*HEP Division, Argonne National Laboratory, Argonne, IL 60439*
[23]*Institut für Theoretische Physik und Astrophysik, Universität Würzburg, D-97074 Würzburg, Germany*
[24]*Royal Holloway University of London, Egham, Surrey. TW20 0EX, UK*
[25]*University College, London, UK*
[26]*University of Florida, Gainesville, FL 32611, USA*
[27]*DESY, Notkestraße 85, D-22603 Hamburg, Germany*
[28]*University of Torino and INFN, Torino, Italy*
[29]*Universitá di Catania and INFN, Via S. Sofia 64, I-95123 Catania, Italy*
[30]*School of Natural Sciences, Inst. for Advanced Study, Princeton, NJ 08540, USA*
[31]*Physics Department, Brookhaven National Laboratory, Upton, NY 11973, USA*
[32]*Dept. of Physics, University of Florence, and INFN, Florence, Italy*
[33]*Departamento de Física, Universidad Católica de Chile, Santiago, Chile*
[34]*Institute for Particle Physics, ETH Zürich, CH-8093 Zürich, Switzerland*
[35]*LPMT, Université de Montpellier II, F-34095 Montpellier Cedex 5, France*
[36]*Laboratoire de Physique Théorique, Université de Paris XI, F-91405 Orsay Cedex, France*
[37]*Department of Physics and Astronomy, University of California, Irvine, CA 92697, USA*
[38]*Sobolev Institute of Mathematics, SB RAS, 630090 Novosibirsk, Russia*
[39]*Department of Physics, University of Oslo, P.O. Box 1048 Blindern, N-0316 Oslo, Norway*
[40]*Ottawa-Carleton Institute for Physics, Dept. of Physics, Carleton University,*

Ottawa K1S 5B6 Canada
[41] *Physikalisches Institut, Universität Bonn, Germany*
[42] *Weizmann Inst. of Science, Dept. of Particle Physics, Rehovot 76100, Israel*
[43] *Theory Group LTP, Paul Scherrer Institut, CH-5232 Villigen PSI, Switzerland*
[44] *Dept. of Physics, Univ. of Wisconsin, Madison, WI 53706*
[45] *ICRR, Tokyo University, Japan*
[46] *Max-Planck-Institut für Physik, Föhringer Ring 6, D-80805 München, Germany*
[47] *Instituto de Física Corpuscular, E-46071 València, Spain*
[48] *Theoretical Physics Department, Fermi National Accelerator Laboratory, Batavia, IL, 60510-0500*
[49] *Institute of Theoretical Physics, Warsaw University, Warsaw, Poland*
[50] *Helsinki Institute of Physics, Helsinki, Finland*
[51] *Inst. f. Hochenergiephysik, Österr. Akademie d. Wissenschaften, Wien, Austria*
[52] *ITEP, Moscow, Russia*
[53] *LAPP-Annecy, F-74941 Annecy-Le-Vieux, France*
[54] *Kobenhavns Univ., Mathematics Inst., Universitetsparken 5, DK-2100 Copenhagen O, Denmark*
[55] *School of Physics, The University of Edinburgh, Edinburgh, UK*
[56] *I. Physik. Institut, RWTH Aachen, D-52074 Aachen, Germany*
[57] *Department of Physics and Astronomy, University of Glasgow, Glasgow, UK*
[58] *School of Physics & Astronomy, University of Southampton, Southampton SO17 1BJ, UK*
[59] *Inst. of Experimental Physics, Warsaw University, Warsaw, Poland*
[60] *Imperial College, London, UK*
[61] *University of Rochester, Rochester, NY 14627, USA*
[62] *Department of Physics, University of Bergen, N-5007 Bergen, Norway*
[63] *University of Manchester, UK*
[64] *Institut für Theoretische Physik, Universität Zürich, CH-8057 Zürich, Switzerland*
[65] *Institute for High Energy Physics, Protvino, Moscow Region, Russia*
[66] *Departament d'Estructura i Constituents de la Matèria, Universitat de Barcelona, E-08028, Barcelona, Catalonia, Spain*
[67] *C.E.R. for Astrophysics, Particle Physics and Cosmology, Univ. de Barcelona, E-08028, Barcelona, Catalonia, Spain*
[68] *Lancaster University, UK*
[69] *Dept. of Physics, Northwestern University, Evanston, IL, USA*
[70] *Dept. of Physics and Astronomy, University of Hawaii, Honolulu, HI 96822, USA*
[71] *Department of Physics and Astronomy, University of Sheffield, Hounsfield Road, Sheffield S3 7RH, UK*
[72] *Enrico Fermi Institute and Department of Physics, University of Chicago, Chicago, IL 60637, USA*
[73] *Institut für Physik, Universität Mainz, D-55099 Mainz, Germany*
[74] *Department of Physics, University of Tokyo, Tokyo 113-0033, Japan*
[75] *Research Center for the Early Universe, University of Tokyo, Japan*

ANL-HEP-PR-04-108, CERN-PH-TH/2004-214, DCPT/04/134, DESY 04-206,
IFIC/04-59, IISc/CHEP/13/04, IPPP/04/67, SHEP-04-33, SLAC-PUB-10764,
UB-ECM-PF-04/31, UCD-04-28, UCI-TR-2004-37

Abstract

Physics at the Large Hadron Collider (LHC) and the International e^+e^- Linear Collider (ILC) will be complementary in many respects, as has been demonstrated at previous generations of hadron and lepton colliders. This report addresses the possible interplay between the LHC and ILC in testing the Standard Model and in discovering and determining the origin of new physics. Mutual benefits for the physics programme at both machines can occur both at the level of a combined interpretation of Hadron Collider and Linear Collider data and at the level of combined analyses of the data, where results obtained at one machine can directly influence the way analyses are carried out at the other machine. Topics under study comprise the physics of weak and strong electroweak symmetry breaking, supersymmetric models, new gauge theories, models with extra dimensions, and electroweak and QCD precision physics. The status of the work that has been carried out within the LHC / ILC Study Group so far is summarised in this report. Possible topics for future studies are outlined.

Contents

1 Introduction and Overview **1**
1.1 Introduction 1
1.1.1 The role of LHC and LC in revealing the nature of matter, space and time 1
1.1.2 Objectives of the study 4
1.2 Overview of the LHC / LC Study 6
1.2.1 Electroweak symmetry breaking 6
1.2.2 Supersymmetric models 13
1.2.3 Gauge theories and precision physics 16
1.2.4 Models with extra dimensions 18
1.2.5 The nature of Dark Matter 19

2 Experimental Aspects of the LHC and LC **23**
2.1 The interaction rate and the environment 24
2.2 Physics cross-sections and backgrounds 25
2.3 The detector performance requirements 27
2.4 Summary of physics capabilities 28

3 Higgs Physics and Electroweak Symmetry Breaking **31**
3.1 Higgs coupling measurements and flavour-independent Higgs searches 34
3.1.1 Model independent determination of the top Yukawa coupling from LHC and LC 36
3.1.2 Associated $t\bar{t}h$ production at the LC and LHC 40
3.1.3 Determining the parameters of the Higgs boson potential . . . 55
3.1.4 Higgs boson decay into jets 60
3.2 Determination of CP properties of Higgs bosons 66
3.2.1 CP studies of the Higgs sector 66
3.3 SUSY Higgs physics 71
3.3.1 Consistency tests and parameter extraction from the combination of LHC and LC results 72
3.3.2 Importance of the $\tilde{\chi}_1^0$ mass measurement for the $A^0, H^0 \to \tilde{\chi}_2^0\tilde{\chi}_2^0$ mass reconstruction 81
3.3.3 The neutral MSSM Higgs bosons in the intense-coupling regime 86
3.3.4 Estimating the precision of a $\tan\beta$ determination with $H/A \to \tau^+\tau^-$ in CMS and $\tau^+\tau^-$ fusion at a high-energy photon collider 93
3.3.5 LHC and LC determinations of $\tan\beta$ 97
3.4 Higgs sector in non-minimal models 101
3.4.1 NMSSM Higgs discovery at the LHC 103
3.4.2 An interesting NMSSM scenario at the LHC and LC 113

3.4.3 Identifying an SM-like Higgs particle at future colliders 121
3.4.4 Synergy of LHC, LC and PLC in testing the 2HDM (II) 124
3.4.5 Enhanced $h^0 \to \gamma\gamma$ decays in fermiophobic Higgs models at the LHC and LC 125
3.4.6 Visible signals of an 'invisible' SUSY Higgs at the LHC 128
3.5 A light Higgs in scenarios with extra dimensions 133
3.5.1 On the complementarity of Higgs and radion searches at LHC and LC 134
3.5.2 Radions at a photon collider 140
3.5.3 Further scenarios 143
3.5.4 Conclusions 144
3.6 Phenomenology of the Littlest Higgs model 144
3.6.1 The Little Higgs at the LHC 146
3.6.2 The Little Higgs at a Linear Collider 148
3.7 Exotic scenarios 151
3.7.1 The CP-conserving MSSM in the decoupling limit 152
3.7.2 The CP-conserving 2HDM with the only light Higgs boson being pseudoscalar – a special non-decoupling limit 153
3.7.3 Maximally-mixed and "Continuum" Higgs models 154
3.7.4 Higgsless models 155

4 Strong Electroweak Symmetry Breaking 157
4.1 Introduction 157
4.2 Low-energy effective theory 158
4.3 Beyond the threshold 160
4.4 Processes at the LHC and the LC 161
4.4.1 Vector-boson scattering at the LHC 161
4.4.2 Vector-boson scattering at the Linear Collider 162
4.4.3 Three-boson production 163
4.4.4 Rescattering 164
4.5 Results 164
4.5.1 Approximations 164
4.5.2 Existing results 165
4.5.3 Ongoing studies 168
4.6 Scenarios where the LHC sees resonances 169
4.7 Conclusions 172

5 Supersymmetric Models 173
5.1 Measurement of supersymmetric particle masses, mixings and couplings at LHC and LC 174
5.1.1 The SPS 1a benchmark scenario 174
5.1.2 A detailed analysis of the measurement of SUSY masses with the ATLAS detector at the LHC 180
5.1.3 Squark and gluino reconstruction with CMS at LHC 202
5.1.4 Measurement of sparticle masses in mSUGRA scenario SPS 1a at a Linear Collider 214

5.1.5 Sparticle mass measurements from LHC analyses and combination with LC results . . . 219
5.1.6 Susy parameter determination in combined analyses at LHC/LC 224
5.1.7 Determination of stop and sbottom sector by LHC and LC . . . 238
5.2 Global fits in the MSSM . . . 242
5.2.1 SFITTER: SUSY parameter analysis at LHC and LC . . . 242
5.2.2 Fittino: A global fit of the MSSM parameters . . . 248
5.3 SUSY and Dark Matter . . . 254
5.3.1 Reach of LHC and LC in Dark Matter allowed regions of the mSUGRA model . . . 254
5.3.2 Impact of the LHC and LC on the accuracy of the predicted Dark Matter relic density . . . 259
5.4 Further SUSY scenarios . . . 265
5.4.1 Non-decoupling effect in sfermion-chargino/neutralino couplings . . . 265
5.4.2 Correlations of flavour and collider physics within supersymmetry . . . 272
5.4.3 Supersymmetric lepton flavour violation at LHC and LC . . . 275
5.4.4 Detection difficulties for MSSM and other SUSY models for special boundary conditions . . . 285
5.5 Determination of mSUGRA parameters and discrimination between SUSY breaking scenarios . . . 290
5.5.1 Complementarity of LHC and Linear Collider measurements of slepton and lighter neutralino masses . . . 290
5.5.2 Discriminating SUSY breaking scenarios . . . 293
5.5.3 Gravitino and goldstino at colliders . . . 295
5.5.4 Reconstructing supersymmetric theories by coherent LHC / LC analyses . . . 303

6 Electroweak and QCD Precision Physics 319
6.1 Top physics . . . 319
6.1.1 Top-quark production . . . 319
6.1.2 Spin correlations in top production and decays . . . 322
6.1.3 Anomalous couplings . . . 325
6.1.4 FCNC in top quark physics . . . 327
6.2 Electroweak precision physics . . . 330
6.2.1 Electroweak precision measurements at the LHC and the LC . . . 330
6.2.2 Constraints on the parameters of the scalar top sector . . . 331
6.2.3 Constraints on the parameters of the MSSM Higgs boson sector 333
6.2.4 Triple gauge boson couplings . . . 334
6.2.5 Conclusions . . . 336
6.3 QCD studies . . . 338
6.3.1 Measurements of α_S . . . 339
6.3.2 BFKL physics . . . 341
6.3.3 Improving the $H \to \gamma\gamma$ background prediction by using combined collider data . . . 347

7 New Gauge Theories **351**
7.1 Scenarios with extra gauge bosons . . . 351
7.1.1 Sensitivity to new physics models . . . 351
7.2 Z′ studies at the LHC . . . 354
7.2.1 Z′mass reaches at the LHC . . . 354
7.2.2 Distinction of models at the LHC . . . 354
7.2.3 Summary: Z′ search at the LHC . . . 356
7.3 Z′ studies at the LC . . . 356
7.3.1 Z′ mass reaches at the LC . . . 356
7.3.2 Distinction of models with the LC . . . 358
7.3.3 Z′ search at GigaZ . . . 359
7.4 Z′ in Little Higgs models . . . 360
7.4.1 Studies at LC . . . 360
7.4.2 Studies at LHC . . . 362
7.5 Charged new gauge bosons . . . 363
7.6 Z′ from a Kaluza-Klein excitation . . . 364
7.6.1 Discovery reach for a Z′ from a Kaluza-Klein excitation . . . 364
7.6.2 Distinguishing a 'conventional' and KK Z′ . . . 366
7.7 Summary . . . 366

8 Models with Extra Dimensions **369**
8.1 Large extra dimensions . . . 369
8.1.1 Indirect effects: graviton exchange . . . 370
8.1.2 Direct production: graviton emission . . . 375
8.1.3 Graviscalar effects in Higgs production . . . 379
8.1.4 Determination of the model parameters . . . 383
8.2 TeV^{-1} extra dimensions . . . 385
8.2.1 Gauge fields in the bulk . . . 385
8.2.2 Universal extra dimensions . . . 393
8.3 Warped extra dimensions . . . 396
8.3.1 Conventional RS model . . . 396
8.3.2 Extensions of the RS model . . . 397
8.3.3 Conclusions . . . 402

9 Conclusions and Outlook **405**

1 Introduction and Overview

1.1 Introduction

1.1.1 The role of LHC and LC in revealing the nature of matter, space and time

The goal of elementary particle physics is to reveal the innermost building blocks of matter and to understand the fundamental forces acting between them. The physics of elementary particles and their interactions played a key role in the evolution of the Universe from the Big Bang to its present appearance in terms of galaxies, stars, black holes, chemical elements and biological systems. Research in elementary particle physics thus addresses some of the most elementary human questions: what are we made of, what is the origin and what is the fate of the Universe?

The past century was characterised by an enormous progress towards an understanding of the innermost secrets of the Universe, which became possible through a cross-fertilisation of breakthroughs on the experimental and theoretical side. The results obtained in particle physics have revealed a complex microphysical world, which however seems to obey surprisingly simple mathematical descriptions, governed by symmetry principles. We now believe that there are four fundamental forces in nature, the strong, electromagnetic, weak and gravitational forces. The seemingly disparate electromagnetic and weak interactions have been found to emerge from the unified electroweak interaction. We have been able to formulate a quantum theory of elementary particles based on the strong and electroweak interactions, which will stand as one of the lasting achievements of the twentieth century. The quantum nature of the interactions means in particular that they arise from the interchange of particles, namely the massless photon, massive W and Z bosons for the electroweak interaction, and the massless gluon for the strong interaction.

According to our current understanding there seem to be indications pointing towards a unification of the strong and electroweak forces, and it appears to be conceivable that also gravity, with the graviton as mediator of the interaction, may be incorporated into a unified framework. We know, however, that our picture of the observed forces and particles — the known particles comprise the constituents of matter, the quarks and leptons, and the mediators of the interactions — is incomplete. There needs to be another ingredient, being related to the origin of mass and the breaking of the symmetry governing the electroweak interaction. Its effects will manifest itself at the energy scales that can be probed at the next generation of colliders. The favourite candidate for this ingredient is the Higgs field, a scalar field that spreads out in all space. Its field quantum is the Higgs particle. If no fundamental Higgs boson exists in nature, electroweak symmetry breaking can occur, for instance, via a new kind of strong interaction.

The Higgs boson is the last missing ingredient of the "Standard Model" (SM) of

particle physics, which was proposed more than three decades ago. The SM has provided an extremely successful description of the phenomena of the electroweak and strong interaction, having passed hundreds of experimental tests at high precision. The direct search for the Higgs boson has excluded a SM Higgs boson with a mass below about 114 GeV [1], which is about 120 times the mass of the proton. The precision tests of the SM, based on the interplay of experimental information obtained at different accelerators, allow one to set an indirect upper bound for a SM Higgs of about 250 GeV [2].

However, even if a SM-like Higgs boson is found, the SM cannot be the ultimate theory, which is obvious already from the fact that it does not contain gravity. There are indications that new physics beyond the SM should manifest itself below an energy scale of about 1 TeV ($\equiv 10^3$ GeV). A particular shortcoming of the SM is its instability against the huge hierarchy of vastly different scales relevant in particle physics. We know of at least two such scales, the electroweak scale at a few hundred GeV and the Planck scale at about 10^{19} GeV, where the strengths of gravity and the other interactions become comparable. The Higgs-, W- and Z-boson masses are all unstable to quantum fluctuations and would naturally be pushed to the Planck scale without the onset of new physics at the scale of few hundred GeV.

There are also direct experimental indications for physics beyond the SM. While in the SM the neutrinos are assumed to be massless, there is now overwhelming experimental evidence that the neutrinos possess non-zero (but very small) masses [3]. A neutrino mass scale in agreement with the experimental observations emerges naturally if there is new physics at a scale of about 10^{16} GeV. We furthermore know that "ordinary" matter, i.e. quarks and leptons, contributes only a small fraction of the matter density of the Universe [4]. There is clear evidence, in particular, for a different kind of "cold Dark Matter", for which the SM does not offer an explanation. The known properties of Dark Matter could arise in particular if new weakly interacting massive particles exist, which requires an extension of the SM.

A very attractive possibility of new physics that stabilises the hierarchy between the electroweak and the Planck scale is supersymmetry (SUSY), i.e. the extension of space and time by new supersymmetric coordinates. Supersymmetric models predict the existence of partner particles with the same properties as the SM particles except that their "spin", i.e. their internal angular momentum, differs by half a unit. Other ideas to solve the hierarchy problem postulate extra spatial dimensions beyond the three that we observe in our every-day life, or new particles at the several TeV scale.

Supersymmetric theories allow the unification of the strong, electromagnetic and weak interactions at a scale of about 10^{16} GeV. In such a "grand unified theory", the strong, electromagnetic and weak interactions can be understood as being just three different manifestations of a single fundamental interaction. (In contrast, in the absence of supersymmetry, the three interactions fail to unify in the SM.) It should be noted that the possible scale of grand unification is approximately the same as the one that would give rise to neutrino masses consistent with the experimental observations. In the minimal supersymmetric extension of the SM the lightest SUSY particle (LSP) is stable. The LSP has emerged as our best candidate for cold Dark Matter in the Universe.

The current understanding of the innermost structure of the Universe will be boosted

by a wealth of new experimental information which we expect to obtain in the near future within a coherent programme of very different experimental approaches. They range from astrophysical observations, physics with particles from cosmic rays, neutrino physics (from space, the atmosphere, from reactors and accelerators), precision experiments with low-energy high-intensity particle beams to experiments with colliding beams at the highest energies. The latter play a central role because new fundamental particles can be discovered and studied under controllable experimental conditions and a multitude of observables is accessible in one experiment.

While the discovery of new particles often requires access to the highest possible energies, disentangling the underlying structure calls for highest possible precision of the measurements. Quantum corrections are influenced by the whole structure of the model. Thus, the fingerprints of new physics often only manifest themselves in tiny deviations. These two requirements — high energy and high precision — cannot normally be obtained within the same experimental approach. While in hadron collisions (collisions of protons with protons or protons with antiprotons) it is technically feasible to reach the highest centre-of-mass energies, in lepton collisions (in particular collisions of the electron and its antiparticle, the positron) the highest precision of measurements can be achieved. This complementarity has often led to a concurrent operation of hadron and lepton colliders in the past and has undoubtedly created a high degree of synergy of the physics programmes of the two colliders. As an example, the Z boson, a mediator of the weak interactions, has been discovered at a proton–antiproton collider, i.e. by colliding strongly interacting particles. Its detailed properties, on the other hand, have only been measured with high precision at electron–positron colliders. These measurements were crucial for establishing the SM. Contrarily, the gluon, the mediator of the strong interactions, has been discovered at an electron–positron collider rather than at a proton collider where the strong interaction dominates.

Within the last decade, the results obtained at the electron–positron colliders LEP and SLC had a significant impact on the physics programme of the Tevatron proton–antiproton collider and vice versa. The electroweak precision measurements at LEP and SLC gave rise to an indirect prediction of the top-quark mass. The top quark was subsequently discovered at the Tevatron with a mass in agreement with the indirect prediction. The measurement of the top-quark mass at the Tevatron, on the other hand, was crucial for deriving indirect constraints from LEP/SLC data on the Higgs-boson mass in the SM, while experimental bounds from the direct search were established at LEP. The experimental results obtained at LEP have been important for the physics programme of the currently ongoing Run II of the Tevatron. There are further examples of this type of synergy between different colliders in the recent past. Following an observed excess of events with high momentum squared at HERA in 1997, and their possible interpretation as leptoquark production, dedicated leptoquark searches at the concurrently running Tevatron were subsequently carried out. These Tevatron searches provided strong constraints on the leptoquark model, information that was in turn fed back to the HERA analyses. The most recent example of the interplay of lepton and hadron colliders is the discovery of the state X(3872) at BELLE [5], which gave rise to a dedicated search at the Tevatron, leading to an independent confirmation of the new state [6,7].

The enormous advance of accelerator science over the last decades has put us in

a situation where both the next generation of hadron and electron–positron colliders are technologically feasible and mature. The Large Hadron Collider (LHC) [8] is under construction at CERN and is scheduled to start taking data in 2007. It will collide protons with an energy of 14 TeV. Since the proton is a composite particle, the actual "hard" scattering process takes place between quarks and gluons at a fraction of the total energy.

The International Linear Collider (ILC) will bring the electron and the positron to collision with an energy of up to approximately 1 TeV and high luminosity [9]. The ILC has been agreed in a world-wide consensus to be the next large experimental facility in high-energy physics. Designs for this machine have been developed in a world-wide effort, and it has been demonstrated that a ILC can be built and reliably operated. The technology for the accelerating cavities has recently been chosen, and the development of an internationally federated design has been endorsed [10].

While the acronym "ILC" refers to the specific machine that is currently designed in a world-wide collaboration [10], the shorthand "LC" is normally used more generically for a Linear Collider. Since most of the text of this report was written prior to the official "ILC" naming, in the following the acronym "LC" is used throughout. Most of the studies in this report were carried out for an ILC-type machine, i.e. an electron–positron Linear Collider with an energy up to about 1 TeV. For studies referring to a Linear Collider with higher energy or to one of the ILC options, like the photon-collider mode, the electron–electron-collider mode or the low-energy electron–positron mode at the Z-boson resonance, this is explicitly indicated in the text.

Ground-breaking discoveries are expected at the LHC and LC. The information obtained from these machines will be indispensable, in particular, for deciphering the mechanism giving rise to the breaking of the electroweak symmetry, and thus establishing the origin of the masses of particles. Furthermore it is very likely that we will be able to determine the new physics responsible for stabilising the hierarchy between the electroweak and the Planck scale, which may eventually lead us to an understanding of the ultimate unification of forces. We expect new insights into the physics of flavour and into the origin for the violation of the charge conjugation and parity (CP) symmetry. This could lead to a more fundamental understanding of the observed matter–antimatter asymmetry in the Universe.

Thus, the physics case is well established for both the LHC and the LC. While the physics programme at each of the machines individually is very rich, further important synergistic effects can be expected from an intimate interplay of the results from the two accelerators. This will lead to mutual benefits for the physics programme of both machines. In this way the physics return for the investment made in both machines will be maximised.

1.1.2 Objectives of the study

The goal of the studies contained in this document is to delineate through detailed examples the complementarity of the LHC and LC programmes and the enormous synergy that will result if the two machines have a very substantial overlap of concurrent operation.

One of the great assets of the LHC is its large mass reach for direct discoveries,

which extends up to typically ∼6–7 TeV for singly-produced particles with QCD-like couplings (e.g. excited quarks) and ∼2–3 TeV for pair-produced strongly interacting particles. The reach for singly produced electroweak resonances (e.g. a heavy partner of the Z boson) is about 5 TeV. The hadronic environment at the LHC, on the other hand, will be experimentally challenging. Kinematic reconstructions are normally restricted to the transverse direction. Since the initial-state particles carry colour charge, QCD cross sections at the LHC are huge, giving rise to backgrounds which are many orders of magnitude larger than important signal processes of electroweak nature. Furthermore, operation at high luminosity entails an experimentally difficult environment such as pile-up events.

The envisaged LC in the energy range of ∼0.5–1 TeV provides a much cleaner experimental environment that is well suited for high-precision physics. It has a well-defined initial state which can be prepared to enhance or suppress certain processes with the help of beam polarisation. The better knowledge of the momenta of the interacting particles gives rise to kinematic constraints which allow reconstruction of the final state in detail. The signal–to–background ratios at the LC are in general much better than at the LHC. Direct discoveries at the LC are possible up to the kinematic limit of the available energy. In many cases the indirect sensitivity to effects of new physics via precision measurements greatly exceeds the kinematic limit, typically reaching up to 10 TeV.

While the complementarity between the LHC and LC is qualitatively obvious, more quantitative analyses of the possible interplay between the LHC and LC have been lacking until recently. They require detailed case studies, involving input about various experimental aspects at both the LHC and LC. In order to achieve this, a close collaboration is necessary between experimentalists from the LHC and LC and theorists.

The LHC / ILC Study Group has formed as a collaborative effort of the hadron collider and linear collider communities. This world-wide working group investigates how analyses carried out at the LHC could profit from results obtained at the LC and vice versa. In order to be able to carry out analyses of this kind, it is necessary to assess in detail the capabilities of the LHC and LC in different scenarios of physics within and beyond the Standard Model. Based on these results, the LHC / ILC Study Group investigates the possible synergy of a concurrent running of the LHC and LC. This synergy can arise from a simultaneous interpretation of LHC and LC data, leading to a clearer physics picture. Furthermore, results from one collider can be directly fed into the analyses of the other collider, so that experimental strategies making use of input from both colliders can be established. The LC results can in this context directly influence the running strategy at the LHC. In particular, the LC could predict properties of new particles, leading to a dedicated search at the LHC. This could involve the implementation of optimised selection criteria or modifications of the trigger algorithms. LC results could also guide decisions on required running time and sharpen the goals for a subsequent phase of LHC running.

In general, the untriggered operation of the LC has the potential to reveal new physics that gives rise to signatures that do not pass the LHC triggers. Such a situation occurred in the past, for instance, at ISR where the discovery of the J/ψ at the electron–positron collider SPEAR (and independently at AGS) lead to a modification of the trigger, and the signal could subsequently be confirmed at ISR. In the TeV

regime one cannot exclude the possibility that unexpected new physics manifests itself in events which will not be selected by the very general trigger strategies adopted by the LHC experiments. Insight from the LC could help in such a case to optimise the search strategy at the LHC.

While the LHC is scheduled to take first data in 2007, the LC could go into operation in about the middle of the next decade. This would allow a substantial period of overlapping running of both machines, since it seems reasonable to expect that the LHC (including upgrades) will run for about 15 years (similarly to the case of the Tevatron, whose physics programme started more than 20 years ago). During simultaneous running of both machines there is obviously the highest flexibility for adapting analyses carried out at one machine according to the results obtained at the other machine.

The results obtained in the framework of the LHC / ILC Study Group are documented in this first working group report. The report should be viewed as a first step that summarises the present status and guides the way towards further studies. Many different scenarios were investigated, and important synergistic effects have been established. Topics under study comprise the physics of weak and strong electroweak symmetry breaking, electroweak and QCD precision physics, the phenomenology of supersymmetric models, new gauge theories and models with extra dimensions. For scenarios where detailed experimental simulations of the possible measurements and the achievable accuracies are available both for the LHC and LC, the LHC / LC interplay could be investigated in a quantitative manner. In other scenarios the assessment of the current situation has revealed the need for further experimental simulations at the LHC and LC as input for studying the interplay between the two machines. Thus, the present work of the LHC and LC physics groups will serve as an important input for future LHC / LC analyses.

1.2 Overview of the LHC / LC Study

In the following, a brief overview of the results obtained in this working group report is given.

1.2.1 Electroweak symmetry breaking

Revealing the mechanism of electroweak symmetry breaking will be the central issue for the LHC and LC. Within the SM, the mass of the Higgs boson is a free parameter. The comparison of the SM predictions with the electroweak precision data point towards a light Higgs boson with $m_h \lesssim 250$ GeV [2]. In the Minimal Supersymmetric extension of the Standard Model (MSSM) the mass of the lightest CP-even Higgs boson can be directly predicted from the other parameters of the model, yielding an upper bound of $m_h \lesssim 140$ GeV [11]. The MSSM predicts four other fundamental Higgs bosons, H, A and $H^{\pm}$. The Higgs sectors of the SM and the MSSM are the most commonly studied realisations of electroweak symmetry breaking.

However, the electroweak precision data do not exclude the possibility of a Higgs sector with unconventional properties. In particular, new physics contributions to electroweak precision observables can in principle compensate the effects of a heavy

Higgs boson, mimicking in this way the contribution from a light SM-like Higgs boson. While a light Higgs boson is also required in extensions of the MSSM, the properties of such a light Higgs boson (and also the other states in the Higgs sector) can significantly differ from the MSSM.

Furthermore, the possibility that no fundamental Higgs particle exists has to be investigated. This necessitates, in particular, the study of scenarios where electroweak symmetry breaking occurs as a consequence of a new strong interaction.

In the following, four different scenarios of electroweak symmetry breaking will be discussed and the impact of the LHC / LC interplay will be highlighted.

1.2.1.1 Scenarios with a light SM-like or MSSM-like Higgs boson

If a state resembling a Higgs boson is detected, it is crucial to experimentally test its nature as a Higgs boson. To this end the couplings of the new state to as many particles as possible must be precisely determined, which requires observation of the candidate Higgs boson in several different production and decay channels. Furthermore the spin and the other CP-properties of the new state need to be measured, and it must be clarified whether there is more than one Higgs state. The LHC will be able to address some of these questions, but in order to make further progress a comprehensive programme of precision Higgs measurements at the LC will be necessary. The significance of the precision Higgs programme is particularly evident from the fact that many extended Higgs theories over a wide part of their parameter space have a lightest Higgs scalar with nearly identical properties to those of the SM Higgs boson. In this so-called decoupling limit additional states of the Higgs sector are heavy and may be difficult to detect both at the LHC and LC. Thus, precision measurements are crucial in order to distinguish the SM Higgs sector from a more complicated scalar sector. In this way the verification of small deviations from the SM may be the path to decipher the physics of electroweak symmetry breaking.

While the LC will provide a wealth of precise experimental information on a light Higgs boson, the LHC may be able to detect heavy Higgs bosons which lie outside the kinematic reach of the LC (it is also possible, however, that the LC will detect a heavy Higgs boson that is not experimentally observable at the LHC due to overwhelming backgrounds). Even in the case where only one scalar state is accessible at both colliders important synergistic effects arise from the interplay of LHC and LC. This has been demonstrated for the example of the Yukawa coupling of the Higgs boson to a pair of top quarks. At a 500 GeV LC the $t\bar{t}h$ coupling can only be measured with limited precision for a light Higgs boson h. The LHC will provide a measurement of the $t\bar{t}h$ production cross section times the decay branching ratio (for $h \to b\bar{b}$ or $h \to W^+W^-$). The LC, on the other hand, will perform precision measurements of the decay branching ratios. Combining LHC and LC information will thus allow one to extract the top Yukawa coupling. A similar situation occurs for the determination of the Higgs-boson self-coupling, which is a crucial ingredient for the reconstruction of the Higgs potential. The measurement of the Higgs self-coupling at the LHC will require precise experimental information on the top Yukawa coupling, the hWW coupling and the total Higgs width, which will be available with the help of the LC. An important synergy between LHC and LC results would even exist if nature had chosen the (very unlikely) scenario of just a SM-type Higgs boson and no other new

physics up to a very high scale. The precision measurements at the LC of the Higgs-boson properties as well as of electroweak precision observables, the top sector, etc. (see Sec. 1.2.3.1), together with the exclusion bounds from the direct searches at the LHC would be crucial to verify that the observed particles are sufficient for a consistent description of the experimental results.

The LHC and LC can successfully work together in determining the CP properties of the Higgs bosons. In an extended Higgs-sector with CP-violation there is a non-trivial mixing between all neutral Higgs states. Different measurements at the LHC and the LC (both for the electron–positron and the photon–photon collider option) have sensitivity to different coupling parameters. In the decoupling limit, the lightest Higgs boson is an almost pure CP-even state, while the heavier Higgs states may contain large CP-even and CP-odd components. Also in this case, high-precision measurements of the properties of the light Higgs boson at the LC may reveal small deviations from the SM case, while the heavy Higgs bosons might only be accessible at the LHC. In many scenarios, for instance the MSSM, CP-violating effects are induced via loop corrections. The CP properties therefore depend on the particle spectrum. The interplay of precision measurements in the Higgs sector from the LC and information on, the SUSY spectrum from the LHC can therefore be important for revealing the CP structure. As an example, if CP-violating effects in the Higgs sector in a SUSY scenario are established at the LC, one would expect CP-violating couplings in the scalar top and bottom sector. The experimental strategy at the LHC could therefore focus on the CP properties of scalar tops and bottoms.

In supersymmetric theories Higgs boson masses can directly be predicted from other parameters of the model, leading, for instance, to the upper bound of $m_h \lesssim 140$ GeV [11] for the mass of the lightest CP-even Higgs boson of the MSSM. A precise determination of the Higgs masses and couplings therefore gives important information about the parameter space of the model. If at the LHC the $h \to \gamma\gamma$ decay mode is accessible, the LHC will be able to perform a first precision measurement in the Higgs sector by determining the Higgs-boson mass with an accuracy of about $\Delta m_h^{\rm exp} \approx 200$ MeV [8]. As a consequence of large radiative corrections from the top and scalar top sector of supersymmetric theories, the prediction for m_h sensitively depends on the precise value of the top-quark mass. For the lightest CP-even Higgs-bosons of the MSSM, an experimental error of 1 GeV in m_t translates into a theory uncertainty in the prediction of m_h of also about 1 GeV. As a consequence, the experimental accuracy of the top-mass measurement achievable at the LHC, $\Delta m_t^{\rm LHC} \approx 1$–2 GeV [12], will not be sufficient to exploit the high precision of the LHC measurement of m_h. Thus, in order to match the experimental precision of m_h at the LHC with the accuracy of the theoretical prediction, the precise measurement of the top-quark mass at the LC, $\Delta m_t^{\rm LC} \lesssim 0.1$ GeV [13], will be mandatory.

If the uncertainty in the predictions for observables in the Higgs sector arising from the experimental error of the top-quark mass is under control (and the theoretical predictions are sophisticated enough so that uncertainties from unknown higher-order corrections are sufficiently small), one can make use of precision measurements in the Higgs sector to obtain constraints on the masses and couplings of the SUSY particles that enter in the radiative corrections to the Higgs sector observables. The results can be compared with the direct information on the SUSY spectrum. In general, the LHC and LC are sensitive to different aspects of the SUSY spectrum, and both machines

will provide crucial input data for the theoretical interpretation of the precision Higgs programme. In a scenario where the LHC and LC only detect one light Higgs boson, precision measurements of its properties at the LC allow to set indirect limits on the mass scale of the heavy Higgs bosons, provided that combined information from the LHC and LC on the SUSY spectrum is available. If the heavy Higgs bosons are directly accessible at the LHC, the combination of the information on the heavy Higgs states at the LHC with the LC measurements of the mass and branching ratios of the light Higgs will allow one to obtain information on the scalar quark sector of the theory. In particular it was demonstrated that the trilinear coupling A_t of the Higgs bosons to the scalar top quarks can be determined in this way.

A promising possibility for the detection of heavy Higgs states at the LHC is from the decay of heavy Higgs bosons into SUSY particles, for instance a pair of next-to-lightest neutralinos. The next-to-lightest neutralino will decay into leptons and the lightest neutralino, which will escape undetected in most SUSY scenarios. For this case it was demonstrated that the reconstruction of the mass of the heavy Higgs bosons at the LHC requires as input the precision measurement of the mass of the lightest neutralino at the LC.

A fundamental parameter in models with two Higgs doublets (e.g., the MSSM) is $\tan\beta$, the ratio of the vacuum expectation values of the two Higgs doublets. It not only governs the Higgs sector, but is also important in many other sectors of the theory. A precise experimental determination of this parameter will be difficult, and it seems very unlikely that it will be possible to extract $\tan\beta$ from a single observable. Instead, a variety of measurements at the LHC and LC will be needed to reliably determine $\tan\beta$. The measurements involve observables in the Higgs sector, the gaugino sector and the scalar tau sector as well as information on the SUSY spectrum.

1.2.1.2 Higgs sector with non-standard properties

The most studied Higgs boson models are the SM and the MSSM because they are the simplest realisations with a minimal field content. However, since we lack a deeper understanding of the origin of electroweak symmetry breaking, it is not sufficient to restrict to certain models based just upon their simplicity. Thus, it is important to explore the extent to which search strategies need to be altered in case of more complicated Higgs sectors.

A possible scenario giving rise to non-standard properties of the Higgs sector is the presence of large extra dimensions, motivated for instance by a "fine-tuning" and "little hierarchy" problem of the MSSM. A popular class of such models comprise those in which some or all of the SM particles live on 3-branes in the extra dimensions. Such models inevitably require the existence of a radion (the quantum degree associated with fluctuations of the distance between the three branes or the size of the extra dimension(s)).

The radion has the same quantum numbers as the Higgs boson and in general the two will mix. Since the radion has couplings that are very different from those of the SM Higgs boson, the two physical eigenstates will have unusual properties corresponding to a mixture of the Higgs and radion properties; the prospects for detecting them at the LHC and LC must be carefully analysed. One finds that there are significant portions of the parameter space for which it will not be possible to

observe the Higgs-like h state at the LHC. For most of this region, the radion-like ϕ state will be observable in the process $gg \to \phi \to ZZ^* \to 4\ell$, leading thus to a situation where one scalar will be detected at the LHC. Disentangling the nature of this scalar state will be a very important but experimentally challenging task.

For instance, if the LHC observes a scalar state with a non-SM-like production or decay rate, it will be unclear from LHC data alone whether this is due to mixing with a radion from extra dimensions or due to the presence of an extended Higgs sector, such as that predicted by the MSSM or its most attractive extension, the Next-to-Minimal Supersymmetric Model (NMSSM), which has two more neutral Higgs bosons. The difficulty in interpreting the LHC experiments would also be severe if an intermediate-mass scalar, with a mass above the SM bound from electroweak precision tests (e.g. $m \sim 400$ GeV), is observed alone. It will then be very challenging to determine whether the observed particle is the radion (with the Higgs particle left undetected), a heavy Higgs boson within a multi-doublet Higgs sector (with additional contributions to precision electroweak observables that compensate for the non-standard properties of the observed scalar) or something else.

In the above scenarios, the LC can observe both the Higgs boson and the radion, and covers most of the parameter space where detection of either state at the LHC is difficult. The Higgs–radion mixing effect would give rise to the same shift in the Higgs couplings g_{hWW}, g_{hZZ} and $g_{h\bar{f}f}$. Thus, ratios of couplings would remain unperturbed and correspond to those expected in the SM. Since the LHC will measure mostly ratios of couplings, the Higgs–radion mixing could easily be missed. The LC, on the other hand, has the capability to measure the absolute values of the couplings to fermions and gauge bosons with high precision. Furthermore, an accurate determination of the total Higgs width will be possible at the LC. These capabilities are crucial in the described scenario, since there would be enough measurements and sufficient accuracy to experimentally establish the Higgs–radion mixing effects. It has been demonstrated in a detailed analysis that the parameter regions for which the Higgs significance is below 5σ at the LHC are covered by the regions where precision measurements of Higgs couplings at the LC establish the Higgs–radion mixing effect. The LHC, on the other hand, will easily observe the distinctive signature of Kaluza–Klein graviton excitation production in these scenarios over a substantial range of the radion vacuum expectation value, Λ_ϕ.

A case where the LHC detects a heavy (500 GeV–1 TeV) SM-like Higgs boson rather than a light CP-even Higgs boson as apparently needed to satisfy precision electroweak constraints can also occur in a general two-Higgs-doublet model. The source of the extra contributions mimicking the effect of a light Higgs boson in the electroweak precision tests may remain obscure in this case. The significant improvement in the accuracy of the electroweak precision observables obtainable at the LC running in the GigaZ mode and at the WW threshold will be crucial to narrow down the possible scenarios.

If nature has chosen a scenario far from the decoupling limit, even in the case of the MSSM, electroweak symmetry breaking dynamics produces no state that closely resembles the SM Higgs boson. Within the MSSM a situation is possible where the neutral Higgs bosons are almost mass-degenerate and $\tan\beta$ is large. In this case, detection of the individual Higgs boson peaks is very challenging at the LHC, whereas the different Higgs boson signals can more easily be separated at the LC. The measured

characteristics at the LC will then allow to determine further Higgs-boson properties at the LHC.

Another situation which was investigated in this report is the case of a fermiophobic Higgs boson (h_f) decaying to two photons with a larger branching ratio than in the SM. In this case the standard Higgs production mechanisms are very much suppressed for moderate to large $\tan\beta$, both at the LC and the LHC. It has been shown that the search for $pp \to H^{\pm}h_f$ should substantially benefit from a previous signal at a LC in the channel $e^+e^- \to Ah_f$, and would provide important confirmation of any LC signal for h_f.

There are many other scenarios where Higgs detection at the LHC can be difficult, or the Higgs signal, while visible, would be hard to interpret. If no clear Higgs signal has been established at the LHC, it will be crucial to investigate with the possibilities of the LC whether the Higgs boson has not been missed at the LHC because of its non-standard properties. This will be even more the case if the gauge sector doesn't show indications of strong electroweak symmetry breaking dynamics. The information obtained from the LC can therefore be crucial for understanding the physics of mass generation and for guiding the future experimental programme in high-energy physics. The particular power of the LC is its ability to look for $e^+e^- \to ZH$ in the inclusive $e^+e^- \to ZX$ missing-mass, M_X, distribution recoiling against the Z boson. Even if the Higgs boson decays completely invisibly or different Higgs signals overlap in a complicated way, the recoil mass distribution will reveal the Higgs boson mass spectrum of the model.

An example studied in this context is a scenario where the Higgs boson decays primarily into hadronic jets, possibly without definite flavor content. Such a situation could be realised for instance in the MSSM if the scalar bottom quark turns out to be very light. A light Higgs boson decaying into jets, undetected at the LHC, could thus lead one to conclude erroneously that the Higgs sector has a more exotic structure than in the MSSM. Such a state could be discovered at the LC and its properties measured with high accuracy. The LHC, on the other hand, should be able to produce, discover, and study in great detail possible new physics at the weak scale (the superpartners in the SUSY example). In order to truly understand electroweak symmetry breaking and the solution of the hierarchy problem, the synergy of the LHC and the LC is crucial. As a further possibility, one might produce superpartners at the LHC that decay through light Higgs bosons as intermediate states into jets and not realise the identity of the intermediate states. In such a situation, it might even be impossible to identify the parent superparticles, despite their having rather ordinary properties from the point of view of the MSSM. The analysis and understanding of data from concurrent operation of the LHC and LC would very likely prove crucial.

New Higgs boson decay modes can also open up in extensions of the MSSM, for instance the NMSSM. A case in which Higgs detection may be difficult occurs if there is a light (CP-even) Higgs boson which dominantly decays into two light CP-odd Higgs bosons, $h \to aa$. Confirmation of the nature of a possible LHC signal at the LC would be vital. For example, the $WW \to h \to aa$ signal, as well as the usual $e^+e^- \to Zh \to Zaa$ signal, will be highly visible at the LC due to its cleaner environment and high luminosity. The LC will furthermore be able to measure important properties of the CP-odd scalar.

Another challenging NMSSM scenario is a singlet dominated light Higgs. While

this state has reasonably large production cross sections at the LHC, it would be difficult to detect as it mainly decays hadronically. Such a state could be discovered at the LC. From the measurement of its properties, the masses of the heavier Higgs bosons could be predicted, guiding in this way the searches at the LHC. For a very heavy singlet dominated Higgs state, on the other hand, the kinematic reach of the LHC will be crucial in order to verify that a non-minimal Higgs sector is realised. Thus, input from both the LHC and the LC will be needed in order to provide complete coverage over the NMSSM parameter space.

Another very difficult scenario for Higgs boson detection would be the case of a "continuum" Higgs model, i.e. a large number of doublet and/or singlet fields with complicated self interactions. This could result in a very significant diminution of all the standard LHC signals. The missing-mass signal from the LC will be crucial in this case to guide the search strategy at the LHC. In all cases with Higgs properties such that the Higgs boson remains undetected at the LHC, experimental information from the LC will be crucial in order to identify the phenomenology responsible for making the Higgs boson "invisible" at the LHC.

1.2.1.3 The Little Higgs scenario

New approaches to electroweak symmetry breaking dynamics have led to phenomenologies that may be quite different from the conventional expectations of weakly coupled multi-Higgs models.

Little Higgs models revive an old idea to keep the Higgs boson naturally light: they make the Higgs particle a pseudo-Nambu-Goldstone boson of a broken global symmetry. The new ingredient of little Higgs models is that they are constructed in such a way that at least two interactions are needed to explicitly break all of the global symmetries that protect the Higgs mass. Consequently, the dangerous quadratic divergences in the Higgs mass are forbidden at one-loop order. In this way a cutoff scale $\Lambda \approx 10$ TeV could be naturally accommodated, solving the "little hierarchy" problem.

The phenomenology of Little Higgs models is normally very rich, giving rise to new weakly coupled fermions, gauge bosons and scalars at the TeV scale. The LHC has good prospects in such a scenario to discover new heavy gauge bosons and the vector-like partner of the top quark. The LC has a high sensitivity to deviations in the precision electroweak observables and in the triple gauge boson couplings, and to loop effects of the new heavy particles on the Higgs boson coupling to photon pairs. Therefore, both the LHC direct observations and the LC indirect measurements will be important to clarify the underlying new physics. If only part of the new states are detectable at the LHC, the high-precision measurements at the LC may allow to set indirect constraints on the masses of new states, indicating in this way a possible route for upgrades in luminosity or even energy for a subsequent phase of LHC running.

1.2.1.4 No Higgs scenarios

If no light Higgs boson exists, quasi-elastic scattering processes of W and Z bosons at high energies provide a direct probe of the dynamics of electroweak symmetry

breaking. The amplitudes can be measured in 6-fermion processes both at the LHC and the LC. The two colliders are sensitive to different scattering channels and yield complementary information.

The combination of LHC and LC data will considerably increase the LHC resolving power. In the low-energy range it will be possible to measure anomalous triple gauge couplings down to the natural value of $1/16\pi^2$. The high-energy region where resonances may appear can be accessed at the LHC only. The LC, on the other hand, has an indirect sensitivity to the effects of heavy resonances even in excess of the direct search reach of the LHC. Detailed measurements of cross sections and angular distributions at the LC will be crucial for making full use of the LHC data. In particular, the direct sensitivity of the LHC to resonances in the range above 1 TeV can be fully exploited if LC data on the cross section rise in the region below 1 TeV are available. In this case the LHC measures the mass of the new resonances and the LC measures their couplings. Furthermore, the electroweak precision measurements (in particular from GigaZ running) at the LC will be crucial to resolve the conspiracy that mimics a light Higgs in the electroweak precision tests. Thus, a thorough understanding of the data of the LC and the LHC combined will be essential for disentangling the new states and identifying the underlying physics.

Besides the mechanism of strong electroweak symmetry breaking, recently Higgsless models have been proposed in the context of higher-dimensional theories. In such a scenario boundary conditions on a brane in a warped 5th dimension are responsible for electroweak symmetry breaking. The unitarity of WW scattering is maintained so long as the KK excitations of the W and Z are not much above the TeV scale and therefore accessible to direct production at the LHC. Experimental information from the LC, in particular electroweak precision measurements, will be important in this case in order to correctly identify the underlying physics scenario.

1.2.2 Supersymmetric models

Experimental information on the masses and couplings of the largest possible set of supersymmetric particles is the most important input to the reconstruction of a supersymmetric theory, in particular of the SUSY breaking mechanism. The lightest supersymmetric particle (LSP) is an attractive candidate for cold Dark Matter in the Universe. A precise knowledge about the SUSY spectrum and the properties of the SUSY particles will be indispensable in order to predict the Dark Matter relic density arising from the LSP (see Sec. 1.2.5 below).

The production of supersymmetric particles at the LHC will be dominated by the production of coloured particles, i.e. gluinos and squarks. Searches for the signature of jets and missing energy at the LHC will cover gluino and squark masses of up to 2–3 TeV [8]. The main handle to detect uncoloured particles will be from cascade decays of heavy gluinos and squarks, since in most SUSY scenarios the uncoloured particles are lighter than the coloured ones. An example of a possible decay chain is $\tilde{g} \to \bar{q}\tilde{q} \to \bar{q}q\tilde{\chi}_2^0 \to \bar{q}q\tilde{\tau}\tau \to \bar{q}q\tau\tau\tilde{\chi}_1^0$, where $\tilde{\chi}_1^0$ is assumed to be the LSP. Thus, fairly long decay chains giving rise to the production of several supersymmetric particles in the same event and leading to rather complicated final states can be expected to be a typical feature of SUSY production at the LHC. In fact, the main background for measuring SUSY processes at the LHC will be SUSY itself.

The LC, on the other hand, has good prospects for the production of the light uncoloured particles. The clean signatures and small backgrounds at the LC as well as the possibility to adjust the energy of the collider to the thresholds at which SUSY particles are produced will allow a precise determination of the mass and spin of supersymmetric particles and of mixing angles and complex phases [9].

In order to establish SUSY experimentally, it will be necessary to demonstrate that every particle has a superpartner, that their spins differ by $1/2$, that their gauge quantum numbers are the same, that their couplings are identical and that certain mass relations hold. This will require a large amount of experimental information, in particular precise measurements of masses, branching ratios, cross sections, angular distributions, etc. A precise knowledge of as many SUSY parameters as possible will be necessary to disentangle the underlying pattern of SUSY breaking. In order to carry out this physics programme, experimental information from both the LHC and the LC will be crucial.

1.2.2.1 Measurement of supersymmetric particle masses, mixings and couplings at LHC and LC

As mentioned above, at the LHC the dominant production mechanism is pair production of gluinos or squarks and associated production of a gluino and a squark. For these processes, SUSY particle masses have to be determined from the reconstruction of long decay chains which end in the production of the LSP. The invariant mass distributions of the observed decay products exhibit thresholds and end-point structures. The kinematic structures can in turn be expressed as a function of the masses of the involved supersymmetric particles. The LHC is sensitive in this way mainly to mass *differences*, resulting in a strong correlation between the extracted particle masses. In particular, the LSP mass is only weakly constrained. This uncertainty propagates into the experimental errors of the heavier SUSY particle masses.

At the LC, the colour–neutral part of the SUSY particle spectrum can be reconstructed with high precision if it is kinematically accessible. It has been demonstrated that experimental information on properties of colour–neutral particles from the LC can significantly improve the analysis of cascade decays at the LHC. In particular, the precise measurement of the LSP mass at the LC eliminates a large source of uncertainty in the LHC analyses. This leads to a substantial improvement in the accuracy of the reconstructed masses of the particles in the decay chain.

In general LC input will help to significantly reduce the model dependence of the LHC analyses. Intermediate states that appear in the decay chains detected at the LHC can be produced directly and individually at the LC. Since their spin and other properties can be precisely determined at the LC, it will be possible to unambiguously identify the nature of these states as part of the SUSY spectrum. In this way it will be possible to verify the kind of decay chain observed at the LHC. The importance of this has been demonstrated, for instance, in a scenario with sizable flavour-changing decays of the squarks. Once the particles in the lower parts of the decay cascades have been clearly identified, one can include the MSSM predictions for their branching ratios into a constrained fit. This will be helpful in order to determine the couplings of particles higher up in the decay chain.

Most of the studies of the LHC / LC interplay in the reconstruction of SUSY par-

ticle masses carried out so far have been done for one particular MSSM benchmark scenario, the SPS 1a benchmark point [14], since only for this benchmark point detailed experimental simulations are available both for the LHC and LC. As an example, the scalar top and bottom mixing angles can be extracted from the reconstructed scalar bottom masses from cascade decays and the measurement of ratios of branching ratios at the LHC in the SPS 1a scenario, provided that precise information on the parameters in the neutralino and chargino mass matrices is available from the LC.

A detailed study of important synergistic effects between LHC and LC has been carried out in the gaugino sector within the SPS 1a scenario. In this analysis the measurements of the masses of the two lightest neutralinos, the lighter chargino, the selectrons and the sneutrino at the LC were used to predict the properties of the heavier neutralinos. It was demonstrated that this input makes it possible to identify the heaviest neutralino at the LHC and to measure its mass with high precision. Feeding this information back into the LC analysis significantly improves the determination of the fundamental SUSY parameters from the neutralino and chargino sector at the LC.

The described analysis is a typical example of LHC / LC synergy. If a statistically not very pronounced (or even marginal) signal is detected at the LHC, input from the LC can be crucial in order to identify its nature. In fact, the mere existence of a LC prediction as input for the LHC searches increases the statistical sensitivity of the LHC analysis. This happens since a specific hypothesis is tested, rather than performing a search over a wide parameter space. In the latter case, a small excess *somewhere* in the parameter space is statistically much less significant, since one has to take into account that a statistical fluctuation is more likely to occur in the simultaneous test of many mass hypotheses. On the other hand, if the LHC does not see a signal which is predicted within the MSSM from LC input, this would be an important hint that the observed particles cannot be consistently described within the minimal model.

In order to establish SUSY experimentally and to determine the SUSY-breaking patterns, it is necessary to accurately measure as many Lagrangian parameters as possible. Since most observables depend on a variety of parameters, one will have to perform a global fit of the SUSY model to a large number of experimental observables. As the measurements at the LHC and the LC in general probe different sectors of the MSSM Lagrangian, the combination of LHC and LC data will be crucial in order to obtain comprehensive information on the underlying structure of the model. For the studied cases, it has been demonstrated that only the combination of measurements of both the LHC and the LC offers a complete picture of the MSSM model parameters in a reasonably model independent framework. In fact, it turned out that attempts to fit only individual sectors of the theory are unsuccessful, and a converging fit is only obtained from the combination of LHC and LC data.

As mentioned above, most of the studies of the LHC / LC interplay in the reconstruction of SUSY particle masses carried out so far have been done for the SPS 1a benchmark scenario [14]. The SPS 1a benchmark point is a favourable scenario both for the LHC and LC. The interplay between the LHC and LC could be qualitatively rather different in different regions of the MSSM parameter space. It seems plausible that synergistic effects from the LHC / LC interplay will be even more important in parameter regions which are more challenging for both colliders. In order to allow a quantitative assessment of the LHC / LC interplay also for other parameter regions,

more experimental simulations for the LHC and LC are required.

1.2.2.2 Distinction between different SUSY-breaking scenarios and extrapolation to physics at high scales

The importance of a precise knowledge of the fundamental SUSY parameters for discriminating between different SUSY-breaking scenarios has been demonstrated for several examples. In general, a per-cent level accuracy appears to be mandatory in order to have a suitable sensitivity to discriminate between different scenarios. This will require detailed experimental information from both the LHC and LC.

The interplay between the LHC and LC is also important for the determination of the nature of the lightest and next-to-lightest SUSY particle (LSP and NLSP). In a scenario where the long-lived NLSP is a charged slepton, methods have been established to discover a massive gravitino, and thereby supergravity, at the LHC and LC. It is crucial to verify supergravity predictions for the NLSP lifetime as well as angular and energy distributions in 3-body NLSP decays. With the gravitino mass inferred from kinematics, the measurement of the NLSP lifetime will test an unequivocal prediction of supergravity. It has been demonstrated that the characteristic couplings of the gravitino, or goldstino, can be tested even for very small masses.

Combining the experimental results from the LHC and LC, stable extrapolations can be performed from the electroweak scale to the grand unification scale, provided that the low-energy spectrum can be fully reconstructed. This has been done by studying the evolution of the three gauge couplings and of the soft supersymmetry breaking parameters, which approach universal values at the GUT scale in minimal supergravity scenarios. For the example of the SPS 1a benchmark point it has been shown that from LHC data alone no reliable extrapolation to the GUT scale can be performed. The coherent analyses based on combined information from the LHC and LC, in which the measurements of SUSY particle properties at the LHC and LC mutually improve each other, result in a comprehensive and detailed picture of the supersymmetric particle system. In particular, the gaugino sector and the non-coloured scalar sector are under excellent control.

Though minimal supergravity has been chosen as a specific example, the methodology can equally well be applied to more general supersymmetric theories. High-precision high-energy experiments at the LHC and LC, providing accuracies at the level of per-cent to per-mille, allow a thorough analysis of the mechanism of supersymmetry breaking and give access to the structure of nature at scales where gravity is linked with particle physics.

1.2.3 Gauge theories and precision physics

1.2.3.1 Standard Model gauge sector

A detailed analysis of the properties in the gauge sector is important for determining the structure of the underlying physics and for distinguishing between different models. Examples of extensions of the SM that however have the same gauge sector as the SM are the MSSM or more general two-Higgs-doublet models.

Models possessing the same gauge sector can be distinguished via quantum corrections that are influenced by the whole structure of the model. The LC provides precision data obtained from running at the $t\bar{t}$ threshold, from fermion pair production at high energies, from measurements in the Higgs sector, etc. Furthermore, running the LC in the GigaZ mode yields extremely precise information on the effective weak mixing angle, the total Z-boson width, the Z partial widths and the mass of the W boson (the latter from running at the WW threshold). Comparing these measurements with the predictions of different models provides a very sensitive test of the theory, in the same way as many alternatives to the SM have been found to be in conflict with the electroweak precision data in the past. In this way, the electroweak precision tests can give access to effects of heavy particles which are beyond the direct reach of the LHC and the LC. However, in order to fully exploit the sensitivity to new physics, as much information as possible is necessary about the part of the spectrum that is directly accessible experimentally. This will most likely require measurements from both the LHC and the LC.

Interesting LHC / LC synergy can also be expected in the determination of the self-couplings of the gauge bosons. The couplings among the gauge bosons can be measured at both colliders independently. Therefore the combination of the uncorrelated LHC and LC measurements may lead to a significantly higher accuracy than the individual measurements. Deviations from the prediction of a SM-like gauge sector could reveal the existence of new (and so far unknown) high mass scales.

The physics of the top quark plays an important role as a possible window to new physics. The top quark is the heaviest elementary particle found so far. Since it decays much faster than the typical time for formation of top hadrons, it provides a clean source of fundamental information. Accurate measurements of the top quark properties, such as its mass, couplings, in particular the couplings to gauge bosons and Higgs fields, and branching ratios of rare decay modes, probe possible deviations from the SM predictions in a sensitive way. Since there are many possibilities of anomalous couplings of the top quark to gauge bosons, one will greatly benefit from the combined results of the LHC and LC. The analysis of spin correlations between production and decay of the top quarks is of particular interest in this context. For example, the top-quark pair production at the LHC involves the strong coupling of gluons to the top quark. In order to probe deviations from the SM structure for this coupling via spin correlations one needs to take into account the information on the Wtb coupling structure which occurs in the top-quark decay. The latter can be accurately measured at the LC. Such an information from the LC could also be useful for measuring the b-quark structure function via single top-quark production at the LHC.

An interesting interplay between the LHC and LC can also occur in QCD analyses. For instance, the clean experimental environment at the LC will allow important measurements relevant for determining fragmentation functions. This information can lead to an improvement of the understanding of two-photon events at the LHC.

1.2.3.2 New gauge theories

Many kinds of extensions of the SM lead to an enlarged gauge-boson sector. Determining the nature of the new gauge bosons will require a variety of detailed experi-

mental results that can be provided by the interplay of the LHC and LC. The LHC has a large mass reach for direct detection of new gauge bosons, while the LC has a large indirect reach arising from virtual effects of the new states that result in deviations from the SM predictions. The indirect search reach of the LC is substantially larger than the direct discovery reach achievable at the LHC.

The LC is sensitive to Z–Z' interference effects through the fermion pair-production process, $e^+e^- \to f\bar{f}$, running at its highest energy. If the mass of the Z' is known from the LHC, the LC information on the ratio of the $Z'f\bar{f}$ couplings and the Z' mass can be used to determine the Z' couplings with high precision. Furthermore, the measurements of the electroweak precision observables in the GigaZ mode of the LC yield important information for distinguishing different models of new physics. This input can be helpful for optimising the search strategies at the LHC.

Careful analyses are required to distinguish a Z' from other possible manifestations of new physics, which can have a somewhat similar phenomenology, but a completely different physical origin. An example is the study of the lightest Kaluza–Klein (KK) excitations of the SM electroweak gauge bosons, which arise in models with large extra dimensions. Little Higgs models provide a class of models with an extended gauge sector. Detailed experimental information is necessary in order to determine the structure of Little Higgs models from the properties of the observed new particle states. In all these cases, combined information from the LHC and LC can be crucial.

1.2.4 Models with extra dimensions

Collider signatures for the presence of extra spatial dimensions are wide and varied, depending on the geometry of the additional dimensions. The basic signal is the observation of a KK tower of states corresponding to a particle propagating in the higher dimensional space-time. The measurement of the properties of the KK states determines the size and geometry of the extra dimensions.

In the scenario of large extra dimensions, where gravity alone can propagate in the bulk, the indirect effects and direct production of KK gravitons are both available at the LHC and at the LC. For the indirect effects of KK gravitons, the search reach of the LC exceeds that of the LHC for an LC centre of mass energy of $\sqrt{s} \gtrsim 800$ GeV. Measurement of the moments of the resulting angular distributions at the LC can identify the spin-2 nature of the graviton exchange. If positron polarisation is available, then azimuthal asymmetries can extend the search for graviton exchange by a factor of two, probing fundamental scales of gravity up to 21 TeV for $\sqrt{s} = 1$ TeV with 500 fb^{-1} of integrated luminosity. In the case of direct KK graviton production, the LHC and LC have comparable search reaches. However, the LHC is hampered by theoretical ambiguities due to a break-down of the effective theory when the parton-level centre of mass energy exceeds the fundamental scale of gravity. Measurements of direct graviton production at two different centre of mass energies at the LC can determine the number of extra dimensions, and the absolute normalisation of the cross section can determine the fundamental scale. Simultaneous determination of all the model parameters has been examined in a quantitative fashion with the result that data from the LC and LHC analysed together substantially improves the accuracy of this determination over the LHC data taken alone.

Standard Model fields are allowed to propagate in extra dimensions with size less than TeV^{-1}. Signatures for the KK states of the SM gauge fields mimic those for new heavy gauge bosons in extended gauge theories. The LHC may discover electroweak gauge KK states via direct production in the mass range $M_c \simeq 4$–6 TeV (lower masses are excluded by LEP/SLC data), while indirect detection at the LC is possible for $M_c \lesssim 20$ TeV for $\sqrt{s} = 1$ TeV. Indirect detection of electroweak gauge KK states is also possible at the LHC for $M_c \lesssim 12$ TeV via a detailed study of the shape of the Drell-Yan lepton-pair invariant mass distribution. If discovered, the determination of the mass of the first gauge KK excitation at the LHC, together with indirect effects at the LC can be used to distinguish the production of a KK gauge state from a new gauge field in extended gauge sectors.

The possibility of universal extra dimensions, where all SM fields are in the bulk, can be mistaken for the production of supersymmetric states, since the KK spectrum and phenomenology resembles that of supersymmetry. In fact, the lightest KK state is a Dark Matter candidate. In this case, threshold production of the new (s)particle at the LC can easily determine its spin and distinguish universal extra dimensions from supersymmetry. Spin determination analyses are on-going for the LHC.

Lastly, the presence of warped extra dimensions results in the resonance production of spin-2 gravitons. This produces a spectacular signature at the LHC for the conventional construction of the Randall-Sundrum model. However, extensions to this model, such as the embedding in a higher-dimensional manifold, or the inclusion of kinetic brane terms, may result in reduced coupling strengths and extremely narrow-width graviton KK states. Narrow resonances of this kind, in particular if they are closely spaced, may be difficult to disentangle in a general search at the LHC. This can be the case even for very light KK states. Radiative return at the LC may pinpoint the existence of these states, which can then be confirmed by a dedicated search at the LHC.

1.2.5 The nature of Dark Matter

The properties of Dark Matter as understood today imply that it should be stable, cold, and non-baryonic. This behaviour is not compatible with the particles and interactions of the SM. Thus, the existence of Dark Matter, which is strongly implied from cosmological observations, is unambiguous evidence for new physics.

It seems suggestive that the physics giving rise to Dark Matter is related to the weak scale, possibly closely tied to the origin of electroweak symmetry breaking. Thus, there is an intriguing possibility at the LHC and LC that Dark Matter particles will be produced in the laboratory.

Several of the new physics scenarios discussed above provide possible Dark Matter candidates that give rise to an acceptable relic density. Supersymmetry offers the LSP as a very attractive candidate. In many scenarios the lightest neutralino is the LSP. The cosmological implications of a stable neutralino have been very thoroughly studied in the literature for many years, and it has been shown that the constraints on the SUSY parameter space from cosmology, direct particle searches, electroweak precision tests and flavour physics can be simultaneously satisfied. Besides a neutralino LSP, other manifestations of Dark Matter can occur in SUSY, such as the gravitino. Possible explanations for Dark Matter have also emerged from models with extra dimensions,

for instance 'Kaluza–Klein Dark Matter', 'warped Dark Matter' or 'branons' (see e.g. Ref. [15] for a recent review).

The collider signatures in different kinds of Dark Matter scenarios can be rather similar, giving rise, for instance, to jets and missing energy at the LHC. Measurements at both the LHC and the LC will be crucial in order to identify the underlying physics [16–19]. In particular it will be important to determine the quantum numbers, the spin and the interactions of the possible Dark Matter candidate. Precise measurements of the properties of this particle are indispensable as input for predicting the cold Dark Matter density, which is a decisive test of the hypothesis that a particular physics scenario is in fact the origin of cold Dark Matter in the Universe. Studying decays of heavier particles into the Dark Matter particle can provide a unique window to processes that happened in the early Universe.

Thus, it is of utmost importance to obtain precise and comprehensive experimental information on the Dark Matter candidate and its annihilation channels in a model-independent way. This experimental requirement is analogous to the experimental information necessary to disentangle the mechanism of electroweak symmetry breaking and, within supersymmetric models, the SUSY breaking mechanism.

If the physics responsible for Dark Matter in the Universe is accessible at the next generation of colliders, a major goal of these colliders will be to predict the Dark Matter density at the same level of accuracy as it can be measured experimentally. The WMAP results [20, 21] have led to a measurement of the Dark Matter content at the 10% level. This precision will further improve with the Planck satellite mission, scheduled for 2007, which aims at a 2% measurement [22].

The impact of the LHC and LC for the precision of the predicted Dark Matter density has mainly been studied for SUSY scenarios so far. For the SPS 1a benchmark point, which as mentioned above is a favourable scenario both for the LHC and LC, the prediction of the Dark Matter density has been studied based on the experimental precision achievable at the LHC. Under the theoretical assumption that the minimal supergravity (mSUGRA) scenario is realised in nature, an accuracy of about 3% can be achieved for the full LHC-design integrated luminosity [16,19]. A similar accuracy can be reached at the LC for the SPS 1a point *without* the mSUGRA assumption (and a significantly higher accuracy if mSUGRA is assumed). The prospects at the LHC appear to be much worse for less favourable scenarios [19]. Possible experimental strategies for these scenarios are currently assessed in detailed studies.

Precision measurements of the properties of the LSP at the LC in a model-independent way, in particular of its mass, its couplings and its annihilation channels, will be crucial for a precise prediction of the relic density that can be compared with the results from observational cosmology. Even in the experimentally challenging co-annihilation scenario, a reliable prediction of the Dark Matter density can be obtained at the LC, based on a model-independent determination of the mass of the LSP and the lightest slepton [17]. An additional critical input from the LC is the precise measurement of the top-quark mass. The dependence of the relic density prediction on the precise value of m_t can be very pronounced if a particular SUSY-breaking scenario is assumed, since in this case the top-quark mass enters via the renormalisation group running from the high scale to the low-energy parameters.

In the case where rapid annihilation occurs through resonant Higgs-boson exchange, the LC measurement of the LSP mass and combined LHC and LC information on

the Higgs-boson properties and the heavier neutralinos could be used to reconstruct the relevant SUSY parameters for predicting the Dark Matter density [23]. In the mSUGRA region where the LSP has a significant Higgsino fraction (focus point region), precise measurements of the neutralino masses and of $\tan\beta$ will be crucial. While this scenario may be problematic for the LHC because of its very heavy sfermions, the LC sensitivity to the neutralino sector leads to a coverage up to very large values of the common scalar mass parameter in the WMAP-allowed region of the mSUGRA parameter space [24].

Thus, the combined information from LHC and LC can be crucial in order to disentangle possible collider signatures of Dark Matter and to precisely determine its origin. This could be a breakthrough in the quest to identify the fundamental composition of the Universe.

2 Experimental Aspects of the LHC and LC

The main experimental aspects of the operation at the LHC and at a 0.5-1 TeV Linear Collider are summarized in this Section. Emphasis is given to the comparison between the two machines and their environments leading to complementary experimental approaches to explore the new physics at the TeV scale.

The LHC and LC have, to some extent, similar features as previous hadron and electron colliders. At the same time, they are much more powerful engines than their predecessors in terms of energy and luminosity, which implies more difficult experimental environments than in the past and more challenging detectors.

The main asset of the LHC is its high mass reach for direct discovery, which extends up to typically $\sim$6-7 TeV for singly-produced particles. The high luminosity and the excellent expected performance of the experiments, in particular their trigger capabilities, will allow a very large fraction of New Physics signatures to be covered. In most cases, the backgrounds to New Physics processes will be measured by using the data itself. In particular, processes like e.g. W, Z, and top production will offer high-statistics data samples to calibrate the detector and understand standard physics (e.g. structure functions, higher-order QCD corrections). In addition, it has been shown [8] that several precise measurements of the new particles will be possible, which should provide first constraints on the underlying New Physics.

The main asset of the LC is two-fold: first, within the kinematically accessible range determined by the center-of-mass energy, new particles can be directly produced and their properties can be studied in great detail. In particular new particles can be dicovered even if their production cross sections are fairly low, and even if their decays are complicated (e.g. purely hadronic). Second, high-precision measurements exhibit sensitivity to new phenomena at scales far above the center-of-mass energy due to virtual effects. High precision, like at previous e^+e^- machines, can be achieved thanks to the well known initial momenta, which allows complete reconstruction of the final states with high efficiency and resolution, and to the absence of event pile-up (see Section 2.1). In contrast to LEP a precise determination of the beamstrahlung spectrum is required as discussed below. Both beams can be polarized longitudinally offering the possibility to disentangle the helicity structure of SM and New Physics processes. The center-of-mass energy is tunable allowing for precise mass and quantum number measurements from threshold scans. Optional high-luminosity running at the Z resonance ("Giga-Z") and at the W^+W^- threshold, as well as e^-e^-, $\gamma\gamma$, and γe^- collision modes, offer additional flexibility.

These very different experimental conditions and capabilities of LHC and LC *together* allow for the discovery and structural understanding of the new phenomena at the TeV energy scale and may even open up windows to physics of Grand Unification of forces and Quantum Gravity.

The main experimental features of the LHC and a LC are discussed and compared briefly below. More details can be found in Refs. [8, 9].

2.1 The interaction rate and the environment

The total inelastic proton-proton cross-section is about 80 mb at $\sqrt{s}$ = 14 TeV, therefore the event rate at the LHC is expected to be 10^9 interactions per second when running at design luminosity (10^{34} cm^{-2} s^{-1}). Since the bunch spacing is 25 ns, on average ∼25 soft interactions (minimum-bias events) are expected to be produced at each bunch crossing. This "pile-up" gives rise to e.g. ∼800 charged particles per crossing inside the detector region used for tracking ($|\eta| < 2.5$).

The need of minimizing the impact of this huge pile-up on the physics performance has had a major impact on the technological choices for and the design of ATLAS and CMS [8], leading to three main requirements:

- Fast detector response (typically 25-50 ns), in order to integrate over two bunch-crossings at most and therefore to minimize the number of piled-up minimum-bias events. This implies novel-technology readout electronics.

- Fine detector granularity, in order to minimize the probability that pile-up particles hit the same detector element as an interesting object (e.g. a photon coming from a $H \to \gamma\gamma$ decay). This implies a large number of readout channels, and therefore a challenging detector operation (e.g. in terms of calibration and monitoring).

- High radiation resistance. The detectors are exposed to an intense flux of particles produced by the pp collisions at each bunch-crossing, which has to be integrated over at least ten years of operation. For instance, in ten years the forward calorimeters will absorb neutron fluences of up to 10^{17} neutrons/cm^2 and doses of up to 10^7 Gy.

In spite of these detector features, pile-up is expected to have some residual impact on the physics performance [8]. For example, in the calorimeters pile-up fluctuations contribute an additional (noise) term to the energy resolution. The pile-up noise inside the volume of electromagnetic calorimeter needed to contain an electromagnetic shower has a typical r.m.s. of $E_T \simeq 250$ MeV, giving a contribution of ∼2.5% (∼ 0.25%) to the energy resolution of electrons and photons of $E_T = 10\ (100)$ GeV. The pile-up noise inside a calorimeter cone of size $\Delta R = 0.4$ has an r.m.s. of $E_T \simeq 7$ GeV, giving a contribution of 7% (2%) to the energy resolution of jets with $E_T = 100(300)$ GeV.

In summary, the large pile-up renders the operation at the LHC more challenging than at previous hadron colliders, and the experimental environment more dirty, and represents a high price to be payed for the huge machine luminosity.

Another challenging issue at the LHC is the trigger. Since the interaction rate is 10^9 events/s (dominated by minimum-bias and QCD interactions, see Section 2.2), whereas the maximum affordable rate-to-storage is of the order of 100 Hz, a powerful and highly-selective trigger system, providing a rate reduction of 10^7 while preserving a high efficiency for the interesting physics processes, is needed. The ATLAS and CMS trigger will be based on a multi-level selection, where the first-level trigger is provided by fast hardware signals from the calorimeters and the muon spectrometers, and the higher-level triggers by software algorithms using the information from all sub-detectors.

The situation is much simpler at a LC, in spite of a even higher peak luminosity than at the LHC, in the range 2-6$\times 10^{34}$ cm^{-2} s^{-1} depending on the exact center-of-mass energy. The average bunch-crossing rate will be 15-30 kHz (with bunch trains whose structure depends on the chosen technology) and the interaction rate will be dominated by $\gamma\gamma$ interactions ($\sim$0.1 events per crossing). Because of such a low rate, the experiment can be run in continual "triggerless" mode, so that the acceptance for physics is maximized, allowing for an unbiased search for new phenomena. In this scenario the LC detector [9] will have no hardware level-one trigger, but only a software-based relatively loose selection.

Beam-related backgrounds, although smaller than the LHC pile-up, are much more severe than at previous e^+e^- colliders because of the high luminosity. The main source of beam-related backgrounds are beam-beam interactions. The high charge density of the colliding beams produces intense emission of beamstrahlung photons (about $6{\cdot}10^{10}$ photons per crossing when running at $\sqrt{s} \simeq 500$ GeV, carrying a total energy of about $3{\cdot}10^{11}$ GeV). These photons, although they disappear in the beam pipe, have two main effects. First, they broaden the energy spectrum of the colliding beams towards lower energies, with typically 85-90% of the luminosity being produced at energies higher than 95% of the nominal center-of-mass energy. The energy loss due to beamstrahlung is roughly of the same size as initial state radiation. Second, beamstrahlung photons give rise to secondary particles, among which particularly dangerous are e^+e^- pairs from photon conversions in the interaction region. If a sufficiently high magnetic field (3-4 T) is used in the detector, as it is indeed planned (see below), most of these pairs are confined inside a cylinder of radius < 3 cm around the beam line, thereby affecting mainly the first layer of the vertex detector. However, these pairs tend to move longitudinally in z towards the machine quadrupoles, where they create a large number of secondaries. The latter are potentially a harmful source of background for the detectors, which must be shielded with suitable masks [9].

2.2 Physics cross-sections and backgrounds

In addition to the backgrounds and challenges related to the environment discussed in the previous Section, other sources of (physics) backgrounds need to be considered.

At the LHC, the physics cross-sections are dominated by QCD jet production, which is many orders of magnitude larger than the production of the most interesting physics channels. The latter are usually characterized by electroweak cross-sections, or are expected to yield low rates because they involve new massive particles.

Figure 2.1 shows the production cross-sections for several representative processes at hadron colliders, as a function of the center-of-mass energy (left panel). It can be seen, for instance, that at the LHC energies the cross-section for jets with $p_T > 100$ GeV is five orders of magnitude larger than the cross-section for a Higgs boson of mass 150 GeV. As a consequence, there is no hope to detect a Higgs boson (or a W, or a Z boson) in the fully-hadronic decay modes (unless it is produced in association with something else), since such final states are swamped by the much higher, and to a large extent irreducible, jet background (hereafter referred to as "QCD background"). Decays into leptons and photons have to be used instead, and since they usually have smaller branching ratios than decays into quarks, a good part of the *a-priori* large pro-

duction cross-section is *de facto* not used at the LHC.

Small signal-to-background ratios, due to the large QCD cross-sections compared to electroweak cross-sections, are a general feature of hadron colliders. However, the situation deteriorates with increasing center-of-mass energy, because the small-x region of the proton structure functions, where the gluon distribution has a huge enhancement, becomes more and more accessible. At the LHC, which is essentially a gluon-gluon collider, the large contribution of gluon-gluon and gluon-quark interactions enhances tremendously the QCD cross-sections compared to the (qq-dominated) electroweak cross-sections. This renders the signal-to-background ratio smaller than e.g. at the Tevatron. As an example, the ratio (e/jet) between the inclusive rate of electrons (coming e.g. from W and Z decays) and the inclusive rate of jets with $p_T > 20$ GeV is e/jet $\simeq 10^{-3}$ at the Tevatron and $\simeq 10^{-5}$ at the LHC. This implies that the particle identification capabilities of the LHC detectors must be two orders of magnitude better than those of the Tevatron experiments.

Signal-to-background ratios are much more favorable at e^+e^- colliders, as shown in the right panel of Fig. 2.1. For instance, in the case of a light Higgs boson of mass ~120 GeV, the signal production cross-section is only two orders of magnitude smaller than that of the backgrounds (e.g. WW and qq production), which in addition are to a large extent reducible. With high luminosity, many physics scenarios can be explored in a few years of operation. For some physics processes, relatively low signal rates call for very high integrated luminosity, and therefore require several years of operation in order to achieve high accuracy in the precision measurements.

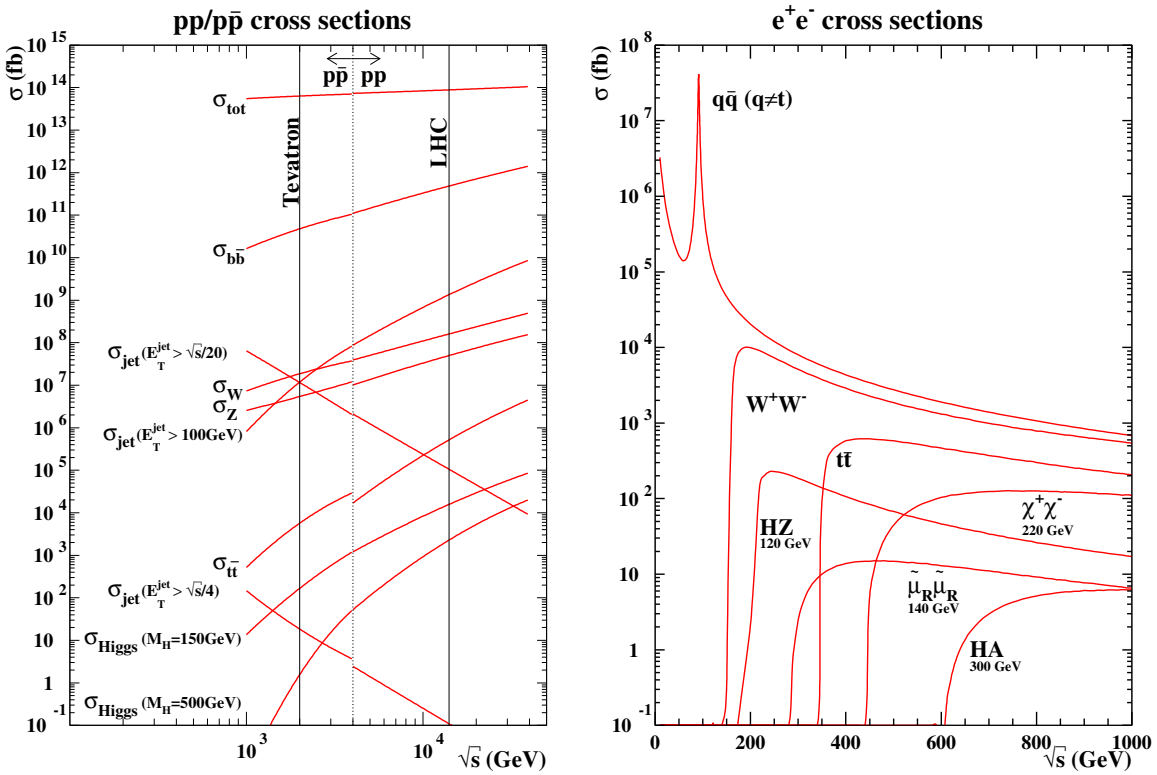

Figure 2.1: Production cross-sections for several representative processes at hadron colliders (left) and e^+e^- colliders (right), as a function of the machine center-of-mass energy.

2.3 The detector performance requirements

Numerous detector performance requirements emerge from the above considerations and from the physics goals of the two machines [8, 9]. The main issues are listed below:

- Measurements of leptons and jets over unprecedented dynamic ranges, extending from a few GeV up to several hundreds GeV (LC) or up to a few TeV (LHC). This is needed in order to detect light particles, like the soft leptons produced in B-hadron decays, as well as the very energetic objects which may be produced in the decay of new massive particles.

- Detector hermeticity. At both machines, full coverage in ϕ and coverage down to $\sim 1^\circ$ from the beam axis in θ are needed mainly for a reliable measurement of the event missing (transverse) energy, a signature of the production of weakly-interacting particles which are expected in many New Physics processes (e.g. SUSY, Higgs production through WW-fusion at a LC, etc.). At the LHC, calorimetric coverage over the above-mentioned angular range is also needed to detect the forward jets produced in association with a Higgs boson in the WW-fusion process.

- Excellent energy and momentum resolution. At the LHC, a mass resolution of $\sim 1\%$ for particles of masses up to a few hundreds GeV decaying into photons, electrons or muons is needed, for instance to extract a possible $H \rightarrow \gamma\gamma$ signal on top of the irreducible $\gamma\gamma$ background.

  At a LC, an excellent track momentum resolution is required in particular to measure the di-lepton mass, and hence the mass of the recoiling system, in the HZ process with $Z \rightarrow \ell\ell$. This should give access to the detection and study of Higgs production independently of the Higgs decay modes. The goal momentum resolution of $\sigma(1/p_T) \leq 5 \cdot 10^{-5}$ (GeV/c)$^{-1}$, which is needed to suppress the combinatorial background, calls for large tracking volumes and high magnetic fields ($\sim$4 T).

  Accurate energy flow measurements is also a must at a LC. Indeed, most signatures from new physics involve final states with many jets, coming e.g. from top-quark or multiple W and Z production and decays. These jets must be efficiently and precisely reconstructed in order to reduce the backgrounds. In addition, enhanced beamstrahlung, as compared to previous e^+e^- colliders, render the kinematic constraints from the knowledge of the initial state weaker than in the past, which puts more weight on energy measurements provided by the detector. The goal energy-flow resolution for hadronic event is $\sigma/E \sim 30\%/\sqrt{E}$, which is necessary e.g. to separate hadronic W and Z decays. This in turn requires a fine 3-dimensional detector granularity, a coil located outside the calorimetry in order to minimize the amount of upstream material, and excellent detector energy resolution and particle identification capabilities.

- Particle identification. Several stringent requirements on the identification of electrons, photons, b-jets, taus, etc. must be satisfied at the LHC in order to

reject the huge QCD backgrounds. As an example, excellent electron/jet and photon/jet separation capabilities are needed. Jets faking photons must be rejected by a factor of $\sim 10^3$, for a photon efficiency of ∼80%, in order to observe a possible $H \rightarrow \gamma\gamma$ signal on top of the background. As already mentioned, an unprecedented suppression factor against jets faking electrons of $10^5 - 10^6$ is needed to extract an inclusive clean electron signal.

At a LC, one of the strongest particle identification requirements is flavor-tagging capabilities (vertexing), since several channels from New Physics (e.g. SUSY) involve b-quarks or τ-leptons. Moreover, a detailed study of the Higgs sector, which requires the individual measurements of the Higgs decay branching ratios into $bb, cc, gg, \tau\tau$, is only possible with an excellent vertex detector, and an innermost layer as close as possible to the beam pipe ($\leq$ 2 cm). The goal performance is to achieve an impact parameter resolution of about 5 μm in both z and $R\phi$.

- At the LC, precision cross section measurements require an excellent luminosity measurement (10^{-4}), which has to be matched by equally precise theoretical predictions. Luminosity measurement requires fast and highly granular forward calorimetry down to angles of approximately 5 mrad. Beam polarization has to be determined to a precision of at least 0.5%. A quasi-continuous monitoring of the differential luminosity spectrum is also necessary.

2.4 Summary of physics capabilities

A detailed discussion of the physics goals of both machines and of their interplay is the subject of the next Sections of this document.

Here only a few general (and fairly gross) conclusions are given:

- The LHC has the highest mass reach for the direct discovery of new particles. This reach extends up to masses of ∼5-6 TeV for singly-produced electroweak particles (e.g. possible new gauge bosons W' and Z'), up to ∼7 TeV for singly-produced strongly-interacting particles (e.g. possible excited quarks), and up to $\sim$ 3 TeV for pair-produced SUSY particles with strong interactions.

  The direct mass reach of a LC is much more modest, being limited by the available center-of-mass energy to less than 1 TeV for the case considered in this document. However, due to the cleaner environment, also direct signals of particles which are produced with low cross sections or which only decay into hadrons or which leave only a small amount of visible energy in the detector can be discovered.

- A Linear Collider has an indirect discovery sensitivity to New Physics, through precise measurements of known processes (e.g. two-fermion production) and the detection of permil-level deviations from the Standard Model expectation, which extends up to energies of ∼10 TeV. Therefore a 1 TeV LC should be able to probe New Physics lying at energy scales much higher than the machine $\sqrt{s}$ through the measurements of the low-energy (quantum-level) tails of the theory.

Because precise measurements are more difficult at hadron colliders for the reasons mentioned above, the LHC indirect sensitivity to New Physics is more modest, except for some strongly-interacting scenarios (like Compositeness) which are expected to manifest themselves through anomalous contributions to di-jet production.

- Precision measurements are the strongest asset of a LC. In general, all particles and processes which are kinematically accessible and produced can be measured with typical precisions ranging from the permil to the percent level, irrespective of the precise physics scenario. Such a precision allows for the exploration of quantum-level effects and yields the possibility to extrapolate the observations to energy scales far above the center-of-mass energy in a model-independent way. Ultimately, GUT or Planck scale physics could be probed.

  Several precise measurements should also be possible at the LHC, thanks mainly to the large available event statistics. As an example, if SUSY exists the LHC experiments should be able to perform several measurements of the sparticle masses, and therefore to constrain the fundamental parameters of the underlying theory to $\sim 10\%$ or better (at least in minimal models). Therefore, in addition to being a very powerful and motivated discovery machine, the LHC should also provide a first and possibly quite deep exploration of the structure of New Physics. There are however two main limitations. First, in general the extent and the precision of the measurements are poorer than at a LC. For instance, the LHC can only measure some of the Higgs couplings, and with an accuracy $(10 - 20\%)$ which is not competitive with that of a LC ($\sim 1\%$). Second, a complete, model-independent and conclusive study of the new theory is *a priori* not granted and looks difficult in most cases.

These features give rise to a nice complementarity between the two machines, and lead to synergy effects which are discussed in more detail in the rest of this document.

3 Higgs Physics and Electroweak Symmetry Breaking

The search for the fundamental dynamics that is responsible for electroweak symmetry breaking is the central challenge for particle physics today. This dynamics, whose fundamental origin is as yet unknown, is ultimately responsible for the generation of the masses of the quarks, charged leptons and the massive gauge bosons. Two broad classes of electroweak symmetry breaking mechanisms have been pursued theoretically. In one class of theories, electroweak symmetry breaking dynamics is weakly-coupled, and in the second class of theories the dynamics is strongly-coupled.

The electroweak symmetry breaking dynamics that is employed by the Standard Model is governed by a self-interacting complex doublet of scalar fields [25]. The Higgs potential is chosen so that the neutral component of the scalar doublet acquires a vacuum expectation value, $v = 246$ GeV, which sets the mass scale of electroweak symmetry breaking. Consequently, three massless Goldstone bosons are generated which provide the longitudinal degrees of freedom for the $W^{\pm}$ and Z^0, while the fourth scalar degree of freedom that remains in the physical spectrum is the CP-even neutral Higgs boson. It is further assumed in the Standard Model that the scalar doublet also couples to fermions via the Yukawa interactions. After electroweak symmetry breaking, these interactions are responsible for the generation of quark and charged lepton masses. The couplings of the Higgs boson to the Standard Model particles is then fixed (and proportional to the corresponding particle mass). However the Higgs mass is proportional to the strength of the Higgs self-coupling, and is therefore not (directly) fixed by present day observations.

Although the Higgs boson has not been directly observed, its virtual effects (primarily via its contributions to the $W^{\pm}$ and Z boson vacuum polarization) can influence electroweak observables. Consequently, one can obtain constraints on the Higgs boson mass (m_h) through a global Standard Model fit to the electroweak data. The results of the LEP Electroweak Working Group analysis yield [26]: $m_h = 114^{+69}_{-45}$ GeV, and provides a one-sided 95% CL upper limit of $m_h < 260$ GeV. These results reflect the logarithmic sensitivity to the Higgs mass via the virtual Higgs loop contributions to the various electroweak observables. The 95% CL upper limit is consistent with the direct searches at LEP [27] that show no conclusive evidence for the Higgs boson, and imply that $m_h > 114.4$ GeV at 95% CL. This range of Higgs masses is consistent with a weakly-coupled Higgs scalar that is the result of the Standard Model scalar dynamics.

In the weakly-coupled approach to electroweak symmetry breaking, the Standard Model is very likely embedded in a supersymmetric theory [28] in order to stabilize the large energy gap between the electroweak and the Planck scales in a natural way [29]. These theories predict a spectrum of Higgs scalars [30], with an expected mass of the lightest CP-even Higgs boson below 200 GeV [31] (less than 135 GeV in the simplest supersymmetric models [32]), and a spectrum of additional neutral and

charged Higgs bosons with masses up to of order 1 TeV. Moreover, over a significant fraction of the supersymmetric parameter space, the properties of the lightest Higgs scalar closely resemble those of the Standard Model (SM) Higgs boson.

An alternative approach to weakly-coupled scalar dynamics posits that electroweak symmetry breaking is driven by the dynamics of a new strongly-interacting sector of particles [33]. Initial models of this kind introduced QCD-like strong interactions near the TeV-scale [34], with numerous variations subsequently explored. More recently, so-called "little Higgs models" have been proposed in which the scale of the new strong interactions is pushed up above 10 TeV [35], and the lightest Higgs scalar resembles the weakly-coupled SM Higgs boson. These models typically contain additional particles, such as new gauge bosons and vector-like fermions, which populate the TeV mass region. In a more speculative direction, a new approach to electroweak symmetry breaking has been explored in which extra space dimensions beyond the usual $3 + 1$ dimensional spacetime are introduced [36] with characteristic sizes of order $(\mathrm{TeV})^{-1}$. In scenarios of this type, it is possible to devise a mechanism for electroweak symmetry breaking that is inherently extra-dimensional [37]. In such models, the resulting phenomenology can be significantly different [38] from the dominant paradigm of the weakly-coupled electroweak symmetry breaking sector. Typically, the spectrum of the TeV-scale will look quite different from the standard weak-coupling approaches. Kaluza-Klein excitations of the Standard Model particles can play a significant role in the resulting phenomenology. In some cases, the light Higgs boson is completely absent from the low-energy spectrum, in so-called higgsless models of electroweak symmetry breaking [39].

Although there is as yet no direct evidence for the origin of electroweak symmetry breaking dynamics, present data can be used to discriminate among the different approaches. As noted above, the precision electroweak data, accumulated in the past decade at LEP, SLC, the Tevatron and elsewhere, seem to be consistent with the Standard Model (or its supersymmetric extension), with a weakly-coupled Higgs boson whose mass lies roughly between 100 and 250 GeV [26]. Moreover, the contribution of new physics, which can enter through $W^{\pm}$ and Z boson vacuum polarization corrections [40], is severely constrained. This fact has already served to rule out nearly all of the initially proposed models of strongly-coupled electroweak symmetry breaking dynamics, and provides strong constraints on any alternative to the Standard Model and its supersymmetric extensions.

It is still possible that the Tevatron will yield the first hints of a SM-like Higgs boson prior to the start of the LHC. However, the most likely scenario is one where the LHC provides the definitive initial discovery of the physics of the electroweak symmetry breaking sector [41]. This will be either in the form of a candidate Higgs boson, or evidence that the electroweak symmetry breaking dynamics is driven by some mechanism that does not involve scalar fields in a fundamental way. Any program of Higgs physics at future colliders must address a number of important questions. First, does the SM Higgs boson (or a Higgs scalar with similar properties) exist? If yes, how many physical Higgs states are associated with the scalar sector? Moreover, how can one prove that a newly discovered scalar is a Higgs boson? To answer these questions, one must observe the Higgs boson in more than one production and decay channel, and map out its properties in detail. One must verify that the spin of the candidate Higgs boson is consistent with spin-zero. It is essential to measure a vari-

ety of Higgs couplings and demonstrate that these do indeed scale in proportion to the corresponding masses. The LHC will be able to address some of these questions with a program of Higgs measurements that can determine the Higgs couplings to the top-quark, tau-lepton, W and Z to an accuracy in the range 10–30%, assuming an integrated luminosity of 300 fb^{-1} [42]. Note, however, that LHC measurements only weakly constrain the Higgs coupling to $b\bar{b}$, even though the latter is the dominant Higgs decay channel for Higgs masses below 135 GeV.

To make further progress requires a comprehensive program of precision Higgs measurements. Such measurements with typical accuracies in some channels approaching the 1% level, are necessary to fully decipher the dynamics responsible for electroweak symmetry breaking. Such a program can only be achieved at the LC. The significance of the precision Higgs program is especially evident in the so-called decoupling limit [43], in which the properties of the lightest Higgs scalar are nearly identical to those of the SM Higgs boson. This limiting case arises in many extended Higgs theories over a significant fraction of the parameter space. Moreover, additional scalars of the Higgs sector are heavy in the decoupling limit and may not be so easily discovered at the next generation of colliders. Thus precision measurements that can distinguish the SM Higgs sector from a more complicated scalar sector are especially important if only one scalar state is discovered. In particular, small deviations from the Standard Model encode the physics of electroweak symmetry breaking, as well as being sensitive to new physics that lies beyond the Standard Model.

Additional information is required in order to fully probe the underlying scalar dynamics responsible for electroweak symmetry breaking. Ideally, one aims to reconstruct the Higgs potential and directly demonstrate the mechanism of electroweak symmetry breaking. This requires precision measurements of Higgs self-couplings, which may only be possible at a very high energy LC. One would like to know whether there are CP-violating phenomena associated with the Higgs sector. Near the decoupling limit, the couplings of the lightest Higgs boson are CP-conserving to a very good approximation, whereas CP-violating couplings among the heavier Higgs states can be unsuppressed. The former certainly requires the precision Higgs program of the LC, whereas the latter may depend on the LHC if the heavier Higgs bosons are too massive to be produced at the LC.

If the Higgs sector is weakly-coupled, one would be very interested in testing the consistency with the constraints of supersymmetry. In this case, knowledge of the spectrum of supersymmetric particles is especially significant for the precision Higgs program. The supersymmetric particle spectrum enters in a crucial way in the radiative corrections to Higgs masses and couplings. The LHC and LC are sensitive to different aspects of the supersymmetric spectrum, and both machines will provide crucial input data for the theoretical interpretation of the precision Higgs program.

If nature chooses a scenario far from the decoupling limit, then electroweak symmetry breaking dynamics produces no state that closely resembles the SM Higgs boson. In this case, it is likely that there will exist many new light states (below a TeV in mass) with a rich phenomenology.[1] In particular, new approaches to electroweak symmetry breaking dynamics have led to phenomenologies that may be quite differ-

[1]The possibility that no light states exist below 1 TeV seems remote given the standard interpretation of the precision electroweak data. Nevertheless, such possibilities cannot yet be excluded with complete certainty.

ent from the conventional expectations of weakly coupled multi-Higgs models (with or without supersymmetry). It will be essential to formulate strategies for using precision Higgs studies at future colliders to distinguish among the many possibilities.

This chapter describes a number of studies that exploit the complementarity of the LHC and LC for exploring the origin of electroweak symmetry breaking. Section 3.1 focuses on precision studies of the lightest CP-even Higgs boson, with the motivation of determining how close its properties are to that of the SM Higgs boson. Section 3.2 studies the CP-properties of the Higgs bosons. Section 3.3 focuses on Higgs physics in the minimal supersymmetric extension of the Standard Model (MSSM), while section 3.4 examines non-minimal approaches (both supersymmetric and non-supersymmetric) to the extended Higgs sector. In section 3.5, Higgs physics in the context of extra-dimensional models are studied, and in section 3.6, the consequences of the so-called littlest Higgs model is explored. Finally, a number of miscellaneous topics are treated in section 3.7.

3.1 Higgs coupling measurements and flavour-independent Higgs searches

In this section, we examine how complementary measurements from the LHC and the LC can contribute to the precision Higgs program at future colliders. Here we shall assume that the lightest CP-even Higgs boson of the scalar spectrum has a mass in the range of 100 to 200 GeV. This assumption is consistent with the standard interpretation of the LEP Higgs search and the implications of the global fit to the precision electroweak data based on the Standard Model (SM). The former implies that $m_h > 114.4$ GeV at 95% CL [27] (in the context of the MSSM, this limit is somewhat weaker, $m_h > 91.0$ GeV at 95% CL [44]), whereas the latter implies that $m_h < 260$ GeV at 95% CL [26].

The LHC will provide the first opportunity for precision Higgs measurements. For example, using methods developed in refs. [45–47], the Higgs couplings to the top-quark, tau-lepton, W and Z can be determined at the LHC to an accuracy in the range 10–30%, assuming an integrated luminosity of 300 fb^{-1} [42]. At the LC, the expectations for precision Higgs measurements are well documented [48]. Significant improvements can be obtained in many channels, approaching accuracies in the range of a few percent or better in a number of cases.

However, there are two important Higgs observables for which the expected accuracy of the LC running at $\sqrt{s} = 500$ GeV is not particularly impressive. These are the Higgs-top Yukawa coupling and the triple Higgs self-coupling. At the LC, the Higgs-top Yukawa coupling is obtained via measurements of $e^+e^- \to t\bar{t}h$ production and the determination of the triple Higgs coupling requires the observation of $e^+e^- \to Zhh$ and/or $e^+e^- \to \nu\bar{\nu}W^*W^* \to \nu\bar{\nu}hh$ production. At $\sqrt{s} = 500$ GeV, the cross-sections for these processes are quite small (due primarily to the phase space suppression of the three and four body final states); consequently, the LC alone can only make crude measurements of these Higgs observables, (assuming sufficient luminosity). It is here where the LHC can play a strong complementary role. Given the large LHC energy and luminosity, the main challenge for the LHC is to suppress backgrounds efficiently enough in order to produce a Higgs signal of significance from which the Higgs-top

Yukawa coupling and the triple Higgs coupling can be extracted.

In this section, we present two studies of the determination of the Higgs-top quark Yukawa coupling. In the contribution of K. Desch and M. Schumacher, an experimental method is proposed to determine the Higgs-top quark Yukawa couplings in a model-independent way at the LHC and LC. By combining the results of the measurements at both colliders, the most accurate determination of this coupling can be achieved. The contribution of S. Dawson *et al.* focuses on the theoretical uncertainties due to higher order QCD corrections that arise in the computation of the cross section for $t\bar{t}h$ associated production at the LHC and LC. The detection of a number of different Higgs decay channels is considered (including $b\bar{b}$, W^+W^-, $\gamma\gamma$ and $\tau^+\tau^-$). Finally, a brief discussion of the Higgs-top Yukawa coupling determination in the MSSM is given. In the latter case, new channels enter if the non-minimal Higgs states of the MSSM (H, A and $H^\pm$) are not too heavy. The complementarity of the LHC and LC for measuring the $t\bar{t}h$ coupling becomes less compelling once higher energies are available for the LC. For example, for the LC with $\sqrt{s} = 800$–1000 GeV and an integrated luminosity of 1 ab^{-1}, the Higgs-top-quark Yukawa coupling could be determined with an accuracy that is significantly more precise than the corresponding $t\bar{t}h$ coupling determination at the LHC.

We also present one study that contrasts the capabilities of the LHC and LC in the measurement of the triple-Higgs coupling. Ultimately, this is the first step required in a program to experimentally determine the parameters of the Higgs boson potential. Center-of-mass energies at the LC ranging from 500 GeV to 1 TeV were considered. In fact, the lower center-of-mass energy provided the more accurate measurement of the triple-Higgs coupling for Higgs masses below about 140 GeV. The prospects for a significant LHC measurement in this mass range are poor. For Higgs masses in the range of 150–200 GeV, the relevant Higgs cross-sections at the LC are becoming too small to allow for a useful measurement, whereas LHC data can yield the more accurate determination of the triple-Higgs coupling. However, the latter can be reliably accomplished only with the input of other precision Higgs properties obtained from measurements at the LC. Nevertheless, the initial accuracies for the triple-Higgs couplings (for $m_h < 200$ GeV) will be crude at best, and higher energy and/or luminosity colliders will be needed to make significant improvements.

Most of the above discussion assumes a pattern of Higgs boson partial widths that is close to the Standard Model expectations. However, if this assumption proves false, the Higgs search strategies (for both discovery and precision measurements) will have to be reconsidered. For example, flavor-independent techniques can be critical for Higgs searches if the theory of the Higgs sector deviates from Standard Model expectations. In the contribution of E.L. Berger, T.M.P. Tait and C.E.M. Wagner, the phenomenology of a Higgs boson that decays predominantly into jets of hadrons with no significant b-quark flavor content is examined. This condition may be realized, for instance, in supersymmetric models in which a light bottom squark is present in the spectrum and in models in which the dominant Higgs decay is into a pair of of light CP-odd scalars. Berger *et al.* emphasize that in these scenarios, the viability of the standard Higgs discovery channels at the LHC (say, for $m_h = 120$ GeV) is significantly degraded. In contrast, the Higgs discovery potential and precision Higgs measurements at the LC are generally much less sensitive to assumptions about the specific pattern of Higgs partial widths. In particular, the Higgs boson can be observed (and

its mass determined) independently of its final state decays in hZ production via the missing mass recoiling against the Z.

In probing the physics of the Higgs sector, it is essential to elucidate the nature of the TeV-scale physics associated with the mechanism of electroweak symmetry breaking. The well known naturalness arguments associated with understanding the origin of the electroweak scale make plausible the existence of new TeV-scale physics beyond the Standard Model. In nearly all models considered, the LHC, with its enormous energy and luminosity, is ideally suited to discover the new TeV-scale phenomena, and provide the initial opportunity for probing the underlying new dynamics. Thus, even if the observation of Higgs bosons at the LHC is problematical or ambiguous, one anticipates a rich phenomenology of TeV-scale physics that is accessible to the LHC. At the LC, the success of the Higgs program for $m_h \lesssim 200$ GeV is guaranteed, independently of the details of the Higgs model. This illustrates another way in which the complementarity of the LHC and the LC can be essential for providing a broad understanding of the physics of electroweak symmetry breaking.

3.1.1 Model independent determination of the top Yukawa coupling from LHC and LC

3.1.1.1 Motivation

The Yukawa coupling of the Higgs boson to the heaviest quark, the top quark, is of great interest for the study of the nature of electroweak symmetry breaking and the generation of masses. While the Yukawa couplings to bottom and charm quarks and to tau leptons and muons are in principle accessible through the Higgs boson decay branching ratios, the Higgs boson decay into top quark pairs is kinematically forbidden for light Higgs bosons as they are favoured by theory and electroweak precision data. The only Standard Model process that probes the top Yukawa coupling at tree level is the associated production of a $t\bar{t}$ pair with a Higgs boson. This process occurs at the LHC (mainly $gg{\rightarrow}t\bar{t}H^0$) as well as at the LC ($e^+e^-{\rightarrow}t\bar{t}H^0$). In the latter case the cross section is only significant at centre–of–mass energies in excess of 800 GeV. At the LHC, the final states that have been investigated so far are $t\bar{t}b\bar{b}$ [49–52] and $t\bar{t}W^+W^-$ [53, 54], the $t\bar{t}\tau^+\tau^-$ final state is under study [55, 56]. At tree level, their production rates are proportional to $g^2_{ttH}\,\mathrm{BR}(H^0 \rightarrow b\bar{b})$ and $g^2_{ttH}\,\mathrm{BR}(H^0 \rightarrow W^+W^-)$, respectively. The absolute values of $\mathrm{BR}(H^0 \rightarrow b\bar{b})$ and $\mathrm{BR}(H^0 \rightarrow W^+W^-)$ can be measured accurately in a model independent way at the LC from the corresponding decay branching ratios [57]. These can be measured already at a first phase of the LC ($\sqrt{s}$ between 350 and 500 GeV). Thus, the combination of the measurements of both machines can be used to determine the value of g_{ttH} without model assumptions and presumable before a second phase of the LC ($\sqrt{s} \sim 1$ TeV) would come into operation.

3.1.1.2 Measurements at the LHC

The results from the following ATLAS analyses of the $t\bar{t}H^0$ process are used:

1. $t\bar{t}H^0$ with $t\bar{t}{\rightarrow}$bbq$\ell\nu$ and $H^0{\rightarrow}b\bar{b}$ [49];
2. $t\bar{t}H^0$ with $H^0{\rightarrow}W^+W^-$ and two like-sign leptons [53];
3. $t\bar{t}H^0$ with $H^0{\rightarrow}W^+W^-$ and three leptons [53].

The expected numbers of selected signal and background events in the three channels for various Higgs masses and total integrated luminosities of 30 fb^{-1} and 300 fb^{-1} are listed in Tables 3.1 and 3.2. The results obtained in this sub-section are based on the anticipated data sample of *one* LHC detector, with the luminosity per detector quoted below.

m_H	30fb^{-1}		300fb^{-1}	
(GeV)	$t\bar{t}H^0$ $H^0\to bb$	background	$t\bar{t}H^0$ $H^0\to bb$	background
100	83.4	303.4	279.0	1101.3
110	63.0	275.7	232.5	1140.6
120	43.0	234.1	173.1	1054.2
130	26.5	200.1	112.5	1015.8
140	13.9	178.2	62.4	947.1

Table 3.1: Expected number of signal and background events for the $t\bar{t}H^0$ with $t\bar{t}\to$bbq$\ell\nu$ and $H^0\to b\bar{b}$ analysis at LHC [49].

m_H	30 fb^{-1}				300 fb^{-1}			
	$t\bar{t}H^0$ $H^0\to WW(2\ell)$		$t\bar{t}H^0$ $H^0\to WW(3\ell)$		$t\bar{t}H^0$ $H^0\to WW(2\ell)$		$t\bar{t}H^0$ $H^0\to WW(3\ell)$	
(GeV)	signal	bckgr	signal	bckgr	signal	bckgr	signal	bckgr
120	4.4	19.6	2.7	21.2	12.7	80.6	10.5	97.6
140	15.0	19.6	8.7	21.2	50.0	80.6	33.7	97.6
160	21.1	19.6	13.0	21.2	72.3	80.6	55.3	97.6
180	17.3	19.6	10.3	21.2	60.9	80.6	41.7	97.6
200	10.5	19.6	5.7	21.2	43.2	80.6	26.4	97.6

Table 3.2: Expected number of signal and background events for the $t\bar{t}H^0$ with $H^0\to W^+W^-$ (two like-sign leptons and three leptons, respectively) analyses at LHC [53].

From the expected event numbers we first estimate the uncertainty (statistical and systematic) on the measured cross section σ_{tth}^{data}. Further uncertainties arise when σ_{tth}^{data} is compared to the theoretical prediction as a function of g_{tth}.

The uncertainty on the observed cross section σ_{tth}^{data} is calculated as

$$(\Delta\sigma_{tth}^{data}/\sigma_{tth}^{data})^2 \;=\; (S+B)/S^2 + (\Delta B_{syst})^2/S^2 + (\Delta\mathcal{L})^2/\mathcal{L}^2 + (\Delta\epsilon)^2/\epsilon^2.$$

Here, $S(B)$ is number of signal (background) events. ΔB_{syst} is the uncertainty on the background determination from sideband data (10% in the $h\to b\bar{b}$ channel at high luminosity, 5% otherwise). $\Delta\mathcal{L}$ is the error on the integrated luminosity (5%) and $\Delta\epsilon$ is the error on the determination of the efficiency. This error involves uncertainties on the tagging efficiency for individual b-jets (3%) and leptons (3% from isolation requirement and 2% from reconstruction efficiency) and an overall detector efficiency uncertainty of 2% (following [47]). The total value of $\Delta\epsilon$ is then calculated for each channel individually depending on the number of leptons and b-jets.

The expeced error inclduing systematic uncertainties and taking into account only the statistical error of each channel is shown in Table 3.3. For the $H^0\to W^+W^-$decay mode the signal and background from the two lepton and three lepton channels

m_H	30 fb^{-1}		300 fb^{-1}	
(GeV)	$H^0 \to bb$	$H^0 \to WW$	$H^0 \to bb$	$H^0 \to WW$
100	0.398(0.236)		0.249(0.133)	
110	0.476(0.292)		0.287(0.159)	
120	0.598(0.387)	1.023(0.974)	0.345(0.202)	0.732(0.611)
130	0.840(0.568)	0.524(0.492)	0.488(0.299)	0.362(0.295)
140	1.444(0.997)	0.370(0.339)	0.804(0.509)	0.252(0.193)
160		0.287(0.254)		0.196(0.137)
180		0.331(0.300)		0.221(0.163)
200		0.486(0.454)		0.282(0.222)

Table 3.3: Expected relative precision on $\sigma_{ttH} \times BR(H \to X)$ for the various LHC $t\bar{t}H^0$ analyses including systemtatic uncertainties (statistical error only). For $H^0 \to W^+W^-$ the expected signal and background in the two and three lepton final state have been added.

m_H (GeV)	ΔBR(bb)/BR(bb)	ΔBR(WW)/BR(WW)
100	0.024	
120	0.024	0.051
140	0.026	0.025
160	0.065	0.021
200		0.021

Table 3.4: Relative precision on the branching ratio for $H^0 \to b\bar{b}$ and $H^0 \to W^+W^-$ expected for a LC running at $\sqrt{s}$= 350 GeV with 500 fb^{-1}.

are added together since their signal contributions are exclusive and the overlap in the background is small. The obtained result is consistent with the study presented in [47].

In the next step the uncertainty on $g^2_{ttH} * BR(H \to b\bar{b}/WW)$ which arises when the observed $\sigma_{ttH} * BR(H \to b\bar{b}/WW)$ is compared to its theoretical prediction. These uncertainties consist of the uncertainties in the proton structure functions (5% [58, 59]) and uncertainties in the calculation of the production cross section. Recent full NLO calculations estimate the uncertainty of the cross section prediction to be approximately 15% from a variation of the hard scale [60–63]. The total theoretical uncertainty $\Delta\sigma^{theo}_{ttH}$ is obtained by adding the above two sources in quadrature.

Finally, the total uncertainty $\Delta(g^2_{ttH} * BR(H \to b\bar{b}/W^+W^-))$ is obtained according to

$$\Delta(g^2_{ttH} * BR(H \to b\bar{b}/W^+W^-))^2/(g^2_{ttH} * BR(H \to b\bar{b}/W^+W^-)^2 \quad = \\ (\Delta\sigma^{theo}_{ttH})^2/(\sigma^{theo}_{ttH})^2 + (\Delta\sigma^{data}_{ttH})^2/(\sigma^{data}_{ttH})^2.$$

3.1.1.3 Measurements at the LC

At the LC, the decay branching ratios into b quark pairs and W boson pairs can be measured at $\sqrt{s}$= 350 GeV to the precision listed in Table 3.4 [57].

3.1.1.4 Results

For an extraction of the top quark Yukawa coupling at each Higgs mass we combine the LHC rate measurement of $t\bar{t}H^0$with $H^0 \to b\bar{b}$ or $H^0 \to W^+W^-$ with the corresponding measurement of the branching ratio at the LC. We make the tree level assumption that the cross section σ_{ttH} is proportional to g^2_{ttH}. Thus, the relative error on g_{ttH} is simply given by $\Delta g_{tth}/g_{ttH} = 0.5\Delta\sigma_{ttH}/\sigma_{ttH}$. The relative error on σ_{ttH} is obtained by adding in quadrature the statistical and systematic uncertainties as described above and the error of the LC branching ratio measurement. The combination of the $b\bar{b}$ and W^+W^- final states is performed by

$$\left(\frac{\Delta g_{tth}}{g_{ttH}}\right)^{-2}_{comb.} = \left(\frac{\Delta g_{tth}}{g_{ttH}}\right)^{-2}_{WW} + \left(\frac{\Delta g_{tth}}{g_{ttH}}\right)^{-2}_{b\bar{b}}.$$

The relative accuracies on the top quark Yukawa coupling that are achievable are summarised in Table 3.5. In Fig. 3.1 the relative accuracy from the $H \to b\bar{b}$ and $H \to WW$ channels are shown individually and combined both for low and high luminosity at the LHC. Also shown are the results that would be obtained if all systematic errors were neglected. For 300 fb^{-1}at the LHC and 500 fb^{-1}at the LC, the obtainable relative uncertainty is approximately 15% for a Higgs boson mass between 120 and 200 GeV. The purely statisical uncertainty ranges from 7% to 11% as shown in Fig. 3.2.

The size of the obtained uncertainties is comparable to those obtained for the LHC alone [47] but in contrast to the latter no model-dependent assumptions are made. In Fig. 3.2 we also show the precision which can be achieved at the LC alone if operated at 800 GeV center-of-mass energy [64] from the measurement of the $e^+e^- \to t\bar{t}H^0$ process with $H^0 \to b\bar{b}$ and and $H^0 \to W^+W^-$ combined.

m_H	30 fb^{-1}			300 fb^{-1}		
(GeV)	bb	WW	bb+WW	bb	WW	bb + WW
100	0.22(0.12)			0.15(0.07)		
110	0.25(0.15)			0.17(0.08)		
120	0.31(0.19)	0.52(0.49)	0.27(0.18)	0.19(0.10)	0.38(0.31)	0.17(0.10)
130	0.43(0.28)	0.28(0.25)	0.23(0.19)	0.26(0.15)	0.20(0.15)	0.16(0.11)
140	0.72(0.50)	0.20(0.17)	0.19(0.16))	0.41(0.26)	0.15(0.10)	0.14(0.09)
150		0.18(0.14)		1.88(1.21)	0.14(0.08)	0.14(0.08)
160		0.16(0.13)			0.13(0.07)	
170		0.17(0.13)			0.13(0.07)	
180		0.18(0.15)			0.14(0.08)	
190		0.22(0.19)			0.15(0.10)	
200		0.26(0.23)			0.16(0.11)	

Table 3.5: Expected relative error on the top Yukawa coupling g_{ttH} from the rate measurement including all systematic uncertainties (statistic errors only) at the LHC and from the branching ratio measurement at the LC.

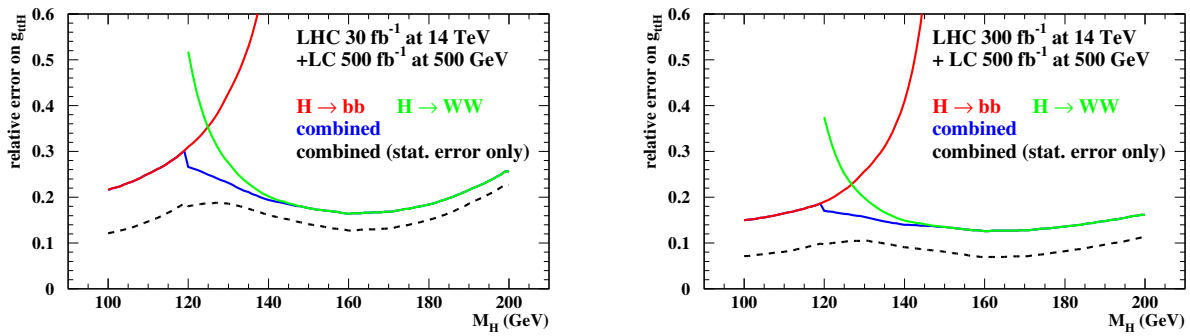

Figure 3.1: Achievable precision on the top Yukawa coupling from 30 fb^{-1}at the LHC and 500 fb^{-1}at the LC (left), and from 300 fb^{-1}at the LHC and 500 fb^{-1}at the LC (right). The red curve shows the precision obtainable from the $H^0 \to b\bar{b}$ final state, the green from the $H^0 \to W^+W^-$ final state and the blue curve from the combination of the two. The dashed lines show the expected precision taking into account only statistical errors.

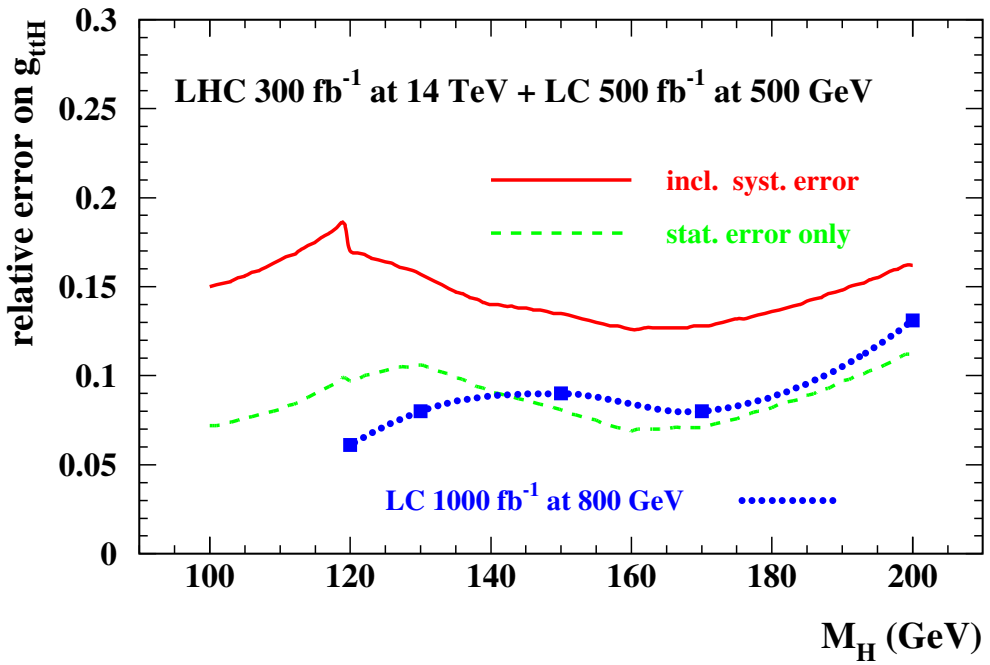

Figure 3.2: Achievable precision on the top Yukawa coupling from 300 fb^{-1}at the LHC and 500 fb^{-1}at the LC at 500 GeV taking into account all systematic uncertainties (full red curve) and using only statistical errors (dashed green curve) . For comparison the expected precision from 1000 fb^{-1}at the LC at 800 GeV alone (dotted blue curve) is also shown.

3.1.2 Associated $t\bar{t}h$ production at the LC and LHC

Once the Higgs boson has been discovered, it is crucial to measure its couplings to fermions and gauge bosons. The couplings to the gauge bosons can be measured through the associated production processes, $e^+e^- \to Zh$, $q\bar{q}' \to W^{\pm}h$, and $q\bar{q} \to Zh$, and through vector boson fusion, $W^+W^- \to h$ and $ZZ \to h$. The couplings of the Higgs boson to fermions are more difficult to measure. We focus on prospects for

measuring the top quark Yukawa coupling.

At a Linear Collider (LC) with an energy $\sqrt{s} = 500$ GeV, a Higgs boson with mass less than around 200 GeV will be copiously produced in association with a Z boson, $e^+e^- \to Zh$. The magnitude of the production rate probes the ZZh coupling. Using missing mass techniques, the LC can measure the Higgs branching ratios (and hence couplings) for many decays [65, 66]. The decay rates measure the individual Yukawa couplings in a model independent fashion and with small errors. It is not possible, however, to probe the top quark Yukawa coupling (g_{tth}) through the decay $h \to t\bar{t}$ for a light Standard Model (SM) Higgs boson ($M_h < 200$ GeV), since this decay is not kinematically accessible.

The LHC, on the other hand, will measure products of Higgs boson production cross sections times Higgs boson branching fractions. Ratios of various decay rates can then be extracted in a model independent way, while measurements of individual Higgs boson couplings to fermions and gauge bosons can be obtained under specific assumptions [45]. The dominant source of Higgs bosons, gluon fusion ($gg \to h$), proceeds through a top quark loop and in principle is sensitive to the top quark Yukawa coupling. However, heavy colored particles beyond the Standard Model would contribute to the $gg \to h$ process and invalidate the interpretation of this production process as a measurement of the top quark Yukawa coupling.

At both a linear and a hadron collider the top Yukawa coupling is only directly accessible through the associated $t\bar{t}h$ production mode. At a LC, the event rate for $e^+e^- \to t\bar{t}h$ is tiny for $\sqrt{s} = 500$ GeV and peaks for an energy scale between $\sqrt{s} = 700$-800 GeV for $M_h \sim 120$-130 GeV. At the LHC, $pp \to t\bar{t}h$ is an important discovery channel for a relatively light Higgs boson ($M_h < 130$ GeV). Although the event rate is small, the signature is quite distinctive. The total cross sections for $pp, p\bar{p}, e^+e^- \to t\bar{t}h$ are known at next-to-leading order (NLO) in QCD and we review the status of current theoretical calculations.

For Higgs boson mass $M_h < 135$ GeV the Higgs boson mainly decays into $h \to b\bar{b}$, while above this threshold $h \to W^+W^-$ dominates. In the following discussion we will consider the decays $h \to b\bar{b}, \tau^+\tau^-$ and W^+W^- and the corresponding measurements of the top quark Yukawa coupling which can be obtained at the LHC and a linear collider. A LC running at $\sqrt{s} = 800$ GeV will be able to determine g_{tth} at the 4–5% level ($M_h = 120$ GeV, $L = 1000$ fb^{-1}), while at lower energies the accuracy on this coupling deteriorates quickly. The LHC, on the other hand, could, under some assumptions, measure g_{tth} at the 10-20% level ($M_h = 110$-120 GeV, $L = 100$-300 fb^{-1} per detector). However, by combining the precisely measured branching ratios for the Higgs boson decay to the lighter fermions and to gauge bosons, which could be obtained at a $\sqrt{s} = 500$ GeV LC, with a measurement of $t\bar{t}h$ production at the LHC, the LHC could extract a measurement of the top quark Yukawa coupling which is free of theoretical uncertainties about the other Higgs boson decay rates.

In the Standard Model, the couplings of the Higgs boson to fermions are completely determined in terms of the corresponding fermion masses, $g_{ffh} = M_f/v$, where $v = (\sqrt{2}G_F)^{-1/2}$ and so the top quark-Higgs boson coupling is the largest Yukawa coupling. In extensions of the Standard Model, however, the Yukawa couplings can be significantly different. They are no longer strictly proportional to the fermion masses, but depend on the parameters of the model. The minimal supersymmetric extension of the Standard Model (MSSM) provides a useful benchmark for comparison with the

Standard Model.

In the following sections, we compare the $t\bar{t}h$ production rates in hadronic and e^+e^- collisions and examine the various Higgs decay channels. We also discuss the possibility of probing the top-Higgs Yukawa coupling by measuring the threshold energy dependence of the $e^+e^- \to t\bar{t}$ cross section. The current state of experimental studies of the $t\bar{t}h$ process is surveyed, with an emphasis on the extraction of the top quark Yukawa coupling. Unless stated otherwise, we concentrate entirely on the Standard Model Higgs boson.

3.1.2.1 Linear Collider

- $t\bar{t}h$ **Production Rates**

The production of a $t\bar{t}h$ final state in e^+e^- collisions proceeds at the tree level through the Feynman diagrams shown in Fig. 3.3 [67].

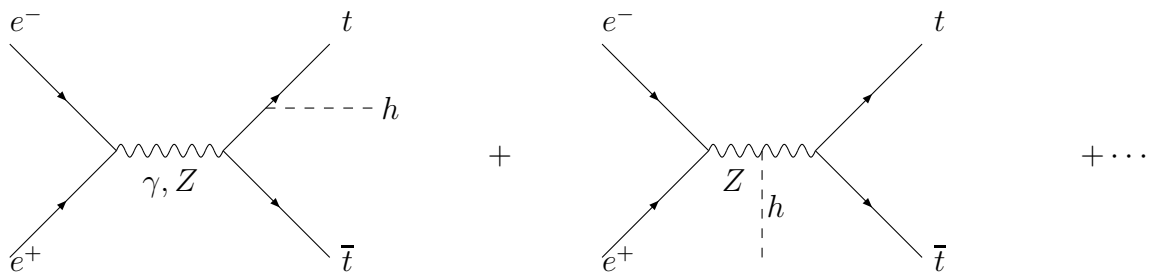

Figure 3.3: Feynman diagrams contributing to the lowest order process, $e^+e^- \to t\bar{t}h$.

To the extent to which the Higgs boson radiation from the $s-$channel Z-exchange is negligible, the cross section is directly proportional to g^2_{tth}. In Fig. 3.4, the total rate from photon exchange only is compared with the total contribution, showing that the effect of Z exchange is only a few percent correction, in particular at low center-of-mass energies. Fig. 3.4 contains only the tree level cross section: at higher orders, the QCD and electroweak radiative corrections could significantly change the relative contributions of the γ and Z exchange. The process has an optimal energy since the rate peaks around $\sqrt{s} \sim$ 700-800 GeV ($\sigma_{t\bar{t}h} \simeq 2.5$ fb for $M_h \sim 120$ GeV). At $\sqrt{s} = 500$ GeV and for $M_h \sim 120$ GeV, the cross section is of order 0.5 fb.

QED corrections due to initial state radiation effects (bremsstrahlung and beamtrahlung, the former being dominant) significantly distort the $t\bar{t}h$ lineshape. The main effect is to shift the maximum of the cross section towards higher $\sqrt{s}$. As a result, the cross section at $\sqrt{s} = 500$ GeV is reduced by a factor $\simeq 2$, *i.e.* $\sigma_{t\bar{t}h} \simeq 0.2$ fb for $M_h \sim 120$ GeV [69,70].

The first order QCD corrections to this process, which turn out to be important near the $t\bar{t}$ threshold, have been computed including only γ exchange in Ref. [68] and with the complete γ and Z contributions in Ref. [71]. The QCD corrected rate, as a function of M_h and for different center-of-mass energies, is compared to the uncorrected one in Fig. 3.5. At $\sqrt{s} = 500$ GeV, the corrections are large and positive, with a strong dependence on M_h ($K_{NLO} \simeq 1.5$, for $\mu = \sqrt{s}$ and $M_h = 120$ GeV). At $\sqrt{s} = 1$ TeV, they

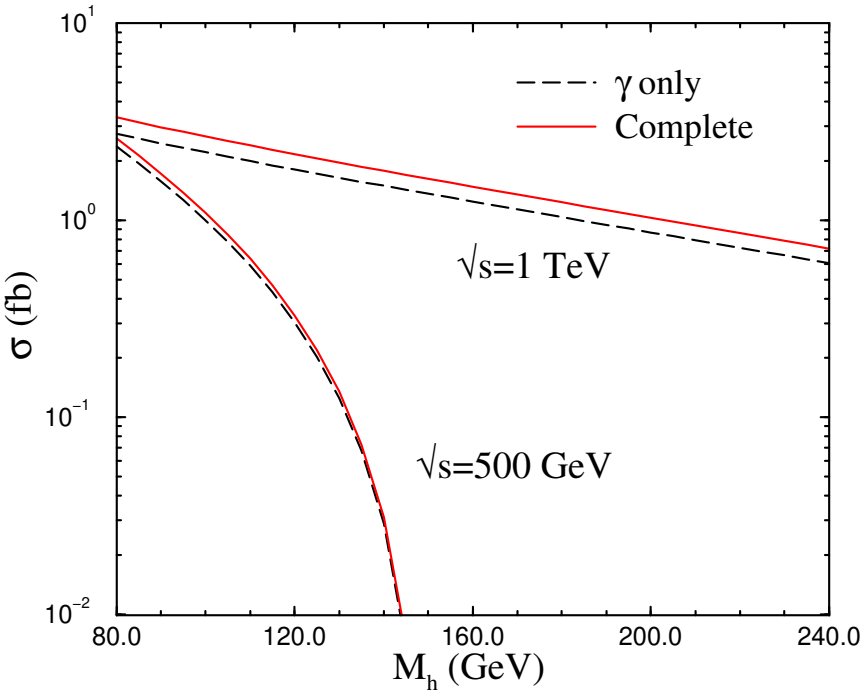

Figure 3.4: Lowest order cross section for $e^+e^- \to t\bar{t}h$ at $\sqrt{s} = 500$ GeV and $\sqrt{s} = 1$ TeV. The curve labeled *complete* includes both γ and Z exchange, along with bremsstrahlung from the Z boson [68].

are small and negative ($K_{NLO} \simeq 0.9$, for $\mu = \sqrt{s}$), and essentially independent of M_h. The only scale dependence at NLO is the running of the strong coupling constant, $\alpha_s(\mu)$. Changing the scale parameter by a factor of 2 induces roughly a 10% change in σ_{NLO}, indicating that higher order QCD corrections may be important to match the experimental precision of a high energy LC.

The electroweak corrections to $e^+e^- \to t\bar{t}h$ are also important and have been computed by three groups [72–74]. At $\sqrt{s} = 500$ GeV, the QCD corrections are significantly larger than the electroweak corrections, while at $\sqrt{s} = 1$ TeV, the electroweak corrections are roughly the same size as the QCD corrections but opposite in sign, as shown in Fig. 3.6.

- $\boldsymbol{h \to b\bar{b}}$

The Higgs decays predominantly to $b\bar{b}$ pairs for $M_h < 135$ GeV. The final state of interest is then

$$e^+e^- \to t\bar{t}h \to t\bar{t}b\bar{b} \ . \tag{3.1}$$

The possibility of fully reconstructing the two top quarks in the final state allows efficient discrimination of the signal over the background, and together with a good b-tagging efficiency is crucial for extracting the signal and for increasing the precision with which the top Yukawa coupling can be measured. Both the semi-leptonic final state

$$e^+e^- \to (bl\nu) + (bq\bar{q}') + (h \to b\bar{b}) \ , \tag{3.2}$$

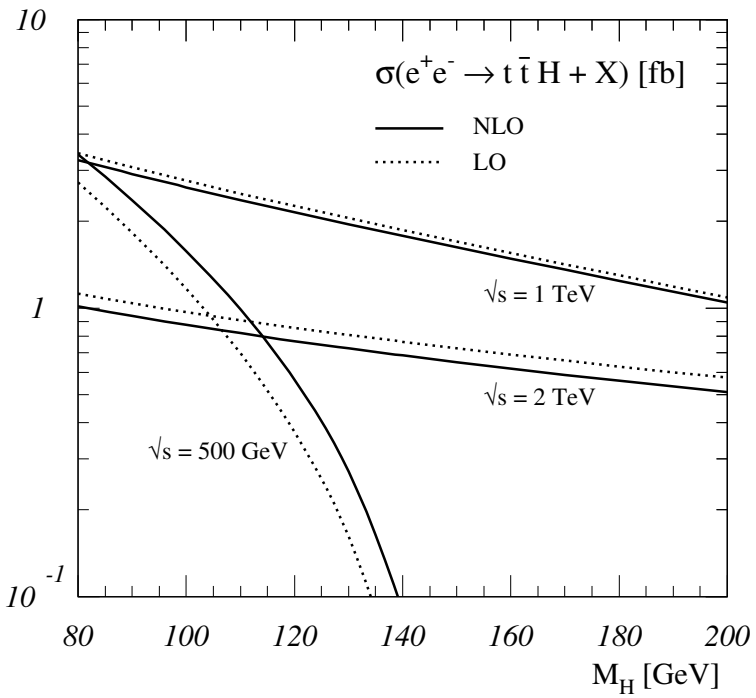

Figure 3.5: LO and NLO cross sections for $e^+e^- \to t\bar{t}h$ as a function of the Higgs mass M_h for $\sqrt{s}=500$ GeV, 1 TeV and 2 TeV. The renormalization scale is set to $\mu=\sqrt{s}$ [71].

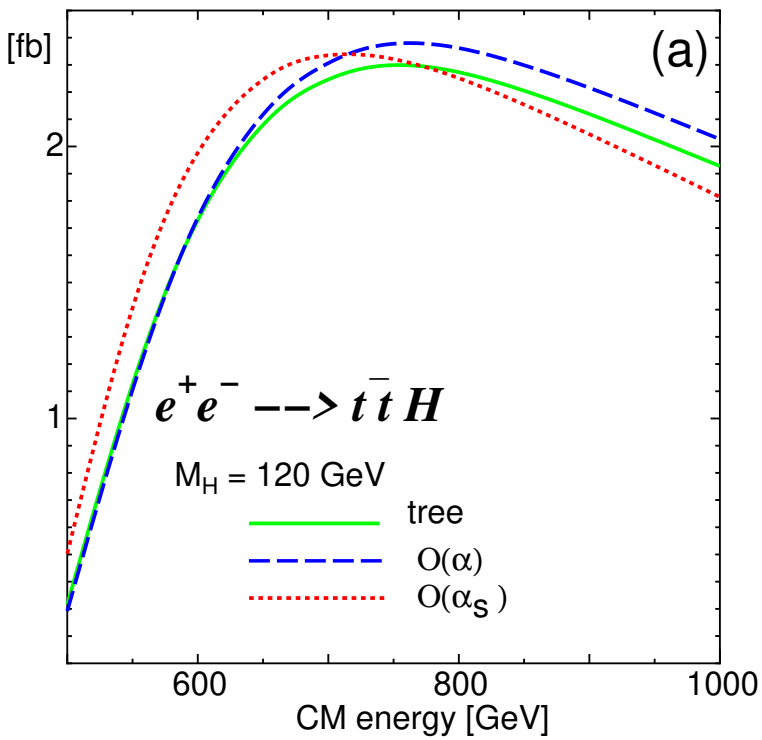

Figure 3.6: LO and NLO cross sections for $e^+e^- \to t\bar{t}h$ showing the effect of the QCD and electroweak corrections to the total cross section for $M_h = 120$ GeV. [72].

and the fully hadronic final state

$$e^+e^- \to (bq_1\bar{q}_1') + (bq_2\bar{q}_2') + (h \to b\bar{b}) \tag{3.3}$$

can be observed.

In the semi-leptonic decay, the final state is 4 b-jets, 2 light quark jets, a high p_T isolated lepton and missing energy from the neutrino. The largest interfering background is the QCD background from the gluon splitting process, $e^+e^- \to t\bar{t}g^*(g^* \to b\bar{b})$. The $b\bar{b}$ pairs resulting from the gluon splitting, however, tend to peak at low values of the $b\bar{b}$ invariant mass. There is also an electroweak background, of which the dominant contribution is $e^+e^- \to Zt\bar{t}$. Although the electroweak background is formally smaller than the QCD background, the $Z \to b\bar{b}$ decay resonates in close proximity to the expected Higgs signal. A parton level calculation of these interfering backgrounds has been performed [75] for the following final state:

$$e^+e^- \to b\bar{b}b\bar{b}l\nu q\bar{q}' \ , \tag{3.4}$$

using helicity amplitudes and no factorization of the production and decay channels.

A feasibility study of the measurement of the top quark Yukawa coupling was performed in Ref. [76], including both semileptonic and fully hadronic decay channels. This study considered the production process $e^+e^- \to t\bar{t}b\bar{b}$, with QCD radiation, hadronization and particles decays (including the top quark), including a toy detector simulation, handled by ISAJET [77]. The analysis also included full reconstruction of the top quark and W boson masses. The fully hadronic channel for $e^+e^- \to t\bar{t}h$ has the advantage of initially higher rates than the semi-leptonic channel due to the large W boson hadronic branching fraction. However, in attempting mass reconstructions, a greater combinatoric problem is presented. The two studies [75, 76] found agreement on the size of the backgrounds, lending validity to the use of the factorization approximation for the decays.

At $\sqrt{s} = 500$ GeV and $M_h = 120$ GeV, a jet $b-$tagging efficiency ϵ_b, and an integrated luminosity L, the precision on the top quark Yukawa coupling obtained by combining the semi-leptonic channel with the hadronic channel is predicted [76] to be:

$$\frac{\delta g_{tth}}{g_{tth}} \sim 21\% \sqrt{\frac{1000 \text{ fb}^{-1}}{L\epsilon_b^4}} \ . \tag{3.5}$$

For $M_h = 130$ GeV, the precision declines to

$$\frac{\delta g_{tth}}{g_{tth}} \sim 44\% \sqrt{\frac{1000 \text{ fb}^{-1}}{L\epsilon_b^4}} \ , \tag{3.6}$$

primarily due to the suppression of the rate for the heavier Higgs mass.

A more detailed preliminary study was performed for $\sqrt{s} = 500$ GeV and $L = 1000 \text{ fb}^{-1}$, assuming $M_h = 120$ GeV, and considering so far only the semileptonic channel [70]. The analysis included both reducible and irreducible backgrounds, realistic detector effects, and reconstruction efficiencies. The main sources of efficiency loss are from limitations of the jet-clustering algorithm and b-tagging performances in a high jet multiplicity environment. Signal and backgrounds are discriminated by making use of a combination of highly efficient preselections and multivariate techniques

involving Neural Networks. Because of the large backgrounds, it is crucial that they are well modeled both in normalization and shape. A conservative estimate of 5% in the overall background normalization was included. The estimated total uncertainty in the top quark Yukawa coupling is approximately 33%. From the optimization of this analysis (improved b-tagging performance, dedicated τ selections, extensive use of kinematical information), together with the combination with the hadronic channel and using NLO K-factors, an ultimate accuracy of $\leq 20\%$ is expected. The increased signal rate and reduced non-interfering backgrounds at higher $\sqrt{s}$ allow for a more precise measurement of the top quark Yukawa coupling.

A feasibility study [69], comparable in level of sophistication to the previous one, but considering both semileptonic and hadronic decay channels at $\sqrt{s}=800$ GeV and for $M_h = 120$ GeV, has been performed. Assuming $L = 1000$ fb^{-1}, the estimated total uncertainty in the top-Higgs Yukawa coupling is:

$$\frac{\delta g_{tth}}{g_{tth}} \sim 5.5\% \ . \tag{3.7}$$

Including only the statistical error, the precision becomes 4.2%.

• $\boldsymbol{h \rightarrow WW^*}$

Within the SM and for $M_h \simeq 135$ GeV, the branching ratio for $h \rightarrow WW^*$ is comparable in size with that for $h \rightarrow b\bar{b}$. For larger Higgs masses, $h \rightarrow WW^*$ becomes the dominant decay mode. Therefore, it is important to explore the potential of this channel to further increase the sensitivity to the top-Higgs decay Yukawa coupling up to higher values of M_h.

The process under consideration contains 4 W bosons and 2 b-jets in the final state:

$$e^+e^- \rightarrow t\bar{t}h \rightarrow W^+bW^-\bar{b}WW^*. \tag{3.8}$$

The final state is fully determined by the W boson decay modes, thus offering a wide variety of experimental signatures:

$$\begin{aligned}
\text{fully hadronic (10 jets)}: &\quad \text{BR} \simeq 20.8\% \ ; \\
\text{semileptonic (1 lepton + 8 jets)}: &\quad \text{BR} \simeq 40.0\% \ ; \\
2 \text{ opposite} - \text{sign leptons} + 6 \text{ jets}: &\quad \text{BR} \simeq 19.3\% \ ; \\
2 \text{ same} - \text{sign leptons} + 6 \text{ jets}: &\quad \text{BR} \simeq 9.6\% \ ; \\
3 \text{ leptons} + 4 \text{ jets}: &\quad \text{BR} \simeq 9.3\% \ ; \\
4 \text{ leptons} + 2 \text{ jets}: &\quad \text{BR} \simeq 1.0\% \ .
\end{aligned}$$

A feasibility study has been performed for $\sqrt{s} = 800$ GeV in the "2 same-sign leptons+jets" final state [64]. This channel is expected to have low backgrounds and therefore a relatively simple topological selection appears to be sufficient. A 5% systematic uncertainty in the overall background normalization has been included. Assuming $L = 1000$ fb^{-1}, the estimated total uncertainty in the top-Higgs Yukawa coupling is found to be $\simeq 15\%$ for $140 \leq M_h \leq 180$ GeV.

In terms of statistics, the semileptonic channel is the most promising one, although the backgrounds are expected to be much larger that for the "2 same-sign leptons+jets" one. This process could be analyzed with a similar strategy to the one applied to the semileptonic channel in $e^+e^- \to t\bar{t}h(h \to b\bar{b})$. Indeed, the increased jet multiplicity in the final state makes it more challenging. Preliminary studies [78, 79] indicate a significant improvement in the total uncertainty on g_{tth} by combining it with the "2 same-sign leptons+jets" channel.

Finally, the results of Refs. [78, 79] suggest that the combination of the $h \to b\bar{b}$ and $h \to WW^*$ decay channels could yield an ultimate uncertainty of

$$\frac{\delta g_{tth}}{g_{tth}} \leq 15\% \tag{3.9}$$

for $M_h \leq 200$ GeV, assuming $\sqrt{s} = 800$ GeV and $L = 1000$ fb^{-1}.

• **$t\bar{t}$ Threshold Scan**

The total cross section for $e^+e^- \to t\bar{t}$ as a function of center-of-mass energy is quite sensitive to the top quark mass, m_t, [80]. It is also sensitive to a lesser degree to the strong coupling constant α_s, the total top quark decay width, Γ_t, and the top quark Yukawa coupling, g_{tth}. By measuring the threshold energy dependence of the forward backward asymmetry and the position of the peak of the top quark momentum distribution, additional sensitivity to Γ_t and g_{tth} can be obtained [81, 82], although the sensitivity to the top quark Yukawa coupling is quite small in all observables.

The total $e^+e^- \to t\bar{t}$ cross section at threshold has been calculated including some of the next-to-next-to-leading logarithms, [83]. The complete set of next-to-next-to-leading logarithmic contributions is not yet complete, but the large size of the corrections relative to the next-to-leading logarithmic terms [84] suggests that the uncertainty on the cross section measurement will be slightly larger than previously estimated, $\delta\sigma_{tt}/\sigma_{tt} \sim \pm 6\%$.

In Ref. [82] an experimental study of the precision on g_{tth} has been performed which we will summarize in the following. The study assumes an integrated luminosity of 300 fb^{-1} and $M_h = 120$ GeV. Theoretical predictions are based on the TOPPIK program [85]. By fixing all variables except g_{tth} and assuming a 3% systematic uncertainty on the total cross section, a measurement of

$$\frac{\delta g_{tth}}{g_{tth}} = {}^{+0.18}_{-0.25} \tag{3.10}$$

could be obtained from the threshold scan. Of course, a more realistic analysis would include the uncertainties on the other variables. Leaving m_t and α_s free with assumed errors

$$\begin{aligned} \Delta\alpha_s &= 0.001\,, \\ \Delta m_t &= 27\text{MeV}\ , \end{aligned} \tag{3.11}$$

but fixing Γ_t to the Standard Model value (and assuming a systematic error of $\delta\sigma_{tt}/\sigma_{tt} = 1\%$), the precision would be reduced to

$$\frac{\delta g_{tth}}{g_{tth}} = {}^{+0.33}_{-0.54}\ . \tag{3.12}$$

Finally, when also leaving Γ_t free,

$$\frac{\delta g_{tth}}{g_{tth}} = {}^{+0.35}_{-0.65} \quad . \tag{3.13}$$

This precision is not competitive with that which can be obtained through $e^+e^- \to t\bar{t}h$ at $\sqrt{s} = 500$ GeV. In view of the possibility of a systematic experimental error on the total $t\bar{t}$ threshold cross section of 1%, the effects of electroweak radiative corrections [86] also need to be included. Interpreting the top quark threshold measurements as a measurement of g_{tth} requires the assumption that there be no new physics in the $\gamma t\bar{t}$ and $Zt\bar{t}$ vertices. Additionally, in the realistic multi-parameter fit discussed above, the Yukawa coupling is 83% correlated with the top quark mass, adding to the difficulty of the interpretation of the threshold cross section as a measurement of the Yukawa coupling.

3.1.2.2 LHC

- **Production Rates**

The $pp \to t\bar{t}h$ channel can be used in the search for an intermediate mass Higgs boson, $M_h < 130$ GeV, at the LHC. In this region, the cross section for the associated production of a Higgs boson with a pair of top quarks is still smaller than the leading $gg \to h$ and $qq \to qqh$ cross sections, but the final state $t\bar{t}h$ signatures are quite distinctive. At the Tevatron, however, the Standard Model cross section for $p\bar{p} \to t\bar{t}h$ is probably too small to be observed [60, 62, 87].

At the LHC energy, $\sqrt{s} = 14$ TeV, the dominant subprocess for $t\bar{t}h$ production is $gg \to t\bar{t}h$, but the other subprocesses, $q\bar{q} \to t\bar{t}h$ and $g(q,\bar{q}) \to t\bar{t}h(q,\bar{q})$ are relevant and cannot be neglected. The cross section for $pp \to t\bar{t}h$, at LO and NLO of QCD corrections, is shown in Fig. 3.7 as a function of the Higgs boson mass M_h, for two different values of the renormalization/factorization scale μ. The major effect of the higher order corrections is to reduce the unphysical scale dependence and to increase the rate from the lowest order prediction by a factor of 1.2–1.6, depending on the value of the scale μ and on the set of parton distribution functions (PDFs) used [60, 61, 63]. The overall theoretical uncertainty of the NLO cross section, including the residual scale dependence, the error on m_t, and the uncertainty in the PDFs, can be estimated around 15–20%.

The cross section for $pp \to t\bar{t}h$ is directly proportional to the top quark Yukawa coupling and can be instrumental to the measurement of this coupling at the LHC. In spite of the fact that the LHC does not allow for a completely model independent determination of the Higgs boson couplings, strategies have been proposed to extract individual couplings with reasonably good precision under some not too restrictive assumptions [45–47]. Typically both g_{WWh}/g_{ZZh} and $g_{bbh}/g_{\tau\tau h}$ ratios are assumed to be SM like [45], and the Higgs boson width is assumed to be saturated by the allowed SM Higgs decay channels. In this picture, the top quark Yukawa coupling could be determined from future LHC measurement with a precision of about 10-15% [45]. Using the $pp \to t\bar{t}h$ channel with both $h \to b\bar{b}$ and $h \to \tau^+\tau^-$ allows one to measure the $g_{bbh}/g_{\tau\tau h}$ ratio in a model independent way [46, 47]. Even in this more general scenario, provided a good accuracy on $pp \to t\bar{t}h, h \to b\bar{b}$ and $pp \to t\bar{t}h, h \to \tau^+\tau^-$ is con-

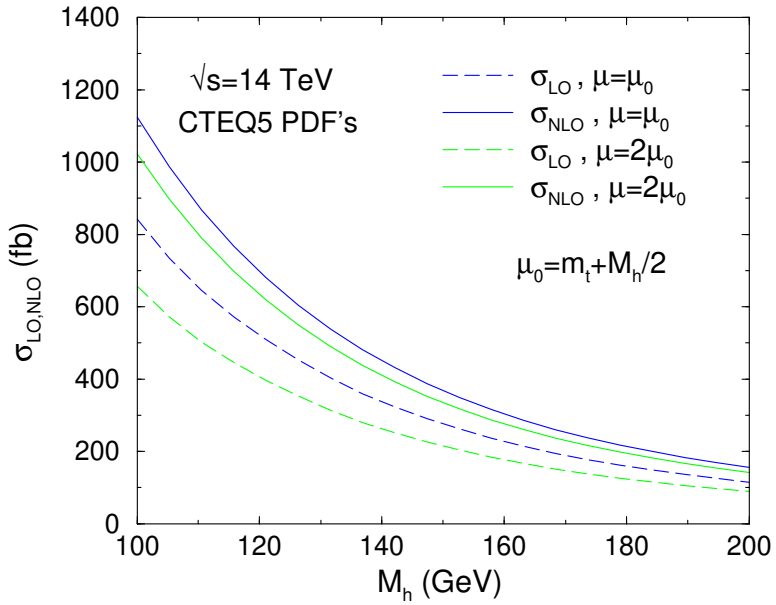

Figure 3.7: Leading order (LO) and next-to-leading order (NLO) rates for $pp \to t\bar{t}h$ at the LHC, $\sqrt{s} = 14$ TeV. The rates are shown for two values of the unphysical factorization/renormalization scale, μ [63].

firmed by dedicated experimental analyses, the precision on the top quark Yukawa coupling stays of the order of $10-15\%$ [46] for Higgs boson masses below 130 GeV.

Moreover, both in the low and the high Higgs boson mass region, $pp \to t\bar{t}h$, with $h \to \tau^+\tau^-$ in one case [46] and $h \to W^+W^-$ in the other [54], will allow the measurement of the ratio g_{tth}/g_{ggh} in a model independent way. With enough experimental accuracy, unambiguous evidence for contributions to $gg \to h$ from exotic colored degrees of freedom could be provided.

Finally, in the most promising scenario, the LHC and a high energy LC will complement each other. A LC with center of mass energy $\sqrt{s} = 500$ GeV will be able to measure all Higgs couplings, except g_{tth}, at the few percent level. We could therefore imagine to use this knowledge of the $Br(h \to b\bar{b}, \tau^+\tau^-, W^+W^-, ZZ, \ldots)$ at the LHC to extract the top quark Yukawa coupling from $pp \to t\bar{t}h$ with better precision . This is indeed close to the philosophy adopted by most of the existing experimental analyses of $pp \to t\bar{t}h$. In the following we summarize some of the existing results.

- $\boldsymbol{h \to b\bar{b}}$

One of the most important channels is the $t\bar{t}h, h \to b\bar{b}$ channel, which is the dominant channel for $M_h < 135$ GeV [51, 52, 88, 89]. The final state consists of two W bosons and four b-jets. One W boson is required to decay leptonically in order to provide a trigger, while the second W is reconstructed from the decay to a $\bar{q}q'$ pair. This decay pattern yields eight fermions:

$$\begin{aligned} t\bar{t}h &\to W^+bW^-\bar{b}\,b\bar{b} \\ &\to l\nu q\bar{q}'b\bar{b}b\bar{b} \ . \end{aligned} \tag{3.14}$$

Both top quarks can be fully reconstructed, and this reduces most of the W + jets background. The main backgrounds are the irreducible continuum QCD $t\bar{t}b\bar{b}$ background, the irreducible resonant $t\bar{t}Z$ background, and the reducible backgrounds which contain jets misidentified as b-jets. After the reconstruction of the two top quarks, the most dangerous background is $t\bar{t}b\bar{b}$.

Fig. 3.8 shows the signal and background shapes from a CMS simulation for $M_h = 115$ GeV and 30 fb^{-1} of integrated luminosity [52]. This study obtains a value of $S/\sqrt{B} \sim 5$, yielding a value of

$$\frac{\delta g_{tth}}{g_{tth}} \sim 12\text{–}15\% \ , \tag{3.15}$$

assuming that the branching ratio for $h \to b\bar{b}$ is known with a negligible error.

Results for the $h \to b\bar{b}$ channel have also been obtained by the ATLAS collaboration [49,89]. The ATLAS analysis assumes a full reconstruction of the final state in order to eliminate combinatoric backgrounds. Assuming a K factor of 1.0 and a Higgs mass of $M_h = 115$ GeV, ATLAS finds a value of $S/\sqrt{B} = 2.4$ with 30 fb^{-1} [49]. After adjusting for the different assumptions about efficiencies and the different cross sections (due to differing choices of the scale factors and PDFs), the ATLAS and CMS analyses are in agreement for the signal and the reducible background. The CMS analysis, however, finds a significantly smaller reducible $t\bar{t}b\bar{b}$ background than does the ATLAS study.

- $\boldsymbol{h \to \gamma\gamma}$

Because of the small rate, the $h \to \gamma\gamma$ channel is useful only at high luminosity [51,89].

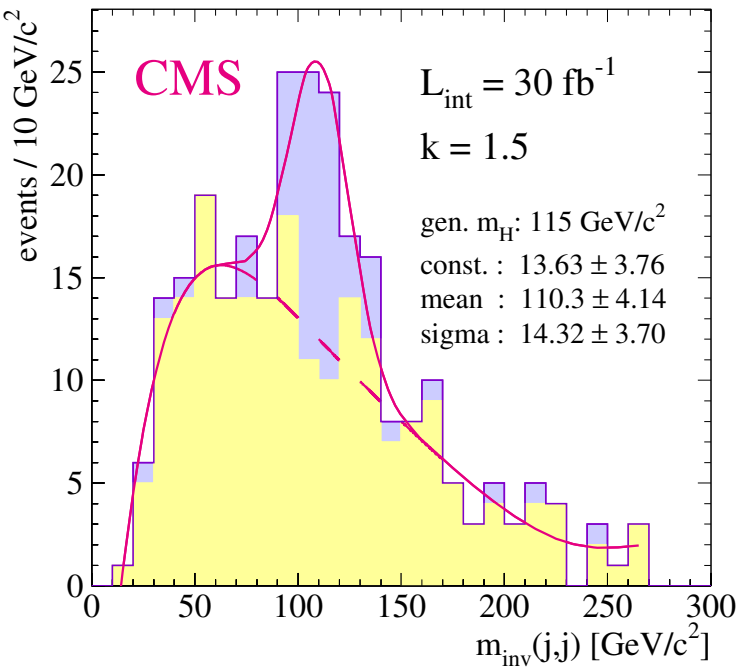

Figure 3.8: Signal and background at the LHC for $pp \to t\bar{t}h \to l\nu q\bar{q}'b\bar{b}b\bar{b}$ with the CMS detector and for $M_h = 115$ GeV. (The NLO corrections are estimated using a k factor of 1.5 slightly higher than the actual value) [52].

• $h \to \tau^+\tau^-$

For $M_h < 130$–135 GeV, the decay $h \to \tau^+\tau^-$ is useful as part of a general strategy to determine Higgs boson couplings with very few theoretical assumptions [46, 47]. It offers the possibility of determining in a completely model independent way the ratio $g_{bbh}/g_{\tau\tau h}$ by measuring the ratio of $pp \to t\bar{t}h, h \to b\bar{b}$ to $pp \to t\bar{t}h, h \to \tau^+\tau^-$. Combining $pp \to t\bar{t}h$, $gg \to h$, and $qq \to qqh$ channels, it also allows a model independent determination of the g_{tth}/g_{ggh} ratio.

First studies assumed that one of the top quarks decays leptonically, while the other decays hadronically [46] . The parton level signature is $b\bar{b}l\nu q\bar{q}'\tau^+\tau^-$, which has the irreducible background $t\bar{t}\tau^+\tau^-$, where the τ pair originates from a Z boson or a photon. The other backgrounds are much smaller. Ref. [46] considered only the τ decays to 1 or 3 charged pions and found that with 100 fb^{-1} an accuracy of about 20% on $\delta\sigma/\sigma$ could be obtained for $M_h < 120$ GeV, declining to 50% for $M_h = 140$ GeV. For larger Higgs masses the rate becomes too small for this decay channel to be observed.

• $h \to W^+W^-$

For $M_h > 135$ GeV, the dominant decay mode is $h \to WW^*$ and the process $pp \to t\bar{t}h,\ h \to WW^*$ can be observed despite the low signal and the lack of a reconstructed mass peak. By measuring the ratio of

$$\frac{\sigma(pp \to t\bar{t}h, h \to b\bar{b})}{\sigma(pp \to t\bar{t}h, h \to WW^*)} \tag{3.16}$$

a measurement of g_{bbh}/g_{WWh} can be made in which many of the systematic uncertainties cancel [54]. Combining $pp \to t\bar{t}h, h \to WW^*$ with $gg \to h, h \to WW^*$, the ratio g_{tth}/g_{ggh} can be measured in a model independent way [46, 47].

The process $pp \to t\bar{t}h, h \to W^+W^-$ gives the final state $W^+W^-W^+W^-b\bar{b}$. The decays can then be classified according to the number of leptonic W decays [53]. Ref. [54] performs a parton model study where the background is reduced by requiring both b decays be tagged with an efficiency $\epsilon_b = 0.6$. The reconstruction of the top quarks is not required and $p_T > 20$ GeV for one trigger lepton is required. With 300 fb^{-1} of data, one can achieve an accuracy of

$$\frac{\delta g_{tth}}{g_{tth}} \sim 16\%\,,\ 8\%\,,\ 12\% \tag{3.17}$$

for $M_h = 130$, 160 and 190 GeV respectively, as illustrated in Fig. 3.9 [54]. The ATLAS collaboration [53] has found that in the most favorable case, $M_h = 160$ GeV, the cross section for $pp \to t\bar{t}h, h \to WW^*$, can be measured with $\delta\sigma/\sigma \sim 26\ \%\ (15\%)$ accuracy with a luminosity of $30\ fb^{-1}$ $(300\ fb^{-1})$ by combining several final states.

The $t\bar{t}h,\ h \to b\bar{b}$ and $t\bar{t}h,\ h \to W^+W^-$ channels can be combined to get a measurement of the relative decay widths $\Gamma(h \to b\bar{b})/\Gamma(h \to W^+W^-)$ with a $50-60\%$ accuracy assuming a luminosity of 300 fb^{-1} for $M_h \lesssim 140$ GeV. [47] This measurement is free of theoretical assumptions. With further assumptions about the $h \to W^+W^-$ width, a value for the $hb\bar{b}$ coupling can be extracted from this channel [47].

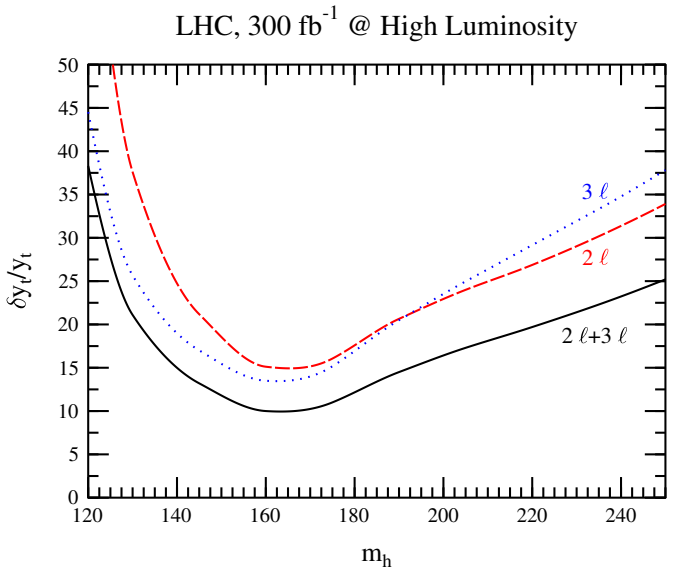

Figure 3.9: Measurement of the top quark Yukawa coupling at the LHC in the $t\bar{t}h$, $h \to W^+W^-$ channel [54].

3.1.2.3 SUSY Higgs Sector

There are two important differences between the Higgs sector in the Standard Model and in a supersymmetric model. First, there are 5 Higgs bosons, $A, h, H, H^{\pm}$, in the minimal SUSY model, so there are more associated top quark-Higgs boson processes:

$$e^+e^-, pp \to t\bar{t}h\,,\, t\bar{t}H\,,\, t\bar{t}A \quad ,$$
$$e^+e^-, pp \to t\bar{b}H^- + b\bar{t}H^+ \quad . \tag{3.18}$$

At a linear collider, the additional Higgs bosons give important new contributions, for example, $e^+e^- \to AH, A \to t\bar{t}$. Secondly, the Higgs boson couplings to the fermions are changed from those of the Standard Model, and depend on the parameters of the model, typically $\tan\beta$.

The NLO QCD corrections to $e^+e^- \to t\bar{t}h$ are modest [90, 91] and the QCD corrected rate for the production of the neutral Higgs bosons is shown in Fig. 3.10. For large $\tan\beta$, the associated production of the lighter Higgs boson, h, is significantly suppressed due to the suppressed coupling of the top quark to the lightest SUSY Higgs boson. The SUSY couplings have the property that the $t\bar{t}h$ and $t\bar{t}H$ production rates are complementary, as demonstrated in Fig. 3.11. The associated production of the pseudoscalar Higgs boson, $e^+e^- \to t\bar{t}A$, is significantly smaller than that of the scalars for all values of the parameter space.

The LC can make precision measurements of the rates for the $t\bar{t}h\,(H, A)$ production modes and use them to discriminate between different models of supersymmetry breaking [92]. A comparison of the rates in gauge mediated SUSY breaking models, anomaly mediated SUSY breaking models, and the mSUGRA model suggest that this channel is sensitive to the mechanism of SUSY breaking for roughly $M_A < 300$ GeV.

The NLO QCD corrections to $e^+e^- \to tbH^{\pm}$ have been computed in Ref. [93]. This process could be important in the energy regime where it is not possible to pair pro-

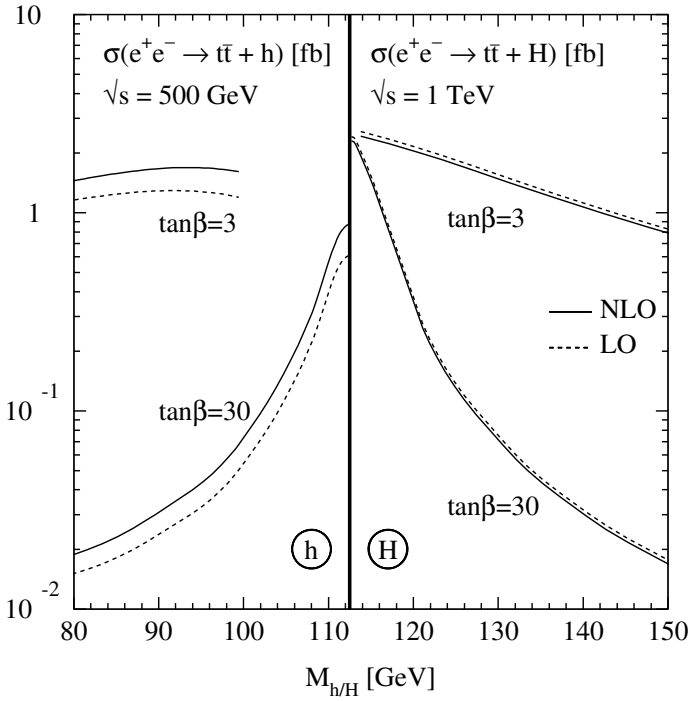

Figure 3.10: The LO and NLO corrected rates for $e^+e^- \to t\bar{t}h$ and $e^+e^- \to t\bar{t}H$ in the MSSM [90].

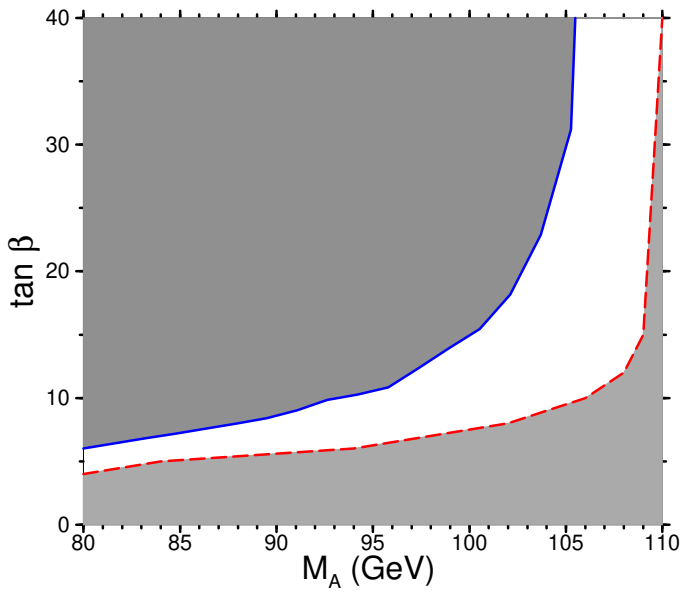

Figure 3.11: Regions of parameter space where the QCD corrected NLO rate for $e^+e^- \to t\bar{t}h$ ($e^+e^- \to t\bar{t}H$) is larger than 0.75 fb, bottom right (upper shading), at $\sqrt{s}=500$ GeV [91].

duce the charged Higgs boson through the process $e^+e^- \to H^+H^-$. Unfortunately, at $\sqrt{s}=500$ GeV, the rate is always small, $\sigma<0.03$ fb for $M_H=260$ GeV and $\tan\beta=40$.

At the LHC, the primary effect in $t\bar{t}h$ production of introducing a supersymmetric model is to change the Higgs couplings to the top quark. The rate for $pp \to t\bar{t}h, h \to b\bar{b}$

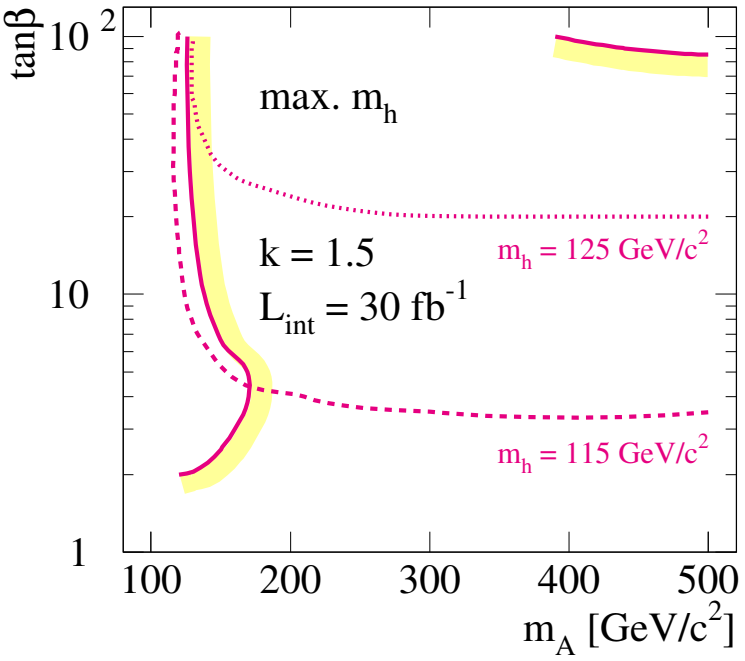

Figure 3.12: 5σ discovery regions with 30 fb^{-1} at the LHC using the CMS detector and the process $pp \to t\bar{t}h, h \to b\bar{b}$ in the MSSM. The plot is obtained by rescaling the Standard Model results by the appropriate SUSY couplings. The discovery region is to the side of the shaded area [52]. The SUSY mixing parameters are chosen to give the maximum value of M_h for a given M_A and $\tan\beta$.

is proportional to $g_{tth}g_{bbh}$ which has only a weak dependence on $\tan\beta$. For a wide choice of parameters and SUSY models, the rate for $pp \to t\bar{t}h$ production is never suppressed by more than 10% [92]. The 5σ discovery contours at the LHC for 30 fb^{-1} are shown in Fig. 3.12. This curve is obtained simply by rescaling the Standard Model results by the appropriate SUSY couplings [52]. The discovery region is to the side of the shaded area.

3.1.2.4 Conclusion

The associated production of a Higgs boson with a pair of $t\bar{t}$ quarks will be the only way of directly measuring the top quark Yukawa coupling at both a high energy LC and the LHC. An e^+e^- collider with $\sqrt{s}=500$ GeV can make a preliminary measurement of the top quark Yukawa coupling. However, the small rate at $\sqrt{s} = 500$ GeV implies that a precision measurement will require a higher energy. At $\sqrt{s}$ = 800-1000 GeV, the top quark Yukawa coupling will be determined with a 4-5% precision.

The LHC measures the product of the production cross section multiplied by the Higgs branching ratios and will be instrumental in obtaining a first set of measurements of ratios of Higgs coupling constants. In order to extract the top quark Yukawa coupling, it is typically assumed that the Higgs decays with Standard Model branching ratios. With this assumption, the LHC will obtain absolute couplings in some channels. This assumption could be removed with precision measurements of the Higgs branching ratios at a Linear Collider.

3.1.3 Determining the parameters of the Higgs boson potential

The LHC is widely regarded as capable of directly observing the agent responsible for electroweak symmetry breaking and fermion mass generation. This is generally believed to be a light Higgs boson [26]. The LHC will easily find a light SM Higgs boson with very moderate luminosity [94, 95] and have significant capability to determine many of its properties, such as its decay modes and couplings [45, 46, 52, 54, 95, 96]. An e^+e^- linear collider could significantly improve these preliminary measurements, in some cases by an order of magnitude in precision [57].

Starting from the requirement that the Higgs boson has to restore unitarity of weak boson scattering at high energies in the SM [97], perhaps the most important measurement after the Higgs boson discovery is of the Higgs potential itself, which requires measurement of the Higgs boson self-couplings. These can be probed directly only by multiple Higgs boson production. Several studies of Higgs boson pair production in e^+e^- collisions have been conducted over the past few years [98–100], deriving quantitative sensitivity limits for the trilinear Higgs self-coupling for several proposed linear colliders for $m_H \leq 140$ GeV. The potential of hadron colliders has been examined only recently [101–103], investigating Higgs pair production via gluon fusion and various subsequent decays. They established that future hadron machines can probe the Higgs potential over a wide range of Higgs mass.

To show the complementarity of hadron and lepton colliders we add to the existing literature by looking at Higgs boson pair production for $m_H \leq 140$ GeV at hadron colliders, and estimate the prospects for probing the Higgs boson self-coupling at a linear collider if $m_H \geq 150$ GeV. Using this input we determine how well the Higgs potential could be reconstructed. We closely follow our argument in Ref. [104].

The trilinear and quartic Higgs boson couplings λ and $\tilde{\lambda}$ are defined through the potential

$$V(\eta_H) = \frac{1}{2} m_H^2 \eta_H^2 + \lambda v \eta_H^3 + \frac{1}{4} \tilde{\lambda} \eta_H^4, \tag{3.19}$$

where η_H is the physical Higgs field. In the SM, $\tilde{\lambda} = \lambda = \lambda_{SM} = m_H^2/(2v^2)$. Regarding the SM as an effective theory, the Higgs self-couplings λ and $\tilde{\lambda}$ are *per se* free parameters. S-matrix unitarity constrains $\tilde{\lambda}$ to $\tilde{\lambda} \leq 8\pi/3$ [97]. Since future collider experiments likely cannot probe $\tilde{\lambda}$, we focus on the trilinear coupling λ in the following.

3.1.3.1 A low mass Higgs boson ($m_H \leq 140$ GeV)

• LHC/SLHC

At LHC energies, inclusive Higgs boson pair production is dominated by gluon fusion, although weak boson fusion production and weak boson or top quark pair associated production are also possible. Since Higgs pair production is already rate limited, we consider only the gluon fusion process in the following.

For $m_H < 140$ GeV, the dominant decay mode of the SM Higgs boson is $H \to b\bar{b}$. Unfortunately, the $4b$ channel (both Higgs bosons decaying to $b\bar{b}$) is completely overwhelmed by the enormous QCD background, which is larger by more than two orders of magnitude. For completeness, we performed a calculation of the signal and background, including the effects of NLO-QCD corrections to the signal via a

multiplicative factor. After including kinematic cuts and realistic efficiency factors for the b jets, a χ^2 test on the m_{vis} distribution for $m_H = 120\,\text{GeV}$ we obtained meaningless 1σ bounds of $-6.8 < \Delta\lambda_{HHH} < 10.1$, where $\Delta\lambda_{HHH} = \lambda/\lambda_{SM} - 1$.

A more advantageous S/B is conceivable if one of the Higgs bosons in $gg \to HH$ decays into a τ pair. In this case, the main contributions to the background arise from continuum $b\bar{b}\tau^+\tau^-$ and $t\bar{t}$ production. The τ-pair invariant mass can be reconstructed with fairly good resolution. We considered the leptonic-hadronic decay channel of the τ pair, to satisfy detector trigger requirements. Unfortunately, no limit can be extracted for the LHC. Even for a luminosity-upgraded LHC (SLHC) achieving 3000 fb^{-1}, we expect a possible 1σ limit extraction of only $-1.6 < \Delta\lambda_{HHH} < 3.1$, too weak to be useful. We find even worse results for the final state $b\bar{b}\mu^+\mu^-$: while background rejection is much better, this channel suffers from simple lack of signal rate due to the extremely small Higgs boson branching ratio to muon pairs - we could expect only about 2 events at the SLHC.

The best strategy appears to be to consider the rare decay of one Higgs boson to a photon pair, while allowing the other to decay to its dominant channel, $b\bar{b}$ [103]. The background consists of QCD $b\bar{b}\gamma\gamma$ production and numerous similar QCD processes where one or more of the b jets or photons is a fake from charm or light jets. We also must include contributions from single Higgs boson production in association with photons and jets, as well as double parton scattering and fakes from multiple interactions. The latter are of little concern at the LHC, so we may employ a single b-tag strategy: for $\epsilon_b = 50\%$, this retains three times the number of signal events as double b-tagging. However, multiple interactions is a serious problem at an SLHC, which we bring under control with double b-tagging.

We impose kinematic cuts to enhance the signal relative to background, and use conservative estimates for the efficiency to identify the final state, $\epsilon_\gamma = 80\%$ and $\epsilon_b = 50\%$, as well as the more pessimistic probabilities from ATLAS for charm and light jets to fake the signal final state: $P_{c\to b} = 1/13$, $P_{j\to b} = 1/140(1/23)$ and $P_{j\to\gamma} = 1/1600$ for the LHC(SLHC). Under these conditions we expect to observe about 6(21) signal events at the LHC(SLHC), on a background of 14(25) events. The S/B ratio is quite respectable, but the statistics are low at the LHC. A χ^2-test yields limits of $-1.1 < \Delta\lambda_{HHH} < 1.9$ for 600 fb^{-1} at the LHC, and $-0.66 < \Delta\lambda_{HHH} < 0.82$ for 6000 fb^{-1} at the SLHC. These limits improve by about 15% if the more optimistic ATLAS estimate of $P_{j\to\gamma} = 1/2500$ can be achieved. Another promising approach is to subtract the backgrounds after measuring them in other kinematic regions, a technique already used by CDF. In this case, the expected limits improve to $-0.74(0.46) < \Delta\lambda_{HHH} < 0.94(0.52)$ at the LHC(SLHC).

• LC

We now turn our attention to Higgs boson pair production in e^+e^- collisions. A detailed study of how well the Higgs boson self-coupling for $m_H = 120$ GeV could be measured in $e^+e^- \to ZHH$ at $\sqrt{s} = 500$ GeV can be found in Ref. [100].

Associated ZHH production followed by $HH \to b$+jets is the dominant source of HH events in the SM if $m_H \leq 140$ GeV. The main backgrounds in this channel are $\bar{t}t$ and W^+W^- production. These are efficiently suppressed by performing a NN analysis. Such an analysis, including a detailed detector simulation, was presented in Ref. [100] for $m_H = 120$ GeV and $\sqrt{s} = 500$ GeV. It concluded that λ could be de-

termined with a precision of about 23% if an integrated luminosity of 1 ab^{-1} could be achieved. The limits achievable at hadron colliders for $m_H = 120$ GeV are significantly weaker.

Since the ZHH cross section and its sensitivity to λ decrease with increasing collider energy, a linear collider operating at 500 GeV offers the best chance for a precise measurement of λ for $m_H \leq 140$ GeV; the bounds we obtain for $\sqrt{s} = 500$ GeV are up to a factor 1.4 (1.9) more stringent than those achievable for $\sqrt{s} = 800$ GeV ($\sqrt{s} = 1$ TeV). The advantage of operating at 500 GeV gradually disappears with increasing Higgs boson mass, due to the reduced phase space. The sensitivity limits achievable weaken by a factor 1.8 (1.2) for $\sqrt{s} = 500$ GeV ($\sqrt{s} = 1$ TeV) if m_H increases from 120 GeV to 140 GeV; for $m_H = 140$ GeV one will not be able to probe λ with a precision of better than 50% for unpolarized beams. If both the electron and positron beams could be polarized, the bounds derived here improve by a factor 1.3, assuming 80% polarization for the electron beam and 60% for the positron beam, and the same integrated luminosity as for unpolarized beams.

We conclude that a 0.5–1 TeV linear collider offers a significantly better chance to probe λ for the mass range from 120 GeV to 140 GeV, although an upgraded LHC could provide convincing proof of spontaneous symmetry breaking.

3.1.3.2 A heavier Higgs boson ($m_H \geq 140$ GeV)

For $m_H \geq 140$ GeV, the principal Higgs boson decay is to W pairs. This completely changes the phenomenology of Higgs pair production.

• LHC/SLHC

We have previously examined this mass range for the LHC [102]. Due to the huge QCD backgrounds in multijet final states, we can use only multiplepton subsamples, where two same-sign W bosons decay leptonically and the other two give four jets, or where three W's decay leptonically and the events have only two extra jets. Summarizing our previous results, the LHC could give 1σ constraints of $-0.4 < \Delta\lambda_{HHH} < 1.9$ [102, 105] for $m_H = 180$ GeV. This is sufficient to exclude the case of no self-coupling to slightly better than 95% c.l. for $150 \lesssim m_H \lesssim 200$ GeV, proving the existence of spontaneous symmetry breaking, and is a fortuitous effect of the destructive interference of the two diagrams in the gluon fusion process. An SLHC could instead make a $20 - 30\%$ measurement (95% CL) of the self-coupling over the mass range $160 < m_H < 180$ GeV.

• LC

If $m_H > 140$ GeV, the channels yielding the largest event rates are $e^+e^- \to ZHH$ with $Z \to jj$ and $HH \to 8$ jets or $\ell\nu + 6$ jets. Final states of similar structure and complexity are encountered in $t\bar{t}H$ production. The main background processes contributing both to $e^+e^- \to ZHH$ and $e^+e^- \to t\bar{t}H$ are $WW+$ jets, $t\bar{t}+$jets and QCD multijet production. Instead of using a NN analysis, we investigate how the sensitivity bounds for λ depend on the signal efficiencies and the signal to background ratio. We then explore the prospects for determining the Higgs boson self-coupling in ZHH production for $m_H > 140$ GeV using some rough guidelines.

Since the number of signal events is small, we combine the $\ell\nu + 8$ jet and 10 jet

final states and use the total cross section to derive sensitivity limits. For the likely case that efficiencies and S/B are similar to the values obtained in the $t\bar{t}H$ analysis, a first-generation LC could obtain only very loose bounds on λ_{HHH}. Using the values quoted in Ref. [104], one finds $-4.1 < \Delta\lambda_{HHH} < 1.0$ at the 1σ level for $m_H = 180$ GeV, $\sqrt{s} = 1$ TeV and 1 ab^{-1}. The achievable limits improve by about a factor 1.3 for electron and positron beam polarizations of 80% and 60%, respectively, and if the same integrated luminosity as in the unpolarized case could be reached. We reach similar conclusions for $m_H = 160$ GeV and $\sqrt{s} = 800$ GeV. For $m_H < 160$ GeV and $m_H > 180$ GeV, fewer than 5 signal events would be seen if efficiencies are smaller than 0.5, disallowing bounds to be placed on λ_{HHH}.

At higher collision energies, one should consider $e^+e^- \to \nu\bar{\nu}HH$ production, which dominates over ZHH above about $\sqrt{s} = 1 - 1.5$ TeV, depending on the Higgs mass. We do not address this channel here, as it is under investigation elsewhere [106].

3.1.3.3 Reconstructing the Higgs Potential

The results presented above can be used to compare the capabilities of future lepton and hadron colliders to reconstruct the Higgs potential. In order to translate bounds on $\Delta\lambda_{HHH}$ into constraints on the Higgs potential which can be graphically displayed, it is convenient to consider the scaled Higgs potential

$$\frac{2}{v^2 m_H^2} V(x) = x^2 + \lambda_{HHH} x^3 + \frac{1}{4}\tilde{\lambda}_{4H} x^4 \ , \tag{3.20}$$

where $x = \eta_H/v$ and $\tilde{\lambda}_{4H} = \tilde{\lambda}/\lambda_{SM}$ is the four Higgs boson self-coupling normalized to the SM value, η_H is the physical Higgs field, and v is the vacuum expectation value. In the following we assume $\tilde{\lambda}_{4H} = 1$.

It should be noted that the scaled Higgs potential of Eq. (3.20) is valid only in the vicinity of $x = 0$. The presence of a non-SM HHH coupling requires higher dimensional terms in an effective Lagrangian which would modify $\tilde{\lambda}_{4H}$ and also create terms proportional to x^n with $n > 4$. These terms are ignored in Eq. (3.20). Eq. (3.20) with $\tilde{\lambda}_{4H} = 1$ thus represents a good approximation to the true scaled Higgs potential only if the contributions of terms proportional to x^n, $n \geq 4$, are much smaller than that of the x^3 term. This is guaranteed for sufficiently small values of x. We restrict the range of x for which we show the scaled Higgs potential to $|x| \leq 0.2$. Provided that the coefficients of the x^n, $n \geq 4$, terms are not much larger than λ_{HHH}, this guarantees that Eq. (3.20) is indeed a good approximation of the true Higgs potential.

In Fig. 3.13 we show how well the scaled Higgs potential could be reconstructed for a Higgs boson of mass $m_H = 120$ GeV and $m_H = 180$ GeV. Hadron colliders indeed have only very limited capabilities to probe λ if $m_H \leq 140$ GeV, although with sufficient luminosity they can provide proof of spontaneous symmetry breaking. The best channel appears to be the semi-rare decay to $b\bar{b}\gamma\gamma$ final states. This channel should now be studied with full detector simulation. In contrast, a 500 GeV linear collider with an integrated luminosity of 1 ab^{-1} could measure $\Delta\lambda_{HHH}$ with a precision of about 20% [100], reconstructing the Higgs potential fairly accurately. We draw similar conclusions for other Higgs boson masses in the range $120\ \mathrm{GeV} < m_H < 140$ GeV. The limits achievable for $\Delta\lambda_{HHH}$ both at lepton and hadron colliders gradually weaken by about a factor 2 if m_H is increased from 120 GeV to 140 GeV.

If the Higgs boson decays predominantly into a pair of W-bosons, i.e. if $m_H \geq 150$ GeV, a completely different picture emerges. While LHC experiments will only be able to put mild constraints on $V(x)$, a luminosity upgrade of the LHC will make it possible to reconstruct the Higgs potential quite precisely for this m_H range. Of course, to control systematic uncertainties associated with knowledge of the Higgs branching ratios and top Yukawa coupling, ideally one would have precision input from a linear collider. Thus, having both collider data sets at hand would greatly increase our understanding of the Higgs potential in this mass region.

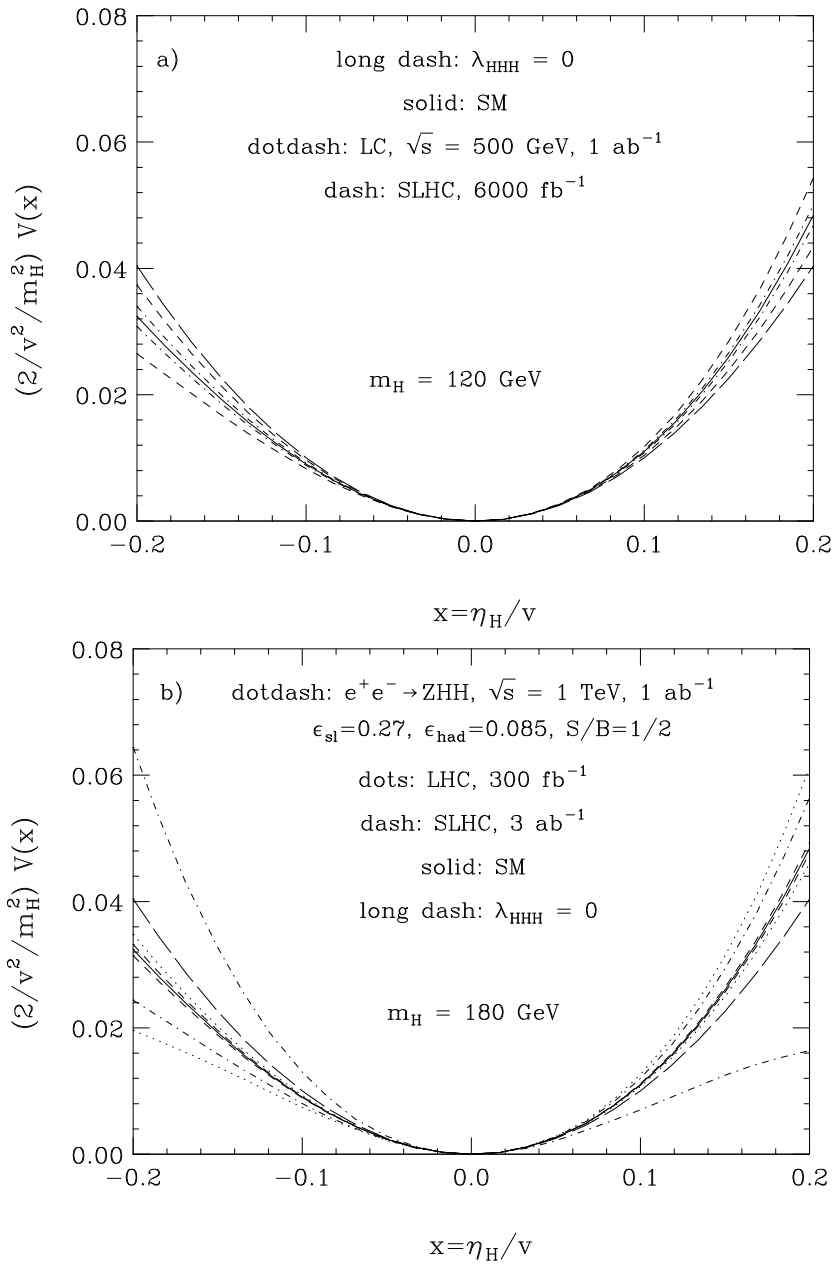

Figure 3.13: Constraints on the scaled Higgs potential for a) $m_H = 120$ GeV and b) 180 GeV. The allowed region is between the two lines of equal texture. The solid line represents the SM Higgs potential, and the long-dashed line shows the result for a vanishing Higgs boson self-coupling.

At a linear collider with a center of mass energy in the 0.8—1 TeV range and an integrated luminosity of 1 ab^{-1}, the number of Higgs boson pair events is very limited. The dominant $WW+$ jets and $t\bar{t}+$ jets backgrounds are several orders of magnitude larger than the signal. As a result, it will be difficult to constrain the Higgs potential using linear collider data if $m_H \geq 150$ GeV. This point is illustrated in Fig. 3.13b assuming the efficiencies and the signal to background ratios to be equal to Ref. [69] for $e^+e^- \to t\bar{t}H$. We obtain results similar to those shown in Fig. 3.13 for $m_H = 160$ GeV.

It should be noted that the prospects to determine the Higgs boson self-coupling and to reconstruct the Higgs potential at an e^+e^- collider for a Higgs boson with mass larger than 150 GeV improve dramatically at larger energies.

3.1.3.4 Conclusions

Our results show that hadron colliders and e^+e^- linear colliders with $\sqrt{s} \leq 1$ TeV are complementary: for $m_H \leq 140$ GeV, linear colliders offer significantly better prospects in measuring the Higgs boson self-coupling, λ; for a Higgs boson in the range $m_H \geq 150$ GeV, the opposite is true. However, to actually perform a meaningful measurement at a hadron collider would demand precision Higgs boson properties input for the top quark Yukawa coupling, the HWW coupling, and the total Higgs boson decay width.

While the LHC can obtain meaningful information on the Higgs total width [47, 105], this is at best at the 15% level for $m_H \geq 160$ GeV, and about a factor of 2 worse in the lower mass region. For individual couplings, the LHC would measure the HWW coupling to about $10(25)\%$ in the upper(lower) mass region, and the top Yukawa coupling at about the $25-30\%$ level. These values constitute large enough systematics to seriously complicate LHC HH measurements. A LC is vastly superior for the HWW coupling and total Higgs width, with a precision at the few percent level. For the top Yukawa coupling, a LC with center of mass energy up to 1 TeV is superior in the lower m_H region, where it can improve the precision to about 15% (see Sec. 2.1.2). It is possibly competitive closer to the WW threshold, although the status of these studies is still not fully mature. A laudable goal would be to remove many of the systematic uncertainty assumptions both LHC and LC studies currently make, to provide more accurate estimates of the ultimate precision achievable, as it would greatly affect the interpretation of LHC results.

3.1.4 Higgs boson decay into jets

3.1.4.1 Introduction

Current strategies for the discovery and measurement of the properties the neutral scalar Higgs particle h with $m_h < 135$ GeV rely heavily on the presumption that the principal branching fractions are close to those predicted in the standard model (SM) or in the usual minimal supersymmetric standard model (MSSM). For masses in this range, the decay width of the SM Higgs boson is dominated by its decay into a pair of bottom quarks, $b\overline{b}$. Since the SM bottom-quark Yukawa coupling is small, these assumptions are not warranted in the presence of non-standard light particles with order one couplings to the Higgs boson. Searches can become particularly difficult

at hadron colliders if the Higgs boson decays predominantly into these new particles and if these particles decay mainly into jets, with no significant bottom or charm flavor content. Ref. [107] shows explicitly that this situation can arise in the MSSM in the presence of light bottom squarks ($\tilde{b}$'s), with mass smaller than about 10 GeV. In this case, $\tilde{b}$ is the lightest supersymmetric particle (LSP). The bottom squarks are assumed to decay primarily into a pair of light quarks via an R-parity-violating interaction. The main results of our study, however, are applicable to a general class of models in which the main modification to the Higgs boson branching ratios is induced by the appearance of an additional decay mode into hadron jets.

The possibility that the Higgs boson decays with substantial branching ratio into jets is not unique to the light bottom squark scenario. It results also in models in which there is a light CP-odd scalar in the spectrum whose mass is less than $2m_b$. The Higgs boson then can decay into a pair of these scalars (and in general, owing to the smallness of the bottom Yukawa coupling, it will unless the coupling to the CP-odd scalars is very small). This possibility was discussed in Ref. [108] in a model in which the CP-odd scalar behaves like an axion. It may arise also in general two-Higgs-doublet models, and even in the MSSM with explicit CP-violation [109]. Quite generally, if the mass of the CP-odd scalar is above a few GeV, but below twice the bottom quark mass, the CP-odd scalar decay into jets will overwhelm the decay into two photons. The Higgs boson would then decay in a way that resembles the results in the light bottom squark scenario, namely, it will decay predominantly into two scalars that subsequently decay into jets. The exact phenomenology of the light CP-odd scalar scenario will be different from that of the light bottom squark scenario, and it should be analyzed in more detail. For instance, one should determine the values of the branching ratio of the CP-odd scalar into two photons that would permit observation of the Higgs boson in the photon plus jet channel. For the aims of this work, we assume that the branching ratio of the Higgs boson decay into photons plus jets is sufficiently small, so that this search channel is not suitable.

3.1.4.2 Higgs decays in a model with a light bottom squark

To exemplify quantitatively the modifications of the branching ratios to SM particles, we summarize the case of Higgs boson decay to light bottom squarks. The possible existence of a light bottom squark $\tilde{b}$ (and a light gluino $\tilde{g}$) is advanced in Ref. [110] to address the excess rate of bottom quark production at hadron colliders. [2] We work in the decoupling limit in which the mass of the CP-odd Higgs boson (m_A) is large compared to m_Z, and we assume that the ratio of Higgs boson vacuum expectation values $\tan\beta$ is large. Under these conditions, $\Gamma_{\tilde{b}}/\Gamma_b \propto (\mu \tan\beta/m_h)^2$, where μ is the Higgsino mass parameter. In the case of light bottom squarks, the dominant decay of h is into a $\tilde{b}\tilde{b}^*$ pair[3] [107, 112], and the total decay width of the h may become several orders of magnitude larger than the width for the decay into $b\bar{b}$. A plot of the Higgs branching fractions is presented in Fig. 3.14 as a function of $\mu \tan\beta/m_h$. Note that the partial Higgs widths into SM decay modes (excluding the gg and $\gamma\gamma$

[2] Various experimental constraints and phenomenological implications are examined in Ref. [111].
[3] Here, $\tilde{b}^*$ is the anti-particle of $\tilde{b}$.

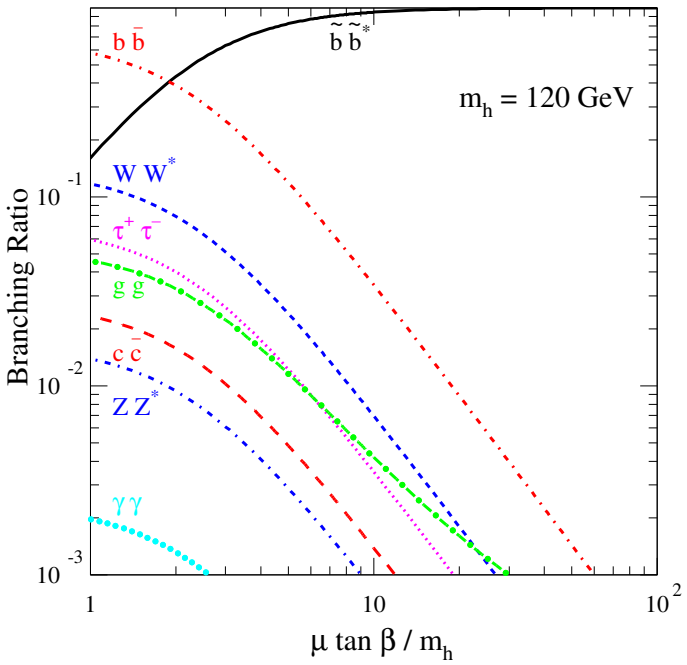

Figure 3.14: *Branching fractions for various Higgs boson decay channels as a function of the ratio* $\mu \tan\beta/m_h$*, with* $m_h = 120$ *GeV and* $m_{\tilde{b}} = 5$ *GeV. The partial widths for Higgs decay into* WW^**,* ZZ^**,* $b\overline{b}$*,* $c\overline{c}$ *and* $\tau^+\tau^-$ *are assumed to be equal to their SM values. The partial widths for Higgs decay into* gg *and* $\gamma\gamma$ *include the effects of the light bottom squarks in the corresponding loop amplitudes.*

modes[4]) are assumed to be given by their SM values (in particular, we assume that radiative corrections to these widths due to supersymmetric particle exchanges are negligible). Consequently, the Higgs branching fractions into SM decay channels are reduced from their SM values by a factor proportional to $\tan^{-2}\beta$ once the $\tilde{b}\tilde{b}^*$ decay mode is dominant. At $m_h = 120$ GeV, the $b\overline{b}$ and $\tilde{b}\tilde{b}^*$ branching fractions cross each other for $\mu \tan\beta/m_h \simeq 1.9$, where each of the branching fractions is about 0.4.

3.1.4.3 Higgs boson decay to jets at the LHC

Having demonstrated the feasibility of the scenario under study, we concentrate on searches for such a Higgs boson. At the Large Hadron Collider (LHC), a SM-like Higgs boson of mass less than ~ 135 GeV is expected to be discovered through a variety of production processes and decay modes [41, 89, 113]. These standard searches look for Higgs boson decays into SM particles. As indicated in Fig. 3.14, the presence of an additional, dominant decay mode into hadron jets may suppress the branching ratios of these decay modes by a factor of order of ten to several hundred, depending on the coupling of the Higgs boson to the new particles. This reduction raises serious questions as to the capability of experiments at the LHC to discover the Higgs boson.

[4]The partial Higgs widths into gg and $\gamma\gamma$ (these decay modes are absent at tree-level and only arise at the loop level) include the effects of the light bottom squarks in the corresponding loop amplitudes.

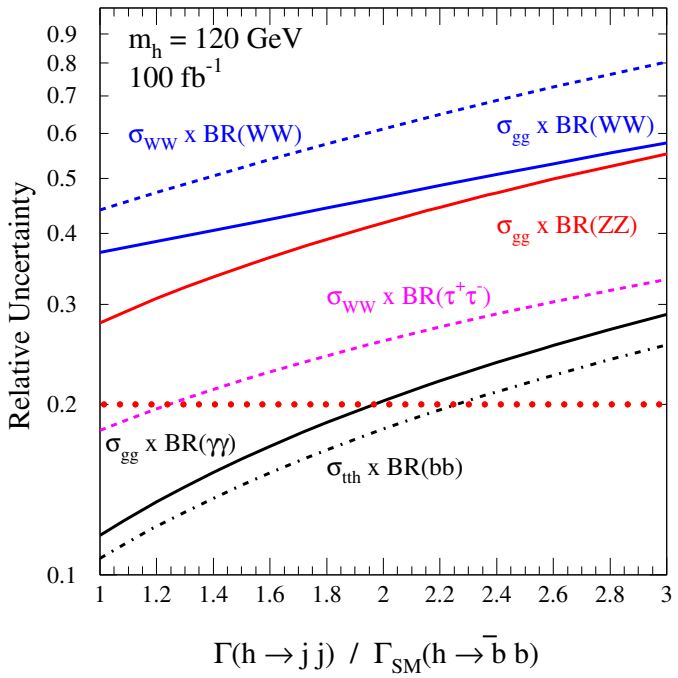

Figure 3.15: *Expected accuracy in LHC measurements of the product of production cross sections and branching ratios for the WW, ZZ, $b\bar{b}$, $\gamma\gamma$, and $\tau^+\tau^-$ decay modes of a Higgs boson with mass 120 GeV as a function of the ratio of the jet-jet and the $b\bar{b}$ widths. The horizontal dotted line at 0.2 indicates the 5σ discovery reach under the assumption $B \gg S$. The partial widths for Higgs decay into WW^*, ZZ^*, $b\bar{b}$, $c\bar{c}$, gg, $\gamma\gamma$, and $\tau^+\tau^-$ and the production cross sections are assumed to be equal to their SM values.*

The more standard decays are suppressed, and the principal decay mode into jets suffers from enormous QCD backgrounds.

At the LHC, it is difficult to obtain information about the Higgs boson couplings in a model-independent way because it is impossible to observe all possible decays in a single production mode. One must be content with measurements of cross sections times branching ratios and cannot make definitive statements about the couplings themselves. In Fig. 3.15, for $m_h = 120$ GeV, we show the accuracies that we expect could be achieved at the LHC (assuming a total integrated luminosity of $100\ \mathrm{fb}^{-1}$) for measurements of the rates (cross sections times branching ratios) of gluon fusion into a Higgs boson followed by $h \to \gamma\gamma$, WW^*, and ZZ^*, and for weak boson fusion into a Higgs boson followed by the decays $h \to WW^*$ and $h \to \tau^+\tau^-$. The accuracies are shown as a function of the ratio of the jet-jet and the $b\bar{b}$ widths. By presenting the plot in this way, the results are more general than the specific supersymmetric model discussed above, and apply to any model of new physics in which the Higgs couplings to light quarks and gluons are modified. In particular, the jet-jet width is the sum of the partial widths for decay into the new hadron channel ($\tilde{b}\tilde{b}^*$ in the supersymmetry example given above), plus $b\bar{b}$, $c\bar{c}$, and gg. The Higgs cross-sections[5] and partial Higgs

[5]Details on the Higgs cross-sections used in this analysis can be found in in Ref. [107].

widths into SM decay modes are assumed to be given by their SM values (that is, radiative corrections to these widths due to supersymmetric particle exchanges are neglected.) In the SM, $\Gamma(h \to \text{jets})/\Gamma(h \to b\bar{b}) = 1.12$, primarily due to the WW^* (where the W^* decays hadronically), gg and $c\bar{c}$ Higgs decay modes.[6] The relative uncertainties contain statistical effects, $\sqrt{S+B}/S$, where we use estimates of the backgrounds and SM signal rates presented in Refs. [114] and [45]. The production through weak boson fusion followed by decay into W bosons is based on leptonic W decays into one electron and one muon, and includes a presumed systematic uncertainty of 30%.

For values of the branching ratio $\text{BR}(h \to \text{jets})$ larger than two to five times that into bottom quarks, the large QCD jet backgrounds will make observation of the h very difficult in Tevatron and LHC experiments. In the particular example of light bottom squarks, however, experiments at these colliders may see evidence of low-energy supersymmetry and/or the heavy SUSY Higgs bosons (note, however, the standard missing-energy signature of conventional SUSY is compromised if a charged $\tilde{b}$ is the LSP).

3.1.4.4 Higgs boson decay to jets at the LC

We now consider a Higgs boson decaying into jets at a high energy e^+e^- linear collider. For a light Higgs boson the dominant production process is $e^+e^- \to Z^0h$ via an intermediate Z^0 [115]. Once the Z^0 is identified, the Higgs boson is discovered, independent of the Higgs boson decay modes, as a clean enhancement in the distribution of mass recoiling from the Z^0 [115], and the mass of the Higgs boson can be measured. The backgrounds from the W fusion and Z^0 fusion processes are small. Because the Zh cross section depends on the hZZ coupling strength, observation of the Higgs boson determines this coupling with an expected accuracy of $\sim 1.2\%$ [115] and can establish the Higgs boson as the principal scalar responsible for electroweak symmetry breaking. These statements remain valid if the Higgs boson decays primarily into a pair of jets since the method does not depend on the Higgs boson decay products.

In the weak boson fusion process, the jet-jet Higgs boson decay channel can also be used to determine the hWW coupling at large $\mu \tan\beta/m_h$ with significantly greater anticipated accuracy than from the $b\bar{b}$ channel [7]. In Fig. 3.16, we show the accuracies that we expect could be achieved in the measurements of the $b\bar{b}$ branching fraction, the hZZ and hWW coupling strengths, and the total width of the Higgs boson, all as a function of the ratio of the jet-jet and the $b\bar{b}$ widths. We distinguish the accuracies to be expected for the hWW coupling strength depending upon whether the $b\bar{b}$ or jet-jet

[6] Note that the left-most edge of the plot in Fig. 3.15, *i.e.* $\Gamma(h \to \text{jets})/\Gamma(h \to b\bar{b}) = 1$, would correspond to a case in which the Higgs decay to bottom quarks is the only hadronic decay mode of the Higgs boson.

[7] To obtain the uncertainty on the branching fraction into a pair of jets, we must first estimate the number of signal and background events in the jet-jet channel. We begin with the numbers presented in Ref. [66] of simulated signal and background events for $h \to b\bar{b}$ in the process $e^+e^- \to Zh$. We remove the b-tag requirement, increasing both signal and background by $(1/0.75)^2$. The signal sample is then multiplied by (1/0.69), the inverse of the SM $b\bar{b}$ branching fraction, and by the jet-jet branching fraction in our model. Since the primary background arises from Z decay, the background is increased by $1/R_b \simeq 1/0.21$, where R_b is the measured fraction of the hadronic width of the Z into $b\bar{b}$.

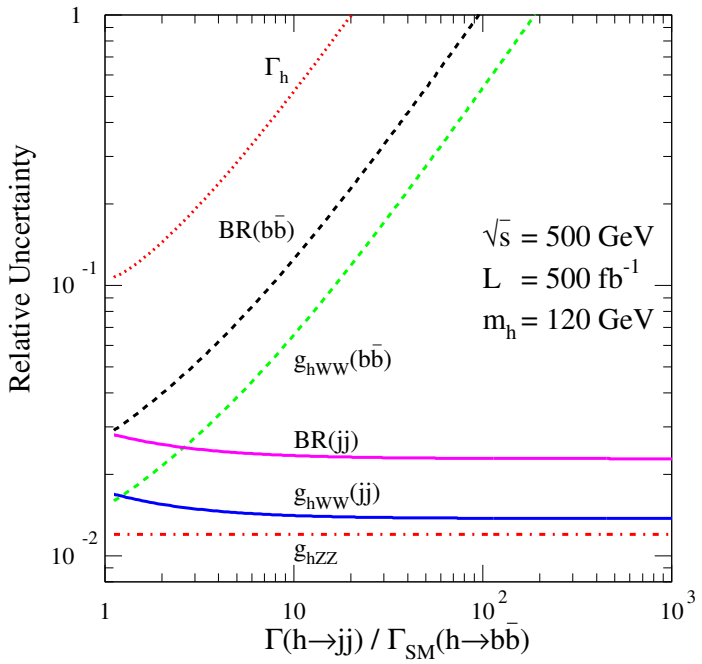

Figure 3.16: *Expected accuracy in the measurements of the $b\bar{b}$ and jet-jet branching fractions, the hZZ and hWW coupling strengths, and the total width of the Higgs boson, as a function of the ratio of the jet-jet and the $b\bar{b}$ widths. The Higgs boson partial widths to $b\bar{b}$, $c\bar{c}$, gg, ZZ^*, and WW^* are taken to be equal to their SM values.*

decay mode of the Higgs boson is used. In this plot, the jet-jet width includes the partial widths into the new non-standard particles ($\tilde{b}\tilde{b}^*$ in the MSSM example), plus gg, $b\bar{b}$ and $c\bar{c}$ (the partial Higgs widths for the latter three channels are fixed to their SM values).

Because they rely principally on the production process $e^+e^- \to hZ^0$, experiments at proposed e^+e^- linear colliders remain fully viable for direct observation of the h and measurement of its mass and some of its branching fractions [107]. The possibility of measuring the Higgs boson width, however, is diminished owing to the large suppression of the decay branching ratio into the weak gauge bosons. If the width exceeds about 2 GeV, a direct measurement should be possible from the invariant mass distribution in the jet-jet channel.

3.1.4.5 Conclusions

In the scenario considered here, the Higgs boson decays to a large extent into hadronic jets, possibly without definite flavor content. Measurements of various properties of the Higgs boson, such as its full width and branching fractions, may therefore require a substantial improvement in the experimental jet-jet invariant mass resolution and a more thorough understanding of backgrounds in the jet-jet channel. Full event and reconstruction studies done for the SM decay $h \to gg$ (where the SM branching frac-

tion is $\sim 5\%$ for $m_h = 120$ GeV) should be pursued further to establish the extent to which properties of the Higgs boson can be determined solely from the jet-jet mode.

The existence of a light Higgs boson, observable at the LHC, is often considered the hallmark of the *minimal* supersymmetric standard model. A light Higgs boson decaying into bottom squarks, undetected at the LHC could thus lead one to conclude erroneously that the underlying effective theory is more exotic than the minimal supersymmetric extension. On the other hand, a Higgs boson that decays into jets can be studied quite well at a linear collider (LC), a point that emphasizes the complementary nature of the LHC and a LC in this scenario. The LHC, with enormous energy and luminosity should be able to produce, discover, and study in great detail possible new physics at the weak scale (the super-partners in the supersymmetry example). The LC can discover and study the Higgs boson. In order to truly understand electroweak symmetry breaking and the solution of the hierarchy problem, both aspects are crucial. As a further possibility, one might produce super-partners at the LHC that decay 'through' light Higgs bosons into jets and not realize what the intermediate state is. In a situation such as this one, it might even be impossible to identify the parent super-particles, despite their having properties rather ordinary from the point of view of the MSSM. The analysis and understanding of data from concurrent operation of the LHC and a LC may prove crucial.

3.2 Determination of CP properties of Higgs bosons

In this section we briefly summarise the information on determination of CP properties of Higgs bosons at different colliders and identify areas of investigations to study the issue of LHC-LC synergy.

3.2.1 CP studies of the Higgs sector

3.2.1.1 Introduction

Studies of the CP properties of the Higgs sector, which will involve establishing the CP eigenvalue(s) for the Higgs state(s) if CP is conserved, and measuring the mixing between the CP-even and CP-odd states if it is not, will certainly be part of the physics studies at future colliders [57, 116, 117]. CP violation in the Higgs sector [118], possible in multi-Higgs models, is indeed an interesting option to generate CP violation beyond that of the SM, possibly helping to explain the observed Baryon Asymmetry of the Universe [119].

In order to identify the CP nature of a Higgs boson, one must probe the structure of its couplings to known particles, in either its production or decay. At tree level, the couplings of a neutral Higgs boson ϕ, which may or may not be a CP eigenstate,[8] to fermions and vector bosons can be written as

$$f\bar{f}\phi: \ -\bar{f}(v_f + ia_f\gamma_5)f\,\frac{gm_f}{2m_W}, \qquad VV\phi: \ c_V\,\frac{gm_V^2}{m_W}\,g_{\mu\nu} \tag{3.21}$$

[8] For CP eigenstates, a pure scalar will be denoted by H and a pure pseudoscalar by A. Otherwise we use the generic notation ϕ.

where g is the usual electroweak coupling constant; v_f, a_f give the Yukawa coupling strength relative to that of a SM Higgs boson, and c_V ($V = W,\ Z$) are the corresponding relative couplings to gauge bosons. In the SM, for a CP-even Higgs $v_f = c_V = 1$ and $a_f = 0$. A purely CP-odd Higgs boson has $v_f = c_V = 0$ and $a_f \neq 0$, with the magnitude of a_f depending on the model. In CP-violating models, v_f, a_f and c_V may all be non-zero at tree level. In particular, in the case of a general 2HDM or the MSSM with CP violation, there are three neutral Higgs bosons ϕ_i, $i = 1, 2, 3$, which mix with each other and share out between them the couplings to the Z, W and fermions; various sum rules are given in [120–122]. Due to this fact, limits on the MSSM (and 2HDM) Higgs sector implied by LEP data are strongly affected by the presence of CP violation [109, 121, 123].

In most formulations of CP-violating Higgs sectors [109, 122, 124–127] the amount of CP mixing is small, being generated at the loop level, with only one of the couplings to gauge bosons or fermions sizable. In most cases, the predicted CP mixing is also a function of the CP-conserving parameters of the model, along with the CP-violating phases.[9] Thus observation and measurement of this mixing at the LC may give predictions for LHC physics; for instance for sparticle phenomenology in the MSSM. Moreover, experiments at different colliders have different sensitivities to the various couplings of eq. 3.21. Hence a combination of LHC, LC and photon collider (PLC) measurements of both CP-even and CP-odd variables may be necessary to completely determine the coupling structure of the Higgs sector. These are two ways in which the high potential of LHC-LC synergy for CP studies can be realized.

In what follows, we give an overview of the LHC, LC, and PLC potentials for CP studies in the Higgs sector. An example of the LHC-LC synergy is presented as well.

3.2.1.2 CP Studies at the LHC

There are several ways to study the CP nature of a Higgs boson at the LHC. In the resonant s-channel process $gg \to \phi \to f\bar{f}$, the scalar or pseudoscalar nature of the Yukawa coupling gives rise to $f\bar{f}$ spin-spin correlations in the production plane [130]. A more recent study [131] looks at this process in the context of a general 2HDM.

In the process $gg \to t\bar{t}\phi$, the large top-quark mass enhances the $v^2 - a^2$ contribution, allowing a determination of the CP-odd and CP-even components of a light Higgs Boson [132, 133]. While this method should provide a good test for verifying a pure scalar or pseudoscalar, examination of a mixed CP state would be far more challenging, requiring $600\ \mathrm{fb}^{-1}$ to distinguish an equal CP-even/CP-odd mixture at $\sim 1.5\,\sigma$ [132].

Higgs decay into two real bosons, $\phi \to ZZ$, with $Z \to l^+l^-$, [134,135] can be used to rule out a pseudoscalar state by examining the azimuthal or polar angle distributions between the decay lepton pairs. Below the threshold, $\phi \to Z^*Z$, extra information is provided by the threshold behavior of the virtual Z boson invariant mass spectrum. This way, one could rule out a pure 0^- state at $> 5\sigma$ with $100\ \mathrm{fb}^{-1}$ in the SM. An extension of these studies to scalar-pseudoscalar mixing is under progress.

In weak boson fusion, the Higgs boson is produced in association with two tagging jets, $qq \to W^+W^-qq \to \phi qq$. As with the decay to ZZ, the scalar and pseu-

[9] For the MSSM with explicit CP violation, computational tools for the Higgs sector are available [128, 129].

doscalar couplings lead to very different azimuthal distributions between the two tagging jets [136]. A similar idea may be employed in $\phi + 2jets$ production [137] in gluon fusion. Higher order corrections [138] may, however, reduce this correlation effect strongly.

Another approach uses the exclusive (inclusive) double diffractive process $pp \to p + \phi + p$ ($pp \to X + \phi + Y$) [139–141] with large rapidity gaps between the ϕ and the (dissociated) protons. The azimuthal angular distribution between the tagged forward protons or the transverse energy flows in the fragmentation regions reflect the CP of the ϕ and can be used to probe CP mixing. This process is particularly promising for the region $m_\phi < 60$ GeV, in which a Higgs signal may have been missed at LEP due to CP violation.

3.2.1.3 CP Studies at an e^+e^- Linear Collider

In e^+e^- collisions, the main production mechanisms of neutral Higgs bosons ϕ are (a) Higgsstrahlung $e^+e^- \to Z\phi$, (b) WW fusion $e^+e^- \to \phi\,\nu\bar{\nu}$, (c) pair production $e^+e^- \to \phi_i\,\phi_j$ ($i \neq j$) and (d) associated production with heavy fermions, $e^+e^- \to f\bar{f}\phi$. Studies of CP at the Linear Collider aim at extracting the relevant couplings mentioned in eq. 3.21. Recall that a pure pseudoscalar of the 2HDM or MSSM does not couple to vector bosons at tree level. The observation of all three ϕ_i ($i = 1, 2, 3$) in a given process, e.g. $e^+e^- \to Z\phi_{1,2,3}$, therefore represents evidence of CP violation [142–144].

In the Higgsstrahlung process, if ϕ is a pure scalar the Z boson is produced in a state of longitudinal polarization at high energies [145, 146]. For a pure pseudoscalar, the process proceeds via loops and the Z boson in the final state is transversally polarized. The angular distribution of $e^+e^- \to ZH$ is thus $\propto \sin^2\theta_Z$, where θ_Z is the production angle of the Z boson w.r.t. to the beam axis in the lab frame, while that of $e^+e^- \to ZA$ is $\propto (1 + \cos^2\theta_Z)$. A forward-backward asymmetry would be a clear signal of CP violation. Furthermore, angular correlations of the $Z \to f\bar{f}$ decay can be used to test the J^{PC} quantum numbers of the Higgs boson(s). Measurements of the threshold excitation curve can give useful additional information [147, 148]. A study in [57] parametrized the effect of CP violation by adding a small ZZA coupling with strength η to the SM matrix element, $\mathcal{M} = \mathcal{M}_{ZH} + i\eta\mathcal{M}_{ZA}$, and showed that η can be measured to an accuracy of 0.032 with 500 fb^{-1}.

Angular correlations of Higgs decays can also be used to determine the CP nature of the Higgs boson(s), independent of the production process; see [149–151] and references therein. The most promising channels are $\phi \to \tau^+\tau^-$ ($m_\phi < 2m_W$) and $\phi \to t\bar{t}$ ($m_\phi > 2m_t$) which in contrast to decays into WW or ZZ allow equal sensitivity to the CP-even and CP-odd components of ϕ.

A detailed simulation of $e^+e^- \to ZH$ followed by $H \to \tau^+\tau^-$ and $\tau^\pm \to \rho^\pm\bar{\nu}_\tau(\nu_\tau)$ [152–154] showed that CP of a 120 GeV SM-like Higgs boson can be measured to $\geq 95\%$ C.L. at a 500 GeV e^+e^- LC with 500 fb^{-1} of luminosity. In case of CP violation, the mixing angle between the scalar and pseudoscalar states may be determined to about 6 degrees [155], the limiting factor being statistics.

3.2.1.4 CP Studies at a Photon Collider

A unique feature of a PLC is that two photons can form a $J_z = 0$ state with both even and odd CP. As a result a PLC has a similar level of sensitivity for both the CP-odd and CP-even components of a CP-mixed state:

$$\mathrm{CP-even}: \epsilon_1 \cdot \epsilon_2 = -(1+\lambda_1\lambda_2)/2, \quad \mathrm{CP-odd}: [\epsilon_1 \times \epsilon_2] \cdot k_\gamma = \omega_\gamma i \lambda_1 (1+\lambda_1\lambda_2)/2, \quad (3.22)$$

ω_i and λ_i denoting the energies and helicities of the two photons respectively; the helicity of the system is equal to $\lambda_1 - \lambda_2$. This contrasts the e^+e^- case, where it is easy to discriminate between CP-even and CP-odd particles but may be difficult to detect small CP-violation effects for a dominantly CP-even Higgs boson [156]. For the PLC, one can form three polarization asymmetries in terms of helicity amplitudes which give a clear measure of CP mixing [157]. In addition, one can use information on the decay products of WW, ZZ, $t\bar{t}$ or $b\bar{b}$ coming from the Higgs decay. Furthermore, with circular beam polarization almost mass degenerate (CP-odd) A and (CP-even) H of the MSSM may be separated [158–160].

A measurement of the spin and parity of the Higgs boson may also be performed using the angular distributions of the final-state fermions from the Z boson decay, which encode the helicities of Z's. A detailed study was performed for above and below the ZZ threshold in [134]. A realistic simulation based on this analysis was made recently in [161].

The same interference effects as mentioned above can be used in the process $\gamma\gamma \to \phi \to t\bar{t}$ [162, 163] to determine the $t\bar{t}\phi$ and $\gamma\gamma\phi$ couplings for a ϕ with indefinite CP parity.

3.2.1.5 Example of LHC-LC synergy

As an example of the LHC-LC synergy, we consider the SM-like, type II 2HDM with CP-violation [161, 164]. We study production of ϕ_2 in the mass range 200 to 350 GeV, decaying to VV, $V = W/Z$, at the LHC, LC and PLC. In particular, we investigate the interplay of different experiments for the determination of $\tan\beta$ and mixing angle Φ_{HA}.

Figure 3.17 shows the expected rates for ϕ_2 with $m_{\phi_2} = 250$ GeV relative to the SM ones, as a function of $\tan\beta$ and Φ_{HA}. For a SM Higgs boson, the expected precision on $\sigma \times BR(H \to VV)$ is $\sim 15\%$ at the LHC [165, 166] and better than 10% at LC and PLC [167, 168]. A PLC will allow to measure $\Gamma_{\gamma\gamma}$ with a precision of 3–8% and the phase of the $\phi \to \gamma\gamma$ amplitude, $\Phi_{\gamma\gamma}$, to $40 - 120$ mrad [168].

Figure 3.18 shows the $1\,\sigma$ bands for determination of $\tan\beta$ and Φ_{HA}, at the LHC, LC and PLC for a particular choice of parameters : $\tan\beta = 0.7$ and $\Phi_{HA} = -0.2$. The chosen point is indicated by a star. For the PLC, information from $\Gamma_{\gamma\gamma}$ and $\Phi_{\gamma\gamma}$ is included. As can be seen, an accurate determination of both parameters requires combination of data from all three colliders.

3.2.1.6 Summary

The LHC, an e^+e^- LC, and a LC in the photon collider option (PLC) will be able to provide nontrivial information on the CP quantum numbers of the Higgs boson(s).

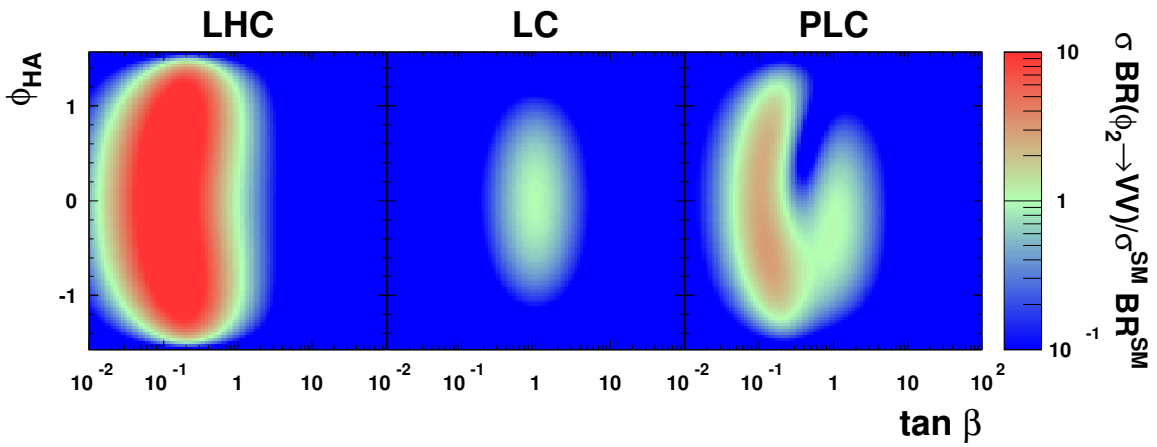

Figure 3.17: $\sigma\times$ BR for $\phi_2 \to VV$ with $V = W/Z$, relative to the SM expectation for the same for a mass of 250 GeV, as a function of $\tan\beta$ and Φ_{HA} for LHC, LC and PLC.

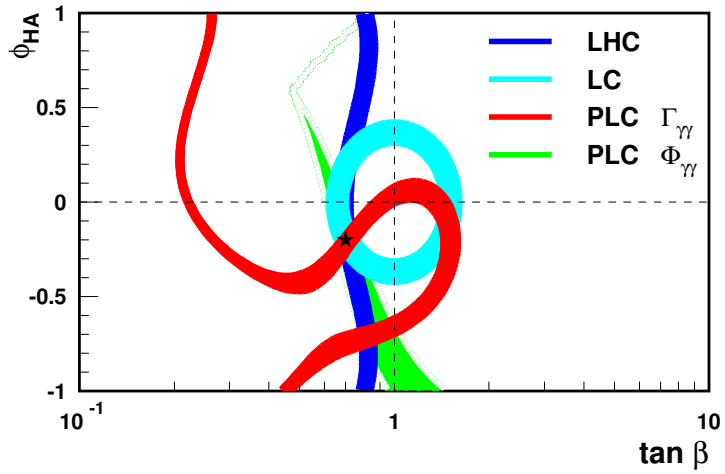

Figure 3.18: 1-σ bands for the determination of $\tan\beta$ and Φ_{HA} from measurements at LHC, LC and PLC, for the case $\tan\beta = 0.7$ and $\Phi_{HA} = -0.2$. The assumed parameter values are indicated by a star ($\star$).

We have summarized the potentials of the different colliders in this document and discussed the possible LHC-LC synergy.

In the MSSM, for instance, the size of CP-violating effects in the Higgs sector depends in part on the sparticle spectrum. Observation and measurement of Higgs-sector CP mixing at the LC can hence give predictions for phenomenology at the LHC in the CP-conserving sector, thus providing a high potential of LHC-LC synergy. A detailed study of this issue is, however, still missing.

Moreover, experiments at different colliders have different sensitivities to the various couplings of eq. 3.21. Hence a combination of LHC and LC/PLC measurements of both CP-even and CP-odd variables may be necessary to completely determine the coupling structure of the Higgs sector. In this document we have presented a first analysis which exemplifies this realization of LHC-LC synergy. While the example presented shows a high potential of the LHC-LC synergy for CP studies, detailed realistic simulations still need to be performed.

Another possibility within CP-violating Higgs scenarios is the following: there are

parameter choices (the CPX model) for which rather light Higgs bosons would not have been discovered at LEP [109] and would also escape LHC detection in the standard channels because of the types of difficulties discussed earlier. The $WW \to h \to aa \to jj\tau^+\tau^-$ channel (where $j = b$ if $m_a > 2m_b$) has not been examined in the context of this model. It can be anticipated (see also Sect. 3.4.1) that an excess in the $2j2\tau$ mass distribution might be observable, but that its confirmation as a Higgs signal would require observation in the $4b$ final state and probably also at the LC.

3.3 SUSY Higgs physics

The prediction of a firm upper bound on the mass of the lightest Higgs boson is one of the most striking predictions of Supersymmetric theories whose couplings stay in the perturbative regime up to a high energy scale. Disentangling the structure of the Higgs sector and establishing possible deviations from the SM will be one of the main goals at the next generation of colliders.

In order to implement electroweak symmetry breaking consistently into the MSSM, two Higgs doublets are needed. This results in eight degrees of freedom, three of which are absorbed via the Higgs mechanism to give masses to the $W^\pm$ and Z bosons. The remaining five physical states are the neutral CP-even Higgs bosons h and H, the neutral CP-odd state A, and the two charged Higgs bosons $H^\pm$. At lowest order, the Higgs sector of the MSSM is described by only two parameters in addition to the gauge couplings, conventionally chosen as M_A and $\tan\beta$, where the latter is the ratio of the vacuum expectation values of the two Higgs doublets.

The tree-level upper bound on the mass of the lightest CP-even Higgs boson, $m_h < M_Z$ in the MSSM, arising from the gauge structure of the theory, receives large radiative corrections from the Yukawa sector of the theory. Taking corrections up to two-loop order into account, it is shifted by about 50% [32]. As a consequence, loop effects, in particular from the top and scalar top sector and for large values of $\tan\beta$ also from the bottom and scalar bottom sector, are very important for SUSY Higgs phenomenology.

While the Higgs sector of the MSSM is CP-conserving at tree level, CP-violating effects can enter via loop corrections. The Higgs sector in extensions of the MSSM contains further matter structure, for instance additional Higgs singlets.

The LC will provide precision measurements of the properties of all Higgs bosons that are within its kinematic reach. Provided that a Higgs boson couples to the Z boson, the LC will observe it independently of its decay characteristics. At the LHC, on the other hand, Higgs boson detection can occur in various channels. In many cases complementary information from more than one channel will be accessible at the LHC. In particular, the LHC has a high potential for detecting heavy Higgs states which might be beyond the kinematic reach of the LC.

In the following, the possible interplay between LHC and LC results in SUSY Higgs physics is investigated for several examples. In Section 3.3.1 first a scenario is analysed where the LHC can detect the heavy Higgs states of the MSSM, while the LC provides precise information on the branching ratios of the light Higgs boson. This allows to perform a sensitive consistency test of the MSSM and to obtain indirect information on the mixing in the scalar top sector. Furthermore a scenario where LHC

and LC only detect one light Higgs boson is investigated and it is demonstrated how constraints on M_A can be derived from combined LHC and LC data. In Section 3.3.2 the decay of the heavy Higgs bosons H and A into a pair of neutralinos is studied at the LHC. This decay can be used to determine M_A, provided that a precise measurement of the mass of the lightest neutralino from the LC is available. Section 3.3.3 investigates the situation where the neutral Higgs bosons are almost mass-degenerate and $\tan\beta$ is large. In this case detection of the individual Higgs boson peaks is very challenging at the LHC, while the different Higgs boson signals can more easily be separated at the LC. The measured characteristics at the LC will then allow to determine further Higgs-boson properties at the LHC. In Sections 3.3.4 and 3.3.5 the determination of $\tan\beta$ from combined LHC and LC information (including also LC running in the $\gamma\gamma$ mode) is investigated.

3.3.1 Consistency tests and parameter extraction from the combination of LHC and LC results

3.3.1.1 Introduction

The Higgs sector of the MSSM is fully determined at lowest order by only two parameters in addition to the gauge couplings, M_A and $\tan\beta$. If the heavy Higgs states H and A (and possibly the charged states $H^\pm$) are accessible at the LHC, their detection will provide experimental information on both these parameters [114]. Thus, in principle the phenomenology of the light CP-even Higgs boson can be predicted if experimental results on the heavy Higgs bosons are available. Comparing these predictions with experimental results on the light CP-even Higgs boson constitutes an important test of the MSSM. Deviations may reveal physics beyond the MSSM.

A realistic analysis of such a scenario, however, needs to take into account that the Higgs-boson sector of the MSSM is affected by large radiative corrections, which arise in particular from the top/stop sector (for large values of $\tan\beta$ also loops of scalar bottom quarks can be important). In this way additional parameters become relevant for predicting the properties of the light CP-even Higgs boson. Experimental information on the parameters entering via large radiative corrections will therefore be crucial for SUSY Higgs phenomenology. This refers in particular to a precise knowledge of the top-quark mass, m_t, from the LC [9,169,170] and information about the SUSY spectrum from both LHC and LC (see Sect. 5 below). An analysis within the Higgs sector thus becomes much more involved. Furthermore, while detection of the heavy Higgs states at the LHC will provide a quite accurate determination of M_A, the experimental information on $\tan\beta$ will be rather limited [114]. On the other hand, the LHC will also be able to detect scalar top and bottom quarks over a wide mass range, so that it can be expected that additional experimental information on the scalar quark sector will be available.

In the following, two examples of a possible interplay between LHC and LC results in SUSY Higgs physics are investigated [171]. They are based on the benchmark scenarios SPS 1a and SPS 1b [14]. In Section 3.3.1.2 a scenario is analyzed where the LHC can detect the heavy Higgs states of the MSSM (see e.g. Ref. [114]), providing experimental information on both tree-level parameters of the MSSM Higgs sector, M_A and $\tan\beta$. The LC, on the other hand, provides precise information on the branching

ratios of the light Higgs boson, which can be compared with the theory prediction. This allows in particular to obtain indirect information on the mixing in the scalar top sector, which is very important for fits of the SUSY Lagrangian to (prospective) experimental data [172].

In Section 3.3.1.3 another scenario is analyzed where no heavy Higgs bosons can be detected at LHC and LC. The combined information about the SUSY spectrum from the LHC and LC and of Higgs-boson branching ratio measurements at the LC is used to obtain bounds on the mass of the CP-odd Higgs boson, M_A, in the unconstrained MSSM (for such analyses within mSUGRA-like scenarios, see Refs. [92, 173]). Since a realistic analysis requires the inclusion of radiative corrections, the achievable sensitivity to M_A depends on the experimental precision of the additional input parameters and the theoretical uncertainties from unknown higher-order corrections. This means in particular that observed deviations in the properties of the light CP-even Higgs boson compared to the SM case cannot be attributed to the single parameter M_A. We analyze in detail the impact of the experimental and theory errors on the precision of the M_A determination. Our analysis considerably differs from existing studies of Higgs boson branching ratios in the literature [174]. In these previous analyses, all parameters except for the one under investigation (i.e. M_A) have been kept fixed and the effect of an assumed deviation between the MSSM and the SM has solely been attributed to this single free parameter. This would correspond to a situation with a complete knowledge of all SUSY parameters without any experimental or theoretical uncertainty, which obviously leads to an unrealistic enhancement of the sensitivity to the investigated parameter.

3.3.1.2 Scenario where LHC information on heavy Higgs states is available

In this section we analyze a scenario where experimental results at the LHC are used as input for confronting the predictions for the branching ratios of the light CP-even Higgs boson with precision measurements at the LC. We consider the SPS 1b benchmark scenario [14], which is a 'typical' mSUGRA scenario with a relatively large value of $\tan\beta$. In particular, this scenario yields an M_A value of about 550 GeV, $\tan\beta = 30$, and stop and sbottom masses in the range of 600–800 GeV. More details about the mass spectrum can be found in Ref. [14].

We assume the following experimental information from the LHC and the LC:

- $\Delta M_A = 10\%$
  This prospective accuracy on M_A is rather conservative. The assumption about the experimental accuracy on M_A is not crucial in the context of our analysis, however, since for $M_A \gg M_Z$ the phenomenology of the light CP-even Higgs boson depends only weakly on M_A.

- $\tan\beta > 15$
  The observation of heavy Higgs states at the LHC in channels like $b\bar{b}H/A, H/A \to \tau^+\tau^-, \mu^+\mu^-$ will be possible in the MSSM if $\tan\beta$ is relatively large [114]. An attempted determination of $\tan\beta$ from the comparison of the measured cross section with the theoretical prediction will suffer from sizable QCD uncertainties, from the experimental errors of the SUSY parameters entering the theoretical prediction, and from the experimental error of the measured cross section.

Nevertheless, the detection of heavy Higgs states at the LHC will at least allow to establish a lower bound on $\tan\beta$. On the other hand, if $\tan\beta \lesssim 10$ the LC will provide a precise determination from measurements in the chargino and neutralino sector. Thus, assuming a lower bound of $\tan\beta > 15$ seems to be reasonable in the scenario we are analyzing.

- $\Delta m_{\tilde{t}}, \Delta m_{\tilde{b}} = 5\%$
  We assume that the LHC will measure the masses of the scalar top and bottom quarks with 5% accuracy. This could be possible if precise measurements of parameters in the neutralino and chargino sector are available from the LC, see Sec. 5.1 below. On the other hand, the measurements at the LHC (combined with LC input) will only loosely constrain the mixing angles in the scalar top and bottom sectors. Therefore we have not made any assumption about their values, but have scanned over the whole possible parameter space (taking into account the $SU(2)$ relation that connects the scalar top and bottom sector). It should be noted that for the prospective accuracy on the scalar top and bottom reconstruction at the LHC we have taken the results of studies at lower values of $\tan\beta$ ($\tan\beta = 10$). While the stop reconstruction should not suffer from the higher $\tan\beta$ value assumed in the present study, sbottom reconstruction is more involved, see Sec. 5.1 below. We assume that the reconstruction of hadronic τ's from the decay $\chi_2^0 \to \tau^+\tau^-\chi_1^0$ will be possible and the di-tau mass spectrum can be used for a mass measurement of the scalar bottom quarks at the 5% level. This still has to be verified by experimental simulation.

  In the scenario we are studying here the scalar top and bottom quarks are outside the kinematic limit of the LC.

- $\Delta m_h = 0.5$ GeV
  At the LC the mass of the light Higgs boson can be measured with an accuracy of 50 MeV. In order to account for theoretical uncertainties from unknown higher-order corrections we assume an accuracy of $\Delta m_h = 0.5$ GeV in this study. This assumes that a considerable reduction of the present uncertainty of about 3 GeV [32] will be achieved until the LC goes into operation.

- $\Delta m_t = 0.1$ GeV
  The top-quark mass (according to an appropriate short-distance mass definition) can be determined from LC measurements at the $t\bar{t}$ threshold with an accuracy of $\Delta m_t \lesssim 0.1$ GeV [9,169].

The experimental information from the heavy Higgs and scalar quark sectors that we have assumed above can be used to predict the branching ratios of the light Higgs boson. Within the MSSM, the knowledge of these experimental input quantities will significantly narrow down the possible values of the light Higgs branching ratios. Comparing this prediction with the precise measurements of the branching ratios carried out at the LC will provide a very sensitive consistency test of the MSSM.

This is shown in Fig. 3.19 for the branching ratios BR($h \to b\bar{b}$) and BR($h \to WW^*$). The light shaded (yellow) region indicates the full parameter space allowed for the two branching ratios within the MSSM. The medium shaded (light blue) region corresponds to the range of predictions in the MSSM being compatible with the assumed experimental information from the LHC as discussed above, i.e. $\Delta M_A = 10\%$,

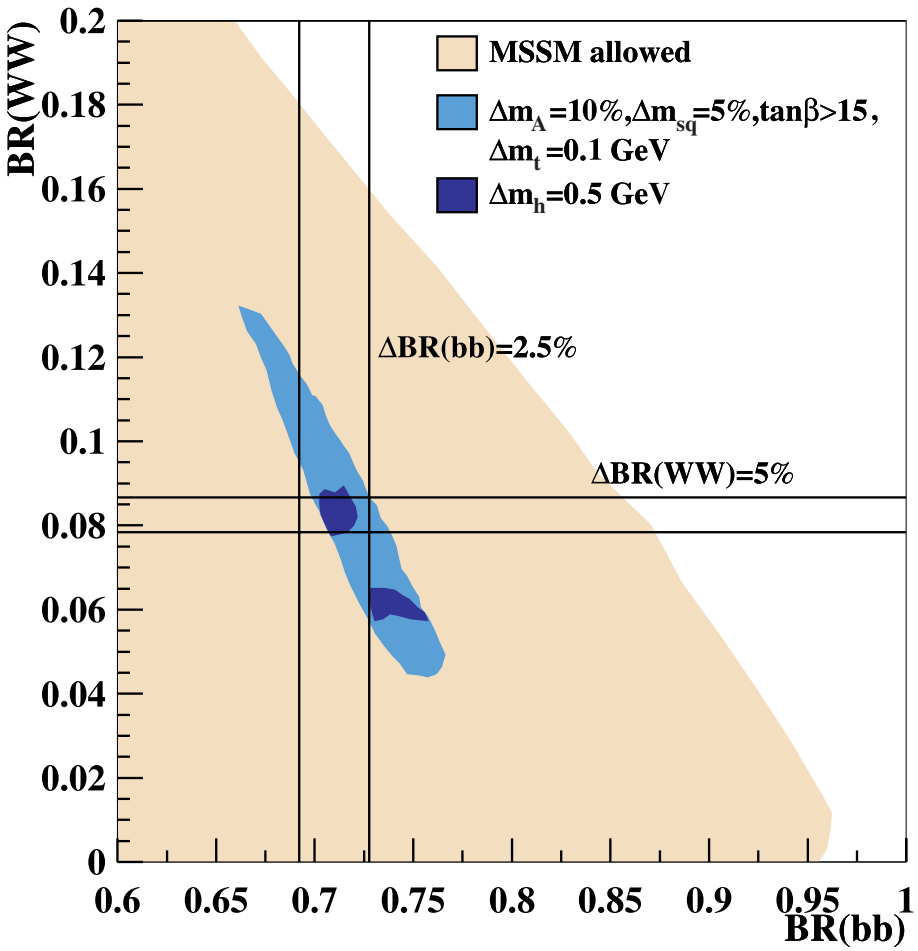

Figure 3.19: The experimental accuracies for the branching ratios BR($h \to b\bar{b}$) and BR($h \to WW^*$) at the LC of about 2.5% and 5%, indicated by a vertical and horizontal band, respectively, are compared with the theoretical prediction in the MSSM. The light shaded (yellow) region indicates the full allowed parameter space. The medium shaded (light blue) region indicates the range of predictions in the MSSM being compatible with the assumed experimental information from LHC and LC, $\Delta M_A = 10\%$, $\tan\beta > 15$, $\Delta m_{\tilde{t}}, \Delta m_{\tilde{b}} = 5\%$, $\Delta m_t = 0.1$ GeV. The dark shaded (dark blue) region arises if furthermore a measurement of the light CP-even Higgs mass, including a theory uncertainty of $\Delta m_h = 0.5$ GeV, is assumed.

$\tan\beta > 15$, $\Delta m_{\tilde{t}}, \Delta m_{\tilde{b}} = 5\%$. The dark shaded (dark blue) region arises if furthermore a measurement of the light CP-even Higgs mass of $m_h = 116$ GeV, including a theory uncertainty of $\Delta m_h = 0.5$ GeV, is assumed. The predictions are compared with the prospective experimental accuracies for BR($h \to b\bar{b}$) and BR($h \to WW^*$) at the LC of about 2.5% and 5%, respectively [9,175].

Agreement between the branching ratios measured at the LC and the theoretical prediction would constitute a highly non-trivial confirmation of the MSSM at the quantum level. In order to understand the physical significance of the two dark-shaded regions in Fig. 3.19 it is useful to investigate the prediction for m_h as a function of the trilinear coupling A_t (see also Ref. [170]). If the masses of the scalar top and bottom quarks have been measured at the LHC (using LC input), a precise measurement of m_h will allow an indirect determination of A_t up to a sign ambiguity. It should be

noted that for this determination of A_t the precise measurement of m_t at the LC is essential [170]. It also relies on a precise theoretical prediction for m_h, which requires a considerable reduction of the theoretical uncertainties from unknown higher-order corrections as compared to the present situation [32], as discussed above. Making use of a prospective measurement of m_h for predicting BR($h \to b\bar{b}$) and BR($h \to WW^*$), on the other hand, is less critical in this respect, since the kinematic effect of the Higgs mass in the prediction for the branching ratios is not affected by the theoretical uncertainties.

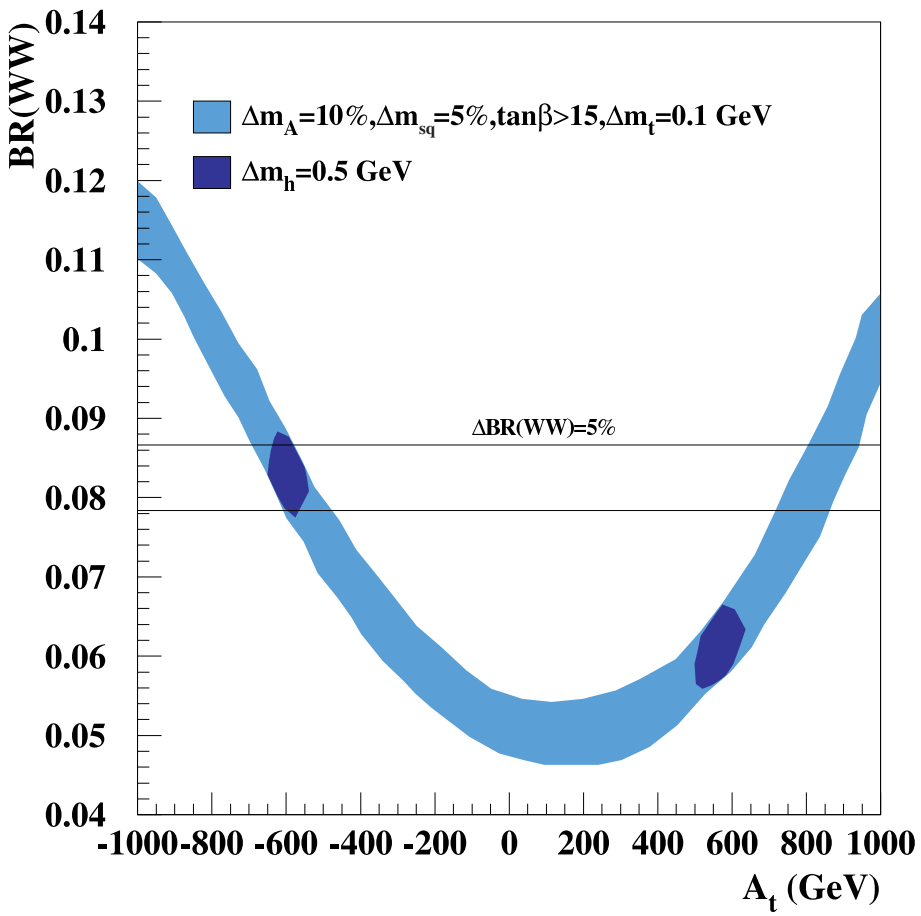

Figure 3.20: The branching ratio for $h \to WW^*$ is shown as a function of the trilinear coupling A_t. The light shaded (light blue) region indicates the range of predictions in the MSSM being compatible with the assumed experimental information, $\Delta M_A = 10\%$, $\tan\beta > 15$, $\Delta m_{\tilde{t}}, \Delta m_{\tilde{b}} = 5\%$, $\Delta m_t = 0.1$ GeV. The dark shaded (dark blue) region arises if furthermore a measurement of the light CP-even Higgs mass, including a theory uncertainty of $\Delta m_h = 0.5$ GeV, is assumed. The experimental accuracy for BR($h \to WW^*$) at the LC of about 5% is indicated by an horizontal band.

Fig. 3.19 shows that the LC measurements of the branching ratios of the light CP-even Higgs boson allow to discriminate between the two dark-shaded regions. From the discussion above, these two regions can be identified as corresponding to the two possible signs of the parameter A_t. This is illustrated in Fig. 3.20, where BR($h \to WW^*$) is shown as a function of A_t. It is demonstrated that the sign ambiguity of A_t

can be resolved with the branching ratio measurement. The determination of A_t in this way will be crucial in global fits of the SUSY parameters to all available data [172].

3.3.1.3 Indirect constraints on M_A from LHC and LC measurements

In the following, we analyze an SPS 1a based scenario [14], where we keep M_A as a free parameter. We study in particular the situation where the LHC only detects one light Higgs boson. For the parameters of the SPS 1a scenario this corresponds to the region $M_A \gtrsim 400$ GeV.

The precise measurements of Higgs branching ratios at the LC together with accurate determinations of (parts of) the SUSY spectrum at the LHC and the LC will allow in this case to obtain indirect information on M_A (for a discussion of indirect constraints on M_A from electroweak precision observables, see Ref. [176]). When investigating the sensitivity to M_A it is crucial to take into account realistic experimental errors of the other SUSY parameters that enter the prediction of the Higgs branching ratios. Therefore we have varied all the SUSY parameters according to error estimates for the measurements at LHC and LC in this scenario. The sbottom masses and the gluino mass can be obtained from mass reconstructions at the LHC with LC input, see Sec. 5.1 below. We have assumed a precision of $\Delta m_{\tilde{g}} = \pm 8$ GeV and $\Delta m_{\tilde{b}_{1,2}} = \pm 7.5$ GeV. We furthermore assume that the lighter stop (which in the SPS 1a scenario has a mass of about 400 GeV, see Ref. [14]) will be accessible at the LC, leading to an accuracy of about $\Delta m_{\tilde{t}_1} = \pm 2$ GeV. The impact of the LC information on the stop mixing angle, $\theta_{\tilde{t}}$, will be discussed below. For $\tan\beta$ we have used an uncertainty of $\Delta \tan\beta = 10\%$ (this accuracy can be expected from measurements at the LC in the gaugino sector for the SPS 1a value of $\tan\beta = 10$ [177]). We have assumed a LC measurement of $m_h = 116$ GeV, but included a theory error from unknown higher-order corrections of ± 0.5 GeV [32].

In our analysis we compare the theoretical prediction [178] for the ratio of branching ratios

$$r \equiv \frac{\left[\mathrm{BR}(h \to b\bar{b})/\mathrm{BR}(h \to WW^*)\right]_{\mathrm{MSSM}}}{\left[\mathrm{BR}(h \to b\bar{b})/\mathrm{BR}(h \to WW^*)\right]_{\mathrm{SM}}} \tag{3.23}$$

with its prospective experimental measurement. Even though the experimental error on the ratio of the two BR's is larger than that of the individual ones, the quantity r has a stronger sensitivity to M_A than any single branching ratio.

In Fig. 3.21 the theoretical prediction for r is shown as a function of M_A, where the scatter points result from the variation of all relevant SUSY parameters within the 3 σ ranges of their experimental errors. The constraint on the SUSY parameter space from the knowledge of m_h is taken into account, where the precision is limited by the theory uncertainty from unknown higher-order corrections. The experimental information on m_h gives rise in particular to indirect constraints on the heavier stop mass and the stop mixing angle. Without assuming any further experimental information, two distinct intervals for the heavier stop mass (corresponding also to different intervals for $\theta_{\tilde{t}}$) are allowed. This can be seen from the upper plot of Fig. 3.21. The interval with lower values of $m_{\tilde{t}_2}$ corresponds to the SPS 1a scenario, while the interval with higher $m_{\tilde{t}_2}$ values can only be realized in the unconstrained MSSM. In the lower plot

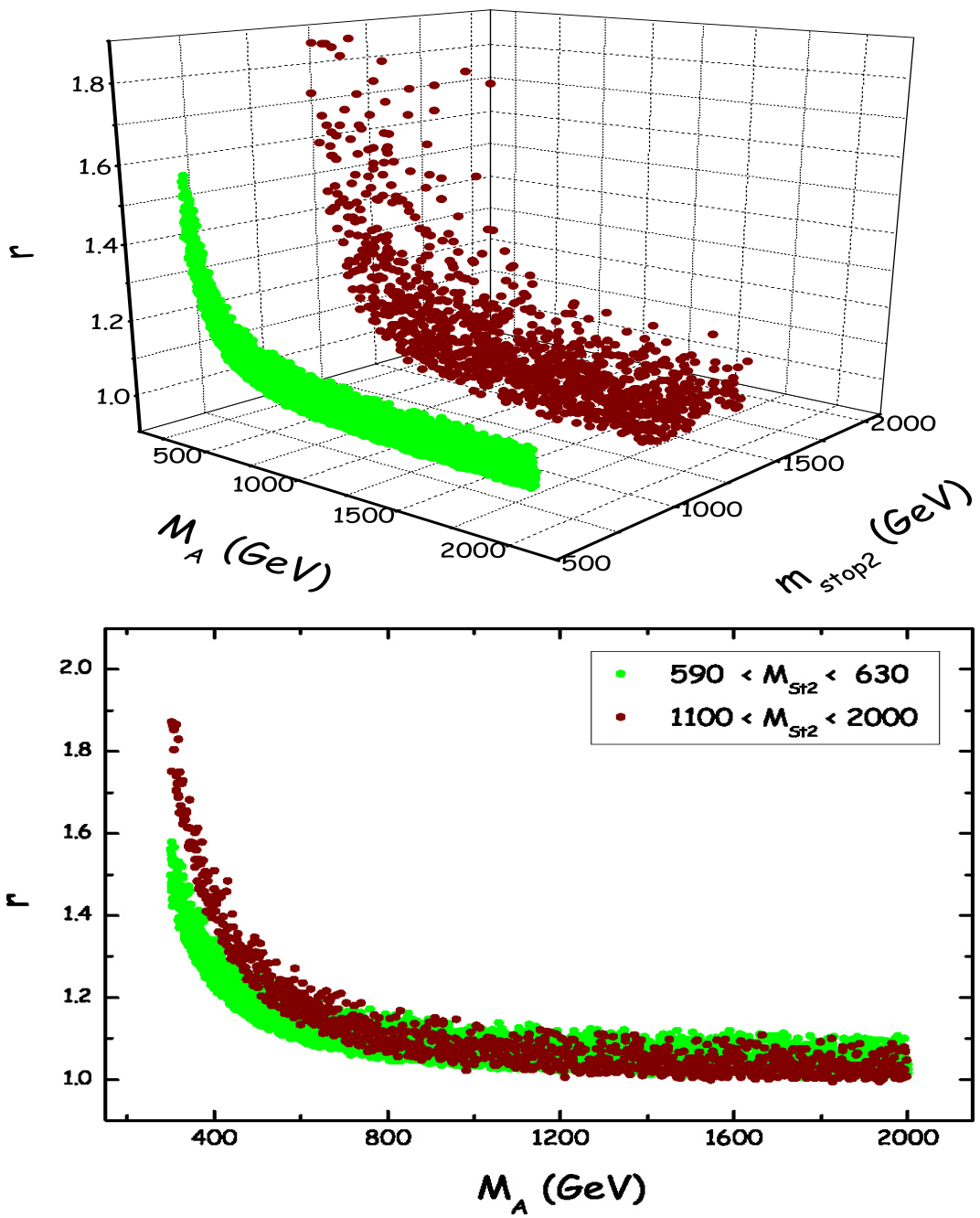

Figure 3.21: The ratio of branching ratios r, see eq. (3.23), is shown as a function of M_A in the SPS 1a scenario. The other SUSY parameters have been varied within the 3 σ intervals of their experimental errors (see text). The upper plot shows the three-dimensional M_A–$m_{\tilde{t}_2}$–r parameter space, while the lower plot shows the projection onto the M_A–r plane.

the projection onto the M_A–r plane is shown, giving rise to two bands with different slopes. Since the lighter stop mass is accessible at the LC in this scenario, it can be expected that the stop mixing angle will be determined with sufficient accuracy to distinguish between the two bands. This has an important impact on the indirect determination of M_A.

The central value of r obtained from the band which is realized in the SPS 1a sce-

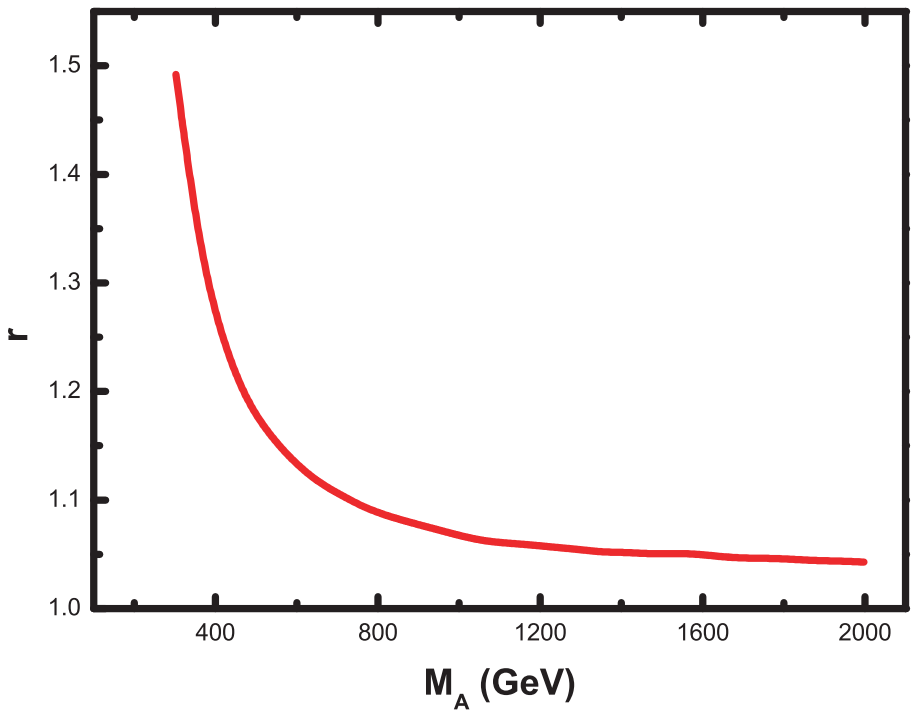

Figure 3.22: The central value of M_A corresponding to the central value of a prospective r measurement is shown for the SPS 1a scenario. This relation between r and M_A would be obtained if all experimental and theoretical uncertainties were negligible (see text).

nario is shown as a function of M_A in Fig. 3.22. The plot shows a non-decoupling behavior of r, i.e. r does not go to 1 for $M_A \to \infty$. This is due to the fact that the SUSY masses are kept fixed in the SPS 1a scenario. In order to find complete decoupling, however, both M_A and the mass scale of the SUSY particles have to become large, see e.g. Ref. [179]. It should be noted that the sensitivity of r to M_A is not driven by this non-decoupling effect. In fact, for larger values of the SUSY masses the slope of $r(M_A)$ even increases (one example being the second band depicted in Fig. 3.21). Thus, even stronger indirect bounds on M_A could be obtained in this case.

The comparison of the theoretical prediction for r with the experimental result at the LC allows to set indirect bounds on the heavy Higgs-boson mass M_A. The relation between r and M_A shown in Fig. 3.22 corresponds to an idealised situation where the experimental errors of all input parameters in the prediction for r (besides M_A) and the uncertainties from unknown higher-order corrections were negligibly small. Assuming a certain precision of r, Fig. 3.22 therefore allows to read off the best possible indirect bounds on M_A as a function of M_A, resulting from neglecting all other sources of uncertainties. This idealised case is compared with a more realistic situation based on the SPS 1a scenario in Fig. 3.23.

For the experimental accuracy of r we consider two different values: a 4% accuracy resulting from a first phase of LC running with $\sqrt{s} \lesssim 500$ GeV [9, 175], and a 1.5% accuracy which can be achieved from LC running at $\sqrt{s} \approx 1$ TeV [180]. In Fig. 3.23 the resulting 1 σ bounds on M_A are shown (the corresponding value of r can be read off from Fig. 3.22) for the experimental precisions of r of 4% and 1.5%, respectively, where the estimated experimental errors on the parameters $\tan\beta, m_{\tilde{b}_{1,2}}, m_{\tilde{t}_1}, m_{\tilde{g}}, m_h$,

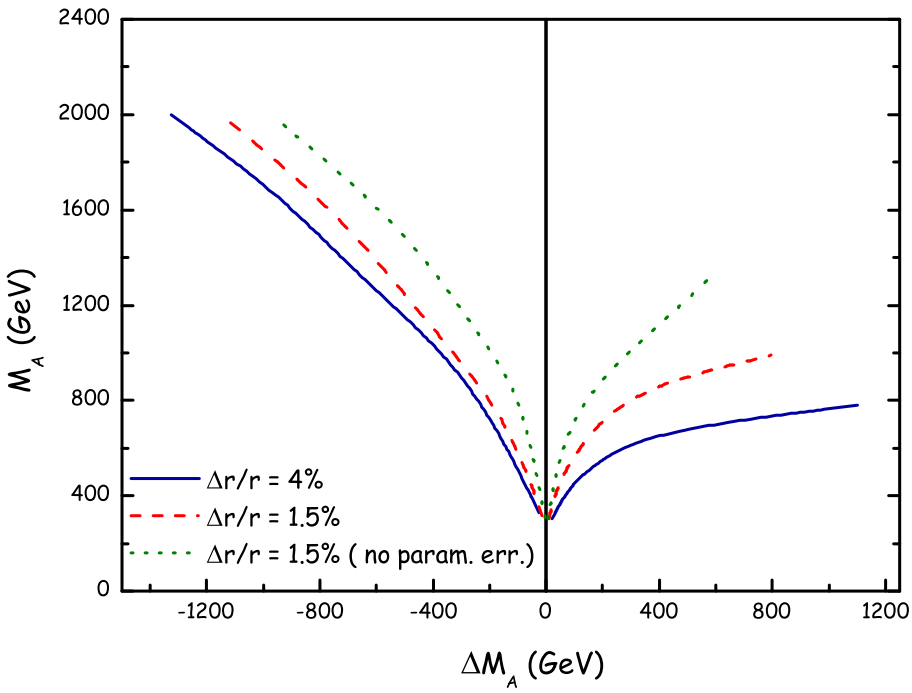

Figure 3.23: The 1 σ bound on M_A, ΔM_A, versus M_A obtained from a comparison of the precision measurement of r (see text) at the LC with the MSSM prediction. The results for ΔM_A are shown for a 4% accuracy of r (full line) and a 1.5% accuracy of r (dashed line). The parametric uncertainties in the prediction of r resulting from LHC/LC measurement errors on $\tan\beta, m_{\tilde{b}_{1,2}}, m_{\tilde{t}_1}, m_{\tilde{g}}, m_h$, and m_t are taken into account. Also shown is the accuracy on M_A which would be obtained if these uncertainties were neglected (dotted line).

and m_t based on the SPS 1a scenario are taken into account. Also shown is the 1 σ error for $\Delta r/r = 1.5\%$ which would be obtained if all SUSY parameters (except M_A) were precisely known, corresponding to the idealised situation of Fig. 3.22.

Fig. 3.23 shows that a 4% accuracy on r allows to establish an indirect upper bound on M_A for M_A values up to $M_A \lesssim 800$ GeV (corresponding to an r measurement of $r \gtrsim 1.1$). With an accuracy of 1.5%, on the other hand, a precision on $\Delta M_A/M_A$ of approximately 20% (30%) can be achieved for $M_A = 600$ (800) GeV. The indirect sensitivity extends to even higher values of M_A. The comparison with the idealised situation where all SUSY parameters (except M_A) were precisely known (as assumed in Ref. [174]) illustrates the importance of taking into account the parametric errors as well as the theory errors from unknown higher-order corrections. Detailed experimental information on the SUSY spectrum and a precision measurement of m_t are clearly indispensable for exploiting the experimental precision on r.

3.3.1.4 Conclusions

We have investigated indirect constraints on the MSSM Higgs and scalar top sectors from measurements at LHC and LC in the SPS 1a and SPS 1b benchmark scenarios. In a situation where the LHC detects heavy Higgs bosons (SPS 1b) the combination of the LHC information on the heavy Higgs states with precise measurements of the

mass and branching ratios of the lightest CP-even Higgs boson at the LC gives rise to a sensitive consistency test of the MSSM. In this way an indirect determination of the trilinear coupling A_t becomes possible. The measurement of m_h alone allows to determine A_t up to a sign ambiguity, provided that a precise measurement of the top-quark mass from the LC is available. With the measurements of the branching ratios $\mathrm{BR}(h \to b\bar{b})$ and $\mathrm{BR}(h \to WW^*)$ at the LC the sign ambiguity can be resolved and the accuracy on A_t can be further enhanced.

In a scenario where LHC and LC only detect one light Higgs boson (SPS 1a, where M_A is taken as a free parameter), indirect constraints on M_A can be established from combined LHC and LC data. Taking all experimental and theoretical uncertainties into account, an indirect determination of M_A with an accuracy of about 20% (30%) seems to be feasible for $M_A = 600$ (800) GeV. In order to achieve this, a precise measurement of the branching ratios $\mathrm{BR}(h \to b\bar{b})$ and $\mathrm{BR}(h \to WW^*)$ at the LC and information on the parameters of the scalar top and bottom sector from combined LHC / LC analyses will be crucial.

3.3.2 Importance of the $\tilde{\chi}_1^0$ mass measurement for the $A^0, H^0 \to \tilde{\chi}_2^0\tilde{\chi}_2^0$ mass reconstruction

3.3.2.1 Introduction

In the MSSM, the couplings of the heavier neutral A^0 and H^0 bosons to down-type fermions are enhanced at high $\tan\beta$:

$$g_{A^0 b\bar{b}} \sim m_b \tan\beta \qquad g_{H^0 b\bar{b}} \sim m_b \frac{\cos\alpha}{\cos\beta} \tag{3.24}$$

at the expense of the couplings to up-type fermions. This results in an important production mechanism for H^0 and A^0 Higgs bosons in association with $b\bar{b}$ pairs at the LHC: $gg \to H^0, A^0 b\bar{b}$. For the same reasons, the dominant decay modes of the heavy neutral Higgs bosons are $H^0, A^0 \to b\bar{b}$ and $H^0, A^0 \to \tau\bar{\tau}$. The $b\bar{b}$ channel has large difficulties to overcome the experimental trigger thresholds at the LHC and therefore does not show much potential; the $H^0, A^0 \to \tau\bar{\tau}$ mode on the other hand, where both the hadronic and leptonic τ decaus can be exploited, allows to discover the heavy neutral Higgs bosons over a large part of the parameter space, notably for high and intermediate values of $\tan\beta$. Also the $H^0, A^0 \to \mu\bar{\mu}$ channel shows some interesting potential, in spite of the very small braching ratio of Higgs into muons $\mathcal{O}(10^{-4})$, since muons are objects that can be experimentally measured with high precision and efficiency.

In spite of the good coverage of the large $\tan\beta$ region, the low and intermediate $\tan\beta$ domain remains largely inaccessible for the previously mentioned channels, and new channels need to be found. Apart from the Higgs couplings to fermions (3.24), also some of the Higgs couplings to gauge bosons might be exploited:

$$\begin{aligned} g_{H^0VV} &\sim \cos(\beta-\alpha) \qquad & g_{H^0A^0Z^0} &\sim \sin(\beta-\alpha) \\ g_{A^0VV} &= 0 \qquad & g_{H^0H^0Z^0} &= g_{A^0A^0Z^0} = 0 \end{aligned} \tag{3.25}$$

where $V = W^{\pm}, Z^0$. Since $\cos(\beta - \alpha)$ is very close to zero for $m_A > 200$ GeV, the only substantial coupling is $g_{H^0A^0Z^0}$. In the Standard Model this coupling is not viable since the masses of H^0 and A^0 differ with only a few GeV, however supersymmetry dictates that the coupling remains the same if two of the three particles are replaced by their superpartners: $H^0\widetilde{A}^0\widetilde{Z}^0$. We thus arrive at a sizeable coupling of the heavy neutral MSSM Higgs bosons to mixtures of higgsinos and gauginos, i.e. neutralinos and charginos, whose masses can be much below the Higgs mass.
The discovery reach of the Higgs decay modes to neutralinos and charginos at the LHC has been studied in [181, 182]. It was found that the most promising channel is the decay of the heavy neutral Higgs bosons into two next-to-lightest neutralinos, with each of the neutralinos in turn decaying as $\widetilde{\chi}_2^0 \to l^+l^-\widetilde{\chi}_1^0$, i.e. into two (isolated) leptons + E_T^{miss}, thus leading to

$$H^0, A^0 \to \widetilde{\chi}_2^0\,\widetilde{\chi}_2^0 \to 4\,l^{\pm} \;+\; E_T^{miss} \qquad (l \;=\; e,\,\mu) \tag{3.26}$$

This results in a clean four lepton final state signature accompanied by a large amount of missing transverse energy.
In the following we will briefly discuss the selection criteria that allow to suppress the Standard Model and supersymmetric backgrounds and can lead to a clearly visible signal. Next, various methods to reconstruct the Higgs mass are proposed, all of which require a precise knowledge of the $\widetilde{\chi}_1^0$ mass. This sensitivity to the mass of the $\widetilde{\chi}_1^0$ is further quantified for the SPS1a benchmark scenario. Finally, it is concluded that a precise determination of the $\widetilde{\chi}_1^0$ mass, coming from a future Linear Collider is needed for an optimal reconstruction of the mass of the heavy Higgs bosons with the neutralino channel.

3.3.2.2 The $H^0, A^0 \to \widetilde{\chi}_2^0\widetilde{\chi}_2^0$ channel at the LHC

Two categories of background to the Higgs signal (3.26) have to be considered: Standard Model processes and SUSY backgrounds.
The main SM backgrounds are Z^0Z^0 and $t\bar{t}$ production. They are dangerous because of their large cross sections at the LHC. The Z^0Z^0 events can result in four isolated leptons but do not have no additional missing transverse energy. The $t\bar{t}$ background can also lead to four leptons, however since two of the must come from a b decay they will in general be soft and non-isolated.
In the SUSY backgounds, one can identify the squark/gluino production, characterised by a large number of energetic jets and a significant amount of E_T^{miss}; the slepton and sneutrino pair production (the second one being more dangereous because the sneutrinos can decay into two charged leptons each) ; and neutrino and chargino pair production, especially $\widetilde{\chi}_2^0\widetilde{\chi}_2^0$ production, possibly mimicking the signal but with much smaller cross sections due to the strongly suppressed coupling of gauginos to a Z^0/γ intermediate state.
One can suppress the SM and MSSM background processes, while preserving most of the Higgs signal, by applying the following selection criteria:

- two pairs of isolated leptons (electrons or muons) with opposite sign and same flavour are required, with transverse momentum larger than 20, 15, 15 and 10 GeV resepctively and within $|\eta| < 2.4$. The isolation criterion demands that

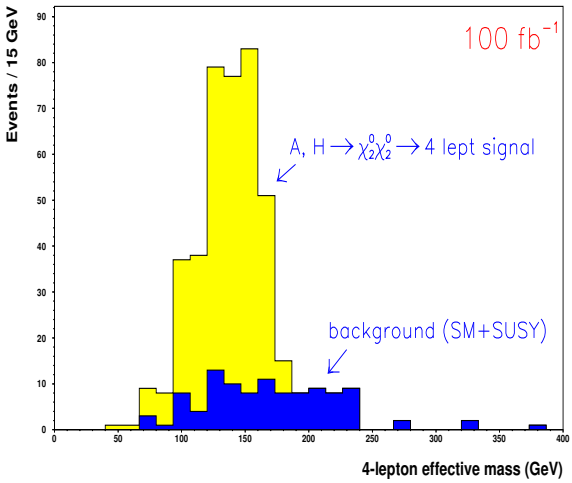

Figure 3.24: Four lepton invariant mass for signal versus background (SM + SUSY) for the SPS1a scenario where m_A = 393 GeV and $\tan\beta$ = 10 (for an integrated luminosity of 100 fb^{-1}).

there are no charged particles with $p_T > 1.5$ GeV in a cone of radius $\Delta R = \sqrt{(\Delta\phi)^2 + (\Delta\eta)^2}$ = 0.3 rad around each lepton track, and that the sum of the transverse energy in the deposited in the electromagnetic calorimeter between ΔR = 0.05 and ΔR = 0.3 rad is smaller than 3 GeV.

- a Z^0-veto is imposed, i.e. all dilepton pairs of opposite sign and same flavour that have an invariant mass in the range $m_{Z^0} \pm 10$ GeV are rejected.
- events must have a missing transverse energy in the interval 20 GeV $< E_T^{miss}$ $<$ 150 GeV. The lower limit suppresses the Z^0Z^0 events while the upper limit reduces the squark/gluino background.
- if needed, one can apply ceilings to the jet multiplicity and the transverse energy of the jets to further suppress squark and gluino events if these particles would be light (and therefore copiously produced).
- further optimization can be done by introducing upper limits to the transverse momentum of the leptons and the four lepton invariant mass, however they depend on the specific MSSM scenario.

After such a selection procedure, a clear signal remains visible on top of the (mainly SUSY) backgrounds, as can be seen in Figure 3.24 for the SPS1a benchmark scenario [183] where m_A = 393 GeV and $\tan\beta$ = 10, M_1 = 100 GeV, M_2 = 192 GeV, μ = 352 GeV, $m_{\tilde{l_L}}$ = 202 GeV, $m_{\tilde{l_R}}$ = 142 GeV, $m_{\tilde{q_L}}$ = 540 GeV, $m_{\tilde{q_R}}$ = 520 GeV, $m_{\tilde{g}}$ = 595 GeV.

3.3.2.3 Higgs mass reconstruction with the $H^0, A^0 \rightarrow \widetilde{\chi}_2^0\widetilde{\chi}_2^0$ channel

In order to reconstruct the mass of the H^0, A^0 Higgs boson we can exploit an interesting kinematical property of the disintegration process. The decay of the next-to-lightest neutralino to leptons features a kinimatical endpoint in the dilepton invari-

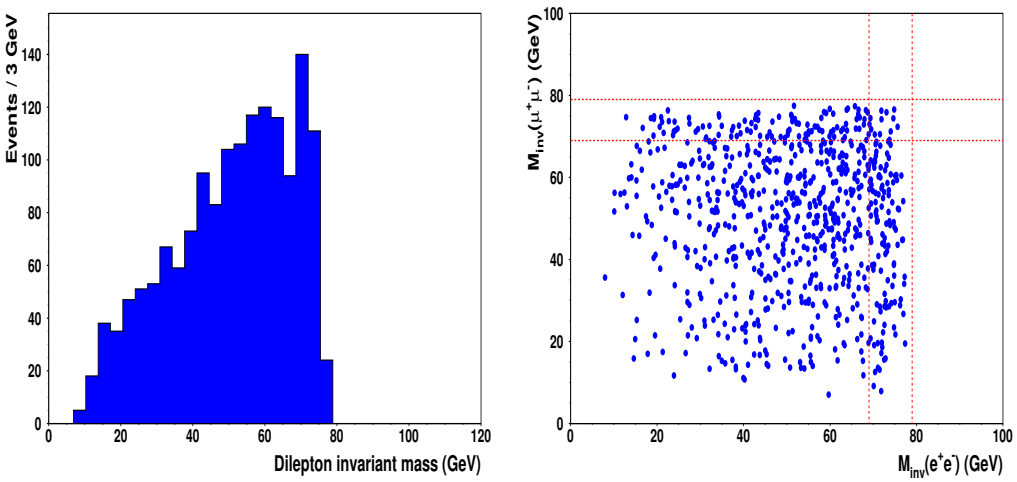

Figure 3.25: (a) Kinematical endpoint at $m_{\widetilde{\chi}_2^0} - m_{\widetilde{\chi}_1^0}$ in the dilepton invariant mass distribution. (b) Double kinematical edge in the di-electron versus dimuon invariant mass distribution.

ant mass spectrum near the mass difference between the $\widetilde{\chi}_2^0$ and the $\widetilde{\chi}_1^0$, or if sleptons are intermediate in mass, near $\sqrt{(m^2_{\widetilde{\chi}_2^0} - m^2_{\tilde{l}})(m^2_{\tilde{l}} - m^2_{\widetilde{\chi}_1^0})/m_{\tilde{l}}}$. In Figure 3.25a this dilepton invariant mass spectrum is plotted for the previously considered scenario. Since there are two $\widetilde{\chi}_2^0$'s present in the Higgs decay channel, a double kinematical edge is visible if one selects only the events containing two electrons and two muons and then plots the di-electron invariant mass versus the dimuon invariant mass. In Figure 3.25b these distributions are plotted for the previously considered scenario. Selecting events in which both dilepton pairs are close to the kinematical edge allows in principle for the direct reconstruction of the A^0 / H^0 mass (provided the statistics are sufficient). By selecting dilepton pairs that have an invariant mass near the kinematical endpoint, one can reconstruct the four-momentum of the χ_2^0:

$$\begin{aligned} \vec{p}_{\widetilde{\chi}_2^0} &= \left(1 + \frac{M_{\widetilde{\chi}_1^0}}{M_{ll}}\right) \vec{p}_{ll} \\ M_{\widetilde{\chi}_2^0} &= M_{\widetilde{\chi}_1^0} + M_{ll} \end{aligned}$$

The Higgs mass is then calculated as the invariant mass of the two $\widetilde{\chi}_2^0$'s, provided the mass of the $\widetilde{\chi}_1^0$ is known. However, as illustrated in Figure 3.25b, even in favourable scenarios and with 600 fb^{-1} of data only a small number of events survive this selection, thereby limiting the statistical accuracy of the Higgs mass obtained with this method. An extension of this method may lead to a much better stastistical significance [184].

An alternative way to determine the Higgs mass consists of fitting the four-lepton invariant mass, which reflects the Higgs mass, with the Monte Carlo distribution for a given m_A. Figure 3.26 shows the fitted four lepton invariant mass for a Higgs mass of m_A = 393 GeV in scenario SPS1a. The average four-lepton invariant mass is 135 GeV. The large discrepancy between this number and the Higgs mass is due to the escaping $\widetilde{\chi}_1^0$ particles.

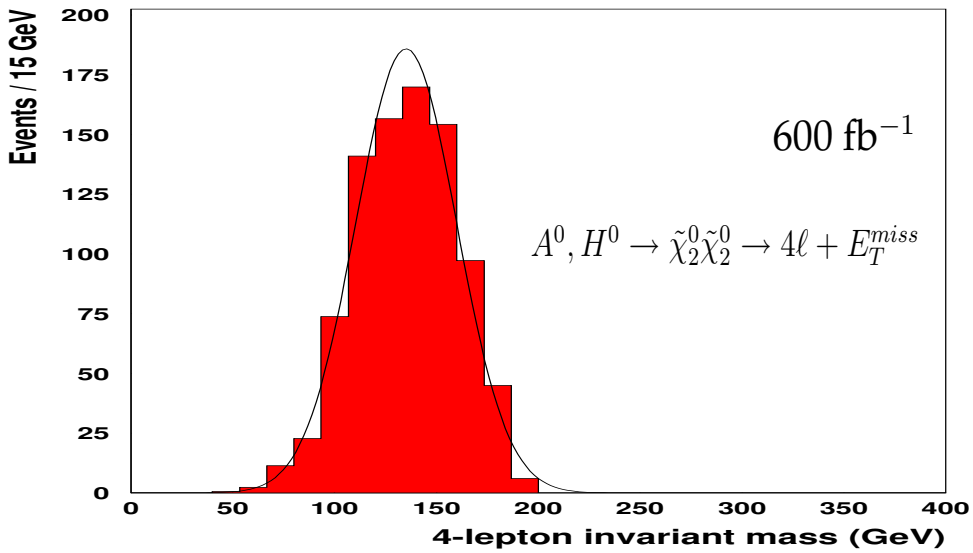

Figure 3.26: Fit of the 4-lepton invariant mass to the Monte Carlo distribution for scenario SPS1a, for a total integrated luminosity of 600 fb^{-1}.

The four lepton invariant mass distribution is only mildly sensitive to the mass of the A^0 boson (the mass of the H^0 boson is typically a few GeV's higher). A shift of m_A by 10 (20) GeV leads to a shift of $\langle M_{lll} \rangle$ by 4 (8) GeV. This behaviour is illustrated in Figure 3.27a where the four lepton invariant mass distributions are shown for m_A = 373, 393 and 413 GeV.
Because of the two $\widetilde{\chi}_1^0$'s escape during the decay of the Higgs boson., the M_{lll} distribution is also sensitive to the mass of the $\widetilde{\chi}_1^0$. A shift of $m_{\widetilde{\chi}_1^0}$ by 5 (10) GeV leads to a shift of $\langle M_{lll} \rangle$ by 5 (15) GeV. Figure 3.27b illustrates this dependency by showing the four lepton invariant mass for three values of $m_{\widetilde{\chi}_1^0}$ = 90, 100 and 110 GeV.
Since the M_{lll} distribution is sensitive to both m_A and $m_{\widetilde{\chi}_1^0}$, the mass of the $\widetilde{\chi}_1^0$ needs to be known with good precision in order to suppress this source of error in the determination of the Higgs mass. Assuming an ultimate LHC integrated luminosity of 600 fb^{-1}, the statistical error on M_{lll} in the above scenario is $\sim$1%. This can lead to a precision on m_A of about 3%, provided the mass of the $\widetilde{\chi}_1^0$ can be determined to better than 1%.

3.3.2.4 Conclusion

Supersymmetric decay modes of the heavy MSSM Higgs bosons offer interesting possibilities to discover these particles in the low and intermedate $\tan\beta$ region of the MSSM parameter space. In particular, the $A^0, H^0 \to \tilde{\chi}_2^0\tilde{\chi}_2^0$ decay can lead to a cleanly observable $4\ell + E_T^{miss}$ final state, provided neutralinos and sleptons are sufficiently light. In this contribution we have investigated the importance of a precise measurement of the $\tilde{\chi}_1^0$ mass at a future LC for the Higgs mass reconstruction in this channel at the LHC. Probably the best way to determine the mass of the A, H bosons is to use the 4-lepton invariant mass m_{4l} as an estimator for the Higgs mass, comparing

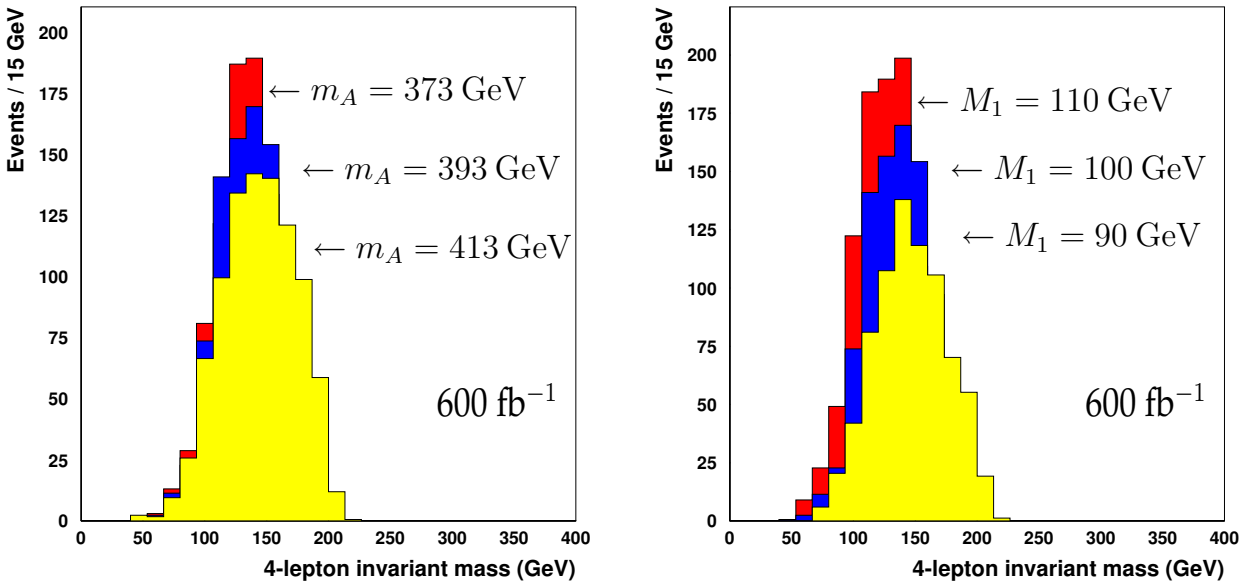

Figure 3.27: Four lepton invariant mass distribition (a) for M_A = 393 $\pm$ 20 GeV; (b) for M_1 = 100 $\pm$ 10 GeV and the other parameters fixed as described in the text.

its distribution for various values of m_A using Monte Carlo simulations. However, the m_{4l} distribution also depends strongly on the mass of the lightest neutralino $\tilde{\chi}_1^0$. Therefore, an accurate measurement of the $\tilde{\chi}_1^0$ mass with a precision better than about 1% at the LC would be needed for an optimal measurement of m_A (i.e. with a statistical error of 3% after 600 fb^{-1} for the SPS1a scenario considered in this contribution) through the neutralino channel at the LHC.

3.3.3 The neutral MSSM Higgs bosons in the intense-coupling regime

3.3.3.1 The intense-coupling regime

In the MSSM Higgs sector, the intense-coupling regime [185,186] is characterized by a rather large value of $\tan\beta$, and a pseudoscalar Higgs boson mass that is close to the maximal (minimal) value of the CP-even h (H) boson mass, $M_A \sim M_h^{\max}$, almost leading to a mass degeneracy of the neutral Higgs particles, $M_h \sim M_A \sim M_H$. In the following, we will summarize the main features of this scenario. For the numerical illustration, we will use HDECAY [187], fix the parameter $\tan\beta$ to the value $\tan\beta = 30$ and choose the maximal mixing scenario, where the trilinear Higgs–stop coupling is given by $A_t \simeq \sqrt{6} M_S$ with the common stop masses fixed to $M_S = 1$ TeV; the other SUSY parameter will play only a minor role.

Figure 1 (left) displays the masses of the MSSM Higgs bosons as a function of M_A. As can be seen, for M_A close to the maximal h boson mass, which in this case is $M_h^{\max} \simeq 130$ GeV, the mass differences $M_A - M_h$ and $M_H - M_A$ are less than about 5 GeV. The $H^\pm$ boson mass, given by $M_{H^\pm}^2 \sim M_A^2 + M_W^2$, is larger: in the range $M_A \lesssim 140$ GeV, one has $M_{H^\pm} \lesssim 160$ GeV, implying that charged Higgs bosons can

always be produced in top-quark decays, $t \to H^+ b$. The couplings of the CP-even Higgs bosons to fermions and gauge bosons normalized to the SM Higgs boson couplings are also shown in Fig. 1 (right). For small M_A values, the H boson has almost SM couplings, while the couplings of the h boson to W, Z, t (b) are suppressed (enhanced); for large M_A values the roles of h and H are interchanged. For medium values, $M_A \sim M_h^{\rm max}$, the couplings of both h and H to gauge bosons $V = W, Z$ and top quarks are suppressed, while the couplings to b quarks are strongly enhanced. The normalized couplings of the CP-even Higgs particle are simply $g_{AVV} = 0$ and $g_{Abb} = 1/g_{Att} = \tan\beta = 30$.

These couplings determine the branching ratios of the Higgs particle, which are shown in Fig. 2. Because the enhanced couplings, the three Higgs particle branching ratios to $b\overline{b}$ and $\tau^+\tau^-$ are the dominant ones, with values $\sim 90\%$ and $\sim 10\%$ respectively. The decays $H \to WW^*$ do not exceed the level of 10%, even for small M_A values [where H is almost SM-like] and in most of the M_A range the decays $H, h \to WW^*$ are suppressed to the level where they are not useful. The decays into ZZ^* are one order of magnitude smaller and the decays into $\gamma\gamma$ are very strongly suppressed for the three Higgsses and cannot be used anymore. Finally, note that the branching ratios for the decays into muons, $\Phi \to \mu^+\mu^-$, are constant in the entire M_A range exhibited, at the level of 3×10^{-4}.

Summing up the partial widths for all decays, the total decay widths of the three Higgs particles are shown in the left-hand side of Fig. 3. As can be seen, for $M_A \sim 130$ GeV, they are at the level of 1–2 GeV, i.e. two orders of magnitude larger than the width of the SM Higgs boson for this value of $\tan\beta$ [the total width increases as $\tan^2\beta$]. The right-hand side of the figure shows the mass bands $M_\Phi \pm \Gamma_\Phi$ and, as can be seen, for the above value of M_A, the three Higgs boson masses are overlapping.

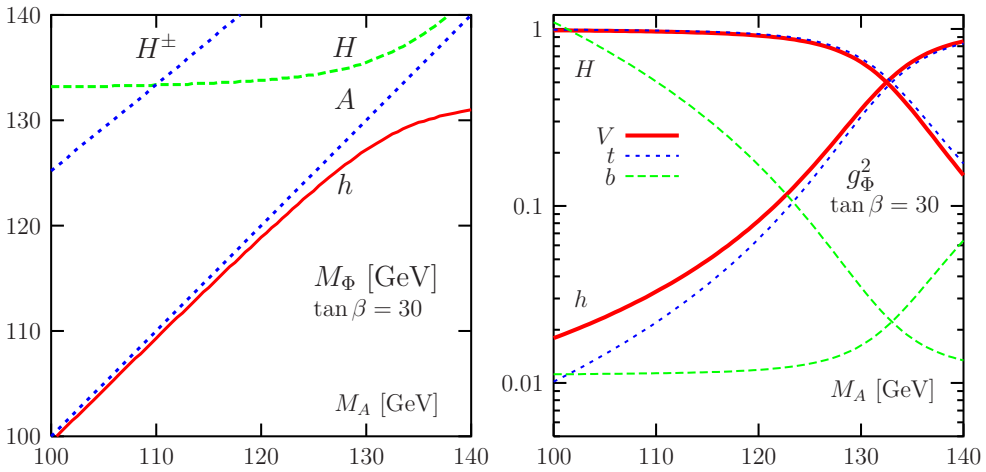

Figure 3.28: *The masses of the MSSM Higgs bosons (left) and the normalized couplings of the CP-even Higgs bosons to vector bosons and third-generation quarks (right) as a function of M_A and $\tan\beta = 30$. For the b-quark couplings, the values $10 \times g^{-2}_{\Phi bb}$ are plotted.*

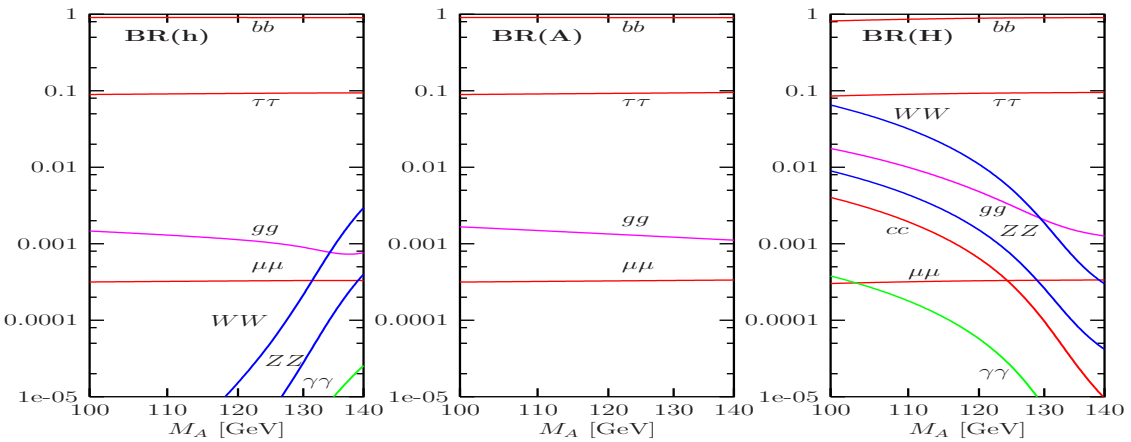

Figure 3.29: *The branching ratios of the neutral MSSM Higgs bosons h, A, H for the various decay modes as a function of M_A and for $tan\beta = 30$.*

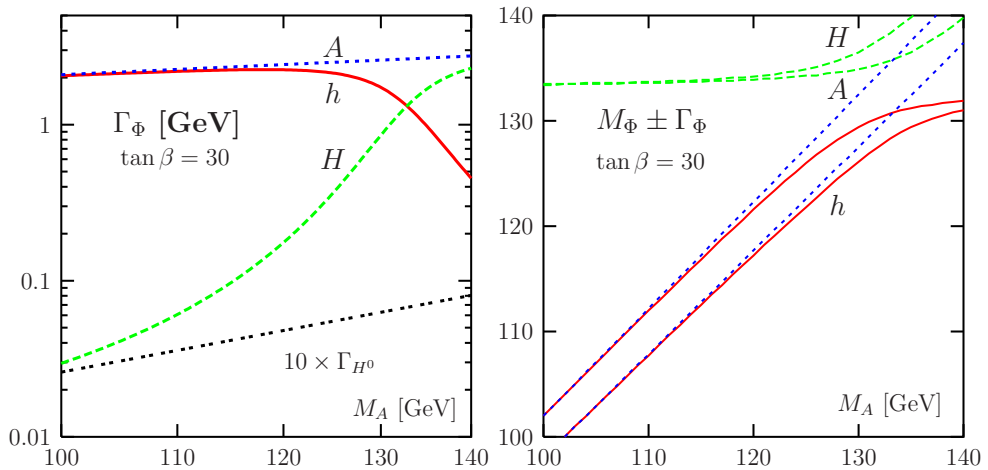

Figure 3.30: *Total decay widths Γ_Φ (left) and the mass bands $M_\Phi \pm \Gamma_\Phi$ (right) for the neutral MSSM Higgs bosons as a function of M_A and for $tan\beta = 30$.*

3.3.3.2 Discrimination of the three Higgs bosons at the LHC

The most difficult problem we must face in the intense-coupling regime, is to resolve between the three peaks of the neutral Higgs bosons when their masses are close to one another. The only decays with large branching ratios on which we can rely are the $b\bar{b}$ and $\tau^+\tau^-$ modes. At the LHC, the former has too large QCD background to be useful, while for the latter channel [which has been shown to be viable for discovery] the expected experimental resolution on the invariant mass of the $\tau^+\tau^-$ system is of the order of 10 to 20 GeV, and thus clearly too large. One would then simply observe a relatively wide resonance corresponding to A and h and/or H production. Since the branching ratios of the decays into $\gamma\gamma$ and $ZZ^* \to 4\ell$ are too small, a way out is to use the Higgs decays into muon pairs: although the branchings ratio is rather small,

BR($\Phi \to \mu^+\mu^-$) $\sim 3.3 \times 10^{-4}$, the resolution is expected to be as good as 1 GeV, i.e. comparable to the total width, for $M_\Phi \sim 130$ GeV.

Because of the strong enhancement of the Higgs couplings to bottom quarks, the three Higgs bosons will be produced at the LHC mainly[10] in the gluon–gluon process, $gg \to \Phi = h, H, A \to \mu^+\mu^-$, which is dominantly mediated by b-quark loops, and the associated production with $b\overline{b}$ pairs, $gg/q\overline{q} \to b\overline{b} + \Phi \to b\overline{b} + \mu^+\mu^-$. We have generated both the signals and backgrounds with the program CompHEP [188]. For the backgrounds to $\mu^+\mu^-$ production, we have included only the Drell–Yan process $pp \to \gamma^*, Z^* \to \mu^+\mu^-$, which is expected to be the largest source. But for the $pp \to \mu^+\mu^- b\overline{b}$ final state, however, we have included the full 4-fermion background, which is mainly due to the process $pp \to b\overline{b}Z$ with $Z \to \mu^+\mu^-$.

The differential cross sections are shown for the scenario $M_A = 125$ GeV and $\tan\beta = 30$, which leads to $M_h = 123.3$ GeV and $M_H = 134.3$ GeV, as a function of the invariant dimuon mass in Fig. 4 (left), for $pp(\to h, H, A) \to \mu^+\mu^-$. As can be seen, the signal rate is fairly large but when put on top of the huge Drell–Yan background, the signal becomes completely invisible. We thus conclude, that already at the level of a "theoretical simulation", the Higgs signal will probably be hopeless to extract in this process for $M_H \lesssim 140$ GeV. In the right-hand side of Fig. 4, we display, again for the same scenario, the signal from $pp \to \mu^+\mu^- b\overline{b}$ and the complete 4-fermion SM background as a function of the dimuon system. The number of signal events is an order of magnitude smaller than in the previous case, but one can still see the two peaks, corresponding to h/A and H production, on top of the background.

In order to perform a more realistic analysis, we have generated unweighted events for the full 4-fermion background $pp \to \mu^+\mu^- + b\overline{b}$ and for the signal. With the help of the new CompHEP–PYTHIA interface [189], the unweighted events have been processed through PYTHIA 6.2 [190] for fragmentation and hadronization. To simulate detector effects, such as acceptance, muon momentum smearing, and b–jet tagging, we take the example of the CMS detector. The details have been given in Ref. [186] and the main points are that: 1) the mass resolution on the dimuons is about 1%, and 2) the efficiency for b–jet tagging is of the order of 40%. The results of the simulation for a luminosity of 100 fb^{-1} are shown in Fig. 5, where the number of $\mu^+\mu^- b\overline{b}$ events in bins of 0.25 GeV is shown as a function of the mass of the dimuon system. The left-hand side shows the signals with and without the resolution smearing as obtained in the Monte-Carlo analysis, while the figures in the right-hand side show also the backgrounds, including the detector effects.

For the point under consideration, the signal cross section for the heavier CP-even H boson is significantly smaller than the signals from the lighter CP-even h and pseudoscalar A bosons; the latter particles are too too close in mass to be resolved, and only one single broad peak for h/A is clearly visible. To resolve also the peak for the H boson, the integrated luminosity should be increased by a factor of 3 to 4. We have also performed the analysis for $M_A = 130$ and 135 GeV. In the former case, it would be possible to see also the second peak, corresponding to the H boson signal with a luminosity of 100 fb^{-1}, but again the h and A peaks cannot be resolved. In the latter

[10] The Higgs-strahlung and vector-boson fusion processes, as well as associated production with top quarks, will have smaller cross sections since the Higgs couplings to the involved particles are suppressed.

case, all three h, A and H bosons have comparable signal rates, and the mass differences are large enough for us to hope to be able to isolate the three different peaks, although with some difficulty.

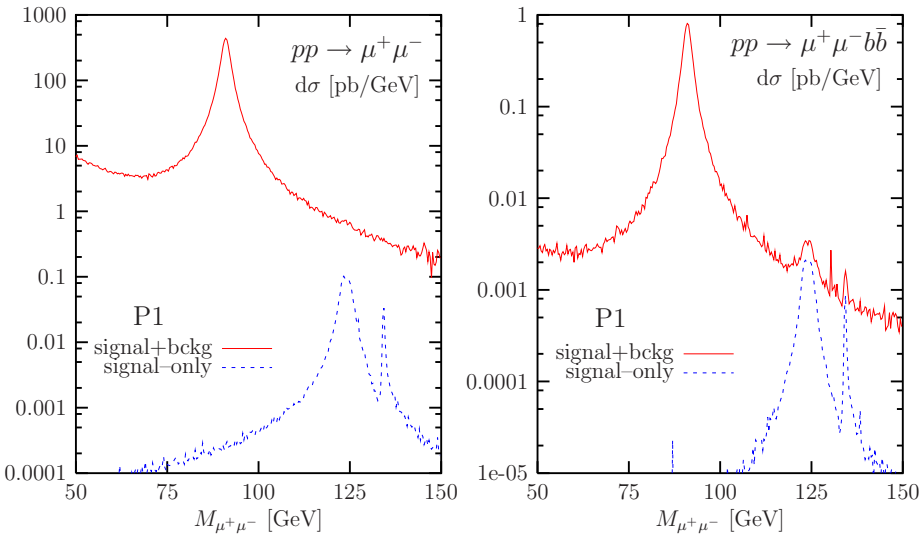

Figure 3.31: *The differential cross section in pb/GeV as a function of the dimuon mass for the point P1, for both the signal and signal plus background in the processes* $pp(\to \Phi) \to \mu^+\mu^-$ *(left figure) and* $pp(\to \Phi b\bar{b}) \to \mu^+\mu^- b\bar{b}$ *(right figure).*

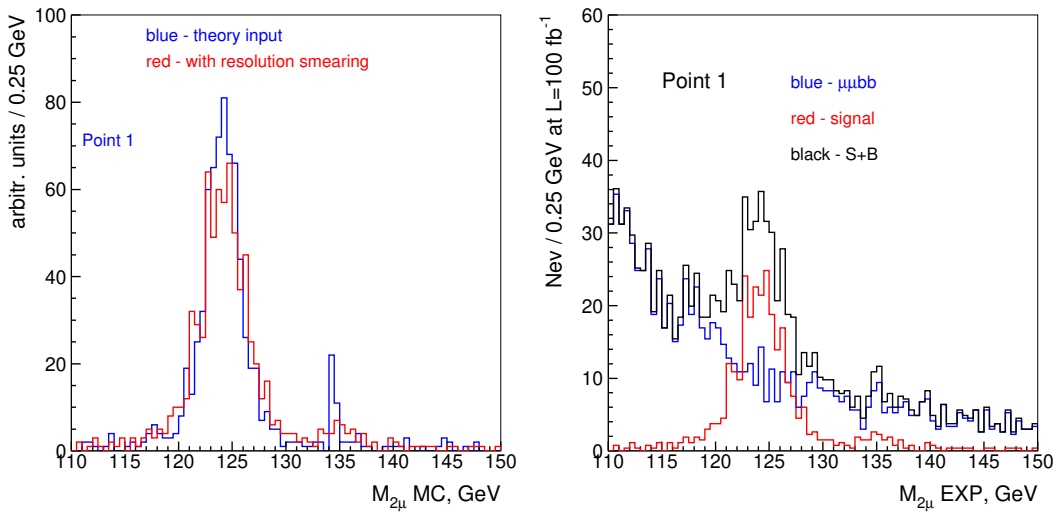

Figure 3.32: $\mu^+\mu^-$ *pair invariant mass distributions for the signal before and after detector resolution smearing (left) and for the signal and the background (right) for* $M_A = 125$ *GeV.*

3.3.3.3 Discrimination in e^+e^- collisions

In e^+e^- collisions, the CP-even Higgs bosons can be produced in the bremsstrahlung, $e^+e^- \to Z + h/H$, and vector-boson fusion, $e^+e^- \to \nu\overline{\nu} + h/H$, processes. The CP-odd Higgs particle cannot be probed in these channels since it has no couplings to gauge bosons at the tree level, but it can be produced in association with h or H bosons in the process $e^+e^- \to A + h/H$. The cross sections for the bremsstrahlung and the pair production as well as the cross sections for the production of h and H are mutually complementary, coming either with a coefficient $\sin^2(\beta-\alpha)$ or $\cos^2(\beta-\alpha)$ and one has:

$$\begin{aligned} \sigma(e^+e^- \to Z + h/H) &= \sin^2/\cos^2(\beta-\alpha)\sigma_{\rm SM} \\ \sigma(e^+e^- \to A + h/H) &= \cos^2/\sin^2(\beta-\alpha)\overline{\lambda}\sigma_{\rm SM} \end{aligned}$$

where $\sigma_{\rm SM}$ is the SM Higgs cross section and $\lambda \sim 1$ for $\sqrt{s} \gg M_A$ accounts for the P–wave suppression near threshold. Since $\sigma_{\rm SM}$ is rather large, being of the order of 100 fb at a c.m. energy of $\sqrt{s} = 300$ GeV [11] the production and the collective detection of the three Higgs bosons is easy with the integrated luminosity, $\int \mathcal{L} \sim 1$ ab^{-1}, which is expected for the TESLA machine for instance [57].

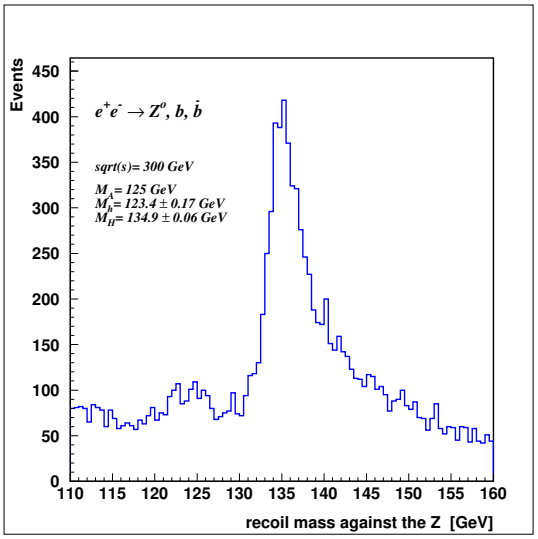

Figure 3.33: *The recoil mass distribution for the signal and backgrounds including ISR and beamstrahlung for the parameter point P1*

In e^+e^- collisions, the Higgs–strahlung processes offer a first way to discriminate between the three Higgs particles, since the pseudoscalar A boson is not involved in this process. For the SM Higgs boson the measurement of the recoil mass in both leptonic and hadronic Z boson decay channels allows a very good determination of

[11] Small $\sqrt{s}$ should be considered for this scenario, $M_\Phi \sim 130$ GeV, since the above two processes are mediated by s-channel gauge boson exchange and the cross sections scale like $1/s$

the Higgs mass of $M_H \sim 120$ GeV with a precision of $\Delta M_H \sim 40$ MeV [57]. In the discussed scenario when two scalar Higgs bosons h and H contribute with different rates the influence of the initial state radiation and a beamstrahlung are more important and should be carefully taken into account. Detail simulation including all the main backgrounds by means of the CompHEP and PYTHIA programs and the detector effects by means of the SIMDET program [191] shows that the most promising way to measure h and H masses is to select first the $Zb\bar{b}$ event sample and then use the recoil mass technique for that sample. Results of simulations for the case of TESLA and for the MSSM parameter point P1 are shown in the Fig. 6. An accuracy of $\Delta M_H \sim 60$ MeV could be reached for the heavy H boson and of $\Delta M_H \sim 170$ MeV for the light h boson.

The complementary pair production channels $e^+e^- \to A + h/H$ will allow to probe the pseudoscalar A boson. Since the h and H boson masses will be known, as discussed previously, one can concentrate on the A particle and measure its mass either via reconstruction in the $b\bar{b}$ and $\tau^+\tau^-$ final states or through a scan in the threshold region. The first method has been discussed in Ref. [192] for heavy Higgs bosons in the $e^+e^- \to HA \to 4b$ final state topology at a c.m. energy $\sqrt{s} = 800$ GeV and with a luminosity of 200 fb^{-1}, with the conclusion that a value $\Delta M_A/M_A \sim 0.2\%$ can be obtained for A boson masses far below the beam energy. Since the c.m. energy that should be considered in our scenario is much smaller, $\sqrt{s} = 350$ GeV, this leads to a larger [about a factor of 5 if there is no coupling suppression] cross section with a luminosity which is also larger. If we take this conservative number as a reference, one could then measure the pseudoscalar mass with a precision of $\Delta M_A \lesssim 200$–300 MeV, which is much smaller than $M_A - M_h$ or $M_H - M_A$.

Higher accuracies could be obtained by measuring the $e^+e^- \to A + h/H$ cross sections near the respective thresholds and which rise as $\sigma \sim \beta^3$, if one makes the analogy with slepton pair production in e^+e^- collisions, which has similar characteristics as our process. Indeed, it has been shown in Ref. [193] that a slepton mass of order 100 GeV can be measured with a precision of less than 0.1% in a threshold scan at TESLA. If this holds also true for $A + h/H$ production [the cross sections are smaller but the final states are cleaner], this is more than enough to discriminate all Higgs bosons in our scenario.

The results quoted here are from an extrapolation of SM–like searches where only one isolated Higgs boson is produced. A dedicated analysis, including a detector simulation, of the intense coupling regime in e^+e^- collisions and the prospect for measuring the A Higgs boson mass is needed. [194].

3.3.3.4 LHC and LC interplay

Once Higgs boson masses will be measured at a e^+e^- LC one can study a problem of a complete parameter measurement for the corresponding MSSM parameter point. In this sense one can use the measured masses and extracted branching ratios BR($\Phi \to b\bar{b}$) at the linear collider to measure $glue - glue - Higgs$ couplings, branching ratios BR($\Phi \to \mu^+\mu^-$) and $b - \overline{b} - Higgs$ couplings via the discussed processes $pp(\to \Phi) \to \mu^+\mu^-$ and $pp(\to \Phi b\bar{b}) \to \mu^+\mu^- b\bar{b}$ at the LHC. Obviosly this can not be done at LC alone.

3.3.3.5 Conclusions

We have shown that in the intense-coupling regime, i.e. when the h, H and A MSSM bosons have masses too close to the critical point $M_h^{\max}$ and when the value of $\tan\beta$ is large, the detection of the individual Higgs boson peaks is very challenging at the LHC. It is only in the associated Higgs production mechanism with $b\bar{b}$ pairs, with at least one tagged b-jet, and with Higgs particles decaying into the clean muon-pair final states, that there is a chance of observing the three signals and resolve between them. This would be possible only if the Higgs mass differences are larger than about 5 GeV.

In e^+e^- collisions, thanks to the clean environment and the complementarity of the production channels, one expects the three Higgs bosons to be more easily separated. The Higgs–strahlung processes allow from the very beginning to probe the h and H bosons and to measure their masses by studying the recoiling Z boson. The associated CP-even and CP-odd Higgs production would then allow to probe the pseudoscalar A boson, either in the direct reconstruction of its final decay products or via a threshold scan. The measured characteristics at the LC allow then to measure several others, like glue-glue-Higgs couplings and BR($\Phi \to \mu^+\mu^-$) at the LHC. From the other hand, in case if the Higgs masses will be not possible to resolve completely at the LHC the information on a overall peak position from the LHC will help to make more proper choice of the energy at LC.

3.3.4 Estimating the precision of a $\tan\beta$ determination with $H/A \to \tau^+\tau^-$ in CMS and $\tau^+\tau^-$ fusion at a high-energy photon collider

3.3.4.1 The uncertainty of the $\tan\beta$ measurement with $H/A \to \tau^+\tau^-$ in CMS

If Higgs bosons will be discovered at the LHC, the determination of their properties will be of high relevance in order to unravel the underlying model. In the minimal supersymmetric extension (MSSM) of the Standard Model (SM) as well as a general type-II Two-Higgs-Doublet-Model one of the most important parameters is $\tan\beta$, the ratio of the two vacuum expectation values $v_{1,2}$. In this work the accuracy of the tanβ measurement is estimated in the $H/A \to \tau^+\tau^-$ decay channels by investigating the final states $e\mu$, $\ell\ell$ ($\ell\ell = e\mu, ee, \mu\mu$) [195], lepton+jet [196] and two-jets [197]. The associated Higgs boson production cross section $gg \to b\bar{b}H/A$ is approximately proportional to $\tan^2\beta$ at large $\tan\beta$. Due to this feature the uncertainty of the $\tan\beta$ measurement is only half of the uncertainty of the rate measurement. However, due to the presence of potentially large radiative corrections [198] the extracted value has to be considered as an effective parameter $\tan\beta_{eff}$. The determination of the fundamental $\tan\beta$ value requires knowledge of the model behind.

The event rates of $H/A \to \tau^+\tau^-$ decay channels are studied in Refs. [195, 197]. The CMS trigger efficiencies and thresholds [199] are taken into account. Event selections to suppress the backgrounds include lepton isolation, τ jet identification, τ tagging with impact parameter, b tagging and jet veto. The effective $\tau^+\tau^-$ mass is reconstructed assuming that the neutrinos are emitted collinear with the measured tau decay products. The signal events were simulated with the following values of

MSSM SUSY parameters: M_2 = 200 GeV/c^2, μ = 300 GeV/c^2, $M_{\tilde{g}}$ = 800 GeV/c^2, $M_{\tilde{q},\tilde{\ell}}$ = 1 TeV/c^2 and A_t is set to 2450 GeV/c^2. The top mass is set to 175 GeV/c^2 and Higgs boson decays to SUSY particles are allowed. We have not included the uncertainties related to the MSSM parameters, but kept them fixed at our chosen values. The uncertainty of the background estimation as well as the uncertainty of the signal selection efficiency have not yet been taken into account in this study. We expect, however, that the background uncertainty and uncertainty of the signal selection will be of the order of 5%. The statistical errors from different $\tau^+\tau^-$ final states are combined using the standard weighted least-squares procedure described in [200].

In addition to event rates, the accuracy of the $\tan\beta$ measurement depends on the systematic uncertainty from the luminosity measurement and on the theoretical uncertainty of the cross section calculation. A 5% uncertainty of the luminosity measurement was taken. The theoretical accuracy of the cross section depends on the transverse momentum range of the two spectator quarks and reduces to 10-15% with the requirement of $p_T^{b,\overline{b}} \gtrsim$ 20 GeV/c [201, 202]. However, since the associated b jets are very soft, reconstructing and b tagging them is difficult. In order to minimize the total measurement error, only one b jet is assumed to be b tagged and a theoretical uncertainty of about 20% is adopted accordingly [201, 203]. The branching ratio $BR(H/A \to \tau\tau)$ is approximately constant at large $\tan\beta$, and the uncertainty of the branching ratio due to the SM input parameters is about 3%.

Since the value of the cross section depends on the Higgs boson mass, the uncertainty of the mass measurement leads to an uncertainty in the signal rate. The Higgs mass is measured using the different final states, and the cross section uncertainties due to mass measurement errors are combined. The mass resolution is almost constant as a function of M_A, $\sim$ 24% for the leptonic final states, $\sim$ 17% for the lepton+jet final state and $\sim$ 12% for the hadronic final state [195]. The uncertainty of the mass measurement is calculated from the gaussian fit of the mass peak as $\sigma_{Gauss}/\sqrt{N_S}$, and the error induced in the cross section ($\Delta\sigma(\Delta m)$) is estimated by varying the cross section for Higgs masses M_0 and $M_0 \pm \sigma_{Gauss}/\sqrt{N_S}$. At the 5$\sigma$ limit where the signal statistics is lowest, the uncertainty of the mass measurement generates 5–6% uncertainty in the $\tan\beta$ measurement.

Table 3.6 shows the statistical uncertainty of the $\tan\beta$ measurement and the cross-section uncertainty due to the mass measurement for each individual final state and for the combined final states from $H/A \to \tau^+\tau^-$ for 30 fb^{-1}. The total estimated uncertainty including theoretical and luminosity errors are shown for the combined final states. The results are shown for the region of the (M_A, $\tan\beta$) parameter space where the statistical significance exceeds 5σ. Close to the 5σ limit the statistical uncertainty is of the order of 11–12%, but it decreases rapidly for increasing $\tan\beta$. As shown in the table, the highest statistical accuracy, about 5% for M_A = 200 GeV/c^2 and $\tan\beta$ = 20, is obtained with the lepton+jet final state. Combining other channels with the lepton+jet channel in this mass range improves the precision only slightly.

Figure 3.34 shows the error on the $\tan\beta$ measurement with error bars for the combined $e\mu + \ell j + jj$ channel for 30 fb^{-1} at low luminosity. The statistical uncertainties are depicted by the smaller error bars and gray area, the uncertainties including the systematic errors are presented with longer error bars. The errors are shown in the region with signal significance larger than 5σ. The statistical uncertainty is largest close to the 5σ limit, where combining the different final states improves the accuracy

30 fb^{-1}	M_A = 200 GeV/c^2 $\tan\beta$ = 20		M_A = 200 GeV/c^2 $\tan\beta$ = 30		M_A = 500 GeV/c^2 $\tan\beta$ = 30		M_A = 500 GeV/c^2 $\tan\beta$ = 40	
	Δstat	$\Delta\sigma(\Delta m)$	Δstat	$\Delta\sigma(\Delta m)$	Δstat	$\Delta\sigma(\Delta m)$	Δstat	$\Delta\sigma(\Delta m)$
$H/A \to \tau^+\tau^- \to e\mu$	8.95%	4.82%	4.85%	3.27%	-	-	-	-
$H/A \to \tau^+\tau^- \to \ell\ell$	7.96%	3.50%	4.08%	2.37%	-	-	-	-
$H/A \to \tau^+\tau^- \to \ell j$	4.81%	2.46%	2.84%	1.65%	-	-	8.40%	4.82%
$H/A \to \tau^+\tau^- \to jj$	13.7%	4.73%	8.25%	3.21%	12.4%	5.82%	8.45%	4.44%
Combined $e\mu + \ell j + jj$	4.05%	1.99%	2.35%	1.34%	9.09%	4.28%	5.96%	3.26%
	$\Delta\tan\beta/\tan\beta$		$\Delta\tan\beta/\tan\beta$		$\Delta\tan\beta/\tan\beta$		$\Delta\tan\beta/\tan\beta$	
	20.1%		17.7%		27.4%		23.3%	
Combined $\ell\ell + \ell j + jj$	3.94%	1.85%	2.24%	1.25%	9.09%	4.28%	5.96%	3.26%
	$\Delta\tan\beta/\tan\beta$		$\Delta\tan\beta/\tan\beta$		$\Delta\tan\beta/\tan\beta$		$\Delta\tan\beta/\tan\beta$	
	19.9%		17.5%		27.4%		23.3%	

Table 3.6: Statistical uncertainties of the $\tan\beta$ measurement and the uncertainties due to mass measurement for individual $H/A \to \tau^+\tau^-$ and combined final states in four (M_A,$\tan\beta$) parameter space point for 30 fb^{-1}. The total error includes statistical error, mass measurement error, theoretical uncertainty of the cross section (20%) and the branching ratio (3%), and the luminosity uncertainty (5%).

most. With one tagged b jet in the event the value of $\tan\beta$ can be determined in the $H/A \to \tau^+\tau^-$ decay channels with an accuracy of better than $\sim$ 35% after collecting 30 fb^{-1}.

3.3.4.2 The uncertainty of the $\tan\beta$ measurement in $\tau^+\tau^-$ fusion at a photon collider

At a high-energy photon collider light h and heavy H and A Higgs bosons will be produced in $\tau^+\tau^-$ fusion

$$\gamma\gamma \to (\tau^+\tau^-) + (\tau^+\tau^-) \to \tau^+\tau^- + h/H/A \tag{3.27}$$

within the MSSM for large values of $\tan\beta$ with a rate which enables a measurement of $\tan\beta$ with high accuracy. The production cross sections grow with the square of $\tan\beta$ for large values of this parameter. $\tau^+\tau^-$ fusion at a photon collider is superior to $b\bar{b}$ fusion due to the larger electric τ charge. The cross sections range between about 1 and 10 fb so that the expected event rates at a photon collider with 600 GeV c.m. energy allow for a good statistical accuracy of the cross sections. The size of the cross sections can be estimated by using the equivalent particle approximation which reduces the hard process to $\tau^+\tau^-$ fusion $\tau^+\tau^- \to \Phi$ ($\Phi = h, H, A$) [204].

The dominant Higgs boson decays are those into $b\bar{b}$ pairs, if decays into supersymmetric particles are forbidden or rare. The background of $\tau^+\tau^- b\bar{b}$ production can be sufficiently suppressed by appropriate cuts on the minimal angle of the τ leptons and their minimal energy. By requiring the τ leptons to go into opposite hemispheres and the invariant $b\bar{b}$ mass to be in a narrow window of $\pm 0.05\ M_\Phi$ around the Higgs mass M_Φ the background can be strongly suppressed to a negligible level for heavy Higgs masses, i.e. 2–3 orders of magnitude below the signal processes. This can be understood from the feature that the background is dominated by $\tau^+\tau^- \to b\bar{b}$ in

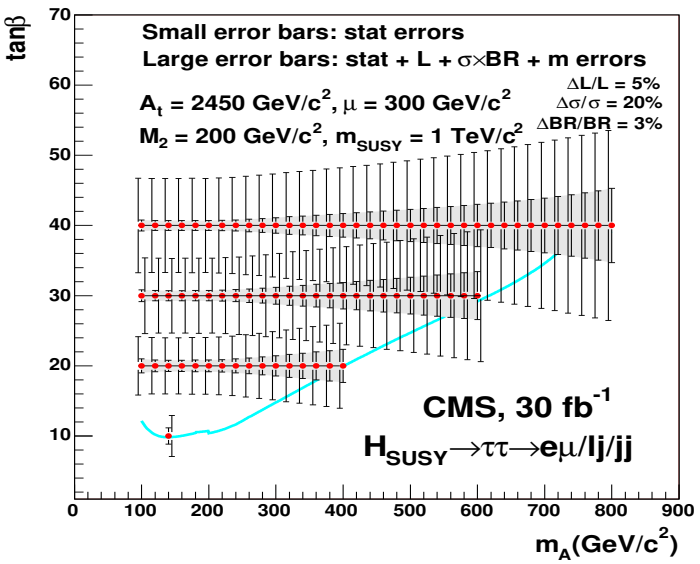

Figure 3.34: The uncertainty of the $\tan\beta$ measurement shown as error bars. The small error bars and gray area show the statistical errors only. The large error bars exhibit the uncertainty if statistical errors, the mass measurement uncertainties, the luminosity uncertainty (5%) and the theoretical uncertainty of the production cross section (20%) and the branching ratio (3%) are taken into account. The solid curve corresponds to the 5σ-discovery contour.

the equivalent particle approximation and diffractive $\gamma\gamma \to (\tau^+\tau^-)(b\bar{b})$ events, the pairs scattering off each other by Rutherford photon exchange. The latter can be suppressed by requiring a large invariant mass for the $(b\bar{b})$ pair and the τ leptons to go into opposite hemispheres. The first process will mainly be diminished by the invariant $b\bar{b}$ mass cut.

$\Delta\tan\beta$	M_A [GeV/c^2]	
	200	400
Δstat	0.53	0.78
Δtot	0.90	1.31

Table 3.7: Absolute errors on the $\tan\beta$ measurement based on H/A production for $M_A = 200$ and 400 GeV/c^2 at a photon collider with c.m. energy of 600 GeV and an integrated luminosity of 200 fb^{-1}, valid for $\tan\beta > 10$. The first line labelled with Δstat shows the statistical error, while the second line presents the total expected accuracy after taking into account the experimental efficiencies, i.e. $\epsilon_{b\bar{b}} = 0.7$ and $\epsilon_{\tau^+\tau^-} = 0.5$ [205]. All errors include the sum over H and A Higgs bosons. Since the background can be suppressed to a negligible level, the absolute errors on $\tan\beta$ are independent of $\tan\beta$ at large values.

A first theoretical signal and background analysis leads to the results presented in Table 3.7 for the expected accuracies of the $\tan\beta$ measurement at a photon collider [204]. They range between about 1 and 10%. Thus, $\tau^+\tau^-$ fusion provides a further significant observable to a global determination of $\tan\beta$ at high values.

3.3.5 LHC and LC determinations of $\tan\beta$

An important goal if SUSY is discovered will be a precise determination of the value of $\tan\beta$. If the heavy Higgs boson, H and A, masses are such that their production rates are large, Ref. [206] has shown that substantial sensitivity to $\tan\beta$ will derive from measurements, at both the LHC and a high-luminosity linear collider, of the H and A production processes, branching fractions and decay widths. These are all largely determined by the ratio of vacuum expectation values that defines $\tan\beta$, and each can be very accurately measured at an LC over a substantial range of the relevant $\tan\beta$ values, $1 < \tan\beta < 60$. In particular, there are several Higgs boson observables which are potentially able to provide the most precise measurement of $\tan\beta$ when $\tan\beta$ is very large. In the context of the MSSM, there is a particularly large variety of complementary methods at the LC that will allow an accurate determination of $\tan\beta$ when $m_A \lesssim \sqrt{s}/2$ so that $e^+e^- \to HA$ pair production is kinematically allowed. We will employ the sample case of $m_A = 200$ GeV at a LC with $\sqrt{s} = 500$ GeV. [Although $m_A = 200$ GeV is excluded by LEP limits in the MSSM context for some choices of parameters, *e.g.* for $\tan\beta \lesssim 3$ in the maximal-mixing scenario with $M_{SUSY} = 1$ TeV, our results will be representative of what can be achieved whenever $\sqrt{s}$ is large enough for $e^+e^- \to HA$ pair production without much phase space suppression. Outside the MSSM context, $m_A = 200$ GeV is completely allowed.] The complementarity has been demonstrated of employing:

a) the $b\bar{b}A,\ b\bar{b}H \to b\bar{b}b\bar{b}$ rate;

b) the $HA \to b\bar{b}b\bar{b}$ rate;

c) a measurement of the average H, A total width in HA production;

d) the $H^+H^- \to t\bar{b}\,\bar{t}b$ rate; and

e) the total $H^\pm$ width measured in $H^+H^- \to t\bar{b}\,\bar{t}b$ production.

By combining the $\tan\beta$ errors from all these processes in quadrature, we obtain the net statistical errors on $\tan\beta$ shown in Fig. 3.35 by the lines [solid for SUSY scenario (I) and dashed for SUSY scenario (II)], assuming a multi-year integrated luminosity of $\mathcal{L} = 2000$ fb^{-1}. The scenarios are defined as:

(I) $m_A = 200$ GeV, $m_{\tilde{g}} = 1$ TeV, $\mu = M_2 = 250$ GeV,
$m_{\tilde{t}_L} = m_{\tilde{b}_L} = m_{\tilde{t}_R} = m_{\tilde{b}_R} \equiv m_{\tilde{t}} = 1$ TeV,
$A_\tau = A_b = 0$, $A_t = \mu/\tan\beta + \sqrt{6}m_{\tilde{t}}$ (maximal mixing);

(II) $m_A = 200$ GeV, $m_{\tilde{g}} = 350$ GeV, $\mu = 272$ GeV, $M_2 = 120$ GeV,
$m_{\tilde{t}_L} = m_{\tilde{b}_L} = 356$ GeV, $m_{\tilde{t}_R} = 273$ GeV, $m_{\tilde{b}_R} = 400$ GeV,
$A_\tau = 0$, $A_b = -672$ GeV, $A_t = -369$ GeV.

We see that, independent of the scenario, the Higgs sector will provide an excellent determination of $\tan\beta$ at small and large $\tan\beta$ values, leading to an error on $\tan\beta$ of 10% or better, provided systematic errors can be kept below the statistical level. If SUSY decays of the $H, A, H^\pm$ are significant [SUSY scenario (II)], the $\tan\beta$ error will be smaller than 13% even in the more difficult moderate $\tan\beta$ range. However, if SUSY decays are not significant [SUSY scenario (I)] there is a limited range of moderate $\tan\beta$ for which the error on $\tan\beta$ would be large, reaching about 50%. In general, it will be

important to establish the light SUSY particle spectrum (using a combination of LHC and LC data) in order to avoid systematic errors in the $\tan\beta$ determination deriving from the influence of non-Higgs model parameters upon predictions for Higgs decays and production rates.

Regardless of the relative magnitude of the LHC versus LC $\tan\beta$ errors, the clean LC environment will provide an important and independent measurement that will complement any LHC determination of $\tan\beta$. Different uncertainties will be associated with the determination of $\tan\beta$ at a hadron and an e^+e^- collider because of the different backgrounds. Further, the LHC and LC measurements of $\tan\beta$ will be highly complementary in that the experimental and theoretical systematic errors involved will be very different.

Combining all the different LC measurements as above does not fully account for the fact that the "effective" $\tan\beta$ value being measured in each process is only the same at tree-level. The $\tan\beta$ values measured via the $H \to b\bar{b}$ Yukawa coupling, the $A \to b\bar{b}$ Yukawa coupling and the $H^+ \to t\bar{b}$ Yukawa coupling could all be influenced differently by the MSSM one-loop corrections. For some choices of MSSM parameters, the impact of MSSM radiative corrections on interpreting these measurements can be substantial [213]. However, if the masses of the SUSY particles are known, so that the important MSSM parameters entering these radiative corrections (other than $\tan\beta$) are fairly well determined, then a uniform convention for the definition of $\tan\beta$ can be adopted and, in general, an excellent determination of $\tan\beta$ (with accuracy similar to that obtained via our tree-level procedures) will be possible using the linear collider observables considered here. Even for special SUSY parameter choices such that one of the Yukawa couplings happens to be significantly suppressed, the observables a)-e) would provide an excellent opportunity for pinning down all the Yukawa couplings and checking the consistency of the MSSM model.

To illustrate the relation between the other MSSM model parameters and the systematic errors in the $\tan\beta$ determination, we give one example. For $\tan\beta = 5$, $m_A = m_H = 200$ GeV, M_2 large enough that there are no SUSY decays of the H and A, $A_t = A_b = 0$ and $m_0 = 1$ TeV for the 1st and 2nd generations, one finds

$$\begin{array}{llll} \mathrm{BR}(H \to b\bar{b}) = 0.61 & \text{and} & \mathrm{BR}(A \to b\bar{b}) = 0.87 & \text{for } m_{\tilde{t}} = m_{\tilde{b}} = 500\ \mathrm{GeV}, \\ \mathrm{BR}(H \to b\bar{b}) = 0.69 & \text{and} & \mathrm{BR}(A \to b\bar{b}) = 0.88 & \text{for } m_{\tilde{t}} = m_{\tilde{b}} = 1000\ \mathrm{GeV}. \end{array} \tag{3.28}$$

The resulting $HA \to b\bar{b}b\bar{b}$ rate differs by about 14% between the two scenarios. The bottom and stop masses would need to be known to within about 150 GeV in order to bring the systematic uncertainty from this source below the roughly 5% statistical uncertainty shown in Fig. 3.35. Dependence on the stop and sbottom sector mixing angles, the gluino mass and so forth are non-negligible as well. The precision of SM parameters, in particular m_t and m_b (the latter enters directly into the $b\bar{b}$ coupling strength of the H and A) will also contribute to the systematic uncertainty. Of course, because $\tan\beta$ is not a directly measurable quantity, other techniques for determining $\tan\beta$ suffer from similar systematics issues.

Finally, it is important to note that the LC techniques employed for the $\tan\beta$ determination discussed above can also be employed in the case of other Higgs sector models. For example, in the general (non-SUSY) 2HDM, if the only non-SM-like Higgs boson with mass below $\sqrt{s}$ is the A [321], then a good determination of $\tan\beta$

will be possible at high $\tan\beta$ from the $b\bar{b}A \to b\bar{b}b\bar{b}$ production rate. Similarly, in models with more than two Higgs doublet and/or triplet representations, the Yukawa couplings of the Higgs bosons, and, therefore, the analogues of the 2HDM parameter $\tan\beta$, will probably be accurately determined through Higgs production observables in e^+e^- collisions.

Now, we will compare the LC results summarized in Fig. 3.35 [206] to the $\tan\beta$ accuracies that can be achieved at the LHC based on $H, A, H^\pm$ production and decay processes. First note that there is a wedge-shaped window of moderate $\tan\beta$ and $m_A \gtrsim 200$ GeV for which the A, H and $H^\pm$ are all unobservable (see, for example, Refs. [8, 207]). In this wedge, the only Higgs boson that is detectable at the LHC is the light SM-like Higgs boson, h. Precision measurements of the properties of the h typically only provide weak sensitivity to $\tan\beta$, and will not be considered here. The lower $\tan\beta$ bound of this moderate-$\tan\beta$ wedge is defined by the LEP-2 limits [208], which are at $\tan\beta \sim 3$ for $m_A \sim 200$ GeV, falling to $\tan\beta \sim 2.5$ for $m_A \gtrsim 250$ GeV, assuming the maximal mixing scenario [see SUSY scenario (I) defined earlier]. The upper $\tan\beta$ limit of the wedge is at $\tan\beta \sim 7$ for $m_A \sim 200$ GeV rising to $\tan\beta \sim 15$ at $m_A \sim 500$ GeV. For either smaller or larger $\tan\beta$ values, the heavy MSSM Higgs bosons can be detected and their production rates and properties will provide sensitivity to $\tan\beta$.

We will now summarize the results currently available regarding the determination of $\tan\beta$ at the LHC using Higgs measurements (outside the wedge region) assuming a luminosity of $\mathcal{L} = 300$ fb^{-1}. The methods employed are those proposed in [209] as reanalyzed from a more experimental perspective by the ATLAS and/or CMS collaborations. The reactions that have been studied at the LHC are the following.

1. $gg \to H \to ZZ \to 4\ell$ [89].

   The best accuracy that can be achieved at low $\tan\beta$ is obtained from the $H \to ZZ \to 4\ell$ rate. One finds $\Delta\tan\beta/\tan\beta = \pm 0.1$ at $\tan\beta = 1$ rising to $> \pm 0.3$ by $\tan\beta = 1.5$ for the sample choice of $m_H = 300$ GeV. For $m_H < 2m_Z$, $\tan\beta$ cannot be measured via this process. (Of course, in the MSSM maximal mixing scenario, such low values of $\tan\beta$ are unlikely in light of LEP-2 limits on m_h.)

2. $gg \to H + gg \to A \to \tau^+\tau^-, \mu^+\mu^-$ and $gg \to b\bar{b}H + b\bar{b}A \to b\bar{b}\tau^+\tau^-, b\bar{b}\mu^+\mu^-$ [89].

   At high $\tan\beta$ and taking $m_A = 150$ GeV, Fig. 19-86 of [89] shows that the $gg \to H \to \tau^+\tau^-$, $gg \to A \to \tau^+\tau^-$, and $gg \to b\bar{b}A + b\bar{b}H \to b\bar{b}\tau^+\tau^-$ rates can, in combination, be used to determine $\tan\beta$ with an accuracy of ± 0.15 at $\tan\beta = 5$, improving to ± 0.06 at $\tan\beta = 40$. The corresponding rates with $H, A \to \mu^+\mu^-$ yield a somewhat better determination at higher $\tan\beta$: ± 0.12 at $\tan\beta = 10$ and ± 0.05 at $\tan\beta = 40$.

   Interpolating, using Figs. 19-86 and 19-87 from [89], we estimate that at $m_A \sim 200$ GeV (our choice for this study) the error on $\tan\beta$ based on these rates would be smaller than ± 0.1 for $\tan\beta \gtrsim 13$, asymptoting to ± 0.05 at large $\tan\beta$.

   The importance of including the $gg \to H$, $gg \to A$ as well as the $gg \to b\bar{b}H + gg \to b\bar{b}A$ processes in order to obtain observable signals for $\tan\beta$ values as low as 10 in the $\mu^+\mu^-$ channels is apparent from [210]. For $\mathcal{L} = 300$ fb^{-1} and $m_A = 200$ GeV, they find that the $b\bar{b}\mu^+\mu^-$ final states can only be isolated for

$\tan\beta > 30$ whereas the inclusive $\mu^+\mu^-$ final state from all production processes becomes detectable once $\tan\beta > 10$.

3. $gg \to t\bar{b}H^- + \bar{t}bH^+$ with $H^\pm \to \tau^\pm\nu$ [211].

   The $tbH^\pm \to tb\tau\nu$ rate gives a fractional $\tan\beta$ uncertainty, $\Delta\tan\beta/\tan\beta$, ranging from ± 0.074 at $\tan\beta = 20$ to ± 0.054 at $\tan\beta = 50$.

The above error estimates are purely statistical. All three techniques will have systematic errors deriving from imprecise knowledge of the gluon distribution function and QCD corrections. Background uncertainties might also enter, although not at the highest $\tan\beta$ values for the $\tan\beta$-enhanced processes that have very high rates. Additional systematic error will, as in the LC case, derive from the need to have precise measurements of SUSY masses and mixing angles in order to precisely relate the $b\bar{b}$ Yukawa couplings of the H and A to the $\tan\beta$ parameter. Finally, in the case of techniques [1.] and (for $\tan\beta < 20 - 30$) [2.], the $\tan\beta$ sensitivity is largely due to the loop-induced $gg \to A$ and $gg \to H$ production processes. Interpreting gg-induced rates in terms of $\tan\beta$ requires significant knowledge of the particles, including SUSY particles, that go into the loops responsible for the $gg \to H$ and $gg \to A$ couplings.

Sensitivity to $\tan\beta$ deriving from direct measurements of the decay widths has not been studied by the LHC experiments. One can expect excellent $\tan\beta$ statistical accuracy at the higher $\tan\beta$ values for which the $gg \to b\bar{b}\mu^+\mu^-$ signal for the H and A is detectable. Further, the direct width measurement would avoid systematic errors deriving from uncertainties in the gluon distribution function or the $gg \to H, A$ loop-induced couplings.

We now discuss the interplay between the LHC errors and the LC errors for $\tan\beta$, assuming $m_A = 200$ GeV. This discussion is based upon statistical errors only. As already noted, to keep systematic errors at a level below the statistical errors will require substantial input on other model parameters (e.g. sparticle masses and mixings in the MSSM context) from both the LHC and the LC. First, consider $\tan\beta \leq 10$. As summarized above, the LHC error on $\tan\beta$ is ± 0.12 at $\tan\beta \sim 10$ and at $\tan\beta \sim 1$, and the error becomes very large for $1.5 \lesssim \tan\beta \lesssim 5$. Meanwhile, the LC error from Fig. 3.35 ranges from roughly ± 0.03 to ± 0.05 for $2 \lesssim \tan\beta \lesssim 5$ rising to about ± 0.1 at $\tan\beta \sim 10$ [in the less favorable SUSY scenario (I)]. Therefore, for $\tan\beta \lesssim 10$ the LC provides the best determination of $\tan\beta$ using Higgs observables related to their Yukawa couplings. (In the MSSM context, other non-Higgs LHC measurements would allow a good $\tan\beta$ determination at low to moderate $\tan\beta$ based on other kinds of couplings.) In the middle range of $\tan\beta$ (roughly $13 < \tan\beta < 30$ at $m_A \sim 200$ GeV), the heavy Higgs determination of $\tan\beta$ at the LHC might be superior to that obtained at the LC. This depends upon the SUSY scenario: if the heavy Higgs bosons can decay to SUSY particles, the LC will give $\tan\beta$ errors that are quite similar to those obtained at the LHC; if the heavy Higgs bosons do not have substantial SUSY decays, then the expected LC $\tan\beta$ errors are substantially larger than those predicted for the LHC. At large $\tan\beta$, the LC measurement of the heavy Higgs couplings and the resulting $\tan\beta$ determination at the LC is numerically only slightly more accurate than that obtained at the LHC. For example, both are of order ± 0.05 at $\tan\beta = 40$. (At this level of statistical error, the ability to reduce the systematic error by combined LC and LHC systematic studies will be particularly important.) The statistical error

comparisons are summarized in Table 3.8. It is possible that the net LHC $\tan\beta$ error would be somewhat smaller than the LC error for $\tan\beta \gtrsim 40$ if both ATLAS and CMS can each accumulate $\mathcal{L} = 300\ \mathrm{fb}^{-1}$ of luminosity; combining the two data sets would presumably roughly double the statistics and decrease errors by a factor of order $1/\sqrt{2}$. Inclusion of the direct width measurement at the LHC would also decrease the error. In any case, a very small statistical error on $\tan\beta$ will be achievable for all $\tan\beta$ by combining the results from the LC with those from the LHC.

Table 3.8: A comparison of fractional statistical errors, $\Delta\tan\beta/\tan\beta$, achievable for $\mathcal{L} = 2000\ \mathrm{fb}^{-1}$ at the LC with those expected at the LHC for $\mathcal{L} = 300\ \mathrm{fb}^{-1}$, assuming $m_A = 200\ \mathrm{GeV}$ in the MSSM. LC results are given for both SUSY scenarios (I) and (II), where Higgs boson decays to SUSY particles are disallowed, respectively allowed. LHC results are estimated by roughly combining the determinations of $\tan\beta$ based on H, A production from [89] with those using $H^\pm$ production from [211], both of which assume the standard MSSM maximal mixing scenario. All entries are approximate.

$\tan\beta$ range	LHC	LC (case I)	LC (case II)
1	0.12	0.15	0.1
1.5–5	very large	0.03–0.05	0.03–0.05
10	0.12	0.1	0.05
13–30	0.05	0.6–0.1	0.05–0.1
40–60	0.05–0.03	0.05–0.025	0.05–0.025

Finally, we wish to emphasize that the above LHC versus LC comparisons have been made based only on $H, A, H^\pm$ processes and for the particular choice of $m_A = 200\ \mathrm{GeV}$ in the MSSM, assuming $\sqrt{s} = 500\ \mathrm{GeV}$ for the LC. For given $\tan\beta$, the LC accuracies would decline if $m_A > \sqrt{s}/2$, since then HA and H^+H^- pair production would not be possible. The LHC accuracies will decrease with increasing m_A at fixed $\tan\beta$ simply as a result of decreasing event rates. Detailed studies would be worthwhile.

3.4 Higgs sector in non-minimal models

In this section we discuss examples of models with a nonminimal Higgs sector or with a light Higgs that has nonstandard decays/branching ratios, emphasizing possible LHC-LC complementarity and cross talk.

The NMSSM is one of the most interesting extensions of the MSSM. The NMSSM Higgs sector contains one additional scalar and one additional pseudoscalar Higgs boson beyond the MSSM Higgs states. The MSSM Higgs states then share their couplings to fermions and gauge bosons with the additional states. New Higgs decay modes also open up. A case that might make Higgs detection difficult is that in which there is a light (CP-even) Higgs boson which dominantly decays into two CP-odd light Higgs bosons. If these CP-odd Higgs bosons do not decay significantly to supersymmetric modes, it is shown that the NMSSM Higgs discovery is close to being guaranteed even in this case if the usually considered LHC detection modes are supplemented by the $WW \to h \to aa$ mode, with $aa \to b\bar{b}\tau^+\tau^-$. The resulting signal would be the only LHC signal for Higgs bosons. Confirmation of the nature of the

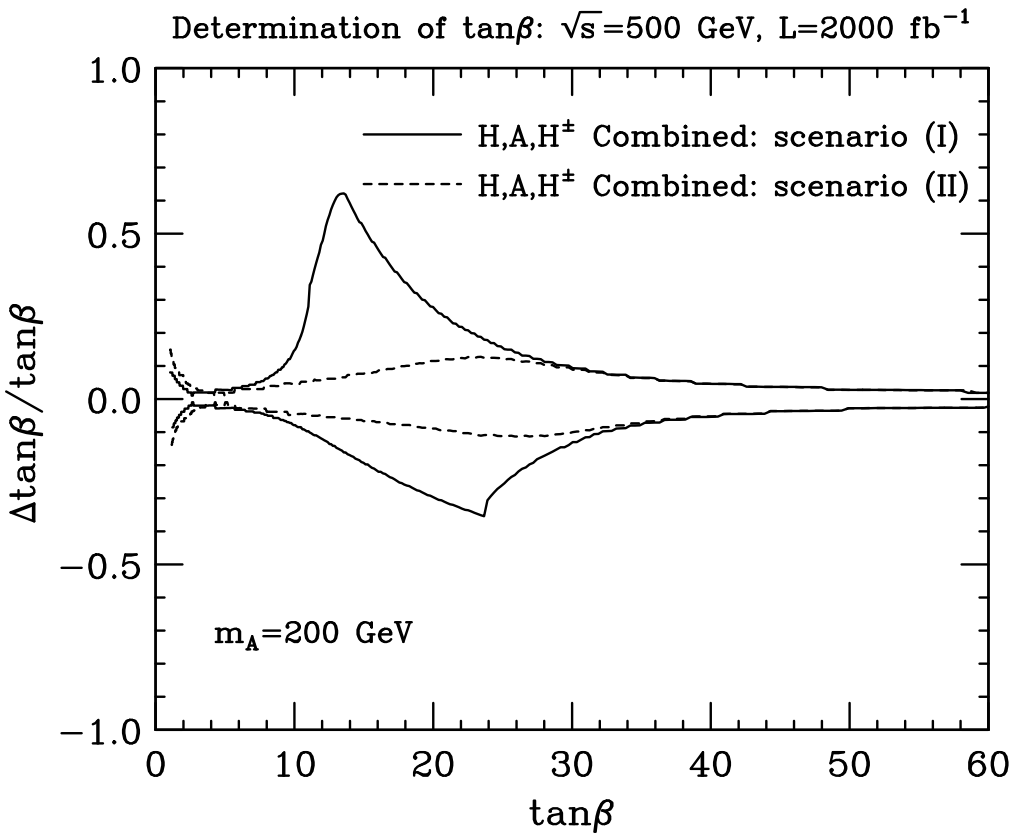

Figure 3.35: For the MSSM, with $m_{H^\pm} \sim m_A = 200$ GeV, and assuming $\mathcal{L} = 2000$ fb^{-1} at $\sqrt{s} = 500$ GeV, we plot the 1σ statistical upper and lower bounds, $\Delta \tan\beta / \tan\beta$, as a function of $\tan\beta$ based on combining (in quadrature) the described LC Higgs boson studies. Results are shown for the SUSY scenarios (I) and (II) described in the text.

signal at the LC would be vital. It is shown that the $WW \to h \to aa$ signal, as well as the usual $e^+e^- \to Zh \to Zaa$ signal, will be highly visible at the LC due to its cleaner environment and high luminosity. Further, the LC will be able to observe both the $aa \to \tau^+\tau- \to b\bar{b}$ and the $aa \to b\bar{b}b\bar{b}$ final states, thus allowing a definitive check that the ratio $BR(a \to \tau^+\tau^-)/BR(a \to b\bar{b})$ is that expected for a CP-odd scalar.

Next we discuss the very interesting scenario that at the Tevatron, LHC and e^+e^- Linear Collider only one light Higgs boson will be found, with properties as expected in the Standard Model. It is possible to realize this SM-like scenario in a Two-Higgs-Doublet Model both with and without decoupling. It is shown how precise measurements of the Higgs boson coupling to gluons at the LHC and to photons at a Photon Collider can allow one to determine which scenario is realized in nature.

After this is discussed the case of a fermiophobic Higgs boson (h_f) decaying to two photons with a larger branching ratio than in the SM. In this case the standard production mechanisms are very suppressed for moderate to large $\tan\beta$, both at the LC and the LHC. It is shown here that the search for $pp \to H^\pm h_f$ should substantially benefit from a previous signal at a LC in the channel $e^+e^- \to A^0 h_f$, and would provide important confirmation of any LC signal for h_f.

Should a light Higgs have substantial branching ratio in 'invisible' channels, as may well happen for a supersymmetric Higgs with mass less than ~ 130 GeV and

nonuniversal gaugino masses at the high scale, its search at the LHC in the standard channels may get compromised. Such a Higgs can be seen at an LC with ease, allowing even a measurement of its 'invisible' branching ratio. Signals at the LHC which can be searched for, so as confirm the lack of signal at LHC in the usual channel due to these effects are discussed.

3.4.1 NMSSM Higgs discovery at the LHC

One of the most attractive supersymmetric models is the Next to Minimal Supersymmetric Standard Model (NMSSM) (see [214, 216] and references therein) which extends the MSSM by the introduction of just one singlet superfield, $\widehat{S}$. When the scalar component of $\widehat{S}$ acquires a TeV scale vacuum expectation value (a very natural result in the context of the model), the superpotential term $\widehat{S}\widehat{H}_u\widehat{H}_d$ generates an effective $\mu\widehat{H}_u\widehat{H}_d$ interaction for the Higgs doublet superfields. Such a term is essential for acceptable phenomenology. No other SUSY model generates this crucial component of the superpotential in as natural a fashion. Thus, the phenomenological implications of the NMSSM at future accelerators should be considered very seriously. One aspect of this is the fact that the $h, H, A, H^\pm$ Higgs sector of the MSSM is extended so that there are three CP-even Higgs bosons ($h_{1,2,3}$, $m_{h_1} < m_{h_2} < m_{h_3}$), two CP-odd Higgs bosons ($a_{1,2}$, $m_{a_1} < m_{a_2}$) (we assume that CP is not violated in the Higgs sector) and a charged Higgs pair ($h^\pm$). An important question is then the extent to which the no-lose theorem for MSSM Higgs boson discovery at the LHC (after LEP constraints) is retained when going to the NMSSM; *i.e.* is the LHC guaranteed to find at least one of the $h_{1,2,3}$, $a_{1,2}$, $h^\pm$? The first exploration of this issue appeared in [215], with the conclusion that for substantial portions of parameter space the LHC would be unable to detect any of the NMSSM Higgs bosons. Since then, there have been improvements in many of the detection modes and the addition of new one. These will be summarized below and the implications reviewed. However, these improvements and additions do not address the possibly important $h \to aa$ type decays that could suppress all other types of signals [108, 215].

One of the key ingredients in the no-lose theorem for MSSM Higgs boson discovery is the fact that relations among the Higgs boson masses are such that decays of the SM-like Higgs boson to AA are only possible if m_A is quite small, a region that is ruled out by LEP by virtue of the fact that $Z \to hA$ pair production was not detected despite the fact that the relevant coupling is large for small m_A. In the NMSSM, the lighter Higgs bosons, h_1 or h_2, can be SM-like (in particular being the only Higgs with substantial WW/ZZ coupling) without the a_1 necessarily being heavy. In addition, this situation is not excluded by LEP searches for $e^+e^- \to Z^* \to h_{1,2}a_1$ since, in the NMSSM, the a_1 can have small Zh_2a_1 (Zh_1a_1) coupling when h_1 (h_2) is SM-like. [In addition, sum rules require that the Zh_1a_1 (Zh_2a_1) coupling is small when the h_1WW (h_2WW) couplings are large.] As a result, NMSSM parameters that are not excluded by current data can be chosen so that the $h_{1,2}$ masses are moderate in size ($\sim 100 - 130$ GeV) and the $h_1 \to a_1a_1$ or $h_2 \to a_1a_1$ decays are dominant. Dominance of such decays falls outside the scope of the usual detection modes for the SM-like MSSM h on which the MSSM no-lose LHC theorem largely relies.

In Ref. [216], a partial no-lose theorem for NMSSM Higgs boson discovery at the LHC was established. In particular, it was shown that the LHC would be able to detect at least one of the Higgs bosons (typically, one of the lighter CP-even Higgs states) throughout the full parameter space of the model, excluding only those parameter choices for which there is sensitivity to the model-dependent decays of Higgs bosons to other Higgs bosons and/or superparticles. Here, we will address the question of whether or not this no-lose theorem can be extended to those regions of NMSSM parameter space for which Higgs bosons can decay to other Higgs bosons. We find that the parameter choices such that the "standard" discovery modes fail *would* allow Higgs boson discovery if detection of $h \to aa$ decays is possible. (When used generically, the symbol h will now refer to $h = h_1$, h_2 or h_3 and the symbol a will refer to $a = a_1$ or a_2). Detection of $h \to aa$ will be difficult since each a will decay primarily to $b\bar{b}$ (or 2 jets if $m_a < 2m_b$), $\tau^+\tau^-$, and, possibly, $\widetilde{\chi}_1^0\widetilde{\chi}_1^0$, yielding final states that will typically have large backgrounds at the LHC.

In [216] we scanned the parameter space, removing parameter choices ruled out by constraints from LEP on Higgs boson production, $e^+e^- \to Zh$ or $e^+e^- \to ha$ [217], and eliminating parameter choices for which one Higgs boson can decay to two other Higgs bosons or a vector boson plus a Higgs boson. For the surviving regions of parameter space, we estimated the statistical significances ($N_{SD} = S/\sqrt{B}$) for all Higgs boson detection modes so far studied at the LHC [218]. These are (with $\ell = e, \mu$)

1) $gg \to h/a \to \gamma\gamma$;
2) associated Wh/a or $t\bar{t}h/a$ production with $\gamma\gamma\ell^\pm$ in the final state;
3) associated $t\bar{t}h/a$ production with $h/a \to b\bar{b}$;
4) associated $b\bar{b}h/a$ production with $h/a \to \tau^+\tau^-$;
5) $gg \to h \to ZZ^{(*)} \to 4$ leptons;
6) $gg \to h \to WW^{(*)} \to \ell^+\ell^-\nu\overline{\nu}$;
7) $WW \to h \to \tau^+\tau^-$;
8) $WW \to h \to WW^{(*)}$.

For an integrated luminosity of $300\ \mathrm{fb}^{-1}$ at the LHC, all the surviving points yielded $N_{SD} > 10$ after combining all modes, including the W-fusion modes. Thus, NMSSM Higgs boson discovery by just one detector with $L = 300\ \mathrm{fb}^{-1}$ is essentially guaranteed for those portions of parameter space for which Higgs boson decays to other Higgs bosons or supersymmetric particles are kinematically forbidden.

In this work, we investigate the complementary part of the parameter space, where *at least one* Higgs boson decays to other Higgs bosons. To be more precise, we require at least one of the following decay modes to be kinematically allowed:

$$\begin{aligned} &i)\ h \to h'h'\ , \quad ii)\ h \to aa\ , \quad iii)\ h \to h^\pm h^\mp\ , \quad iv)\ h \to aZ\ , \\ &v)\ h \to h^\pm W^\mp\ , \quad vi)\ a' \to ha\ , \quad vii)\ a \to hZ\ , \quad viii)\ a \to h^\pm W^\mp\ . \end{aligned} \tag{3.29}$$

After searching those regions of parameter space for which one or more of the decays $i) - viii)$ is allowed, we found that the only subregions for which discovery of a Higgs boson in modes 1) – 8) was not possible correspond to NMSSM parameter choices for which (a) there is a light CP-even Higgs boson with substantial doublet content that decays mainly to two still lighter CP-odd Higgs states, $h \to aa$, and (b) all the other Higgs states are either dominantly singlet-like, implying highly suppressed production rates, or relatively heavy, decaying to $t\bar{t}$, to one of the "difficult" modes

$i) - viii)$ or to a pair of sparticles. In such cases, the best opportunity for detecting at least one of the NMSSM Higgs bosons is to employ $WW \to h$ production and develop techniques for extracting a signal for the $h \to aa$ final state. We have performed a detailed simulation of the $aa \to b\bar{b}\tau^+\tau^-$ final state and find that its detection may be possible after accumulating $300\ \mathrm{fb}^{-1}$ in both the ATLAS and CMS detectors. Further, we show that the $WW \to h \to aa$ signal is extremely robust at an LC.

We consider the simplest version of the NMSSM [214], where the term $\mu\widehat{H}_1\widehat{H}_2$ in the superpotential of the MSSM is replaced by (we use the notation $\widehat{A}$ for the superfield and A for its scalar component field)

$$\lambda\widehat{H}_1\widehat{H}_2\widehat{S} \ + \ \frac{\kappa}{3}\widehat{S}^3 \ , \tag{3.30}$$

so that the superpotential is scale invariant. We make no assumption on "universal" soft terms. Hence, the five soft supersymmetry breaking terms

$$m^2_{H_1}H_1^2 \ + \ m^2_{H_2}H_2^2 \ + \ m^2_S S^2 \ + \ \lambda A_\lambda H_1 H_2 S \ + \ \frac{\kappa}{3}A_\kappa S^3 \tag{3.31}$$

are considered as independent. The masses and/or couplings of sparticles will be such that their contributions to the loop diagrams inducing Higgs boson production by gluon fusion and Higgs boson decay into $\gamma\gamma$ are negligible. In the gaugino sector, we chose $M_2 = 1$ TeV (at low scales). Assuming universal gaugino masses at the coupling constant unification scale, this yields $M_1 \sim 500$ GeV and $M_3 \sim 3$ TeV. In the squark sector, as particularly relevant for the top squarks which appear in the radiative corrections to the Higgs potential, we chose the soft masses $m_Q = m_T \equiv M_{susy} = 1$ TeV, and varied the stop mixing parameter

$$X_t \equiv 2\,\frac{A_t^2}{M^2_{susy} + m_t^2}\left(1 - \frac{A_t^2}{12(M^2_{susy} + m_t^2)}\right) \ . \tag{3.32}$$

As in the MSSM, the value $X_t = \sqrt{6}$ – so called maximal mixing – maximizes the radiative corrections to the Higgs boson masses, and we found that it leads to the most challenging points in the parameter space of the NMSSM. We adopt the convention $\lambda, \kappa > 0$, in which $\tan\beta$ can have either sign. We require $|\mu_{\rm eff}| > 100$ GeV; otherwise a light chargino would have been detected at LEP. The only possibly light SUSY particle will be the $\widetilde{\chi}^0_1$. A light $\widetilde{\chi}^0_1$ is a frequent characteristic of parameter choices that yield a light a_1.

We have performed a numerical scan over the free parameters. For each point, we computed the masses and mixings of the CP-even and CP-odd Higgs bosons, h_i ($i = 1, 2, 3$) and a_j ($j = 1, 2$), taking into account radiative corrections up to the dominant two loop terms, as described in [219]. We eliminated parameter choices excluded by LEP constraints [217] on $e^+e^- \to Zh_i$ and $e^+e^- \to h_i a_j$. The latter provides an upper bound on the Zh_ia_j reduced coupling, R'_{ij}, as a function of $m_{h_i} + m_{a_j}$ for $m_{h_i} \simeq m_{a_j}$. Finally, we calculated $m_{h^\pm}$ and required $m_{h^\pm} > 155$ GeV, so that $t \to h^\pm b$ would not be seen.

In order to probe the complementary part of the parameter space as compared to the scanning of Ref. [216], we required that at least one of the decay modes $i) - viii)$ is allowed. For each Higgs state, we calculated all branching ratios including those

for modes $i) - viii)$, using an adapted version of the FORTRAN code HDECAY [278]. We then estimated the expected statistical significances at the LHC in all Higgs boson detection modes 1) – 8) by rescaling results for the SM Higgs boson and/or the MSSM h, H and/or A. The rescaling factors are determined by R_i, t_i and $b_i = \tau_i$, the ratios of the VVh_i, $t\bar{t}h_i$ and $b\bar{b}h_i, \tau^+\tau^-h_i$ couplings, respectively, to those of a SM Higgs boson. Of course $|R_i| < 1$, but t_i and b_i can be larger, smaller or even differ in sign with respect to the SM. For the CP-odd Higgs bosons, $R'_i = 0$ at tree-level; t'_j and b'_j are the ratios of the $i\gamma_5$ couplings for $t\bar{t}$ and $b\bar{b}$, respectively, relative to SM-like strength. A detailed discussion of the procedures for rescaling SM and MSSM simulation results for the statistical significances in channels 1) – 8) will appear elsewhere.

In our set of randomly scanned points, we selected those for which all the statistical significances in modes 1) – 8) are below 5σ. We obtained a lot of points, all with similar characteristics. Namely, in the Higgs spectrum, we always have a very SM-like CP-even Higgs boson with a mass between 115 and 135 GeV (*i.e.* above the LEP limit), which can be either h_1 or h_2, with a reduced coupling to the gauge bosons $R_1 \simeq 1$ or $R_2 \simeq 1$, respectively. This state decays dominantly to a pair of (very) light CP-odd states, a_1a_1, with m_{a_1} between 5 and 65 GeV. The singlet component of a_1 cannot be dominant if we are to have a large $h_1 \to a_1a_1$ or $h_2 \to a_1a_1$ branching ratio when the h_1 or h_2, respectively, is the SM-like Higgs boson. Further, when the h_1 or h_2 is very SM-like, one has small Zh_1a_1 or Zh_2a_1 coupling, respectively, so that $e^+e^- \to h_1a_1$ or $e^+e^- \to h_2a_1$ associated production places no constraint on the light CP-odd state at LEP. We have selected six difficult benchmark points, displayed in Table 3.9. These are such that $a_1 \to \widetilde{\chi}^0_1\widetilde{\chi}^0_1$ decays are negligible or forbidden. (Techniques for cases such that $\widetilde{\chi}^0_1\widetilde{\chi}^0_1$ decay modes are important are under development.) For points 1 – 3, h_1 is the SM-like CP-even state, while for points 4 – 6 it is h_2. We have selected the points so that there is some variation in the $h_{1,2}$ and a_1 masses. The main characteristics of the benchmark points are displayed in Table 3.9. Note the large $BR(h \to a_1a_1)$ of the SM-like h ($h = h_1$ for points 1 – 3 and $h = h_2$ for points 4 –6). For points 4 – 6, with $m_{h_1} < 100$ GeV, the h_1 is mainly singlet. As a result, the Zh_1a_1 coupling is very small, implying no LEP constraints on the h_1 and a_1 from $e^+e^- \to h_1a_1$ production.

We note that in the case of the points 1 – 3, the h_2 would not be detectable either at the LHC or the LC. For points 4 – 6, the h_1, though light, is singlet in nature and would not be detectable. Further, the h_3 or a_2 will only be detectable for points 1 – 6 if a super high energy LC is eventually built so that $e^+e^- \to Z \to h_3a_2$ is possible. Thus, we will focus on searching for the SM-like h_1 (h_2) for points 1 – 3 (4 – 6) using the dominant $h_1(h_2) \to a_1a_1$ decay mode.

In the case of points 2 and 6, the $a_1 \to \tau^+\tau^-$ decays are dominant. The final state of interest will be $jj\tau^+\tau^-$, where the jj actually comes primarily from $a_1a_1 \to \tau^+\tau^-\tau^+\tau^-$ followed by jet decays of two of the τ's: $\tau^+\tau^- \to jj + \nu's$. (The contribution from direct $a_1 \to jj$ decays to the $jj\tau^+\tau^-$ final state is relatively small for points 2 and 6.) In what follows, when we speak of $\tau^+\tau^-$, we refer to those τ's that are seen in the $\tau^+\tau^- \to \ell^+\ell^- + \nu's$ final state ($\ell = e, \mu$). For points 1 and 3 – 5 $BR(a_1 \to b\bar{b})$ is substantial. The relevant final state is $b\bar{b}\tau^+\tau^-$. Nonetheless, we begin with a study of the backgrounds and signals without requiring b-tagging. With our latest cuts, we will see that b-tagging is not necessary to overcome the apriori large Drell-Yan $\tau^+\tau^-$+jets background. It is eliminated by stringent cuts for finding the highly energetic forward / backward jets characteristic of the WW the fusion process. As a result, we

Point Number	1	2	3	4	5	6
Bare Parameters						
λ	0.2872	0.2124	0.3373	0.3340	0.4744	0.5212
κ	0.5332	0.5647	0.5204	0.0574	0.0844	0.0010
$\tan\beta$	2.5	3.5	5.5	2.5	2.5	2.5
$\mu_{\rm eff}$ (GeV)	200	200	200	200	200	200
A_λ (GeV)	100	0	50	500	500	500
A_κ (GeV)	0	0	0	0	0	0
CP-even Higgs Boson Masses and Couplings						
m_{h_1} (GeV)	115	119	123	76	85	51
R_1	1.00	1.00	-1.00	0.08	0.10	-0.25
t_1	0.99	1.00	-1.00	0.05	0.06	-0.29
b_1	1.06	1.05	-1.03	0.27	0.37	0.01
Relative gg Production Rate	0.97	0.99	0.99	0.00	0.01	0.08
$BR(h_1 \to b\overline{b})$	0.02	0.01	0.01	0.91	0.91	0.00
$BR(h_1 \to \tau^+\tau^-)$	0.00	0.00	0.00	0.08	0.08	0.00
$BR(h_1 \to a_1 a_1)$	0.98	0.99	0.98	0.00	0.00	1.00
m_{h_2} (GeV)	516	626	594	118	124	130
R_2	-0.03	-0.01	0.01	-1.00	-0.99	-0.97
t_2	-0.43	-0.30	-0.10	-0.99	-0.99	-0.95
b_2	2.46	-3.48	3.44	-1.03	-1.00	-1.07
Relative gg Production Rate	0.18	0.09	0.01	0.98	0.99	0.90
$BR(h_2 \to b\overline{b})$	0.01	0.04	0.04	0.02	0.01	0.00
$BR(h_2 \to \tau^+\tau^-)$	0.00	0.01	0.00	0.00	0.00	0.00
$BR(h_2 \to a_1 a_1)$	0.04	0.02	0.83	0.97	0.98	0.96
m_{h_3} (GeV)	745	1064	653	553	554	535
CP-odd Higgs Boson Masses and Couplings						
m_{a_1} (GeV)	56	7	35	41	59	7
t_1'	0.05	0.03	0.01	-0.03	-0.05	-0.06
b_1'	0.29	0.34	0.44	-0.20	-0.29	-0.39
Relative gg Production Rate	0.01	0.03	0.05	0.01	0.01	0.05
$BR(a_1 \to b\overline{b})$	0.92	0.00	0.93	0.92	0.92	0.00
$BR(a_1 \to \tau^+\tau^-)$	0.08	0.94	0.07	0.07	0.08	0.90
m_{a_2} (GeV)	528	639	643	560	563	547
Charged Higgs Mass (GeV)	528	640	643	561	559	539
Most Visible of the LHC Processes 1)-8)	2 (h_1)	2 (h_1)	8 (h_1)	2 (h_2)	8 (h_2)	8 (h_2)
$N_{SD} = S/\sqrt{B}$ Significance of this process at L =300 fb^{-1}	0.48	0.26	0.55	0.62	0.53	0.16
$N_{SD}(L = 300\ \text{fb}^{-1})$ for $WW \to h \to aa \to jj\tau^+\tau^-$ at LHC	50	22	69	63	62	21
$S(L = 500\ \text{fb}^{-1})$ for $WW \to h \to aa \to jj\tau^+\tau^-$ at LC	36	320	45	45	45	320

Table 3.9: Properties of selected scenarios that could escape detection at the LHC. In the table, $R_i = g_{h_iVV}/g_{h_{SM}VV}$, $t_i = g_{h_it\overline{t}}/g_{h_{SM}t\overline{t}}$ and $b_i = g_{h_ib\overline{b}}/g_{h_{SM}b\overline{b}}$ for $m_{h_{SM}} = m_{h_i}$; t_1' and b_1' are the $i\gamma_5$ couplings of a_1 to $t\overline{t}$ and $b\overline{b}$ normalized relative to the scalar $t\overline{t}$ and $b\overline{b}$ SM Higgs couplings. We also give the gg fusion production rate ratio, $gg \to h_i/gg \to h_{SM}$, for $m_{h_{SM}} = m_{h_i}$. Important absolute branching ratios are displayed. For points 2 and 6, the decays $a_1 \to jj$ ($j \neq b$) have $BR(a_1 \to jj) \simeq 1 - BR(a_1 \to \tau^+\tau^-)$. For the heavy h_3 and a_2, we give only their masses. For all points 1 – 6, the statistical significances for the detection of any Higgs boson in any of the channels 1) – 8) are tiny; the third-to-last row gives their maximum together with the process number and the corresponding Higgs state. The next-to-last row gives the statistical significance of the new $WW \to h \to aa \to jj\tau^+\tau^-$ [$h = h_1$ ($h = h_2$) for points 1–3 (4–6)] LHC signal explored here. The final row gives the signal rate S at the LC for $40 < M_{jj\tau^+\tau^-} < 120$ GeV, where $B = 0$.

will find good signals for all 6 of our points.

In principle, one could explore final states other than $b\bar{b}\tau^+\tau^-$ (or $jj\tau^+\tau^-$ for points 2 and 6). However, all other channels will be much more problematical at the LHC. A $4b$-signal would be burdened by a large QCD background even after implementing b-tagging. A $4j$-signal would be completely swamped by QCD background. Meanwhile, the 4τ-channel (by which we mean that all decay leptonically) would not allow one to reconstruct the h_1, h_2 resonances.

In the case of the $2b2\tau$ (or $2j2\tau$) signature, we identify the τ's through their leptonic decays to electrons and muons. Thus, they will yield some amount of missing (transverse) momentum, $p^T_{\rm miss}$. This missing transverse momentum can be projected onto the visible e, μ-momenta in an attempt to reconstruct the parent τ-direction.

Results for the LHC

Let us now focus on the $WW \to h \to aa$ channel that we believe provides the best hope for Higgs detection in these difficult NMSSM cases. (We reemphasize that the h_1 [cases 1 – 3] or h_2 [cases 4 – 6] has nearly full SM strength coupling to WW.) The $b\bar{b}\tau^+\tau^-$ (or $2j\tau^+\tau^-$, for points 2 and 6) final state of relevance is complex and subject to large backgrounds, and the a_1 masses of interest are very modest in size. In order to extract the WW fusion $2j2\tau$ NMSSM Higgs boson signature, it is crucial to strongly exploit forward and backward jet tagging on the light quarks emerging after the double W-strahlung preceding WW-fusion. We also require two additional central jets (from one of the a's) and two opposite sign central leptons ($\ell = e, \mu$) coming from the the $\tau^+\tau^-$ emerging from the decay of the other a. By imposing stringent forward / backward jet tagging cuts, we remove the otherwise very large background from Drell-Yan $\tau^+\tau^- + jets$ production. In the end, the most important background is due to $t\bar{t}$ production and decay via the purely SM process, $gg \to t\bar{t} \to b\bar{b}W^+W^- \to b\bar{b}\tau^+\tau^- + p^T_{\rm miss}$, in association with forward and backward jet radiation.

We have employed numerical simulations based on a version of `HERWIG v6.4` [220–222] modified to allow for appropriate NMSSM couplings and decay rates. Calorimeter emulation was performed using the `GETJET` code [223]. Since the a_1 will not have been detected previously, we must assume a value for m_{a_1}. In practice, it will be necessary to repeat the analysis for densely spaced m_{a_1} values and look for the m_{a_1} choice that produces the best signal. We look among the central jets for the combination with invariant mass M_{jj} closest to m_{a_1}. In the top plot of Fig. 3.36, we show the $M_{jj\tau^+\tau^-}$ invariant mass distribution obtained after cuts, but before b-tagging or inclusion of K factors — the plot presented assumes that we have hit on the correct m_{a_1} choice.

The selection strategy adopted is a more refined (as regards forward / backward jet tagging) version of that summarized in [224]. It is clearly efficient in reconstructing the h_1 (for points 1–3) and h_2 (for points 4–6) masses from the $jj\tau^+\tau^-$ system, as one can appreciate by noting the peaks appearing in the LHC plot of Fig. 3.36 at $M_{jj\tau^+\tau^-} \approx 100$ GeV. In contrast, the heavy Higgs resonances at m_{h_2} for points 1–3 and the rather light resonances at m_{h_1} for points 4–6 (recall Table 3.9) do not appear, the former mainly because of the very poor production rates and the latter due to the fact that either the $h_1 \to a_1a_1$ decay mode is not open (points 4, 5) or – if it is – the b-quarks and e/μ-leptons eventually emerging from the a_1 decays are too soft to pass the acceptance cuts (point 6, for which $m_{a_1} = 7$ GeV and $m_{h_1} = 51$ GeV). For all six NMSSM setups, the Higgs resonance produces a bump below the end of the low mass tail of the $t\bar{t}$ background (see the insert in the top frame of Fig. 3.36). Note how

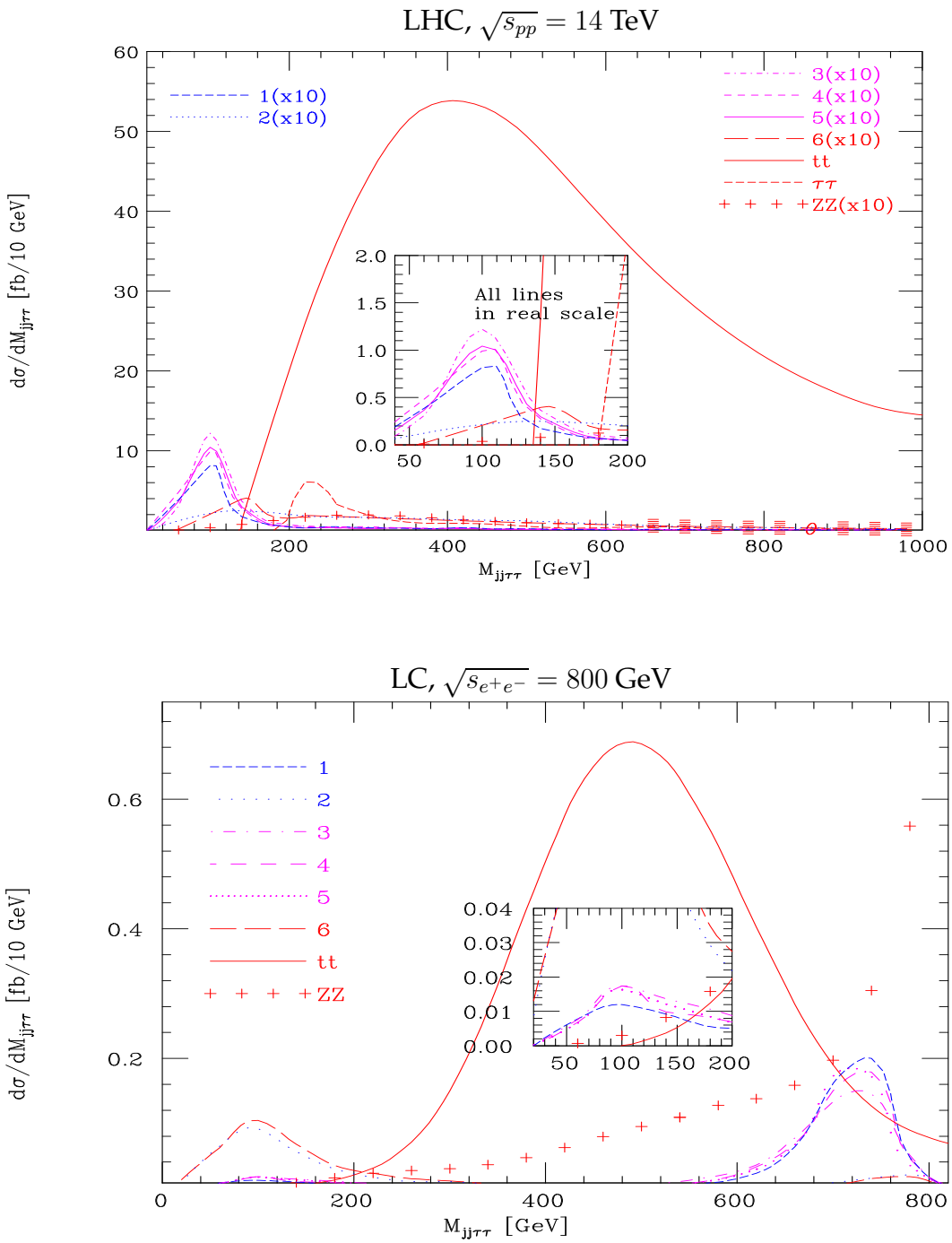

Figure 3.36: We plot $d\sigma/dM_{jj\tau^+\tau^-}$ [fb/10 GeV] vs $M_{jj\tau^+\tau^-}$ [GeV] for signals and backgrounds after basic event selections, but before b tagging. The upper (lower) figure is that for the LHC (LC). In both plots, the lines corresponding to points 4 and 5 are visually indistinguishable. No K factors are included.

small the DY $\tau^+\tau^-$ background is after strong forward / backward jet tagging. Since the main surviving background is from $t\bar{t}$ production, b tagging is not helpful. For points 2 and 6, for which the signal has no b'is in the final state, anti-b-tagging might be useful, but has not been considered here.

To estimate $S/\sqrt{B}$, we assume $L = 300\ \mathrm{fb}^{-1}$, a K factor of 1.1 for the WW fusion signal and K factors of 1, 1 and 1.6 for the DY $\tau^+\tau^-$, ZZ production and $t\bar{t}$ backgrounds, respectively. (These K factors are not included in the plot of Fig. 3.36.) We sum events over the region $40 \leq M_{jj\tau^+\tau^-} \leq 150$ GeV. (Had we only included masses below 130 GeV, we would have had no $t\bar{t}$ background, and the $S/\sqrt{B}$ values would be enormous. However, we are concerned that this absence of $t\bar{t}$ background below $130\ \mathrm{GeV}$ might be a reflection of limited Monte Carlo statistics. As a result we have taken the more conservative approach of at least including the first few bins for which our Monte Carlo does predict some $t\bar{t}$ background.)

For points 1, 2, 3, 4, 5 and 6, we obtain signal rates of about $S = 1636$, 702, 2235, 2041, 2013, and 683, respectively. The $t\bar{t}$+jets background rate is $B_{tt} \sim 795$. The ZZ background rate is $B_{ZZ} \sim 6$. The DY $\tau^+\tau^-$ background rate is negligible. (We are continuing to increase our statistics to get a fully reliable estimate.) The resulting $N_{SD} = S/\sqrt{B}$ values for points 1-6 are 50, 22, 69, 63, 62, and 21, respectively. The smaller values for points 2 and 6 are simply a reflection of the difficulty of isolating and reconstructing the two jets coming from the decay of a very light a_1. Overall, these preliminary results are very encouraging and suggest that a no-lose theorem for NMSSM Higgs detection at the LHC is close at hand.

The LC scenario

While further examination of and refinements in the LHC analysis may ultimately lead us to have full confidence in the viability of the NMSSM Higgs boson signals discussed above, an enhancement at low $M_{b\bar{b}\tau^+\tau^-}$ of the type shown (for some choice of m_{a_1}) will nonetheless be the only evidence on which a claim of LHC observation of Higgs bosons can be based. Ultimately, a means of confirmation and further study will be critical. Thus, it is important to summarize the prospects at the LC, with energy up to 800 GeV, in the context of the difficult scenarios 1 — 6 of Table 3.9 discussed here. In the following, $h = h_1$ for points 1–3 and $h = h_2$ for points 4–6 in Table 3.9.

Because the ZZh coupling is nearly full strength in all cases, and because the h mass is of order 100 GeV, discovery of the h will be very straightforward via $e^+e^- \to Zh$ using the $e^+e^- \to ZX$ reconstructed M_X technique which is independent of the "unexpected" complexity of the h decay to a_1a_1. This will immediately provide a direct measurement of the ZZh coupling with very small error [225]. This approach is completely independent of the final state decay mode(s) and will thus work for all the points 1 – 6, including, in particular, points 2 and 6 for which the final state does not contain b's. The next stage will be to look at rates for the various h decay final states, F, and extract $BR(h \to F) = \sigma(e^+e^- \to Zh \to ZF)/\sigma(e^+e^- \to Zh)$. For the NMSSM points 1 and 3 – 5, the main channels would be $F = b\bar{b}b\bar{b}$, $F = b\bar{b}\tau^+\tau^-$ and $F = \tau^+\tau^-\tau^+\tau^-$. For points 2 and 6, the relevant final states are $F = 4j, jj\tau^+\tau^-, \tau^+\tau^-\tau^+\tau^-$. At the LC, a fairly accurate determination of $BR(h \to F)$ should be possible for both sets of the three final states F. This information would allow us to determine $BR(h \to a_1a_1)$ independently.

Here, we consider the equally (or perhaps more) useful vector-vector fusion mode that will be active at a LC. At 800 GeV or above, it is the dominant Higgs boson

production channel for CP-even Higgs bosons in the intermediate mass range. Contrary to the case of the LHC though, the dominant contribution (from WW fusion) does not allow for forward and backward particle tagging, as the incoming electron and positron convert into (anti)neutrinos, which escape detection. Although the ZZ fusion contribution would allow tagging of forward/backward e^- and e^+, the cross section is a factor of 10 smaller (see Fig. 4 of Ref. [225]) in comparison. At the LC the ZZ background plays a fairly significant role. It has been simulated in our HERWIG and (LC-adjusted) GETJET numerical analysis.

At a LC, the optimal signature will thus be different than at the LHC and a different set of selection criteria are needed (see [224] for details). We have chosen selection criteria that retain both the WW and the ZZ fusion Higgs boson production processes. Basic requirements include the presence of at least two central jets — we look among the central jets for the combination with invariant mass M_{jj} closest to m_{a_1}. We also require two oppositely charged central leptons ($\ell = e, \mu$). After ensuring that these are not back-to-back, we resolve the $p^T_{\rm miss}$ along their directions and reconstruct the invariant mass $M_{\tau^+\tau^-}$. Finally, we note that we have included Initial State Radiation (ISR) and beam-strahlung effects, as predicted using the HERWIG default. These tend to introduce an additional unresolvable missing longitudinal momentum, although to a much smaller extent than do the Parton Distribution Functions (PDFs) in hadron-hadron scattering at the LHC. Further discussion of the details of the cuts and simulation will be presented elsewhere.

At the LC, the $jj\tau^+\tau^-$ background is again very small. As a result, we do not need to employ b tagging — it is sufficient to simply require two non-forward / backward jets; these happen to be b's for points 1 and 3 – 5 and light quark jets for points 2 and 6.

The bottom plot of Fig. 3.36 gives the resulting $M_{jj\tau^+\tau^-}$ invariant mass distributions for the signal and several backgrounds. We note that it is not fruitful to place cuts on the invariant masses M_{jj} and $M_{\tau^+\tau^-}$ that exclude $M_{jj}, M_{\tau^+\tau^-} \sim m_Z$ in an attempt to reduce the ZZ background. This is because the SM-like h mass is typically of order 115 GeV, *i.e.* not so far from m_Z, and the experimental resolutions in the two masses M_{jj} and $M_{\tau^+\tau^-}$ are poor, either because of the large number of hadronic tracks or the missing longitudinal momenta of the (anti) neutrinos, respectively.

From Fig. 3.36, we see that the $M_{jj\tau^+\tau^-}$ distribution reconstructed at the LC displays resonance mass peaks (again centered at 100 GeV) for the SM-like h_1 (points 1 – 3) or h_2 (points 4 – 6) that are very clearly visible above both the $t\bar{t}$ and ZZ backgrounds, particularly for the case of points 2 and 6 (see insert in the bottom frame of Fig. 3.36). Assuming $L = 500$ fb^{-1}, the points 1,3,4,5 yield 36,45,45,45 events in the $40 \leq M_{jj\tau^+\tau^-} \leq 120$ GeV interval where the background is essentially zero. This would constitute a convincing signal given the very small size predicted for the background. For points 2 and 6, we get about 320 events over this same background-free mass interval. The much larger signal for these points is mainly due to two reasons. Firstly, the overall $BR(h_1/h_2 \to a_1a_1 \to 2j2\ell)$ is largest in these cases, as follows from the branching ratios in Table 3.9 and simple combinatorics. Secondly, there is a kinematic difference related to the much smaller m_{a_1} in cases 2 and 6 that we now discuss. Notice that, although assigning the entire missing transverse momentum to the τ-lepton system may seem not entirely appropriate (given the forward/backward (anti)neutrinos from the incoming electrons and positrons in WW fusion), this does

not hamper the ability to reconstruct the Higgs mass peaks. However, there will be a proportion of the signal events that tend to reproduce the overall $\sqrt{s_{e^+e^-}}$ value in the $M_{jj\tau^+\tau^-}$ distribution. The effect is more pronounced for points 1 and 3–5, which is where the a_1 mass is larger (see Table 3.9) so that most of the hadronic tracks composing the emerging jets easily enter the detector region. For points 2 and 6, where m_{a_1} is below 10 GeV, this may often not be true and it appears that the consequent effect of these hadrons escaping detection is that of counterbalancing the $p^T_{\rm miss}$ contributions related to the neutrinos left behind in WW fusion reactions. For the case of the ZZ noise, in the limit of full coverage and perfect resolution of the detector, one would have $M_{jj\tau^+\tau^-} \equiv \sqrt{s_{e^+e^-}}$, which explains the concentration of events with $M_{jj\tau^+\tau^-}$ around 800 GeV. (The "tails" beyond $\sqrt{s_{e^+e^-}}$ are due to the smearing of the visible tracks in our Monte Carlo analysis.)

In summary, we have obtained a statistically very significant LHC signal in the $jj\tau^+\tau^-$ final state of WW fusion for cases in which the NMSSM parameters are such that the most SM-like of the CP-even Higgs bosons, h, is relatively light and decays primarily to a pair of CP-odd Higgs states, $h \to aa$ with $a \to b\bar{b}, \tau^+\tau^-$ if $m_a > 2m_b$ or $a \to jj, \tau^+\tau^-$ if $m_a < 2m_b$. The statistical significances are (at least) of order 50 to 70 for points with $m_a > 2m_b$ and of order 20 for points with $m_a < 2m_b$. These high significances were obtained by imposing stringent cuts requiring highly energetic forward / backward jets in order to isolate the WW fusion signal process from backgrounds such as DY $\tau^+\tau^-$ pair production. Still, this signal will be the only evidence for Higgs bosons at the LHC. The LC will be absolutely essential in order to confirm that the enhancement seen at the LHC really does correspond to a Higgs boson. At the LC, discovery of a light SM-like h is guaranteed to be possible in the Zh final state using the recoil mass technique. Further, we have seen that WW, ZZ fusion production of the h will also produce a viable signal in the $jj\tau^+\tau^-$ final state (and perhaps in the $4j$ and $\tau^+\tau^-\tau^+\tau^-$ final states as well, although we have not examined these [226]); for some parameter choices the jj will be a $b\bar{b}$ pair as can be determined by b-tagging. Finally, we have yet to explore the cases in which the $a_1 \to \widetilde{\chi}^0_1\widetilde{\chi}^0_1$ decay has a large branching ratio. Detecting a Higgs signal in such cases will require a rather different procedure. Work on the $WW \to h \to$ invisible signal is in progress [226].

As we have stressed, for parameter space points of the type we have discussed here, detection of any of the other MSSM Higgs bosons is likely to be impossible at the LHC and is likely to require an LC with $\sqrt{s_{e^+e^-}}$ above the relevant thresholds for $h'a'$ production, where h' and a' are heavy CP-even and CP-odd Higgs bosons, respectively.

Although results for the LHC indicate that Higgs boson discovery will be possible for the type of situations we have considered, it is clearly important to refine and improve the techniques for extracting a signal. This will almost certainly be possible once data is in hand and the $t\bar{t}$ background can be more completely modeled.

Clearly, if SUSY is discovered and $WW \to WW$ scattering is found to be perturbative at WW energies of 1 TeV (and higher), and yet no Higgs bosons are detected in the standard MSSM modes, a careful search for the signal we have considered should have a high priority.

Finally, we should remark that the $h \to aa$ search channel considered here in the NMSSM framework is also highly relevant for a general two-Higgs-doublet model, 2HDM. It is really quite possible that the most SM-like CP-even Higgs boson of a

2HDM will decay primarily to two CP-odd states. This is possible even if the CP-even state is quite heavy, unlike the NMSSM cases considered here. If CP violation is introduced in the Higgs sector, either at tree-level or as a result of one-loop corrections (as, for example, is possible in the MSSM), $h \to h'h''$ decays will generally be present. The critical signal will be the same as that considered here.

3.4.2 An interesting NMSSM scenario at the LHC and LC

3.4.2.1 Introduction

The Next-to-Minimal Supersymmetric Standard Model (NMSSM) provides an elegant solution to the μ problem of the MSSM by introducing an extra complex scalar Higgs superfield. The extra fields have no gauge couplings and are principally only manifest through their mixing with the other states. This leads to scenarios where Higgs boson couplings are reduced in comparison to the MSSM, presenting a challenge to the next generation of colliders. In this contribution, we will examine the phenomenology of one of these scenarios at the LHC and a future e^+e^- Linear Collider and demonstrate a synergy between the two machines.

The NMSSM has already been discussed in Section 3.4.1 of this study, in the context of establishing a "no-lose" theorem for the discovery of at least one Higgs boson at the next generation of colliders (see also Ref. [227]). It was seen that for some exceptional NMSSM parameter choices the discovery of *any* Higgs boson at all will be difficult at the LHC, but for the majority of choices at least one Higgs boson will be discovered. Here we adopt a different philosophy and examine a "typical" NMSSM scenario point. While not representative of scenarios over the entire range of parameters, the chosen scenario is certainly not unusual and a wide range of parameter choices will result in similar phenomenology, differing only in numerical detail and not in general structure. This scenario therefore presents an interesting illustrative picture of the Higgs sector that might be waiting for us at the next generation of colliders.

3.4.2.2 The Model

The NMSSM has the same field content as the minimal model augmented by an additional neutral singlet superfield $\hat{S}$. Its superpotential is given by

$$W = \hat{u}^c \, \mathbf{h_u} \hat{Q} \hat{H}_u - \hat{d}^c \, \mathbf{h_d} \hat{Q} \hat{H}_d - \hat{e}^c \, \mathbf{h_e} \hat{L} \hat{H}_d + \lambda \hat{S} (\hat{H}_u \hat{H}_d) + \frac{1}{3} \kappa \hat{S}^3, \tag{3.33}$$

where $\hat{H}_u$ and $\hat{H}_d$ are the usual Higgs doublet superfields with $\hat{H}_u \hat{H}_d \equiv \hat{H}_u^+ \hat{H}_d^- - \hat{H}_u^0 \hat{H}_d^0$. $\hat{Q}$ and $\hat{L}$ represent left handed quark and lepton weak isospin doublets respectively, while $\hat{u}^c$, $\hat{d}^c$ and $\hat{e}^c$ are the right handed quark and lepton fields; $\mathbf{h_u}$, $\mathbf{h_d}$ and $\mathbf{h_e}$ are matrices of Yukawa couplings where family indices have been suppressed. The usual μ-term of the MSSM, $\mu \hat{H}_u \hat{H}_d$, has been replaced by a term coupling the new singlet field to the usual Higgs doublets, $\lambda \hat{S} \hat{H}_u \hat{H}_d$. When the new singlet field gains a vacuum expectation value (VEV), an effective μ-term is generated with an effective Higgs-higgsino mass parameter given by $\mu_{\text{eff}} = \lambda \langle S \rangle$. (We adopt the notation

that the superfields are denoted by expressions with a "hat", while their scalar components are denoted by the same expression without the hat.) The superpotential resulting from this substitution (not yet Eq.(3.33)) contains an extra symmetry — a $U(1)$ "Peccei-Quinn" (PQ) symmetry [228], which will be broken during electroweak symmetry breaking. As is the case when any global symmetry is dynamically broken, this results in a massless Nambu-Goldstone boson which is in this instance a pseudoscalar Higgs state. Since this Higgs state has not been observed in experiment we have only two possibilities: we must either break the Peccei-Quinn symmetry explicitly, giving the pseudoscalar a mass and putting it out of the kinematical reach of past experiments, or we must decouple it from the other particles by setting $\lambda \ll 1$. Here we adopt the former possibility[12] and introduce an explicit Peccei-Quinn symmetry breaking term $\frac{1}{3}\kappa\hat{S}^3$. This results in the superpotential given in Eq.(3.33). We will not elaborate on the formal details of the model here except to elucidate our parameter choice — for a more detailed examination of the model see Ref. [230] and references therein.

At tree level, the NMSSM Higgs sector has seven parameters: the Higgs couplings from the superpotential, λ and κ; their two associated soft supersymmetry breaking parameters, A_λ and A_κ ; and the VEVs of the three neutral Higgs fields, which we re-express as two ratios of VEVs, $\tan\beta = \langle H_u^0\rangle/\langle H_d^0\rangle$ and $\tan\beta_s = \sqrt{2}\langle S\rangle/v$, and the electroweak scale $v/\sqrt{2} = \sqrt{\langle H_u^0\rangle^2 + \langle H_d^0\rangle^2}$. The scenario to be considered here has parameters given by $\lambda = 0.3$, $\kappa = 0.1$, $\tan\beta = \tan\beta_s = 3$ and $A_\kappa = -60$ GeV. The parameter A_λ is replaced by the mass scale M_A which is chosen to be the diagonal entry of the pseudoscalar Higgs boson mass-squared matrix that returns to the value of the physical MSSM pseudoscalar Higgs boson mass in the MSSM limit (i.e. $\lambda \to 0$, $\kappa \to 0$ while keeping λ/κ and μ_{eff} fixed). This choice allows the reader a more intuitive connection with the MSSM. M_A will not be fixed, but will be allowed to vary over the physical range. Finally, we take $v = 246$ GeV.

3.4.2.3 The Mass Spectrum

The Higgs mass spectrum for our parameter choice, evaluated at one-loop precision [231], can be seen in Fig.(3.37), as a function of M_A. This spectrum looks remarkably like that of the MSSM with the addition of two extra Higgs fields — a scalar state and a pseudoscalar state. As in the MSSM, the heavy pseudoscalar, scalar and charged Higgs bosons all lie around the mass scale M_A, while a lighter scalar state has mass around 115-130 GeV. However, in addition we see extra scalar and pseudoscalar states with masses of order 100 GeV and below; these are the Higgs states which are dominated by the extra singlet degrees of freedom.

Making an expansion in the (often) small parameters $1/\tan\beta$ and M_Z/M_A allows us to obtain simple approximate forms for the masses of these extra singlet dominated Higgs bosons [229]. One finds that the singlet dominated pseudoscalar Higgs fields has a mass given approximately by

$$M_{A_1}^2 \approx -\frac{3}{\sqrt{2}}\kappa v_s A_\kappa, \tag{3.34}$$

[12]For a description of the decoupled case, see Ref. [229].

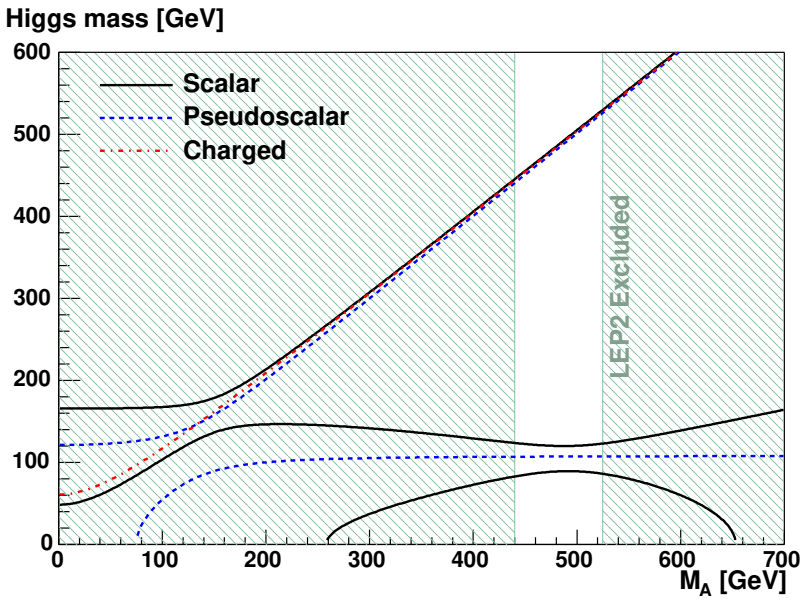

Figure 3.37: *The one-loop Higgs mass spectrum as a function of M_A for $\lambda = 0.3$, $\kappa = 0.1$, $\tan\beta = \tan\beta_s = 3$ and $A_\kappa = -60$ GeV. Also shown by the shaded area are the values of M_A that are ruled out by LEP2 [1] for this parameter choice.*

while the singlet dominated scalar has a mass which is maximized at $M_A \approx 2\mu_{\rm eff}/\sin 2\beta$ where it is given by

$$M_{H_1}^2 \approx \frac{1}{2}\kappa v_s(4\kappa v_s + \sqrt{2}A_\kappa). \tag{3.35}$$

It must be stressed that these expressions are very approximate and are not applicable over the entire parameter range; the one-loop expressions for the masses should be used in preference, as in Fig.(3.37). However, the approximate expressions are useful in determining the qualitative behaviour of the masses as the parameters are varied. [Although approximate, these expressions do surprisingly well in estimating the singlet dominated masses. For example, for the present parameter choice they give $M_{A_1} \approx 96.2$ GeV and $M_{H_1} \approx 88.1$ GeV, which compare favourably with the one-loop results, 107.3 GeV and 89.5 GeV respectively at $M_A = 495$ GeV. This is in part due to the suppression of couplings to quarks, which reduces the impact of radiative corrections.]

In particular, the masses are strongly dependent only on the quantities κv_s and A_κ [and M_A]. The dependence on κv_s (which is a measure of how strongly the PQ symmetry is broken) is straightforward: as κv_s increased the masses also increase. Since one expects v_s to be of the order of v and κ is restricted by $\kappa^2 + \lambda^2 \lesssim 0.5$ when one insists on perturbativity up to the unification scale, it is natural (though not mandatory) for this mass scale to be rather low, and the extra Higgs states rather light. In contrast, the A_κ contribution to the masses has opposite sign for scalar and pseudoscalar. The dependence of the pseudoscalar mass, Eq.(3.34), on A_κ indicates that A_κ should be negative, while Eq.(3.35) insists that its absolute value does not become too large. These effects are nicely summarized by the approximate mass sum rule (at

$M_A \approx 2\mu_{\rm eff}/\sin 2\beta$):

$$M_{H_1}^2 + \frac{1}{3} M_{A_1}^2 \approx 2\,(\kappa v_s)^2. \tag{3.36}$$

The overall scale for the masses is set by κv_s, while increasing the scalar mass leads to a decrease in the pseudoscalar mass and vice versa.

Fig.(3.37) also shows the values of M_A that, for this parameter choice, are already ruled out by LEP (the shaded region). Although a SM Higgs boson with mass below 114.4 GeV is now ruled out with 95% confidence by the LEP experiments [1], lighter Higgs bosons are still allowed if their coupling to the Z boson is reduced. In the NMSSM, since the extra singlet fields have no gauge couplings, the couplings of the singlet dominated fields to the Z boson come about only through mixing with the neutral doublet Higgs fields. When this mixing is small their couplings are reduced and they can escape the Higgs-strahlung dominated LEP limits. For the LEP limits shown here we take into account decays to both $b\overline{b}$ [1] and $\gamma\gamma$ [232], as well as decay mode independent searches carried out by the OPAL detector [233]. As expected, the limits are dominated by the decay $H_1 \to b\overline{b}$.

The dependence of the lightest Higgs boson mass on M_A also makes a prediction for the mass of the heavy states. The lightest Higgs boson mass must be kept large enough to escape the current LEP limits. However, since this mass decreases rapidly to either side of its maximum (see Fig.(3.37) we are forced to constrain M_A, and thus the heavy Higgs boson masses, to around $M_A \approx 2\mu_{\rm eff}/\sin 2\beta \approx \mu_{\rm eff}\tan\beta$.

There is still significant room for a rather light Higgs bosons to be found the LHC and/or a LC. It is essential that these light Higgs bosons be ruled out or discovered at the next generation of colliders. In the following we will focus on the production of a light singlet dominated scalar Higgs boson at the LHC and a LC and its subsequent decay, but one should bear in mind that there is also a light pseudoscalar Higgs boson which also deserves study.

3.4.2.4 Branching ratios for the light scalar

The dominant branching ratios of the lightest scalar Higgs boson are shown in Fig.(3.38) as a function of M_A. For a SM Higgs boson of the same mass (around $80-90$ GeV) one would expect the dominant decays to be to bottom quarks, τ leptons, and charm quarks, with the addition of loop induced decays to gluons and photons. These are indeed also the dominant decays of the singlet dominated scalar for most of the allowed M_A range, but the branching ratios now show significant structure at approximately 463 GeV and again at around 490 GeV due to the suppression of various couplings.

The couplings of the lightest Higgs scalar to up-type and down-type quarks and leptons are given in terms of the SM Higgs couplings by

$$g^{\rm NMSSM}_{H_1 u\overline{u}} = (\ O^H_{11}\cot\beta + O^H_{21})\ g^{\rm SM}_{Hu\overline{u}}, \tag{3.37}$$

$$g^{\rm NMSSM}_{H_1 d\overline{d}} = (-O^H_{11}\tan\beta + O^H_{21})\ g^{\rm SM}_{Hd\overline{d}}, \tag{3.38}$$

respectively, where O^H_{11} and O^H_{21} are elements of the scalar Higgs mixing matrix. The relative minus sign between terms in Eq.(3.37) and Eq.(3.38) has the same origin as the relative minus sign between the $hu\overline{u}$ and $hd\overline{d}$ couplings in the MSSM.

The first structure seen in Fig.(3.38), at around 463 GeV, is due to the cancellation of $-O^H_{11}\tan\beta$ with O^H_{21} in Eq.(3.38), forcing the $H_1 \to b\overline{b}$ and $H_1 \to \tau^+\tau^-$ branching

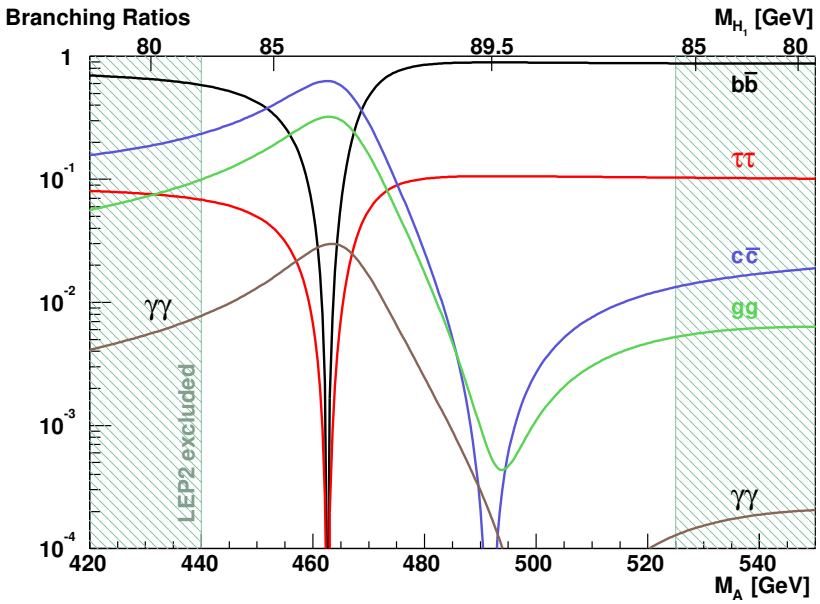

Figure 3.38: *The dominant branching ratios for the lightest scalar Higgs boson as a function of* M_A *for* $\lambda = 0.3$, $\kappa = 0.1$, $\tan\beta = \tan\beta_s = 3$ *and* $A_\kappa = -60$ *GeV. The complicated structure is due to the switching off of the Higgs boson couplings to up-type and down-type quarks and leptons.*

ratios to vanish. As M_A is increased, O^H_{21} passes smoothly through zero, eventually canceling with $O^H_{11}\cot\beta$ in Eq.(3.37). This provides the structure at around 490 GeV where the $H_1 \to c\bar{c}$ branching ratio vanishes.

The decays to gg and $\gamma\gamma$ are mediated by loop diagrams giving a more complex behaviour. $H_1 \to gg$ is dominated by top and stop loops and consequently shows a marked decrease as the $H_1 t\bar{t}$ coupling switches off; although the top-loop contribution will pass through zero here, stop loops and bottom (s)quark loops prevent the branching ratio from vanishing. In addition to top and bottom (s)quark loops the $\gamma\gamma$ branching ratio is mediated by virtual W bosons, charged Higgs bosons and charginos. The dominant effect is from the W bosons and the top loops and so we see a broad suppression over the range where these couplings vanish.

3.4.2.5 LHC Production

Cross-sections for the production of the lightest scalar Higgs boson in various channels at the LHC are shown in Fig.(3.39). The total production cross-section is dominated by gluon-gluon fusion, and is sizable over the entire range. Other significant production channels are vector boson fusion ($VV \to H_1$), Higgs-strahlung ($W \to WH_1$ and $Z \to ZH_1$) and associated production together with top and bottom quarks ($gg \to H_1 t\bar{t}$ and $gg \to H_1 b\bar{b}$ respectively). As we saw for the branching ratios we again see structures which are associated with the couplings of the Higgs boson to various particles passing through zero. However, in contrast to the earlier discussion, there are now three, rather than two, significant values of M_A where structure appears. The coupling of the Higgs boson to a vector boson $V = W,\ Z$ with respect to the SM is

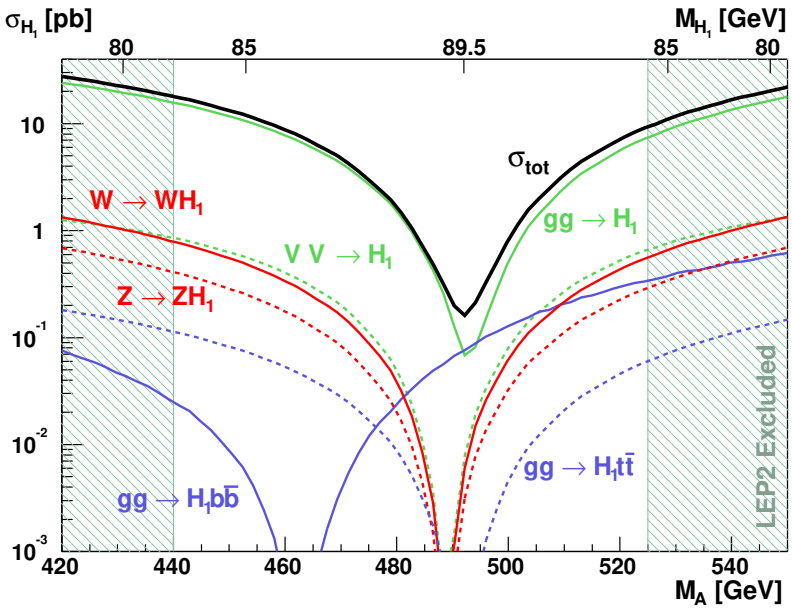

Figure 3.39: *Production cross-sections for the lightest scalar Higgs boson at the LHC, as a function of* M_A *for* $\lambda = 0.3$, $\kappa = 0.1$, $\tan\beta = \tan\beta_s = 3$ *and* $A_\kappa = -60$ *GeV.*

given by

$$g^{\rm NMSSM}_{H_1VV} = O^H_{21}\, g^{\rm SM}_{H_1VV}, \tag{3.39}$$

where O^H_{21} is the same element appearing in Eqs.(3.37–3.38), so when this mixing element vanishes the vector boson fusion and Higgs-strahlung cross-sections will disappear. This M_A point is very close to the point where the $H_1 t\bar{t}$ couplings vanish because the first term on the right-hand-side of Eq.(3.37) is suppressed by $1/\tan\beta$.

For the lower values of M_A, where the Higgs decay to $b\bar{b}$ is suppressed, this Higgs boson may be visible via its decay to $\gamma\gamma$ (with a branching ratio $\gtrsim 0.1\%$ for $M_A \lesssim 480$ GeV). However, as the $\gamma\gamma$ branching ratio is turned off at higher M_A, seeing this Higgs boson will become much more challenging. Although the cross-section remains relatively large, the Higgs boson almost always decays hadronically and the signal has a very large QCD background. The only significant non-hadronic decay is the Higgs decay to τ-pairs with a branching fraction of approximately 10%, but this also has large SM backgrounds.

The chosen scenario is extremely challenging for the LHC, but it is by no means a "worst-case scenario". For example, increasing the value of $\tan\beta$ would increase the separation between the b-quark and vector boson switch-off points, moving the M_A range with an enhanced $H_1 \to \gamma\gamma$ branching ratio out of the allowed region. Alternatively, increasing the value of κv_s slightly would lead to a light Higgs boson sitting right on top of the Z-peak, making it very difficult to disentangle from the SM backgrounds. If the value of κv_s is significantly larger (and $|A_\kappa|$ not too large), the singlet dominated scalar would be heavy enough to decay to a vector boson pair, making its detection much easier. However, if the value of M_A is such that the coupling of Eq.(3.39) vanishes, these golden channels would be lost.

3.4.2.6 LC Production

The vanishing of the HVV couplings in the region of interest is particularly significant for a LC since the most promising production mechanisms are vector boson fusion, e.g. $e^+e^- \to W^+W^-\nu\overline{\nu} \to H_1\nu\overline{\nu}$, and Higgs-strahlung, $e^+e^- \to Z^* \to ZH_1$. The cross-sections for these processes at a $\sqrt{s} = 500$ GeV LC are plotted in Fig.(3.40) for our parameter choice, as a function of M_A, and show the distinctive vanishing of

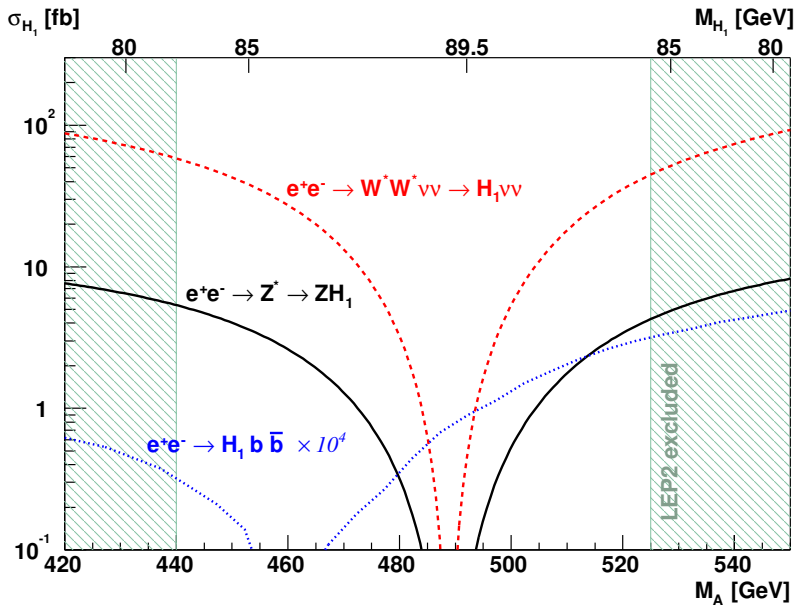

Figure 3.40: *Production cross-sections for the lightest scalar Higgs boson at a* $\sqrt{s} = 500$ *GeV LC, as a function of* M_A *for* $\lambda = 0.3$, $\kappa = 0.1$, $\tan\beta = \tan\beta_s = 3$ *and* $A_\kappa = -60$ *GeV. The cross-section for* $e^+e^- \to H_1 b\overline{b}$ *has been multiplied by* 10^4.

the H_1VV coupling. Nevertheless, the lightest scalar Higgs boson would be seen by these channels for all of the M_A range except for a small window around 490 GeV. In contrast to the LHC, for most of the the observable region decays to $b\overline{b}$ and/or $\tau^+\tau^-$ could be easily used due the LC's relatively background free environment. For M_A values where the bottom and τ couplings vanish, the decays to $\gamma\gamma$ and charm may be used instead.

It is difficult to see what production mechanism could be used to close the remaining window around the critical point where the HVV couplings vanish. Higgs production in association with a top quark pair, $e^+e^- \to H_1t\overline{t}$, is vanishingly small here because of the proximity of the H_1VV and $H_1t\overline{t}$ "turning-off" points (they will move even closer as $\tan\beta$ is increased). The production in association with bottom quarks is shown in Fig.(3.40), multiplied by a factor of 10^4 to be visible on the same scale. Generally, this production process has three contributing sub-processes: Higgs-strahlung, $e^+e^- \to ZH_1$, followed by the Z decay to a bottom quark pair; Higgs pair production, $e^+e^- \to H_1A_i$ $(i = 1, 2)$ followed by the pseudoscalar decaying to bottom quarks; and bottom quark pair production, $e^+e^- \to b\overline{b}$ followed by the radiation of H_1 off a bottom quark. The first contribution is very closely related to the Higgs-strahlung already shown in Fig.(3.40) [simply multiplied by the $Z \to b\overline{b}$ branching ratio], so

contains no new information and is *not* included in the $e^+e^- \to H_1 b\bar{b}$ cross-section shown. The second contribution is only kinematically allowed for the lightest pseudoscalar Higgs boson and is vanishingly small because two small mixings are needed (neither scalar nor pseudoscalar singlet fields have a Z coupling). Therefore the remaining process is dominated by Higgs radiation off bottom quarks, and although this switches off at a different M_A value, it is too small to be useful because of the small bottom quark Yukawa coupling.

At a LC with $\sqrt{s} = 800$ GeV, these cross-sections are modified as shown in Fig.(3.41). The t-channel W-fusion cross-section increases, while the s-channel Higgs-strahlung

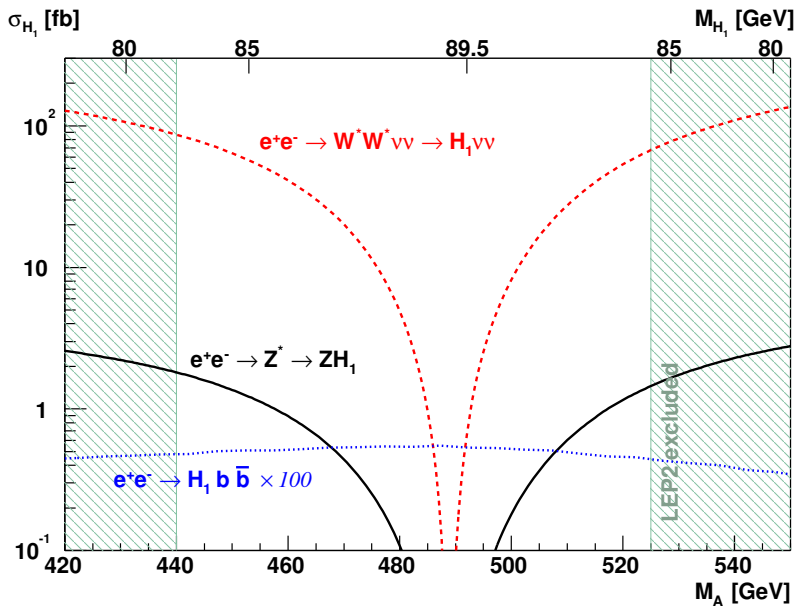

Figure 3.41: *Production cross-sections for the lightest scalar Higgs boson at a* $\sqrt{s} = 800$ *GeV LC, as a function of* M_A *for* $\lambda = 0.3$, $\kappa = 0.1$, $\tan\beta = \tan\beta_s = 3$ *and* $A_\kappa = -60$ *GeV. The cross-section for* $e^+e^- \to H_1 b\bar{b}$ *has been multiplied by* 100.

cross-section decreases, but the overall M_A dependence remains the same, with both cross-sections vanishing at around 490 GeV. The $e^+e^- \to H_1 b\bar{b}$ associated production cross-section has increased dramatically due to the opening up of $e^+e^- \to H_1 A_2$, which was kinematically disallowed at $\sqrt{s} = 500$ GeV. Since this new contribution contains no $H_1 b\bar{b}$ coupling, the cross-section no longer vanishes at around 460 GeV, but unfortunately it is still too small to be of practical use[13].

Increasing κv_s and thus the singlet dominated masses only reduces the production cross-sections in line with the expectations of a reduced phase space. If the singlet dominated scalar is heavy enough, and M_A is far enough away from its critical value, the scalar will decay to vector bosons, making its discovery easier.

[13] This cross-section has been calculated under the assumption of a fixed width (of 1 GeV) for A_2, and is only intended to present an order of magnitude estimate.

3.4.2.7 Conclusions

In this contribution we have considered a particularly challenging NMSSM scenario, presenting masses, branching ratios and production cross-sections at both the LHC and a future e^+e^- LC. Such scenarios have a Higgs spectrum very similar to the MSSM, i.e. nearly degenerate heavy charged, scalar and pseudoscalar states and a light Higgs boson at around 120–140 GeV, supplemented by an additional singlet dominated scalar and pseudoscalar. We have seen that there is still room allowed by LEP for the singlet dominated Higgs boson to be very light, i.e. $\lesssim M_Z$. Despite having reasonably large production cross-sections at the LHC, this light Higgs boson would be difficult to see since its mainly hadronic decays cannot be easily untangled from the SM backgrounds. At a LC, this light scalar can be seen via vector boson fusion and Higgs-strahlung for most of the parameter range, except for a small region where the Higgs-vector boson coupling vanishes. If this Higgs boson is discovered at a LC but is missed at the LHC, LC input would be vital in providing information for trigger and background removal when the LHC endeavours to confirm the discovery.

We have also seen that a such a light Higgs boson may place restrictions on the masses of the heavier Higgs bosons. For small κv_s, in order to avoid detection of the light scalar at LEP, we require $M_A \approx \mu \tan\beta$. [The veracity of the pre-condition "small κv_s" may be ascertained by also observing the singlet dominated pseudoscalar, by e.g. $e^+e^- \to t\bar{t}A_1$, and making use of the approximate sum rule of Eq.(3.36).] This prediction for the heavy Higgs boson masses would be invaluable to the LHC.

In this scenario the H_2, H_3 and A_2 will be present, looking very much like the MSSM Higgs bosons h, H and A respectively with slightly altered couplings and could be detected in the usual way.

For heavier singlet dominated states, the position of the LHC is more favourable, since the clean decay to vector bosons opens up [although again, this is not useful over the entire M_A range]. Also the LHC's kinematic reach will prove useful in discovering or ruling out very heavy singlet dominated Higgs states. On the other hand, if the extra singlet dominated Higgs boson is found to be almost degenerate with the lightest doublet dominated Higgs boson, LC precision may be required to disentangle the two states.

In summary, in order to provide complete coverage over the NMSSM parameter space, both the LHC and an e^+e^- LC will be needed. Not only can the LC probe areas where the LHC cannot, it can provide valuable input to the LHC investigation of the NMSSM Higgs sector.

3.4.3 Identifying an SM-like Higgs particle at future colliders

3.4.3.1 SM-like scenario.

One of the great challenges at future colliders will be the SM-like scenario that no new particle will be discovered at the Tevatron, the LHC and electron-positron Linear Collider (LC) except the Higgs boson with partial decay widths, for the basic channels to fundamental fermions (up- and down-type) and vector bosons W/Z, as in the SM:

$$\left|\frac{\Gamma_i^{\rm exp}}{\Gamma_i^{\rm SM}} - 1\right| = \left|\left(\frac{g_i}{g_i^{\rm SM}}\right)^2 - 1\right| \lesssim \delta_i \ll 1, \text{ where } i = u, d, V. \tag{3.40}$$

New physics may still be seen via deviations of some observables from the SM predictions. The Higgs-boson loop couplings with photons or gluons are very promising for such studies. In the SM and in its extensions, all fundamental charged particles, with mass arising from a Higgs mechanism, contribute to the Higgs boson effective couplings with photons, and, similarly, all quarks contribute to the Higgs boson coupling to gluons. These couplings are absent in the SM at tree level, and therefore, the relevant background will be relatively low.

Results from the LHC and LC can be combined and thus facilitate in distinguishing models. We stress here in particular the role of the $\gamma\gamma$ mode of a linear collider (Photon Collider), where the expected accuracy of the measurement of the two-photon width for Higgs mass equal to 120 GeV is of the order of 2% [234] in comparison to the LHC and LC with the corresponding accuracy 15–20% [8,57].

Here we assume that one neutral Higgs particle has been found at the LHC with all basic couplings, within the experimental accuracy, as expected in the SM. So, we have for relative couplings:

$$\chi_i = \frac{g_i}{g_i^{\rm SM}}, \quad \text{with } \chi_i^{\rm obs} = \pm(1-\epsilon_i), \quad \text{and } |\epsilon_i| \le \delta_i \quad \text{for } i = u, d, V. \tag{3.41}$$

Additional constraints on these ϵ_i follow from the considered model.

We consider the Two-Higgs-Doublet Model (2HDM) with no or weak CP-violation, using the soft Z_2-violation potential as given by [235–238]. We introduce a parameter μ via the real part of the coefficient of the bilinear mixing term $\Re(m_{12}^2) = 2\mu^2 v_1 v_2/v^2$ [238]. For $\mu^2 \gg |\lambda_i| v^2$ the SM-like scenario with decoupling is realized. The SM-like scenario can also be realized for $\mu < v$ with non-decoupling, in particular for $M_{H\pm} \approx M_H \approx 700\,\text{GeV}$, $M_A \approx 600\,\text{GeV}$ and M_h=120 GeV, $\mu < 0.3\, M_{H\pm}$, with λ_i within perturbativity and even unitarity constraints. The Yukawa interactions are of Type II with the basic couplings constrained by $(\chi_u+\chi_d)\chi_V = 1+\chi_u\chi_d$ (pattern relation [238]), valid for each neutral Higgs boson, even in the general CP-violating case.

The SM-like scenario corresponds to the observation of either h or H. We distinguish solutions A and B (see ref. [238] and table 3.10) for the realization of an SM-like scenario for the observed Higgs particle with mass 110 to 250 GeV. In solutions A all basic (relative) couplings are close to 1 or all are close to -1. Note that only solution A_{h+} is realized in the decoupling limit. In solutions B, one basic coupling, χ_u or χ_d, has opposite sign to the other two, and obviously one expects here larger deviations from the SM than for solutions A. One can see that the decay width $h(H)Z\gamma$ is less sensitive to the discussed effects of 2HDM than the $h(H)\gamma\gamma$ one.[14]

solution	basic couplings	$\lvert\chi_{gg}\rvert^2$	$\lvert\chi_{\gamma\gamma}\rvert^2$	$\lvert\chi_{Z\gamma}\rvert^2$
$A_{h\pm}/A_{H_-}$	$\chi_V \approx \chi_d \approx \chi_u \approx \pm 1$	1.00	0.90	0.96
$B_{h\pm d}/B_{H_- d}$	$\chi_V \approx -\chi_d \approx \chi_u \approx \pm 1$	1.28	0.87	0.96
$B_{h\pm u}$	$\chi_V \approx \chi_d \approx -\chi_u \approx \pm 1$	1.28	2.28	1.21

Table 3.10: *SM-like realizations in the 2HDM II [238], together with ratios of partial widths to their SM values for $M_{h(H)} \approx 120$ GeV for the case $|\chi_i| = 1$, $M_{H^\pm}$ =700 GeV and $\mu \lesssim 0.3 M_{H^\pm}$.*

[14] The process $e\gamma \to eh(H)$ with large transverse momentum of the scattered electron, has a sensitivity from the $h(H)Z\gamma$ vertex, with Z far from the mass shell, similar to that of $h(H) \to \gamma\gamma$ [239].

3.4.3.2 The two-gluon decay width.

The two-gluon width will be measured at the LHC. This quantity is for solutions A practically equal to the SM prediction (see table 1).

In the SM the contributions of t and b quarks partly cancel, while for solutions B they add, giving larger deviations from the SM predictions. In Fig. 1 (left) the solid curve corresponds to the case $\chi_u = -\chi_d = \pm 1$ for all solutions B. The shaded bands reflecting $1\ \sigma$ experimental uncertainties correspond to the B_{h+u} case only.

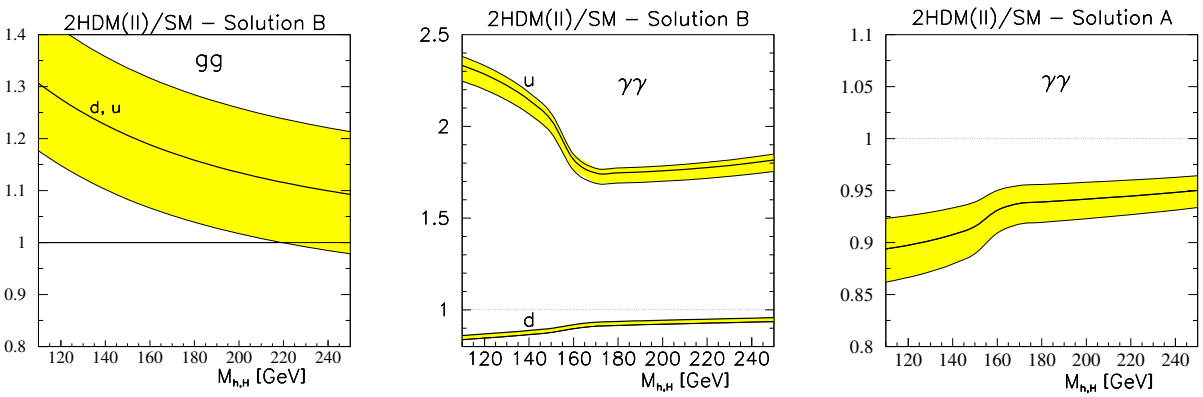

Figure 3.42: *Ratios of the Higgs boson decay widths in the SM-like 2HDM II and the SM as functions of $M_{h,H}$ for solutions B and A for $M_{H^\pm}$=700 GeV and $\mu \lesssim 0.3 M_H^\pm$.*

3.4.3.3 The two-photon decay width.

For solutions A the widths $h(H) \to \gamma\gamma$ and $h(H) \to Z\gamma$ will differ from the SM predictions due to the charged Higgs boson contribution, proportional to the trilinear coupling hH^+H^- (HH^+H^-), so we have:

$$\chi_{H^\pm} \equiv -\frac{v g_{hH^+H^-}}{2M^2_{H^\pm}} = \left(1 - \frac{M_h^2}{2M^2_{H^\pm}}\right)\chi_V + \frac{M_h^2 - \mu^2}{2M^2_{H^\pm}}(\chi_u + \chi_d), \tag{3.42}$$

and similarly for H. The value of $\chi_{H^\pm}$ is close to $\chi_V \approx \pm 1$ (non-decoupling) at the considered small values of $(M_h^2/2M^2_{H^\pm})$ for solutions A and $(\mu^2/M^2_{H^\pm})$ for solutions B.

For solutions $B_{h\pm d}$ the main deviation from that of the SM is like for solution A given by the contribution of $H^\pm$. For the solution B_{h+u} the effect of the change of sign of the coupling $ht\bar{t}$ dominates.

The ratios of the two-photon Higgs widths to the SM value are shown in Fig. 1 (see also table 1) for solutions B (center) and A (right). The results are presented without (solid lines) and with realistic $1\ \sigma$ uncertainties (shaded bands) around the SM values of the measured basic couplings [57].

3.4.3.4 Conclusion

We analyse, using realistic estimates of experimental uncertainties, the potential of future colliders to determine the nature of an SM-like Higgs boson, SM or 2HDM, for mass 110–250 GeV. It is crucial to combine precise measurements of loop couplings involving gluons at LHC and photons at a Photon Collider, as only couplings to photons are sensitive to the decoupling property of the model.

3.4.4 Synergy of LHC, LC and PLC in testing the 2HDM (II)

Interplay of LHC, LC and PLC in testing the 2HDM (II) [164] has been studied for Higgs boson h with mass 200 to 350 GeV, decaying to W^+W^- and ZZ. Figure 3.43 shows the expected rate, relative to SM, as a function of relative (to SM) couplings to top quark, χ_t, and vector bosons, χ_V. At LHC, cross section sensitive mainly to χ_t can be measured with precision (SM case) of about 15% [165, 166], while at LC, for cross section depending predominantly on χ_V, the precision is $4-7\%$ [167]. The two-photon width of the Higgs boson, to be measured with accuracy of $4-9\%$ at PLC [168], depends both on χ_t and χ_V. At PLC also the phase of $h \to \gamma\gamma$ amplitude, $\phi_{\gamma\gamma}$, can be measured to $40-120$ mrad [168]. By combining these measurements, couplings of the Higgs boson can be precisely determined, as shown in Fig. 3.44 (assumed parameter values are $\chi_V = 0.9$, $\chi_t = -1$, $\chi_b = 1$).

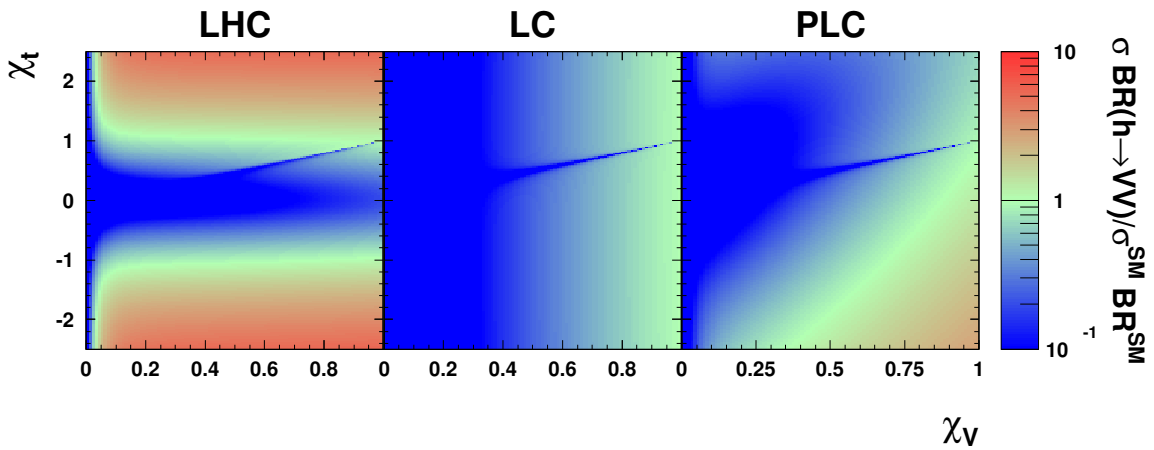

Figure 3.43: h (250 GeV) production rates at LHC, LC and PLC, relative to SM.

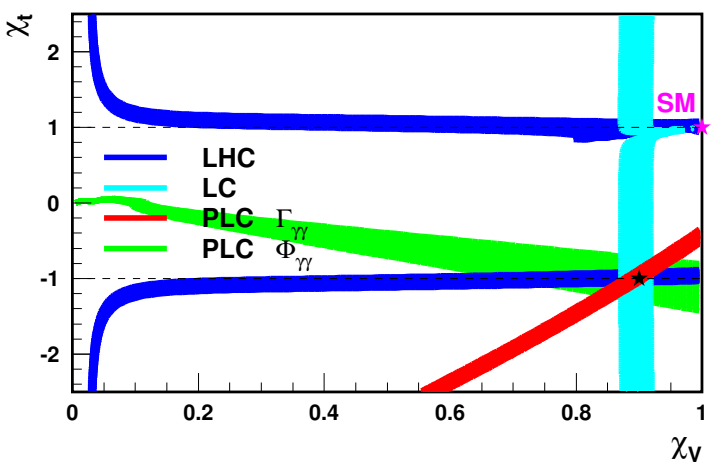

Figure 3.44: Values of χ_V and χ_t determined from measurements at LHC, LC and PLC, for assumed parameters indicated by ($\star$).

3.4.5 Enhanced $h^0 \to \gamma\gamma$ decays in fermiophobic Higgs models at the LHC and LC

3.4.5.1 Introduction

We study the production of a fermiophobic Higgs [240] (h_f) followed by $h_f \to \gamma\gamma$ decay at a e^+e^- high energy linear collider (LC) and the Large Hadron Collider (LHC). A h_f has very suppressed or zero couplings to fermions and so its dominant decay modes are to bosons, either $\gamma\gamma$ (for $m_{h_f} < 95$ GeV) or WW^* (for $m_{h_f} > 95$ GeV) [241]. In this paper we shall consider $h_f \to \gamma\gamma$ decays only. Higgs boson production mechanisms which depend on the Higg-fermion-fermion coupling (such as gluon-gluon fusion $gg \to h_f$) are very suppressed. Hence h_f is best searched for by mechanisms which involve its couplings to vector bosons ($V = W^{\pm}, Z$) and/or other Higgs bosons. At the LHC there are two standard ways to produce h_f, for which experimental simulations have been performed in the context of the SM Higgs (ϕ^0). These are:

(i) $pp \to W^* \to Wh_f$, $W \to l\nu$ (Higgsstrahlung) [242]

(ii) $pp \to qqh_f$ (Vector boson fusion) [243]

At a e^+e^- LC one has the following mechanisms:

(iii) $e^+e^- \to h_f Z$ (Higgsstrahlung) [244]

(iv) $e^+e^- \to h_f \nu\overline{\nu}$ (W boson fusion) [244]

At a $\gamma\gamma$ collider:

(v) $\gamma\gamma \to h_f$ [245], [92, 173]

All these mechanisms have been shown to be effective for the SM Higgs ϕ^0 and for h^0 of the MSSM [92, 173], since both these Higgs bosons have substantial couplings to vector bosons. This is not the case in a general 2 Higgs Doublet Model (2HDM), in which a h_f may arise. In the 2HDM the above mechanisms (i) to (v) for h_f are all suppressed by $\sin^2(\beta - \alpha)$, which in the fermiophobic scenario ($\alpha \to \pi/2$) in the 2HDM (Model I) reduces to:

$$VVh_f \sim \cos^2\beta \ \ (\equiv 1/(1 + \tan^2\beta)) \tag{3.43}$$

This is a severe suppression for $\tan\beta \geq 10$ and renders all the above mechanisms unobservable (for an earlier discussion with just mechanism (i) see [246]). This is shown in Fig. 3.45, where we apply the results of the signal/background ($S^{\phi}/\sqrt{B}$) simulations for $\phi^0 \to \gamma\gamma$ to the case of a h_f. To do this we need to scale the SM Higgs signal S^{ϕ} by the factor BR($h_f \to \gamma\gamma$)/BR($\phi^0 \to \gamma\gamma$), and include the $\cos^2\beta$ suppression in the production cross–sections. Since all the above simulations presented results for $m_{\phi^0} = 120$ GeV we will consider a h_f of this mass. For $m_{h_f} = 120$ GeV on has [247]:

$$BR(h_f \to \gamma\gamma)/BR(\phi^0 \to \gamma\gamma) \approx 10 \tag{3.44}$$

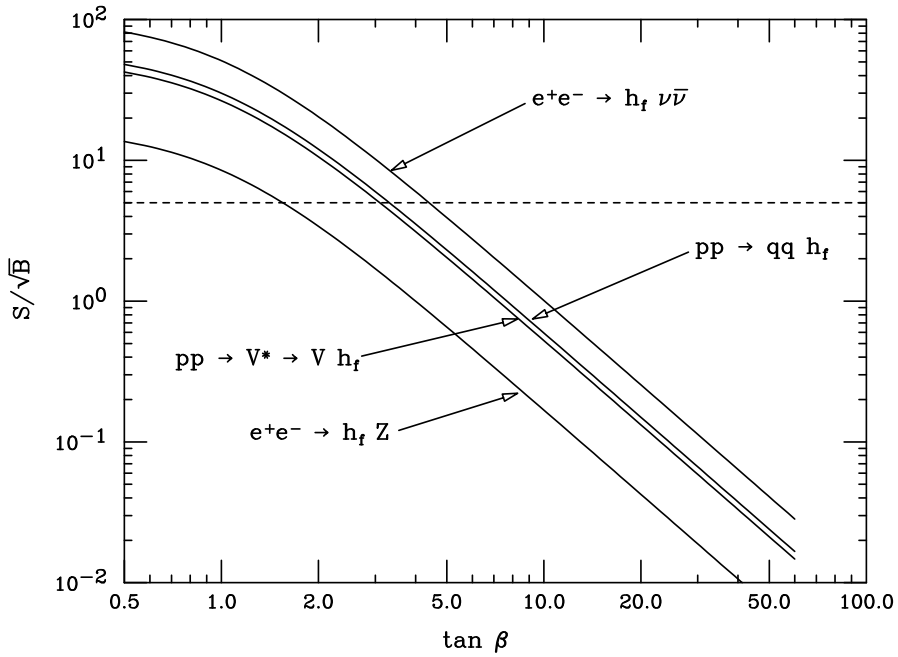

Figure 3.45: $S/\sqrt{B}$ as a function of $\tan\beta$ for various h_f production processes.

In Fig. 3.45 we plot $S/\sqrt{B}$ for h_f as a function of $\tan\beta$. We include the production mechanisms (i)-(iv) and take $m_{h_f} = 120$ GeV. We are not aware of a simulation for mechanism (v). Each curve is of the simple form:

$$S/\sqrt{B} = 10K_i \cos^2\beta \tag{3.45}$$

where K_i ($i = 1, 4$) corresponds to the SM Higgs $S^\phi/\sqrt{B}$ for each of the mechanisms (i)-(iv) for the chosen luminosities ($\mathcal{L}$) in Refs. [242] → [244], which are 50 fb^{-1} for (i),(ii) and 1000 fb^{-1} for (iii),(iv), with $\sqrt{s} = 500$ GeV. For other choices of $\mathcal{L}$ the $S/\sqrt{B}$ scales as $\sqrt{\mathcal{L}}$. One can see that all the mechanisms offer spectacular signals ($S/\sqrt{B} >> 5$) *when* there is little suppression in the cross-section at low $\tan\beta$. Importantly, each collider can discover h_f in two distinct channels, thus providing valuble confirmation of any initial signal. However, $S/\sqrt{B}$ falls rapidly as $\tan\beta$ increases, and $S/\sqrt{B} < 5$ at some critical value $\tan\beta_C$. In Fig. 3.45, $\tan\beta_C$ varies between 2 and 5. Hence unless $\tan\beta$ is fairly small a relatively light h_f (even $m_{h_f} << 120$ GeV) may escape detection at both the LHC and LC.

Fortunately there are alternative mechanisms $\sim \sin^2\beta$, which are thus unsuppressed in the region of large $\tan\beta$ [248]:

(vi) At the LHC: $pp \to H^\pm h_f, A^0 h_f$

(vii) At a LC: $e^+e^- \to A^0 h_f$

For $\sin^2\beta >> \cos^2\beta$ only the above channels offer reasonable rates, and thus all three should be exploited in order to first discover h_f and thereafter provide confirmatory signals. We are not aware of explicit signal–background simulations for these channels. The cross–sections at Tevatron energies for the mechanisms in (vi) were studied in [249]. The mechanism $pp \to H^\pm h_f$, followed by $H^\pm \to h_f W^*$ (which

would have a large branching ratio) and $W^{\pm} \to l^{\pm}\nu$ would lead to a signature $\gamma\gamma + l$ similar to that from mechanism (i). Moreover, there is also the possibility of $\gamma\gamma\gamma\gamma$ final states [248]. Mechanism (vii) is usually absent in discussions of the MSSM Higgs bosons at a LC, due to its strong suppression of $\cos^2(\beta - \alpha)$ for $m_A \geq m_Z$. However for a h_f in the larger $\tan\beta$ region it provides promising rates.

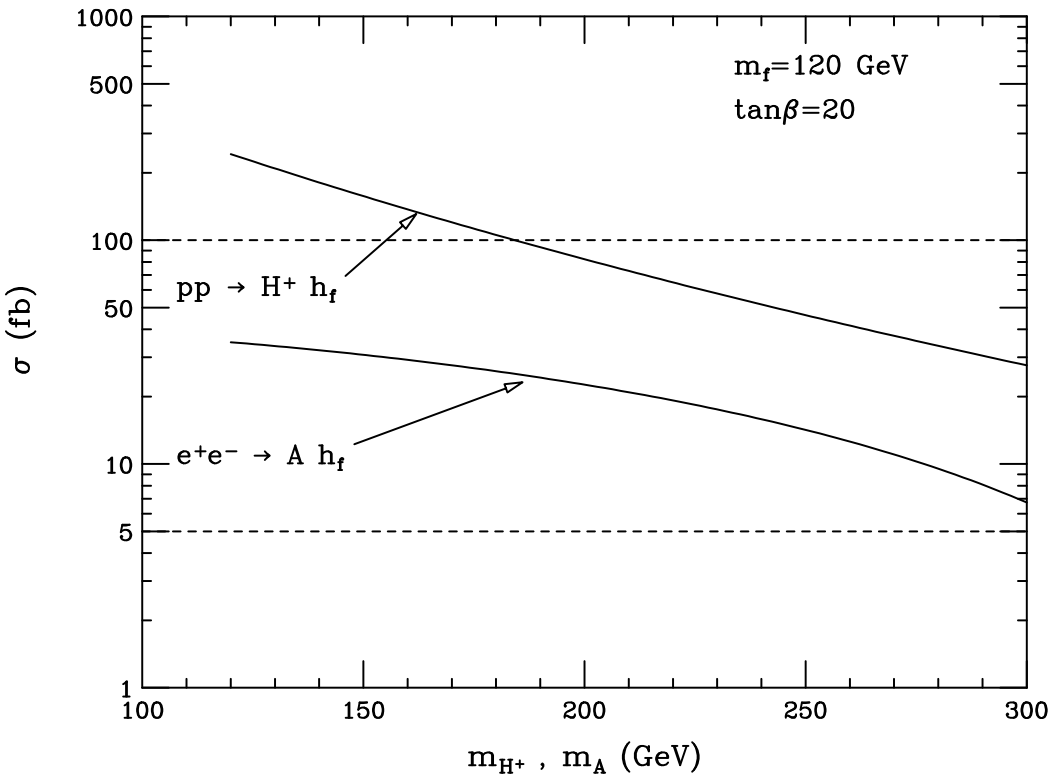

Figure 3.46: $\sigma(pp \to H^{\pm}h_f)$ and $\sigma(e^+e^- \to A^0h_f)$ as a function of m_A or $m_{H^{\pm}}$, for $m_{h_f} = 120$ GeV.

In Fig. 3.46 we plot $\sigma(pp \to H^{\pm}h_f)$ and $\sigma(e^+e^- \to A^0h_f)$ as a function of Higgs mass $m_{H^{\pm},A^0}$ for $m_{h_f} = 120$ GeV and fixing $\tan\beta = 20$ (i.e. $\sin^2\beta \sim 1$). We do not plot $\sigma(pp \to A^0h_f)$ which has a value approximately half that of $\sigma(pp \to H^{\pm}h_f)$, for $m_{H^{\pm}} = m_A$. One can see that $\sigma(e^+e^- \to A^0h_f)$ would offer a sizeable number of events for $\mathcal{L} = 500$ fb^{-1}, and backgrounds would be smaller than for the mechanisms at the LHC. Detection prospects for $e^+e^- \to A^0h_f, h_f \to \gamma\gamma$ at larger $\tan\beta$ might be comparable to those for the Higgsstrahlung channel $e^+e^- \to Zh_f$ at low $\tan\beta$. It is not clear which cross–section for $pp \to H^{\pm}h_f$ and $pp \to A^0h_f$ would be observable. Detection prospects may be marginal due to the sizeable backgrounds at the LHC. In this region of larger $\tan\beta$, it is more likely that h_f is detected first at a LC in the channel $e^+e^- \to A^0h_f$, while both $e^+e^- \to h_fZ$ and $e^+e^- \to h_f\nu\overline{\nu}$ are unobservable due to the aforementioned suppression of $\cos^2\beta$. With just one such signal for h_f, confirmatory signals at the LHC would be of great urgency. Prior knowledge of the Higgs masses from the LC in the observed channel $e^+e^- \to A^0h_f$ should facilitate the search for the analogous process $pp \to A^0h_f$ at the LHC. In the same way, possible discovery of $H^{\pm}$ in $e^+e^- \to H^+H^-$ would aid the search for $pp \to H^{\pm}h_f$. We encourage experimental simulations of the mechanisms $e^+e^- \to A^0h_f$ and $pp \to H^{\pm}h_f, A^0h_f$ followed by $h_f \to \gamma\gamma$ decay.

Producing a h_f in as many channels as possible is of utmost importance. It is here that the interplay of the LC and LHC would be greatly beneficial in the studied region of larger $\tan\beta$. Discovery of such a particle would strongly constrain the possible choices of the underlying Higgs sector.

3.4.6 Visible signals of an 'invisible' SUSY Higgs at the LHC

3.4.6.1 Introduction

Sparticles can affect the discovery of a Higgs of mass $\sim 125GeV$ in two ways. The loop effects due a light stop of mass around that of a t quark can reduce the ggh coupling and hence the production to a level low enough to preclude the discovery of h at the LHC [250, 251]. If the assumption of the gaugino mass unification at the GUT scale is given up, the latest LEP and Tevatron data together with cosmological constraints still allow the lightest supersymmetric Higgs to have a large branching fraction into invisible neutralinos [252, 253].

If it is the light stop that makes the Higgs 'invisible' it might still be possible to recover the Higgs signal in the $\tilde{t}_1\tilde{t}_1^* h/\tilde{t}_1\tilde{t}_2 h$ channel [250,251,254]. The large values of the 'invisible' branching fractions (B_{invis}) can make the h 'invisible' reducing the branching ratio into the $\gamma\gamma$ and $b\overline{b}$ channels that are considered to be the optimal channels to search for a h at the LHC, in this mass range in the inclusive and the associated production modes respectively. In this case strategies for a dedicated search of a h with 'invisible' decay products have to be devised. It is possible to search for an 'invisible' Higgs at the LHC in the WW fusion channel [255, 256] upto an invisible branching ratio of ~ 0.25, and in its associated production with a Z [257, 258] or in the $t\bar{t}$ [259, 260] channel for somewhat larger values of the invisible branching ratio depending on the mass of the Higgs. The vector boson fusion channel is quite promising but issues of QCD backgrounds to the signal for an 'invisible' Higgs are yet to be completely resolved.

On the other hand an LC in the first stage would be able to see such a Higgs with ease, further allowing a measurement of its branching ratio into the 'invisible' channel. Combining this with the possible signal for the 'invisible' Higgs at the LHC, one can use specific features of the sparticle phenomenology to test the hypothesis that the 'invisibility' of the Higgs at the LHC is supersymmetric in origin.

In the next section we first discuss the possible depletion in the inclusive Higgs signal for the case of a light stop quark. Then we present predicted values of the B_{invis} over the supersymmetric parameter space, while still being consistent with the data from the LEP, Tevatron as well as the WMAP DM constraints [20]. Next we present special features of the neutralino phenomenology that such a scenario will imply at the LC as well as at the LHC. The $\tilde{\chi}_1^0$ is a mixed gaugino-higgsino state in this case, causing an enhancement of the cross-section for associated production of h with a pair of neutralinos or equivalently production of h in decays of $\tilde{\chi}_j^0$. We point out how the associated production of the h with a pair of $\tilde{\chi}_i^0$ at the LHC and the LC will reflect this scenario as well as comment how the second lightest neutral Higgs might also have substantial 'invisible' branching ratio in this case, thus affecting the Higgs phenomenology further.

3.4.6.2 Invisible Higgs due to Supersymmetric Effects at the LHC

Direct decays of the lightest supersyemmetric Higgs into a pair of sfermions are not possible in view of the upper limit on m_h in SUSY *and* the lower limits on the sparticle masses implied by the LEP data. As far as the loop induced hgg and $h\gamma\gamma$ couplings are concerned, it is the light $\tilde{t}_1, \tilde{b}_1$ loops that can have the largest effect. For large values of squark mixing (trilinear term $A_t - \mu/\tan\beta$) and a light stop ($m_{\tilde{t}_1} \sim 160 - 170$) GeV, the $\tilde{t}_1$ loop contribution can interfere destructively with that of the t loop. This would cause a reduction in $\Gamma(gg \to h)$ and an increase in the $\Gamma(h \to \gamma\gamma)$ relative to the expectations in the Standard Model. Due to the dominance of the latter by $W-$ loop, the reduction in $gg \to h$ width and hence in the inclusive production cross-section by light $\tilde{t}_1$ loop has a much more significant role to play. Thus in this situation a reduction by about a factor of 5 or more in the product of the production cross section $\sigma(gg \to h)$ and the $\Gamma(h \to \gamma\gamma)$ is possible [250, 251]. This is illustrated in Fig. 3.47 which shows the ratio $R_{gg\gamma\gamma} = \frac{\Gamma^{SUSY}(h\to gg)\times BR^{SUSY}(h\to\gamma\gamma)}{\Gamma^{SM}(h\to gg)\times BR^{SM}(h\to\gamma\gamma)}$. $R_{\gamma\gamma}$ is defined similar to $R_{gg\gamma\gamma}$. The two panels show clearly, that $R_{gg\gamma\gamma}$ can fall well below 0.6, making the Higgs boson h 'invisible' in the inclusive channel in the $\gamma\gamma$ mode at the LHC, given the expected significance level of the signal as given by the experimental studies by ATLAS and CMS [116]. Two facts are worth noting though. We notice that large reductions in $R_{gg\gamma\gamma}$ occur for parameter values where $R_{\gamma\gamma}$ rises above unity thus facilitating the search of the Higgs in the Wh, Zh channel using the $\gamma\gamma$ decay of h. Further, the larger reductions in $R_{gg\gamma\gamma}$ happen for heavier Higgses, for which the signal in the $\gamma\gamma$ channel remains statistically significant in spite of the reduction in $R_{gg\gamma\gamma}$. The reduction in $R_{gg\gamma\gamma}$ becomes less pronounced with increasing values of $\tan\beta$. Further, if the invisibility of the Higgs signal is caused by a light stop, the branching ratio into $b\bar{b}$ channel is unaffected, thus keeping the prospects of the search is associated production mode with the decay of the h in the $b\bar{b}$ channel alive.

In view of the LEP bound on the chargino mass, the effect of the sparticles other than the $\tilde{t}$ on the loop induced decay widths of the light higgs is rather small [252]. For the case of universal gaugino masses at high scale, the LEP bound on $\tilde{\chi}_1^{\pm}$ mass implies a lower bound on $\tilde{\chi}_1^0$ mass and hence on the possible value that $\Gamma_{\chi\chi} = \Gamma(h \to \tilde{\chi}_1^0\tilde{\chi}_1^0)$ can have. However, in models with nonuniversal gaugino masess at the high scale, it is possible to have large values for $\mathcal{B}_{\chi\chi} = B.R.(h \to \tilde{\chi}_1^0\tilde{\chi}_1^0)$ while still being consistent with the nonobservation of any effects of the sparticles in the chargino-neutralino sector [252, 253]. For the decay to be kinematically possible, consistent with the LEP constraints, one needs M_1/M_2 at the EW scale to be less than the value of ~ 0.5 that it has in models with universal gaugino masses. Further to maximise the value of the $h\tilde{\chi}_1^0\tilde{\chi}_1^0$ coupling and hence that of $\Gamma_{\chi\chi}$, one needs the LSP to be a mixture of gaugino and higgsino. This along with maximising the h mass for a given choice of parameters is achieved by choosing small value of the higssino mass parameter μ and moderate values of $\tan\beta$. We will see later that indeed values of $\mathcal{B}_{\chi\chi}$ upto 0.6–0.7 are possible. $R_{\gamma\gamma}$ and $R_{b\bar{b}}$ defined similarly are given approximately by $1.0 - \mathcal{B}_{\chi\chi}$. The large values of $\mathcal{B}_{\chi\chi}$ cause a reduction in the branching fraction into the $\gamma\gamma$ channel and $b\bar{b}$ channel. Reduction in the former affects the inclusive search, whereas the latter is used for the search when the Higgs is produced in association with a $W/Z/t\bar{t}$ or via the Vector Boson Fusion. Reductions in these branching fractions then can reduce the reach of the search via these channels. Of course, the large values of $\mathcal{B}_{\chi\chi}$ give rise to new

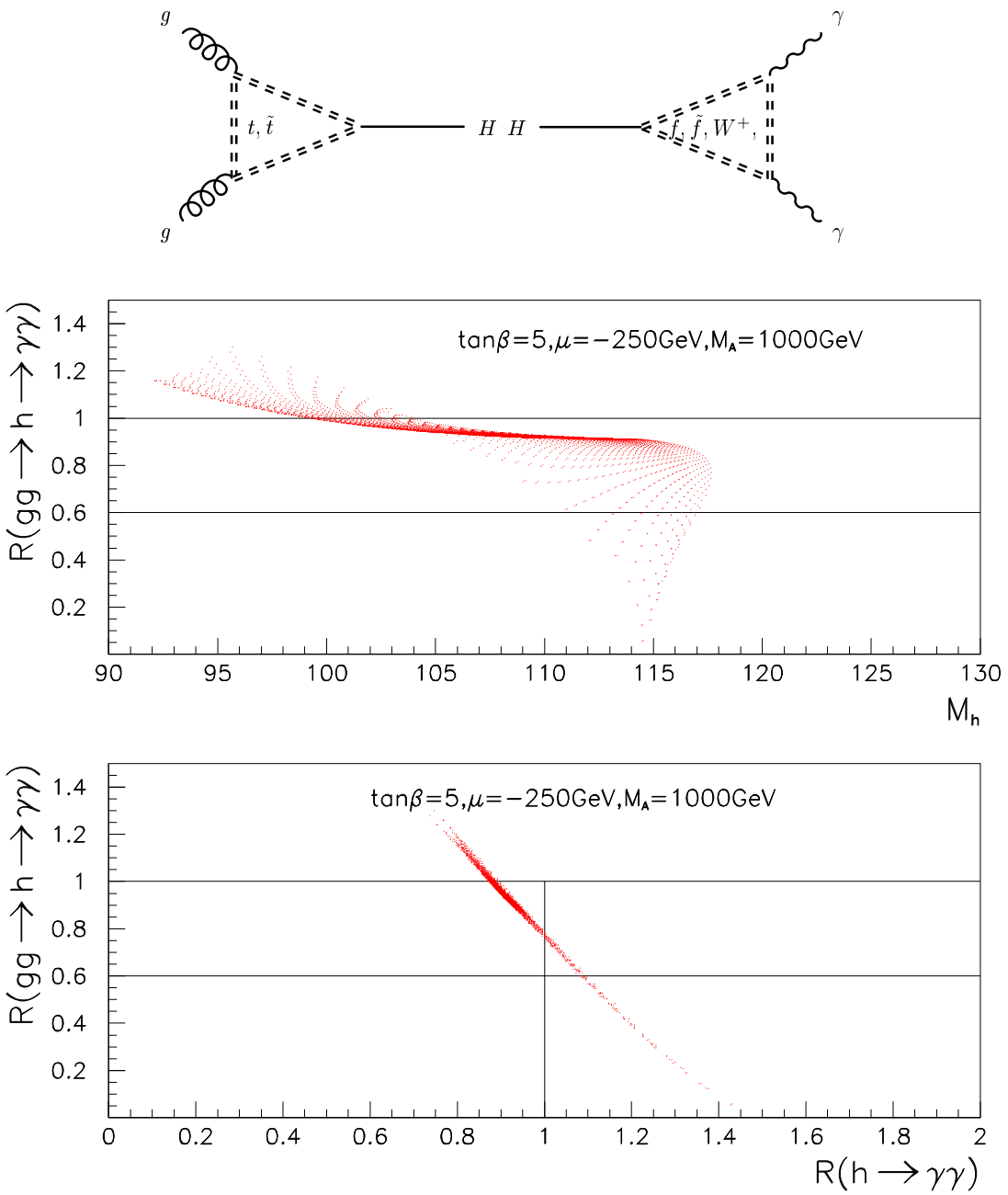

Figure 3.47: Correlation of the ratio $R_{gg\gamma\gamma}$ with $R_{\gamma\gamma}$ and m_h for a chosen set of values of A_t, μ and $\tan\beta$, for light top squarks [251]

search channels where the Higgs decays into invisible products.

In this case the 'invisibility' of the Higgs is caused by the mixed nature of Higgsino-Gaugino content of the LSP and its small mass. A light $\tilde{\chi}_1^0$ with such couplings has implications for the relic density of the neutralinos in the Universe, as the latter is decided by $\sigma(\tilde{\chi}_1^0\tilde{\chi}_1^0 \rightarrow f^+f^-)$. For a light $\tilde{\chi}_1^0$, the Z/h-mediated s channel process contributes to the annihilation. If the $\tilde{l}_R$ is light the cross-section also receives a contribution from the t-channel $\tilde{l}_R$ exchange. There is a clear correlation between the expected 'invisible' branching ratio for the h and the relic density of the $\tilde{\chi}_1^0$ as the same

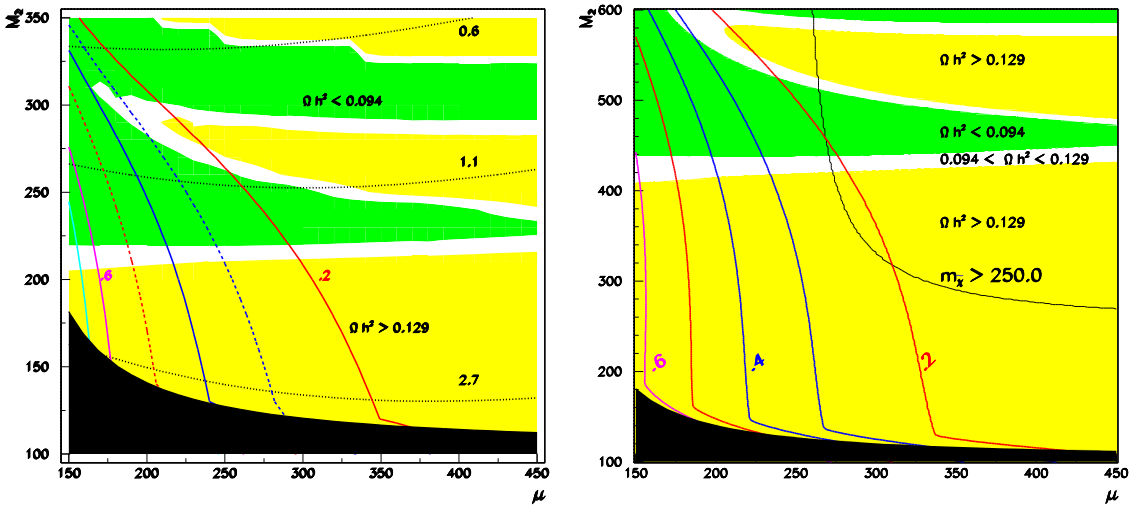

Figure 3.48: Left and right panel shows contours of $B.R.(h \to \tilde{\chi}_1^0\tilde{\chi}_1^0)$ for $r = M_1/M_2|_{EW} = 0.2$ and 0.1 respectively, along with the DM and LEP constraints. The white region corresponds to $0.094 < \Omega h^2 < 0.129$. Parameter m_0 determining the slepton mass [252,253] takes values 90 and 94 GeV for the left and right panel respectively. $\tan\beta = 5$ and $m_h = 125$ GeV. The black region is the LEP-excluded region. The lightly and heavily shaded regions correspond to $\Omega h^2 > 0.129$ and $\Omega h^2 < 0.094$ respectively.

couplings are involved. Left and right panels of figure 3.48 show results [253, 261] Obtained for $r = M_1/M_2|_{EW} = 0.2(0.1)$, $\tan\beta = 5$ and $m_{\tilde{l}_R} \sim 100$ GeV using the micrOMEGAs [262] program to calculate the relic density. These show that the requirement of an acceptable relic density does constrain the M_2–μ plane quite substantially. However, there exist large regions of this plane where the 'invisible' branching ratio of h is as large as 0.5–0.6, even for 'large' ($\sim$ 200 GeV) $\tilde{l}_R$, consistent with the LEP constraints and with an acceptable relic density.

3.4.6.3 Implications for the sparticle phenomenology at the LHC and the LHC-LC interplay

In a scenario where the lightest MSSM Higgs h signal in the $\gamma\gamma$ or $b\bar{b}$ channel is invisible at the LHC due to one of the two reasons mentioned above, it is imperative to ask two questions : 1) whether it is possible to recover the Higgs signal in some other channel and 2) whether the particular scenario responsible for making the h 'invisible' can be tested at the LHC. Of course information that even a first stage LC could provide about such a h which is 'invisible' at the LHC will be very crucial in this exercise.

If it is the light $\tilde{t}_1$ that makes the h 'invisible', the signal for the h can be recovered at the LHC in the channel $\tilde{t}_1\tilde{t}_1 h$ and $\tilde{t}_1\tilde{t}_2 h$ as the cross-section for this process will then be substantial. It may be that the Tevatron might be able to see a $\tilde{t}_1$ with $m_{\tilde{t}_1} \sim 160 - 170$ GeV. Feasibility of observation of a $\tilde{t}_1$ in this mass range, should $c\tilde{\chi}_1^0$ be its dominant decay mode, has still not been properly investigated. The large QCD backgrounds at the LHC might not make it very easy. On the other hand, even a first phase LC will be able to probe this mass range for the $\tilde{t}$ very easily and thoroughly. If it is

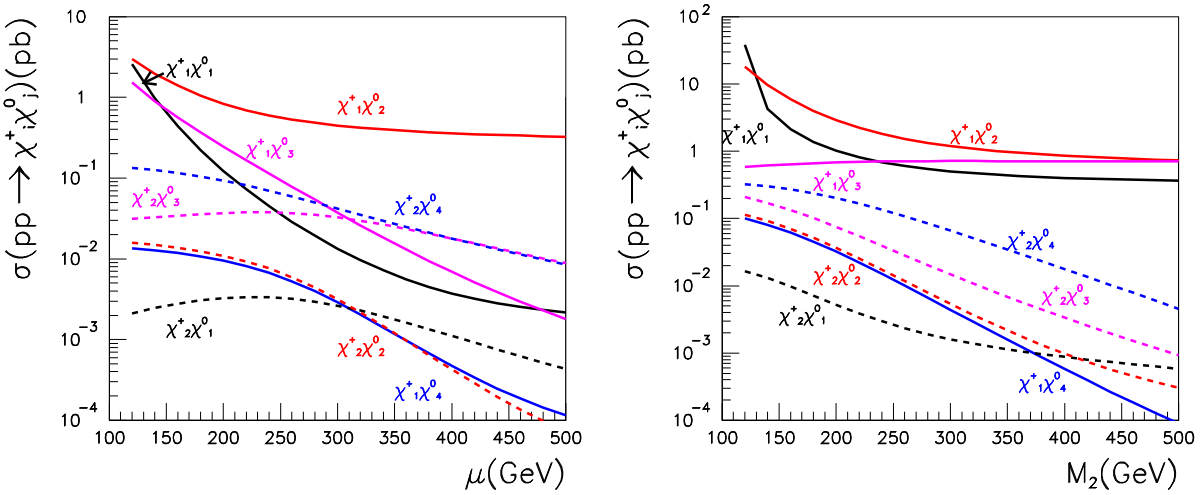

Figure 3.49: Associated Production of chargino and neutralino at the LHC at LO for $M_2 = M_1/10$ a) as a function of μ for $M_2 = 250$GeV. b) as a function of M_2 for $\mu = 150$GeV .

the nonuniversal gaugino masses that make the h 'invisible' then the smaller mass of the $\tilde{\chi}_1^0$ as well its mixed nature will cause the trilepton signal at the Tevatron to be qualitatively different from that expected in the universal case. Thus this scenario may be tested at the Tevatron via the hadronically quiet trilepton events. At the LHC eventhough the EW production of $\tilde{\chi}^{\pm}\tilde{\chi}^0$ is subdominant, usual $b\overline{b}$ and $\gamma\gamma$ signatures of the Higgs, production of charginos and neutralino is quite substantial[15]. Fig. 3.49 shows that, for values of $\mu - M_2$ where $R_{\gamma\gamma}$ is below .6, all neutralinos and charginos can be produced. For instance with $M_2 = 250$GeV, the cross section for $\tilde{\chi}_4^0\tilde{\chi}_2^+$ is in excess of 100 fb while $\tilde{\chi}_2^0\tilde{\chi}_1^+$ is above 1 pb. In our analysis we had taken masses of all the sfermions and heavier Higgses to be in the TeV range. If the gluino/squarks are in the mass range of about 500 GeV, the cascade production of $\tilde{\chi}^{\pm}\tilde{\chi}^0$ is then quite substantial. A correlation between the observations in the chargino-neutralino sector, a possible non observation of the Higgs at the LHC and a signal at the LC for a Higgs with 'invisible' decay mode can thus unravel the issue completely.

If we now look at the (lightest) Higgs that can be produced through cascade decays in these processes, one sees from Fig. 3.50 that, through essentially $\tilde{\chi}_3^0$ decays, associated Higgs cross sections of about 30fb are possible. Nonetheless, again, it is in these regions with highest yield that the Higgs has a large branching ratio into invisible and would be difficult to track. The h search in neutralino decays at the LHC, in this scenario is being investigated and should certainly provide clean examples of the possible LHC-LC interplay.

The implications of this scenario for the SUSY phenomenology at LC have been recently investigated [263]. It has been shown there that, for the region of small values of μ where the Higgs can become 'invisible' for nonuniversal gaugino masses, for the range of nonuniversality parameter 0.03 – 0.5 (the universal case) and $\tan\beta$ values from 10–50, the production cross-section will be at an observable level ($> 1fb$ at a 500 GeV LC) for at least one of the sparticle pairs from among $\tilde{\chi}^+\tilde{\chi}^-, \tilde{\chi}_1^0\tilde{\chi}_3^0, \tilde{\chi}_1^0\tilde{\chi}_2^0$.

[15]Production of light sleptons, as constrained from cosmology in these scenarios, is on the other hand quite modest at the LHC.

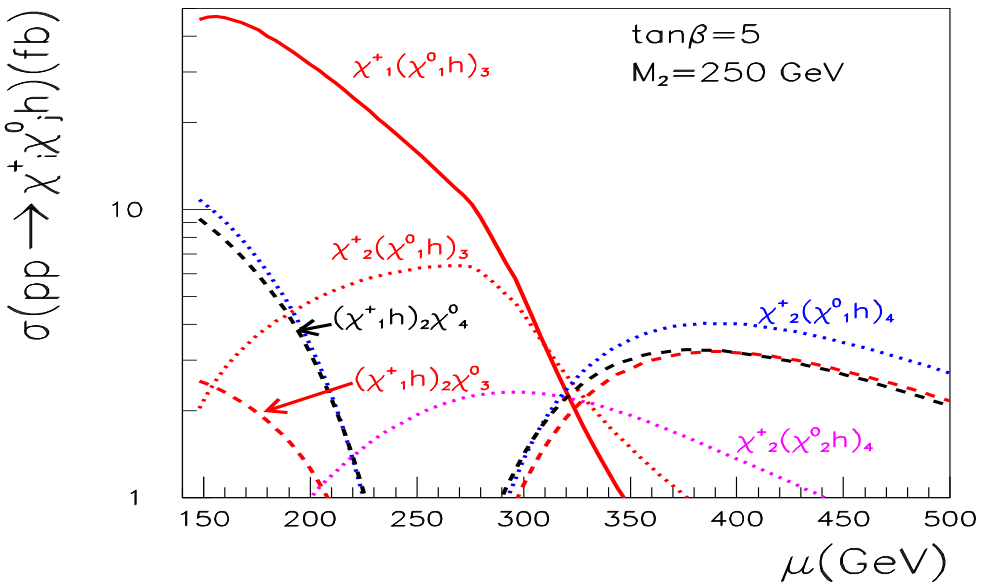

Figure 3.50: Higgs yield through charginos and neutralinos decays as a function of μ, $M_2 = 250$GeV, $\tan\beta = 5$, maximal mixing and $M_1 = M_2/10$. The subscript for the parentheses $(\quad)_j$ indicates the parent neutralino or chargino.

For smaller values of m_0, even the slepton signal will be large and observable. In this case even the $\tilde{\chi}_1^+\tilde{\chi}_1^-\gamma$ production cross-section will be appeciable. Thus not only can an LC see an 'invisible' Higgs easily, but it should be able to see the sparticles, thus testing whether SUSY is responsible for the nonobservation of the light Higgs at the LHC. Further, measurements of the invisible decay width at the LC, can provide useful pointers for the sfermion and neutralino/chargino phenomenology at the LHC. Implications for this scenario for lower masses of the Pseudoscalar Higgs have yet to be investigated fully.

3.5 A light Higgs in scenarios with extra dimensions

In this section we discuss the detectability of a light Higgs at the LHC, and the corresponding complementarity of a LC, for scenarios beyond the SM based on extra dimensions. Models with 3-branes in extra dimensions typically imply the existence of a radion, ϕ, that can mix with the Higgs, h, thereby modifying the Higgs properties and the prospects for its detectability at the LHC. The presence of the ϕ will affect the scope of the LHC searches. Detection of both the ϕ and the h might be possible. We report on a study on the complementarity of the observation of $gg \to h$, with $h \to \gamma\gamma$ or $h \to Z^0 Z^{0*} \to 4\,\ell$, and $gg \to \phi \to Z^0 Z^{0(*)} \to 4\,\ell$ at the LHC in the context of the Randall-Sundrum model. The potential for determining the nature of the detected scalar(s) at the LHC and at an e^+e^- linear collider is discussed, both separately and in combination. Also the virtues of measurements from a low energy photon collider are discussed.

3.5.1 On the complementarity of Higgs and radion searches at LHC and LC

3.5.1.1 Introduction

One particularly attractive extra-dimensional model is that proposed by Randall and Sundrum (RS) [264], in which there are two 3+1 dimensional branes separated in a 5th dimension. A central prediction of this theory is the existence of the radion, a graviscalar which corresponds to fluctuations in the size of the extra dimension. Detection and study of the radion will be central to the experimental probe of the RS and related scenarios with extra dimensions. There is already an extensive literature on the phenomenology of the radion, both in the absence of Higgs-radion mixing [265–269] and in the presence of such a mixing [270–276].

In this section we discuss the complementarity of the search for the Higgs boson and the radion at the LHC. As the Higgs-radion mixing may suppress the main discovery process $gg \to H \to \gamma\gamma$ for a light Higgs boson, we study the extent to which the appearance of a $gg \to \phi \to Z^0 Z^{0(*)} \to 4\,\ell$ signal ensures that LHC experiments will observe at least one of the two scalars over the full parameter phase space. The additional information, which could be extracted from a TeV-class e^+e^- linear collider (LC), is also considered. More details on the theoretical framework are given in [277]

3.5.1.2 Radion and Higgs Boson Search Complementarity

Here we address two issues. The first is whether there is a complementarity between the Higgs observability, mostly through $gg \to h \to \gamma\gamma$, and the $gg \to \phi \to Z^0 Z^{0(*)} \to 4\,\ell$ reaction, thus offering the LHC the discovery of at least one of the two particles over the full parameter space. The second, and related, issue,discussed in the next section, concerns the strategies available to understand the nature of the discovered particle.

The couplings of the h and ϕ to Z^0Z^0, W^+W^- and $f\overline{f}$ are given relative to those of the SM Higgs boson, denoted by H, by:

$$\frac{g_{hWW}}{g_{HWW}} = \frac{g_{hZZ}}{g_{HZZ}} = \frac{g_{hf\overline{f}}}{g_{Hf\overline{f}}} = d + \gamma b\,, \quad \frac{g_{\phi WW}}{g_{HWW}} = \frac{g_{\phi ZZ}}{g_{HZZ}} = \frac{g_{\phi f\overline{f}}}{g_{Hf\overline{f}}} = c + \gamma a\,. \tag{3.46}$$

with $\gamma \equiv v/\Lambda_\phi$ and $a, b, c, d,$ are functions of the mixing angle defined e.g. in [277]. Couplings of the h and ϕ to $\gamma\gamma$ and gg receive contributions not only from the usual loop diagrams but also from trace-anomaly couplings to $\gamma\gamma$ and gg. Thus, these couplings are not simply directly proportional to those of the SM H. Of course, in the limit of $\xi = 0$, the h has the same properties as the SM Higgs boson.

The effects of the mixing of the radion with the Higgs boson have been studied [276] by introducing the relevant terms in the HDECAY program [278], which computes the Higgs couplings, including higher order QCD corrections. Couplings and widths for the radion have also been implemented.

Results have been obtained by comparing the product of production and decay rates for the h and ϕ to those expected for a light SM H. The LHC sensitivity has been extracted by rescaling the results for Higgs observability, obtained assuming SM couplings. We define Higgs observability as a $> 5\ \sigma$ excess over the SM background

for the combination of the inclusive channels: $gg \to h \to \gamma\gamma$; $t\bar{t}h$, with $h \to b\bar{b}$ and $gg \to h \to Z^0 Z^{0(*)} \to 4\ell$, after rescaling the SM Higgs results. We define ϕ observability as a $> 5\,\sigma$ signal in the $gg \to \phi \to Z^0 Z^{0(*)} \to 4\ell$ channel only. We study the results as a function of four parameters: the Higgs mass M_h, the radion mass M_ϕ, the scale Λ_ϕ and the mixing parameter ξ.

Due to the suppression, from radion mixing, of the loop-induced effective couplings of the h (relative to the SM H) to gluon and photon pairs, the key process $gg \to h \to \gamma\gamma$ may fail to provide a significant excess over the $\gamma\gamma$ background at the LHC. Other modes that depend on the gg fusion production process are suppressed too. For $M_\phi > M_h$, this suppression is very substantial for large, negative values of ξ. This region of significant suppression becomes wider at large values of M_ϕ and Λ_ϕ. In contrast, for $M_\phi < M_h$, the $gg \to h \to \gamma\gamma$ rate is generally only suppressed when $\xi > 0$. All this is shown, in a quantitative way, by the contours in Figures 3.51, 3.52 and 3.53. In all these figures, the outermost, hourglass shaped contours define the theoretically

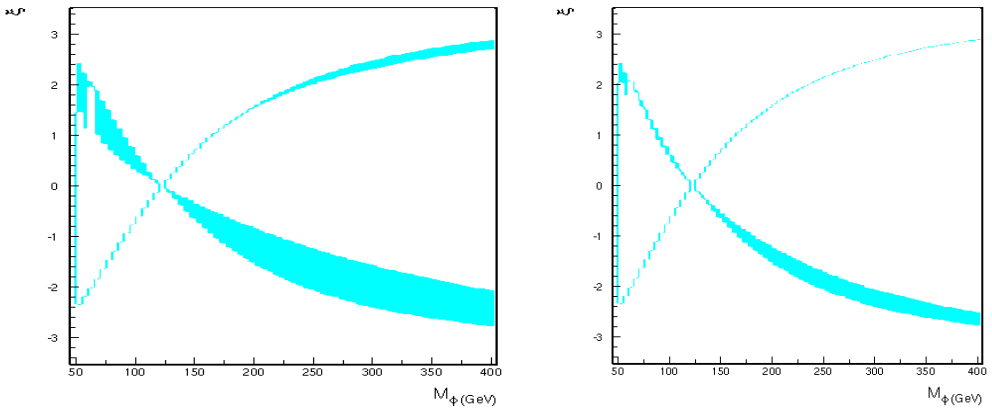

Figure 3.51: *Regions in (M_ϕ, ξ) parameter space of h non-detectability (including $gg \to h \to \gamma\gamma$ and other modes) at the LHC for one experiment and 30 fb^{-1} (left) and 100 fb^{-1} (right). We take $\Lambda_\phi = 5$ TeV and $M_h = 120$ GeV.*

allowed region. As shown in Figure 3.51, three main regions of non-detectability may appear. Two are located at large values of M_ϕ and $|\xi|$. A third region appears at low M_ϕ and positive ξ, where the above-noted $gg \to h \to \gamma\gamma$ suppression sets in. This latter region becomes further expanded when $2M_\phi < M_h$ and the decay channel $h \to \phi\phi$ opens up, thus reducing the $h \to \gamma\gamma$ branching ratio. Figure 3.52 shows how the regions of non-detectability shrink (expand) when $M_\phi < M_h$ ($M_\phi > M_h$) as Λ_ϕ increases. Figure 3.53 shows that the non-detectability regions shrink as M_h increases from 115 GeV to 180 GeV. The detectability is increasing as additional channels, in particular $gg \to h \to Z^0 Z^{0*} \to 4\,\ell$, become available for Higgs discovery. For large Higgs boson masses the region of non-detectability is reduced to a narrow strip along the lower ξ edge.

Figure 3.51 shows that the non-detectability regions are reduced by considering a larger data set. In particular, we see that an integrated luminosity of 100 fb^{-1} would remove the regions at large positive ξ in the $\Lambda_\phi = 5$ and 7.5 TeV plots of Figure 3.52. Similarly, including the qqh, $h \to WW^* \to \ell\ell\nu\overline{\nu}$ channel in the list of the discovery modes removes the same two regions and reduces the large region of h non-

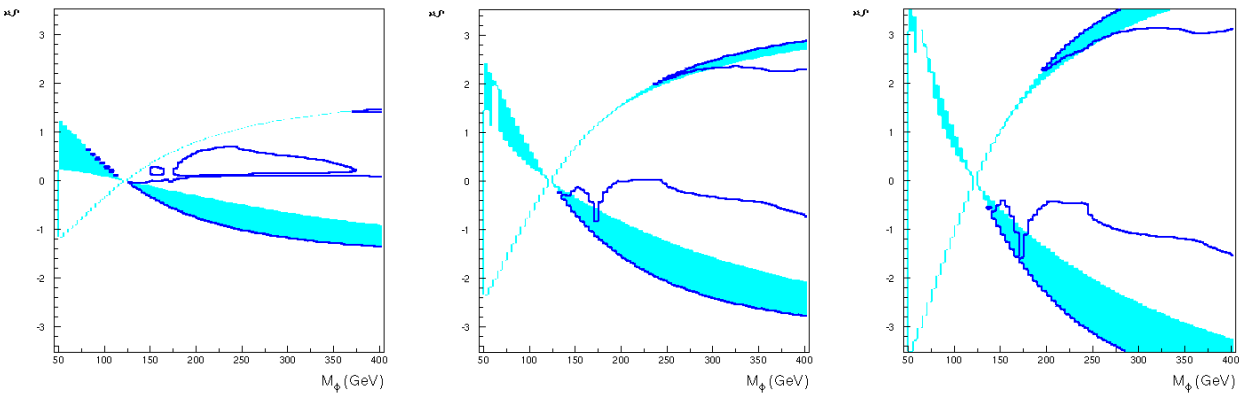

Figure 3.52: *Regions in (M_ϕ, ξ) parameter space of h detectability (including $gg \to h \to \gamma\gamma$ and other modes) and of $gg \to \phi \to Z^0 Z^{0(*)} \to 4\ \ell$ detectability at the LHC for one experiment and 30 fb^{-1}. The outermost, hourglass shaped contours define the theoretically allowed region. The light grey (cyan) regions show the part of the parameter space where the net h signal significance falls below $5\ \sigma$. The thick grey (blue) curves indicate the regions where the significance of the $gg \to \phi \to Z^0 Z^{0(*)} \to 4\ \ell$ signal exceeds $5\ \sigma$. Results are presented for M_h=120 GeV and Λ_ϕ= 2.5 TeV (left), 5.0 TeV (center) and 7.5 TeV (right).*

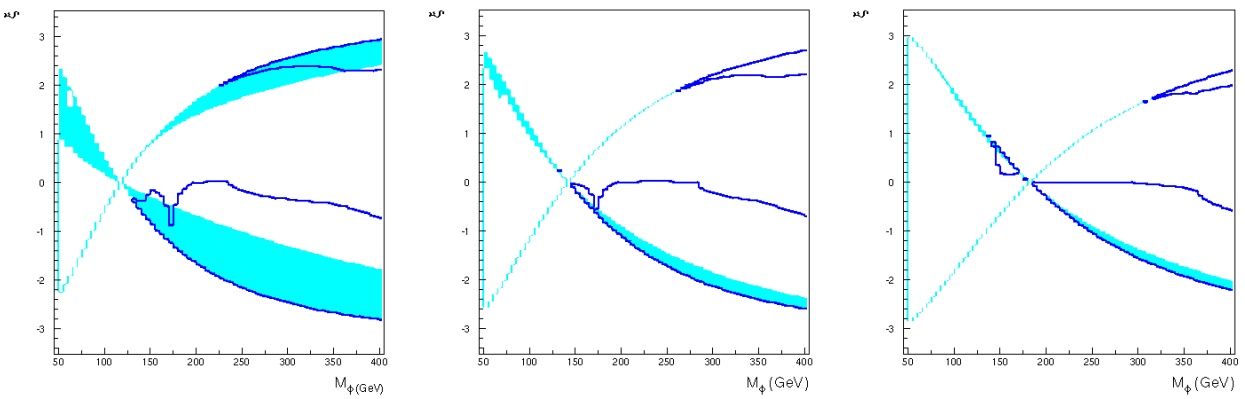

Figure 3.53: *Same as Figure 3.52 but for M_h = 115 GeV (left), M_h = 140 GeV (center) and M_h = 180 GeV (right). Λ_ϕ has been fixed to 5.0 TeV.*

observability at negative ξ values.

In all these regions, a complementarity is potentially offered by the process $gg \to \phi \to Z^0 Z^{0(*)} \to 4\ \ell$, which becomes important for $M_\phi > 140$ GeV. At the LHC, this process would have the same event structure as the golden SM Higgs mode $H \to Z^0 Z^{0*} \to 4\ \ell$, which has been thoroughly studied for an intermediate mass Higgs boson. By computing the $gg \to \phi \to Z^0 Z^{0(*)} \to 4\ \ell$ rate relative to that for the corresponding SM H process and employing the LHC sensitivity curve for $H \to Z^0 Z^{0(*)}$, the significance for the ϕ signal in the $4\ \ell$ final state at the LHC can be extracted. Results are overlayed on Figures 3.52 and 3.53, assuming 30 fb^{-1} of data.

Two observations are in order. The observability of ϕ production in the four lepton channel fills most of the gaps in (M_h, ξ) parameter space in which h detection is not

possible (mostly due to the suppression of the loop-induced $gg \to h \to \gamma\gamma$ process). The observation of at least one scalar is thus guaranteed over almost the full parameter space, with the following exceptions. (a) In the region of large positive ξ with $M_\phi < M_h$ the ϕ couplings are suddenly suppressed (as opposed to the $M_\phi > M_h$ side of the hourglass) making the $gg \to \phi$ production rate too small for ϕ observation in either the $\gamma\gamma$ or $Z^0Z^{0*} \to 4\ell$ final state. (The $Z^0Z^{0*} \to 4\ell$ mode is also phase space suppressed for smaller M_ϕ.) (b) There is a narrow region at $M_\phi \simeq 170$ GeV due to the ramp-up of the $\phi \to W^+W^-$ channel, where a luminosity of order 100 fb^{-1} is required to reach a $\geq 5\,\sigma$ signal for $\phi \to Z^0Z^{0*}$. We should also note that the $\phi \to Z^0Z^0$ decay is reduced for $M_\phi > 2M_h$ by the onset of the $\phi \to hh$ decay, which can become the main decay mode. The resulting $hh \to b\bar{b}b\bar{b}$ topology, with di-jet mass constraints, may represent a viable signal for the LHC in its own right, but detailed studies will be needed. Figures 3.52 and 3.53 also exhibit regions of (M_ϕ, ξ) parameter space in which *both* the h and ϕ mass eigenstates will be detectable. In these regions, the LHC will observe two scalar bosons somewhat separated in mass with the lighter (heavier) having a non-SM-like rate for the the gg-induced $\gamma\gamma$ (Z^0Z^0) final state. Additional information will be required to ascertain whether these two Higgs bosons derive from a multi-doublet or other type of extended Higgs sector or from the present type of model with Higgs-radion mixing.

An e^+e^- LC should guarantee observation of both the h and the ϕ even in most of the regions within which detection of either at the LHC might be difficult. Thus, this scenario provides an illustration of the complementarity between the two machines in the study of the Higgs sector. In particular, in the region with $M_\phi > M_h$ the hZ^0Z^0 coupling is enhanced relative to the SM HZ^0Z^0 coupling and h detection in e^+e^- collisions would be even easier than SM H detection. Further, assuming that e^+e^- collisions could also probe down to ϕZ^0Z^0 couplings of order $g^2_{\phi ZZ}/g^2_{HZZ} \simeq 0.01$, the left panel of Figure 3.55 shows that the ϕ would be seen in almost the entirety of the $M_\phi > M_h$ region, aside from a narrow cone near $\xi \sim 0$. In the $M_\phi < M_h$ region, the hZ^0Z^0 coupling is suppressed, but only by a modest amount; $e^+e^- \to Z^0h$ would be easily detected. As seen in Figure 3.55, detection of the ϕ in the $M_\phi < M_h$ part of parameter space will only be possible if ξ is near the edges of the hourglass region. This would include the large $\xi > 0$ region (a) defined above. In regions where both $e^+e^- \to Z^0h$ and $e^+e^- \to Z^0\phi$ can be seen the *four* measured quantities $g^2_{Z^0Z^0h}$, $g^2_{Z^0Z^0\phi}$, M_h and M_ϕ would significantly constrain the values of the ξ and Λ_ϕ parameters of the model, often leaving only a two-fold ambiguity in their determination.

3.5.1.3 Determining the Nature of the Observed Scalar

The interplay between the emergence of the Higgs boson and of the radion graviscalar signals opens up the question of the identification of the nature of the newly observed particle(s).

After observing a new scalar at the LHC, some of its properties will be measured with sufficient accuracy to determine if they correspond to those expected for the SM H, i.e. for the minimal realization of the Higgs sector [279, 280]. In the presence of extra dimensions, further scenarios emerge. For the present discussion, we consider two scenarios. The first has a light Higgs boson, for which we take M_h = 120 GeV, with couplings different from those predicted in the SM. The question here

is if the anomaly is due to an extended Higgs sector, such as in Supersymmetry, or rather to the mixing with an undetected radion. The second scenario consists of an intermediate-mass scalar, with 180 GeV $< M <$ 300 GeV, observed alone. An important issue would then be the question of whether the observed particle is the SM-like Higgs boson or a radion, with the Higgs particle left undetected. This scenario is quite likely at large negative ξ and large M_ϕ — see Figures 3.52 and 3.53.

In the first scenario, the issue is the interpretation of discrepancies in the measured Higgs couplings to gauge bosons and fermions. These effects increase with $|\xi|$, $1/\Lambda_\phi$ and M_h/M_ϕ. The LHC is expected to measure some ratios of these couplings [280]. In the case of the SM H, the ratio g_{HZZ}/g_{HWW} can be determined with a relative accuracy of 15% to 8% for 120 GeV $< M_H <$ 180 GeV, while the ratio $g_{H\tau\tau}/g_{HWW}$ and that of the effective coupling to photons, $g^{effective}_{H\gamma\gamma}/g_{HWW}$ can be determined to 6% to 10% for 120 GeV $< M_h <$ 150 GeV. Now, the Higgs-radion mixing would induce the same shifts in the direct couplings g_{hWW}, g_{hZZ} and $g_{h\overline{f}f}$, all being given by $d + \gamma b$ times the corresponding H couplings — see Eq. (3.46). Although this factor depends on the Λ_ϕ, M_ϕ and ξ parameters, ratios of couplings would remain unperturbed and correspond to those expected in the SM. Since the LHC measures mostly ratios of couplings, the presence of Higgs-radion mixing could easily be missed. One window of sensitivity to the mixing would be offered by the combination $g^{effective}_{h\gamma\gamma}/g_{hWW}$. But the mixing effects are expected to be limited to relative variation of $\pm 5\%$ w.r.t. the SM predictions. Hence, the LHC anticipated accuracy corresponds to deviations of one unit of σ, or less, except for a small region at $\Lambda_\phi \simeq 1$ TeV. Larger deviations are expected for the absolute rates [276], especially for the $gg \to h \to \gamma\gamma$ channel which can be dramatically enhanced or suppressed relative to the $gg \to H \to \gamma\gamma$ prediction for larger ξ values due to the large changes in the $gg \to h$ coupling relative to the $gg \to H$ coupling. Of course, to detect these deviations it is necessary to control systematic uncertainties for the absolute $\gamma\gamma$ rate. All the above remarks would also apply to distinguishing between the light Higgs of supersymmetry, which would be SM-like assuming an approximate decoupling limit, and the h of the Higgs-radion scenario. In a non-decoupling two-doublet model, the light Higgs couplings to up-type and down-type fermions can be modified differently with respect to those of the SM H, and LHC measurements of coupling ratios would detect this difference.

A TeV-class LC has the capability of measuring the *absolute* coupling strengths to all fermions separately. For the SM H, accuracies of order 1%-5% for the couplings are achieved. Further, a determination of the total H width to 4% - 6% accuracy is possible. These capabilities are important for the scenario we propose since there would be enough measurements and sufficient accuracy to detect Higgs-radion mixing for moderate to large ξ values [281]. This is shown in Figure 3.54 by the additional contours, which indicate the regions where the discrepancy with the SM predictions for the Higgs couplings to pairs of b quarks and W bosons exceeds 2.5 σ.

It is worth emphasizing that one of the basic predictions of the model is that the W^+W^-, Z^0Z^0 and $f\overline{f}$ couplings of the h should all be changed by exactly the same factor. The above discussion shows that it will be possible to check this at a basic level at the LHC (in that ratios of branching ratios should be the same as in the SM) and with some precision at the LC.

We note that the *combination* of the direct observation of $\phi \to Z^0Z^{0*}$ at the LHC and the precision measurements of the Higgs properties at a e^+e^- LC will extend

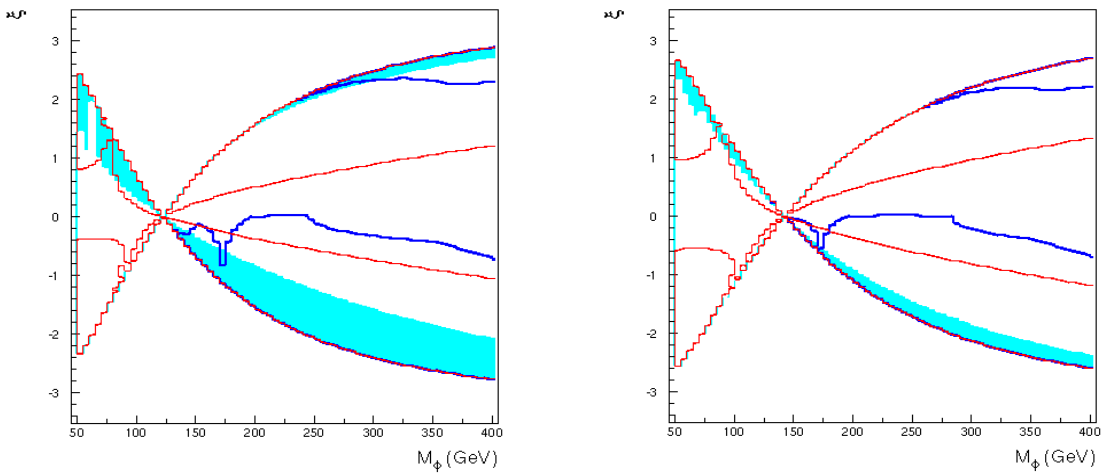

Figure 3.54: *Same as Figures 3.52 and 3.53 for M_h = 120 GeV (left), 140 GeV (right) and Λ_ϕ = 5 TeV with added contours, indicated by the medium grey (red) curves, showing the regions where the LC measurements of the h couplings to $b\bar{b}$ and W^+W^- would provide a $> 2.5\ \sigma$ evidence for the radion mixing effect.*

our ability to distinguish between the Higgs-radion mixing scenario and the SM H scenario to a large portion of the regions where at the LHC only the h or only the ϕ is detected and determining that the observed boson is not the SM H is difficult. Finally, we reemphasize the fact that h will be detected in $e^+e^- \to Z^0h$ throughout the entire (M_ϕ, ξ) parameter space and that $e^+e^- \to Z^0\phi$ can be detected in all but the region exemplified, for $M_h = 120$ GeV and $\Lambda_\phi = 5$ TeV, in the left panel of Figure 3.55. This, in particular, guarantees the observability of the ϕ in the low M_ϕ, large $\xi > 0$ region that is most difficult for the LHC.

If, at the LHC, an intermediate mass scalar is observed alone, its non-SM-like nature can, in some cases, be determined through measurement of its production yield and its couplings. In particular, in the region at large, negative ξ values where ϕ production is visible whereas h production is not, the yield of $Z^0Z^0 \to 4\ \ell$ from ϕ decay can differ by a factor of 2 or more from that expected for a SM H (depending upon the value of M_ϕ — see Figure 13 of Ref. [276]). For $M_\phi < 2\ M_h$ the deviations arise from the substantial differences between the $gg \to \phi$ coupling and the $gg \to H$ coupling. For $M_\phi > 2M_h$, this rate is also sensitive to $\mathrm{B}R(\phi \to hh)$. Defining $R \equiv \mathrm{B}R(\phi \to Z^0Z^{0(*)})/\mathrm{B}R(H \to Z^0Z^{0(*)})$, one finds $R > 0.9$ for $M_\phi < 2M_h$. Such a small deviation would not have a big impact compared to the possibly large deviations of $gg \to h/gg \to H$ relative to unity. However, past the threshold for $\phi \to hh$ decays, the Z^0Z^0 branching fraction is significantly affected; for example, $R < 0.7$ for a substantial portion of the $|\xi| < 1.5$ part of the $M_\phi > 2M_h$ region when $M_h = 120$ GeV and $\Lambda_\phi = 5$ TeV. The combination of a reduced $Z^0Z^0 \to 4\ \ell$ rate and the possibility to observe $\phi \to hh$ decays, ensures that the LHC could positively identify the existence of the radion in the region $M_\phi > 2M_h$, $\xi\widetilde{\chi}_0^0$.

Finally, we should note that the distinctive signature of KK graviton excitation production at the LHC [266, 268] will be easily observed for a substantial range of Λ_ϕ.

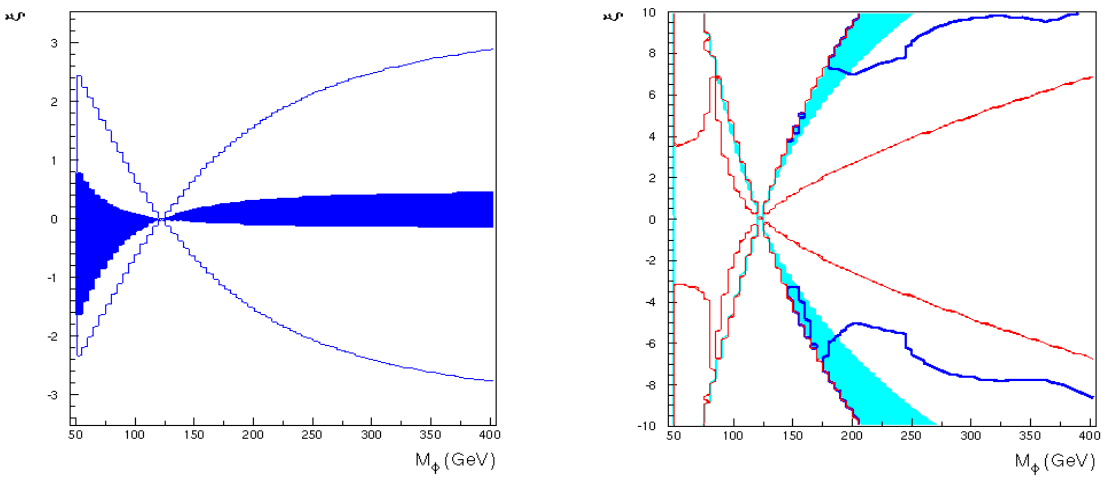

Figure 3.55: *Left: Contour in* (M_ϕ, ξ) *parameter space with* $g^2_{\phi ZZ}/g^2_{HZZ} < 0.01$ *indicated by the dark region, for* M_h *= 120 GeV and* $\Lambda_\phi = 5$ *TeV. Right: Same as Figure 3.54, for* M_h *= 120 GeV and* Λ_ϕ*=30 TeV.*

This will not only serve as a warning to look for a possibly mixed Higgs-radion sector but will also allow us to determine Λ_ϕ from the measurements of m_1 and m_0/M_{Pl}. Note that m_1, the mass of the first KK graviton excitation, given by

$$m_1 = x_1 \frac{m_0}{M_{Pl}} \frac{\Lambda_\phi}{\sqrt{6}} \tag{3.47}$$

where m_0 is the curvature parameter and x_1 is the first zero of the Bessel function J_1 ($x_1 \sim 3.8$). m_0/M_{Pl} can be determined from the KK excitation profile. The 95% CL limit for detecting the first KK excitation, with an integrated luminosity of 100 fb^{-1}, is given in terms of m_0/M_{Pl} by $m_1(\mathrm{TeV}) = 6.6 + 2\ln_{10}\left(\frac{m_0}{M_{Pl}}\right)$ [266]. Using Eq. (3.47), we find that the signal for the first KK excitation will be below the 95% CL for $\Lambda_\phi > \frac{\sqrt{6}}{x_1}\left(\frac{M_{Pl}}{m_0}\right)\left[6.6 + 2\ln_{10}\left(\frac{m_0}{M_{Pl}}\right)\right]$ TeV. For example, for $m_0/M_{Pl} = 0.1$ this corresponds to $\Lambda_\phi \geq 30$ TeV, which is also consistent with precision electroweak constraints [282]. In this case, the Higgs-radion sector becomes absolutely crucial for revealing the RS scenario. This is illustrated in the right panel of Figure 3.55 where we show that Higgs-radion phenomenology can be explored at the LHC for a large section of parameter space when $\Lambda_\phi = 30$ TeV.

3.5.2 Radions at a photon collider

In this section, we demonstrate the important complementarity of a photon collider (PC) for probing the Higgs-radion sector of the Randall-Sundrum (RS) model [264]. In [283] a SM Higgs boson with $m_H = 115$ GeV was examined. After the cuts, one obtains per year about $S = 3280$ and $B = 1660$ in the $\gamma\gamma \to H \to b\bar{b}$ channel, corresponding to $S/\sqrt{B} \sim 80$!

We will assume that these numbers do not change significantly for a Higgs mass of 120 GeV. After mixing, the S rate for the h will be rescaled relative to that for the the SM H. Of course, B will not change. The rescaling is shown in Fig. 3.56. The S for the ϕ can also be obtained by rescaling if $M_\phi \sim 115$ GeV. For $M_\phi < 120$ GeV, the $\phi \to b\bar{b}$ channel will continue to be the most relevant for ϕ discovery, but studies have not yet been performed to obtain the S and B rates for low masses.

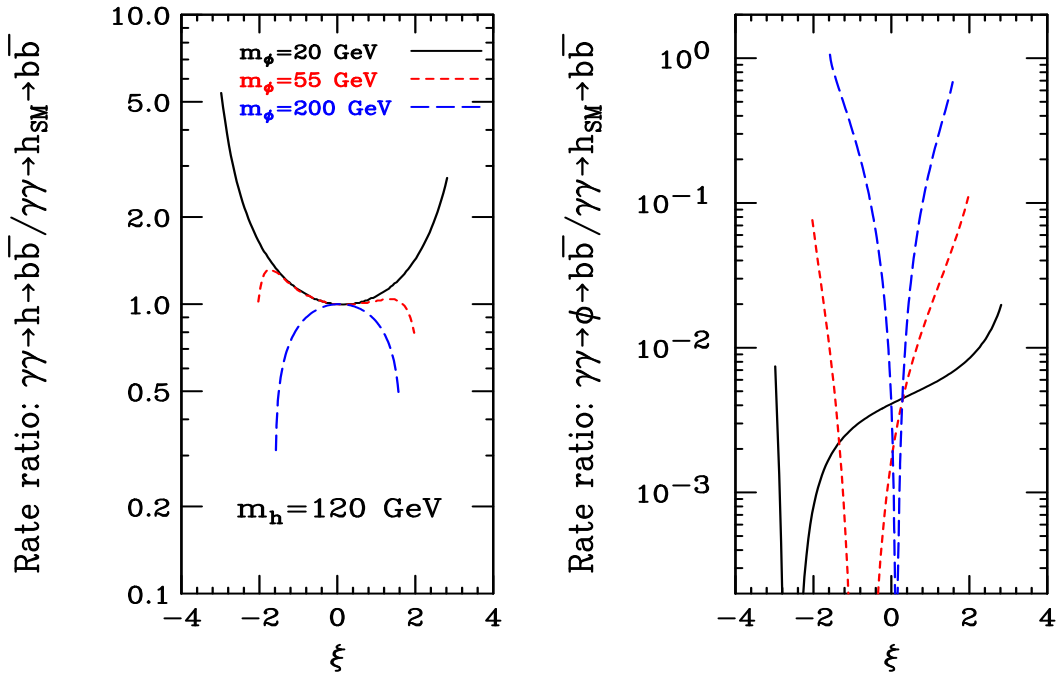

Figure 3.56: The rates for $\gamma\gamma \to h \to b\bar{b}$ and $\gamma\gamma \to \phi \to b\bar{b}$ relative to the corresponding rate for a SM Higgs boson of the same mass. Results are shown for $m_h = 120$ GeV and $\Lambda_\phi = 5$ TeV as functions of ξ for $M_\phi = 20$, 55 and 200 GeV.

Observe that for $M_\phi < m_H$ we have either little change or enhancement, whereas significant suppression of the $gg \to H \to \gamma\gamma$ rate was possible in this case for positive ξ. Also note that for $M_\phi > m_H$ and large $\xi < 0$ (where the LHC signal for the h is marginal) there is much less suppression of $\gamma\gamma \to H \to b\bar{b}$ than for $gg \to H \to \gamma\gamma$ — at most a factor of 2 vs a factor of 8 (at $M_\phi = 200$ GeV). This is no problem for the PC since $S/\sqrt{B} \sim \frac{1}{2}80 \sim 40$ is still a very strong signal. In fact, we can afford a reduction by a factor of 16 before we hit the 5σ level! Thus, *the $\gamma\gamma$ collider will allow h discovery (for $m_H = 120$) throughout the entire hourglass shown in Fig. 3.51*, which is something the LHC cannot absolutely do.

Using the factor of 16 mentioned above it is apparent that the ϕ with $M_\phi < 120$ GeV is very likely to elude discovery at the $\gamma\gamma$ collider. (Recall that it also eludes discovery at the LHC for this region.) The only exceptions to this statement occur at the very largest $|\xi|$ values for $M_\phi \geq 55$ GeV where $S_\phi > S_H/16$.

Of course, we need to have signal and background results after cuts for these lower masses to know if the factor of 16 is actually the correct factor to use. To get the best signal to background ratio we would want to lower the machine energy and readjust cuts and so forth. This study should be done. For the $M_\phi > m_H$ region, we will need

results for the WW and ZZ modes that are under study.

Overall, the PC is more than competitive with the LHC for h discovery. In particular, the PC can see the h where the LHC signal will be marginal (i.e. at the largest theoretically allowed ξ values). Of course, the marginal LHC regions are not very big for full L. Perhaps even more interesting is the fact that there is a big part of the hourglass where the h will be seen at both colliders. When the LHC achieves $L > 100$ fb^{-1}, this comprises most of the hourglass, shown in 3.51. Simultaneous observation of the h at the two different colliders will greatly increase our knowledge about the h since the two rates measure different things. The LHC rate in the $\gamma\gamma$ final state measures $\Gamma(h \to gg)\Gamma(h \to \gamma\gamma)/\Gamma^h_{\rm tot}$ while the PC rate in the $b\bar{b}$ final state determines $\Gamma(h \to \gamma\gamma)\Gamma(h \to b\bar{b})/\Gamma^h_{\rm tot}$. Consequently, the ratio of the rates gives us $\frac{\Gamma(H\to gg)}{\Gamma(H\to b\bar{b})}$, in terms of which we may compute

$$R_{hgg} \equiv \left[\frac{\Gamma(H \to gg)}{\Gamma(H \to b\bar{b})}\right]\left[\frac{\Gamma(H \to gg)}{\Gamma(H \to b\bar{b})}\right]^{-1}_{SM}. \tag{3.48}$$

This is a *very* interesting number since it directly probes for the presence of the anomalous ggh coupling. In particular, $R_{hgg} = 1$ if the only contributions to $\Gamma(H \to gg)$ come from quark loops and all quark couplings scale in the same way. A plot of R_{hgg} as a function of ξ for $M_H = 120$ GeV, $\Lambda_\phi = 5$ TeV and $M_\phi = 20$, 55 and 200 GeV appears in Fig. 3.57.

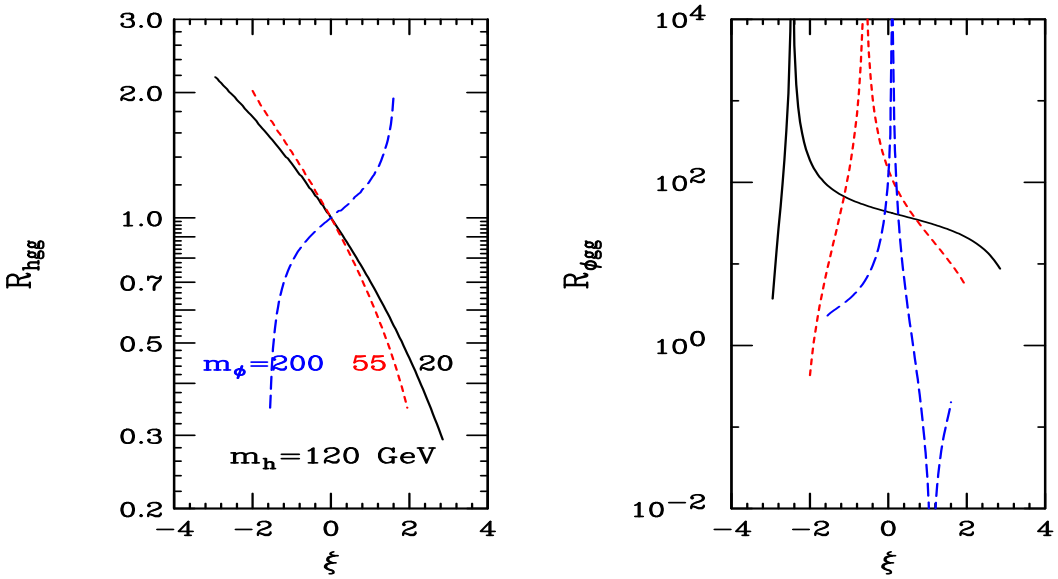

Figure 3.57: *We plot the ratios R_{Hgg} and $R_{\phi gg}$ of the Hgg and ϕgg couplings-squared including the anomalous contribution to the corresponding values expected in its absence. Results are shown for $m_h = 120$ GeV and $\Lambda_\phi = 5$ TeV as functions of ξ for $M_\phi = 20$, 55 and 200 GeV. (The same type of line is used for a given M_ϕ in the right-hand figure as is used in the left-hand figure.)*

We can estimate the accuracy with which R_{hgg} can be measured as follows. Assuming the maximal reduction of 1/2 for the signal rate (S) rescaling at the $\gamma\gamma$ CLIC collider, we find that $\Gamma(H \to \gamma\gamma)\Gamma(H \to b\bar{b})/\Gamma^h_{tot}$ can be measured with an accuracy of about $\sqrt{S+B}/S \sim \sqrt{3200}/1600 \sim 0.035$. The dominant error will then be from the

LHC which will typically measure $\Gamma(H \to gg)\Gamma(H \to \gamma\gamma)/\Gamma^h_{tot}$ with an accuracy of between 0.1 and 0.2 (depending on parameter choices and available L). From Fig. 3.57, we see that 0.2 fractional accuracy will reveal deviations of R_{hgg} from 1 for all but the smallest ξ values. The ability to measure R_{hgg} with good accuracy may be the strongest reason in the Higgs context for having the PC as well as the LHC. Almost all non-SM Higgs theories predict $R_{hgg} \neq 1$ for one reason another, unless one is in the decoupling limit.

Depending on L at the LHC, there might be a small part of the hourglass (large $|\xi|$ with $M_\phi > m_H$) where *only* the ϕ will be seen at the LHC and the h will only be seen at the PC. This is a nice example of complementarity between the two machines. By having both machines we maximize the chance of seeing both the h and ϕ.

As regards the ϕ, we have already noted from Fig. 3.56 that the $b\overline{b}$ final state rate (relevant for the $M_\phi = 20$ and 55 GeV cases) will only be detectable in the latter case (more generally for 55 GeV$< M_\phi < 2m_W$), and then only if $|\xi|$ is as large as theoretically allowed. If $\gamma\gamma \to \phi \to b\overline{b}$ can be observed, Fig. 3.57 shows that a large deviation for $R_{\phi gg}$ relative to the value predicted for a SM H of the same mass is typical (but not guaranteed). For $M_\phi > 2m_W$, $\mathrm{B}R(\phi \to b\overline{b})$ will be very small and detection of $\gamma\gamma \to \phi \to b\overline{b}$ will not be possible. We are currently studying $\gamma\gamma \to \phi \to WW, ZZ$ final states in order to assess possibilities at larger M_ϕ.

Overall, there is a strong case for the PC in the RS model context, especially if a Higgs boson is seen at the LHC that has non-SM-like rates and other properties.

3.5.3 Further scenarios

3.5.3.1 Beyond Higgs-radion mixing

Motivations for going beyond the simple RS model are easily found. The one that will most obviously have an influence on Higgs-radion mixing physics is the fact that in the strict RS model the radion is massless, which is to say that the distance between the branes is not stable. The above studies simply introduce a mass for the radion by hand. Several explicit mechanisms for giving mass to the radion have been discussed. One example is the Goldberger-Wise mechanism [288] that relies on introducing an additional scalar field that propagates in the bulk. However, in the approach of [288] the scalar field potential employed does not yield an exact solution to the Einstein equations. The result is brane curvature, which might impact Higgs phenomenology. Possible impacts have not been worked out.

In a more recent approach [289], the additional scalar field is introduced in the bulk with a vacuum profile chosen so that the RS metric (with no curvature) is an exact solution of the Einstein equations while at the same time the radion becomes massive. However, there are inevitable consequences for the Higgs sector. One finds that the quantum fluctuations of this additional bulk scalar field (which include the full tower of KK excitation fluctuations) will all mix with the Higgs and radion. The phenomenology of the extended Higgs-radion-KK excitation mixing matrix has not been worked out. But, it is sure to lead to additional freedom in the phenomenology of the Higgs-radion sector that could possibly pose further challenges for experimental study and an even greater need for having both the LHC and LC available for this study.

3.5.3.2 Universal extra dimension models

In the universal extra dimension models, all particles propagate in the extra dimension(s). There has been relatively little discussion of impacts on Higgs physics in the context of these models. Perhaps the most important observation made to date is that the Higgs mass can be quite large without conflicting with precision electroweak constraints if the extra dimension is as large as allowed by other constraints [290]. If the Higgs mass is near the upper limit of about 800 GeV, only the LHC will be able to detect it if the LC energy is restricted to $\sqrt{s} \lesssim 1$ TeV.

Contributions of various KK excitation modes to one-loop induced Higgs couplings (e.g. the $h\gamma\gamma$ coupling) will generally be measurable [291]. The complexity of understanding how to relate precision Higgs measurements to the full KK structure will surely require both the LHC and the LC — probably the LHC will be needed to probe the KK excitations while the LC will most clearly reveal deviations from SM expectations for the couplings most strongly influenced by the KK modes.

3.5.4 Conclusions

In summary, for almost the entire region of the parameter phase space where the suppression of the Higgs signal yield causes the overall signal significance at the LHC to drop below 5 σ, the radion eigenstate ϕ can be observed in the $gg \to \phi \to Z^0 Z^{0(*)} \to 4\,\ell$ process instead. An e^+e^- linear collider or a low energy PC linear collider would effectively complement the LHC both for the Higgs observability, including the most difficult region at low M_ϕ and positive ξ values, and for the detection of the radion mixing effects, through the precision measurements of the Higgs particle couplings to various types of particle pairs.

Finally, we note that the Higgs-radion sector is not the only means for probing the Randall-Sundrum type of model. The scenarios considered here will also yield the distinctive signature of KK graviton excitation production at the LHC [268]. This easily observed signal will serve as a warning to look for a possibly mixed Higgs-radion sector and allow to fix Λ_ϕ.

3.6 Phenomenology of the Littlest Higgs model

The Standard Model (SM) of the strong and electroweak interactions has passed stringent tests up to the highest energies accessible today. The precision electroweak data [292] point to the existence of a light Higgs boson in the SM, with mass $m_H \lesssim 200$ GeV. The Standard Model with such a light Higgs boson can be viewed as an effective theory valid up to a much higher energy scale Λ, possibly all the way up to the Planck scale. In particular, the precision electroweak data exclude the presence of dimension-six operators arising from strongly coupled new physics below a scale Λ of order 10 TeV [293]; if new physics is to appear below this scale, it must be weakly coupled. However, without protection by a symmetry, the Higgs mass is quadratically sensitive to the cutoff scale Λ via quantum corrections, rendering the theory with $m_H \ll \Lambda$ rather unnatural. For example, for $\Lambda = 10$ TeV, the "bare" Higgs mass-squared parameter must be tuned against the quadratically divergent radiative corrections at the

1% level. This gap between the electroweak scale m_H and the cutoff scale Λ is called the "little hierarchy".

Little Higgs models [294–301] revive an old idea to keep the Higgs boson naturally light: they make the Higgs particle a pseudo-Nambu-Goldstone boson [302] of a broken global symmetry. The new ingredient of little Higgs models is that they are constructed in such a way that at least two interactions are needed to explicitly break all of the global symmetry that protects the Higgs mass. This forbids quadratic divergences in the Higgs mass at one-loop; the Higgs mass is then smaller than the cutoff scale Λ by *two* loop factors, making the cutoff scale $\Lambda \sim 10$ TeV natural and solving the little hierarchy problem.

From the bottom-up point of view, in little Higgs models the most important quadratic divergences in the Higgs mass due to the top quark, gauge boson, and Higgs boson loops are canceled by loops of new weakly-coupled fermions, gauge bosons, and scalars with masses around a TeV. In contrast to supersymmetry, the cancellations in little Higgs models occur between loops of particles with the *same* statistics. Electroweak symmetry breaking is triggered by a Coleman-Weinberg [303] potential, generated by integrating out the heavy degrees of freedom, which also gives the Higgs boson a mass at the electroweak scale.

The "Littlest Higgs" model [296], which we focus on here, is a minimal model of this type. It consists of a nonlinear sigma model with a global SU(5) symmetry which is broken down to SO(5) by a vacuum condensate $f \sim \Lambda/4\pi \sim$ TeV. The gauged subgroup [SU(2)×U(1)]^2 is broken at the same time to its diagonal subgroup SU(2)×U(1), identified as the SM electroweak gauge group. The breaking of the global symmetry leads to 14 Goldstone bosons, four of which are eaten by the broken gauge generators, leading to four massive vector bosons: an SU(2) triplet Z_H, $W_H^\pm$, and a U(1) boson A_H. The ten remaining uneaten Goldstone bosons transform under the SM gauge group as a doublet h (which becomes the SM Higgs doublet) and a triplet ϕ (which gets a mass of order f). A vector-like pair of colored Weyl fermions is also needed to cancel the divergence from the top quark loop, leading to a new heavy vector-like quark with charge $+2/3$.

The particle content and interactions are laid out in detail in Ref. [304]. Here we summarize the features important for the collider phenomenology. The Littlest Higgs model contains six new free parameters, which can be chosen as follows:

1) $\tan\theta = s/c = g_1/g_2$, where $g_{1,2}$ are the couplings of the two SU(2) gauge groups, with $g^{-2} = g_1^{-2} + g_2^{-2}$.

2) $\tan\theta' = s'/c' = g'_1/g'_2$, where $g'_{1,2}$ are the couplings of the two U(1) gauge groups, with $g'^{-2} = g_1'^{-2} + g_2'^{-2}$.

3) f, the symmetry breaking scale, $\mathcal{O}$(TeV).

4) v', the vacuum expectation value (vev) of the triplet ϕ; $v' < v^2/4f$.

5) M_H, the SM-like Higgs boson mass.

6) M_T, the top-partner mass (together with m_t and f, this fixes the top-partner couplings up to a two-fold ambiguity).

In what follows we describe the prospects for little Higgs studies at the LHC and the LC. This summary is based on Refs. [304, 305].

3.6.1 The Little Higgs at the LHC

3.6.1.1 Z_H and W_H

The heavy SU(2) gauge bosons Z_H and W_H can be produced via Drell-Yan at the LHC (and at the Tevatron, if they are light enough). In the Littlest Higgs model, the SU(2) fermion doublets are chosen to transform under the $SU(2)_1$ gauge group; their couplings to Z_H and W_H are therefore proportional to $\cot\theta$, leading to a Drell-Yan cross section proportional to $\cot^2\theta$. In Fig. 3.58(a) we show the cross section for Z_H production at the Tevatron and LHC for $\cot\theta = 1$. In the region of small $\cot\theta \simeq 0.2$,

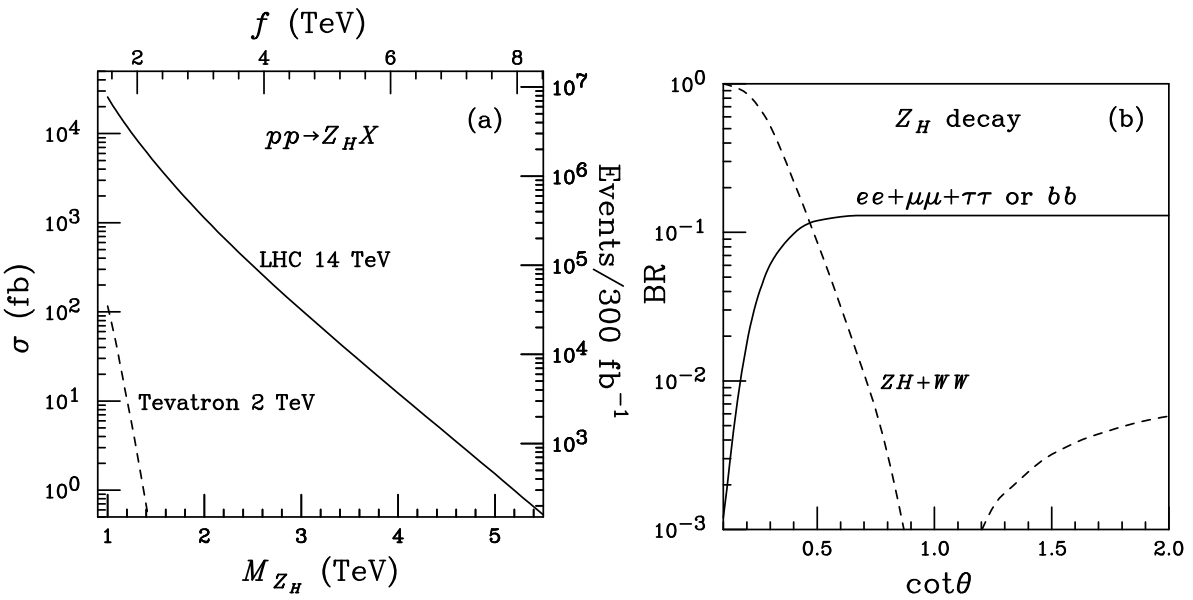

Figure 3.58: (a) Cross section for Z_H production in Drell-Yan at the LHC and Tevatron, for $\cot\theta = 1$. From Ref. [304]. (b) Branching ratios of Z_H into SM particles as a function of $\cot\theta$, neglecting final-state mass effects.

which is favored [306] by the precision electroweak data, the cross section shown in Fig. 3.58(a) must be scaled down by $\cot^2\theta \simeq 0.04$. Even with this suppression factor, a cross section of 40 fb is expected at the LHC for $M_{Z_H} \simeq 2$ TeV, leading to 4,000 events in 100 fb^{-1} of data. The production and decay of Z_H and W_H at the LHC has also been studied in Ref. [307].

The decay branching fractions of Z_H are shown in Fig. 3.58(b). The decays to fermion pairs follow an equipartition among the left-handed fermion doublets. Neglecting final-state particle masses, the branching fraction into three flavors of charged leptons is equal to that into one flavor of quark ($\simeq 1/8$ for $\cot\theta \gtrsim 0.5$), due to the equal coupling of Z_H to all SU(2) fermion doublets. The partial widths to fermion pairs are proportional to $\cot^2\theta$. The Z_H also decays into ZH and W^+W^- with equal partial widths (again neglecting final-state mass effects). These decays come from the coupling of Z_H to the components of the Higgs doublet h, applying the Goldstone boson equivalence theorem for the Goldstone modes eaten by the Z and W bosons. The partial widths to ZH and W^+W^- are proportional to $\cot^2 2\theta$. The total width of Z_H depends on $\cot\theta$; for $\cot\theta \sim 0.2$ the Z_H width is about 1% of the Z_H mass.

The different dependence of the bosonic and fermionic Z_H decay modes on $\cot\theta$ offers a method to distinguish the Littlest Higgs model from a "big Higgs" model with the same gauge group in which the Higgs doublet transforms under only one of the SU(2) groups [307], in which case the ZH and W^+W^- partial widths would also be proportional to $\cot^2\theta$.

The $W_H^\pm$ couplings to fermion doublets are larger by a factor of $\sqrt{2}$ than the Z_H couplings; this together with the parton distribution of the proton leads to a $W_H^\pm$ cross section at the LHC about 1.5 times that of Z_H [307]. As for the W_H decays, the branching fraction into three lepton flavors is equal to that into one generation of quarks ($\simeq 1/4$ for $\cot\theta \gtrsim 0.5$). At low $\cot\theta$, $W_H^\pm$ decays predominantly into $W^\pm H$ and $W^\pm Z$ with partial widths proportional to $\cot^2 2\theta$.

The general features of the production and decay of Z_H and W_H should extend to other little Higgs models in which the SM SU(2) gauge group comes from the diagonal breaking of two SU(2) groups; this is true, e.g., for the model in Ref. [297]. The decays to ZH, WH will however be modified in this model since it contains two Higgs doublets.

3.6.1.2 A_H

The heavy U(1) gauge boson is the lightest new particle in the Littlest Higgs model. Its couplings to fermions are more model dependent than those of the heavy SU(2) gauge bosons, since they depend on the U(1) charges of the fermions (see Ref. [304] for details). Even the presence of A_H is somewhat model-dependent, since one can remove this particle from the Littlest Higgs model by gauging only one U(1) group (hypercharge) without adding a significant amount of fine-tuning [306]. Nevertheless, we show in Fig. 3.59 the cross section and branching ratios of A_H for the simplest anomaly-free choice of fermion U(1) charges given in Ref. [304].

3.6.1.3 T

The heavy top-partner T can be pair produced via QCD interactions with a cross section that depends only on the T mass. However, this production mode is suppressed by phase space due to the typically high mass of the T. The single T production mode, $W^+b \to T$, is dominant at the LHC for M_T above about a TeV. The cross section for single T production depends on the W^+bT coupling, which in turn depends on the amount of mixing between T and the left-handed top quark. This coupling is fixed in terms of M_T and f, up to a two-fold ambiguity for M_T/f above its minimum value of $2m_t/v$. The cross sections are shown in Fig. 3.60. The top-partner T decays into tH, tZ and bW with branching fractions of 1/4, 1/4, and 1/2, respectively. These decays come from the coupling of T to the Higgs doublet h and the 3rd generation quark doublet, applying the Goldstone boson equivalence theorem for the Goldstone modes eaten by the Z and W bosons.

The structure of the top sector in many of the other little Higgs models in the literature is quite similar to the Littlest Higgs model, so these general features of T production and decay should carry over. Some models contain more than one top-partner [297–299, 301, 310], or contain partners for the two light generations of fermions as well [298, 300]; in these cases the phenomenology will be modified.

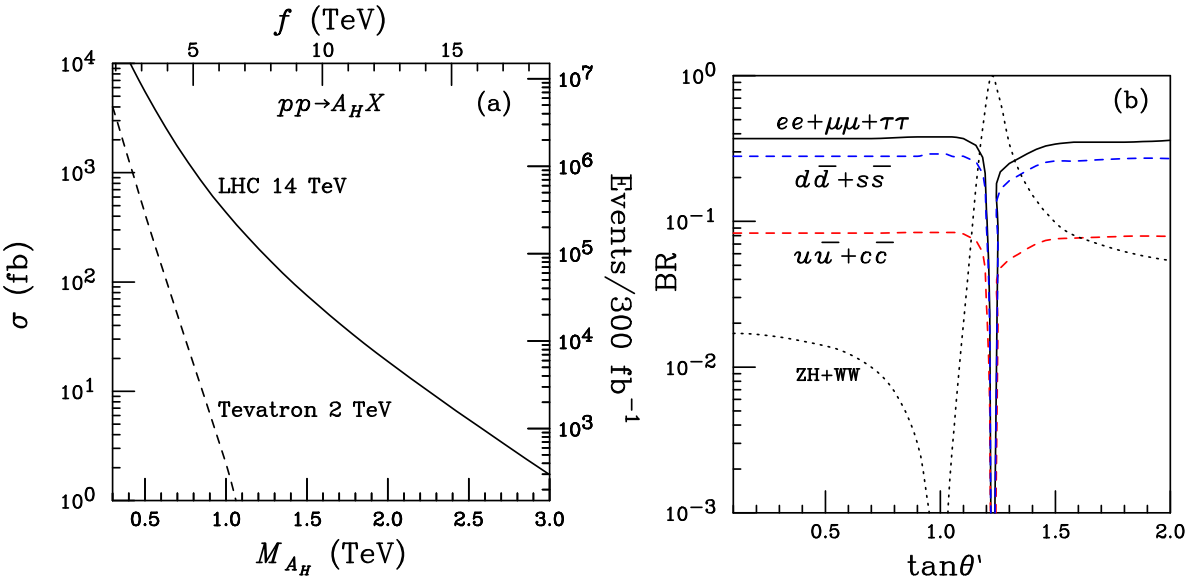

Figure 3.59: (a) Cross section for A_H production in Drell-Yan at the LHC and Tevatron, for $\cot\theta' = 1$. From Ref. [304]. (b) Branching ratios of A_H into fermions and $ZH + WW$ as a function of $\tan\theta'$, neglecting final-state mass effects.

3.6.1.4 Φ^{++}

The doubly charged component Φ^{++} of the Higgs triplet can be singly produced through the resonant process $W^+W^+ \to \Phi^{++} \to W^+W^+$. The cross section for this process is proportional to the square of the triplet vev v', which must be quite small in the Littlest Higgs model: $v' < v^2/4f$. This may make resonant Φ^{++} production difficult to see due to lack of rate. The doubly charged Higgs boson could also be found via pair production from photon or Z exchange, if it is not too heavy. The doubly charged Higgs boson can in principle decay to a pair of like-sign charged leptons via the dimension-four operator $L\Phi L$, offering a more distinctive signature than the decay into a pair of like-sign W bosons; however, the coupling is highly model dependent and care must be taken to avoid generating too large a neutrino mass from the triplet vev.

3.6.2 The Little Higgs at a Linear Collider

3.6.2.1 Electroweak precision measurements

The Littlest Higgs model introduces corrections to the precision electroweak observables, which have been studied in Refs. [306, 308, 309]. These corrections lead to constraints on the model parameter space and a lower bound on the scale f from existing electroweak data. The constraints come from Z pole data from LEP and SLD, low-energy neutrino-nucleon scattering, atomic parity violation, and the W boson mass measurement from LEP-II and the Tevatron. Together, these measurements probe contributions from the exchange of virtual heavy gauge bosons between fermion pairs, the mixing of the heavy SU(2) and U(1) gauge bosons with the Z boson that modifies the Z couplings to fermions, and a shift in the ratio of the masses of the W

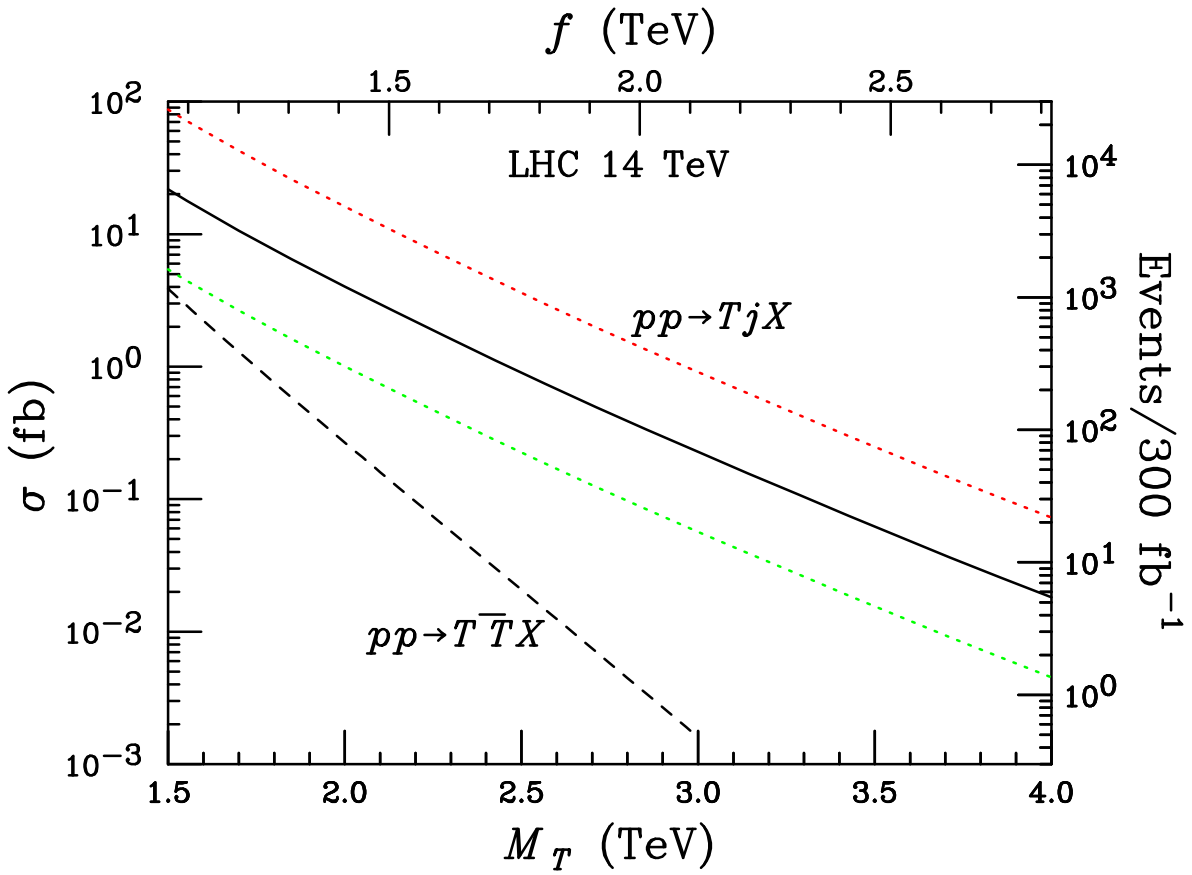

Figure 3.60: Cross sections for T production at the LHC. The single-T cross section is shown for $M_T/f = 2m_t/v$ (solid line) and $M_T/f = 2.5m_t/v$ (dotted lines). The QCD pair production cross section is shown for comparison (dashed line). The top axis shows the corresponding f value for $M_T/f = 2m_t/v$. From Ref. [304].

and Z due both to mixing of the W and Z bosons with the heavy gauge bosons and to the nonzero triplet vev.

A linear collider will achieve high-precision measurements of the top quark and Higgs boson masses, which are important inputs to the SM electroweak fit. LC improvement in the W boson mass measurement, together with an order-of-magnitude improvement in the measurements of the Z-pole observables at a "Giga-Z" machine, should turn up a deviation from the SM fit due to the little Higgs model contributions.

3.6.2.2 Triple gauge boson couplings

The WWZ triple gauge boson coupling in the Littlest Higgs model is modified from its SM form due to the modification of G_F by W_H exchange [304]:

$$g_1^Z = \kappa_Z = 1 + \frac{1}{\cos 2\theta_W}\left\{\frac{v^2}{8f^2}\left[-4c^2s^2 + 5(c'^2 - s'^2)^2\right] - \frac{2v'^2}{v^2}\right\}, \qquad (3.49)$$

where the form-factors are defined according to [311]

$$\mathcal{L}_{WWV} = ig_{WWV}\left[g_1^V(W^+_{\mu\nu}W^{-\mu} - W^{+\mu}W^-_{\mu\nu})V^\nu + \kappa_V W^+_\mu W^-_\nu V^{\mu\nu} + \frac{\lambda_V}{m_W^2}W^{+\nu}_\mu W^{-\rho}_\nu V^\mu_\rho\right]. \tag{3.50}$$

At present, the constraints from the WWZ coupling are weak compared to those from electroweak precision measurements. However, at a future linear collider, a precision of $10^{-3} - 10^{-4}$ on g_1^Z and κ_Z should be achievable; this would be sensitive to $f \sim (15-50)v \sim 3.5 - 12$ TeV for generic values of c, c' and v'. Unfortunately for this measurement, the region of parameter space that loosens the electroweak precision bound on f (small c and v' and $c' \simeq s'$) also suppresses the little Higgs contribution to g_1^Z and κ_Z.

3.6.2.3 Loop-induced Higgs boson decays

The decay partial widths of the Higgs boson into gluon pairs or photon pairs are modified in the Littlest Higgs model by the new heavy particles running in the loop and by the shifts in the Higgs couplings to the SM W boson and top quark [305]. These modifications of the Higgs couplings to gluon or photon pairs scale like $1/f^2$, and thus decouple at high f scales. The range of partial widths for given f values accessible by varying the other model parameters are shown in Fig. 3.61.

Are these corrections observable? For $f \geq 1$ TeV, the correction to $\Gamma(H \to gg)$ is always less than 10%. This is already smaller than the remaining SM theoretical uncertainty on the gluon fusion cross section due to uncalculated higher-order QCD corrections [312]. For the partial width to photons, the situation is more promising because the QCD corrections are well under control. At the LHC, the $H \to \gamma\gamma$ decay rate can be measured to 15–20% [313]; this probes $f < 600$ GeV at 1σ. A linear e^+e^- collider has only comparable precision since the $H \to \gamma\gamma$ branching ratio measurement is limited by statistics [57, 314, 315]. The most promising measurement would be done at a photon collider, where the $\gamma\gamma \to H \to b\bar{b}$ rate can be measured to about 2% [316] for a Higgs boson with mass around 115–120 GeV. (The uncertainty rises to 10% for $m_H = 160$ GeV.) Combining this with a measurement of the branching ratio of $H \to b\bar{b}$ to about 1.5–2% at the e^+e^- collider [57, 314, 317] allows the extraction of $\Gamma(H \to \gamma\gamma)$ with a precision of about 3%. Such a measurement would be sensitive to $f < 1.5$ TeV at the 1σ level, or $f < 1.1$ TeV at the 2σ level. A 5σ deviation is possible for $f < 700$ GeV. For comparison, the electroweak precision constraints require $f \gtrsim 1$ TeV in the Littlest Higgs model [306].

The biggest model dependence in the loop-induced Higgs decays in little Higgs models comes from the content of the Higgs sector at the electroweak scale. In models with only one light Higgs doublet, our general conclusions should hold, up to factors related to the multiplicity and detailed couplings of the new heavy particles. However, many little Higgs models [295, 297–300] contain two light Higgs doublets. In this case, mixing between the two neutral CP-even Higgs particles and the contribution of a relatively light charged Higgs boson running in the loop can lead to large deviations in the couplings of the lightest Higgs boson to gluon or photon pairs, swamping the effects from the heavy states.

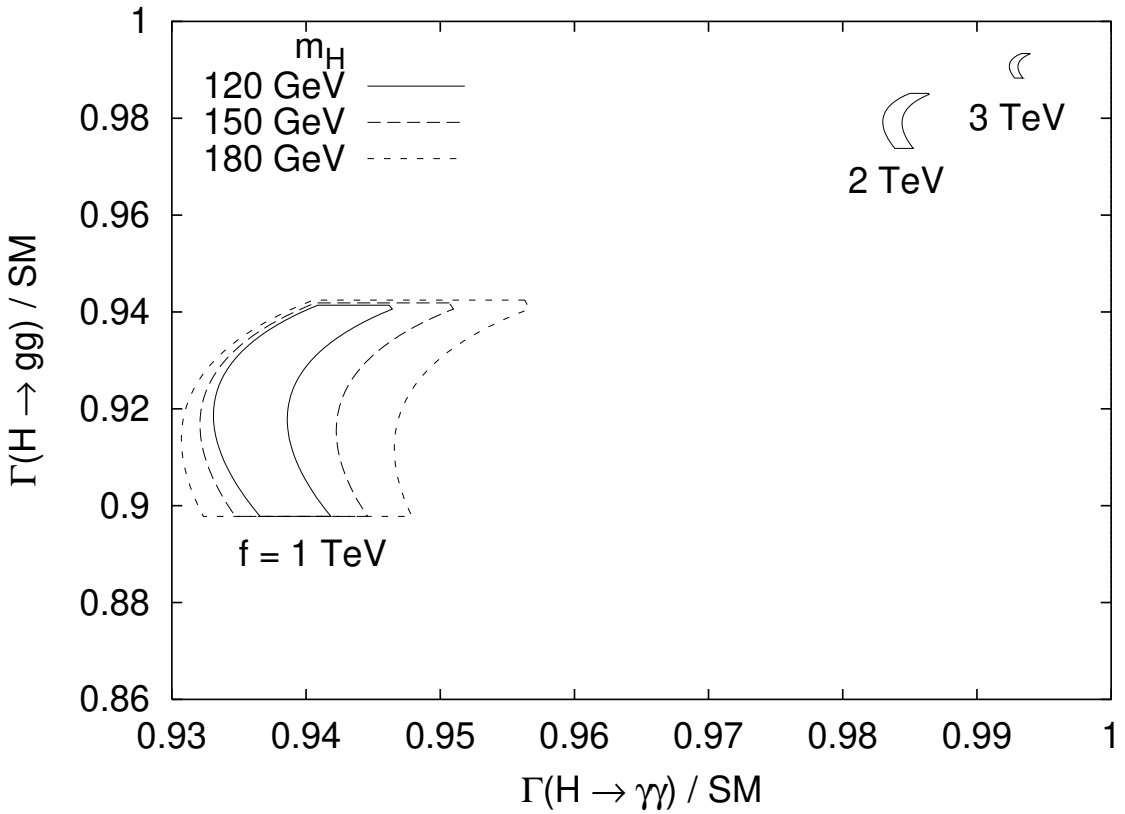

Figure 3.61: Range of values of $\Gamma(H \to gg)$ versus $\Gamma(H \to \gamma\gamma)$ accessible in the Littlest Higgs model normalized to the SM value, for $m_H = 120$, 150, 180 GeV and $f = 1$, 2, 3 TeV. From Ref. [305].

3.7 Exotic scenarios

In this section, we focus on a few additional situations in which the available experimental signals for Higgs physics could be difficult to detect at the LHC or the LC and the extent to which these two machines (including also the photon-collider γC option) will complement one another. Whether the scenarios considered should all be termed "exotic" is not clear. Some of the models of this type involve substantial extensions of more standard models. Other relevant scenarios arise simply by virtue of choosing particular, theoretically motivated parameters and/or boundary conditions within the context of very attractive and fairly simple models. The examples are chosen to highlight how the LC can usually provide a clear signal for Higgs physics in models for which the LHC cannot or vice versa, or to illustrate how a first signal at one type of machine can be clarified and studied in greater detail at the other collider. In particular, even if a scalar particle is detectable at the LHC, a full precision study of its properties will typically require a high luminosity LC. Additional examples of relevance for the LHC/LC complementarity, such as the NMSSM, radion-Higgs mixing and so forth are given more detailed treatment in earlier sections of this report.

3.7.1 The CP-conserving MSSM in the decoupling limit

A very probable MSSM scenario is one in which the the $H, A, H^{\pm}$ are fairly heavy (and rather degenerate) while the h is light and has very SM properties. As reviewed in earlier sections, it may be possible at the LHC and LC to detect deviations in the properties of the h that reveal that it is not precisely SM-like and that provide some indication for the presence of the more complicated MSSM Higgs sector. However, if the $(m_A, \tan\beta)$ parameter space point is in the LHC wedge of moderate $\tan\beta$ and $m_A \gtrsim 300$ GeV, direct detection of the $H, A, H^{\pm}$ may not be possible at the LHC. In addition, their detection at an LC with $\sqrt{s} < 600$ GeV will also not be possible in this same wedge region [318]. This is because pair production, $e^+e^- \to HA, H^+H^-$, is kinematically inaccessible while the Yukawa radiation processes, $e^+e^- \to b\bar{b}H, b\bar{b}A, t\bar{t}H, t\bar{t}A$ all have a very low rate for moderate $\tan\beta$.

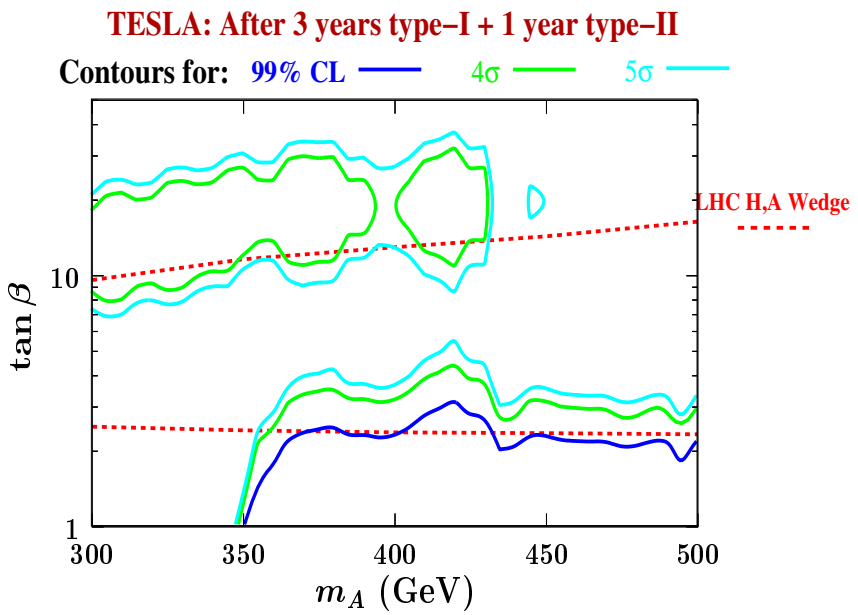

Figure 3.62: Contours for 4σ and 5σ discovery and 99% CL exclusion in the $\gamma\gamma \to H, A \to b\bar{b}$ channel after 1 year of TESLA $\gamma\gamma$ operation in the laser photon-electron polarization configuration II (designed for H, A masses near the maximum reach point of $m_A, m_H \sim 0.8\sqrt{s}$) and 3 years of operation in polarization configuration I (designed to maximize sensitivity to moderate H, A masses). For details, see [319, 320]. The dashed lines show the LHC wedge region where H, A detection is not possible; the LC wedge is even larger for $\sqrt{s} \lesssim 800$ GeV.

However, there are options at the LC that would allow H, A and $H^{\pm}$ detection. First, the LC energy will eventually be upgraded to $\gtrsim 1$ TeV, allowing HA and H^+H^- pair production up to masses $\gtrsim 500$ GeV. Second, it has been shown [319, 320] (see also [158, 159]) that the photon-collider (γC) option at a $\sqrt{s} = 600$ GeV LC has an excellent chance of allowing direct discovery of the H and A for masses up to about 500 GeV in the channel $\gamma\gamma \to H, A \to b\bar{b}$. A plot from [320] is presented in Fig. 3.62. This plot shows that after 4 years of operation of a TESLA-based γC it would be possible to detect the H, A signal precisely in the wedge of $(m_A, \tan\beta)$ parameter space where their detection would not be possible at either the LHC or LC. The only region

within the wedge for which the $b\bar{b}$ final state signal is weak is the part of the wedge with the lowest $\tan\beta$ values. Here, the $t\bar{t}$ decays of the H and A become important and the $t\bar{t}$ final state would be likely to provide a strong signal. This channel has not yet been studied in detail.

3.7.2 The CP-conserving 2HDM with the only light Higgs boson being pseudoscalar – a special non-decoupling limit

The easiest way to satisfy precision electroweak constraints in the two-Higgs-doublet model (2HDM) context is if the Higgs potential parameters are chosen so that the decoupling limit applies. In the decoupling limit, the lightest CP-even Higgs boson, the h, is SM-like by virtue of all the other Higgs bosons (the $H, A, H^{\pm}$) being heavy. However, this is not the only way to achieve consistency with the precision electroweak data. As shown in [321,322] (see also [323]), it is possible to choose 2HDM parameters in such a way that the only light Higgs boson is the A, all the other Higgs bosons (h, H and $H^{\pm}$) having masses of order a TeV. The h in this kind of model will be SM-like and will give sizable $\Delta T < 0$ and $\Delta S > 0$ contributions that would lead to inconsistency with the precision constraints. However, for parameters such that there is a small non-zero $m_{H^{\pm}} - m_H > 0$ mass difference (an isospin splitting) there will be a large $\Delta T > 0$ that will more than compensate the large $\Delta T < 0$ contribution from the heavy h. This is easily understood algebraically. When the A is relatively light while the h is heavy and SM-like, one finds

$$\Delta\rho = \frac{\alpha}{16\pi m_W^2 c_W^2}\left\{\frac{c_W^2}{s_W^2}\frac{m_{H^{\pm}}^2 - m_{H^0}^2}{2} - 3m_W^2\left[\log\frac{m_{h^0}^2}{m_W^2} + \frac{1}{6} + \frac{1}{s_W^2}\log\frac{m_W^2}{m_Z^2}\right]\right\}$$

The large negative contribution from the heavy SM-like h arising from the 2nd term in brackets is compensated by an even larger positive contribution from the first term proportional to $(m_{H^{\pm}} - m_H)(m_{H^{\pm}} + m_H)$. The resulting predictions of the 2HDM give postive shifts of $\mathcal{O}(0.1)$ to both S and T (assuming $U = 0$). In this scenario, the LHC would discover a $\sim 500\ \mathrm{GeV} - 1\ \mathrm{TeV}$ SM-like h (for example, in the $h \to ZZ \to 4\ell$ channel) instead of a light CP-even Higgs boson (with SM-like WW, ZZ couplings) as apparently needed to satisfy precision electroweak constraints. The current precision electroweak constraints would then imply that additional contributions to S and/or T are required, but their source and nature would be obscure. For example, instead of the 2HDM scenario considered here, the negative ΔT and positive ΔS from the heavy SM-like h could equally well be compensated by new physics yielding a sizable $\Delta S < 0$ contribution with small ΔT (that would yield a net S, T prediction in the lower left corner of the ellipse) or new physics giving $\Delta T > 0$ and $\Delta S < 0$ contributions (that would return the net S, T prediction to near the center of the ellipse).

Clarification of the situation would be difficult. In the 2HDM scenario being considered, and assuming a moderate $\tan\beta$ value, the A would not be directly detectable at either the LHC or the LC — it falls into the wedge region described in the previous subsection. The $h \to AA$ decay, if allowed kinematically, would typically have a reasonable branching ratio despite the presence of the on-shell ZZ, WW decay modes. Its detection would be very important to unraveling the situation. Of course, the (S, T) prediction remains within the 90% CL ellipse even if m_A is as large as $500\ \mathrm{GeV}$,

for which $h \to AA$ decays would be forbidden and direct detection of the A (as well as of the $H^\pm$ and H) in e^+e^- collisions would require a much higher energy LC. A γC might play a crucial role. Detection of the A in the $\gamma\gamma \to A \to b\bar{b}$ channel would generally be possible for $m_A \lesssim 0.8\sqrt{s}$, i.e. for $m_A \lesssim 800$ GeV for $\sqrt{s} \lesssim 1$ TeV. See [319] for details.

Considerable clarification would result from a Giga-Z run at the future LC (combined with a WW threshold scan sufficient to obtain $\Delta m_W = 7MeV$). Given the LHC measurement of m_h, one could determine with considerable accuracy the additional ΔT and/or ΔS from the additional new physics with a (correlated) 1σ error of order $\delta\Delta T \sim \delta\Delta S \sim \pm 0.05$. Some scenarios would be excluded, but many possibilities would remain, since one could not be sure that the observed deviation was the result of the presence of undetected Higgs bosons or some of the other types of new physics discussed in earlier sections of this report.

3.7.3 Maximally-mixed and "Continuum" Higgs models

We first describe the general type of model we wish to consider in this section and some of the related experimental considerations. We then use the continuum Higgs model as a particular example.

In unconstrained CP-conserving two-doublet models away from the decoupling limit, the scalars can mix strongly with one another and have similar masses and many couplings possibilities. In CP-conserving models with more than two-doublets and/or doublets plus one or more complex singlets there will be mixing among the pseudoscalars as well as among the scalars. In CP-violating Higgs sectors (including the MSSM two-doublet Higgs sector with CP-violation from loop corrections), the mixing possibilities will be even greater. Such mixing typically results in a sharing of the WW/ZZ coupling among the CP-even (or all the CP-mixed) Higgs bosons, thereby substantially reducing key high-mass-resolution LHC signals such as $gg \to h \to ZZ^{(*)} \to 4\ell$ and especially $gg \to h \to \gamma\gamma$. At the same time, the Higgs bosons can have masses that differ by an amount of order the experimental resolution in other critical channels that do not rely on the WW/ZZ coupling, such as $gg \to t\bar{t}h$ with $h \to b\bar{b}$ or $h \to \tau^+\tau^-$. Such reduced and overlapping signals will be much more difficult to separate from background than in the SM Higgs case. In addition, heavier Higgs bosons can decay to lighter ones, further complicating the search possibilities.

Even in the absence of h decays to other Higgs bosons, the $WW \to h \to \tau^+\tau^-$ detection channel will take a "double-hit". First, the production rate for each h would be suppressed due to reduced WWh coupling. Second, the poor mass resolution in the final state would mean that signals for several different h's (separated in mass by, say, 10 GeV) will overlap and make peak detection impossible. Instead, one must try to determine the presence of a broad excess in the $M_{\tau\tau}$ distribution.

Because of these possibilities, it is often fairly easy to find model parameters such that the LHC will have difficulty detecting the Higgs boson signals. The power of the LC is its ability to look for $e^+e^- \to Zh$ in the inclusive $e^+e^- \to ZX$ missing-mass channel approach by simply looking for a bump in the reconstructed M_X. Even if the signals from different Higgs bosons overlap somewhat and their strength is maximally shared, the excess in the M_X distribution will be apparent at the LC. And, of course, the inclusive M_X peak or broad excess is independent of how the Higgs

bosons decay.

Another general point is that even if the LHC does not find a direct signal for a set of relatively light but strongly mixed and overlapping Higgs bosons we will know that they (or some alternative source of electroweak symmetry breaking) are present below the TeV scale by virtue of the fact that $WW \to WW$ scattering measurements will be consistent with perturbative expectations.

We now very briefly review a particular model in which the above considerations have been shown to be relevant. This model [324] was explicitly constructed as a worst case scenario for Higgs detection. The idea is to imagine a large number of doublet and/or singlet Higgs fields with complicated self interactions. In general, the Higgs sector could be CP-violating. The worst case arises if these many Higgs bosons are spaced in mass at intervals slightly less than the mass resolution in $M_{b\bar{b}}$, $M_{\tau^+\tau^-}$ and M_X. They will mix with one another and the heavier ones will decay to the lighter ones. In general, they will share the WW/ZZ coupling strength. Using continuum limit notation, the only constraints are

$$\int dm_h K(m_h) = 1\,, \qquad \int dm_h K(m_h) g^2_{ZZh} m_h^2 \lesssim (200\ \mathrm{GeV})^2 \tag{3.51}$$

where $g^2_{ZZh} = K(m_h) g^2_{ZZh_{SM}}$. The latter constraint relies on either assuming that these Higgs bosons are entirely responsible for explaining the precision electroweak data (a constraint that can be avoided if there is substantial isospin splitting between the charged Higgs and scalar Higgs of the model) or if one demands perturbativity of the model up to the Planck scale.

The result is very substantial diminution of all the standard LHC signals. In particular, the high resolution $gg \to h \to \gamma\gamma$ and $gg \to h \to ZZ \to 4\ell$ final states have very low production rate for any one of the h's due to the sharing of the WW/ZZ coupling-squared. Other channels with more limited resolution will not exhibit separated mass peaks. There will only be a spread out signal that must be detected as a broad excess in some type of mass distribution such as $M_{b\bar{b}}$ or $M_{\tau^+\tau^-}$ or $M_{b\bar{b}\tau^+\tau^-}$ (the latter being relevant for heavier Higgs bosons that decay to a pair of lighter Higgs bosons). The recent study of [325], which claims that a signal can be seen in the $WW \to \sum_i h_i \to WW \to 2\ell 2\nu$ channel, neglects the possibility of Higgs decays to much lighter Higgs bosons (that have very weak WW/ZZ coupling and do not contribute to the above sum rules). Allowing for this possibility, it would seem impossible to guarantee an observable LHC signal for the continuum Higgs scenario.

As discussed in [324], the broad M_X excess in the $e^+e^- \to ZX$ channel that would arise in this model *will* be detectable with enough ($L \gtrsim 100 \div 200\ \mathrm{fb}^{-1}$) integrated luminosity at the LC. Further, with $L \sim 500\ \mathrm{fb}^{-1}$ it will be possible to determine the extent of the excess in bins with size of order $10\ \mathrm{GeV}$ as well as to examine the dominant final states in each such bin.

3.7.4 Higgsless models

We simply mention the recently proposed Higgsless model [326] in which boundary conditions on a brane in a warped 5th dimension are responsible for electroweak symmetry breaking. The unitarity of WW scattering is maintained so long as the KK excitations of the W and Z are not much above the TeV scale and therefore accessible

to direct production at the LHC. These higher KK excitations also work together in such a way as to avoid tree-level violation of the $\rho = 1$ constraint and to make only a small contribution to the S parameter.

The exact nature of the LHC signals for the W and Z excitations has not been worked out. However, it is clear that understanding what is happening in WW scattering and electroweak symmetry breaking will require detecting all the relevant excitations and determining details of their couplings to one another. This will be a challenging task.

An LC (with $\sqrt{s} \lesssim 1$ TeV) might have some difficulty studying all the relevant KK excitations. Thus, this is a case in which the LHC might be superior for understanding electroweak symmetry breaking. Still, the LC measurements of the M_X distribution would be very revealing in that no excess (at masses below a few hundred GeV) would be observed and one could then be more certain that the KK resonances observed at the LHC were indeed the entire story.

4 Strong Electroweak Symmetry Breaking

4.1 Introduction

The experimental data which were obtained in recent years have established the validity of the description of electroweak interactions by a spontaneously broken gauge theory. The masses of fermions and electroweak gauge bosons are generated by the Higgs mechanism [327], which involves the condensation of a scalar multiplet with non-vanishing hypercharge and weak isospin quantum numbers. This includes the Goldstone bosons associated with the spontaneous breaking of the electroweak $SU(2)_L \times U(1)_Y$ symmetry, which are identified with the longitudinal degrees of freedom of the massive W and Z gauge bosons.

The Standard Model (SM) [328] is the simplest theory of electroweak interaction that is complete in the sense that its predictions can be extrapolated up to energies far beyond the electroweak scale,

$$v = (\sqrt{2}G_F)^{-1/2} = 246\,\mathrm{GeV}, \tag{4.1}$$

where G_F is the Fermi constant. The Higgs mechanism identifies v with the vacuum expectation value of the Higgs field. In the SM, fluctuations around this expectation value are associated with a scalar particle, the Higgs boson. This hypothesis is consistent with the electroweak precision data [329].

Nevertheless, the absence of a light Higgs boson is a logical possibility, supported by the fact that the Higgs has not been observed at LEP. Actually, the best fit of the SM to the data predicts its mass to be below $100\,\mathrm{GeV}$, which is already excluded by direct searches [330].

If no Higgs boson exists, the Higgs mechanism is still valid formally, but the electroweak symmetry cannot be linearly realized on the multiplet of Goldstone bosons. As a consequence, the model is non-renormalisable, and scattering amplitudes of Goldstone bosons are unbounded at high energies. The predictivity of extrapolations is limited to energies below the scale

$$\Lambda = 4\pi v = 3.1\,\mathrm{TeV}, \tag{4.2}$$

where the tree-level amplitudes saturate perturbative unitarity. This scale provides a cutoff to the low-energy effective theory. Higher-dimensional operators are expected to contribute corrections of order $v^2/\Lambda^2 = 1/(4\pi)^2$ to low-energy observables and could mimic the existence of a light Higgs boson.

In fact, the lowest threshold where without the Higgs boson a tree-level scattering amplitude would violate unitarity (if naively extrapolated) is already at $1.2\,\mathrm{TeV}$ [331]. Thus, new experiments which probe amplitudes in the TeV range with sufficient precision will observe dynamics which cannot be inferred from our present knowledge about electroweak interactions. While Goldstone bosons by themselves are unphysical degrees of freedom, their identification with the longitudinal components of W

and Z bosons makes this new dynamics observable in the scattering amplitudes of vector bosons:

$$W_L W_L \to W_L W_L, \quad W_L W_L \to Z_L Z_L, \quad \ldots \tag{4.3}$$

In this no-Higgs scenario, it is not clear what physics we can expect in the TeV range. The simplest model of strong electroweak symmetry breaking is minimal technicolour [332], where the paradigm of QCD is transferred to electroweak interactions, assuming the existence of technifermions which are confined at the scale Λ. In this model, a strong vector resonance (the technirho) is predicted in WW scattering, analogous to pion scattering in the GeV range. However, technicolour does not account for fermion masses and thus must be extended by additional interactions, and it does not predict the correct sign and magnitude of the shifts in the low-energy precision observables. More realistic models involve more complicated spectra and scale patterns and differ in their statements about TeV-scale phenomenology [333].

The LHC and the Linear Collider both have the capabilities to shed light onto this new sector of high-energy physics by measurements of the vector boson scattering amplitudes (4.3). The two facilities are complementary in several respects. Clearly, the LHC with its c.m. energy of $14\,\mathrm{TeV}$ is able in principle to collect data beyond the unitarity saturation threshold. However, the fast falloff of the relevant cross section limits its actual reach for the processes we are considering here, and the signals are contaminated by a large background of SM processes. Backgrounds are much less severe at an e^+e^- collider. There, the machine itself limits the energy reach, but the high luminosity anticipated for a Linear Collider makes it more than comparable in sensitivity in the range below $1\,\mathrm{TeV}$, where the new strong interactions determine the precise pattern of the rise of vector boson scattering amplitudes with energy.

At present, no theoretical or experimental analysis is available that compares and combines the capabilities of both machines in the context of strongly interacting W and Z bosons. This will be a goal of the ongoing LHC/LC workshop. The purpose of this note is to review the theoretical and phenomenological background, to discuss the principal properties of the relevant processes at both colliders, and to summarise the studies that have been completed or are under way, on a common basis.

4.2 Low-energy effective theory

Below the cutoff Λ there is a generic effective-theory description of electroweak interactions that relies only on the established facts about symmetries [334]. The electroweak Goldstone bosons w^a ($a = 1, 2, 3$) are used for the parameterisation of a unitary 2×2 matrix Σ,

$$\Sigma(x) = \exp\left(-\frac{i}{v} w^a(x)\, \tau^a\right), \tag{4.4}$$

where τ^a are the Pauli matrices. The Σ field is normalised to unit vacuum expectation value,

$$\langle \Sigma \rangle = \mathbf{1}, \tag{4.5}$$

and serves as the Higgs field in the electroweak effective Lagrangian,

$$\begin{aligned}\mathcal{L} = &-\tfrac{1}{2}\,\mathrm{tr}\,[\mathbf{W}_{\mu\nu}\mathbf{W}^{\mu\nu}] - \tfrac{1}{2}\,\mathrm{tr}\,[\mathbf{B}_{\mu\nu}\mathbf{B}^{\mu\nu}] - \tfrac{v^2}{4}\,\mathrm{tr}\,[V_\mu V^\mu] + \Delta\rho\,\tfrac{v^2}{8}\,\mathrm{tr}\,[TV_\mu]\,\mathrm{tr}\,[TV^\mu] \\ &+ \mathcal{L}_{\mathrm{fermion}} + \mathcal{L}_{\mathrm{gauge-fixing}} + \mathcal{L}_{\mathrm{ghost}}.\end{aligned} \tag{4.6}$$

The additional building blocks of this Lagrangian are the left- and right-handed fermions, the weak and hypercharge gauge bosons W^a ($a = 1, 2, 3$) and B with

$$\mathbf{W}_\mu = W^a_\mu \tfrac{\tau^a}{2}, \qquad \mathbf{B}_\mu = B_\mu \tfrac{\tau^3}{2}, \tag{4.7}$$

and the corresponding field strengths $\mathbf{W}_{\mu\nu}$ and $\mathbf{B}_{\mu\nu}$. The derived fields V_μ and T are given by

$$V_\mu = \Sigma(D_\mu\Sigma)^\dagger = -ig\mathbf{W}_\mu + ig'B_\mu + \ldots \quad \text{and} \quad T = \Sigma\tau^3\Sigma^\dagger = \tau^3 + \ldots, \tag{4.8}$$

where D_μ is the gauge-covariant derivative. In physical terms, V_μ represents the longitudinal gauge bosons which are identified with the Goldstone bosons in observable scattering amplitudes. The omitted terms involve Goldstone fields and their derivatives. These vanish in the unitary gauge, where Fadeev-Popov ghost and Goldstone fields are set to zero and the Σ field is set to unity.

From the structure of the generic Lagrangian (4.6) one can infer the leading term proportional to E^2/v^2 in the rise of the longitudinal vector boson scattering amplitudes. This is called the Low-Energy Theorem (LET) [335]. Transversal gauge bosons provide contributions that are constant in energy and suppressed by the gauge couplings, but enhanced by the larger number of degrees of freedom. For $\Delta\rho = 0$, the LET is given by

$$A(W_L^- W_L^- \to W_L^- W_L^-) = -\frac{s}{v^2} \tag{4.9}$$

$$A(W_L^+ W_L^- \to W_L^+ W_L^-) = -\frac{u}{v^2} \tag{4.10}$$

$$A(W_L^+ W_L^- \to Z_L Z_L) = \frac{s}{v^2} \tag{4.11}$$

$$A(Z_L Z_L \to Z_L Z_L) = 0 \tag{4.12}$$

Subleading corrections (proportional to E^4/v^4) are parameterised by the additional operators $\mathcal{L}_1$ to $\mathcal{L}_{11}$ [334]:

$$\mathcal{L}_1 = \alpha_1 g g' \operatorname{tr}\left[\Sigma\mathbf{B}_{\mu\nu}\Sigma^\dagger\mathbf{W}^{\mu\nu}\right] \tag{4.13}$$

$$\mathcal{L}_2 = i\alpha_2 g' \operatorname{tr}\left[\Sigma\mathbf{B}_{\mu\nu}\Sigma^\dagger[V^\mu, V^\nu]\right] \tag{4.14}$$

$$\mathcal{L}_3 = i\alpha_3 g \operatorname{tr}\left[\mathbf{W}_{\mu\nu}[V^\mu, V^\nu]\right] \tag{4.15}$$

$$\mathcal{L}_4 = \alpha_4 (\operatorname{tr}\left[V_\mu V_\nu\right])^2 \tag{4.16}$$

$$\mathcal{L}_5 = \alpha_5 (\operatorname{tr}\left[V_\mu V^\mu\right])^2 \tag{4.17}$$

$$\mathcal{L}_6 = \alpha_6 \operatorname{tr}\left[V_\mu V_\nu\right] \operatorname{tr}\left[TV^\mu\right] \operatorname{tr}\left[TV^\nu\right] \tag{4.18}$$

$$\mathcal{L}_7 = \alpha_7 \operatorname{tr}\left[V_\mu V^\mu\right] \operatorname{tr}\left[TV_\nu\right] \operatorname{tr}\left[TV^\nu\right] \tag{4.19}$$

$$\mathcal{L}_8 = \tfrac{1}{4}\alpha_8 g^2 (\operatorname{tr}\left[T\mathbf{W}_{\mu\nu}\right])^2 \tag{4.20}$$

$$\mathcal{L}_9 = \tfrac{i}{2}\alpha_9 g \operatorname{tr}\left[T\mathbf{W}_{\mu\nu}\right] \operatorname{tr}\left[T[V^\mu, V^\nu]\right] \tag{4.21}$$

$$\mathcal{L}_{10} = \tfrac{1}{2}\alpha_{10} (\operatorname{tr}\left[TV_\mu\right] \operatorname{tr}\left[TV_\nu\right])^2 \tag{4.22}$$

$$\mathcal{L}_{11} = \alpha_{11} g \epsilon^{\mu\nu\rho\lambda} \operatorname{tr}\left[TV_\mu\right] \operatorname{tr}\left[V_\nu \mathbf{W}_{\rho\lambda}\right] \tag{4.23}$$

In this list, we have omitted terms which involve fermions or violate CP invariance.

Although in the Higgs-less scenario the point $\alpha_i \equiv 0$ has no special properties, the couplings α_1 to α_{11} are often referred to as *anomalous couplings*. Their values are

expected to be of the order $v^2/\Lambda^2 = 1/16\pi^2$ or larger [336]. Two of them (α_1 and α_8) have been constrained at LEP1. Together with $\Delta\rho$ in (4.6), they are equivalent to the set of electroweak precision observables S, T, U [337]. Four additional parameters ($\alpha_{2,3,9,11}$) modify the interactions of one transversal with two longitudinal gauge bosons and thus are equivalent to the triple-gauge couplings $\kappa_\gamma, \kappa_Z, g_1^Z, g_5^Z$ [338]. In a strong-interaction scenario, these parameters are given by the leading Taylor coefficients of the W/Z form factors. Finally, the parameters $\alpha_{4,5,6,7,10}$ describe independent deviations in the four-point interactions of longitudinal gauge bosons and thus determine the quasielastic W and Z scattering amplitudes.

4.3 Beyond the threshold

As stated in the Introduction, the extrapolated tree-level scattering amplitudes of Goldstone bosons violate unitarity in the high-energy range above $1.2\,\mathrm{TeV}$. Depending on the actual values of the α_i parameters, the limits may be lower or higher. In any case, the low-energy effective theory does not predict scattering amplitudes beyond a certain threshold.

Given the fact that even in the well-known QCD case strong interactions are poorly understood, we have no calculational methods which would provide us with reliable quantitative predictions in that range. Therefore, phenomenological models are used to give results that are at least internally consistent. By comparing different models the resolving power of an experiment in a certain energy range can be estimated. If no new degrees of freedom are introduced, unitarity in the $2 \to 2$ scattering channels of Goldstone bosons is a necessary requirement. Therefore, models are often based on the unitarisation of extrapolated scattering amplitudes.

Since low-energy pion scattering (QCD) exhibits resonances in several channels, it is reasonable to expect similar effects for new strong interactions in the electroweak sector. This is implemented by the Padé unitarisation model [339], which is based on the assumption that each scattering channel is dominated by a single resonance (or dip) in the cross section. By contrast, the K-matrix model [340] exhibits saturation of the Goldstone boson scattering amplitudes without resonances. Alternatives and refinements of these scenarios are also considered in the studies mentioned below.

It should be stressed that such models serve as test cases for sensitivity estimates in a region where otherwise no prediction would be possible. Once real data are available, signals of new strong interactions will be extracted from data without model assumptions. Apart from effects in Goldstone scattering, models of strong electroweak symmetry breaking typically predict additional new particles with properties that can be studied in various ways [333]. However, since no particular model is preferred (such as the MSSM in the weakly-interacting case), this is not easily taken into account in a generic analysis. In the studies discussed in the present paper, no degrees of freedom beyond the known particles are included.

4.4 Processes at the LHC and the LC

Since vector bosons are unstable particles, they are accessible only by their couplings to fermion pairs and photons. Thus, at tree level, a process, which depends on massive four-boson interaction amplitudes, typically involves the production of six fermions in the final state. There are two cases:

1. Vector boson scattering:

$$ff \to ff + V^*V^* \to ff + VV \to 6f \tag{4.24}$$

2. Three-boson production:

$$ff \to V^* \to VVV \to 6f \tag{4.25}$$

Furthermore, at one-loop order, four-boson interactions modify the imaginary part of vector boson pair production (rescattering):

$$ff \to V^* \to V^*V^* \to VV \to 4f \tag{4.26}$$

In the analysis of the processes listed above, we can make use of the generic properties of Goldstone-boson scattering amplitudes. Since the relative impact of the anomalous couplings rises with the energy of the $2 \to 2$ scattering, the strongest effect occurs at large pair invariant masses of the vector bosons. Using angular correlations of the decay fermions, one can enhance the fraction of longitudinally polarised vector bosons in the event sample. Finally, forward scattering of vector bosons is dominated by transversal vector boson exchange which does not involve the symmetry-breaking sector, hence large-angle scattering is most sensitive to anomalous four-boson interactions.

4.4.1 Vector-boson scattering at the LHC

At the LHC, four channels of vector boson scattering (4.24) are accessible:

$$pp \to jj + W^+W^- \tag{4.27}$$
$$pp \to jj + W^\pm W^\pm \tag{4.28}$$
$$pp \to jj + ZZ \tag{4.29}$$
$$pp \to jj + W^\pm Z \tag{4.30}$$

In each case, detection is easiest for leptonic decays of the vector boson. Obviously, $ZZ \to \ell^+\ell^-\ell^+\ell^-$ is the *golden channel* since the vector boson pair can be completely reconstructed from the final state. In the leptonic W decay $W \to \ell\nu$, the neutrino prohibits an unambiguous determination of the invariant mass of the vector boson pair. Semileptonic modes (one vector boson decays hadronically, one leptonically) are more difficult due to the QCD background, but have a larger branching ratio. Finally, in the fully hadronic modes the QCD background is a major problem.

A necessary ingredient for background reduction is the tagging of the two extra jets in (4.27–4.30), which are found in the forward region. This is due to the fact that

at high energies, where the W and Z masses can be neglected, they are emitted from quarks essentially on-shell by the splitting processes $q \to qZ$ and $q \to q'W$ which are peaked in the collinear region. Generically, the forward jets retain a large fraction of the original parton energy, while the transverse momentum is of the order $M_W/2$.

Since there are five independent anomalous couplings which affect the four-boson interactions at subleading order, one would need at least five measurements for their determination. At the LHC, this cannot be done using cross sections alone, since in the subprocesses

$$W^+W^-/ZZ \to W^+W^- \quad \text{and} \quad W^+W^-/ZZ \to ZZ \tag{4.31}$$

the initial state cannot be traced.

An obvious advantage of the LHC is the accessibility of the high-energy range beyond $1\,\mathrm{TeV}$. For a rough estimate, one can regard vector boson scattering as the result of the splittings $p \to q$ and $q \to W/Z$, which allows for an effective subprocess energy up to about $2\,\mathrm{TeV}$. Whether this range can actually be exploited depends on the presence of resonances. As a guideline, one can take the searches for the Higgs boson in the high-mass region, which for $M_H = 1\,\mathrm{TeV}$ is merely a broad resonance in vector boson scattering. While narrow resonances are likely to be observed, the measurement of a structureless scattering amplitude becomes difficult in this range.

4.4.2 Vector-boson scattering at the Linear Collider

At an e^+e^- collider, the relevant processes are

$$e^+e^- \to \nu\overline{\nu}W^+W^- \quad \text{and} \tag{4.32}$$
$$e^+e^- \to \nu\overline{\nu}ZZ, \tag{4.33}$$

which contain the subprocesses

$$W^+W^- \to W^+W^- \quad \text{and} \quad W^+W^- \to ZZ, \tag{4.34}$$

respectively. The signatures are characterised by a large missing invariant mass due to the two neutrinos. The W and Z final states can be detected and measured in all decay channels (except $Z \to \nu\overline{\nu}$), hence no reduction due to low branching ratios applies.

The difficult backgrounds are

$$e^+e^- \to e^\pm\nu W^\mp Z \quad \text{and} \quad e^+e^- \to e^+e^-W^+W^-, \tag{4.35}$$

which are induced by photons and thus have a cross section enhanced by large logarithms $\ln s/m_e^2$. Clearly, in the hadronic modes the separation of W and Z is important both for disentangling the signals and for reducing the background. To achieve this, the jet pair invariant mass resolution has to be better than the mass difference $M_Z - M_W$. Furthermore, it is essential to detect and veto forward-going electrons.

For the Linear Collider designs which are currently considered, the energy is initially limited to about $1\,\mathrm{TeV}$. There is no particular reason to expect a resonance structure in that range (with the possible exception of a physical Higgs boson). However, a

precise analysis of the rise of the scattering processes in the sub-threshold region will significantly add to any information on the high-energy region obtainable at LHC.

By measuring the cross sections of the two processes mentioned above, two linear combinations of the five parameters $\alpha_{4,5,6,7,10}$ can be determined. To further separate their contributions, one can exploit angular distributions or investigate additional scattering processes. These are

$$e^+e^- \to e^\pm \nu W^\mp Z, \tag{4.36}$$
$$e^+e^- \to e^+e^- W^+W^-, \tag{4.37}$$
$$e^+e^- \to e^+e^- ZZ, \tag{4.38}$$

which have the subprocesses

$$W^\mp Z \to W^\mp Z, \quad ZZ \to W^+W^-, \quad \text{and} \quad ZZ \to ZZ, \tag{4.39}$$

respectively. To reduce the large contribution of photon-induced irreducible background for the first two cases, the electron(s) in the final state have to be observed away from the very forward region. Unfortunately, the eeZ coupling is small, so that ZZ-induced processes have a cross section an order of magnitude smaller than WW-induced ones.

Finally, the process

$$e^-e^- \to \nu\nu W^-W^- \tag{4.40}$$

reveals an additional channel of WW scattering, which requires running the machine in e^-e^- mode.

For all W-induced processes, the signal can be further enhanced by a factor of up to four if the initial beams are polarised.

4.4.3 Three-boson production

While the vector-boson scattering processes discussed above have a cross section that logarithmically increases with energy, the cross section of three-boson production processes falls off like $1/s$. This limits their usefulness to subprocess energies in the lower range where the cross section of the fusion processes is still small.

At the LHC, four channels are present:

$$pp \to qq \to W^+W^-W^\pm, \quad W^+W^-Z, \quad W^\pm ZZ, \quad ZZZ, \tag{4.41}$$

where the latter channel is additionally suppressed, cf. (4.12). At the Linear Collider there are only two processes,

$$e^+e^- \to W^+W^-Z, \quad ZZZ. \tag{4.42}$$

Note that the Higgs-strahlung mode of Higgs boson production with $H \to W^+W^-$ or $H \to ZZ$ decay is a special case of this, where a low-lying resonance (the Higgs boson) is present in the spectrum.

4.4.4 Rescattering

The process

$$e^+e^- \to W^+W^- \to 4f \tag{4.43}$$

can be investigated with great precision at a Linear Collider. Therefore, it is conceivable to extract the imaginary part of the amplitude, which is the result of the rescattering $W^+W^- \to W^+W^-$. To leading order, this imaginary part can be derived from (4.9), while at subleading order anomalous contributions come into play. In this process, WW rescattering takes place at the full collider energy.

It should be noted that the real part of the WW pair production amplitude is also a sensitive probe of a strongly-interacting symmetry breaking sector. By making full use of polarisation and angular distributions at a Linear Collider, the real and imaginary parts of all individual form factors can be disentangled [341], which in the present context amounts to a precise measurement of the parameters $\alpha_{2,3,9,11}$. Together with results on vector boson pair production at the LHC, these data have to be taken as an input for the analysis of vector boson scattering both at LHC and at the LC. This is important since the parameters $\alpha_{3,9,11}$ also affect the quartic vector boson couplings and therefore must be known if an unambiguous determination of all independent parameters in the low-energy effective Lagrangian is intended.

4.5 Results

4.5.1 Approximations

Several studies have been done in the past, both for the LC and the LHC. Since vector-boson scattering is embedded in complicated six-fermion processes where for a given final state thousands of Feynman graphs contribute, approximations which simplify the problem are welcome. Many of the studies listed below use one or more of the following:

1. Equivalence Theorem (ET) [342]. The scattering of longitudinal vector bosons is replaced by the scattering of Goldstone bosons. This is important for the implementation of unitarisation models in the high-energy region, and it is justified since parametrically the corrections (partly due to transversal gauge bosons) are suppressed by factors of $M_W^2/\hat{s}$ and g^2. However, this suppression is typically overcome by the multiplicity of transversal polarisation directions and the larger structure functions of transversal gauge bosons.

2. Effective W approximation (EWA) [343]. The process is separated into the splitting of the initial fermions into vector bosons and the subsequent scattering, i.e.

   $$f \to f' + V \quad \text{and} \quad VV \to VV. \tag{4.44}$$

   This approach introduces parton distribution functions for the W and Z vector bosons, which differ for longitudinal and for transversal polarisation. It allows us to estimate event rates when the ET is used for evaluating the amplitudes. The EWA is formally valid up to corrections of order $M_W^2/\hat{s}$ and g^2, where $\hat{s}$

is the invariant mass squared of the W pair, and g is the weak coupling. Unfortunately, neither M_W nor g are small enough for this approximation to be quantitatively reliable in realistic applications. This is mainly due to the large number of numerically important Feynman diagrams which are neglected in this approach. Another problem with the EWA is the transverse momentum of the W pair which is set to zero. This kinematic variable is essential for background reduction.

3. Narrow-width approximation for the vector bosons in the final state. The process is separated into the on-shell production of vector bosons and their decay, i.e.

$$ff \to ffVV \quad \text{and} \quad V \to ff. \tag{4.45}$$

This approximation is justified since non-resonant electroweak six-fermion contributions are typically very small in the kinematical range of interest. Since the angular correlations of fermions are important, polarisation information should be carried through. However, for technical reasons this information is often discarded. For a realistic simulation, the V mass (W or Z) must be smeared by hand, which introduces an arbitrariness in the results.

4. Leading-order approximation. In fact, complete next-to-leading order (NLO) results, which will be needed for precision studies of real data, are not available for any of the processes we are discussing here. Only for on-shell W scattering the NLO corrections ($O(g^2/16\pi^2)$) are known [344]. However, these results have to be embedded in the narrow-width and effective W approximations, where other $O(g^2)$ contributions are neglected. The only effect that can easily be included is the leading-logarithmic scale dependence of the anomalous couplings, which is proportional to $v^2/\Lambda^2 = 1/16\pi^2$, not suppressed by g^2.

While these approximations are quite useful for studying the overall properties of the processes under consideration and for developing experimental strategies, for detailed numerical comparisons and, in particular, for the analysis of real data they are insufficient. The use of complete calculations in Monte-Carlo generators has only begun, and on the experimental side the inclusion of detector effects is essential as well. Since many of the studies lack this level of sophistication, numerical results should be compared or combined with care.

4.5.2 Existing results

A variety of studies has been done for LC [341, 345–350] and LHC [89, 101, 351–355]. For the TGCs the situation is relatively clear. A fast-simulation study basically without approximations exists which has shown that the coupling parameters belonging to the dimension four operators ($g_1^Z, \kappa_\gamma, \kappa_Z$) can be measured at $\sqrt{s} = 800\,\mathrm{GeV}$ about an order of magnitude better than at LHC, resulting in 1σ errors of $\Delta\alpha_2 = 0.0004$ and $\Delta\alpha_3 = 0.0002$ (see figure 4.1) [57, 350]. The correlations with the dimension-six operators $\lambda_\gamma, \lambda_Z$ are small, making the result robust.

The situation is more complicated for the quartic couplings. A complete six-fermion fast simulation study using $e^+e^- \to W^+W^-\nu\nu$ and $e^+e^- \to ZZ\nu\nu$ at $\sqrt{s} = 800\,\mathrm{GeV}$

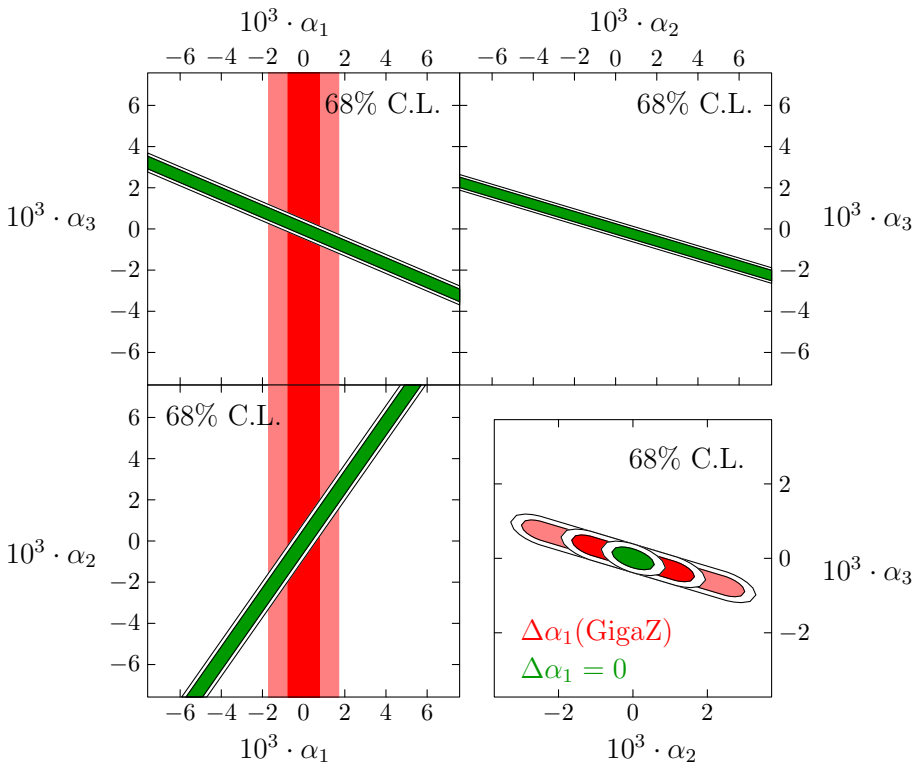

Figure 4.1: Sensitivity to the effective couplings $\alpha_{1,2,3}$ from the measurement of the triple gauge couplings at a linear collider and from the Z-pole precision data. For the Z-pole constraint the outer region is without and the inner region with the accurate m_W measurement. In the lower right plot the $\alpha_2 - \alpha_3$ plane with $\alpha_1 = 0$ or with the Z-pole constraint is shown.

shows that α_4, α_5 can be measured at the linear collider with a precision of 0.005 and 0.03 assuming $SU(2)_c$ invariance. The results of the two subprocesses are shown in figure 4.2 [349]. This seems to be somewhat better than what is possible at LHC (see figure 4.3) [354]. The situation gets more complicated if also the $SU(2)_c$ violating couplings $\alpha_{6,7,10}$ are allowed to differ from zero. The process $e^+e^- \to W^+W^-\nu\nu$ contains only the subprocess $W^+W^- \to W^+W^-$ which is sensitive to α_4 and α_5 while $e^+e^- \to ZZ\nu\nu$ contains only $W^+W^- \to ZZ$, sensitive to $\alpha_4 + \alpha_6$ and $\alpha_5 + \alpha_7$. The $\alpha_4 - \alpha_5$ contour from $e^+e^- \to W^+W^-\nu\nu$ only thus remains valid while the one from $e^+e^- \to ZZ\nu\nu$ had to be understood as a contour in $(\alpha_4 + \alpha_6) - (\alpha_5 + \alpha_7)$.

At the LHC it cannot be decided on an event by event basis if a process is induced by W^+W^- or by ZZ, so that in general all processes are sensitive to all couplings. This makes the LC superior to the LHC for these two processes, even if the LHC can reach higher centre of mass energies. However, further information can be obtained from $W^\pm W^\pm \to W^\pm W^\pm$ and $ZZ \to ZZ$. The first process is sensitive to α_4 and α_5 only, however with a different correlation than $W^+W^- \to W^+W^-$. At LC this process can only be assessed in e^-e^- running which needs additional running time with a factor three lower luminosity where not much else can be done. At the LHC this process is even preferred at large x_{Bj} where valence quarks dominate and easy to select with a same sign dilepton pair in the final state. $ZZ \to ZZ$ is sensitive to all α_i. At LC it is strongly suppressed due to the small Z-lepton coupling. At LHC with its quark initial states this suppression is much weaker and ZZ with at least one leptonically decaying Z is easy to detect and the full kinematics can be reconstructed.

With the present studies it is not possible to combine the estimated results for LC and LHC. However, it has already become clear that both colliders are able to probe quartic anomalous couplings down to their expected values in the percent range, and that combining the two colliders significantly reduces the correlations between the α parameters. Also the precise measurement of the triple couplings at the LC will improve the interpretation of the quartic couplings at the LHC.

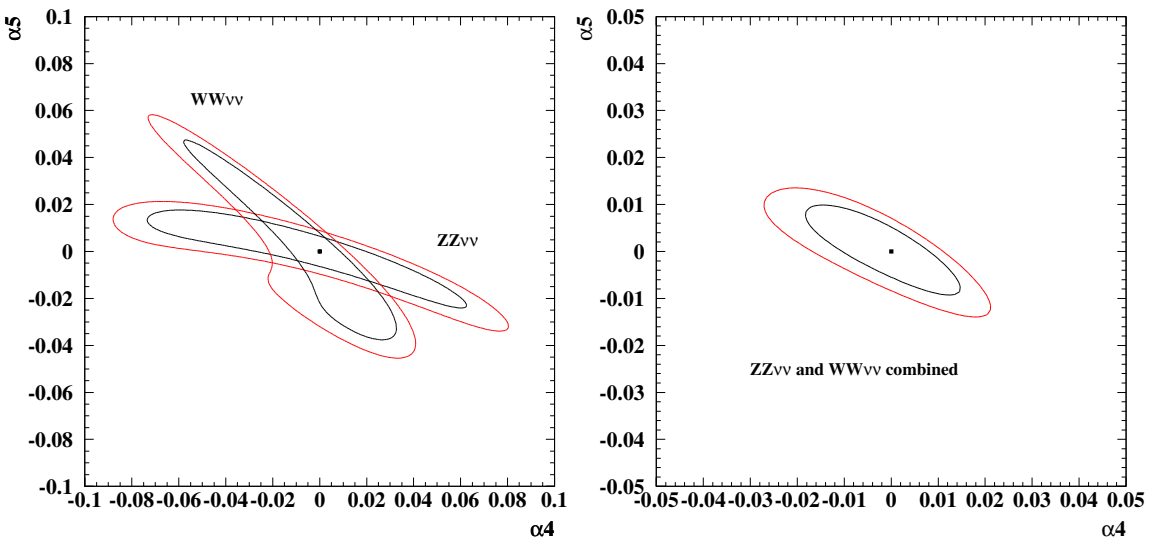

Figure 4.2: Sensitivity to α_4 and α_5 at a linear collider with $\sqrt{s} = 800\,\mathrm{GeV}$ from $e^+e^- \to \nu\nu W^+W^-$ and $e^+e^- \to \nu\nu ZZ$. The inner and outer contours represent 68% and 90% c.l.

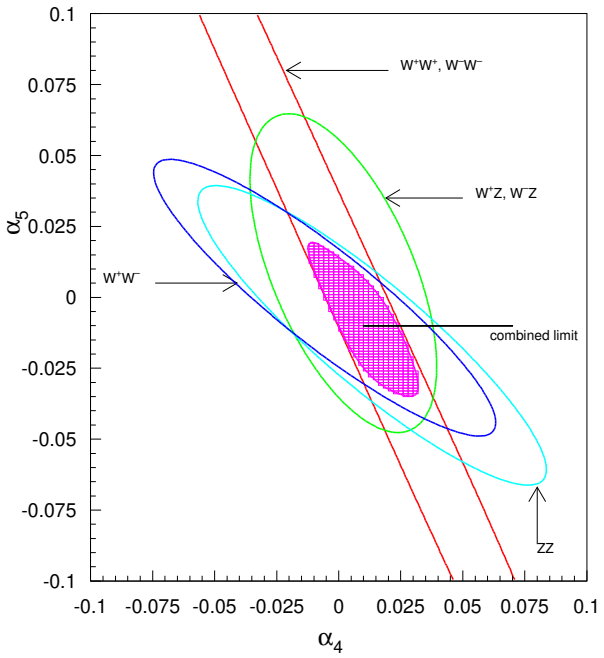

Figure 4.3: Sensitivity to α_4 and α_5 (90% c.l.) at LHC.

4.5.3 Ongoing studies

New studies are currently under way both for the LHC and the LC. These studies are performed with contacts between the different groups from the beginning so that a LC-LHC combination of the results should be possible.

4.5.3.1 LHC

In the CMS collaboration, a new analysis of strong WW scattering is under way [356]. This study will use a Monte Carlo generator which simulates all six-fermion final states in pp interactions, currently being developed in Torino [357]. Events will be processed through the GEANT simulation of the CMS apparatus, and then passed through the online selection and reconstruction programs.

While the six-fermion final state generator is being developed, the group is currently conducting an exploratory study of WW scattering in the semileptonic mode $WW \to \mu\nu jj$. The simulation of the signal and backgrounds ($t\bar{t}X, Wjj, WX$) is based on the PYTHIA [358] and CompHEP [359] generators, along with the fast simulation package of CMS [360]. Requiring a central high-p_T muon, two central jets compatible with the W mass, two forward jets, and two rapidity gaps, the preliminary result is an efficiency of about 15 % for the signal and of less than 0.2 % for the backgrounds considered. A detailed investigation of the signal to background ratio is in progress.

In the ATLAS collaboration, it is planned to extend the parton-level study of Butterworth et al. [355] by an experimental analysis based on the ATLAS detector simulation.

4.5.3.2 Linear Collider

Two new studies of WW scattering at the Linear Collider [361, 362] proceeds along similar lines. In addition to the backgrounds considered in [349], the $\gamma\gamma$ production of top and W pairs is taken into account. Also the processes $e^-e^- \to W^-W^-$, $e^+e^- \to ZZe^+e^-$ and $e^+e^- \to WZe\nu$ will be considered.

Also a study of WWZ and ZZZ production in e^+e^- has started [363]. Also this study will use Whizard [364] and the fast simulation program SIMDET [191]. Both studies will be combined in a common fit for $\alpha_{4,5,6,7,10}$.

4.6 Scenarios where the LHC sees resonances

A LC can help interpret resonances that are seen in vector-boson scattering at the LHC. The LHC should be able to detect directly scalar and vector resonances with masses up to about $2\,\mathrm{TeV}$ [355]. Vector resonances with masses in this range induce anomalous values for α_2 and α_3 which can readily be measured at a $500\,\mathrm{GeV}$ LC [365]. In analogy with the pair-production of charged pions in e^+e^- annihilation near the ρ resonance, a form factor F_T can be used to describe the effects of vector resonances on the pair production of longitudinally polarised W bosons in e^+e^- annihilation. The real part of $F_T - 1$ is proportional to $\alpha_2 + \alpha_3$, and is related well below threshold to the masses of the vector resonances by [366]

$$F_T = 1 + s \sum_k \frac{a_k}{M_k^2}\,, \tag{4.46}$$

where $\sqrt{s}$ is the e^+e- centre of mass energy, M_k are the masses of the vector resonances ordered by $M_1 < M_2 < ...$, and a_k are their relative weights with $\sum a_k = 1$. In ordinary QCD with vector meson dominance, $a_1 \approx 1$.

A $500\,\mathrm{GeV}$ LC could measure the mass of a $1\,\mathrm{TeV}$ $(1.5\,\mathrm{TeV})$ vector resonance with an accuracy of $,\mathrm{GeV}$ $(27\,\mathrm{GeV})$ by measuring $\alpha_2 + \alpha_3$ under the assumption $a_1 = 1$. A measurement of $\alpha_2 + \alpha_3$ which was consistent with the mass of the LHC resonance would provide evidence for spin-1. By measuring both the real and imaginary parts of F_T a $500\,\mathrm{GeV}$ LC would also provide a measurement of the vector resonance width Γ_1 with an error of $19\,\mathrm{GeV}$ $(90\,\mathrm{GeV})$ for a $1\,\mathrm{TeV}$ $(1.5\,\mathrm{TeV})$ vector resonance.

It is also possible to drop the assumption $a_1 = 1$ and measure a_1 directly. Measurements of the real and imaginary parts of F_T at two different centre of mass energies can be used to extract a_1 along with the mass and width of the first vector resonance, assuming $M_1 \ll M_2$. With $250\,\mathrm{fb}^{-1}$ luminosity at $\sqrt{s} = 0.35\,\mathrm{TeV}$ and $250\,\mathrm{fb}^{-1}$ luminosity at $\sqrt{s} = 0.5\,\mathrm{TeV}$, the mass, width and weight parameter a_1 of a 1 TeV vector resonance can be measured with accuracies of 101 GeV, 26 GeV, and 26%, respectively.

At $\sqrt{s} = 1\,\mathrm{TeV}$ a LC would be sitting on top of a $1\,\mathrm{TeV}$ vector resonance and would measure the mass and width with a statistical accuracy of 0.08 GeV and 0.02 GeV, respectively, assuming $a_1 = 1$ and a luminosity of $1000\,\mathrm{fb}^{-1}$. Again, a_1 can be measured by combining results from two different centre of mass energies. Assuming $500\,\mathrm{fb}^{-1}$ luminosity at $\sqrt{s} = 0.5\,\mathrm{TeV}$ and $1000\,\mathrm{fb}^{-1}$ at $\sqrt{s} = 1\,\mathrm{TeV}$, the mass, width, and weight parameter a_1 of a 1 TeV vector resonance can be measured with accuracies of 0.08 GeV, 0.8 GeV, and 1.4%, respectively. If the vector resonance has a mass

of 1.5 TeV the same three parameters can be measured With accuracies of 44 GeV, 16 GeV, and 10%, respectively, assuming the same combination of LC energies and luminosities.

If the resonance which was being produced at the LHC were a scalar, then the $500\,\mathrm{GeV}$ LC would measure a value for $\alpha_2 + \alpha_3$ which was inconsistent with vector resonance production. Hence the $500\,\mathrm{GeV}$ LC result could rule out a spin-1 interpretation. A $0.8 - 1.0\,\mathrm{TeV}$ LC could also estimate the mass of a scalar resonance well above $1\,\mathrm{TeV}$ by measuring the enhancement in the vector-boson scattering cross-section due to a scalar resonance. The leading order correction to the Low Energy Theorem (LET) cross-section σ_{LET} for WW scattering due to a scalar resonance of mass M_0 is given by

$$\sigma(M_0) = \left(1 + \frac{8}{3}\frac{s}{M_0^2}\right)\sigma_{\mathrm{LET}}$$

where $\sqrt{s}$ is the WW centre of mass energy [367]. With $1\,\mathrm{ab}^{-1}$ at $\sqrt{s} = 1\,\mathrm{TeV}$ for example, a LC could measure the mass of a $1.5\,\mathrm{TeV}$ scalar resonance with a 17% accuracy [366].

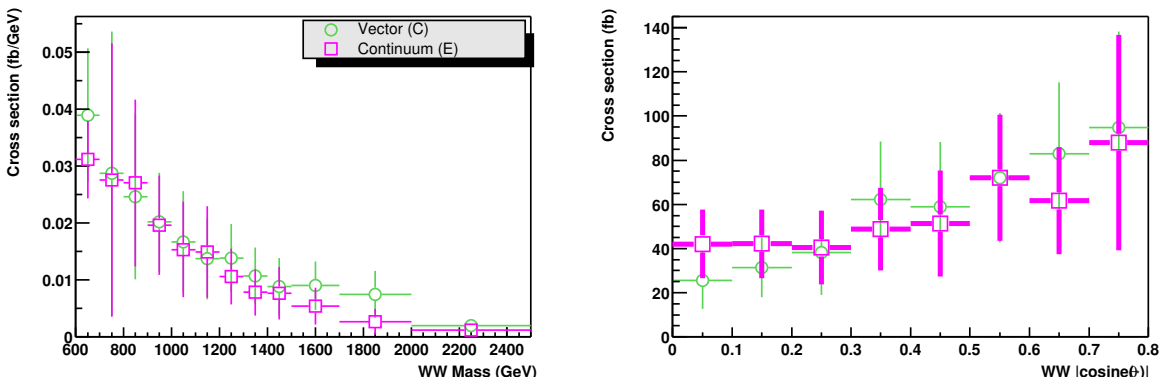

Figure 4.4: Differential cross section measurements at LHC assuming $100\,\mathrm{fb}^{-1}$ of luminosity and $\sqrt{s} = 14$ TeV: (left) $d\sigma/dM_{WW}$ and (right) $d\sigma/d|\cos\theta^*|$. The green circles are measurements assuming a single 1.9 TeV vector resonance, while the red squares are measurements assuming a model without resonances.

It is instructive to study in more detail a specific example. Figure 4.4 shows the precision with which the LHC can measure the WW scattering differential cross sections $d\sigma/dM_{WW}$ and $d\sigma/d|\cos\theta^*|$, where M_{WW} is the WW mass and $\cos\theta^*$ is the cosine of the W scattering angle in the WW rest frame [355]. Results for two WW scattering models are shown: a model with a single 1.9 TeV vector resonance and a model with no resonances. The precision with which the LHC can measure the mass, width, and peak cross section for a 1.9 TeV vector resonance can be obtained by fitting the $d\sigma/dM_{WW}$ distribution of Figure 4.4 to the sum of a polynomial and a Gaussian function. In order to obtain a lower bound on resonance parameter precision, it is assumed that the polynomial is fixed by sideband measurements, and that the only unknowns are the height, position, and width of the Gaussian function. The height of the Gaussian will be proportional to a_1^2, so that the Gaussian fit can be parameterised in terms of a_1, M_1, and Γ_1. The wide tilted green ellipse in the right hand side of Figure 4.5 is the projection of the 3-dimensional covariance ellipse for such a fit projected onto the

$M_1 - a_1$ plane. If the constraint $a_1 = 1$ is imposed, the 1σ error band on M_1 is given by the tall vertical blue band at $a_1 = 1$.

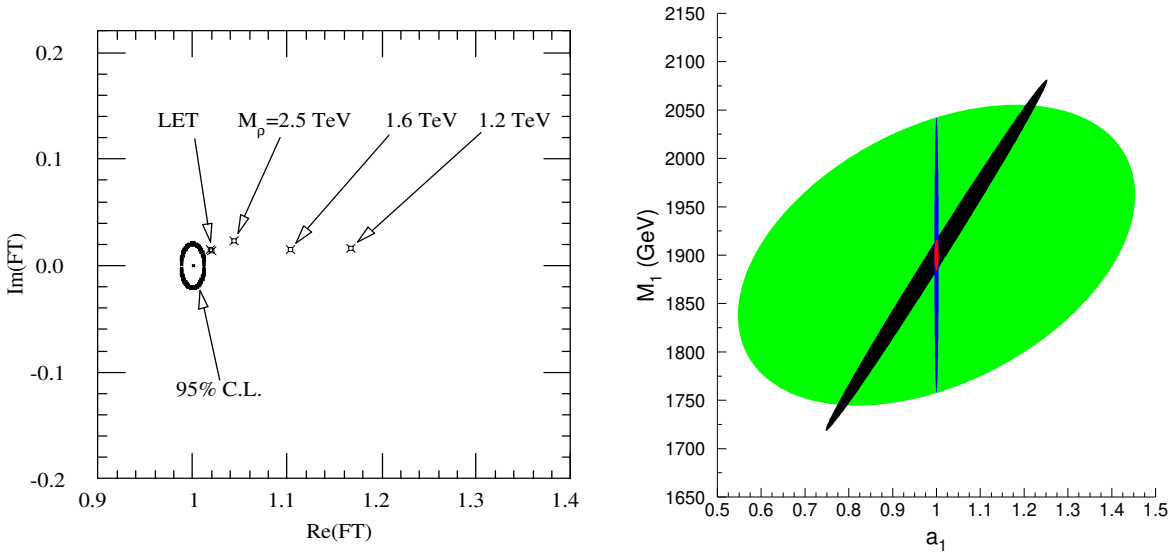

Figure 4.5: Left: The 95% C.L. contour for F_T measured at a LC with $\sqrt{s} = 500$ GeV and $500\,\mathrm{fb}^{-1}$, along with values of F_T for various vector resonance masses, assuming $a_1 = 1$. Right: Three dimensional covariance ellipses for fits of a_1, M_1, Γ_1 projected onto the $M_1 - a_1$ plane. The wide tilted green ellipse (narrow tilted black ellipse) is obtained from LHC (LC) measurements. If it is assumed that $a_1 = 1$ then the 1σ error for M_1 from the LHC (LC) is given by the tall blue (short red) vertical band at $a_1 = 1$.

The LC can help measure the properties of a 1.9 TeV vector resonance. The left hand side of Figure 4.5 shows the accuracy with which a $\sqrt{s} = 500$ GeV LC with $500\,\mathrm{fb}^{-1}$ can measure the form factor F_T, along with the predicted values of F_T for various vector resonance masses assuming $a_1 = 1$. The signal from a 1.9 TeV vector resonance would have a significance of 15σ, and so a $\sqrt{s} = 500$ GeV LC would establish the presence of a vector resonance. A three-parameter fit of a_1, M_1, and Γ_1 can be obtained by combining the LC measurement of F_T at $\sqrt{s} = 500$ GeV with a LC measurement of F_T at $\sqrt{s} = 1000$ GeV assuming a luminosity of $1000\,\mathrm{fb}^{-1}$. The projection of the covariance ellipse for this fit onto the $M_1 - a_1$ plane is given by the narrow tilted black ellipse in the right hand side of Figure 4.5. If the constraint $a_1 = 1$ is imposed then the 1σ error band on M_1 from LC measurements is given by the short vertical red band at $a_1 = 1$.

The LHC is sensitive to vector resonances up to a mass of $1.5\,\mathrm{GeV}$ [89]. The LC can distinguish the Standard Model from the Low Energy Theorem (LET) prediction with 3.7 standard deviations at $\sqrt{s} = 500\,\mathrm{GeV}$ ($\mathcal{L} = 500\mathrm{fb}^{-1}$) and with 10.7 standard deviations at $\sqrt{s} = 1000\,\mathrm{GeV}$ ($\mathcal{L} = 1000\,\mathrm{fb}^{-1}$). The LET prediction is given by the limit of infinite mass. The mass sensitivity is $2.5\,\mathrm{TeV}$ and $4.1\,\mathrm{TeV}$ for $\sqrt{s} = 500\,\mathrm{GeV}$ and $\sqrt{s} = 1000\,\mathrm{GeV}$, where the sensitivity is defines as the mass which can be separated with 3σ from the LET.

4.7 Conclusions

While it is tempting to numerically combine the results of the existing LHC and LC studies of strong WW scattering, this would be premature due to the mixed status of the theoretical and experimental approximations. For a meaningful comparison, it is essential that full six-fermion matrix elements are consistently used together with realistic detector simulations. In particular, the effective-W approximation which has been adopted for most of the LHC studies misses the electroweak radiation of transversally polarised W and Z bosons, which constitutes a numerically important background that needs to be taken into account.

Nevertheless, one can already draw the conclusion that in the low-energy range it will possible to measure anomalous couplings down to the natural scale $1/16\pi^2$. A combination of LC and LHC data will considerably increase the resolving power of the LHC. Furthermore, the direct sensitivity of the LHC to resonances in the range above $1\,\mathrm{TeV}$ can be fully exploited only if LC data on the cross section rise in the sub-TeV region are available.

5 Supersymmetric Models

In order to establish supersymmetry (SUSY) experimentally and to identify its underlying structure, comprehensive experimental information on the properties of new particles will be indispensable. For distinguishing SUSY from other possible kinds of new physics it will in particular be necessary to demonstrate that every particle has a superpartner, that their spins differ by $1/2$, that their gauge quantum numbers are the same, that their couplings are identical and that certain mass relations hold. The lightest supersymmetric particle (LSP) is an attractive candidate for cold Dark Matter in the Universe. Disentangling the underlying pattern of SUSY breaking and probing a possible SUSY nature of Dark Matter will require a detailed knowledge of the SUSY spectrum and a precise measurement of as many SUSY parameters as possible.

The information obtainable at the LHC and the LC will be highly complementary. The production of supersymmetric particles at the LHC will be dominated by the production of coloured particles, i.e. gluinos and squarks. Searches for the signature of jets and missing energy at the LHC will cover gluino and squark masses of up to 2–3 TeV [8]. The main handle to detect uncoloured particles will be from cascade decays of heavy gluinos and squarks, since in most SUSY scenarios the uncoloured particles are lighter than the coloured ones. Thus, fairly long decay chains giving rise to the production of several supersymmetric particles in the same event and leading to rather complicated final states can be expected to be a typical feature of SUSY production at the LHC. In fact, the main background for measuring SUSY processes at the LHC will be SUSY itself. The LC, on the other hand, has good prospects for the production of the light uncoloured particles. The clean signatures and small backgrounds at the LC as well as the possibility to adjust the energy of the collider to the thresholds at which SUSY particles are produced will allow a precise determination of the mass and spin of supersymmetric particles and of mixing angles and complex phases [9].

Many studies have been worked out that exemplify the possible synergy between the LHC and LC in exploring the phenomenology of supersymmetric models. In Section 5.1 it is studied in detail how input from the LC can improve the determination of particle masses, mixings and couplings at the LHC. The implications of the synergy between the LHC and LC for global fits in the MSSM are investigated in Section 5.2. Section 5.3 is devoted to the impact of LHC and LC results on exploring Dark Matter allowed regions of the parameter space and evaluating the Dark Matter relic density. The physics gain of the LHC / LC interplay is investigated for various SUSY scenarios in Section 5.4. In Section 5.5 it is analysed how different SUSY breaking scenarios can be discriminated based on the combined information from the LHC and LC, and the extrapolation to physics at high scales is discussed.

5.1 Measurement of supersymmetric particle masses, mixings and couplings at LHC and LC

The precise measurement of the masses of the largest possible set of supersymmetric particles is the most important input to the reconstruction of the supersymmetric theory, in particular of the SUSY breaking mechanism. At the LHC, the dominant production mechanism is pair production of gluinos or squarks and associated production of a gluino and a squark. For these processes, SUSY particle masses have to be calculated from the reconstruction of long decay chains which end in the LSP. Invariant masses can only be estimated from the endpoints (edges) of invariant mass spectra. In particular the LSP mass is only slightly constrained. This uncertainty propagates into the errors of the heavier SUSY particle masses.

At a LC, the colour–neutral part of the SUSY particle spectrum can be reconstructed with high precision if it is kinematically accessible. In particular, the LSP mass can be reconstructed with a precision significantly better than 1 GeV. If this and further LC measurements are input into the LHC mass fits, significant improvement on the masses which can only be accessed by the LHC (in particular squarks and gluinos) can be achieved.

The following studies focus on an analysis of the SUSY benchmark point SPS 1a, a typical mSugra scenario, but further model points are investigated as well in Section 5.1.3. The main features of the SPS 1a benchmark scenario are summarised in Section 5.1.1 for later reference. Section 5.1.2 outlines simulations for the reconstruction of a large set of SUSY particles in ATLAS. Section 5.1.3 describes the reconstruction of squarks and gluinos in CMS. In Section 5.1.4 SUSY searches at the LC are discussed and the experimental accuracies achievable in the SPS 1a scenario are analysed. The influence of LC mass measurements on the ATLAS and CMS analyses is discussed in detail in Section 5.1.5. In Section 5.1.6 it is demonstrated that LC predictions can be crucial for guiding the LHC search for the heaviest neutralino. In this way the heaviest neutralino can be identified at the LHC and its mass can be measured with high precision. Feeding this information back into the LC analysis leads to an improved accuracy in the determination of the SUSY parameters in the neutralino and chargino sector. Section 5.1.7 focusses on stop and sbottom reconstruction at the LHC using input from the LC.

So far only few detailed case studies for SUSY parameter determinations at LHC and LC exist. Further LC information such as decay branching ratios is likely to be helpful for an extraction of SUSY particle couplings at the LHC. While the studies performed so far have mostly been restricted to the SPS 1a benchmark point, which is a favourable scenario both for LHC and LC, examples of other possible scenarios should be investigated as well. It can be expected that also in this case important synergy effects will arise from the LHC / LC interplay.

5.1.1 The SPS 1a benchmark scenario

5.1.1.1 Introduction

In the unconstrained version of the Minimal Supersymmetric extension of the Standard Model (MSSM) no particular Supersymmetry (SUSY) breaking mechanism is

assumed, but rather a parametrisation of all possible soft SUSY breaking terms is used. This leads to more than a hundred parameters (masses, mixing angles, phases) in this model in addition to the ones of the Standard Model. For performing detailed simulations of experimental signatures within detectors of high-energy physics experiments it is clearly not practicable to scan over a multi-dimensional parameter space. One thus often concentrates on certain "typical" benchmark scenarios.

The "Snowmass Points and Slopes" (SPS) [14] are a set of benchmark points and parameter lines in the MSSM parameter space corresponding to different scenarios in the search for Supersymmetry at present and future experiments. The SPS 1a reference point is a "typical" parameter point of the minimal supergravity (mSUGRA) scenario. It gives rise to a particle spectrum where many states are accessible both at the LHC and the LC, corresponding to a rather favourable scenario for phenomenology at LHC and LC. The SPS 1a benchmark scenario has been studied with detailed experimental simulations at both colliders.

Since for no other parameter point in the MSSM a similar amount of information about the experimental capabilities of both the LHC and the LC is available, most analyses performed in the context of the LHC / ILC Study Group have focussed on this particular parameter point. It should be kept in mind, however, that the interplay between LHC and LC could be qualitatively very different in different regions of the MSSM parameter space. In order to allow a quantitative assessment of the LHC / LC interplay also for other parameter regions, more experimental simulations for LHC and LC are required.

5.1.1.2 Definition of the SPS 1a benchmark point

The SPS benchmark points are defined in terms of low-energy MSSM parameters. The benchmark values for the SPS 1a point are the following (all mass parameters are given in GeV) [14, 368]. The gluino mass $M_{\tilde{g}}$, the Supersymmetric Higgs mass parameter μ, the mass of the CP-odd Higgs boson M_A, the ratio of the vacuum expectation values of the two Higgs doublets $\tan\beta$, and the electroweak gaugino mass parameters M_1 and M_2 have the values

$$M_{\tilde{g}} = 595.2, \quad \mu = 352.4, \quad M_A = 393.6, \quad \tan\beta = 10, \quad M_1 = 99.1, \quad M_2 = 192.7. \tag{5.1}$$

The soft SUSY-breaking parameters in the diagonal entries of the squark and slepton mass matrices have been chosen to be the same for the first and second generation. They have the values (these parameters are approximately equal to the sfermion masses; the off-diagonal entries have been neglected for the first two generations; the index i in $M_{\tilde{q}i_L}$ refers to the generation)

$$M_{\tilde{q}1_L} = M_{\tilde{q}2_L} = 539.9, \quad M_{\tilde{d}_R} = 519.5, \quad M_{\tilde{u}_R} = 521.7, \quad M_{\tilde{e}_L} = 196.6, \quad M_{\tilde{e}_R} = 136.2. \tag{5.2}$$

The soft SUSY-breaking parameters in the diagonal entries of the squark and slepton mass matrices of the third generation have the values

$$M_{\tilde{q}3_L} = 495.9, \quad M_{\tilde{b}_R} = 516.9, \quad M_{\tilde{t}_R} = 424.8, \quad M_{\tilde{\tau}_L} = 195.8, \quad M_{\tilde{\tau}_R} = 133.6, \tag{5.3}$$

while the trilinear couplings of the third generation read

$$A_t = -510.0, \quad A_b = -772.7, \quad A_\tau = -254.2. \tag{5.4}$$

All mass parameters for the benchmark point SPS 1a are to be understood as defined in the $\overline{\rm DR}$ scheme at the scale $Q = 453.6$ GeV. The value of the top-quark mass for all SPS benchmarks is chosen to be $m_t = 175$ GeV.

As mentioned above, these low-energy parameters correspond to a "typical" mSUGRA point with an intermediate value of $\tan\beta$. In order to obtain these low-energy parameters from the high-scale parameters m_0, $m_{1/2}$, A_0 of the mSUGRA scenario a particular code had to be chosen. For the SPS benchmarks this was version 7.58 of the program *ISAJET* [77]. Once the low-energy parameters have been fixed, this choice is no longer relevant. The mSUGRA parameters used for generating the SPS 1a benchmark values are

$$m_0 = 100\text{GeV}, \quad m_{1/2} = 250\text{GeV}, \quad A_0 = -100\text{GeV}, \quad \tan\beta = 10, \quad \mu > 0. \tag{5.5}$$

5.1.1.3 Particle spectrum and decay modes

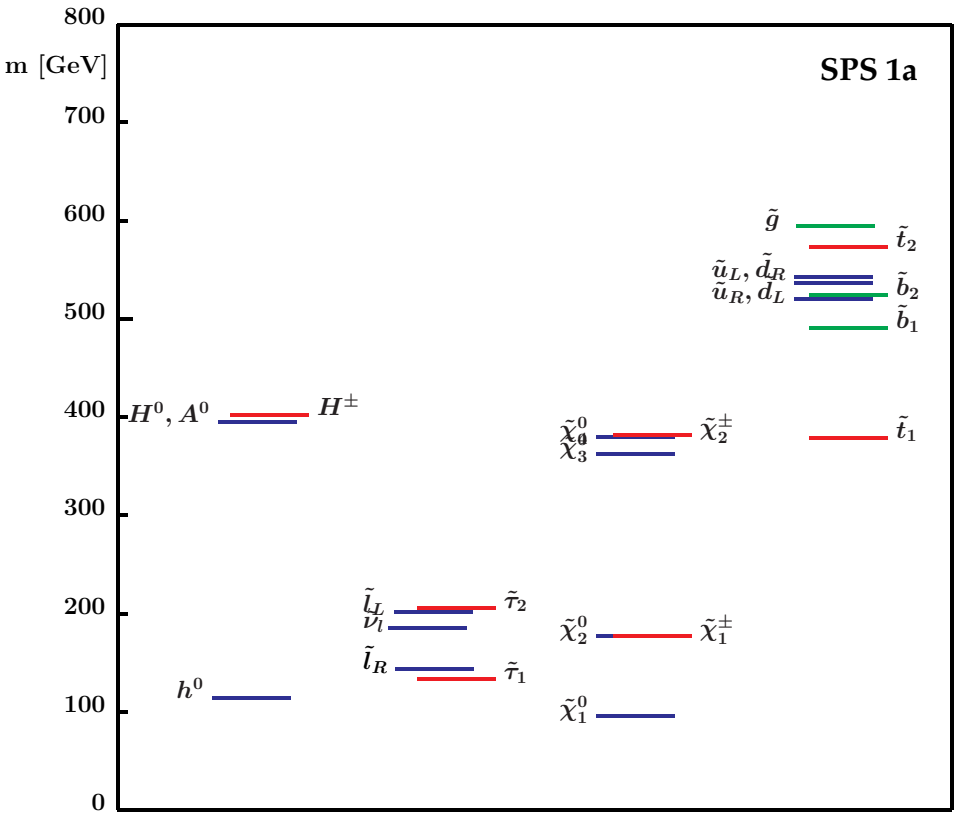

Figure 5.1: The mass spectrum corresponding to the SPS 1a benchmark scenario (from Ref. [369]).

While the low-energy MSSM parameters have been fixed as benchmarks by definition, the particle spectra, branching ratios, etc. for the SPS points should be calculated with an appropriate program according to the specific requirements of the

analysis that is being performed. For simplicity, the spectrum shown in Fig. 5.1 and the branching ratios of the SUSY particles and the Higgs bosons listed in Tab. 5.1–5.4, see Ref. [369], have been obtained with *ISAJET* 7.58, although parts of this code are not state-of-the-art. The resulting spectra and branching ratios have been widely used for exploring the physics potential of LHC and LC.

$\tilde{\ell}$	m [GeV]	decay	$\mathcal{B}$
$\tilde{e}_R$	143.0	$\tilde{\chi}_1^0 e^-$	1.000
$\tilde{e}_L$	202.1	$\tilde{\chi}_1^0 e^-$	0.490
		$\tilde{\chi}_2^0 e^-$	0.187
		$\tilde{\chi}_1^- \nu_e$	0.323
$\tilde{\nu}_e$	186.0	$\tilde{\chi}_1^0 \nu_e$	0.885
		$\tilde{\chi}_2^0 \nu_e$	0.031
		$\tilde{\chi}_1^+ e^-$	0.083
$\tilde{\mu}_R$	143.0	$\tilde{\chi}_1^0 \mu^-$	1.000
$\tilde{\mu}_L$	202.1	$\tilde{\chi}_1^0 \mu^-$	0.490
		$\tilde{\chi}_2^0 \mu^-$	0.187
		$\tilde{\chi}_1^- \nu_\mu$	0.323
$\tilde{\nu}_\mu$	186.0	$\tilde{\chi}_1^0 \nu_\mu$	0.885
		$\tilde{\chi}_2^0 \nu_\mu$	0.031
		$\tilde{\chi}_1^+ \mu^-$	0.083
$\tilde{\tau}_1$	133.2	$\tilde{\chi}_1^0 \tau^-$	1.000
$\tilde{\tau}_2$	206.1	$\tilde{\chi}_1^0 \tau^-$	0.526
		$\tilde{\chi}_2^0 \tau^-$	0.174
		$\tilde{\chi}_1^- \nu_\tau$	0.300
$\tilde{\nu}_\tau$	185.1	$\tilde{\chi}_1^0 \nu_\tau$	0.906
		$\tilde{\chi}_1^+ \tau^-$	0.067

Table 5.1: Slepton masses and significant branching ratios ($\mathcal{B} > 3\%$) in SPS 1a (from Ref. [369]).

$\tilde{\chi}$	m [GeV]	decay	$\mathcal{B}$
$\tilde{\chi}_1^0$	96.1		
$\tilde{\chi}_2^0$	176.8	$\tilde{e}_R^\pm e^\mp$	0.062
		$\tilde{\mu}_R^\pm \mu^\mp$	0.062
		$\tilde{\tau}_1^\pm \tau^\mp$	0.874
$\tilde{\chi}_3^0$	358.8	$\tilde{\chi}_1^\pm W^\mp$	0.596
		$\tilde{\chi}_1^0 Z^0$	0.108
		$\tilde{\chi}_2^0 Z^0$	0.215
$\tilde{\chi}_4^0$	377.8	$\tilde{\chi}_1^\pm W^\mp$	0.526
		$\tilde{\chi}_1^0 h^0$	0.064
		$\tilde{\chi}_2^0 h^0$	0.134

$\tilde{\chi}$	m [GeV]	decay	$\mathcal{B}$
$\tilde{\chi}_1^+$	176.4	$\tilde{\tau}_1^+ \nu_\tau$	0.979
$\tilde{\chi}_2^+$	378.2	$\tilde{\chi}_1^0 W^+$	0.064
		$\tilde{e}_L^+ \nu_e$	0.052
		$\tilde{\mu}_L^+ \nu_\mu$	0.052
		$\tilde{\tau}_2^+ \nu_\tau$	0.056
		$\tilde{\chi}_1^+ Z^0$	0.244
		$\tilde{\chi}_1^+ h^0$	0.170

Table 5.2: Neutralino and chargino masses and significant branching ratios ($\mathcal{B} > 3\%$) in SPS 1a (from Ref. [369]).

The SPS 1a scenario yields a sparticle spectrum, see Fig. 5.1, of which many states are accessible both at LHC and LC. Experimentally important and challenging, however, are the τ-rich neutralino and chargino decays, see Tab. 5.2. This is a generic feature of SUSY scenarios with intermediate or large values of $\tan\beta$ (the parameter space at smaller values of $\tan\beta$ is severely constrained by the exclusion bounds from the LEP Higgs searches [1,370]). A non-negligible mixing leads to a significant mass splitting between the two staus so that the lighter stau becomes the lightest slepton. Neutralinos and charginos therefore decay predominantly into staus and taus, which is experimentally more challenging than the dilepton signal resulting for instance from the decay of the second lightest neutralino into the lightest neutralino and a pair of leptons of the first or the second generation. This effect becomes more pronounced for larger values of $\tan\beta$.

$\tilde{q}$	m [GeV]	decay	$\mathcal{B}$
$\tilde{t}_1$	379.1	$\tilde{\chi}_1^0 t$	0.179
		$\tilde{\chi}_2^0 t$	0.095
		$\tilde{\chi}_1^+ b$	0.726
$\tilde{t}_2$	574.7	$\tilde{\chi}_1^+ b$	0.206
		$\tilde{\chi}_2^+ b$	0.216
		$Z^0 \tilde{t}_1$	0.225
		$h^0 \tilde{t}_1$	0.042
		$\tilde{\chi}_1^0 t$	0.030
		$\tilde{\chi}_2^0 t$	0.080
		$\tilde{\chi}_3^0 t$	0.033
		$\tilde{\chi}_4^0 t$	0.166

$\tilde{q}$	m [GeV]	decay	$\mathcal{B}$
$\tilde{b}_1$	491.9	$\tilde{\chi}_1^0 b$	0.062
		$\tilde{\chi}_2^0 b$	0.362
		$\tilde{\chi}_1^- t$	0.428
		$W^- \tilde{t}_1$	0.133
$\tilde{b}_2$	524.6	$\tilde{\chi}_1^0 b$	0.148
		$\tilde{\chi}_2^0 b$	0.171
		$\tilde{\chi}_3^0 b$	0.053
		$\tilde{\chi}_4^0 b$	0.072
		$\tilde{\chi}_1^- t$	0.213
		$W^- \tilde{t}_1$	0.344

Table 5.3: Stop and sbottom masses and significant branching ratios ($\mathcal{B} > 3\%$) in SPS 1a (from Ref. [369]).

Concerning the compatibility of the benchmark scenario with external constraints, severe restrictions on the MSSM parameter space arise from the requirement that the lightest SUSY particle should give rise to an acceptable dark matter density. The SPS 1a parameter values give rise to a dark matter density in what used to be the "bulk" region of the allowed mSUGRA parameter space. Taking into account the recent precision data from the WMAP Collaboration [20,21], the dark matter density corresponding to the SPS 1a point is slightly outside the allowed region. However, shifting the low-energy MSSM parameters of the SPS 1a point in order to make them fully compatible with the most recent WMAP bound would hardly affect the collider phenomenology of the SPS 1a scenario. It should furthermore be mentioned in this context that allowing a small amount of R-parity violation in the model would leave the collider phenomenology essentially unchanged, while having a drastic impact on the constraints from dark matter relic abundance. The SPS 1a benchmark scenario is in satisfactory agreement with all other experimental constraints.

Higgs	m [GeV]	decay	$\mathcal{B}$
h^0	114.0	$\tau^-\tau^+$	0.051
		$b\bar{b}$	0.847
		$c\bar{c}$	0.035
H^0	394.1	$\tau^-\tau^+$	0.059
		$b\bar{b}$	0.807
		$t\bar{t}$	0.031
		$\tilde{\chi}_1^0\tilde{\chi}_2^0$	0.034
A^0	393.6	$\tau^-\tau^+$	0.049
		$b\bar{b}$	0.681
		$t\bar{t}$	0.092
		$\tilde{\chi}_1^0\tilde{\chi}_2^0$	0.065
		$\tilde{\chi}_2^0\tilde{\chi}_2^0$	0.058
H^+	401.8	$\nu_\tau\tau^+$	0.077
		$t\bar{b}$	0.770
		$\tilde{\chi}_1^+\tilde{\chi}_1^0$	0.130

Table 5.4: Higgs masses and significant branching ratios ($\mathcal{B} > 3\%$) in SPS 1a (from Ref. [369]).

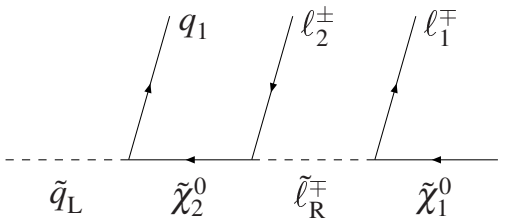

Figure 5.2: A squark decay chain for SPS 1a, where $m_{\tilde{q}_{\mathrm{L}}} \in \{491.9, 537.2, 543.0\}$ GeV, $m_{\tilde{\chi}_2^0} = 176.82$ GeV, $m_{\tilde{\ell}_{\mathrm{R}}} = 142.97$ GeV, $m_{\tilde{\chi}_1^0} = 96.05$ GeV.

5.1.2 A detailed analysis of the measurement of SUSY masses with the ATLAS detector at the LHC

5.1.2.1 Introduction

We here describe a series of analyses performed on Point SPS 1a [14], characterized by the SUGRA parameters

$$\begin{aligned} m_0 = 100\,\mathrm{GeV}, \qquad m_{1/2} = 250\,\mathrm{GeV}, \\ \tan\beta = 10, \qquad A = -100\,\mathrm{GeV}, \qquad \mu > 0, \end{aligned} \tag{5.6}$$

with the aim of providing an input to the studies which evaluate the complementarity of the LHC and of the LC.

5.1.2.2 Analysis of kinematic edges involving $\tilde{\chi}_2^0 \to \tilde{l}_R l$

In this scenario the total SUSY cross section is rather large, and at the LHC squarks and gluinos will be produced abundantly. The gluino is the heaviest particle and decays to a squark and a quark. The squarks decay to neutralinos and charginos, which in turn decay to sleptons or lighter neutralinos and charginos. The sleptons then decay into the LSP, $\tilde{\chi}_1^0$.

Since the LSP will escape detection, it is not a straightforward task to reconstruct SUSY events. A possible approach is to use kinematic edges [14, 89]. Particularly interesting is the decay $\tilde{\chi}_2^0 \to \tilde{l}_R l \to l^+ l^- \tilde{\chi}_1^0$. The two leptons in the final state provide a natural trigger, and the energy resolution is high.

While right-handed squarks decay directly to the LSP, due to the bino-like nature of the χ_1^0 at SPS 1a, left-handed squarks decay to $\tilde{\chi}_2^0$ with a branching ratio $\sim 32\%$. We will in this analysis look at the decay chain shown in Fig. 5.2,

$$\tilde{q}_L \underset{\sim 32\%}{\longrightarrow} q\tilde{\chi}_2^0 \underset{12.1\%}{\longrightarrow} q l_2^{\pm} \tilde{l}_R^{\mp} \underset{100\%}{\longrightarrow} q l_2^{\pm} l_1^{\mp} \tilde{\chi}_1^0 \tag{5.7}$$

where $\tilde{q}_L$ can be $\tilde{d}_L$, $\tilde{u}_L$, $\tilde{b}_2$ or $\tilde{b}_1$. The first two have very similar masses, $m_{\tilde{d}_L} = 543.0$ GeV and $m_{\tilde{u}_L} = 537.2$ GeV, and will in this analysis be grouped together and referred to as $\tilde{q}_L$. For the fraction of the chain in Eq. (5.2) which starts with a sbottom, $\tilde{b}_1$ is responsible for 78%, leaving us insensitive to the contribution from $\tilde{b}_2$. Decay chains involving the stop are not considered. The production cross section of the relevant squarks and their branching fractions to $\tilde{\chi}_2^0$ are

$$\sigma(\tilde{q}_L) = 33\,\mathrm{pb}, \quad BR(\tilde{q}_L \to q\tilde{\chi}_2^0) = 31.4\%$$

$$\sigma(\tilde{b}_1) = 7.6 \text{ pb}, \quad BR(\tilde{b}_1 \to b\tilde{\chi}_2^0) = 35.5\% \tag{5.8}$$

with many of the squarks coming from gluino decay. The stau is the lightest slepton, so it has the largest branching ratio. In this analysis we will however only use final states with electrons and muons.

We shall discuss the precision that can be achieved in the determination of this spectrum at the LHC, reconstructing it back to the squark mass, from measurements of various kinematic edges and thresholds of subsets of decay products. In particular, we shall determine how this precision can be improved with input from a Linear Collider [9].

Kinematics The invariant masses of various subsets of particles can be determined from kinematical edges and thresholds, as discussed in [371],

$$\left(m_{ll}^2\right)^{\text{edge}} = \frac{\left(m_{\tilde{\chi}_2^0}^2 - m_{\tilde{l}_R}^2\right)\left(m_{\tilde{l}_R}^2 - m_{\tilde{\chi}_1^0}^2\right)}{m_{\tilde{l}_R}^2} \tag{5.9}$$

$$\left(m_{qll}^2\right)^{\text{edge}} = \frac{\left(m_{\tilde{q}_L}^2 - m_{\tilde{\chi}_2^0}^2\right)\left(m_{\tilde{\chi}_2^0}^2 - m_{\tilde{\chi}_1^0}^2\right)}{m_{\tilde{\chi}_2^0}^2} \tag{5.10}$$

$$\left(m_{ql}^2\right)_{\text{min}}^{\text{edge}} = \frac{\left(m_{\tilde{q}_L}^2 - m_{\tilde{\chi}_2^0}^2\right)\left(m_{\tilde{\chi}_2^0}^2 - m_{\tilde{l}_R}^2\right)}{m_{\tilde{\chi}_2^0}^2} \tag{5.11}$$

$$\left(m_{ql}^2\right)_{\text{max}}^{\text{edge}} = \frac{\left(m_{\tilde{q}_L}^2 - m_{\tilde{\chi}_2^0}^2\right)\left(m_{\tilde{l}_R}^2 - m_{\tilde{\chi}_1^0}^2\right)}{m_{\tilde{l}_R}^2} \tag{5.12}$$

$$\begin{aligned}\left(m_{qll}^2\right)^{\text{thres}} = {} & [(m_{\tilde{q}_L}^2 + m_{\tilde{\chi}_2^0}^2)(m_{\tilde{\chi}_2^0}^2 - m_{\tilde{l}_R}^2)(m_{\tilde{l}_R}^2 - m_{\tilde{\chi}_1^0}^2) \\ & -(m_{\tilde{q}_L}^2 - m_{\tilde{\chi}_2^0}^2)\sqrt{(m_{\tilde{\chi}_2^0}^2 + m_{\tilde{l}_R}^2)^2(m_{\tilde{l}_R}^2 + m_{\tilde{\chi}_1^0}^2)^2 - 16m_{\tilde{\chi}_2^0}^2 m_{\tilde{l}_R}^4 m_{\tilde{\chi}_1^0}^2} \\ & +2m_{\tilde{l}_R}^2(m_{\tilde{q}_L}^2 - m_{\tilde{\chi}_2^0}^2)(m_{\tilde{\chi}_2^0}^2 - m_{\tilde{\chi}_1^0}^2)]/(4m_{\tilde{l}_R}^2 m_{\tilde{\chi}_2^0}^2)\end{aligned} \tag{5.13}$$

where "min" and "max" refer to minimising and maximising w.r.t. the choice of lepton. Furthermore "thres" refers to the threshold in the subset of the m_{qll} distribution for which the angle between the two lepton momenta (in the slepton rest frame) exceeds $\pi/2$, which corresponds to $m_{ll}^{\text{edge}}/\sqrt{2} < m_{ll} < m_{ll}^{\text{edge}}$.

Monte Carlo simulations In order to assess quantitatively the precision that can be achieved, we have performed Monte Carlo simulations of SUSY production at SPS 1a, using the `PYTHIA 6.2` program [372] and passing the particles through the `ATLFAST` detector simulation [373] before reconstructing invariant masses. We have used a sample corresponding to 100 fb^{-1}, one year at design luminosity. The results documented in this section have been found to be in agreement with results obtained using `HERWIG` [376].

The cuts used to isolate the chain were the following

- At least four jets, the hardest three satisfying:
  $p_{T,1} > 150$ GeV, $p_{T,2} > 100$ GeV, $p_{T,3} > 50$ GeV.
- $M_{\text{eff}} \equiv E_{T,\text{miss}} + p_{T,1} + p_{T,2} + p_{T,3} + p_{T,4} > 600$ GeV

- $E_{T,\mathrm{miss}} > \max(100\ \mathrm{GeV}, 0.2M_{\mathrm{eff}})$

- Two isolated Opposite–Sign Same–Flavour (OS-SF) leptons (not τ) satisfying $p_T(l) > 20\ \mathrm{GeV}$ and $p_T(l) > 10\ \mathrm{GeV}$.

The basic signature of our decay chain are two OS-SF leptons. Two such leptons can also be produced in other processes. If the two leptons are independent of each other, one would expect equal amounts of OS-SF leptons and Opposite–Sign Opposite–Flavour (OS-OF) leptons. Their distributions should also be identical. This allows us to remove the background OS-SF contribution by subtracting the OS-OF events.

In addition to the two OS-SF leptons, our signal event will typically have considerable missing E_T and two very hard jets, one from the decay of the squark in the chain we try to reconstruct, one from the decay of the squark in the other chain.

The only Standard Model process to have all the features of our signal event, is $t\bar{t}$ production where both W's decay leptonically. However, with some help from the underlying event, pile-up and detector effects, other processes might also result in the signatures above. Together with $t\bar{t}$, we therefore considered the following PYTHIA processes: QCD, Z/W+jet, $ZZ/ZW/WW$.

The QCD processes are cut away by the requirement of two leptons and of considerable missing E_T. For the processes involving Z and W the requirement of high hadronic activity together with missing E_T, removes nearly all events. The only Standard Model background to survive the rather hard cuts listed above, is a small fraction of $t\bar{t}$ events. However, the rate of W^+W^- (from the decay of t and $\bar{t}$) going to $e^{\pm}\mu^{\mp}$ is identical to that going to $e^+e^-/\mu^+\mu^-$, so with the subtraction of OS-OF events the $t\bar{t}$ sample gives no net contribution to the mass distribution, only some minor contribution to the fluctuations.

In Fig. 5.3 the invariant mass of the two leptons for events passing the cuts is plotted. The Standard Model background is clearly negligible. The real background to our decay chain consists of other SUSY processes, and as is illustrated in Fig. 5.3, these are effectively removed by the OS-OF subtraction. This subtraction is also included for the invariant mass distribution in Fig. 5.4.

The edge value for m_{ll}, Fig. 5.3, is very accurately determined by fitting it to a triangular shape with Gaussian smearing. For the other distributions, Fig. 5.4, the end points are found with a naive linear fit. This method is known not to be optimal. In fact, by changing the binning or the range fitted, the fit values may change by typically a few GeV. For a more realistic situation one would need to investigate more thoroughly how the theoretical distributions are distorted by sparticle widths, by the detector resolution and the cuts applied. As already discussed in [371], it is not possible at the level of the present studies to perform a detailed estimate of the corresponding systematic errors, therefore we include only the statistical errors from the fitting procedure for each edge. In addition one has the systematic error on the energy scale. We use the ATLAS benchmark values, 0.1% for leptons and 1% for jets. The resulting values for the endpoints and the corresponding errors are given in table 5.5.

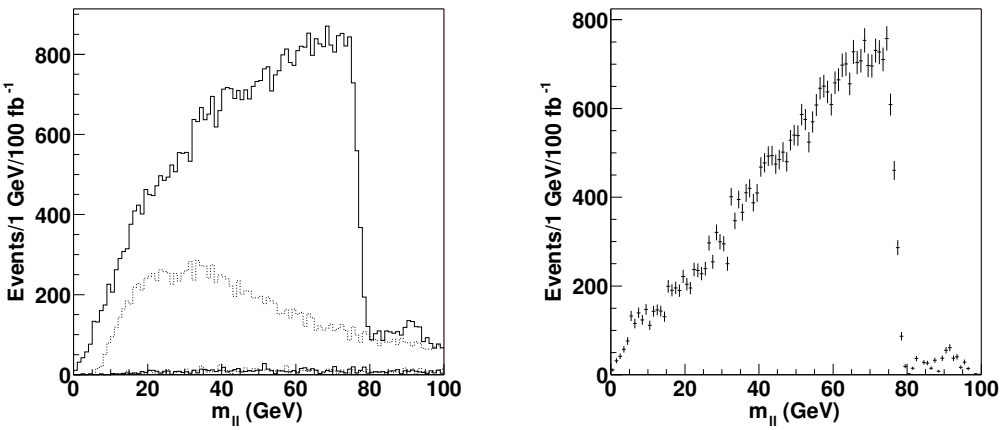

Figure 5.3: Effect of subtracting background leptons, for $\int \mathcal{L}dt = 100$ fb^{-1}. Left: Solid: OS-SF, Dotted: OS-OF, Two upper curves: SUSY+SM, two lower curves: SM alone; Right: OS-SF−OS-OF. The triangular shape of the theoretical expectation is reproduced.

Table 5.5: Endpoint values found from fitting the edges in Fig. 5.3 and Fig. 5.4, for 100 fb^{-1}.

Edge	Nominal Value	Fit Value	Syst. Error Energy Scale	Statistical Error
$m(ll)^{\mathrm{edge}}$	77.077	77.024	0.08	0.05
$m(qll)^{\mathrm{edge}}$	431.1	431.3	4.3	2.4
$m(ql)^{\mathrm{edge}}_{\mathrm{min}}$	302.1	300.8	3.0	1.5
$m(ql)^{\mathrm{edge}}_{\mathrm{max}}$	380.3	379.4	3.8	1.8
$m(qll)^{\mathrm{thres}}$	203.0	204.6	2.0	2.8
$m(bll)^{\mathrm{thres}}$	183.1	181.1	1.8	6.3

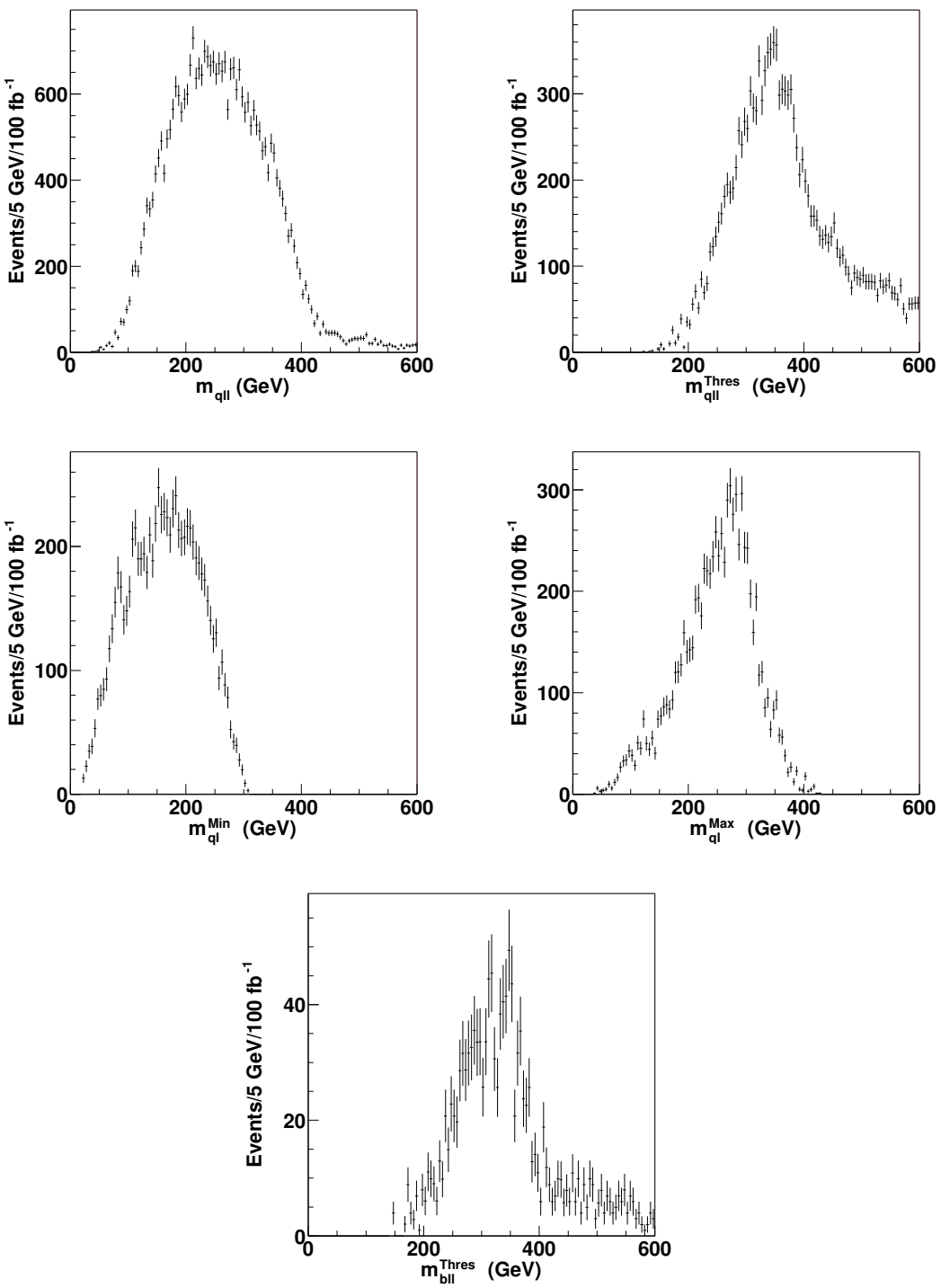

Figure 5.4: Invariant mass distributions with kinematical endpoints, for $\int \mathcal{L}dt = 100$ fb^{-1}.

5.1.2.3 Gluino mass measurement

In the considered point the gluino decays through $\tilde{g} \to \tilde{q}q$, where $\tilde{q}$ is any squark flavour, except $\tilde{t}_2$, for which the decay $\tilde{g} \to \tilde{t}_2 t$ is kinematically forbidden. Thus the reconstruction of the gluino can be attempted adding a quark to an identified $\tilde{q}_L$ decay chain. A particularly favorable situation happens with the b squarks, for which the decay chain includes two b-jets which can be tagged, thereby reducing the combinatorial background. In addition to the cuts given in section 5.1.2.2 we require:

- the invariant mass of the OS-SF lepton pair should be larger than 65 GeV, and lower than the edge shown in Fig. 5.3.
- Exactly two jets tagged as b, of which one must be among the two leading jets in the event, and the second one must have $p_T > 50$ GeV.

Using a technique described e.g. in [89], the $\tilde{\chi}_2^0$ momentum can be approximated by the expression:

$$\vec{p}(\tilde{\chi}_2^0) = \left(1 - \frac{m(\tilde{\chi}_1^0)}{m(\ell\ell)}\right) \vec{p}_{\ell\ell}$$

where $\vec{p}_{\ell\ell}$ is the vector of the sum of the momenta of the two leptons. This approximation works reasonably well for the Point under study as the $\tilde{\chi}_1^0$ momentum is close to zero in the $\tilde{\chi}_2^0$ rest frame near the end-point. For situations with $\tilde{\ell}_R$ close in mass either to $\tilde{\chi}_2^0$ or $\tilde{\chi}_1^0$, this assumption is not justified anymore. If the masses of the $\tilde{\chi}_1^0$ and of the $\tilde{\chi}_2^0$ are known, one can thus calculate the $\tilde{b}$ mass as $m(\tilde{\chi}_2^0 b)$, and the $\tilde{g}$ mass as $m(\tilde{\chi}_2^0 bb)$. The lower cut on $m_{\ell\ell}$ is chosen such as to to optimize the precision on the $\tilde{\chi}_2^0$ momentum, while retaining a reasonable statistics for the analysis. We plot in Fig 5.5 the flavour-subtracted distribution of $m(\tilde{\chi}_2^0 b)$ versus $m(\tilde{\chi}_2^0 bb)$, for both b jets, assuming the nominal values for $m(\tilde{\chi}_1^0)$ and $m(\tilde{\chi}_2^0)$. Two well-separated regions appear in the plot, of which one corresponds to the correct $\tilde{\chi}_2^0 b$ pairing for the reconstruction of the $\tilde{b}$, and shows a strong correlation between the $\tilde{g}$ and the $\tilde{b}$ mass. The second region corresponds to the situation in which $m(\tilde{\chi}_2^0 b)$ is calculated taking the b-jet from the $\tilde{g} \to b\tilde{b}$ decay. We select the interesting region on the 2-dimensional plot by requiring $380 < m(\tilde{\chi}_2^0 b) < 600$ GeV, and $m(\tilde{\chi}_2^0 bb) - m(\tilde{\chi}_2^0 b) > 150$ GeV. The main residual background consists where the cascade identified by OS-SF the lepton pair originates from a squark of the first four generations, and the leading b is part of a different cascade. We suppress this background by requiring that the invariant mass of the $\tilde{\chi}_2^0$ with the leading jet not tagged as b is outside of the interval 400 GeV to 600 GeV. The $m(\tilde{\chi}_2^0 bb)$ after these cuts is shown in Fig. 5.6. Superimposed in blue is the residual background. The width of the distribution is dominated by the $\tilde{\chi}_2^0$ momentum mismeasurement. The statistical uncertainty on the peak position is ~ 4 GeV for 100 fb^{-1} and ~ 2.5 GeV for 300 fb^{-1}, and the central value is ~ 10 GeV lower than the nominal $\tilde{g}$ mass. The displacement of the fit value from the nominal value is related to an underestimate of the energy of part of the b jets.

For this analysis we assume that both $\tilde{\chi}_1^0$ and $\tilde{\chi}_2^0$ would be measured with the technique described in the previous section. As already discussed above, this results in a strong correlation between the measured $\tilde{\chi}_1^0$ and $\tilde{\chi}_2^0$ masses which can be parametrized as:

$$m(\tilde{\chi}_2^0) = 82.85 + 0.977 \times m(\tilde{\chi}_1^0)$$

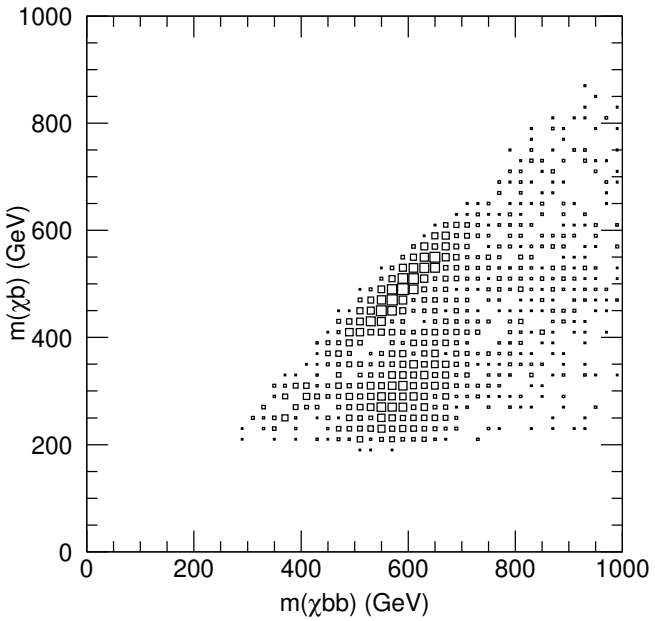

Figure 5.5: Distribution of $m(\tilde{\chi}_2^0 b)$ versus $m(\tilde{\chi}_2^0 bb)$ for events passing the selections.

Therefore, to evaluate the dependence of the measured gluino mass on the assumed $\tilde{\chi}_1^0$ and $\tilde{\chi}_2^0$ masses, we varied only the $\tilde{\chi}_1^0$ mass between 76 and 116 GeV, and the $\tilde{\chi}_2^0$ mass was taken from the above parametrization. For each value of $m(\tilde{\chi}_1^0)$ we performed a full gluino mass evaluation. The results are shown in Fig. 5.7. There is a clear linear dependence of the estimated gluino mass on the $m(\tilde{\chi}_1^0)$ which can be parametrized as:

$$m(\tilde{g}) = 500 + 0.988 \times m(\tilde{\chi}_1^0)$$

The further step in the analysis is the measurement of the mass of the sbottom quark. The gluino decays both to $\tilde{b}_1$ and $\tilde{b}_2$, the selected events are therefore a mixture of the two decay channels. We first select events for which only one of the two possible $m(\chi_2^0 b)$ combinations passes the selection cuts. As clearly seen from Fig. 5.5, the spread due to the approximation on the $\tilde{\chi}_2^0$ momentum measurement affects in the same way the gluino and sbottom mass measurement, and it can to a large extent be factored out by studying the difference $m(\tilde{\chi}_2^0 bb) - m(\tilde{\chi}_2^0 b)$.

The resulting distribution is shown in Fig. 5.8 for an integrated luminosity of 300 fb^{-1}. The observed events, after lepton flavour subtraction, are shown as black dots with error bars. In color we show the different contributions: $\tilde{g} \to \tilde{b}_1 b$ (green), $\tilde{g} \to \tilde{b}_2 b$ (blue), and background (red). The distribution is wider than could be expected from a single resonance. However, the dominant distribution for $\tilde{g} \to \tilde{b}_1 b$ has a non-gaussian shape, because of the mismeasurement of part of the b-jets. In order to experimentally distinguish the two peaks, a detailed understanding of the response function of the detector to b-jets is needed. For the present work, assuming the presence of two peaks, we naively fit the observed distribution to the sum of two gaussian functions. The results are shown in Fig. 5.9, where two peaks separated by approximately the expected ~ 35 GeV are found by the fit. The statistical errors from the fit are

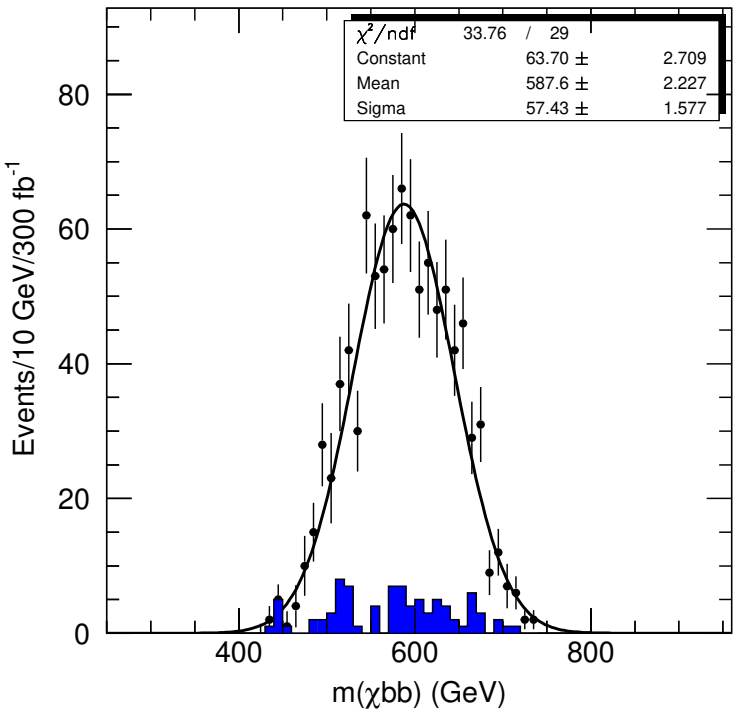

Figure 5.6: $m(\tilde{\chi}_2^0 bb)$ after all cuts. The residual SUSY background is shown in blue. Superimposed is a gaussian fit. The distribution is shown for an integrated statistics of 300 fb^{-1}

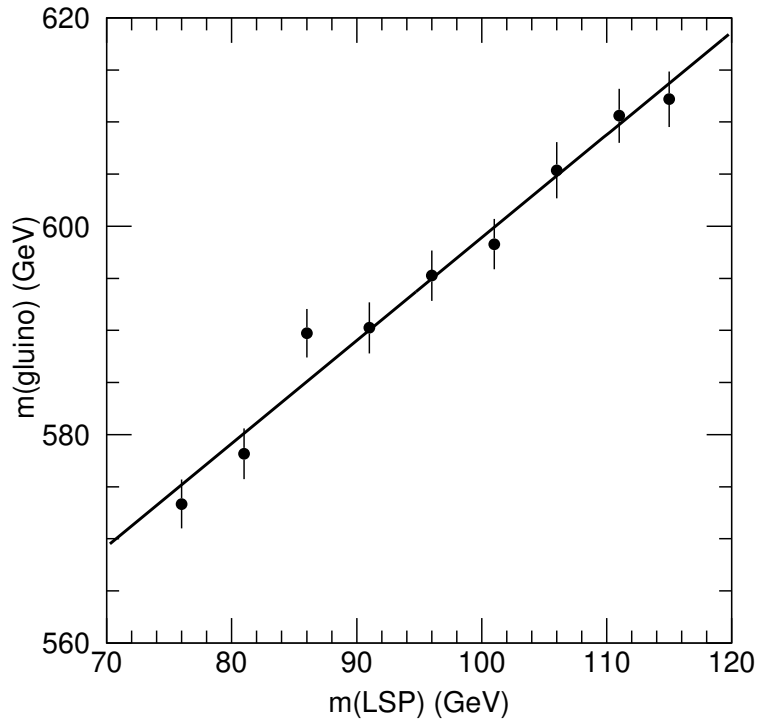

Figure 5.7: *Estimated $m(\tilde{g})$ as a function of the $m(\tilde{\chi}_1^0)$ assumed as input of the fit.*

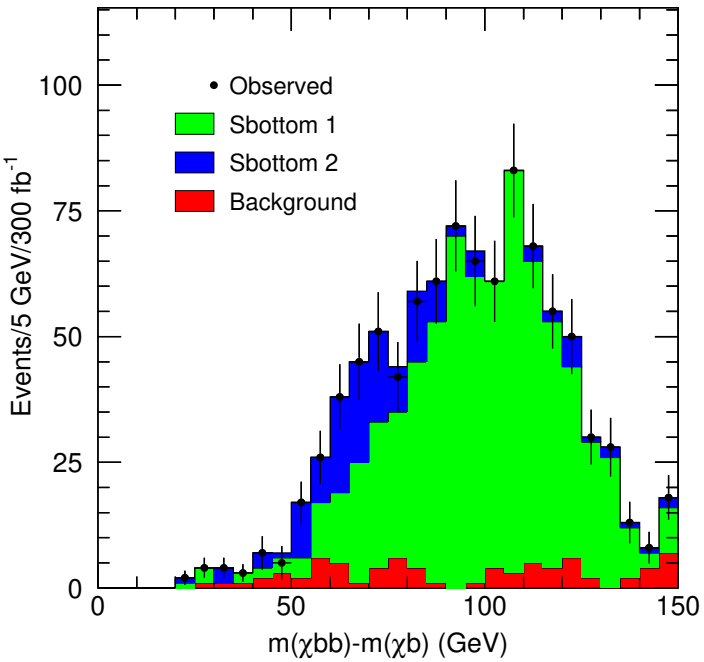

Figure 5.8: Distribution of $m(\tilde{\chi}_2^0 bb) - m(\tilde{\chi}_2^0 b)$ for an integrated luminosity of 300 fb^{-1} (points with error bars). Superimposed are: $\tilde{g} \to \tilde{b}_1 b$ (green), $\tilde{g} \to \tilde{b}_2 b$ (blue), and background (red).

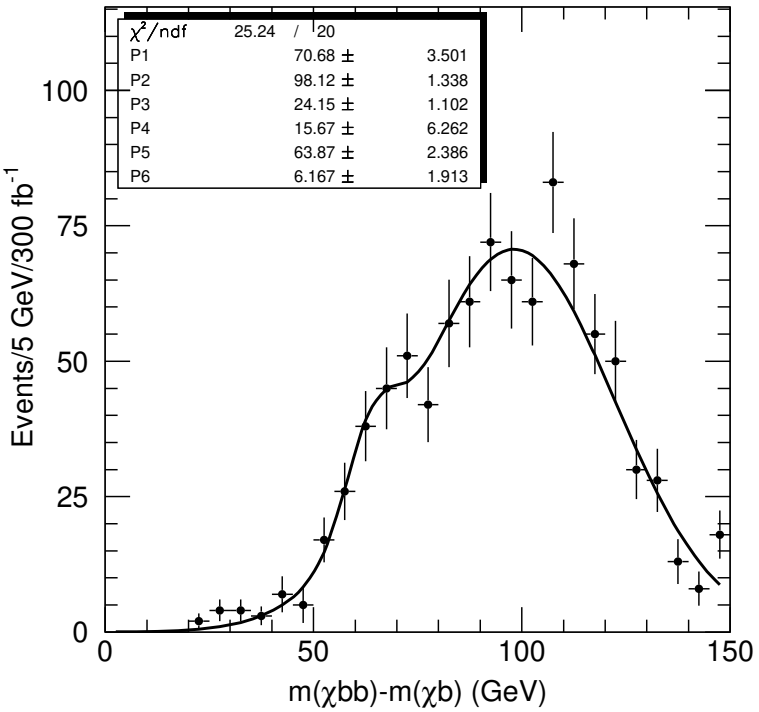

Figure 5.9: Distribution of $m(\tilde{\chi}_2^0 bb) - m(\tilde{\chi}_2^0 b)$ for an integrated luminosity of 300 fb^{-1}. Superimposed is the fit performed assuming the sum of two gaussian distributions.

~ 1.5 GeV for $\tilde{b}_1$ and ~ 2.5 GeV for $\tilde{b}_2$. This result is obtained under the assumption that two peaks do indeed exists, which must be demonstrated by careful experimental analysis. We have verified that the measured gluino-sbottom mass difference has a negligible dependence on the assumed $\tilde{\chi}_1^0$ mass.

Under the assumption that the shape of the response of the ATLAS detector to b-jets can be accurately modeled, it is also possible to estimate the relative population of $\tilde{b}_1$ and $\tilde{b}_2$ decays in the distributions of Fig 5.8 through a likelihood fit and thus extract a measurement of the quantity:

$$\frac{BR(\tilde{g} \to \tilde{b}_2 b) \times BR(\tilde{b}_2 \to \tilde{\chi}_2^0 b)}{BR(\tilde{g} \to \tilde{b}_1 b) \times BR(\tilde{b}_1 \to \tilde{\chi}_2^0 b)} \tag{5.14}$$

An approximate estimate of the achievable statistical error on this measurement can be obtained by considering the number of events in a mass interval chosen to maximize the $\tilde{b}_2$ signal. The number of $\tilde{b}_1$ decays in that interval can be estimated from the $\tilde{b}_1$ decay distribution normalized to the peak at ~100 GeV, and subtracted, thus yielding the number of $\tilde{b}_2$ decays. The total number of flavour-subtracted events in the mass interval 50-80 GeV for 300 fb^{-1} is 913, of which 707 are from $\tilde{b}_1$ decays, 73 from background, and 141 from $\tilde{b}_2$ decays. We assume a 100% error on the background estimate, and we neglect the systematic error on the modeling of the detector response and on the evaluation of the correction factor necessary to take into account the fact that the analysis efficiency is different for $\tilde{b}_1$ and $\tilde{b}_2$ decays. Under these hypotheses, the quantity in Equation 5.14, can be measured to be 0.257+-0.078.

For a lower statistics of 100 fb^{-1}, it would probably be impossible to demonstrate the presence of two peaks, and the average value of the distribution provides a measurement of the quantity:

$$\frac{m(\tilde{b}_1) \times BR(\tilde{g} \to \tilde{b}_1 b) \times BR(\tilde{b}_1 \to \tilde{\chi}_2^0) + m(\tilde{b}_2) \times BR(\tilde{g} \to \tilde{b}_2 b) \times BR(\tilde{b}_2 \to \tilde{\chi}_2^0)}{BR(\tilde{g} \to \tilde{b}_1 b) \times BR(\tilde{b}_1 \to \tilde{\chi}_2^0) + BR(\tilde{g} \to \tilde{b}_2 b) \times BR(\tilde{b}_2 \to \tilde{\chi}_2^0)}$$

with a statistical error of ~ 1.7 GeV.

5.1.2.4 Direct Slepton Production

Sleptons (here taken to mean only selectrons and smuons) are produced by s-channel Z^* exchange with a cross section of 91 fb at SPS 1a. The relatively high $m_{1/2}$ at this point makes for quite a large splitting in the slepton sector. The mass of the right-handed and left-handed sleptons are 142.9 GeV and 201.9 GeV respectively.

At SPS 1a $\tilde{\ell}_R$ always decays to $\tilde{\chi}_1^0$ and a lepton, whereas the probability for this decay from $\tilde{\ell}_L$ is 45%. The two other decay modes for $\tilde{\ell}_L$ (to $\tilde{\chi}_2^0 + \ell$ and $\tilde{\chi}_1^\pm + \nu$) are not considered in this study. The key signature for direct di-slepton production will therefore be 2 opposite-sign same-flavour leptons, $\not\!\!E_T$ from the escaping $\tilde{\chi}_1^0$'s and no jets. Because of the low cross section for the signal we did this study in a high-luminosity environment so in reality a small jet activity is to be expected.

The backgrounds are dilepton production from WW (most signal like), $t\bar{t}$ (most events passing cuts due to the large cross section), WZ (important because of SF excess), and several SUSY backgrounds: chargino-neutralino production, decays from

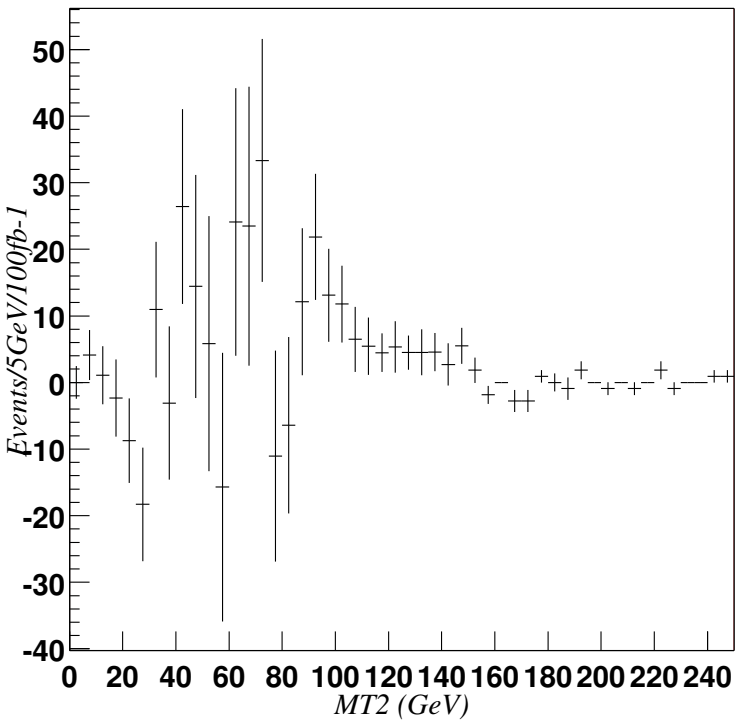

Figure 5.10: Subtracting opposite-flavour events passing the cuts from the passing same-flavour events. The scale is 100 fb^{-1}.

squarks and gluinos, $\tilde{\tau}_1\tilde{\tau}_1$, $\tilde{\nu}\tilde{\nu}$, and $\tilde{\nu}\tilde{\ell}_L$. Both signal and background were generated with PYTHIA 6.210 [372] and the WZ* cross checked with HERWIG [376]. The detector simulation was ATLFAST [373], a fast simulation package for ATLAS.

No direct mass measurement is possible due to the escaping $\tilde{\chi}_1^0$'s but the mass can still be estimated using the M_{T2} variable, suggested by the Cambridge group [377]:

$$M_{T2}^2 = \min_{\not{p}_1+\not{p}_2=\not{p}_T} \left[\max\left\{m_T^2(p_T^{\ell_1}, \not{p}_1), m_T^2(p_T^{\ell_2}, \not{p}_2)\right\}\right]$$

where $\not{p}_1$ and $\not{p}_2$ are the unknown momenta of the neutralinos. The maximum of this distribution is a function of the mass difference between the decaying particle and the mass of the invisible particle (assuming the leptons are massless).

The M_{T2} edge for $\tilde{\ell}_R$ is right on top of the edges for the SM backgrounds but $\tilde{\ell}_L$ is more isolated. Since the $\tilde{\ell}_R$ is produced abundantly from neutralino decay at SPS 1a it is much more realistic to measure its mass there than from direct production.

The result after applying hard cuts and then opposite-flavour subtraction is shown in figure 5.10.

Finally, to estimate what $\tilde{\ell}_L$ mass this corresponds to and how well we could do at the LHC a set of experiments were performed. For each experiment a set of signal SPS 1a events are picked at random and the resulting histogram from background subtraction is compared to a sample of ultra-high statistics signal distributions with varying $\tilde{\ell}_L$ masses, all scaled to 100 fb^{-1}. The mass is then taken as the value with lowest χ_N^2. 10000 such experiments were performed.

Table 5.6: Branching ratios for $\tilde{u}_L$ and $\tilde{d}_L$ at SPS 1a, from ISAJET 7.58 [375].

Decay	BR (%)	Decay	BR (%)
$\tilde{u}_L \to \tilde{\chi}_1^0 u$	0.6	$\tilde{d}_L \to \tilde{\chi}_1^0 d$	2.4
$\tilde{u}_L \to \tilde{\chi}_2^0 u$	31.8	$\tilde{d}_L \to \tilde{\chi}_2^0 d$	31.0
$\tilde{u}_L \to \tilde{\chi}_3^0 u$	0.09	$\tilde{d}_L \to \tilde{\chi}_3^0 d$	0.15
$\tilde{u}_L \to \tilde{\chi}_4^0 u$	1.0	$\tilde{d}_L \to \tilde{\chi}_4^0 d$	4.0
$\tilde{u}_L \to \tilde{\chi}_1^+ d$	65.3	$\tilde{d}_L \to \tilde{\chi}_1^- u$	60.9
$\tilde{u}_L \to \tilde{\chi}_2^+ d$	1.23	$\tilde{d}_L \to \tilde{\chi}_2^- u$	4.06

There are very few signal events; both the signal and the backgrounds, in particular the WW background, fluctuate and this makes it hard to do a precise mass measurement. Most experiments fall within 3 GeV of the expected value, but the distribution shows significant non-gaussian tails. From a gaussian fit to the distribution of results we quote a statistical uncertainty of 2.8 GeV on the determination of the position of the M_{T2} edge.

A test where the Pythia WW background was replaced by a WW sample from Herwig was also performed. The result was very similar but with a somewhat higher uncertainty on the edge position.

5.1.2.5 Heavy gaugino analysis

We present here a brief overview of the full analysis described in [374].
Profiting from the high statistics sample of squarks which will be collected at the LHC for the considered point, we search for the rare decays of the squarks into the heavier gauginos.

The branching fractions of the squarks into gauginos for Point SPS 1a are given in Table 5.6. The decays into $\tilde{\chi}_4^0$ and $\tilde{\chi}_2^+$ dominate the ones into $\tilde{\chi}_3^0$. In fact, after diagonalization of the mixing matrix, whereas the $\tilde{\chi}_3^0$ is almost exclusively higgsino, the $\tilde{\chi}_4^0$ has typically some gaugino admixture, yielding a significant coupling to the $\tilde{q}_L$, and a BR of a few percent. The same is true for the $\tilde{\chi}_2^+$.

A similar signature as the one from the decay $\tilde{\chi}_2^0 \to \tilde{\ell}_R l$ studied in the previous sections can be exploited for the decay of the heavier gauginos. The uncorrelated lepton pairs can still be subtracted using lepton flavour correlation, and the background from $\tilde{\chi}_2^0$ decays is eliminated by simply considering lepton-lepton invariant masses above the $\tilde{\chi}_2^0$ kinematic edge.

Three decay chains for $\tilde{\chi}_4^0$ and one decay chain for $\tilde{\chi}_2^\pm$ do provide a signal with correlated lepton flavour:

$$\begin{array}{lllll} \tilde{q}_L \to & \tilde{\chi}_4^0 & q & & \\ & \big\lfloor\!\to & \tilde{\ell}_R^\pm & \ell^\mp & \\ & & \big\lfloor\!\to \tilde{\chi}_1^0 & \ell^\pm & \qquad [D1] \end{array}$$

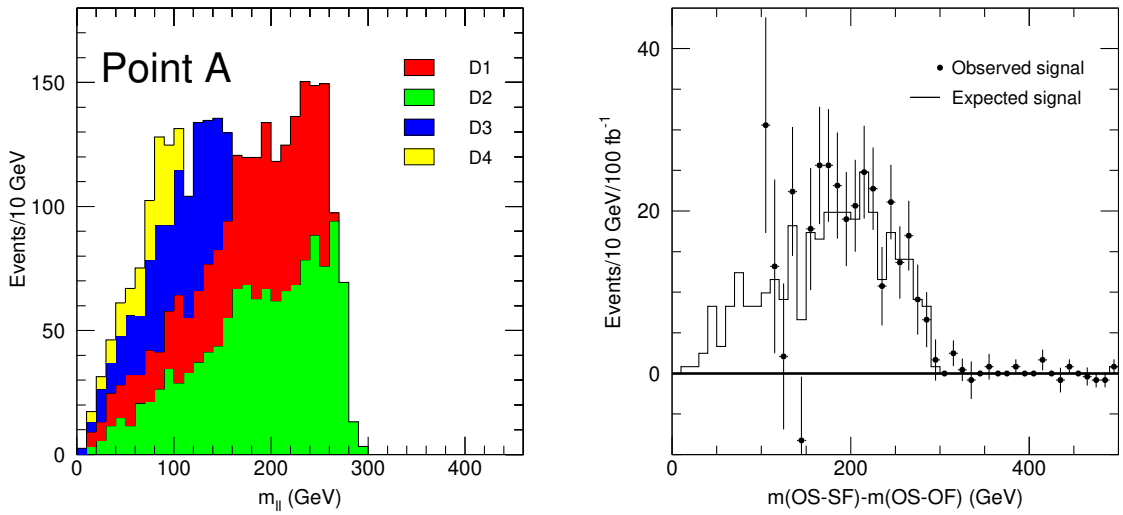

Figure 5.11: Point SPS 1a. Left: distribution of $m_{\ell\ell}$ before cuts for the decay chains [D1] (red), [D2] (green), [D3] (blue) and [D4] (yellow). Right: reconstructed $m_{\ell\ell}$ spectrum after cuts and after subtracting opposite-flavour lepton pairs from same-flavour lepton pairs. The black points show the result of the subtraction, with the statistical errors for 100 fb^{-1}. The full line is the spectrum for events containing the desired decay chains.

$$
\begin{aligned}
\tilde{q}_L \rightarrow\ & \tilde{\chi}_4^0 \quad q \\
& \hookrightarrow\ \tilde{\ell}_L^{\pm}\ \ell^{\mp} \\
& \qquad \hookrightarrow\ \tilde{\chi}_1^0\ \ell^{\pm} \qquad [D2] \\
& \qquad \hookrightarrow\ \tilde{\chi}_2^0\ \ell^{\pm} \qquad [D3] \\
\tilde{q}_L \rightarrow\ & \tilde{\chi}_2^{\pm} \quad q' \\
& \hookrightarrow\ \tilde{\nu}_{\ell}\ \ell^{\pm} \\
& \qquad \hookrightarrow\ \tilde{\chi}_1^{\pm}\ \ell^{\mp} \qquad [D4]
\end{aligned}
$$

The shape of the two-lepton invariant mass for each of the [D1]-[D4] chains displays an edge, which, for each decay $p1 \rightarrow p2\ell^{\pm} \rightarrow p3\ell^{\pm}\ell^{\mp}$ is at the position $m_{l^+l^-}^{max}$ given by the expression:

$$
m_{l^+l^-}^{max} = m_{p1}\sqrt{1-\frac{m_{p2}^2}{m_{p1}^2}}\sqrt{1-\frac{m_{p3}^2}{m_{p2}^2}}
$$

This is illustrated in Figure 5.11. The experimentally observed shape is the sum of the four shapes from the decays [D1] to [D4], shown in different colors in the figure, weighted by the relative production rate. We observe that for Point SPS 1a the outermost edge is from decay [D2].

In order to reduce the Standard Model background below the SUSY background from uncorrelated gauginos decays, we require:

- Exactly two isolated opposite-sign same-flavour leptons with $P_T(1) > 20$ GeV, $P_T(2) > 10$ GeV

Table 5.7: Results after cuts for Point SPS 1a. We show in column 2 the number of signal events, in 3 the statistical significance, in 4 the total background, in 5 the SM background, and in 6 the invariant mass interval chosen to optimize the significance. The assumed statistics is 100 fb^{-1}.

Point	N_{ev} Signal	Significance	Total bck.	SM bck.	Interval (GeV)
SPS 1a	259.1 $\pm$ 21.1	12.3	92.3	27.1	150–290

- $P_T^{miss}>$ 100 GeV, at least four jets, $P_T(j1) > 150$ GeV, $P_T(j2) > 100$ GeV, $M_{eff} > 600$ GeV.
- $M_{T2} > 80$ GeV, where M_{T2} is a special case of a variable discussed in [377].
- $m_{\ell^+\ell^-} > 100$ GeV

The following backgrounds were considered: $\overline{t}t$, Z+jets, W+jets, and produced with the PYTHIA [372] generator.
After these cuts, the SM background is ∼70 events, of which 42 are from $\overline{t}t$ and 28 from Z+jets for an integrated luminosity of 100 fb^{-1}. This is well below the SUSY background which, for the SPS 1a point is ∼250 events.
The efficiency for the signal after cuts is ∼10%.

The $m_{\ell^+\ell^-}$ spectra after subtraction are shown superimposed to the expected signal shape in the right side of Figure 5.11. In Table 5.7 we give the numbers of signal and background events inside the mass bin 150–290 GeV which maximizes the significance.

The invariant mass distribution after background subtraction can be used to extract a measurement of the relevant lepton-lepton edge. The statistical precision of the edge measurement has been determined through a set of Monte Carlo experiments, each corresponding to an integrated luminosity of 100 fb^{-1}. For each experiment the edge position was evaluated using a sliding window algorithm. From this approach, the statistical error on the $\tilde{\chi}_4^0$ edge was evaluated to be $\sim$ 4 GeV for an integrated luminosity of 100 fb^{-1}.

5.1.2.6 Measurement of $\tilde{\tau}_1$ mass

The dominant decay mode of the $\tilde{\chi}_2^0$ in Point SPS 1a is the decay to the pair $\tilde{\tau}_1\tau$, which is favoured over the decay to $\tilde{\ell}_R$ due to the relatively high value of $\tan\beta$. These decays can be identified in the ATLAS detector through the tagging of the hadronic decays of the τ which present a characteristic pattern in the detector. The graph showing the rejection power on quark jets as a function of the τ efficiency, from [89] is shown in Fig. 5.12. A typical figure is a rejection of a factor 100 on QCD jets for a τ efficiency of 50%. The rejection values quoted are referred to low luminosity, and we perform the analysis on an integrated luminosity of 30 fb^{-1}.

The first step is the reduction of the Standard Model background to a manageable level with hard cuts on jet multiplicity and E_T^{miss}. We require therefore:

- At least 4 jets: $p_T > 100, 50, 50, 50$ GeV
- $E_T^{miss} > max(100\ GeV, 0.2 \times M_{eff})$

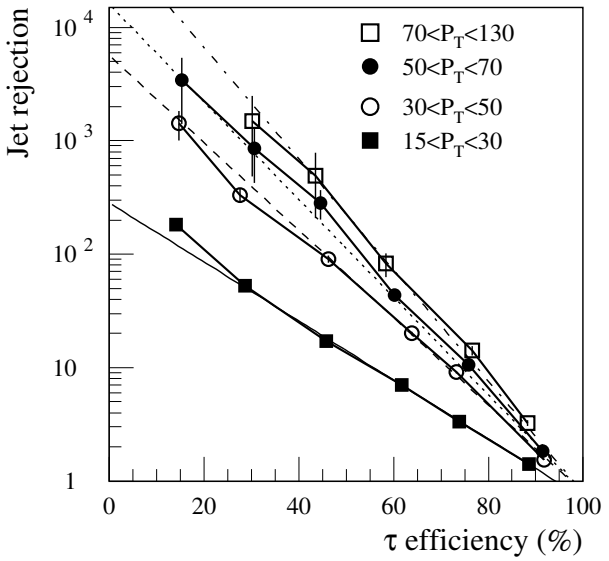

Figure 5.12: Rejection factor of QCD jets as a function of the τ efficiency for different intervals of τ transverse momentum.

- $M_{eff} > 500$ GeV
- two jets tagged as τ with $P_T(\tau_1) > 30$ GeV, and $P_T(\tau_2) > 25$ GeV, with opposite charge.

Backgrounds from QCD jets, W+jets, Z+jets, $\bar{t}t$ were considered and generated with PYTHIA. The use of a parton-shower Monte Carlo to estimate multi-jet backgrounds is known to underestimate the backgrounds, and the present analysis should be considered a preliminary study, waiting for a more detailed study involving specialised generators. After the requirement on tau-tagged jets is applied, the dominant backgrounds are Z+jets and $\bar{t}t$. The total SM background is reduced to about 1/10 of the SUSY backgrounds in the $\tau\tau$ edge region and the conclusions of the analysis would only marginally be affected by a significant increase in background.

The invariant mass distribution for the two τ candidates is shown in Fig. 5.13. The background from QCD jets misidentified as τ jets will have random sign assignment, therefore the distribution of the same-sign τ-candidate pairs, also shown in Fig. 5.13, will give a good description of the dominant SUSY background, constituted by a τ from $\tilde{\chi}_1^{\pm}$ decay and a misidentified jet, and of SM background. Part of the background with two real τ coming from two $\tilde{\chi}_1^{\pm}$ will also have same-sign τ, as the bulk of SUSY production in Point SPS 1a is $\tilde{g}\tilde{g}$ and $\tilde{g}\tilde{q}$ production.

We can thus subtract the same-sign τ pairs from the opposite-sign τ pairs. The result is shown in Fig. 5.14 where the resulting distribution is shown as the full points with error bars. The distribution shown as a full line are the events containing two τ from $\tilde{\chi}_2^0$ decays, and the grey area shows the events from two uncorrelated $\tilde{\chi}_1^{\pm}$ decays. The observed distribution has a clear structure with an end-point corresponding to the edge of the invariant mass distribution of the undecayed τ, shown as a dashed line in Fig. 5.14.

Although the distribution in Fig. 5.14 does not have a sharp edge, it is nonetheless sensitive to the edge position. This has been verified, by producing the same distributions as for the SPS 1a point, but with values of the $\tilde{\tau}_1$ mass such as to displace

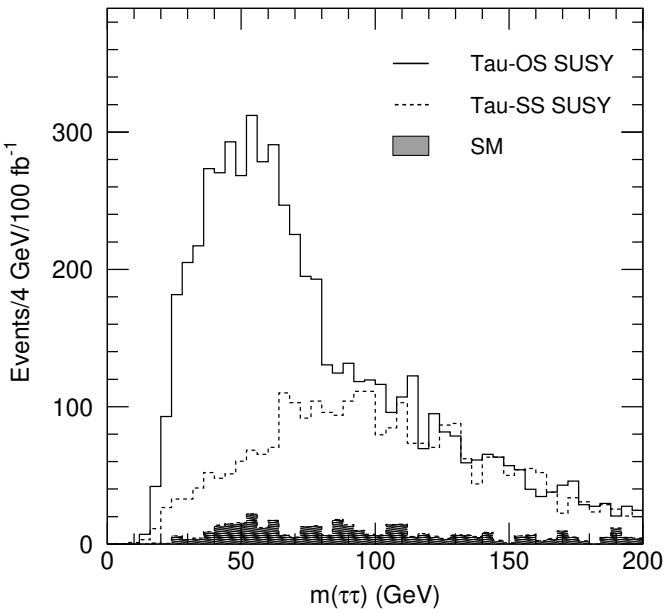

Figure 5.13: Invariant mass distribution of: opposite sign τ-tagged jets (full line); same-sign τ-tagged jets (dashed line), SM background (grey). The integrated luminosity is 30 fb^{-1}.

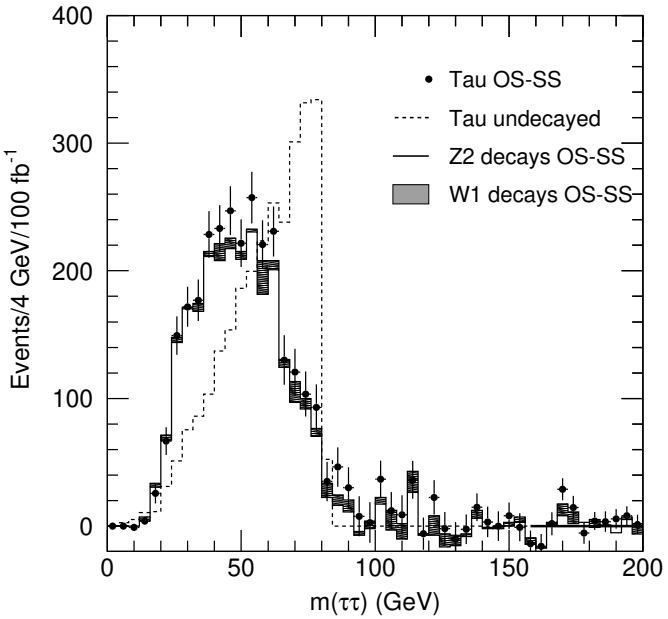

Figure 5.14: Invariant mass distribution of τ-tagged jets after subtraction of same-sign background (full circles). Superimposed are shown the distributions for: $\tilde{\chi}_2^0 \rightarrow \tilde{\tau}_1\tau$ signal (full line), $\tilde{\chi}_1^{\pm}$ decays (grey), undecayed τ's from $\tilde{\chi}_2^0$ (dashed line).

.

the edge position down by five and ten GeV. On a statistical basis two distributions displaced by five GeV can be distinguished. The identification of the actual end-point of the $\tau\tau$ mass distribution requires however a detailed simulation study, outside the scope of this analysis. We conservatively quote a systematic uncertainty of 5 GeV on the determination of the edge position.

5.1.2.7 Measurement of q_R mass

In mSUGRA models the $\tilde{\chi}_1^0$ is essentially a bino, and the $\tilde{\chi}_2^0$ a Wino. Therefore the $\tilde{q}_R$ which has zero SU(2) charge decays with almost 100% BR into the corresponding quark and the $\tilde{\chi}_1^0$.

In the case of SPS 1a, where the squarks are lighter than the gluinos by only a few tens of GeV, the bulk of the SUSY production is given by gluino production. The signature of events where both gluinos decay into two $\tilde{q}_R$ is thus the presence of two low P_T jets from the $\tilde{g} \rightarrow q\tilde{q}_R$ decays, two high P_T jets from the $\tilde{q}_R$ decay, and E_T^{miss}. We apply the same cuts as for the hadronic analysis discussed above, and in addition we require:

- Leading jet with $P_T > 300$ GeV
- At most 4 jets with $P_T > 50$ GeV
- Veto leptons, τ-jets, b-jets

The second and third cut are aimed at reducing the background from $\tilde{q}_L$ and third generation squarks. For the events containing two $\tilde{q}_R$ decaying to $q\tilde{\chi}_1^0$, at the end of the cascade decays there are two particles with the same mass, both decaying to a jet and a $\tilde{\chi}_1^0$. A very useful variable in this situation is the Cambridge M_{T2} variable calculated on the two leading jets. We show in Fig 5.15 the distribution of M_{T2} for the SUSY events, and for the background (in red), for a $m(\tilde{\chi}_1^0) = 96$ GeV. A clear edge structure can be seen, which approximately coincides with the $\tilde{q}_R$ mass. The considerations on SM backgrounds given in 5.1.2.6 apply here as well, from Fig 5.15 the detectability of an edge structure would be guaranteed even in the presence of a much higher SM background.

At this point 65% of the events contain two $\tilde{q}_R$, 30% only one $\tilde{q}_R$, and 5% no $\tilde{q}_R$. The bulk of the surviving SUSY background are events with one $\tilde{q}_L$ produced, decaying either to $q\tilde{\chi}_2^0$ or to $\tilde{\chi}_1^\pm$. For the SUSY background events the resulting edge shape is at a lower value than for the signal, as on the $\tilde{q}_L$ side the mass difference between the squark and the corresponding decay gaugino is smaller than for the $\tilde{q}_R$.

In order to estimate the edge position, we parametrize the M_{T2} shape on a simulated sample of pure $\tilde{q}_R$ decays, and we perform a fit to the distribution of Fig 5.15. The resulting fit is shown in Fig. 5.16. The statistical error on the edge position is ± 3.6 GeV for an integrated luminosity of 30 fb^{-1}. The position of the fitted edge is $\sim$10 GeV lower than the nominal one, as the presence of a significant background with a lower edge distorts the M_{T2} shape. The 10 GeV discrepancy can be taken as an approximate estimate of the systematic uncertainty on the evaluation of the $\tilde{q}_R$ mass through the edge fitting. As already discussed for the $\tilde{q}_L$ evaluation, this value of the uncertainty is quite conservative, since in the real experiment, given that most of

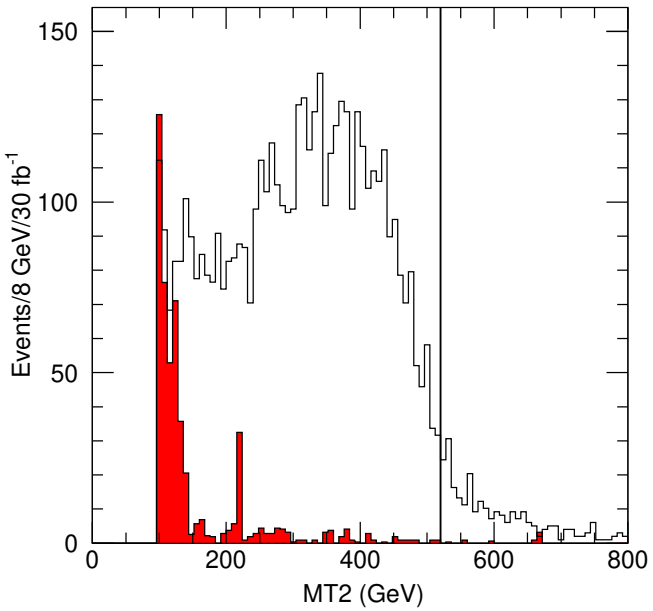

Figure 5.15: Distribution of M_{T2} for the events passing the cuts. In red is shown the Standard Model background. The integrated statistics in the plot is 30 fb^{-1}.

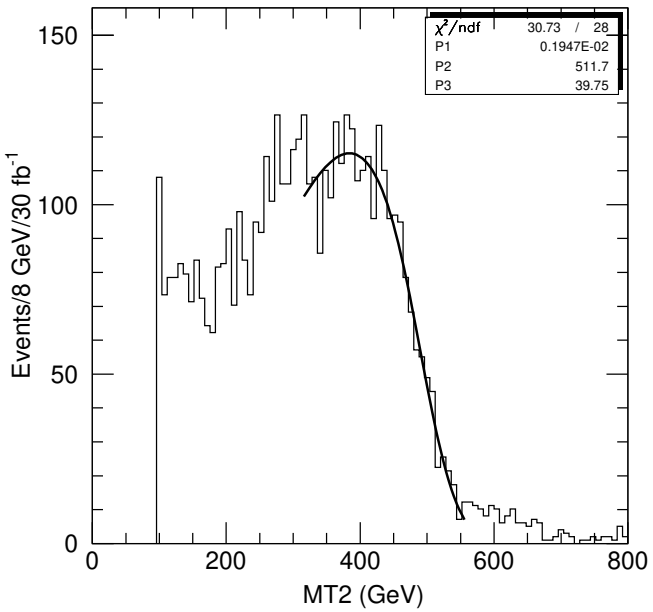

Figure 5.16: Distribution of M_{T2} for events passing the cuts. Superimposed is the fit described in the text.

the involved sparticle masses will be known, it will be possible to estimate the background shape and account for it in the fit. The M_{T2} evaluation relies on the knowledge of $m(\tilde{\chi}_1^0)$. For small variations of $m(\tilde{\chi}_1^0)$, the M_{T2} measurement amounts to measuring $m(\tilde{q}_R) - m(\tilde{\chi}_1^0)$, which should be taken as the output result of this analysis.

5.1.2.8 Measurements in the stop sector

At the LHC, we may be able to access the nature of the stop and sbottom if they are lighter than the gluino ($\tilde{g}$). This is because they copiously arise from the gluino decay. The relevant decay modes for $\tilde{b}_i$ ($i = 1, 2$), $\tilde{t}_1$, to charginos $\tilde{\chi}_j^\pm$ ($j = 1, 2$) or neutralinos $\tilde{\chi}_j^0$ ($j = 1, 2, 3, 4$) are listed below (indices to distinguish a particle and its anti-particle is suppressed unless otherwise stated),

$$\begin{aligned}
(\mathrm{I})_j &\quad \tilde{g} \to b\tilde{b}_1 \to bb\tilde{\chi}_j^0 \ (\to bbl^+l^-\tilde{\chi}_1^0), \\
(\mathrm{II})_j &\quad \tilde{g} \to t\tilde{t}_1 \to tt\tilde{\chi}_j^0, \\
(\mathrm{III})_j &\quad \tilde{g} \to t\tilde{t}_1 \to tb\tilde{\chi}_j^\pm, \\
(\mathrm{III})_{ij} &\quad \tilde{g} \to b\tilde{b}_i \to bW\tilde{t}_1 \to bbW\tilde{\chi}_j^\pm, \\
(\mathrm{IV})_{ij} &\quad \tilde{g} \to b\tilde{b}_i \to tb\tilde{\chi}_j^\pm.
\end{aligned} \tag{5.15}$$

In the previous literature [89, 379], the lighter sbottom $\tilde{b}_1$ is often studied through the mode $(\mathrm{I})_2$, namely the $bb\tilde{\chi}_2^0 \to bbl^+l^-\tilde{\chi}_1^0$ channel. This mode is important when the second lightest neutralino $\tilde{\chi}_2^0$ has substantial branching ratios into leptons. The measurement of sbottom and gluino masses from the study of these decay chains is discussed above.

In Refs. [380, 381] we proposed to measure the edge position of the m_{tb} distribution for the modes $(\mathrm{III})_1$ and $(\mathrm{IV})_{11}$, where m_{tb} is the invariant mass of a top-bottom (tb) system. The decay modes are expected to be dominant in the minimal supergravity model (MSUGRA), as the branching ratios $\mathrm{BR}(\tilde{b}_1(\tilde{t}_1) \to t(b)\tilde{\chi}_1^\pm)$ could be as large as 60%. We focused on the reconstruction of hadronic decays of the top quark, because the m_{tb} distribution of the decay makes a clear "edge" in this case. The parton level m_{tb} distributions for the modes $(\mathrm{III})_j$ and $(\mathrm{IV})_{ij}$ are expressed as functions of $m_{\tilde{g}}$, $m_{\tilde{t}_1}$, $m_{\tilde{b}_i}$, and the chargino mass $m_{\tilde{\chi}_j^\pm}$: $d\Gamma/dm_{tb} \propto m_{tb}$.

The events containing tb are selected by requiring the following conditions in addition to the standard SUSY cuts: 1) Two and only two b-jets. 2) Jet pairs consistent with a hadronic W boson decay, $|m_{jj} - m_W| < 15$ GeV. 3) The invariant mass of the jet pair and one of the b-jets, m_{bjj}, satisfies $|m_{bjj} - m_t| < 30$ GeV. The events after the selection contain misreconstructed events. We use a W sideband method to estimate the background distribution due to misreconstructed events. Monte Carlo simulations show that the distribution of the signal modes (III) and (IV) after subtracting the background is very close to the parton level distribution. The distribution is then fitted by a simple fitting function described with the end point M_{tb}^{fit}, the edge height h per Δm bin, and a smearing parameter. We assume that the signal distribution is sitting on a linearly decreasing background near the edge, which is also determined by the fit.

The edge position (end point) of the m_{tb} distribution M_{tb} for the modes $(\mathrm{III})_j$ and

$(\mathrm{IV})_{ij}$ are written as follows;

$$
\begin{aligned}
M_{tb}^2(\mathrm{III})_j &= m_t^2 + \frac{m_{\tilde{t}_1}^2 - m_{\tilde{\chi}_j^\pm}^2}{2m_{\tilde{t}_1}^2}\left\{(m_{\tilde{g}}^2 - m_{\tilde{t}_1}^2 - m_t^2)\right. \\
&\left. + \sqrt{(m_{\tilde{g}}^2 - (m_{\tilde{t}_1} - m_t)^2)(m_{\tilde{g}}^2 - (m_{\tilde{t}_1} + m_t)^2)}\right\}, \\
M_{tb}^2(\mathrm{IV})_{ij} &= m_t^2 + \frac{m_{\tilde{g}}^2 - m_{\tilde{b}_i}^2}{2m_{\tilde{b}_i}^2}\left\{(m_{\tilde{b}_i}^2 - m_{\tilde{\chi}_j^\pm}^2 + m_t^2)\right. \\
&\left. + \sqrt{(m_{\tilde{b}_i}^2 - (m_{\tilde{\chi}_j^\pm} - m_t)^2)(m_{\tilde{b}_i}^2 - (m_{\tilde{\chi}_j^\pm} + m_t)^2)}\right\}. \qquad (5.16)
\end{aligned}
$$

In some model parameters $M_{tb}(\mathrm{III})_1$ is very close to $M_{tb}(\mathrm{IV})_{11}$. When they are experimentally indistinguishable, it is convenient to define a weighted mean of the end points;

$$
\begin{aligned}
M_{tb}^{\mathrm{w}} &= \frac{\mathrm{BR(III)}M_{tb}(\mathrm{III})_1 + \mathrm{BR(IV)}_{11}M_{tb}(\mathrm{IV})_{11}}{\mathrm{BR(III)} + \mathrm{BR(IV)}_{11}}, \\
\mathrm{BR(III)} &\equiv \mathrm{BR(III)}_1 + \mathrm{BR(III)}_{11} + \mathrm{BR(III)}_{21}. \qquad (5.17)
\end{aligned}
$$

As the final states bbW from the decay chain $\tilde{g} \to b\tilde{b}_i \to bW\tilde{t}_1 \to bbW\tilde{\chi}_1^\pm$ (mode $(\mathrm{III})_{i1}$) could have an irreducible contribution to the tb final state, they are included in the definition of M_{tb}^{w}.

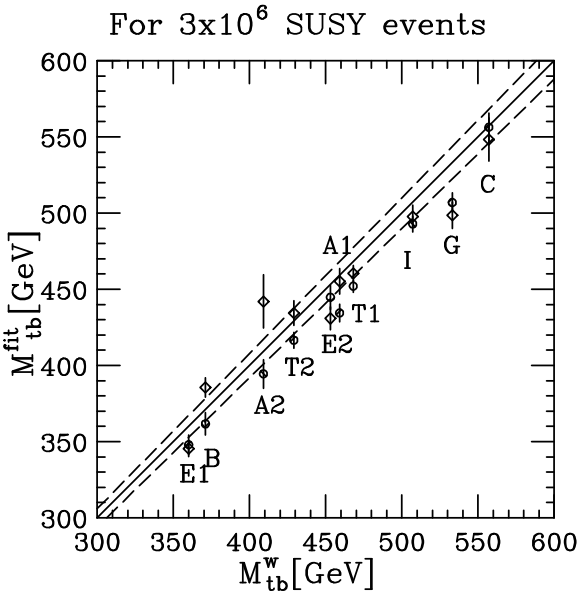

Figure 5.17: Relation between M_{tb}^{w} and M_{tb}^{fit} for the sample points. The solid line corresponds to $M_{tb}^{\mathrm{w}} = M_{tb}^{\mathrm{fit}}$ and dashed lines to $M_{tb}^{\mathrm{w}}(1 \pm 0.02) = M_{tb}^{\mathrm{fit}}$. Bars with a diamond and a circle correspond to PYTHIA and HERWIG samples, respectively. From [381]

We demonstrate the viability of the method by studying the relation between M_{tb}^{w} and M_{tb}^{fit} for several model points, decribed in detail in [381]. The results corresponding to a generated statistics of 3×10^6 SUSY events for each model point are shown in Fig. 5.17. The fitted value M_{tb}^{fit} increases linearly with the weighted end point M_{tb}^{w}.

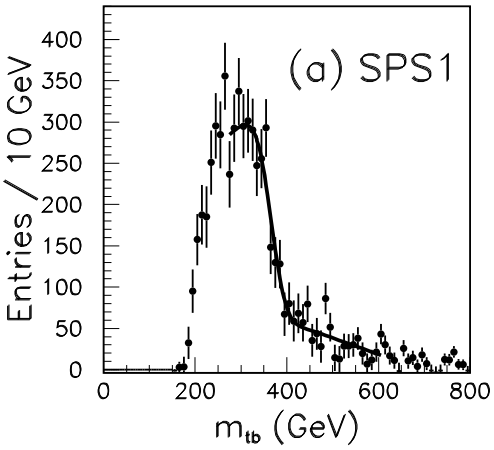

Figure 5.18: The m_{tb} distributions at SPS1. The fit curves are also shown. From [381].

The $M_{tb}^{\rm fit}$ tends to be lower than $M_{tb}^{\rm w}$, which is the effect of particles missed outside the jet cones. This is similar to what is found in previous studies and should be corrected by more careful study including the modification of jet definition.

The $M_{tb}^{\rm fit}$ contains the information on $\tilde{t}_1$ as can be seen in Eq.(5.17). Given the very precise electroweak SUSY parameter measurements and $\tilde{g}$ and $\tilde{b}$ mass measurements with LHC/LC, the remaining dominant uncertainty are in the stop mass $m_{\tilde{t}_1}$, and the stop and sbottom mixing angles θ_t and θ_b. The results of the end point fit at SPS1 for the 3×10^6 Monte Carlo events are $M_{tb}^{\rm fit} = 363.9 \pm 4.8$ GeV and $h = 267.3.2 \pm 20.8$ ($\Delta m = 10$ GeV). We show the m_{tb} distribution and fitting curve in Fig. 5.18.

We will now discuss the relation between the edge height h and the number of reconstructed tb events. The number of the reconstructed "edge" events $N_{\rm edge}$ arising from the decay chains (III) and (IV) may be estimated from $M_{tb}^{\rm fit}$ and h per bin size Δm as follows,

$$N_{\rm edge} \sim N_{\rm fit} = \frac{h}{2}\left(\frac{m_t}{M_{tb}^{\rm fit}} + 1\right) \times \frac{M_{tb}^{\rm fit} - m_t}{\Delta m}. \tag{5.18}$$

This formula is obtained by assuming the parton level distribution, and equating the minimum of the m_{tb} distribution from the decay chain (III) or (IV) to m_t. The consistency between $N_{\rm edge} \sim N_{\rm fit}$ is checked by using the generator information in Ref. [381].

In the MSUGRA model, the decay modes which involve W bosons (modes (II), (III) and (IV)) often dominate the gluino decays to bbX. Because the events with W bosons should remain after the W sideband subtraction, the reconstruction efficiency ϵ_{tb} is expected to be similar for these decay modes. Thus, if the contributions from the stop or sbottom pair productions are negligible, the numbers of events with two bottom quarks are given approximately as

$$\begin{aligned} N_{\rm fit} &\sim \epsilon_{tb}{\rm BR}({\rm edge})\left[2N(\tilde{g}\tilde{g})\left(1-{\rm BR}(\tilde{g}\to bbX)\right)+N(\tilde{g}\tilde{q})+N(\tilde{g}\tilde{q}^*)\right], \\ N_{\rm all} &\sim \epsilon_{tb}{\rm BR}(\tilde{g}\to bbX)\left[2N(\tilde{g}\tilde{g})\left(1-{\rm BR}(\tilde{g}\to bbX)\right)+N(\tilde{g}\tilde{q})+N(\tilde{g}\tilde{q}^*)\right], \end{aligned} \tag{5.19}$$

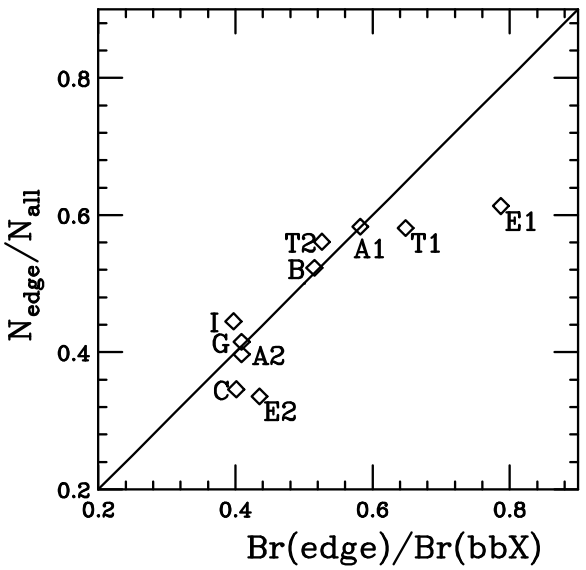

Figure 5.19: Relation between $N_{\rm edge}/N_{\rm all}$ and $\mathrm{BR(edge)}/\mathrm{BR}(\tilde{g} \to bbX)$.

where

$$\mathrm{BR(edge)} \equiv \mathrm{BR(III)}_1 + \mathrm{BR(III)}_{11} + \mathrm{BR(III)}_{21} + \mathrm{BR(IV)}_{11}, \tag{5.20}$$

and $\mathrm{BR}(\tilde{g} \to bbX)$ is the branching ratio of the gluino decaying into stop or sbottom, thus having two bottom quarks in the final state. Therefore $\mathrm{BR(edge)}\ /\mathrm{BR}(\tilde{g} \to bbX) \sim N_{\rm fit}/N_{\rm all}$ is expected.

In Fig. 5.19, we plot the ratio $N_{\rm edge}/N_{\rm all}$ as a function of $\mathrm{BR(edge)}\ /\mathrm{BR}(\tilde{g} \to bbX)$[1]. The points tend to be on the expected line $N_{\rm edge}/N_{\rm all} = \mathrm{BR(edge)}/\mathrm{BR}(\tilde{g} \to bbX)$. Some points in the plots are away from the line: The point "C" is off because the chargino has large branching ratios into leptons. At the point "T1", the stop mass is particularly light and $\tilde{t}_1\tilde{t}_1^*$ productions contributes to $N_{\rm all}$. The points "E1" and "E2" are significantly off because the first and the second generation squarks dominantly decay into the gluino, and the events containing two bottom quarks are not dominant. The description of the points are found in [381]. These exceptional cases will be easily distinguished by looking into the data from LHC/LC.

At the SPS1 point, we find $N_{\rm fit} = 3742.2 \pm 291.2$ and $N_{\rm all} = 5987.5$. This means $N_{\rm fit}/N_{\rm all} = 0.62 \pm 0.05$, while $\mathrm{BR(edge)}\ /\mathrm{BR}(\tilde{g} \to bbX) = 0.55$ is the input.

5.1.2.9 Conclusions

We have reviewed the present level of understanding of the perspectives for SUSY measurements at the LHC with the ATLAS detector. To this effect, we have performed an extensive and detailed study on the benchmark mSUGRA model SPS1a.

The measurement strategy is based on the identification of unique patterns of decay products which characterise exclusive sparticle decay chains. For each of these decays the invariant mass distributions of the observed decay products exhibit thresholds and end-point structures. The kinematic structures can in turn be expressed as a

[1]Here we plot $N_{\rm edge}/N_{\rm all}$ instead of $N_{\rm fit}/N_{\rm all}$, because $N_{\rm fit} \sim N_{\rm edge}$, and the statistical fluctuation of $N_{\rm edge}$ is small ($\sim 2\%$) with a help of the generator information.

function of the masses of the involved sparticles. By applying this procedure to Point SPS1a, we have demonstrated that the measurements possible at the LHC will cover most of the masses of the SUSY particles. Information on sparticle couplings is also provided by some analyses e.g. from detailed studies of the stop-sbottom sector. More studies are however needed in order to assess the full power of the LHC in this field.

5.1.3 Squark and gluino reconstruction with CMS at LHC

5.1.3.1 Introduction

One of the main purposes of the next generation colliders is to search for the Physics beyond the Standard Model. The discovery of superpatners of ordinary particles, as expected in Supersymmetric extension of SM (SUSY) [382], would be a proof of the existence of new physics. If supersymmetry exists at the electroweak scale, it could hardly escape detection at LHC. Thanks, in fact, to the centre of mass energy of 14 TeV, which will be available at LHC, it will be possible to extend the searches of SUSY particles up to masses of 2.5 – 3 TeV. SUSY, if it exists, is expected to reveal itself at LHC via excess of multijet+$\mathrm{E}_{\mathrm{T}}^{miss}$+(multilepton) final states compared to SM expectations [383]. Determining masses of supersymmetric particles, however, is more difficult. A Linear Collider could in this sense be very useful to complement measurement performed at LHC, increasing the degree of our knowledge of the SUSY sector. The main goal of this paper, is to show the potential of the CMS detector [113] to reconstruct SUSY particles and how a Linear Collider could improve on these measurements.

5.1.3.2 Strongly interacting sparticle reconstruction

In this section we present the results of a new study aimed at the reconstruction of the strongly interacting gluinos, sbottoms and squarks. In order to perform this mass reconstruction, two different decay chains $\tilde{g} \to \tilde{b}b$, $\tilde{b} \to \tilde{\chi}_2^0 b$, $\tilde{\chi}_2^0 \to \tilde{\ell}^{\pm}\ell^{\mp} \to \tilde{\chi}_1^0 \ell^+\ell^-$ and $\tilde{g} \to \tilde{q}q$, $\tilde{q} \to \tilde{\chi}_2^0 q$, $\tilde{\chi}_2^0 \to \tilde{\ell}^{\pm}\ell^{\mp} \to \tilde{\chi}_1^0 \ell^+\ell^-$, where $\ell = e, \mu$, have been considered. In the first decay chain two b-jets, two same flavour and opposite charge isolated leptons and large missing transverse momentum due to the escaping $\tilde{\chi}_1^0$ are produced, while the second decay chain presents the same topology except for the presence of two non b-jets. In both cases, the reconstructions are performed starting from the $\tilde{\chi}_2^0 \to \ell^+\ell^-\tilde{\chi}_1^0$ decay, with $\ell = e, \mu$. Leptons from the $\tilde{\chi}_2^0$ decay exhibit a peculiar $\ell^+\ell^-$ invariant mass distribution with a sharp edge, as shown in Fig. 5.20 and Fig. 5.21. If $m_{\tilde{\chi}_2^0} < m_{\tilde{\ell}} + m_{\ell}$ the $\tilde{\chi}_2^0$ decay would be a three body decay mediated by a virtual slepton and the edge would be placed at $m_{\tilde{\chi}_2^0} - m_{\tilde{\chi}_1^0}$. In the opposite case, when $m_{\tilde{\chi}_2^0} > m_{\tilde{\ell}} + m_{\ell}$, the neutralino decay is a two body decay and the edge would be placed at

$$M_{\ell^+\ell^-}^{max} = \frac{\sqrt{\left(m_{\tilde{\chi}_2^0}^2 - m_{\tilde{\ell}}^2\right)\left(m_{\tilde{\ell}}^2 - m_{\tilde{\chi}_1^0}^2\right)}}{m_{\tilde{\ell}}} \tag{5.21}$$

The analysis has been performed in a mSUGRA scenario, considering three different benchmark points, the so called point

- B ($m_{1/2} = 250$, $m_0 = 100$, $\tan\beta = 10$, $\mu > 0$ and $A_0 = 0$),
- G ($m_{1/2} = 375$, $m_0 = 120$, $\tan\beta = 20$, $\mu > 0$ and $A_0 = 0$),
- I ($m_{1/2} = 350$, $m_0 = 180$, $\tan\beta = 35$, $\mu > 0$ and $A_0 = 0$),

of ref. [386]. Point B is very similar to point SPS1a of ref. [387], the only difference being in the value of the A_0 parameter. All the chosen benchmark points are characterized both by relative low value for m_0 and $m_{1/2}$ (high production cross section for strongly interacting sparticles) and different values of $\tan\beta$. Indeed, the branching ratios of $\tilde{\chi}_2^0 \to \tilde{\ell}^{\pm}\ell^{\mp} \to \tilde{\chi}_1^0\ell^+\ell^-$ ($\ell = e, \mu$) decay is strongly dependent on the $\tan\beta$ parameter. This effect is of fundamental importance for our analysis.

The signal events are generated using PYTHIA 6.152 [388] with ISASUGRA 7.51 [389] input parameters, whereas background events ($t\bar{t}$, Z+jets, W+jets and QCD jets) are generated with PYTHIA 6.152 [388]. The detector response has been evaluated using the fast MC package CMSJET [390]. The study has been realized for several different integrated luminosities.

Table 5.8 summarizes the SUSY spectra at Point B, G and I, while in Table 5.9 the total SUSY cross-sections at the three different benchmark points are shown together with the branching ratios for the last decay chain ($\tilde{\chi}_2^0 \to \tilde{\ell}_R^{\pm}\ell^{\mp} \to \tilde{\chi}_1^0\ell^{\pm}\ell^{\mp}$). As can be seen from this Table, while the cross-section and the $\mathcal{B}R$ are quite large at point B, at point G (intermediate $\tan\beta$ region) the situation become worse, while at point I (large $\tan\beta$ region) the $\mathcal{B}R$ for the interesting decay chain becomes even negligible. In the next sections we will see how these effects are reflected in the reconstruction performances.

5.1.3.3 Sbottom and gluino reconstruction

In order to perform the sbottom and gluino reconstruction, through the decay chain $\tilde{g} \to \tilde{b}b$, $\tilde{b} \to \tilde{\chi}_2^0 b$, $\tilde{\chi}_2^0 \to \tilde{\ell}^{\pm}\ell^{\mp} \to \tilde{\chi}_1^0\ell^+\ell^-$, events with at least 2 same flavour opposite sign (SFOS) isolated leptons having $p_T > 15$ GeV and $|\eta| < 2.4$, corresponding to the acceptance of the muon system, and at least 2 jets tagged as b-jets, having $p_T > 20$ GeV and $|\eta| < 2.4$, are selected.

The $\tilde{b}$ reconstruction proceeds in two steps. First the $\tilde{\chi}_2^0 \to \tilde{\ell}_R^{\pm}\ell^{\mp} \to \tilde{\chi}_1^0\ell^{\pm}\ell^{\mp}$ decay chain is considered. As mentioned before, this decay is characterized by a sharp end-point in the dilepton invariant mass distribution. In Fig. 5.20 the SFOS dilepton pair invariant mass distribution is shown for SUSY events superimposed over the SM background. The $t\bar{t}$ component, which represents the main background, gives a wide distribution, while the Z+jets channel is visible for the Z peak which lies quite close to the end-point of the SUSY distribution. To perform the reconstruction a precise knowledge of the edge is necessary. In order to reduce the SM background contribution, the high missing energy content of SUSY events has been exploited. A cut on $E_T^{miss} > 150$ GeV permits to drastically reduce the SM background. This, combined with a cut on the dilepton energy, $E_{\ell\ell} > 100$ GeV, which suppresses other SUSY background sources, gives a very clean dilepton edge, as can be seen in Fig. 5.21. In order to extract the value of the end-point, a fit with a jacobian function can be performed on the clean $M(e^+e^-) + M(\mu^+\mu^-) - M(e^+\mu^-) - M(\mu^+e^-)$ distribution, which,

Particle	Mass (GeV)		
	Point B	Point G	Point I
$\tilde{u}_L$	537.0	773.9	738.4
$\tilde{d}_L$	542.8	778.0	742.7
$\tilde{c}_L$	537.0	773.9	738.4
$\tilde{s}_L$	542.8	778.0	742.7
$\tilde{t}_1$	392.9	587.2	555.4
$\tilde{b}_1$	496.0	701.9	640.3
$\tilde{u}_R$	519.1	747.9	714.9
$\tilde{d}_R$	520.9	745.8	713.2
$\tilde{c}_R$	519.1	747.9	714.9
$\tilde{s}_R$	520.9	745.8	713.2
$\tilde{t}_2$	575.9	778.6	736.0
$\tilde{b}_2$	524.0	748.4	713.3
$\tilde{e}_R$	136.2	183.2	221.3
$\tilde{\mu}_R$	136.2	183.2	221.3
$\tilde{\tau}_2$	200.3	285.4	304.8
$\tilde{e}_L$	196.6	278.9	295.7
$\tilde{\nu}_{e_L}$	179.8	267.1	284.6
$\tilde{\mu}_L$	196.6	278.9	295.7
$\tilde{\nu}_{\mu_L}$	179.8	267.1	284.6
$\tilde{\tau}_1$	127.6	154.1	143.7
$\tilde{\nu}_{\tau_L}$	179.0	263.4	271.2
$\tilde{g}$	595.1	860.8	809.8
$\tilde{\chi}_1^0$	95.6	150.0	139.8
$\tilde{\chi}_2^0$	174.7	277.1	257.9
$\tilde{\chi}_1^\pm$	173.8	276.8	257.6
$\tilde{\chi}_3^0$	339.9	477.9	446.7
$\tilde{\chi}_4^0$	361.0	493.6	462.2
$\tilde{\chi}_2^\pm$	361.6	494.3	463.3

Table 5.8: Spectra at point B, G and I as given by `PYTHIA 6.152` with input parameters taken from `ISASUGRA 7.51`.

according to Eq. 5.21, returns the value $M_{\ell^+\ell^-}^{max} = (77.59 \pm 0.01)$ GeV for an integrated luminosity of 300 fb^{-1}.

To reconstruct the sbottom, opposite charge leptons in a window of about 15 GeV around the edge are selected. This requirement allows to select a kinematical condition in which the leptons are emitted back-to-back in the $\tilde{\chi}_2^0$ rest frame. In this condition the $\tilde{\chi}_2^0$ momentum is reconstructed through the relation:

$$\vec{p}_{\tilde{\chi}_2^0} = \left(1 + \frac{m_{\tilde{\chi}_1^0}}{M_{\ell^+\ell^-}}\right) \vec{p}_{\ell^+\ell^-}. \tag{5.22}$$

At this stage of reconstruction, we use the generated value for $m(\tilde{\chi}_1^0)$.

The $\tilde{\chi}_2^0$ momentum is then summed with the momentum of the highest E_T b-tagged jet and the $\tilde{b}$ is hence reconstructed. To reduce combinatorial background coming from wrong b jets association, further kinematical cuts have been used. All the details

	Point B	Point G	Point I
$\sigma_{SUSY}(pb)$	57.77	8.25	10.14
$\mathcal{B}R(\tilde{\chi}_2^0 \to \tilde{\ell}_R^{\pm}\ell^{\mp} \to \tilde{\chi}_1^0\ell^{\pm}\ell^{\mp})(\%)$	16.44	2.26	0.25

Table 5.9: Total SUSY cross section and $\mathcal{B}R(\tilde{\chi}_2^0 \to \tilde{\ell}_R^{\pm}\ell^{\mp} \to \tilde{\chi}_1^0\ell^{\pm}\ell^{\mp})$ for the three different benchmark points analysed.

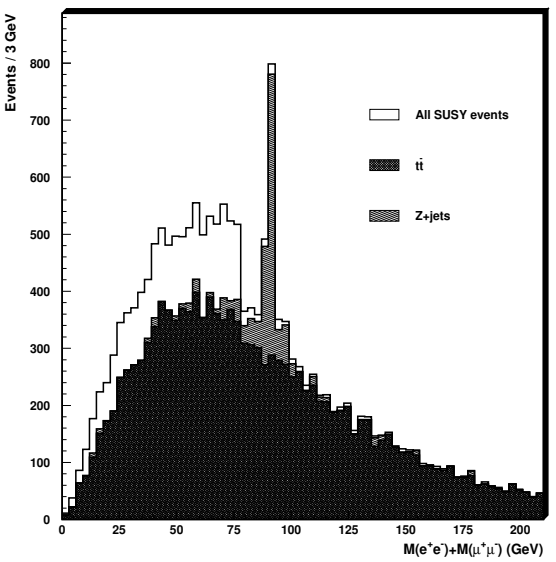

Figure 5.20: Invariant mass distribution of same flavour opposite sign isolated leptons for SUSY events, superimposed on the SM background, for an integrated luminosity of 10 fb^{-1}. The contributions of $t\bar{t}$ and Z+jets events are shown.

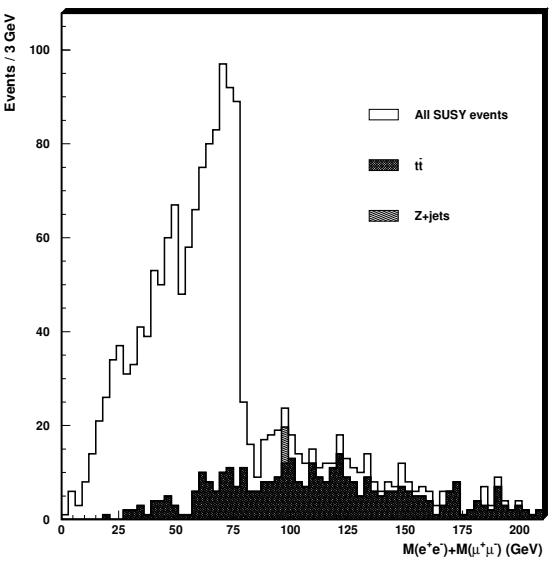

Figure 5.21: Same as in Fig. 5.20 with $E_T^{miss} > 150$ GeV and $E_{ll} > 100$ GeV cuts.

of the reconstruction procedure can be found in [391]. As shown in Fig. 5.22a, with an integrated luminosity of 300 fb^{-1}, a well visible sbottom mass peak, with a resolution well below than 10%, can be reconstructed for point B. The result of the fit, $M(\tilde{b}) = 497 \pm 2$, $\sigma = 36 \pm 3$ GeV, is in good agreement with the generated values of the two sbottoms ($\tilde{b}_1, \tilde{b}_2$), $M(\tilde{b}_1) = 496\,\mathrm{GeV}, M(\tilde{b}_2) = 524\,\mathrm{GeV}$. Indeed, the result of the fit should be considered as the superposition of the two contributions coming from $\tilde{b}_1$ and $\tilde{b}_2$, so we should compare it with the mean of the two masses weighted by the $\sigma \times BR$'s:

$$\overline{M}(\tilde{b}) = \frac{M(\tilde{b}_1) \cdot \sigma \times BR(\tilde{b}_1) + M(\tilde{b}_2) \cdot \sigma \times BR(\tilde{b}_2)}{\sigma \times BR(\tilde{b}_1) + \sigma \times BR(\tilde{b}_2)} = 503.9 \text{ GeV}$$

resulting in good agreement. Unfortunately, however, the separation of the two sbot-

tom contributions seems to be unaccessible even at very high luminosities due to the fact that the detector resolution is larger than the mass difference between the two sbottoms. However, with the ultimate luminosity of 300 fb^{-1}, reachable at the end of the LHC running period, it is possible to perform a double gaussian fit on the sbottom mass distribution. In Fig. 5.23 the two gaussian superimposed to the sbottom mass peak are shown. The results of the fit return $M(\tilde{b}_1) = 487 \pm 7$ GeV, $M(\tilde{b}_2) = 530 \pm 19$ GeV in agreement with the generated value. It is worth noticing that the ratio of the coefficient of the two gaussians, $k_1/k_2 = 2.5$, is in good agreement with the ratio of the $\sigma \times \mathcal{B}R$ for the two sbottom states, $\sigma \times \mathcal{B}R(\tilde{b}_1)/\sigma \times \mathcal{B}R(\tilde{b}_2) = 2.54$.

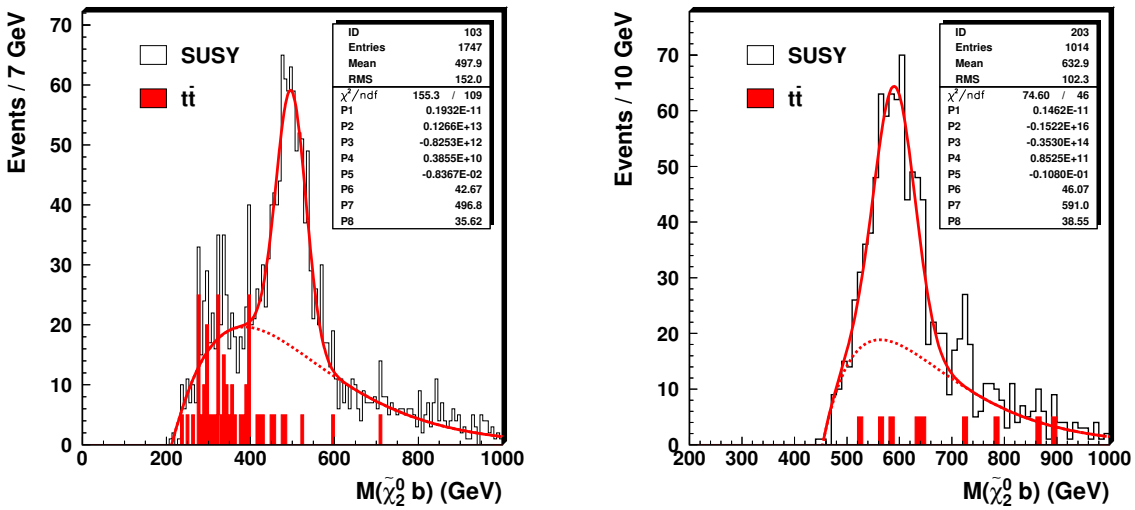

Figure 5.22: (a): $M(\tilde{\chi}_2^0 b)$; (b): $M(\tilde{\chi}_2^0 bb)$ mass distributions for an integrated luminosity of 300 fb^{-1}. In both plots results for mSUGRA point B are presented. Events in the mass window $65\,\text{GeV} < M_{\ell^+\ell^-} < 80\,\text{GeV}$ with $E_T^{miss} > 150\,\text{GeV}, E_{\ell\ell} > 100\,\text{GeV}$ and $E_T^b > 250\,\text{GeV}$ are considered.

The gluino is reconstructed from the sbottom and the b-tagged jet closest in angle. As shown in Fig. 5.22b, a resolution better than 10% is achieved also in this case and the fitted mass value, $M_{\tilde{g}} = 591 \pm 3$, $\sigma = 39 \pm 3$ GeV, is in agreement with the generated value, $M_{\tilde{g}} = 595$ GeV.

All the results shown so far are derived for point B and for an integrated luminosity of 300 fb^{-1}; it is however worth to notice that the analysis at point B can be performed also with lower integrated luminosities: the squark mass peak is visible even with an integrated luminosity of 1 fb^{-1}; sbottom and gluino can be seen with 10 fb^{-1}. The same kind of analysis was repeated also for point G. In this case the higher value of $\tan\beta$ reflects into higher branching ratio for the decay $\tilde{\chi}_2^0 \to \tau^+\tau^-\tilde{\chi}_1^0$ and to a lower signal $\tilde{\chi}_2^0 \to \tilde{\ell}^\pm\ell^\mp \to \tilde{\chi}_1^0\ell^+\ell^-$, $\ell = e, \mu$ (see Table 5.9). In order to reconstruct a clean mass peak for sbottom and gluino, not only the cuts should be tightened but also a larger integrated luminosity is needed. Only with an integrated luminosity of 300 fb^{-1} it is possible to distinguish an edge in the dilepton distribution and to reconstruct the two mass peaks ($\tilde{b}$, $\tilde{g}$) and perform the fits, nonetheless in this case a worse mass resolution is obtained. An attempt was made also to repeat the analysis at point I of ref. [386], which is characterized by a still higher value of $\tan\beta$ ($\tan\beta = 35$), but

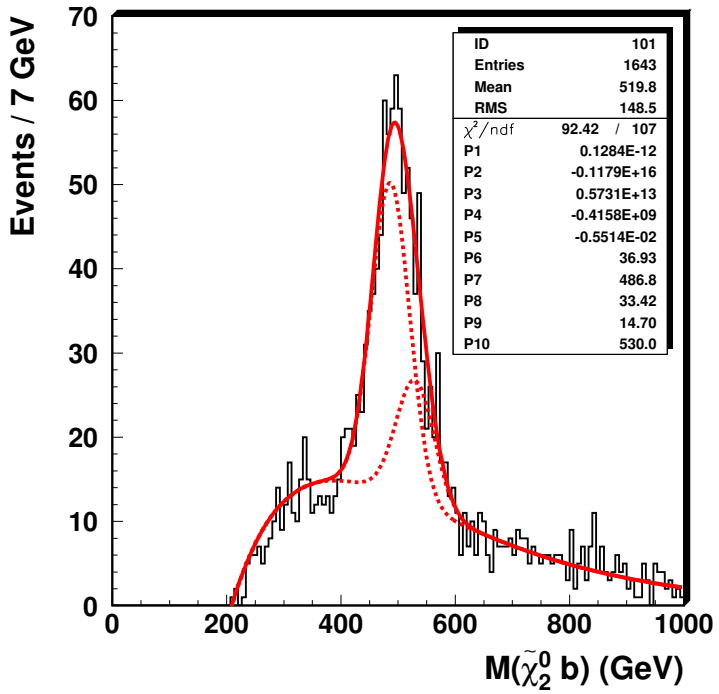

Figure 5.23: $M(\tilde{\chi}_2^0 b)$ mass distribution for an integrated luminosity of 300 fb^{-1}, superimposed with a double gaussian fit.

for that point, since the BR($\tilde{\chi}_2^0 \to \tilde{\ell}^{\pm}\ell^{\mp} \to \tilde{\chi}_1^0 \ell^+ \ell^-$) is almost negligible, even with an integrated luminosity of 300 fb^{-1}, it is not possible to distinghuish the dilepton edge. Hence no reconstruction of sbottoms and gluinos in this channel is possible. Further studies are in progress to understand the capability of reconstruction looking at the $\tau\tau$ final state.
In Table 5.10 the results obtained for the reconstructed masses and resolutions at point B and G, in the hypothesis of a known $\tilde{\chi}_1^0$ mass and at different integrated luminosity, are summarized.

		M($\tilde{b}$)	$\sigma(\tilde{b})$	M($\tilde{g}$)	$\sigma(\tilde{g})$	M($\tilde{g}$)-M($\tilde{b}$)	$\sigma(\tilde{g}$-$\tilde{b})$
Point B	10 fb^{-1}	500 ± 7	42 ± 5	594 ± 7	42 ± 7	92 ± 3	17 ± 4
	60 fb^{-1}	502 ± 4	41 ± 4	592 ± 4	46 ± 3	88 ± 2	20 ± 2
	300 fb^{-1}	497 ± 2	36 ± 3	591 ± 3	39 ± 3	90 ± 2	23 ± 2
Point G	300 fb^{-1}	720 ± 26	81 ± 18	851 ± 40	130 ± 43	127 ± 10	48 ± 11

Table 5.10: Sbottom and gluino mass resolution. All the results are expressed in GeV.

Evaluation of the $\sigma \times BR$ Antother interesting information that can be extracted by this analysis is the achievable precision on the $\sigma \times BR$ of the chain. This can be evaluated just counting events in the peaks corresponding to all the signal process in which a sbottom or a gluino is produced.

Indeed, the precision on the $\sigma \times BR$ measurement, is directly related to the number of observed events in the peak, N_{obs}, through

$$\delta(\sigma \times BR) = \frac{\delta(N_{obs})}{\mathcal{L}_{int} \cdot \epsilon}. \tag{5.23}$$

For an integrated luminosity of 10 fb^{-1}, in the sbottom peak, taking into account the region between $\overline{M} - 2.5\sigma$ and $\overline{M} + 2.5\sigma$, and subtracting the events under the background curve, we count 102 events. This means that the $\sigma \times BR$ for events in which the sbottom is directly produced or arises from a gluino, and then decays into the whole decay chain, can be measured with an error of about 10%. In the gluino peak, with the same procedure, 59 events are counted, which correspond to an error of 13% on the measurement of the gluino $\sigma \times BR$. These results can be improved with larger collected statistics: in the sbottom decay chain a precision of the order of $\sim 4.5\%$ can be achieved at 60 fb^{-1} and of the order of $\sim 1.9\%$ at 300 fb^{-1}. All the previous results have been obtained selecting events in a fixed $M_{\ell\ell}$ window ($65 < M_{\ell\ell} < 80$) around the edge. It is however important to notice that even at 10 fb^{-1} of integrated luminosity, CMS will be able to give a preliminary estimate not only of the masses of sparticles like sbottoms and gluinos, but also of the $\sigma \times BR$ of their production processes and consequent decays.

5.1.3.4 Squark and gluino reconstruction

The supersymmetric partners of the light quarks ($\tilde{u}$, $\tilde{d}$, $\tilde{c}$ and $\tilde{s}$) can be reconstructed with a similar procedure to the sbottom reconstruction, exploiting the decay chain $\tilde{g} \to \tilde{q}q$, $\tilde{q} \to \tilde{\chi}_2^0 q$, $\tilde{\chi}_2^0 \to \tilde{\ell}^{\pm}\ell^{\mp} \to \tilde{\chi}_1^0 \ell^+\ell^-$, where $\ell = e, \mu$, which is identical to the chain considered in the case of the sbottom, apart from the emission of a light quark q instead of a bottom in the decay $\tilde{q} \to \tilde{\chi}_2^0 q$. Non b-jets have to be identified, and the b-tagging capability of the CMS detector has hence to be used in order to veto the presence of b-jets and to perform an anti b-tagging.
Events are selected requiring:

- at least two same flavour opposite sign (SFOS) isolated leptons, with $p_T > 15$ GeV and $|\eta| < 2.4$; as in the previous sections, for leptons we mean only electrons and muons;
- at least two jets, tagged as non b-jets, with $p_T > 20$ GeV and $|\eta| < 2.4$;
- no b-jets.

The reconstruction procedure starts, as in the sbottom case, from the identification of the dilepton edge and hence events in the window 65 GeV $< M_{\ell\ell} <$ 80 GeV are selected and associated to the most energetic jet to get the squark invariant mass distribution. In order to reduce the SM background a cut in the missing energy is imposed, as in the previous reconstruction and also similar kinematical cuts are used to reduce the SUSY combinatorial background. A detailed description of all the cuts imposed can be found in ref. [392]. Given the very high $\sigma \times BR$ for squarks going into the $\tilde{\chi}_2^0$-dilepton chain, which is about four times larger than for the sbottom chain, it is plausible to perform the reconstruction with an integrated luminosity lower than

in the sbottom case. In ref. [391] it has been shown that squark reconstruction will be possible already with an integrated luminosity of 1 fb^{-1}, corresponding to the first two or three months of life of the Large Hadron Collider. The treatment of the combinatorial background is more complicated than for sbottom since in this case the contribution $\tilde{q}\tilde{g}$ and $\tilde{q}\tilde{q}$ processes cannot be neglected. However, similarly to the sbottom case, the use of kinematical cuts allows a good combinatorial reduction. Figure 5.24 shows the squark peak for $E_{j1} > 300$ GeV, for a sample corresponding to 300 fb^{-1} of integrated luminosity. The measured values are:

$$\begin{aligned} M(\tilde{\chi}_2^0 q) &= 536 \pm 1 \text{ GeV} \\ \sigma[M(\tilde{\chi}_2^0 q)] &= 31 \pm 1 \text{ GeV} \end{aligned}$$

Due to the Wino nature of $\tilde{\chi}_2^0$, the decay $\tilde{q} \to \tilde{\chi}_2^0$ occurs almost uniquely for the left squarks, since the right squarks decay through $\tilde{q} \to \tilde{\chi}_1^0 q$ with a BR larger than 0.99. The measured value has hence to be compared with the nominal values of the left squark, which are

$$\begin{aligned} M(\tilde{d}_L) = M(\tilde{s}_L) = 542.8 \text{ GeV} \\ M(\tilde{u}_L) = M(\tilde{c}_L) = 537.0 \text{ GeV} \end{aligned}$$

The resolution of the $\sigma \times BR$ of the entire squark production and decay process can be inferred by the number of events in the peak, which is 18048 at 300 fb^{-1}, leading to a value:

$$\frac{\delta(\sigma \times BR)}{\sigma \times BR} = 0.7\% \tag{5.25}$$

Gluino can be reconstructed going back in the decay chain with a procedure similar to the one used for the sbottom: after removing the most energetic jet from the list of the available jets, the one closest in angle to the reconstructed squark is associated to it. Figure 5.25 shows the final gluino peak for an integrated luminosity of 300 fb^{-1}, after all the kinematical cuts described in ref. [392] are applied. The gaussian fit gives:

$$\begin{aligned} M(\tilde{\chi}_2^0 qq) &= 590 \pm 2 \text{ GeV} \\ \sigma[M(\tilde{\chi}_2^0 qq)] &= 59 \pm 2 \text{ GeV} \end{aligned}$$

which is in agreement with the mass value of the generated gluino: $M(\tilde{g}) = 595.1$ GeV. Although the achieved resolution is worse than the one of the gluino reconstructed into the sbottom chain, this result is remarkable since it has been obtained in a totally indipendent way, and can eventually be combined with that in order to have a better estimate of the gluino mass.

In Table 5.11 the results obtained for the squark and gluino reconstruction for several different luminosities and different benchmark points are summarized. Also for the squark decay chain the study has been repeated at points G and I. Given the larger statistics, the results are slightly improved: the end-point of the dilepton mass distribution can be seen at point G even with 10 fb^{-1}. Nonetheless, the peak reconstructions are possible only with a large integrated luminosity, as reported in Table 5.11. No reconstruction is possible at point I.

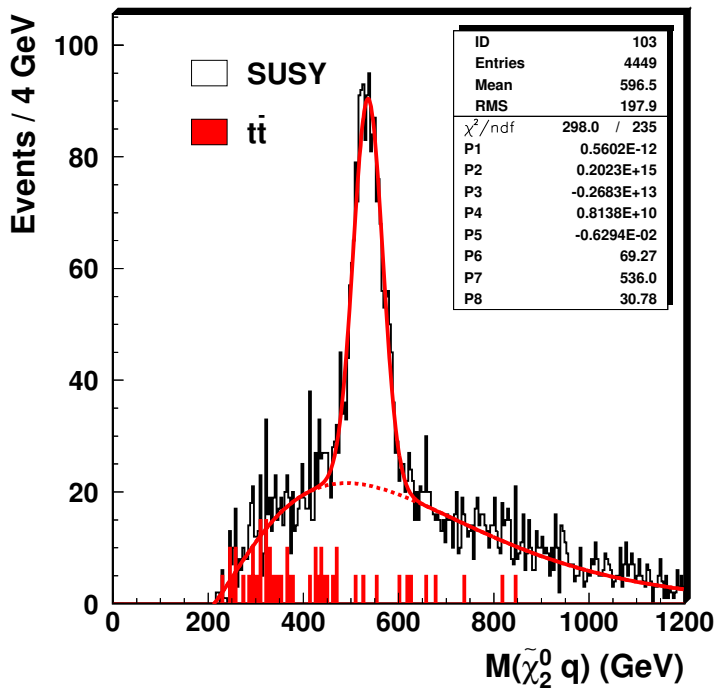

Figure 5.24: Invariant mass of the system $\tilde{\chi}_2^0 q$ for an integrated luminosity of 300 fb^{-1}. Events are selected having 65 GeV$< M_{\ell\ell} <$ 80 GeV, $E_T^{miss} > 100$ GeV and $E_{j1} > 300$ GeV. A fit is performed with a gaussian superimposed over a polynomial to take into account the combinatorial plus Standard Model background.

5.1.3.5 Neutralino mass

All the results shown in the previous sections are obtained in the hypothesis of a known $\tilde{\chi}_1^0$ mass. In a realistic scenario, however, CMS will not be able to detect $\tilde{\chi}_1^0$, this being a weakly interacting particle which escapes the detector, and other strategies have to been devoloped. One possibility is the one already exploited in ref. [89, 393], which makes use of several different end-points, in order to constraint the mass of $\tilde{\chi}_1^0$. However, this can be easily done in a favourable scenario, like the one at point B, while this could be critical if SUSY reveal itself in a scenario like the one at point G where the end-points are difficult to select or even worse in the case of point I.

It is worth noticing, that as both $M(\tilde{b})$ and $M(\tilde{g})$ depend on the $\tilde{\chi}_1^0$ mass, their difference $M(\tilde{g}) - M(\tilde{b})$ is on the contrary independent on $M(\tilde{\chi}_1^0)$. As shown in Fig. 5.26,

		M($\tilde{q}$)	$\sigma(\tilde{q})$	M($\tilde{g}$)	$\sigma(\tilde{g})$	M($\tilde{g}$)-M($\tilde{q}$)	$\sigma(\tilde{g}$-$\tilde{q})$
Point B	10 fb^{-1}	535 ± 3	57 ± 3	592 ± 7	75 ± 5	57 ± 3	9 ± 3
	60 fb^{-1}	532 ± 2	36 ± 1	595 ± 2	59 ± 2	47 ± 2	16 ± 5
	300 fb^{-1}	536 ± 1	31 ± 1	590 ± 2	59 ± 2	44 ± 2	11 ± 2
Point G	300 fb^{-1}	774 ± 9	84 ± 9	853 ± 11	126 ± 11	82 ± 3	35 ± 3

Table 5.11: Squark and gluino mass resolution. All the results are expressed in GeV.

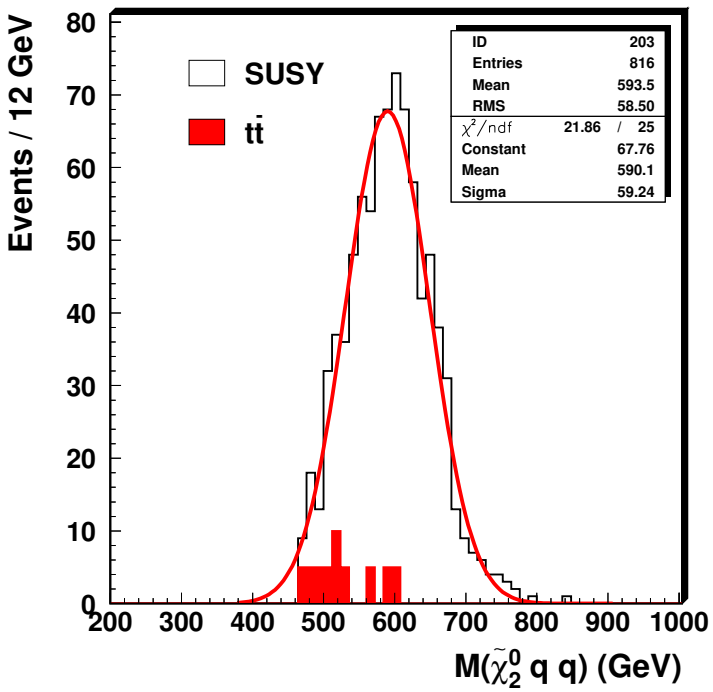

Figure 5.25: Invariant mass of the system $\tilde{\chi}_2^0 qq$ for events having 65 GeV$< M_{\ell\ell} <$ 80 GeV, $E_T^{miss} >$ 50 GeV, $E_{j1} >$ 300 GeV, 390 GeV$< M(\tilde{\chi}_2^0 q) <$ 690 GeV and $E_{j2} <$ 60 GeV. The integrated luminosity is 300 fb^{-1}.

CMS will be able to measure this difference with an error of few percents, independent of any assumption on the sparticle spectrum.

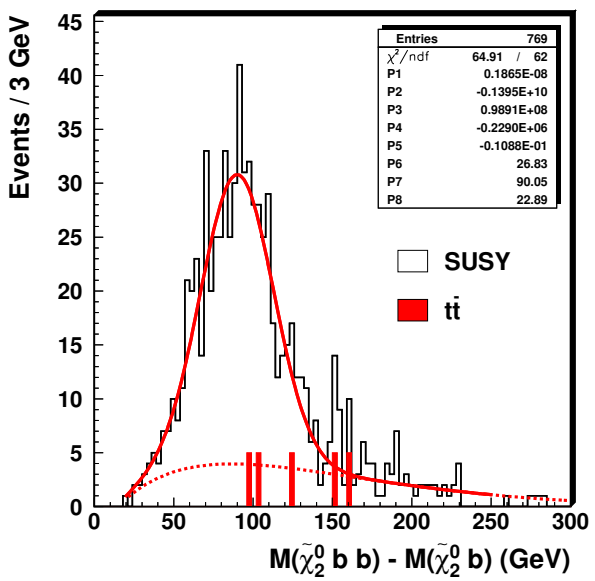

Figure 5.26: $M(\tilde{\chi}_2^0 bb) - M(\tilde{\chi}_2^0 b)$ distribution for the same events as in Fig. 5.22.

In Table 5.10 and 5.11 also the achieved resolution in the $M(\tilde{g}) - M(\tilde{b})$ for the dif-

ferent benchmark points and at several different integrated luminosities are shown.

Of course, a precise $M(\tilde{\chi}_1^0)$ measurement from a Linear Collider could be used as input in our measurements eliminating the biggest source of systematic uncertainties. To evaluate the dependence of sbottom, squark and gluino mass measurement on the accuracy of the $\tilde{\chi}_1^0$ mass knowledge, the reconstruction procedure has been repeated for different $\tilde{\chi}_1^0$ mass values. The dependence of $M(\tilde{b})$ and $M(\tilde{g})$ (sbottom decay chain) and of $M(\tilde{q})$ and $M(\tilde{g})$ (squark decay chain) on $M(\tilde{\chi}_1^0)$ is shown in Fig. 5.27 and in Fig. 5.28, respectively. All the masses of the reconstructed sparticles show a linear dependence. Performing a linear fit, we can deduce:

$$\begin{aligned}
\Delta M(\tilde{\chi}_2^0 b) &= (1.60 \pm 0.03)\Delta M(\tilde{\chi}_1^0) \\
\Delta M(\tilde{\chi}_2^0 bb) &= (1.62 \pm 0.05)\Delta M(\tilde{\chi}_1^0) \\
\Delta M(\tilde{\chi}_2^0 q) &= (1.70 \pm 0.01)\Delta M(\tilde{\chi}_1^0) \\
\Delta M(\tilde{\chi}_2^0 qq) &= (1.68 \pm 0.07)\Delta M(\tilde{\chi}_1^0)
\end{aligned}$$

In the case of the sbottom, for instance, in order to have an uncertainty less than the statistical error achieved at 300 fb^{-1}, we should have $\Delta M(\tilde{\chi}_1^0) < 1.25$ GeV. The Linear Collider should ensure an accuracy on the $\tilde{\chi}_1^0$ mass of the order of $\sim 1\%$ at point B.

This is a conservative estimate of the error on the squark, sbottom and gluino mass peaks due to the $M(\tilde{\chi}_1^0)$ uncertainty. It has in fact been evaluated living $M(\tilde{\chi}_2^0)$ unchanged while changing $M(\tilde{\chi}_1^0)$, in a hypotesis of complet independence between sparticles mass values. Realistically, this error should decrease taking into account the correlation between $M(\tilde{\chi}_2^0)$ and $M(\tilde{\chi}_1^0)$.

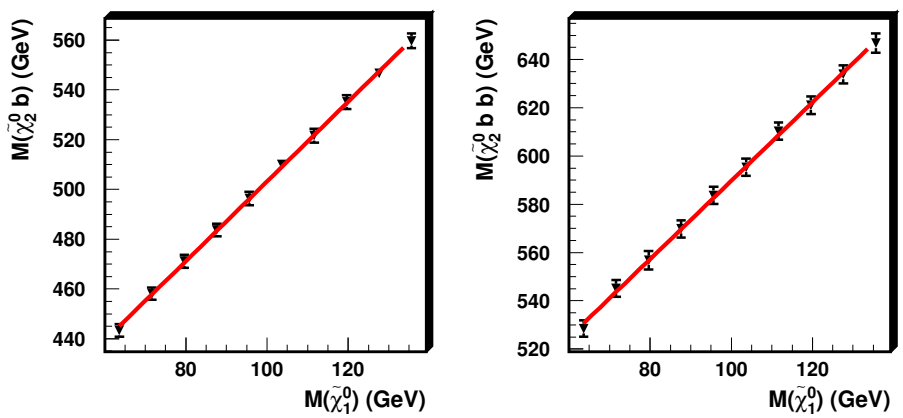

Figure 5.27: Dependence of sbottom and gluino masses (sbottom decay chain) vs $M(\tilde{\chi}_1^0)$.

5.1.3.6 Conclusions

If SUSY exists at the EW scale, the CMS detector will be able to discover it in a very large range of mSUGRA parameters. With the ultimate high luminosity of 300 fb^{-1}, strongly interacting sparticles could be discovered up to masses of 2.5 – 3 TeV.

Altough sparticle reconstruction is more difficult, new analyses have shown that in many cases it will be possible to make exclusive reconstructions. This is the case,

for istance, of the decay $\tilde{g} \rightarrow \tilde{b}b$ and $\tilde{g} \rightarrow \tilde{q}q$ which allow to reconstruct sbottom, squark and gluino masses. Resolutions better than 10% will be attainable in the low $\tan\beta$ region, already after the first year of data taking. In a favourable SUSY scenario, not only the mass of strongly interacting SUSY particles can be measured but also an estimate of the $\sigma \times \mathcal{B}R$ of their production processes and consequent decays will be possible. The combination of LHC/LC measurements will help us to reach a deeper knowledge of the SUSY sector. Detailed studies are going on in order to improve the present analysis and to evaluate the CMS capability to reconstruct SUSY sparticles.

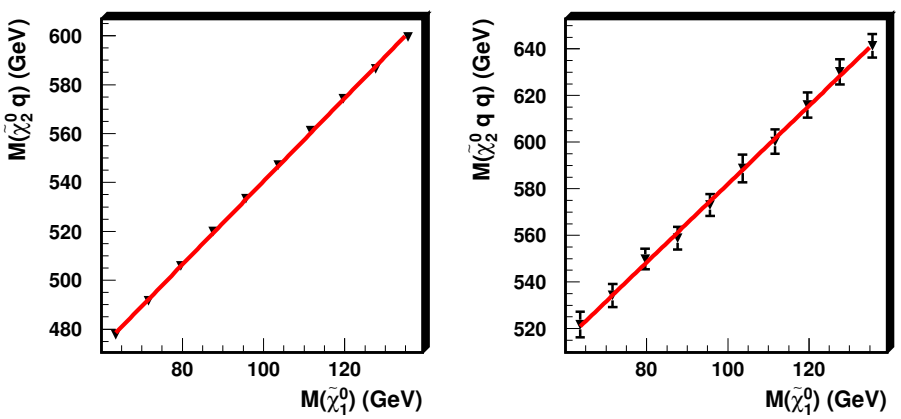

Figure 5.28: Dependence of squark and gluino masses (squark decay chain) vs $M(\tilde{\chi}_1^0)$.

5.1.4 Measurement of sparticle masses in mSUGRA scenario SPS 1a at a Linear Collider

5.1.4.1 Introduction

If low energy supersymmetry will be discovered at the LHC its gross features may be revealed, in particular for the coloured squark and gluino sector. However, a Linear Collider will be indispensible in order to provide complementary information, in particular in the slepton and neutralino/chargino sector, and to scrutinise the characteristics of the underlying SUSY structure. High precision LC experiments have to

- measure the masses, decay widths, production cross sections, mixing angles, etc., of the new particles,
- prove that each particle can be associated to its superpartner with the expected spin and parity, gauge quantum numbers and couplings,
- reconstruct the low energy SUSY breaking parameters which would allow one to uncover the fundamental theory and finally extrapolate its parameters to high (GUT, Planck) scales.

A concurrent operation of the LHC and LC would provide answers to these elementary topics already after a few years of running. A nice example to support their complementarity is the SPS 1a benchmark point [14, 369]. With the recent progress in cavity development TESLA energies of 1 TeV appear achievable, thus the complete slepton and neutralino/chargino spectra as well as the light stop $_1$ would be accessible. A peculiarity of this scenario is the large $\tan\beta = 10$ leading to (incompletely measurable) multi τ final states from $\tilde{\chi}_i^0$, $\tilde{\chi}_i^\pm$ cascade decays. Therefore charged slepton and sneutrino production are very important to measure the masses of the LSP $\tilde{\chi}_1^0$ and the light chargino $\tilde{\chi}_1^\pm$. The advantage of the LC is to explore the spectrum in a bottom-up approach, i.e. selecting particular channels by the appropriate choice of energy and beam polarisations, while suppressing background reactions.

First studies of SPS 1a masses were based on extrapolations and estimates from low $\tan\beta$ scenarios [394]. Meanwhile more reliable simulations have become available. They typicaly assume integrated luminosities of $\mathcal{L} = 250{-}500\,\mathrm{fb}^{-1}$ at $\sqrt{s} = 500\,\mathrm{GeV}$ to be accumulated within a reasonable run time of one to two years. The LC luminosity is expected to scale linearly with energy. Beam polarisations of $\mathcal{P}_{e^-} = \pm 0.8$ and $\mathcal{P}_{e^+} = \pm 0.6$ are assumed. For the determination of sparticle properties of SPS 1a other than masses see [395].

5.1.4.2 Sleptons

Scalar leptons are produced in pairs

$$e^+e^- \;\rightarrow\; \tilde{\ell}_i^+\tilde{\ell}_j^-,\ \tilde{\nu}_\ell\overline{\tilde{\nu}}_\ell \qquad\qquad \ell = e,\ \mu,\ \tau \ \text{ and } \ [i,j = L,R \ \text{ or } \ 1,2] \quad (5.27)$$

via s-channel γ/Z exchange and t-channel $\tilde{\chi}$ exchange for the first generation. The $L,\ R$ states can be determined using beam polarisation, e.g. $\tilde{\ell}_R\tilde{\ell}_R$ production is much

larger for right-handed e_R^- than for left-handed e_L^- electrons; positron polarisation further enhances the effect. The isotropic two-body decays

$$\tilde{\ell}^- \rightarrow \ell^- \tilde{\chi}_i^0 \,, \tag{5.28}$$

$$\tilde{\nu}_\ell \rightarrow \ell^- \tilde{\chi}_i^+ \tag{5.29}$$

allow for a clean identification and lead to a uniform lepton energy spectrum. The minimum and maximum ('endpoint') energies

$$E_{+/-} = \frac{\sqrt{s}}{4}\left(1 - \frac{m_{\tilde{\chi}}^2}{m_{\tilde{\ell}}^2}\right)(1 \pm \beta) \,, \tag{5.30}$$

$$m_{\tilde{l}} = \frac{\sqrt{s}}{E_- + E_+}\sqrt{E_- E_+} \,, \tag{5.31}$$

$$m_{\tilde{\chi}} = m_{\tilde{l}}\sqrt{1 - \frac{E_- + E_+}{\sqrt{s}/2}} \tag{5.32}$$

can be used for an accurate determination of the masses of the primary slepton and the secondary neutralino/chargino.

Charged slepton production in continuum Examples of mass measurements using the lepton energy spectra of $e_L^+e_R^- \rightarrow \tilde{\mu}_R\tilde{\mu}_R$ and $\tilde{e}_R\tilde{e}_R$ production at $\sqrt{s} = 400$ GeV are shown in fig. 5.29 [396]. With a moderate luminosity of $\mathcal{L} = 200$ fb^{-1} the masses can be determined with (highly correlated) errors of $\delta m_{\tilde{\mu}_R} \simeq \delta m_{\tilde{\chi}_1^0} \simeq 0.2$ GeV, respectively $\delta m_{\tilde{e}_R} \simeq \delta m_{\tilde{\chi}_1^0} \simeq 0.1$ GeV. A simultaneous analysis of $\tilde{e}_R\tilde{e}_R$, $\tilde{e}_R\tilde{e}_L$ and $\tilde{e}_L\tilde{e}_L$

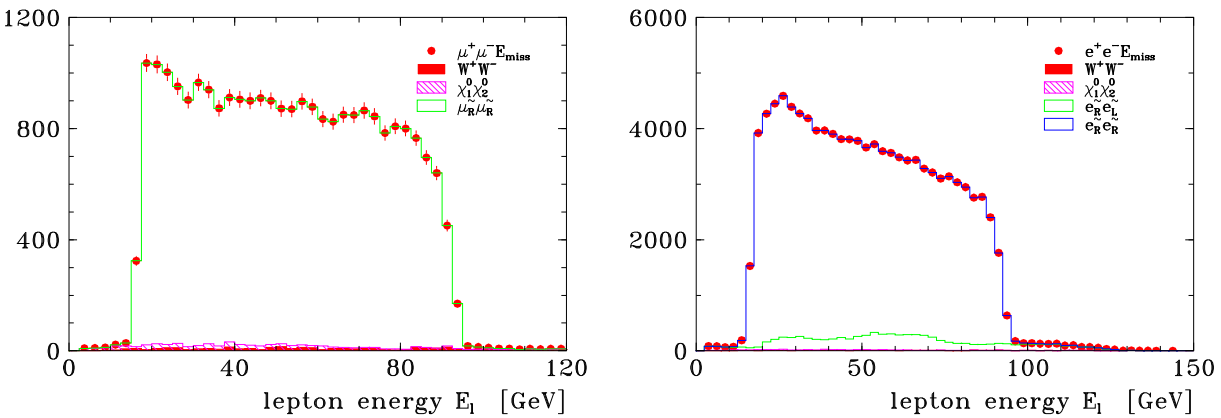

Figure 5.29: Energy spectra of E_μ from the reaction $e_L^+e_R^- \rightarrow \tilde{\mu}_R^+\tilde{\mu}_R^- \rightarrow \mu^+\tilde{\chi}_1^0\ \mu^-\tilde{\chi}_1^0$ (left) and E_e from the reaction $e_L^+e_R^- \rightarrow \tilde{e}_R^+\tilde{e}_R^- \rightarrow e^+\tilde{\chi}_1^0\ e^-\tilde{\chi}_1^0$ (right),SPS 1a at $\sqrt{s} = 400$ GeV and $\mathcal{L} = 200$ fb^{-1}

production makes use of the different energy distributions of the final electrons and positrons [397,398]. The symmetric background is eliminated by a double subtraction of e^- and e^+ energy spectra and opposite electron beam polarisations. This essentially results in a clean $\tilde{e}_R\tilde{e}_L$ sample where the endpoints from $\tilde{e}_R$ and $\tilde{e}_L$ decays are easily measurable. Assuming $\sqrt{s} = 500$ GeV and $\mathcal{L} = 2 \cdot 500$ fb^{-1}, both selectron masses can be determined with an accuracy of $\delta m_{\tilde{e}_R,\tilde{e}_L} \simeq 0.8$ GeV.

In the production of $e_L^+ e_R^- \to \tilde{\tau}_1^+ \tilde{\tau}_1^- \to \tau^+ \tilde{\chi}_1^0\, \tau^- \tilde{\chi}_1^0$ the final τ leptons are incompletely measured, thus spoiling the flat energy distribution of eq. (5.30). However, the hadronic decays $\tau \to \rho\nu_\tau,\ 3\pi\nu_\tau$ are still sensitive to the primary $\tilde{\tau}_1$ mass [396]. From the $E_{3\pi}$ energy spectrum, shown in fig. 5.30, the expected uncertainty is $\delta m_{\tilde{\tau}_1} = 0.3$ GeV, assuming the $\tilde{\chi}_1^0$ mass to be known. The heavier state $\tilde{\tau}_2$ is much more problematic to identify and measure its mass. So far no simulations for continuum production exist.

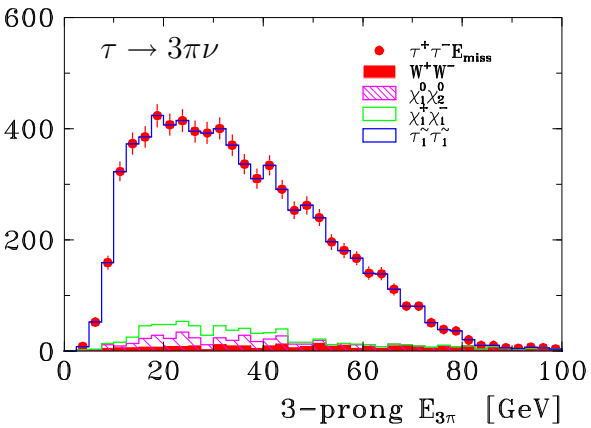

Figure 5.30: Hadron energy spectrum $E_{3\pi}$ of $\tau \to 3\pi\nu_\tau$ decays from the reaction $e_L^+ e_R^- \to \tilde{\tau}_1^+ \tilde{\tau}_1^1 \to \tau^+ \tilde{\chi}_1^0\, \tau^- \tilde{\chi}_1^0$, SPS 1a at $\sqrt{s} = 400\,\text{GeV}$ and $\mathcal{L} = 200\,\text{fb}^{-1}$

Sneutrino production Sneutrinos are very difficult to detect because most of their decays are invisible into a neutrino and a neutralino. Only $\sim 8\%$ can be identified via the decay (5.29) into the corresponding charged lepton and a chargino, which subsequently decays via $\tilde{\chi}_1^\pm \to \tilde{\tau}\nu \to \tau\nu\,\tilde{\chi}_1^0$. In practice only $\tilde{\nu}_e\tilde{\nu}_e$ production with the additional t-channel chargino exchange has a large enough cross section to be observable. A detection and measurement of $\tilde{\nu}_\mu$ and $\tilde{\nu}_\tau$ appears extremely challenging, if not hopeless. The reaction $e^+e_L^- \to \tilde{\nu}_e\tilde{\nu}_e \to \nu_e\tilde{\chi}^0\, e^\pm\tilde{\chi}_1^\mp \to e^\pm\tau^\mp \not{E}$ and $\tau \to \mu\nu\nu$ at $\sqrt{s} = 500$ GeV has been studied [397]. The energy spectrum of the primary electron can be used to determine the electron-sneutrino mass to $\delta m_{\tilde{\nu}_e} = 1.2$ GeV and the chargino mass to $\delta m_{\tilde{\chi}_1^\pm} = 1.4$ GeV.

Threshold scans Masses of accuracy $\mathcal{O}(0.1\,\text{GeV})$ can be obtained by scanning the excitation curve close to production threshold. In e^+e^- annihilation slepton pairs $\tilde{\ell}_i^+\tilde{\ell}_i^-$, except $\tilde{e}_R\tilde{e}_L$, are produced in a P-wave state with a characteristic rise of the cross section $\sigma_{\tilde{\ell}^+\tilde{\ell}^-} \sim \beta^3$, where $\beta = \sqrt{1 - 4\,m_{\tilde{\ell}}^2/s}$. On the other hand in e^-e^- collisions $\tilde{e}_R^-\tilde{e}_R^-$ and $\tilde{e}_L^-\tilde{e}_L^-$ pairs are produced in a S-wave state with a steeper rise of $\sigma_{\tilde{e}^-\tilde{e}^-} \sim \beta$. Thus, the shape of the cross section carries information on the mass and the quantum numbers. The anticipated precision requires to take the finite width $\Gamma_{\tilde{\ell}}$ and higher order corrections into account [399]. Examples of SPS 1a simulations within this frame are shown in fig. 5.31. Using polarised beams and $\mathcal{L} = 50\,\text{fb}^{-1}$ a (highly correlated) two-parameter fit gives $\delta m_{\tilde{e}_R} = 0.20$ GeV and $\delta\Gamma_{\tilde{e}_R} = 0.25$ GeV; the resolution deteriorates by a factor of ~ 2 for $\tilde{\mu}_R\tilde{\mu}_R$ production. For $e_R^-e_R^- \to \tilde{e}_R\tilde{e}_R$ the gain in resolution is substantial, yielding $\delta m_{\tilde{e}_R} = 0.050$ GeV and $\delta\Gamma_{\tilde{e}_R} = 0.045$ GeV with only a tenth of the luminosity, compared to e^+e^- beams. But notice that a LC in e^-e^- mode is expected to provide much lower luminosity, typically reduced by a factor of seven. The precision

on masses can be considerably improved if one is able fix the sparticle width, e.g. by assuming model calculations.

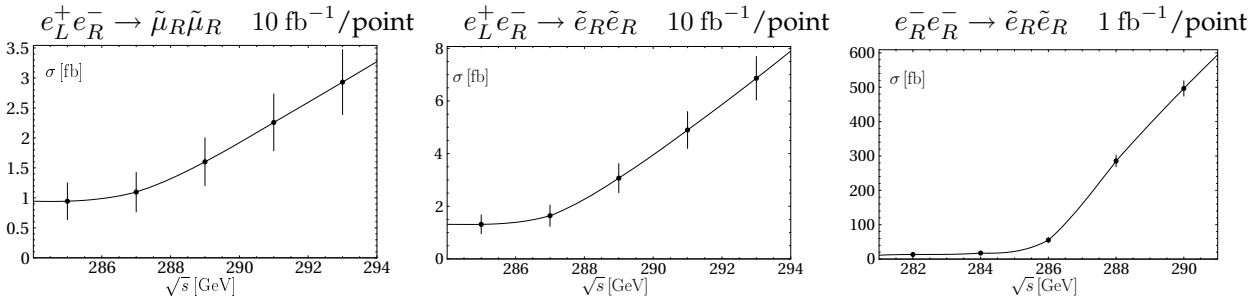

Figure 5.31: Cross sections at threshold for the reactions $e_L^+e_R^- \to \tilde{\mu}_R\tilde{\mu}_R$, $e_L^+e_R^- \to \tilde{e}_R\tilde{e}_R$ and $e_R^-e_R^- \to \tilde{e}_R\tilde{e}_R$ for SPS 1a scenario including background [399]. Error bars correspond to a luminosity of 10 fb^{-1} resp. 1 fb^{-1} per point

Taking the superior mass precision from the $\tilde{e}_R^-\tilde{e}_R^-$ scan and combining it with the energy spectrum of $\tilde{e}_R^+\tilde{e}_R^-$ production in the continuum, see fig. 5.29, one can constrain the neutralino mass to $\delta m_{\tilde{\chi}_1^0} = 0.05$ GeV or better. Such an accurate LSP mass would have immediate consequences for other processes, e.g. the construction of the kinematically allowed minimum mass $m_{\min}(\tilde{\ell})$ [400] yielding for the smuon a resolution of $\delta m_{\tilde{\mu}_R} < 0.05$ GeV [396].

5.1.4.3 Charginos and neutralinos

Charginos and neutralinos are produced in pairs

$$e^+e^- \to \tilde{\chi}_i^+\tilde{\chi}_j^- \qquad [i,j=1,2] \tag{5.33}$$

$$\to \tilde{\chi}_i^0\tilde{\chi}_j^0 \qquad [i,j=1,\ldots,4] \tag{5.34}$$

via s-channel γ/Z exchange and t-channel $\tilde{e}$ or $\tilde{\nu}_e$ exchange. Beam polarisations are important to study the $\tilde{\chi}$ properties and couplings, e.g. by manipulating the $\tilde{\nu}_e$ exchange contribution. Charginos and neutralinos decay into their lighter partners and gauge bosons or sfermion-fermion pairs

$$\tilde{\chi}_i \to Z/W\,\tilde{\chi}_j\,, \tag{5.35}$$

$$\tilde{\chi}_1^\pm \to \tilde{\tau}_1\nu_\tau \to \tau\nu_\tau\,\tilde{\chi}_1^0\,, \tag{5.36}$$

$$\tilde{\chi}_2^0 \to \tilde{\ell}\ell \to \ell\ell\,\tilde{\chi}_1^0\,. \tag{5.37}$$

Chargino production Light charginos are being detected via the process $e_R^+e_L^- \to \tilde{\chi}_1^+\tilde{\chi}_1^1 \to \tau^+\nu_\tau\tilde{\chi}_1^0\,\tau^-\nu_\tau\tilde{\chi}_1^0$. The observed final state particles are the same as in the production of $\tilde{\tau}_1\tilde{\tau}_1$ and $\tilde{\chi}_2^0\tilde{\chi}_1^0 \to \tau\tau\tilde{\chi}_1^0\tilde{\chi}_1^0$, a severe background which may be partially removed by topological cuts. The chargino mass may be reconstructed from the energy spectra of hadronic τ decays. In a model similar to SPS 1a a simulation at $\sqrt{s} = 400$ GeV and $\mathcal{L} = 200$ fb^{-1} yields a mass uncertainty of $\delta m_{\tilde{\chi}_1^\pm} = 1.5$ GeV [401].

Alternatively the cross section at threshold can be scanned which rises fairly steeply as $\sigma_{\tilde{\chi}\tilde{\chi}} \sim \beta$, characteristic for the chargino's spin $1/2$. The excitation curve is shown in fig. 5.32 and provides a chargino mass determination accurate to $\delta m_{\tilde{\chi}^\pm} = 0.55$ GeV.

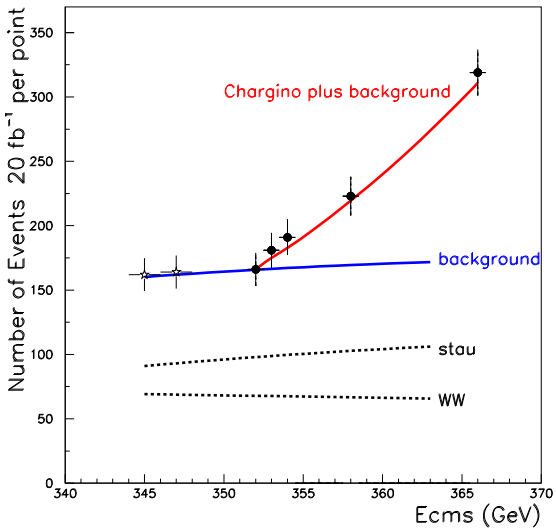

Figure 5.32: Threshold scan of $e^+_R e^-_L \to \tilde{\chi}^+_1 \tilde{\chi}^1_1 \to \tau^+ \nu_\tau \tilde{\chi}^0_1 \, \tau^- \nu_\tau \tilde{\chi}^0_1$ for SPS 1a assuming $\mathcal{L} = 100\,\mathrm{fb}^{-1}$

The heavy chargino may be produced via $e^+e^- \to \tilde{\chi}^\pm_1 \tilde{\chi}^\mp_2$ and identified via the bosonic two-body decays $\tilde{\chi}^\pm_2 \to Z\tilde{\chi}^\pm_1,\ W\tilde{\chi}^0_1$. From the energy distributions of the reconstructed Z, W a resolution of $\delta m_{\tilde{\chi}^\pm_2} \sim 3\,\mathrm{GeV}$ is estimated. Complete simulations of the process don't yet exist.

Neutralino production The continuum production of neutralino $\tilde{\chi}^0_2$ has been studied in the reaction $e^+e^- \to \tilde{\chi}^0_1 \tilde{\chi}^0_2$ followed the dominant decay mode $\tilde{\chi}^0_2 \to \tau\tau\tilde{\chi}^0_1$ [402]. Both τ's are required to be emitted in the same hemisphere, but the SUSY background is still very large. The shape of the $m_{\tau\tau}$ effective mass distribution is sensitive to the neutralino mass within $\delta m_{\tilde{\chi}^0_2} \sim 2\,\mathrm{GeV}$.

More promising is a threshold scan of $e^+_R e^-_L \to \tilde{\chi}^0_2 \tilde{\chi}^0_2 \to 4\,\tau + 2\,\tilde{\chi}^0_1$, which has very low background. Assuming $\mathcal{L} = 100\,\mathrm{fb}^{-1}$ one achieves a precision of $\delta m_{\tilde{\chi}^0_1} = 1.2\,\mathrm{GeV}$.

The simulation of inclusive cascade decays $\tilde{\chi}^0_2 \to e^+e^-\tilde{\chi}^0_1,\ \mu^+\mu^-\tilde{\chi}^0_1$, where the dilepton masses are sensitive to the $\tilde{\chi}^0_2 - \tilde{\chi}^0_1$ mass difference has not yet been tried. These chains are important in the LHC analysess [403,404], but they are difficult to be observed at a LC since the decay modes are an order of magnitude less frequent and the signature competes with a large signal from $\tilde{e}\tilde{e}$, $\tilde{\mu}\tilde{\mu}$ production.

High mass neutralinos $\tilde{\chi}^0_3$, $\tilde{\chi}^0_4$ can be detected via the bosonic Z, W decays (5.35). First studies at $\sqrt{s} = 750\,\mathrm{GeV}$ show that for high luminosity the Z energy spectra can be used to reconstruct the heavy neutralino masses with resolutions of a few GeV [397].

5.1.4.4 Stop production

Light stop production may become accessible if the LC can be operated at $\sqrt{s} = 1\,\mathrm{TeV}$. The observation will be based on the production and decay sequence $e^+e^- \to_{11} \to b\tilde{\chi}^+_1 \bar{b}\tilde{\chi}^-_1 \to b\tau^+\nu\tilde{\chi}^0_1 \bar{b}\tau^+\nu\tilde{\chi}^0_1$, i.e. the signature are 2 b-jets + 2 τ's in the final state. The analysis techniques are similar to those in the slepton sector. One can use the energy spectrum of the b-jets and exploit the $b\,b$ correlations to construct the minimum kinematically allowed mass $m_{\min}()$ assuming $m_{\tilde{\chi}^\pm}$ to be known [400]. With a luminosity of $1000\,\mathrm{fb}^{-1}$ the rate will be sufficient to achieve a mass resolution of $\delta m_{_1} = 2\,\mathrm{GeV}$.

	m [GeV]	Δm [GeV]	Comments
$\tilde{\chi}_1^{\pm}$	176.4	0.55	simulation threshold scan , 100 fb^{-1}
$\tilde{\chi}_2^{\pm}$	378.2	3	estimate $\tilde{\chi}_1^{\pm}\tilde{\chi}_2^{\mp}$, spectra $\tilde{\chi}_2^{\pm} \to Z\tilde{\chi}_1^{\pm}$, $W\tilde{\chi}_1^0$
$\tilde{\chi}_1^0$	96.1	0.05	combination of all methods
$\tilde{\chi}_2^0$	176.8	1.2	simulation threshold scan $\tilde{\chi}_2^0\tilde{\chi}_2^0$, 100 fb^{-1}
$\tilde{\chi}_3^0$	358.8	3 – 5	spectra $\tilde{\chi}_3^0 \to Z\tilde{\chi}_{1,2}^0$, $\tilde{\chi}_2^0\tilde{\chi}_3^0, \tilde{\chi}_3^0\tilde{\chi}_4^0$, 750 GeV, > 1000 fb^{-1}
$\tilde{\chi}_4^0$	377.8	3 – 5	spectra $\tilde{\chi}_4^0 \to W\tilde{\chi}_1^{\pm}$, $\tilde{\chi}_2^0\tilde{\chi}_4^0, \tilde{\chi}_3^0\tilde{\chi}_4^0$, 750 GeV, > 1000 fb^{-1}
$\tilde{e}_R$	143.0	0.05	e^-e^- threshold scan, 10 fb^{-1}
$\tilde{e}_L$	202.1	0.2	e^-e^- threshold scan 20 fb^{-1}
$\tilde{\nu}_e$	186.0	1.2	simulation energy spectrum, 500 GeV, 500 fb^{-1}
$\tilde{\mu}_R$	143.0	0.2	simulation energy spectrum, 400 GeV, 200 fb^{-1}
$\tilde{\mu}_L$	202.1	0.5	estimate threshold scan, 100 fb^{-1} [394]
$\tilde{\tau}_1$	133.2	0.3	simulation energy spectra, 400 GeV, 200 fb^{-1}
$\tilde{\tau}_2$	206.1	1.1	estimate threshold scan, 60 fb^{-1} [394]
$\tilde{t}_1$	379.1	2	estimate b-jet spectrum, $m_{\min}()$, 1TeV, 1000 fb^{-1}

Table 5.12: Sparticle masses and their expected precisions in Linear Collider experiments, SPS 1a mSUGRA scenario.

5.1.4.5 Summary

The results of the SPS 1a sparticle mass studies are summarised in table 5.12, where the best values expected from either production in the continuum or threshold scans are quoted. For most sparticles they are based on realistic Monte Carlo and detector simulations and reasonable assumptions on the LC performance. Only the heavy $\tilde{\chi}^0$, $\tilde{\chi}^{\pm}$ and $_1$ states rely on some plausible estimates. Typical accuracies in the per cent to per mil range can be expected at a Linear Collider. These precision measurements serve as input to explore SUSY scenarios in a model independent way [405]. It should be pointed out once more that LC experiments provide much more valuable information, such as accurate values on mixing angles, couplings and quantum numbers.

The final goal would be to perform a combined analysis of all available experimental information – including masses, cross sections, branching ratios, etc. from the LC and LHC [403, 404] – in order to arrive at a high precision determination of the SUSY Lagrange parameters and to extrapolate them to high scales aiming at reconstructing the fundamental parameters and the mechanism of supersymmetry breaking. This requires also that theoretical calculations have to be developed to the same accuracy as the anticipated experiments. Such a programme is in progress [406].

5.1.5 Sparticle mass measurements from LHC analyses and combination with LC results

The analyses briefly described in the previous sections provide a series of measurements of kinematic quantities which are directly related to sparticle masses and branching fractions through simple algebraic formulae.

Some of the measurements, performed in the framework of both ATLAS and CMS, can be used to extract a direct measurement of the masses of the sparticles. Some others, in particular the analyses in the stop/sbottom sectors provide the measurements

of complex quantities which are used in other sections (see Sec. 5.1.7) to strongly constrain the parameters of the MSSM. We concentrate in this section on the information of masses which can be obtained from the LHC analyses, and on how the information from LHC and LC can be combined.

In order to have a single consistent set, we base ourselves here only on the ATLAS analyses, which address a broader range of signatures than the CMS ones. We have however checked that the CMS results, once different analysis assumptions are correctly taken into account, give results consistent with the ATLAS ones.

We summarize in Table 5.13 all of the used measurements, with the statistical error corresponding to the ultimate integrated luminosity for the LHC of 300 fb^{-1}. The central values of the measured quantities are calculated from the mass spectrum of ISASUSY 7.58.

For all measurements, a systematic error from the uncertainty on the energy scale in the detector is given, corresponding to 1% for the measurements involving hadronic jets, and 0.1% for purely leptonic measurements. For the case of $m_{\tau\tau}^{max}$ and $m(\tilde{q}_R)$, the errors given in the first column (respectively 5 and 10 GeV) are very conservative estimates of the systematic uncertainty on the precision with which the observed structures can be related to the corresponding physical quantities. More detailed studies are needed for a firmer estimate.

Table 5.13: Summary table of the SUSY measurements which can be performed at the LHC with the ATLAS detector. The statistical errors are given for the ultimate integrated luminosity of 300 fb^{-1}. The uncertainty in the energy scale results in an error of 1% for measurements including jets, and of 0.1% for purely leptonic mesurements.

		Errors		
Variable	Value (GeV)	Stat. (GeV)	Scale (GeV)	Total
$m_{\ell\ell}^{max}$	77.07	0.03	0.08	0.08
$m_{\ell\ell q}^{max}$	428.5	1.4	4.3	4.5
$m_{\ell q}^{low}$	300.3	0.9	3.0	3.1
$m_{\ell q}^{high}$	378.0	1.0	3.8	3.9
$m_{\ell\ell q}^{min}$	201.9	1.6	2.0	2.6
$m_{\ell\ell b}^{min}$	183.1	3.6	1.8	4.1
$m(\ell_L) - m(\tilde{\chi}_1^0)$	106.1	1.6	0.1	1.6
$m_{\ell\ell}^{max}(\tilde{\chi}_4^0)$	280.9	2.3	0.3	2.3
$m_{\tau\tau}^{max}$	80.6	5.0	0.8	5.1
$m(\tilde{g}) - 0.99 \times m(\tilde{\chi}_1^0)$	500.0	2.3	6.0	6.4
$m(\tilde{q}_R) - m(\tilde{\chi}_1^0)$	424.2	10.0	4.2	10.9
$m(\tilde{g}) - m(\tilde{b}_1)$	103.3	1.5	1.0	1.8
$m(\tilde{g}) - m(\tilde{b}_2)$	70.6	2.5	0.7	2.6

The values in the table can either be used stand-alone in order to extract a consistent set of mass measurement from the LHC, or combined with equivalent measurements from the LC in order to obtain a global picture of the SUSY mass spectra.

The available measurements are naturally divided into two classes:

- a set of six edge measurements, each involving typically three among the masses of $\tilde{q}_L$, $\tilde{\chi}_2^0$, $\tilde{l}_R$ and $\tilde{\chi}_1^0$
- a set of measurements involving the mass of an additional sparticle and one or more of the sparticles involved in the edge measurement.

A two-step strategy can therefore be used in order to calculate the SUSY mass spectrum from the LHC data alone. The first step consists in solving the system of equations (5.9)–(5.13) for $\tilde{q}_L$, $\tilde{b}_1$, $\tilde{\chi}_2^0$, $\tilde{l}_R$ and $\tilde{\chi}_1^0$. The second step consists, for each additional particle, in calculating explicitly its mass using as an input the mass values for the lighter sparticles calculated using the edge measurements.

The system of equations involving the edge measurements is solved numerically, by finding the set of mass values which minimizes the χ^2 function,

$$\chi^2 = \sum_j \chi_j^2 = \sum_j \left[\frac{E_j^{\text{theory}}(\vec{m}) - E_j^{\text{exp}}}{\sigma_j^{\text{exp}}} \right]^2 . \tag{5.38}$$

Here $E_j^{\text{theory}}(\vec{m})$ is the theoretical value for the masses $\vec{m} = \{m_{\tilde{q}_L}, m_{\tilde{b}_1}, m_{\tilde{\chi}_2^0}, m_{\tilde{l}_R}, m_{\tilde{\chi}_1^0}\}$, E_j^{exp} is the measurement of edge number j, and σ_j^{exp} is the estimated error of the edge measurement.

In order to assess the precision with which ATLAS can determine the sparticle masses from the procedure of fitting kinematic edges, we generate a large number of LHC "experiments". For each "experiment" i we construct a set of edge measurements E_j^i from the estimated errors in the following way

$$E_j^i = E_j^{\text{nom}} + a_j^i \sigma_j^{\text{fit}} + b^i \sigma_j^{Escale}, \tag{5.39}$$

where E_j^{nom} is the nominal value for edge number j, σ_j^{fit} is the combined error on the fit value and σ_j^{Escale} is the energy scale error. Within each "experiment" b^i and a_j^i are picked from Gaussian distributions of mean value 0 and width 1. The resulting masses have a near Gaussian distribution around the nominal values with RMS deviations given in Table 5.13.

Since the analytic formulae for the edge positions, Eqs. (5.9)–(5.13), consist mainly of mass *differences* there are strong correlations between the masses. Due to the very accurate determination of the m_{ll} edge, see Eq. (5.9) and Table 5.5, the two neutralinos and the slepton are very interdependent. If one of them is overestimated, so are the other two. This is illustrated in Fig. 5.33 (left panel) for $\tilde{\chi}_1^0$ and $\tilde{l}_R$. The correlation between $\tilde{\chi}_1^0$ and $\tilde{\chi}_2^0$ or $\tilde{l}_R$ and $\tilde{\chi}_2^0$ are similar. In contrast, the correlation between $\tilde{q}_L$ and the lighter particles is less severe, but still significant, due to the less precise measurements of the edge positions involving a jet. This can be seen in the center panel of Fig. 5.33. Finally, the rather imprecise determination of edges involving a b-quark, leads to the $\tilde{b}_1$ having only a mild correlation with the lighter masses, as seen in the right-hand panel of Fig. 5.33.

Using the mass measurements for the lighter neutralinos obtained through the edge analysis, model-independent mass measurements can be extracted from the measurements in Table 5.13.

The resulting uncertainties are given in Table 5.14, for an integrated luminosity of 300 fb^{-1}. The measurement of $m(\tilde{b}_1)$ obtained with the edges is superseded by the

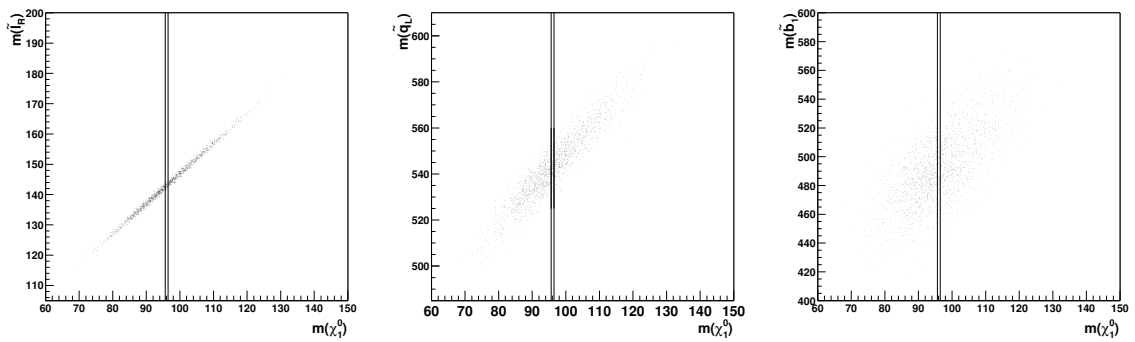

Figure 5.33: Mass correlation plots. Dots: LHC alone. Vertical bands: Fixing $m_{\tilde{\chi}_1^0}$ to within $\pm 2\sigma$ with LC input ($\sigma = 0.2\%$).

one obtained through the study of the gluino decay chain. For the $\tilde{\tau}_1$ and $\tilde{q}_R$ masses the edge measurements given in Table 5.13 include a large systematic error. This is a rough and conservative estimate of the actual uncertainty, due to the fact that the analysis concerned are very preliminary. We expect this uncertainty to be significantly reduced by more detailed analyses. We quote for the mass measurement extracted from these analyses an interval of uncertainties, where the upper value corresponds to using the systematic error in full, and the lower value to putting the systematic uncertainty to zero. The analyses at the LHC are not able to discriminate the production of squarks of the first four flavours, therefore the uncertainty is quoted for generic $\tilde{q}_R$ and $\tilde{q}_L$. The values of the masses are derived from kinematic measurements, not from direct measurement. Therefore, as shown clearly in Fig. 5.33 they are strongly correlated. Therefore any analysis trying to extract a global fit from the LHC measurements should start from the actual measurements rather than from the values of the masses shown. Most of the sparticle measurements shown rely on knowing the values of the lighter sparticles, which are accessible at the LC. The combined result for LHC and LC was therefore obtained by giving as an input to the mass calculation program the LC values for the masses of the sleptons and of the lighter neutralinos, with the errors quoted in Table 5.12. The results are shown in the second column of Table 5.14. One can notice that the improvement on the measurements of the masses of squarks and gluinos are moderate, as the LHC measurements are dominated by the 1% error on the jet energy scale. Achieving this level of uncertainty on the jet scale will require very detailed studies on the part of the LHC collaborations, and it is unlikely that the uncertainty could be reduced below the 1% level. As an academic exercise we evaluated how the mass measurement uncertainty would change if one respectively assumes 0.5% jet energy scale error and no jet energy scale error. Note that by using the sparticle masses determined at a LC the correlations between the masses determined at the LHC can be strongly reduced, as demonstrated in Fig. 5.33. The vertical bands show the 2σ precision with which the mass of $\tilde{\chi}_1^0$ can be determined at a LC. E.g., using $m_{\tilde{\chi}_1^0}$ from the LC basically fixes the mass of the $\tilde{l}_R$ determined from the LHC data.

Table 5.14: The RMS values of the mass distribution in the case of the LHC alone, and combined with measurements from the LC. The results from Table 5.13 and Table 5.12 are used as an input. All numbers in GeV.

	LHC	LHC+LC
$\Delta m_{\tilde{\chi}_1^0}$	4.8	0.05 (LC input)
$\Delta m_{\tilde{\chi}_2^0}$	4.7	0.08
$\Delta m_{\tilde{\chi}_4^0}$	5.1	2.23
$\Delta m_{\tilde{l}_R}$	4.8	0.05 (LC input)
$\Delta m_{\tilde{l}_L}$	5.0	0.2 (LC input)
Δm_{τ_1}	5-8	0.3 (LC input)
$\Delta m_{\tilde{q}_L}$	8.7	4.9
$\Delta m_{\tilde{q}_R}$	7-12	5-11
$\Delta m_{\tilde{b}_1}$	7.5	5.7
$\Delta m_{\tilde{b}_2}$	7.9	6.2
$\Delta m_{\tilde{g}}$	8.0	6.5

Table 5.15: The RMS values of the mass distribution in the case of the LHC alone, and combined with measurements from the LC, under the assumption that an uncertainty on the jet energy scale of 0.5% can be achieved at the LHC. The results from Table 5.13 and Table 5.12 are used as an input. All numbers in GeV.

	LHC (0.5% jet scale)	LHC (0.5% jet scale) + LC
$\Delta m_{\tilde{q}_L}$	7.8	2.6
$\Delta m_{\tilde{b}_1}$	6.0	3.7
$\Delta m_{\tilde{b}_2}$	6.4	4.3
$\Delta m_{\tilde{g}}$	6.0	3.7

Table 5.16: The RMS values of the mass distribution in the case of the LHC alone, and combined with measurements from the LC, for the case where a vanishing uncertainty on the jet energy scale at the LHC is assumed. The results from Table 5.13 and Table 5.12 are used as an input. All numbers in GeV.

	LHC (0% jet scale)	LHC (0% jet scale) + LC
$\Delta m_{\tilde{q}_L}$	7.4	0.8
$\Delta m_{\tilde{b}_1}$	5.4	2.8
$\Delta m_{\tilde{b}_2}$	5.8	3.4
$\Delta m_{\tilde{g}}$	5.2	2.3

5.1.6 Susy parameter determination in combined analyses at LHC/LC

5.1.6.1 Introduction

Supersymmetry (SUSY) is one of the best motivated extensions of the Standard Model (SM). However, since SUSY has to be broken even the minimal version, the unconstrained MSSM, has 105 new parameters. SUSY analyses at future experiments, at the LHC and at a future Linear Collider (LC) [407], will have to focus on the determination of these parameters in as model-independent a way as possible.

With so many new parameters clear strategies will be needed in analysing the experimental data [408]. An interesting possibility to resolve the new physics is to start with the gaugino/higgsino particles which are expected to be among the lightest SUSY particles. In the unconstrained MSSM this sector depends only on 4 parameters at tree level: M_1, M_2, μ and $\tan\beta$ – the U(1) and SU(2) gaugino masses, the higgsino mass parameter and the ratio of the vacuum expectations of the two Higgs fields, respectively.

Some strategies have been worked out for the determination at the tree level the parameters M_1, M_2, μ, $\tan\beta$ even if only the light gaugino/higgsino particles, $\tilde{\chi}_1^0$, $\tilde{\chi}_2^0$ and $\tilde{\chi}_1^\pm$ were kinematically accessible at the first stage of the LC [409]. In this report we demonstrate how such an LC analysis could be strengthened if in addition some information on the mass of the heaviest neutralino from the LHC is available [410]. We consider three scenarios: (i) stand alone LC data, (ii) when the LC data are supplemented by the heavy neutralino mass estimated from the LHC data, and (iii) joint analysis of the LC and LHC data. In particular mass predictions of the heavier states from the LC analysis are possible which lead to an improved possibility to correctly interpret LHC measurements of these particles. The results in the last scenario will clearly demonstrate the essentiality of the LHC and the LC and the benefit from the joint analysis of their data.

In order to work out this hand-in-hand LHC+LC analysis for determining the tree-level SUSY parameters, we assume that only the first phase of a LC with a tunable energy up to $\sqrt{s} = 500$ GeV would overlap with the LHC running. Furthermore, we assume an integrated luminosity of $\int \mathcal{L} \sim 500$ fb^{-1} and polarised beams with $P(e^-) = \pm 80\%$, $P(e^+) = \pm 60\%$. In the following σ_L will refer to cross sections obtained with $P(e^-) = -80\%$, $P(e^+) = +60\%$, and σ_R with $P(e^-) = +80\%$, $P(e^+) = -60\%$. We restrict ourselves to the CP conserving chargino/neutralino sector and take the SPS1a as a working benchmark [14,369]; the inclusion of CP violating phases will be considered elsewhere. While the electroweak scale parameters of the SPS1a scenario are derived from a mSUGRA model, we do not impose any mSUGRA relations anywhere in this analysis. Thus the analysis and the results are qualitatively valid for any MSSM scenario with a similar mass spectrum.

Before presenting our results on the parameter determination, we first briefly recapitulate the main features of chargino and neutralino sectors and sketch our strategy.

5.1.6.2 The gaugino/higgsino sector

a) Chargino sector

The mass matrix of the charged gaugino $\tilde{W}^{\pm}$ and higgsino $\tilde{H}^{\pm}$ is given by[2]

$$\mathcal{M}_C = \begin{pmatrix} M_2 & \sqrt{2} m_W \cos\beta \\ \sqrt{2} m_W \sin\beta & \mu \end{pmatrix} \tag{5.40}$$

As a consequence of possible field redefinitions, the parameter M_2 can be chosen real and positive. The two charginos $\tilde{\chi}^{\pm}_{1,2}$ are mixtures of the charged SU(2) gauginos and higgsinos. Since the mass matrix $\mathcal{M}_C$ is not symmetric, two different unitary matrices acting on the left– and right–chiral $(\tilde{W}, \tilde{H})_{L,R}$ two–component states

$$\begin{pmatrix} \tilde{\chi}^-_1 \\ \tilde{\chi}^-_2 \end{pmatrix}_{L,R} = U_{L,R} \begin{pmatrix} \tilde{W}^- \\ \tilde{H}^- \end{pmatrix}_{L,R} \tag{5.41}$$

define charginos as mass eigenstates. For real $\mathcal{M}_C$ the unitary matrices U_L and U_R can be parameterised as

$$U_{L,R} = \begin{pmatrix} \cos\Phi_{L,R} & \sin\Phi_{L,R} \\ -\sin\Phi_{L,R} & \cos\Phi_{L,R} \end{pmatrix} \tag{5.42}$$

The mass eigenvalues $m^2_{\tilde{\chi}^{\pm}_{1,2}}$ and the mixing angles are given by

$$\begin{aligned} m^2_{\tilde{\chi}^{\pm}_{1,2}} &= \frac{1}{2}(M_2^2 + \mu^2 + 2m_W^2 \mp \Delta_C) \\ \cos 2\phi_{L,R} &= -(M_2^2 - \mu^2 \mp 2m_W^2 \cos 2\beta)/\Delta_C \end{aligned}$$

where $\Delta_C = [(M_2^2 - \mu^2)^2 + 4m_W^4 \cos^2 2\beta + 4m_W^2(M_2^2 + \mu^2) + 8m_W^2 M_2 \mu \sin 2\beta]^{1/2}$.

The $e^+e^- \to \tilde{\chi}^{\pm}_i \tilde{\chi}^{\mp}_j$ production processes occur via the s-channel γ, Z^0 and the t-channel $\tilde{\nu}_e$ exchange. Since the two mixing angles $\Phi_{L,R}$ enter the couplings in the $\tilde{\chi}\tilde{\chi}Z$ and $e\tilde{\chi}\tilde{\nu}_e$ vertices, the chargino production cross sections $\sigma^{\pm}\{ij\} = \sigma(e^+e^- \to \tilde{\chi}^{\pm}_i \tilde{\chi}^{\mp}_j)$ are bilinear functions of $\cos 2\Phi_{L,R}$ [412] and can be written as

$$\sigma^{\pm}\{ij\} = c_1 \cos^2 2\Phi_L + c_2 \cos 2\Phi_L + c_3 \cos^2 2\Phi_R + c_4 \cos 2\Phi_R + c_5 \cos 2\Phi_L \cos 2\Phi_R + c_6 \tag{5.43}$$

We derived the coefficients $c_1, \ldots, c_6$ for the lightest chargino pair production cross section, see Appendix a).

b) Neutralino sector

The neutralino mixing matrix in the $\{\tilde{\gamma}, \tilde{Z}^0, \tilde{H}^0_1, \tilde{H}^0_2\}$ basis is given by

$$\mathcal{M}_N = \begin{pmatrix} M_1 \cos^2_W + M_2 \sin^2_W & (M_2 - M_1)\sin_W \cos_W & 0 & 0 \\ (M_2 - M_1)\sin_W \cos_W & M_1 \sin^2_W + M_2 \cos^2_W & m_Z & 0 \\ 0 & m_Z & \mu \sin 2\beta & -\mu \cos 2\beta \\ 0 & 0 & -\mu \cos 2\beta & -\mu \sin 2\beta \end{pmatrix} \tag{5.44}$$

The neutralino eigenvectors and their masses are obtained with the 4×4 diagonalisation matrix N:

$$N^* \mathcal{M}_N N^{\dagger} = \tilde{f} diag\{m_{\tilde{\chi}^0_1}, \ldots, m_{\tilde{\chi}^0_4}\} \tag{5.45}$$

[2]One should note the difference between our convention of taking $\tilde{\chi}^-$ as "particles" and e.g. the convention of [411].

The parameter M_1 can only be determined from the neutralino sector. The characteristic equation of the mass matrix squared, $\mathcal{M}_N\mathcal{M}_N^\dagger$, can be written as a quadratic equation for the parameter M_1:

$$x_i M_1^2 + y_i M_1 - z_i = 0, \quad \text{for} \quad i = 1,2,3,4 \tag{5.46}$$

where x_i, y_i, z_i are given by:

$$\begin{aligned} x_i &= -m^6_{\tilde{\chi}^0_i} + a_{41} m^4_{\tilde{\chi}^0_i} - a_{21} m^2_{\tilde{\chi}^0_i} + a_{01}, & (5.47)\\ y_i &= a_{42} m^4_{\tilde{\chi}^0_i} - a_{22} m^2_{\tilde{\chi}^0_i} + a_{02}, & (5.48)\\ z_i &= m^8_{\tilde{\chi}^0_i} - a_{63} m^6_{\tilde{\chi}^0_i} + a_{43} m^4_{\tilde{\chi}^0_i} - a_{23} m^2_{\tilde{\chi}^0_i} + a_{03}, & (5.49) \end{aligned}$$

The coefficients a_{kl}, ($k = 0,2,4,6$, $l = 1,2,3$), being invariants of the matrix $\mathcal{M}_N\mathcal{M}_N^T$, can be expressed as functions of M_2, μ and $\tan\beta$. Their explicit form is given in the Appendix b).

The $e^+e^- \to \tilde{\chi}^0_i\tilde{\chi}^0_j$ production processes occur via the s-channel Z^0 and the t- and u-channel $\tilde{e}_L$ and $\tilde{e}_R$ exchanges. Since the neutralino mixing matrix N is parameterised in general by 6 angles, the analytic expressions for the production cross sections are more involved. Their explicit form can be found in [409].

As one can see from eq. (5.46) for each neutralino mass $m_{\tilde{\chi}^0_i}$ one gets two solutions for M_1. In principle, a measurement of two neutralino masses and/or the cross section resolves this ambiguity. However, one has to remember that the mass eigenvalues show different sensitivity to the parameter M_1, depending on their gaugino/higgsino composition. In our scenario, the mass of the lightest neutralino $m_{\tilde{\chi}^0_1}$ depends strongly on M_1 if M_1 is in the range -183 GeV$< M_1 < 180$ GeV, while the others are roughly insensitive, see Fig. 5.34. In a general MSSM, where M_1 and M_2 are independent free parameters, this feature can completely change. We demonstrate this in Fig. 5.34, where the M_1/M_2 GUT relation is relaxed. We choose M_1 as a free parameter and all other parameters as in the SPS1a reference point. It can clearly be seen that the LSP becomes nearly independent but the heavier neutralinos become more sensitive to M_1 with larger and larger $|M_1|$ [413].

c) The strategy

At the initial phase of future e^+e^- linear–collider operations with polarised beams, the collision energy may only be sufficient to reach the production thresholds of the light chargino $\tilde{\chi}^\pm_1$ and the two lightest neutralinos $\tilde{\chi}^0_1$, $\tilde{\chi}^0_2$. From the analysis of this restricted system, nevertheless the entire tree level structure of the gaugino/higgsino sector can be unraveled in analytical form in CP–invariant theories as follows [409, 412].

It is clear from eq.(5.43) that by analysing the $\tilde{\chi}^+_1\tilde{\chi}^-_1$ production cross sections with polarised beams, $\sigma^\pm_L\{11\}$ and $\sigma^\pm_R\{11\}$, the chargino mixing angles $\cos 2\Phi_L$ and $\cos 2\Phi_R$ can be determined [412]. Any two contours, $\sigma^\pm_L\{11\}$ and $\sigma^\pm_R\{11\}$ for example, will cross at least at one point in the plane between $-1 \leq \cos 2\Phi_L, \cos 2\Phi_R \leq +1$, if the chargino and sneutrino masses are known and the SUSY Yukawa coupling is identified with the gauge coupling. However, the contours, being of second order, may

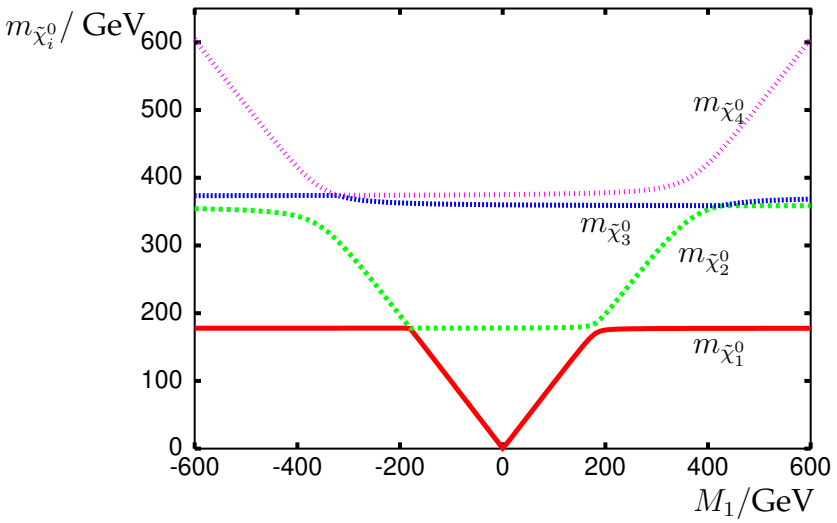

Figure 5.34: *M_1 dependence of the neutralino mass eigenvalues $m_{\tilde{\chi}_i^0}$, $i = 1, \ldots, 4$ with M_2, μ and $\tan\beta$ as in the reference scenario SPS1a.*

cross up to four times. The ambiguity can be resolved by measuring the transverse[3] cross section $\sigma_T^{\pm}\{11\}$, or measuring $\sigma_L^{\pm}\{11\}$ and $\sigma_R^{\pm}\{11\}$ at different beam energies. We have chosen the latter solution.

In the CP conserving case studied in this paper the SUSY parameters M_2, μ and $\tan\beta$ can be determined from the chargino mass $m_{\tilde{\chi}_1^{\pm}}$ and the mixing angles $\cos 2\Phi_L$, $\cos 2\Phi_R$ [412]. It is convenient to define

$$p = \pm \left| \frac{\sin 2\Phi_L + \sin 2\Phi_R}{\cos 2\Phi_L - \cos 2\Phi_R} \right| \tag{5.50}$$

$$q = \frac{1}{p} \frac{\cos 2\Phi_L + \cos 2\Phi_R}{\cos 2\Phi_L - \cos 2\Phi_R} \tag{5.51}$$

Since the $\cos 2\Phi_L$ and $\cos 2\Phi_R$ are derived from $\tilde{\chi}_1^+\tilde{\chi}_1^-$ cross sections, the relative sign of $\sin 2\Phi_L$, $\sin 2\Phi_R$ is not determined and both possibilities in eqn.(5.50), (5.51) have to be considered. From p, q, the SUSY parameters are determined as follows ($r^2 = m^2_{\tilde{\chi}_1^{\pm}}/m_W^2$):

$$M_2 = \frac{m_W}{\sqrt{2}} \left[(p+q)\sin\beta - (p-q)\cos\beta \right] \tag{5.52}$$

$$\mu = \frac{m_W}{\sqrt{2}} \left[(p-q)\sin\beta - (p+q)\cos\beta \right] \tag{5.53}$$

$$\tan\beta = \left[\frac{p^2 - q^2 \pm \sqrt{r^2(p^2+q^2+2-r^2)}}{(\sqrt{1+p^2} - \sqrt{1+q^2})^2 - 2r^2} \right]^{\eta} \tag{5.54}$$

where $\eta = 1$ for $\cos 2\Phi_R > \cos 2\Phi_L$, and $\eta = -1$ otherwise. The parameters M_2, μ are uniquely fixed if $\tan\beta$ is chosen properly. Since $\tan\beta$ is invariant under simultaneous

[3]The measurement of the transverse cross section involves the azimuthal production angle Φ of the charginos. At very high energies their angle coincides with the azimuthal angle of the chargino decay products. With decreasing energy, however, the angles differ and the measurement of the transverse cross section is diluted.

change of the signs of p, q, the definition $M_2 > 0$ can be exploited to remove this overall sign ambiguity.

The remaining parameter M_1 can be obtained from the neutralino data [409]. The characteristic equation for the neutralino mass eigenvalues eq. (5.46) is quadratic in M_1 if M_2, μ and $\tan\beta$ are already predetermined in the chargino sector. In principle, two neutralino masses are then sufficient to derive M_1, as explained in the previous section. The cross sections $\sigma^0_{L,R}\{12\}$ and $\sigma^0_{L,R}\{22\}$ for production of $\tilde{\chi}^0_1\tilde{\chi}^0_2$ and $\tilde{\chi}^0_2\tilde{\chi}^0_2$ neutralino pairs[4] with polarised beams can serve as a consistency check of the derived parameters.

In practice the above procedure may be much more involved due to finite experimental errors of mass and cross section measurements, uncertainties from sneutrino and selectron masses which enter the cross section expressions, errors on beam polarisation measurement, etc. In addition, depending on the benchmark scenario, some physical quantities in the light chargino/neutralino system may turn to be essentially insensitive to some parameters. For example, as seen in fig. 5.34, the first two neutralino masses are insensitive to M_1 if $M_1 \gg M_2,\ \mu$. Additional information from the LHC on heavy states, if available, can therefore be of great value in constraining the SUSY parameters.

Our strategy can be applied only at the tree level. Radiative corrections, which in the electroweak sector can be $\mathcal{O}(10\%)$, inevitably bring all SUSY parameters together [415]. Nevertheless, tree level analyses should provide in a relatively model-independent way good estimates of SUSY parameters, which can be further refined by including iteratively radiative corrections in an overall fit to experimental data.

5.1.6.3 SUSY parameters from the LC data

a) Experimental input at the LC

In this paper we take the unconstrained MSSM and adopt the SPS1a scenario defined at the electroweak scale [14,369]. The relevant SUSY parameters are

$$M_1 = 99.13\,\mathrm{G}eV, \quad M_2 = 192.7\,\mathrm{G}eV, \quad \mu = 352.4\,\mathrm{G}eV, \quad \tan\beta = 10 \tag{5.55}$$

with no GUT or mSUGRA relations assumed. The resulting chargino and neutralino masses, together with the slepton masses of the first generation, are given in table 5.17.

	$\tilde{\chi}^\pm_1$	$\tilde{\chi}^\pm_2$	$\tilde{\chi}^0_1$	$\tilde{\chi}^0_2$	$\tilde{\chi}^0_3$	$\tilde{\chi}^0_4$	$\tilde{e}_R$	$\tilde{e}_L$	$\tilde{\nu}_e$
mass	176.03	378.50	96.17	176.59	358.81	377.87	143.0	202.1	186.0
error	0.55		0.05	1.2			0.05	0.2	0.7

Table 5.17: *Chargino, neutralino and slepton masses in SPS1a, and the simulated experimental errors at the LC [417,418]. It is assumed that the heavy chargino and neutralinos are not observed at the first phase of the LC operating at $\sqrt{s} \leq 500$ GeV. [All quantities are in GeV.]*

[4]The lightest neutralino–pair production cannot be observed. Alternatively, one can try to exploit photon tagging in the reaction $e^+e^- \to \gamma\tilde{\chi}^0_1\tilde{\chi}^0_1$ [414].

In this scenario (which has a rather high $\tan\beta$ value) the $\tilde{\chi}_1^+$ and $\tilde{\chi}_2^0$ decay dominantly into $\tilde{\tau}$ producing the signal similar to that of stau pair production. Therefore the $\tilde{\tau}$ mass and mixing angle are also important for the study of the chargino and neutralino sectors. The mass and mixing angle can be determined as $m_{\tilde{\tau}_1} = 133.2 \pm 0.30$ GeV and $\cos 2\theta_\tau = -0.84 \pm 0.04$, and the stau-pair production cross section ranges from 43 fb to 138 fb depending on the beam polarisation, see [416, 417] for details of the stau parameter measurements. We assume that the contamination of stau production events can be subtracted from the chargino and neutralino production. Below we included the statistical error to our analysis but we did not include the systematic errors.

b) Chargino Sector

As observables we use the light chargino mass and polarised cross sections $\sigma_L^\pm\{11\}$ and $\sigma_R^\pm\{11\}$ at $\sqrt{s} = 500$ GeV and $\sqrt{s} = 400$ GeV. The light charginos $\tilde{\chi}_1^\pm$ decay almost exclusively to $\tilde{\tau}_1^\pm\nu_\tau$ followed by $\tilde{\tau}_1^\pm \to \tau^\pm\tilde{\chi}_1^0$. The signature for the $\tilde{\chi}_1^\pm\tilde{\chi}_1^\mp$ production would be two tau jets in opposite hemispheres plus missing energy.

The experimental errors that we assume and take into account are:

- The measurement of the chargino mass has been simulated for our reference point and the expected error is 0.55 GeV, table 5.17.
- With $\int \mathcal{L} = 500$ fb^{-1} at the LC, we assume 100 fb^{-1} per each polarisation configuration and we take into account 1σ statistical error.
- Since the chargino production is sensitive to $m_{\tilde{\nu}_e}$, we include its experimental error of 0.7 GeV.
- The measurement of the beam polarisation with an uncertainty of $\Delta P(e^\pm)/P(e^\pm) = 0.5\%$ is assumed. This error is conservative; discussions to reach errors smaller than 0.25% are underway [419].

The errors on the production cross sections induced by the above uncertainties, as well as the total errors (obtained by adding individual errors in quadrature), are listed in table 5.18. We assume 100% efficiency for the chargino cross sections due to a lack of realistic simulations.

Now we can exploit the eq. (5.43) and draw $\cos 2\Phi_R = f(\cos 2\Phi_L, \sigma_{L,R}^\pm\{11\})$ consistent with the predicted cross sections within the mentioned error bars, as shown in fig. 5.35. With the $\sqrt{s} = 500$ GeV data alone two possible regions in the plane are selected. With the help of the $\sigma_L^\pm\{11\}$ at $\sqrt{s} = 400$ GeV ($\sigma_R^\pm\{11\}$ is small and does not provide further constraints) the ambiguity is removed and the mixing angles are limited within the range

$$\cos 2\Phi_L = [0.62, 0.72] \quad (5.56)$$

$$\cos 2\Phi_R = [0.87, 0.91] \quad (5.57)$$

Although $\cos 2\Phi_L, \cos 2\Phi_R$ are determined rather precisely at a few per-cent accuracy, an attempt to exploit eqns. (5.52)-(5.54) shows that M_2 is reconstructed within 10 GeV, μ within 40 GeV, and essentially no limit on $\tan\beta$ is obtained (we get $\tan\beta > 6$). The main reason for this result is a relatively large error of the light chargino mass

$\sqrt{s}$	400 GeV		500 GeV	
$(P(e^-), P(e^+))$	$(-80\%, +60\%)$	$(+80\%, -60\%)$	$(-80\%, +60\%)$	$(+80\%, -60\%)$
$\sigma(e^+e^- \to \tilde{\chi}_1^+\tilde{\chi}_1^-)$	215.84	6.38	504.87	15.07
$\delta\sigma_{\text{stat}}$	1.47	0.25	2.25	0.39
$\delta\sigma_{P(e^-)}$	0.48	0.12	1.12	0.28
$\delta\sigma_{P(e^+)}$	0.40	0.04	0.95	0.10
$\delta\sigma_{m_{\tilde{\chi}_1^\pm}}$	7.09	0.20	4.27	0.12
$\delta\sigma_{m_{\tilde{\nu}_e}}$	0.22	0.01	1.57	0.04
$\delta\sigma_{\text{total}}$	7.27	0.35	5.28	0.51

Table 5.18: *Cross sections $\sigma^\pm_{L,R}\{11\} = \sigma_{L,R}(e^+e^- \to \tilde{\chi}_1^+\tilde{\chi}_1^-)$ with polarised beams $P(e^-) = \mp 80\%$, $P(e^+) = \pm 60\%$ at $\sqrt{s} = 400$ and 500 GeV and assumed errors (in fb) corresponding to 100 fb^{-1} for each polarisation configuration.*

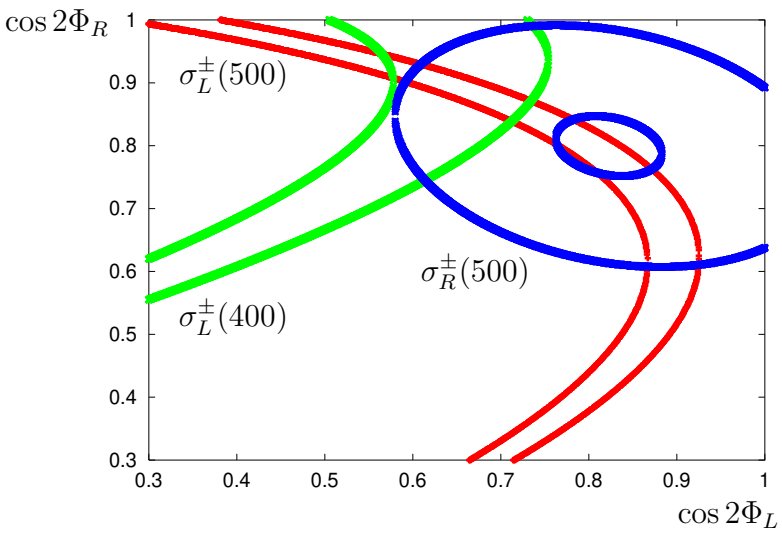

Figure 5.35: $\cos 2\Phi_R$ *as a function of* $\cos 2\Phi_L$ *for* $\sigma^\pm_L\{11\}$ *at* $\sqrt{s} = 500$ *GeV (red), and 400 GeV (green) and* $\sigma^\pm_R\{11\}$ *at* $\sqrt{s} = 500$ *GeV (blue) within the error bounds (theo+exp) as given in table 5.18.*

measurement due to the $\tilde{\chi}_1^+ \to \tilde{\chi}_1^0\tau^+\nu_\tau$ decay mode. Several methods exploiting other sectors of the MSSM have been proposed to measure $\tan\beta$ in the high $\tan\beta$ regime [416, 420]. In the following we will exploit the neutralino sector (with eqns. (5.56), (5.57) as the allowed ranges for the chargino mixing angles) to improve constraints on M_2, μ and $\tan\beta$, and to determine M_1.

c) Neutralino Sector:

As observables we use the two light neutralino masses and polarised cross sections $\sigma^0_{L,R}\{12\}$ and $\sigma^0_{L,R}\{22\}$ at $\sqrt{s} = 400$ GeV and $\sqrt{s} = 500$ GeV. Although the production of $\tilde{\chi}_1^0\tilde{\chi}_3^0$ and $\tilde{\chi}_1^0\tilde{\chi}_4^0$ pairs is kinematically accessible at $\sqrt{s} = 500$ GeV in the chosen reference point SPS1a, the production rates are small and the heavy states $\tilde{\chi}_3^0$ and $\tilde{\chi}_4^0$ decay via cascades to many particles. This feature is quite common in large parts of

the MSSM parameter space when the gaugino and higgsino mass parameters are not too close. Therefore in our analysis we take into account the experimental information available only from the production of the light neutralino pairs.

$\sqrt{s}$	400 GeV		500 GeV	
$(P(e^-), P(e^+))$	$(-80\%, +60\%)$	$(+80\%, -60\%)$	$(-80\%, +60\%)$	$(+80\%, -60\%)$
$\sigma(e^+e^- \to \tilde{\chi}_1^0\tilde{\chi}_2^0)$	148.38	20.06	168.42	20.81
$\delta\sigma_{\text{stat}}$	2.92	1.55	3.47	1.55
$\delta\sigma_{\text{bg}}$	0.44	0.02	0.31	0.03
$\delta\sigma_{P(e^-)}$	0.32	0.05	0.37	0.06
$\delta\sigma_{P(e^+)}$	0.28	0.001	0.31	0.01
$\delta\sigma_{m_{\tilde{\chi}_1^\pm}}$	0.21	0.30	0.16	0.26
$\delta\sigma_{m_{\tilde{e}_L}}$	0.20	0.01	0.17	0.01
$\delta\sigma_{m_{\tilde{e}_R}}$	0.00	0.01	0.00	0.01
$\delta\sigma_{\text{total}}$	3.0	1.58	3.52	1.57

Table 5.19: *Cross sections $\sigma^0_{L,R}\{12\} = \sigma_{L,R}(e^+e^- \to \tilde{\chi}_1^0\tilde{\chi}_2^0)$ with polarised beams $P(e^-) = \mp 80\%$, $P(e^+) = \pm 60\%$ at $\sqrt{s} = 400$ and 500 GeV, and assumed errors (in fb) corresponding to 100 fb^{-1} for each polarisation configuration.*

	400 GeV		500 GeV	
$(P(e^-), P(e^+))$	$(-80\%, +60\%)$	$(+80\%, -60\%)$	$(-80\%, +60\%)$	$(+80\%, -60\%)$
$\sigma(e^+e^- \to \tilde{\chi}_2^0\tilde{\chi}_2^0)$	85.84	2.42	217.24	6.10
$\delta\sigma_{\text{stat}}$	2.4	0.4	3.8	0.6
$\delta\sigma_{P(e^-)}$	0.19	0.05	0.48	0.12
$\delta\sigma_{P(e^+)}$	0.16	0.02	0.41	0.05
$\delta\sigma_{m_{\tilde{\chi}_1^\pm}}$	2.67	0.08	1.90	0.05
$\delta\sigma_{m_{\tilde{e}_L}}$	0.15	0.004	0.28	0.01
$\delta\sigma_{m_{\tilde{e}_R}}$	0.00	0.00	0.00	0.00
$\delta\sigma_{\text{total}}$	3.6	0.41	4.3	0.62

Table 5.20: *Cross sections $\sigma^0_{L,R}\{22\} = \sigma_{L,R}(e^+e^- \to \tilde{\chi}_2^0\tilde{\chi}_2^0)$ with polarised beams $P(e^-) = \mp 80\%$, $P(e^+) = \pm 60\%$ at $\sqrt{s} = 400$ and 500 GeV, and assumed errors (in fb) corresponding to 100 fb^{-1} for each polarisation configuration.*

The neutralino $\tilde{\chi}_2^0$ decays into $\tilde{\tau}_1^\pm\tau^\mp$ with almost 90%, followed by the $\tilde{\tau}_1^\pm \to \tau^\pm\tilde{\chi}_1^0$. Therefore the final states for the $\tilde{\chi}_1^\pm\tilde{\chi}_1^\mp$ and $\tilde{\chi}_1^0\tilde{\chi}_2^0$ are the same (2τ + missing energy), however with different topology. While for the charginos, the τ's tend to be in opposite hemispheres with rather large invariant mass, in the $\tilde{\chi}_1^0\tilde{\chi}_2^0$ process both τ's, coming from the $\tilde{\chi}_2^0$ decay, would be more often in the same hemisphere with smaller invariant mass. This feature allows to separate the processes to some extent exploiting e.g. a cut on the opening angle between the two jets of the $\tau's$. However, in the case of $\tilde{\chi}_1^0\tilde{\chi}_2^0$, significant background from $\tilde{\chi}_1^\pm\tilde{\chi}_1^\mp$ and $\tilde{\tau}_1^\pm\tilde{\tau}_1^\mp$ remains.

We estimate the statistical error on $\sigma(e^+e^- \to \tilde{\chi}_1^0\tilde{\chi}_2^0)$ based on the experimental simulation presented in [418]. This simulation was performed at $\sqrt{s} = 500$ GeV for unpolarised beams yielding an efficiency of 25%. We extrapolate the statistical errors at different $\sqrt{s}$ and different polarisations as $\delta\sigma/\sigma = \sqrt{S+B}/S$ where we calculate

the number of signal (S) and background (B) events from the cross sections and the integrated luminosity (100 fb^{-1}) assuming the same efficiency as achieved for the unpolarised case. Since the cross sections for the SUSY background processes are also known only with some uncertainty, we account for this uncertainty in the background subtraction by adding an additional systematic error ($\delta\sigma_{\mathrm{bg}}$).

For the process $\tilde{\chi}_2^0\tilde{\chi}_2^0 \to \tau^+\tau^-\tau^+\tau^-\tilde{\chi}_1^0\tilde{\chi}_1^0$ no detailed simulation exists. From the τ-tagging efficiency achieved in the $\tilde{\chi}_1^0\tilde{\chi}_2^0$ channel, we assume that this final state can be reconstructed with an efficiency of 15% with negligible background. This is justified since no major SUSY background is expected for the 4-τ final state, BR$(\tilde{\nu}_\tau \to \tau^+\tau^-\tilde{\chi}_1^0)^2$ is only 0.5%. SM backgrounds arise mainly from Z pair production and are small.

For both processes we account in addition for polarisation uncertainties and uncertainties in the cross section predictions from the errors on the chargino and selectron masses. Note that we implicitly assume that the branching ratio $\tilde{\chi}_2^0 \to \tau^+\tau^-\tilde{\chi}_1^0$ is known, which is a simplifaction. A full analysis will have to take into account the parameter dependence of this branching ratio in addition, since it cannot be measured directly.

The neutralino cross sections depend on M_1, M_2, μ, $\tan\beta$ and on slepton masses. We prefer to express M_2, μ, $\tan\beta$ in terms of $m_{\tilde{\chi}_1^\pm}$ and the mixing angles $\cos 2\Phi_L, \cos 2\Phi_R$. Then we consider neutralino cross sections as functions of unknown $M_1, \cos 2\Phi_L, \cos 2\Phi_R$ with uncertainties due to statistics and experimental errors on beam polarisations, $m_{\tilde{\chi}_1^\pm}, m_{\tilde{e}_L}$ and $m_{\tilde{e}_R}$ included (in quadrature) in the total error, see table 5.19 and table 5.20.

d) Results

We perform a $\Delta\chi^2$ test defined as

$$\Delta\chi^2 = \sum_i |\frac{O_i - \overline{O}_i}{\delta O_i}|^2 \tag{5.58}$$

The sum over physical observables O_i includes $m_{\tilde{\chi}_1^0}, m_{\tilde{\chi}_2^0}$ and neutralino production cross sections $\sigma^0_{L,R}\{12\}, \sigma^0_{L,R}\{22\}$ measured at both energies of 400 and 500 GeV. The $\Delta\chi^2$ is a function of unknown $M_1, \cos 2\Phi_L, \cos 2\Phi_R$ with $\cos 2\Phi_L, \cos 2\Phi_R$ restricted to the ranges given in eqns. (5.56),(5.57) as predetermined from the chargino sector. $\overline{O}_i$ stands for the physical observables taken at the input values of all parameters, and δO_i are the corresponding errors.

In fig. 5.36 the contour of $\Delta\chi^2 = 1$ is shown in the $M_1, \cos 2\Phi_L, \cos 2\Phi_R$ parameter space along with its three 2dim projections. The projection of the contours onto the axes determines 1σ errors for each parameter.

Values obtained for $M_1, \cos 2\Phi_L, \cos 2\Phi_R$ together with $m_{\tilde{\chi}_1^\pm}$ can be inverted to derive the fundamental parameters M_2, μ and $\tan\beta$. At the same time masses of heavy chargino and neutralinos are predicted. As can be seen in table 5.21, in the SPS1a scenario the parameters M_1 and M_2 are determined at the level of a few per-mil, μ is reconstructed within a few per-cent, while $\tan\beta$ is found with an error of order 15%.

The errors on the predicted masses of the heavy chargino/neutralinos, which in our SPS1a scenario are predominantly higgsinos, are strongly correlated with the error of μ; the left panel of fig. 5.37 shows the correlation between μ and $m_{\tilde{\chi}_4^0}$. In the right panel of this figure a weaker correlation is observed between $\tan\beta$ and $m_{\tilde{\chi}_4^0}$ (or between

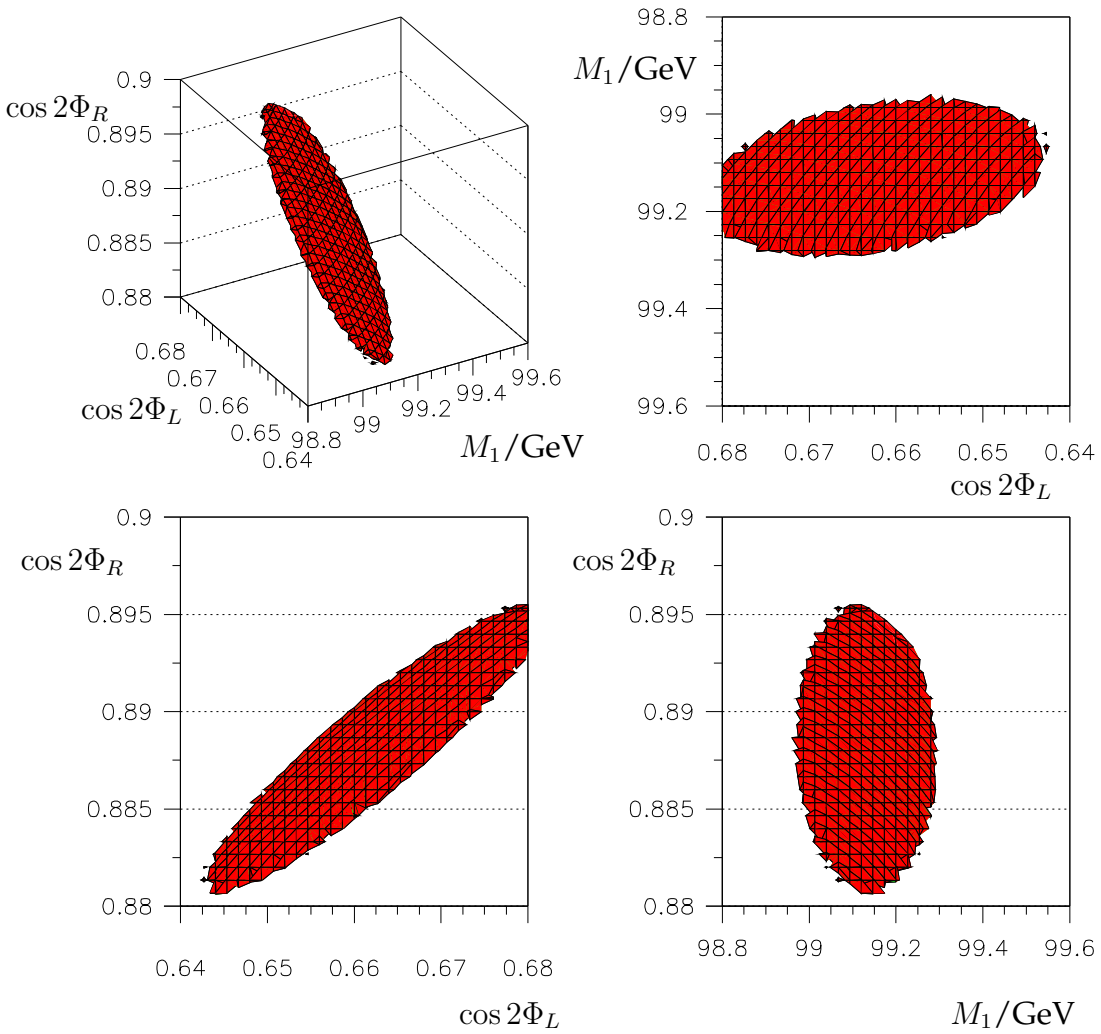

Figure 5.36: *The $\Delta\chi^2 = 1$ contour in the $M_1, \cos 2\Phi_L, \cos 2\Phi_R$ parameter space, and its three 2dim projections, derived from the LC data.*

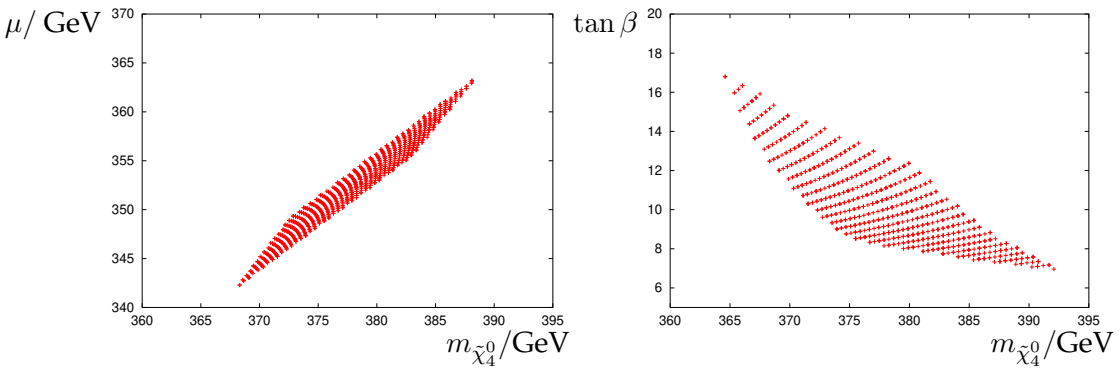

Figure 5.37: *The correlation between predicted values of μ and $m_{\tilde{\chi}_4^0}$ (left panel) and the allowed range of $\tan\beta$ and $m_{\tilde{\chi}_4^0}$ (right panel) from the analysis of the LC data.*

$\tan\beta$ and μ). Therefore, by providing $m_{\tilde{\chi}_4^0}$ from endpoint measurements [403], the

LHC could considerably help to get a better accuracy on μ. At the same time a better determination of $\tan\beta$ can be expected.

SUSY Parameters				Mass Predictions		
M_1	M_2	μ	$\tan\beta$	$m_{\tilde{\chi}_2^\pm}$	$m_{\tilde{\chi}_3^0}$	$m_{\tilde{\chi}_4^0}$
99.1 ± 0.2	192.7 ± 0.6	352.8 ± 8.9	10.3 ± 1.5	378.8 ± 7.8	359.2 ± 8.6	378.2 ± 8.1

Table 5.21: *SUSY parameters with 1σ errors derived from the analysis of the LC data collected at the first phase of operation. Shown are also the predictions for the heavier chargino/neutralino masses.*

5.1.6.4 Combined strategy for the LHC and LC

a) LC data supplemented by $m_{\tilde{\chi}_4^0}$ from the LHC

The LHC experiments will be able to measure the masses of several sparticles, as described in detail for the SPS1a point in [403]. In particular, the LHC will provide a first measurement of the masses of $\tilde{\chi}_1^0$, $\tilde{\chi}_2^0$ and $\tilde{\chi}_4^0$. The measurements of $\tilde{\chi}_2^0$ and $\tilde{\chi}_4^0$ are achieved through the study of the processes:

$$\tilde{\chi}_i^0 \to \tilde{\ell}\ell \to \ell\ell\tilde{\chi}_1^0 \tag{5.59}$$

where the index i can be either 2 or 4. The invariant mass of the two leptons in the final state shows an abrupt edge, which can be expressed in terms of the masses of the relevant sparticles as

$$m_{l^+l^-}^{\max} = m_{\tilde{\chi}_i^0}\sqrt{1-\frac{m_{\tilde{\ell}}^2}{m_{\tilde{\chi}_i^0}^2}}\sqrt{1-\frac{m_{\tilde{\chi}_1^0}^2}{m_{\tilde{\ell}}^2}} \tag{5.60}$$

If one only uses the LHC information, the achievable precision on $m_{\tilde{\chi}_2^0}$ and $m_{\tilde{\chi}_4^0}$ will be respectively of 4.5 and 5.1 GeV for an integrated luminosity of 300 fb^{-1}, see figure 5.38. The correct interpretation of the largest observed $m_{l^+l^-}^{\max}$ as originating from $\tilde{\chi}_4^0$ decays can be facilitated by the prediction of $m_{\tilde{\chi}_4^0}$ from the LC measurements in the MSSM context.

In the case of the $\tilde{\chi}_4^0$, which in the considered scenario is mainly higgsino, this information can be exploited at the LC to constrain the parameter μ with a better precision. If we include this improved precision on $m_{\tilde{\chi}_4^0}$ in the $\Delta\chi^2$ test of eq. (5.58), the resulting $\Delta\chi^2 = 1$ contours get modified and the achievable precision is improved, as shown in table 5.22.

SUSY Parameters				Mass Predictions	
M_1	M_2	μ	$\tan\beta$	$m_{\tilde{\chi}_2^\pm}$	$m_{\tilde{\chi}_3^0}$
99.1 ± 0.2	192.7 ± 0.5	352.4 ± 4.5	10.2 ± 0.9	378.5 ± 4.1	358.8 ± 4.1

Table 5.22: *SUSY parameters with 1σ errors derived from the analysis of the LC data collected at the first phase of operation and with $\delta m_{\tilde{\chi}_4^0} = 5.1$ GeV from the LHC. Shown are also the predictions for the masses of $\tilde{\chi}_2^\pm$ and $\tilde{\chi}_3^0$.*

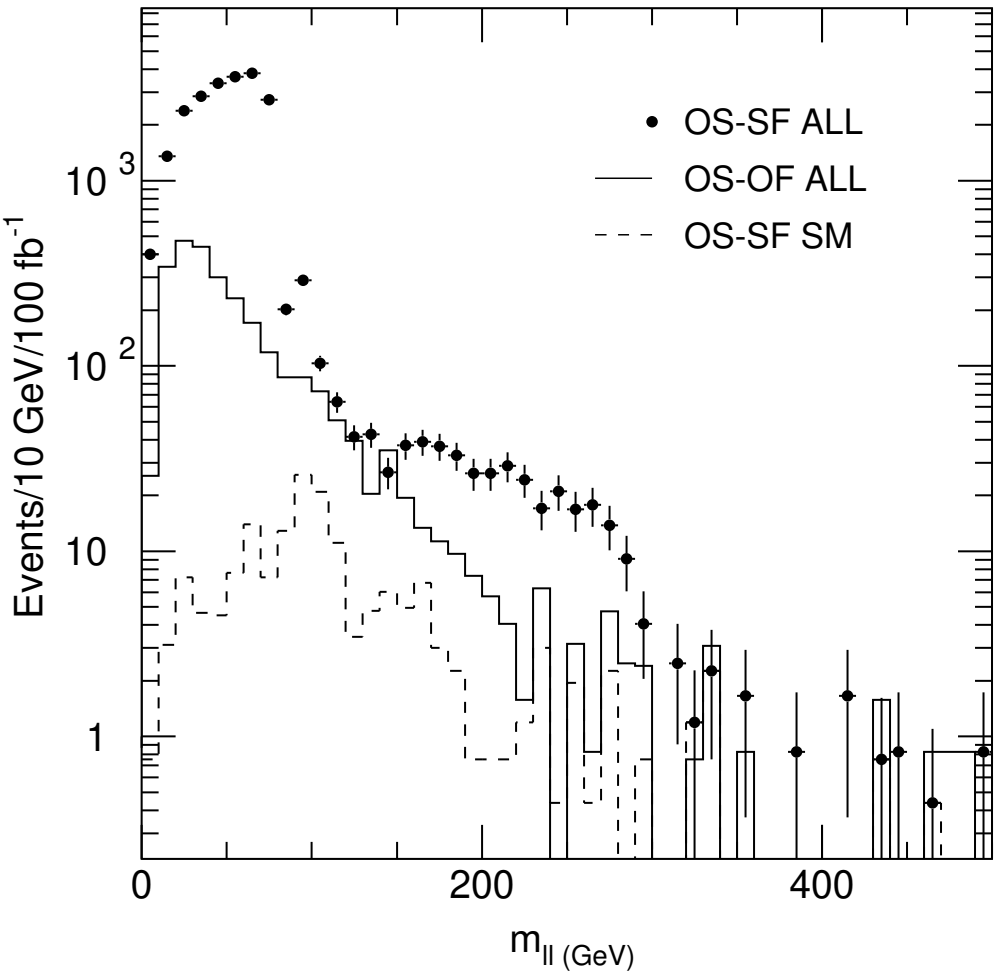

Figure 5.38: *Invariant mass spectrum respectively for: Opposite-Sign Same-Flavour (OS-SF) leptons total (full dots), Opposite-Sign Opposite-Flavour (OS-OF) leptons total (solid line), Opposite-Sign Same-Flavour leptons in the SM (dashed line). The signals of $\tilde{\chi}_2^0$, $\tilde{\chi}_4^0$ consist of OS-SF leptons [403].*

b) Joint analysis of the LC and LHC data

From the consideration of eq. (5.60), one can see that the uncertainty on the LHC measurement of $m_{\tilde{\chi}_2^0}$ and $m_{\tilde{\chi}_4^0}$ depends both on the experimental error on the position of $m_{l^+l^-}^{\max}$, and on the uncertainty on $m_{\tilde{\chi}_1^0}$ and $m_{\tilde{\ell}}$. The latter uncertainty, which for both masses is of 4.8 GeV, turns out to be the dominant contribution. A much higher precision can thus be achieved by inserting in eq. (5.60) the values for $m_{\tilde{\chi}_1^0}$, $m_{\tilde{e}_R}$ and $m_{\tilde{e}_L}$ which are measured at the LC with precisions respectively of 0.05, 0.05 and 0.2 GeV, table 5.17.

With this input the precisions on the LHC+LC measurements of $m_{\tilde{\chi}_2^0}$ and $m_{\tilde{\chi}_4^0}$ become: $\delta m_{\tilde{\chi}_2^0} = 0.08$ GeV and $\delta m_{\tilde{\chi}_4^0} = 2.23$ GeV.

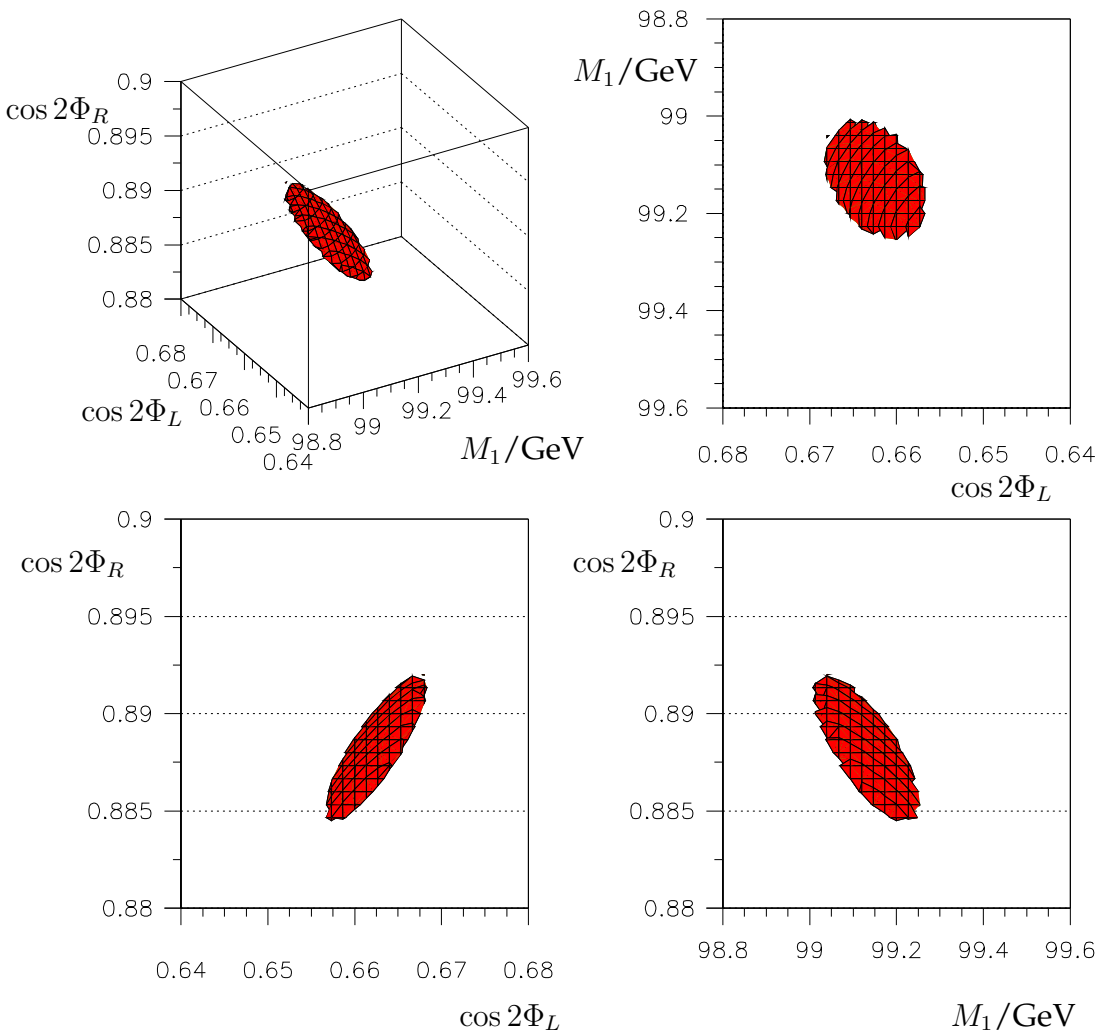

Figure 5.39: *The $\Delta\chi^2 = 1$ contour in the $M_1, \cos 2\Phi_L, \cos 2\Phi_R$ parameter space, and its three 2dim projections, derived from the joint analysis of the LC data and LHC data.*

SUSY Parameters				Mass Predictions	
M_1	M_2	μ	$\tan\beta$	$m_{\tilde{\chi}_2^\pm}$	$m_{\tilde{\chi}_3^0}$
99.1 ± 0.1	192.7 ± 0.3	352.4 ± 2.1	10.2 ± 0.6	378.5 ± 2.0	358.8 ± 2.1

Table 5.23: *SUSY parameters with 1σ errors derived from the combined analysis of the LHC and LC data with $\delta m_{\tilde{\chi}_2^0} = 0.08$ GeV and $\delta m_{\tilde{\chi}_4^0} = 2.23$ GeV derived from the LHC when using the LC input of $\delta m_{\tilde{\chi}_1^0} = 0.05$ GeV.*

From the results of the $\Delta\chi^2$ test one can calculate the improvement in accuracy for the derived parameters by imposing the new mass constraints. The final results are shown in figure5.39 and table 5.23. The accuracy for the parameters μ and particularly $\tan\beta$ is much better, as could be expected from fig. 5.37, where the allowed range of μ and $\tan\beta$ from the LC analysis is considerably reduced once the measured mass $m_{\tilde{\chi}_4^0}$ at the LHC is taken into account. In particular, the precision on $\tan\beta$ becomes better than from other SUSY sectors [416, 420].

5.1.6.5 Summary

We have studied the prospects for the determination of the parameters which govern the chargino/neutralino sector of a general MSSM. We focus on the situation where only the lightest states ($\tilde{\chi}_1^0$, $\tilde{\chi}_2^0$, $\tilde{\chi}_1^\pm$) are accessible at the first stage of a LC. For a specific example of the MSSM, the SPS1a scenario with a rather high $\tan\beta = 10$, we show how the combination of the results from the two accelerators, LHC and LC, allows a precise determination of the fundamental SUSY parameters. The analysis has been performed within the general frame of the unconstrained MSSM. Our strategy does not rely on any particular relations among the fundamental parameters, like the GUT or mSUGRA relations, and therefore is applicable for arbitrary MSSM parameters which lead to a phenomenology similar to the one studied.

Measuring with high precision the masses of the expected lightest SUSY particles $\tilde{\chi}_1^0$, $\tilde{\chi}_2^0$, $\tilde{\chi}_1^\pm$ and their cross sections at the LC, and taking into account simulated mass measurement errors and corresponding uncertainties for the theoretical predictions, we could determine the fundamental SUSY parameters M_1, M_2, μ at tree level for the SPS1a point within a few percent, while $\tan\beta$ is estimated within ~ 15 %. The masses of heavier chargino and neutralinos can also be predicted at a level of a few percent and are used as input for the LHC analysis. The use of polarised beams at the LC is decisive for deriving unique solutions.

If the LC analysis is supplemented with the LHC measurement of the heavy neutralino mass, the errors on μ and $\tan\beta$ can be improved. However, the best results are obtained when first the LSP and slepton masses from the LC are fed to the LHC analyses to get a precise experimental determination of the $\tilde{\chi}_2^0$ and $\tilde{\chi}_4^0$ masses, which in turn are injected back to the analysis of the chargino/neutralino LC data. The combined strategy will provide in particular a precise measurement of the $\tilde{\chi}_4^0$ mass, the μ parameter with an accuracy at the $\leq O(1\%)$ level, and an error on $\tan\beta$ of the order of $\leq 10\%$, reaching a stage where radiative corrections become relevant in the electroweak sector and which will have to be taken into account in future fits [415].

Appendix: Useful expressions for the gaugino/higgsino sector

a) For the lightest chargino pair production, $\sigma^\pm\{11\} = \sigma(e^-(p_1)e^+(p_2) \to \tilde{\chi}_1^+(p_3)\tilde{\chi}_1^-(p_4))$, the coefficients $c_1, \ldots, c_6$ in eq. (5.43) are given by:

$$
\begin{aligned}
c_1 &= \int_C |Z|^2\{c_{LR}L^2 f_2 + c_{RL}R^2 f_1\} \\
c_2 &= \int_C |Z|^2\{c_{LR}L^2(1-4L)(2f_2+f_3) + c_{RL}R^2(1-4R)(2f_1+f_3)\} \\
&\quad - \int_C G\tilde{N}4\{c_{LR}L(2f_2+f_3) + c_{RL}R(2f_1+f_3)\} - \int_C Re(Z)\tilde{N}c_{LR}Lf_3 \\
c_3 &= \int_C |Z|^2(c_{LR}L^2 f_1 + c_{RL}R^2 f_2) - \int_C Z\tilde{N}2c_{LR}Lf_1 + \int_C \tilde{N}^2 c_{LR}f_1 \\
c_4 &= \int_C |Z|^2(1-4L)\{c_{LR}L^2(2f_1+f_3) + c_{RL}R^2(2f_2+f_3)\} + \int_C \tilde{N}^2 2c_{LR}f_1 \\
&\quad + \int_C Re(Z)\tilde{N}c_{LR}L\{-4f_1 - f_3 + 4L(2f_1+f_3)\} + \int_C G\tilde{N}4c_{LR}(2f_1+f_3)
\end{aligned}
$$

$$
\begin{aligned}
& - \int_C GRe(Z)4\{c_{LR}L(2f_1+f_3)+c_{RL}R(2f_2+f_3)\} \\
c_5 &= \int_C |Z|^2(c_{LR}L^2+c_{RL}R^2)f_3 - \int_C Re(Z)\tilde{N}c_{LR}Lf_3 \\
c_6 &= \int_C |Z|^2\{c_{LR}L^2(1-8L)+c_{RL}R^2(1-8L)+16L^2(c_{LR}L^2+c_{RL}R^2)\}(f_1+f_2+f_3) \\
& - \int_C Re(Z)\tilde{N}c_{LR}L(1-4L)(2f_1+f_3) + \int_C G^2(c_{LR}+c_{RL})(f_1+f_2+f_3) \\
& - \int_C Re(Z)G8\{c_{RL}R+c_{LR}L(1-4L)\}(f_1+f_2+f_3) + \int_C \tilde{N}^2 c_{LR}f_1 \\
& + \int_C G\tilde{N}4c_{LR}(2f_1+f_3)
\end{aligned}
$$

where $\int_C = \frac{q_{\tilde{\chi}}}{E_b^3}\frac{1}{2\pi}\int \mathrm{d}\cos\theta$, $L = -\frac{1}{2}+\sin^2\theta_W$, $R = \sin^2\theta_W$, and

$$
G = e^2/s, \quad Z = g^2/\cos^2\theta_W(s-m_Z^2+im_Z\Gamma_Z), \quad \tilde{N} = g^2/(t-m_{\tilde{\nu}_e}^2)
$$

denote the γ, Z and $\tilde{\nu}_e$ propagators,

$$
c_{LR} = (1-P(e^-))(1+P(e^+)), \quad c_{RL} = (1+P(e^-))(1-P(e^+))
$$

are the beam polarisation factors, and

$$
f_1 = (p_1p_4)(p_2p_3), \quad f_2 = (p_1p_3)(p_2p_4), \quad f_3 = s\,m_{\tilde{\chi}_i^\pm}^2/2
$$

are the pure kinematic coefficients.

b) The coefficients a_{kl} ($k = 0,2,4,6$, $l = 1,2,3$), which appear in eqns. (5.47),(5.48) and (5.49), are invariants of the matrix $\mathcal{M}_N\mathcal{M}_N^T$. They can be expressed as functions of the parameters M_2, μ, $\tan\beta$ in the following way:

$$
\begin{aligned}
a_{63} &= M_2^2+2(\mu^2+m_Z^2) \\
a_{41} &= M_2^2+2(\mu^2+m_Z^2\cos^2\theta_W) \\
a_{42} &= -2\mu m_Z^2\sin 2\beta\sin^2\theta_W \\
a_{43} &= 2\mu^2M_2^2+(\mu^2+m_Z^2)^2-2m_Z^2\mu M_2\sin 2\beta\cos^2\theta_W+2m_Z^2M_2^2\sin^2\theta_W \\
a_{21} &= \mu^4+2\mu^2M_2^2+2m_Z^2\mu^2\cos^2\theta_W+m_Z^4\cos^2\theta_W-2m_Z^2M_2\mu\sin 2\beta\cos^2\theta_W \\
a_{22} &= 2[m_Z^4M_2\sin^2\theta_W\cos^2\theta_W-m_Z^2\mu^3\sin^2\theta_W\sin 2\beta-m_Z^2\mu M_2^2\sin^2\theta_W\sin 2\beta] \\
a_{23} &= \mu^4M_2^2+m_Z^4\mu^2\sin^2 2\beta+2m_Z^2\mu^2M_2^2\sin^2\theta_W-2m_Z^2M_2\mu^3\cos^2\theta_W\sin 2\beta+m_Z^4M_2^2\sin^4\theta_W \\
a_{01} &= \mu^4M_2^2+m_Z^4\mu^2\cos^4\theta_W\sin^2 2\beta-2m_Z^2\mu^3M_2\cos^2\theta_W\sin 2\beta \\
a_{02} &= 2m_Z^4\mu^2M_2\sin^2\theta_W\cos^2\theta_W\sin^2 2\beta-2m_Z^2\mu^3M_2^2\sin^2\theta_W\sin 2\beta \\
a_{03} &= m_Z^4\mu^2M_2^2\sin^4\theta_W\sin^2 2\beta
\end{aligned}
$$

5.1.7 Determination of stop and sbottom sector by LHC and LC

5.1.7.1 Fits to stop and sbottom masses and mixings with LC inputs

In this section, we describe the fits to the stop and sbottom masses and mixings at SPS 1 using LHC/LC data. At this point, $\tilde{b}_1$, $\tilde{b}_2 \sim 500\,\mathrm{GeV}$, therefore direct production

of $\tilde{b}$ at LC is not possible without significant extension of the energy. Therefore we consider the fits of the mixing angle using LHC data and LC data at $\sqrt{s} = 500$ GeV.

Note that all sleptons, the lighter chargino $\tilde{\chi}_1^\pm$, and the lightest and the second lightest neutralinos $\tilde{\chi}_1^0$ and $\tilde{\chi}_2^0$ are within the reach of early stage of the LC at $\sqrt{s} = 500$ GeV. The LC measures the accessible sparticles masses precisely [9]. Furthermore, Chargino and neutralino production cross sections and the first generation slepton production cross sections are sensitive to the gaugino masses M_1 and M_2. The expected errors at $\sqrt{s} = 500$ GeV are given in [177].

The LC measurements improve the mass resolution of strongly interacting sparticles at LHC [421]. Errors of sparticles masses are estimated as $\Delta(m_{\tilde{g}} - m_{\tilde{\chi}_1^0}) = 2.5$ GeV, $\Delta(m_{\tilde{g}} - m_{\tilde{b}_1}) = 1.5$ GeV and $\Delta(m_{\tilde{g}} - m_{\tilde{b}_2}) = 2.5$ GeV at SPS 1a in [421] for $\int \mathcal{L}dt = 300$ fb^{-1}. LHC also improve the resolution of weak SUSY parameters. Statistics of $\tilde{\chi}_2^0$ produced from $\tilde{q}$ decay is huge. In addition, $\tilde{\chi}_4^0 (m_{\tilde{\chi}_4^0} = 378$ GeV) arises occasionally from squark decays. The same flavor and opposite sign lepton pair arises from the cascade decay $\tilde{\chi}_2^0 \to \tilde{l}l \to ll\tilde{\chi}_1^0$ and $\tilde{\chi}_4^0 \to \tilde{l}l \to ll\tilde{\chi}_1^0$. The end points of m_{ll} distribution arising would be measured precisely at LHC. The errors of the end points are $\Delta m_{ll} = 0.08(2.3)$ GeV for $\tilde{\chi}_2^0(\tilde{\chi}_4^0)$ respectively [421]. This is translated into the $m_{\tilde{\chi}_4^0}$ error $\Delta m_{\tilde{\chi}_4^0} = 2.23$ GeV which corresponds to $\Delta\mu = 2.1$ GeV. This is an example that the combination of LHC and LC fits determines $M_1, M_2, \mu, \tan\beta$ better.

Given the precise determination of weak SUSY parameters, one can access the structure of sbottom and stop mass matrices. The mass matrices are controlled by the five parameters, $m^2_{\tilde{Q}_{L3}}$, $m^2_{\tilde{b}_R}$, $m^2_{\tilde{t}_R}$, $m^2_{LR}(\tilde{b})$ and $m^2_{LR}(\tilde{t})$. They may be parameterized masses and mixings of sbottom and stop; $m_{\tilde{b}_1}, m_{\tilde{b}_2}, \theta_b$, $m_{\tilde{t}_1}$ and θ_t. Among those parameters, $m_{\tilde{b}_1}$ and $m_{\tilde{b}_2}$ can be measured through the peak position of $m(bb\tilde{\chi}_2^0) - m(bb\tilde{\chi}_2^0)$ distributions. On the other hand, LC measurement determine the possible decay chains of $\tilde{t}$ and $\tilde{b}$ to the weak SUSY particles, such as the decays into $\tilde{\chi}_i^0$ or $\tilde{\chi}_i^\pm$, and they further decays into $\tilde{\nu}$, $\tilde{l}$ and so on. Therefore $\tilde{t}$ and $\tilde{b}$ decay branching ratios are regarded as the functions of the parameters of stop and sbottom sector.

The θ_b and θ_t dependent quantities that can be measured at LHC are discussed in the previous section,

- $\overline{\mathrm{BR}}(\tilde{b}) \equiv BR(\tilde{g} \to b\tilde{b}_2 \to bb\tilde{\chi}_2^0)/BR(\tilde{g} \to b\tilde{b}_1 \to bb\tilde{\chi}_2^0)$
- The weighted end point M_{tb}^{w} of the cascade decays (III)$_1$ $\tilde{g} \to t\tilde{t} \to tb\tilde{\chi}_1^+$ and (IV)$_{i1}$ $\tilde{g} \to b\tilde{b}_i \to tb\tilde{\chi}_1^+$.
- $\overline{\mathrm{BR}}(\tilde{t}) \equiv BR(edge)/BR(\tilde{g} \to bbX)$.

We list the input values and estimated errors on those quantities in Table 5.24, see the previous section for the details. Errors on the weak SUSY breaking parameters M_1, M_2, μ and $\tan\beta$ can be ignored compared to the errors on those observable in the following discussions.

Stop and sbottom mixing angles θ_t and θ_b may be determined from $\overline{BR}(\tilde{b})$ and $\overline{BR}(\tilde{t})$ measurement. Through LHC/LC measurements, we knows $\tilde{\chi}_2^0 \sim \tilde{W}$. Because $\tilde{W}$ couples only to the $\tilde{b}_L$, $BR(\tilde{b}_2 \to b\tilde{\chi}_2^0)/BR(\tilde{b}_2 \to b\tilde{\chi}_2^0)$ becomes a sensitive function of θ_b. As the phase space of $\tilde{g} \to \tilde{b}_i$ is strongly constrained by gluino and sbottom mass measurements, the measured $\overline{BR}(\tilde{b})$ can be translated immediately into the constraint on $BR(\tilde{b}_2 \to b\tilde{\chi}_2^0)/BR(\tilde{b}_2 \to b\tilde{\chi}_2^0)$, thus θ_b.

	input	error
$m_{\tilde{g}} - m_{\tilde{b}_1}$	103.3 GeV	1.5 GeV
$m_{\tilde{g}} - m_{\tilde{b}_2}$	70.6 GeV	2.5 GeV
M_{tb}^{w}	370.9 GeV	4.8(100 fb^{-1} w/o sys)
$\overline{\text{BR}}(\tilde{b})$	0.252	0.078
$\overline{\text{BR}}(\tilde{t})$	0.583	0.05(100 fb^{-1} w/o sys)

Table 5.24: Measurements used for this fit.

On the other hand $\overline{BR}(\tilde{t})$ depends mainly on θ_t. Here, the gluino branching ratio into the edge mode is consisted by the contributions from (III)$_1$ $\tilde{g} \to t\tilde{t}_1 \to tb\tilde{\chi}_1^+$ and (IV)$_{i1}$ $\tilde{g} \to b\tilde{b}_i \to tb\tilde{\chi}_1^+$ and (III)$_{ij}$ $\tilde{g} \to b\tilde{b}_1 \to bW\tilde{t}_1 \to bbW\tilde{\chi}_1^+$. $BR(\tilde{t}_1 \to b\chi_1^+)$ is sensitive to θ_t as wino like $\tilde{\chi}_1^+$ couples only to the $\tilde{t}_L$. The branching ratio of $\tilde{b}_i$ depends on θ_b while the sum of $\tilde{b}_1$ and $\tilde{b}_2$ contributions tends to be stable if both $\tilde{g} \to \tilde{b}_1$ and $\tilde{g} \to \tilde{b}_2$ are open. Altogether, one can measure θ_t from $\overline{BR}(\tilde{t})$, and θ_b from $\overline{BR}(\tilde{b})$.

Finally M_{tb}^{w} is sensitive to $m_{\tilde{t}}$ as the end point depends on the stop mass. It also depends on the $\tilde{b}_i$ masses, and θ_t and θ_b because the end point is expressed as the weighted average of M_{tb}(III)$_1$ and M_{tb}(IV)$_{11}$ Therefore the stop mass determination is possible only when the mixing angle is constrained.

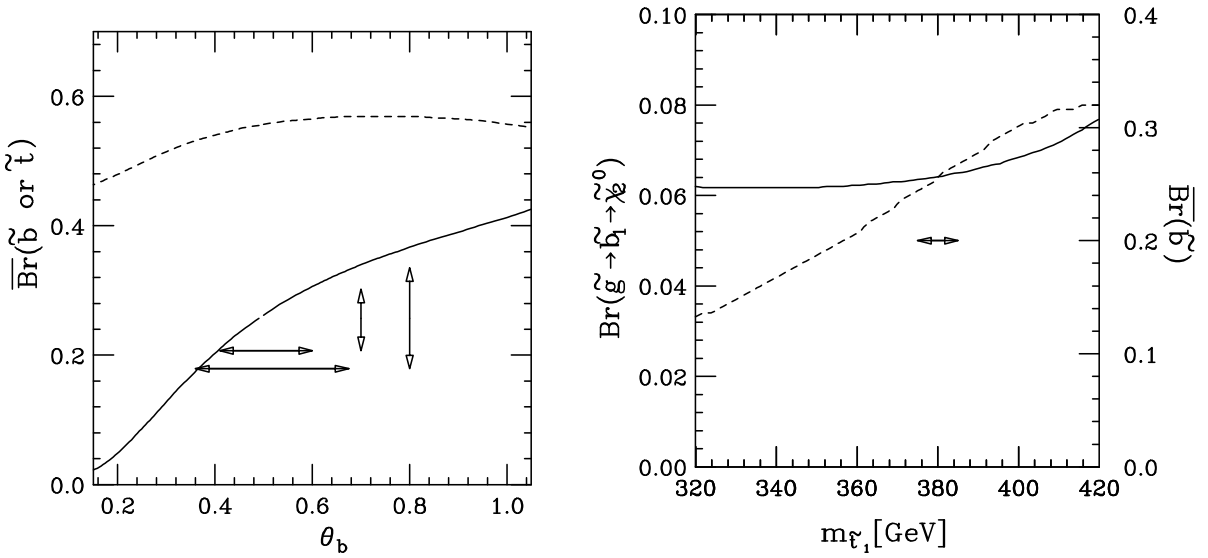

(a) (b)

Figure 5.40: a) $\overline{\text{BR}}(\tilde{b})$ (solid line) and $\overline{\text{BR}}(\tilde{t})$ (dotted line) as a function of θ_b. Errors for $\overline{\text{BR}}(\tilde{b})$ with/without systematical uncertainty are also shown by arrows. See text. The other parameters are fixed to the inputs. b) BR($\tilde{g} \to b\tilde{b} \to bb\tilde{\chi}_2^0$) (solid line) and $\overline{\text{BR}}(\tilde{b})$ (dotted line) as functions of $m_{\tilde{t}}$. θ_t, θ_b, $m_{\tilde{b}_1}$ and $m_{\tilde{b}_2}$ are fixed to SPS 1 inputs. An arrow shows the 1-σ arrowed region for $m_{\tilde{t}_1}$ for fixed θ_t.

We now illustrate the idea described above step by step through theoretical calculation. In Fig. 5.40 a), the solid line shows $\overline{\text{BR}}(\tilde{b})$ as a function of θ_b while fixing other sparticle masses and mixings. It increases monotonically as θ_b increases from 0 to $\pi/2$.

This is because the $\tilde{b}_L$ component of $\tilde{b}_2$ is proportional to $\sin\theta_b$, while the wino-like $\tilde{\chi}_2^0$ couples only to the left handed sparticles. The statistical errors of $\overline{\mathrm{BR}}(\tilde{b})$, with (without) systematic uncertainty and the corresponding errors of θ_b, $\Delta\overline{\mathrm{BR}}(\tilde{b}) = 0.078\,(0.045)$ and $\Delta\theta_b = 0.157\,(0.095)$, are shown by the long (short) vertical and horizontal arrows, respectively.

We note that $\mathrm{BR}(\tilde{g} \to b\tilde{b}_i \to bb\tilde{\chi}_2^0)$ depends on the stop mass $m_{\tilde{t}_1}$ and the mixing θ_t in addition to the sbottom mixing angle θ_b. In Fig. 5.40 Here solid and dotted lines show $\overline{\mathrm{BR}}(\tilde{b})$ and $BR(\tilde{g} \to b\tilde{b}_1 \to bb\tilde{\chi}_2^0)$, respectively, as functions of $m_{\tilde{t}_1}$. The stop mixing angle is fixed as $\theta_t = 0.96$. We see that the branching ratio has strong dependence on the stop mass. This is because the decay $\tilde{b}_i \to W\tilde{t}_1$ dominates the sbottom decay width if $m_{\tilde{b}_i} \gg m_{\tilde{t}_1}$. On the other hand, the stop mass dependence is canceled in $\overline{\mathrm{BR}}(\tilde{b})$ in Fig. 5.40 b). $\overline{\mathrm{BR}}(\tilde{b})$ is therefore independent to the stop sector and useful to extract the sbottom mixing angle. In addition, the uncertainty of the production cross sections and acceptances may be canceled in the ratio.

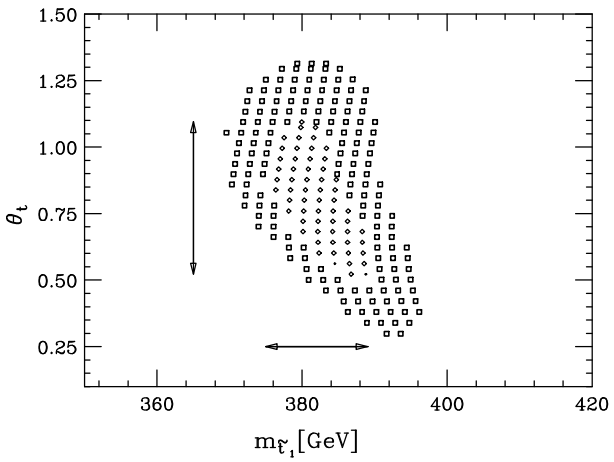

Figure 5.41: Expected 1-σ and 2-σ errors in a $m_{\tilde{t}_1}$ and θ_t plane from $\overline{\mathrm{BR}}(\tilde{t}_1)$ and M_{tb}^{w} measurements. Arrows show the 1-σ errors of θ_t and $m_{\tilde{t}_1}$.

We now discuss the constraint on $m_{\tilde{t}_1}$ and θ_t. In Fig. 5.41, we fix $m_{\tilde{b}_1}$, $m_{\tilde{b}_2}$ and θ_b to the input values, and scan the parameter space of $m_{\tilde{t}_1}$ and θ_t. We define a $\Delta\chi^2$-like function $\Delta\overline{\chi}^2$,

$$\Delta\overline{\chi}^2 \equiv \left(\frac{M_{tb}^{\mathrm{w}} - 370.9\mathrm{GeV}}{4.8\mathrm{GeV}}\right)^2 + \left(\frac{\overline{\mathrm{BR}}(\tilde{t}) - 0.583}{0.05}\right)^2 + \left(\frac{\overline{\mathrm{BR}}(\tilde{b}) - 0.252}{0.078}\right)^2. \qquad (5.61)$$

In Figure 5.41, the diamonds (squares) show the parameter points where $\Delta\chi^2 < 1(4)$, respectively, $\Delta m_{\tilde{t}_1} \sim 7$ GeV and $\Delta\theta_t = 0.287$. The deviation of $\overline{\mathrm{BR}}(\tilde{b})$ is very small over the scanned region because we fixed θ_b. Note that, the θ_b dependence of $\overline{\mathrm{BR}}(\tilde{t})$ is very weak in in Fig. 5.40(a) (a dotted line) within the allowed region of θ_b.

In this contribution we have shown that sbottom and stop mixing angle may be extracted by measuring the ratios of the branching ratios at LHC, provided precise determination of the neutralino mass matrix using LHC and LC data. The measurement of the mixing angle is essential to determine the sbottom mass matrix model

independently, and the information can be extracted only when both LHC and LC data is available.

5.2 Global fits in the MSSM

5.2.1 SFITTER: SUSY parameter analysis at LHC and LC

5.2.1.1 Introduction

While the Standard Model describes all available high energy physics experiments, it still has to be regarded as an effective theory, valid at the weak scale. New physics are expected to appear at the TeV energy scale. The supersymmetric extension ([487]) of the Standard Model is a well motivated extension providing us with a description of physics that can be extended consistently up to the unification scale.

If supersymmetry or any other high-scale extension of the Standard Model is discovered, it will be crucial to determine its fundamental high-scale parameters from weak-scale measurements [488]. The LHC and future Linear Colliders will provide us with a wealth of measurements [8, 9, 489], which due to their complexity require proper treatment to unravel the corresponding high-scale physics. Even in the general weak-scale minimal supersymmetric extension of the standard model (MSSM [490]) without any unification or SUSY breaking assumptions some of the measurements of masses and couplings are not independent measurements; moreover, linking supersymmetric particle masses to weak-scale SUSY parameters involves non-trivial mixing to mass eigenstates in essentially every sector of the theory. On top of that, for example in gravity mediated SUSY breaking scenarios (mSUGRA/cMSSM) a given weak-scale SUSY parameter will always be sensitive to several high-scale parameters which contribute through renormalization group running. Therefore, a fit of the model parameters using all experimental information available will lead to the best sensitivity and make the most efficient use of the information available.

In a fit, the allowed parameter space might not be sampled completely. To avoid boundaries imposed by non-physical parameter points, which can confine the fit to a 'wrong' parameter region, combining the fit with an initial evaluation of a multi-dimensional grid is the optimal approach.

In the general MSSM the weak-scale parameters can vastly outnumber the collider measurements, so that a complete parameter fit is not possible and one has to limit oneself to a consistent subset of parameters. In SFITTER both grid and fit are realised and can be combined. This way, one can ultimately eliminate all dependence on the starting point of the parameter determination. SFITTER also includes a general correlation matrix and the option to exclude parameters of the model from the fit/grid by fixing them to a value. Additionally, SFITTER includes the option to apply a Gaussian smearing to all observables before they enter the fit/grid in order to simulate realistically experimental measurements. In this preliminary study, however, correlations and systematic uncertainties are neglected and the central values are used for the measurements.

Currently, SFITTER uses the predictions for the supersymmetric masses provided by SUSPECT [491], but the conventions of the SUSY Les Houches accord [492] allow us to interface other programs. The branching ratios and e^+e^- production cross

	$m_{\rm SPS1a}$	LHC	LC	LHC+LC		$m_{\rm SPS1a}$	LHC	LC	LHC+LC
h	111.6	0.25	0.05	0.05	H	399.6		1.5	1.5
A	399.1		1.5	1.5	$H+$	407.1		1.5	1.5
χ_1^0	97.03	4.8	0.05	0.05	χ_2^0	182.9	4.7	1.2	0.08
χ_3^0	349.2		4.0	4.0	χ_4^0	370.3	5.1	4.0	2.3
$\chi_1^\pm$	182.3		0.55	0.55	$\chi_2^\pm$	370.6		3.0	3.0
$\tilde{g}$	615.7	8.0		6.5					
$\tilde{t}_1$	411.8		2.0	2.0					
$\tilde{b}_1$	520.8	7.5		5.7	$\tilde{b}_2$	550.4	7.9		6.2
$\tilde{u}_1$	551.0	19.0		16.0	$\tilde{u}_2$	570.8	17.4		9.8
$\tilde{d}_1$	549.9	19.0		16.0	$\tilde{d}_2$	576.4	17.4		9.8
$\tilde{s}_1$	549.9	19.0		16.0	$\tilde{s}_2$	576.4	17.4		9.8
$\tilde{c}_1$	551.0	19.0		16.0	$\tilde{c}_2$	570.8	17.4		9.8
$\tilde{e}_1$	144.9	4.8	0.05	0.05	$\tilde{e}_2$	204.2	5.0	0.2	0.2
$\tilde{\mu}_1$	144.9	4.8	0.2	0.2	$\tilde{\mu}_2$	204.2	5.0	0.5	0.5
$\tilde{\tau}_1$	135.5	6.5	0.3	0.3	$\tilde{\tau}_2$	207.9		1.1	1.1
$\tilde{\nu}_e$	188.2		1.2	1.2					

Table 5.25: Errors for the mass determination in SPS1a, taken from [501]. Shown are the nominal parameter values and the error for the LHC alone, the LC alone, and a combined LHC+LC analysis. All values are given in GeV.

sections are provided by MSMlib [493], which has been used extensively at LEP and cross checked with Ref. [494]. The next-to-leading order hadron collider cross sections are computed using PROSPINO [495]. The fitting program uses the MINUIT package [496]. The determination of χ^2 includes a general correlation matrix between measurements. In its next version SFITTER will be interfaced with the improved branching fraction determination of SDECAY [497], as well as alternative renormalization group codes like SoftSUSY [499], ISAJET [500] or SPHENO [441].

5.2.1.2 mSUGRA/cMSSM Parameter Determination

	SPS1a	StartFit	LHC	$\Delta_{\rm LHC}$	LC	$\Delta_{\rm LC}$	LHC+LC	$\Delta_{\rm LHC+LC}$
m_0	100	500	100.03	4.0	100.03	0.09	100.04	0.08
$m_{1/2}$	250	500	249.95	1.8	250.02	0.13	250.01	0.11
$\tan\beta$	10	50	9.87	1.3	9.98	0.14	9.98	0.14
A_0	-100	0	-99.29	31.8	-98.26	4.43	-98.25	4.13

Table 5.26: Summary of the mSUGRA fits in SPS1a: true values, starting values, fit values and absolute errors from the fit. As in SPS1a we fix $\mu > 0$. The mass values of the fits are based on Tab. 5.25.

Assuming that SUSY breaking is mediated by gravitational interactions (mSUGRA/cMSSM) we fit four universal high-scale parameters to a toy set of collider measurements: the universal scalar and gaugino masses, m_0, $m_{1/2}$, the trilinear coupling A_0 and the ratio of the Higgs vacuum expectation values, $\tan\beta$. The sign of the Higgsino mass parameter μ is a discrete parameter and therefore fixed. In contrast to an earlier study [498] we assume the set of mass measurement at the LHC and at the LC, shown in Tab. 5.25.

The central value for our assumed data set corresponds to the SUSY parameter point SPS1a [14, 369], as computed by SUSPECT. As mentioned in the introduction correlations, systematic errors and theoretical errors are neglected. As the central (true) values are used as measurements in order to study the errors on the determination of the parameters, the χ^2 values are not meaningful and therefore are not quoted.

The starting points for the mSUGRA parameters are fixed to the mean of the lower and upper limit (typically 1 TeV/c^2) of the allowed parameter range, *i.e.* they are not necessarily close to the true SPS1a values. The result of the fit is shown in Tab. 5.26. All true parameter values are reconstructed well within the quoted errors, in spite of starting values relatively far away. The measurements of m_0 and $m_{1/2}$ are very precise, while the sensitivity of the masses on $\tan\beta$ and A_0 is significantly weaker. The results for the LHC alone are generally an order of magnitude less precise than those for the LC, and this qualitative difference is expected to become even more pronounced once we properly include systematical errors.

Because the data set is fit assuming mSUGRA as a unification scenario the absence of measurements of most of the strongly interacting particles, in particular the gluino, does not have a strong impact on the precision of the LC determination. Therefore the results for the combined measurements LHC+LC show only a small improvement.

Assuming an uncorrelated data set, the correlations between the different high-scale SUSY parameters which we obtain from the fit are given in Tab. 5.27. We can understand the correlation matrix step by step [502]: first, the universal gaugino mass $m_{1/2}$ can be extracted very precisely from the physical gaugino masses. The determination of the universal scalar mass m_0 is dominated by the weak-scale scalar particle spectrum, but in particular the squark masses are also strongly dependent on the universal gaugino mass, because of mixing effects in the renormalization group running. Hence, a strong correlation between the m_0 and $m_{1/2}$ occurs. The universal trilinear coupling A_0 can be measured through the third generation weak-scale mass parameters $A_{b,t,\tau}$. However, the $A_{b,t,\tau}$ which appear for example in the off-diagonal elements of the scalar mass matrices, also depend on m_0 and $m_{1/2}$, so that A_0 is strongly correlated with m_0 and $m_{1/2}$. At this point one should stress that the determination of A_0 is likely to be dominated by A_t as it appears in the calculation of the lightest Higgs mass m_h. After taking into account the current theoretical error of 3 GeV on m_h [32] we expect the determination of A_0 to suffer significantly. The experimental errors therefore can be considered a call for an improvement of the theoretical error.

	m_0	$m_{1/2}$	$\tan\beta$	A_0
m_0	1.000	-0.555	0.160	-0.324
$m_{1/2}$		1.000	-0.219	0.617
$\tan\beta$			1.000	0.307
A_0				1.000

Table 5.27: The (symmetric) correlation matrix for the mSUGRA fit given in Tab.5.26 with data set LHC+LC.

In general, $\tan\beta$ can be determined in three sectors of the supersymmetric spectrum: all four Higgs masses, and for large values of m_A in particular the light CP even Higgs mass m_h depend on $\tan\beta$. The mixing between gauginos and Higgsinos in the neutralino/chargino sector is governed by $\tan\beta$. Finally, the stop mixing is

governed by $\mu/\tan\beta$, while the sbottom and stau mixing depends on $\mu\tan\beta$. The correlation of $\tan\beta$ with the other model parameters reflects the relative impact of these three sectors. In an earlier analysis we assumed a uniform error of 0.5% on all mass measurements [498] and saw that in this case $\tan\beta$ is determined through stau mixing, which in turn means that it shows very little correlation with $m_{1/2}$.

For the more realistic scenario in Tab. 5.25 the outcome is the following: the relative errors for the light Higgs mass and for the light neutralino masses at the LC are tiny. The relevant parameter in the Higgs sector is the light stop mass, which is governed by $m_{1/2}$; similarly the gaugino mass $m_{1/2}$ which fixes the light neutralino and chargino masses does not depend strongly on $\tan\beta$. The slepton sector introduces a strong correlation between m_0 and $m_{1/2}$. The resulting correlation matrix is shown in in Tab. 5.27. The results obtained with SFITTER are in agreement with expectation.

5.2.1.3 General MSSM Parameter Determination

	AfterGrid	AfterFit	SPS1a		AfterGrid	AfterFit	SPS1a
$\tan\beta$	100	10.02±3.4	10	$M_{\tilde{u}_R}$	532.1	532.1±2.8	532.1
M_1	100	102.2±0.74	102.2	$M_{\tilde{d}_R}$	529.3	529.3±2.8	529.3
M_2	200	191.79±1.9	191.8	$M_{\tilde{c}_R}$	532.1	532.1±2.8	532.1
M_3	589.4	589.4±7.0	589.4	$M_{\tilde{s}_R}$	529.3	529.3±2.8	529.3
μ	300	344.3±1.3	344.3	$M_{\tilde{t}_R}$	420.2	420.08±13.3	420.2
m_A	399.35	399.1±1.2	399.1	$M_{\tilde{b}_R}$	525.6	525.5±10.1	525.6
$M_{\tilde{e}_R}$	138.2	138.2±0.76	138.2	$M_{\tilde{q}1_L}$	553.7	553.7±2.1	553.7
$M_{\tilde{\mu}_R}$	138.2	138.2±0.76	138.2	$M_{\tilde{q}2_L}$	553.7	553.7±2.1	553.7
$M_{\tilde{\tau}_R}$	135.5	135.48±2.3	135.5	$M_{\tilde{q}3_L}$	501.3	501.42±10.	501.3
$M_{\tilde{e}_L}$	198.7	198.7±0.68	198.7	A_τ	-253.5	-244.7±1428	-253.5
$M_{\tilde{\mu}_L}$	198.7	198.7±0.68	198.7	A_t	-504.9	-504.62±27.	-504.9
$M_{\tilde{\tau}_L}$	197.8	197.81±0.92	197.8	A_b	-797.99	-825.2±2494	-799.4

Table 5.28: Result for the general MSSM parameter determination in SPS1a using the toy sample of all MSSM particle masses with a universal error of 0.5%. Shown are the nominal parameter values, the result after the grid and the final result. All masses are given in GeV.

In this study, the unconstrained weak-scale MSSM is described by 24 parameters in addition to the standard model parameters. The parameters are listed in Tab. 5.28: $\tan\beta$ as in mSUGRA, plus three soft SUSY breaking gaugino masses M_i, the Higgsino mass parameter μ, the pseudoscalar Higgs mass m_A, the soft SUSY breaking masses for the right sfermions, $M_{\tilde{f}_R}$, the corresponding masses for the left doublet sfermions, $M_{\tilde{f}_L}$ and finally the trilinear couplings of the third generation sfermions $A_{t,b,\tau}$.

Toy model with all masses

For testing purposes, we first consider a toy data set which includes all supersymmetric particle masses. The universal error on all mass measurements is set to 0.5%.

In any MSSM spectrum, in first approximation, the parameters M_1, M_2, μ and $\tan\beta$ determine the neutralino and chargino masses and couplings. We exploit this feature to illustrate the option to use a grid before starting the fit. The starting values of the parameters other than M_1, M_2, μ and $\tan\beta$ are set to their nominal values, this study

is thus less general than the one of mSUGRA. The χ^2 is then minimized on a grid using the six chargino and neutralino masses as measurements to determine the four parameters M_1, M_2, μ and $\tan\beta$. The step size of the grid is 10 for $\tan\beta$ and 100 GeV for the mass parameters. After the minimization, the four parameters obtained from grid minimization are fixed and all remaining parameters are fitted. In a final run all model parameters are released and fitted. The results after the grid (including the complementary fit), after the final fit and the nominal values are shown in Tab. 5.28. The smearing option has not been applied. However, the errors on the fitted values (once the fit converges) should not be sensitive to these shortcomings.

The final fit indeed converges to the correct central values within its error. The central values of the fit are in good agreement with generated values, except for the trilinear coupling $A_{b,\tau}$. The problem is using only mass measurements to determine the three entries in a (symmetric) scalar mass matrix: in the light slepton sector there are three masses, left and right scalars plus the sneutrino, so the system is in principle calculable. In the third generation squark sector we have three independent diagonal entries per generation and two off-diagonal entries. But the number of mass measurements is only four, therefore the system is underdetermined in first order. The off-diagonal entry in the mass matrix for down type scalars includes a term $A_{b,\tau}$ and an additional term $\mu\tan\beta$. Even for very moderate values of $\tan\beta$ the extraction of $A_{b,\tau}$ requires precise knowledge of $\tan\beta$. The use of branching ratios and cross section measurements (with polarised beams) which carry information about the scalar mixing angles should significantly improve the determination of $A_{t,b,\tau}$.

Toy model with LHC-LC mass measurements

In the study of the three data sets LHC, LC, and LHC+LC in the MSSM, a fit was performed for the data sets LHC and LC, whereas for LHC+LC additionally the GRID was used for M_1, M_2, μ and $\tan\beta$ with the five chargino and neutralino masses. The starting points were chosen to be the true values (with the exception of the parameters used in the grid). In order to obtain a solvable system, for the LHC data set m_A, $M_{\tilde{t}_R}$, $M_{\tilde{\tau}_L}$, A_τ were fixed. For the LC data set the first and second generation squark soft SUSY breaking masses, the gluino mass M_3, $M_{\tilde{b}_R}$ and A_b were fixed. These parameters were chosen on the basis of the measurements available in Tab. 5.25. The values to which these parameters were fixed is not expected to influence the final result of the fit. The results for the two data sets are shown in Tab. 5.29.

Note that the general rule that the LHC is not sensitive to weakly interacting particle masses is not entirely true: while the LHC has the advantage of measuring the squark and gluino masses, the first and second generation slepton mass parameters are also determined with a precision of the order of percent. The results in Tab. 5.29 show that the LHC alone is well capable of determining for example all gaugino mass parameters as well as most of the scalar mass parameters.

The situation at the LC is slightly different. Only marginal information on the squark sector available at the LC. The measurement of A_t from the Higgs sector should be taken with a grain of salt (theoretical error on the lightest Higgs mass). Adding the stau mixing angle to the set of LC measurements will improve the determination of A_τ. However, the measurements of the parameters, in particular slepton and gaugino parameters are far more precise than at the LHC.

For the LHC+LC data set, a sufficient number of mass measurements is available,

	LHC	LC	LHC+LC	SPS1a
$\tan\beta$	10.22±9.1	10.26±0.3	10.06±0.2	10
M_1	102.45±5.3	102.32±0.1	102.23±0.1	102.2
M_2	191.8±7.3	192.52±0.7	191.79±0.2	191.8
M_3	578.67±15	fixed 500	588.05±11	589.4
$M_{\tilde{\tau}_L}$	fixed 500	197.68±1.2	199.25±1.1	197.8
$M_{\tilde{\tau}_R}$	129.03±6.9	135.66±0.3	133.35±0.6	135.5
$M_{\tilde{\mu}_L}$	198.7±5.1	198.7±0.5	198.7±0.5	198.7
$M_{\tilde{\mu}_R}$	138.2±5.0	138.2±0.2	138.2±0.2	138.2
$M_{\tilde{e}_L}$	198.7±5.1	198.7±0.2	198.7±0.2	198.7
$M_{\tilde{e}_R}$	138.2±5.0	138.2±0.05	138.2±0.05	138.2
$M_{\tilde{q}3_L}$	498.3±110	497.6±4.4	521.9±39	501.3
$M_{\tilde{t}_R}$	fixed 500	420±2.1	411.73±12	420.2
$M_{\tilde{b}_R}$	522.26±113	fixed 500	504.35±61	525.6
$M_{\tilde{q}2_L}$	550.72±13	fixed 500	553.31±5.5	553.7
$M_{\tilde{c}_R}$	529.02±20	fixed 500	531.70±15	532.1
$M_{\tilde{s}_R}$	526.21±20	fixed 500	528.90±15	529.3
$M_{\tilde{q}1_L}$	550.72±13	fixed 500	553.32±6.5	553.7
$M_{\tilde{u}_R}$	528.91±20	fixed 500	531.70±15	532.1
$M_{\tilde{d}_R}$	526.2±20	fixed 500	528.90±15	529.3
A_τ	fixed 0	-202.4±89.5	352.1±171	-253.5
A_t	-507.8±91	-501.95±2.7	-505.24±3.3	-504.9
A_b	-784.7±35603	fixed 0	-977±12467	-799.4
m_A	fixed 500	399.1±0.9	399.1±0.8	399.1
μ	345.21±7.3	344.34±2.3	344.36±1.0	344.3

Table 5.29: Result for the general MSSM parameter determination in SPS1a using the mass measurements given in Tab. 5.25. Shown are the nominal parameter values and the result after fits to the different data sets. All masses are given in GeV.

so that no parameters need to be fixed. The superiority of the combination of the measurements at the two colliders is obvious from this observation and from Tab. 5.29: The LHC contributes to reduce the error in the weak sector (M_2) and the LC in the strongly interacting sector (third generation squarks). Even more important: of 13 parameters undetermined by either the LHC or the LC, 11 are determined with good precision in the combination. For A_τ, A_b, we expect an improvement with the use of branching ratios and cross section measurements.

A complete measurement of all parameters at the weak scale is particularly important if one wants to probe unification scenarios which link subsectors of the parameter space which are independent at the weak scale. An advanced tool like SFITTER can extract the information to probe supersymmetry breaking scenarios from any set of measurements, provided the set is sufficient to overconstrain the model parameters.

5.2.1.4 Conclusions

SFITTER is a new program to determine supersymmetric parameters from measurements. The parameters can be extracted either using a fit, a multi-dimensional grid, or a combination of the two. Correlations between measurements can be specified

and are taken into account. While it is relatively easy to fit a fixed model with very few parameters for example at a high scale to a set of collider measurements, the determination of the complete set of weak-scale MSSM model parameters requires this more advanced tool. A mSUGRA inspired fit does not include the full complexity and power of the combined LHC and LC data compared to the measurements at either collider alone. The results from SFITTER in the MSSM with the three data sets show that only the combination of measurements of both the LHC and the LC offers a complete picture of the MSSM model parameters in a reasonably model independent framework.

5.2.2 Fittino: A global fit of the MSSM parameters

5.2.2.1 Introduction

As for the program SFITTER, the aim of Fittino is the determination of the parameters of the MSSM. It is implemented in C++ and focusses on the determination of the parameters of the soft SUSY breaking Lagrangian $\mathcal{L}_{\text{soft}}$, obeying the following principles:

- No *a priori* knowledge of SUSY parameters is assumed (but can be imposed if desired by the user).
- All measurements from future colliders could be used.
- All correlations among parameters and all influences of loop-induced effects, where parameters of one sector affect observables of other sectors of the theory, are taken into account, as far as they are implemented into the program which provides the theoretical predictions.

In this way an unbiased global fit is obtained. No attempt to extract SUSY parameters at the GUT scale is made, since the evolution of the parameters and their determination at the low scale factorizes. The result of Fittino with the full errors of the low energy SUSY parameters can therefore be used later to extrapolate to the GUT scale.

However, all 105 possible parameters of $\mathcal{L}_{\text{MSSM}}$ cannot be determined simultaneously. Therefore, assumptions on the structure of $\mathcal{L}_{\text{MSSM}}$ are made. All phases are set to 0, no mixing between generations is assumed and the mixing within the first two generations is set to 0. Thus the number of free parameters in the SUSY breaking sector is reduced to 24. Further assumptions can be specified by the user. Observables used in the fit can be

- Masses, limits on masses of unobserved particles
- Widths
- Cross-Sections
- Branching ratios
- Edges in mass spectra

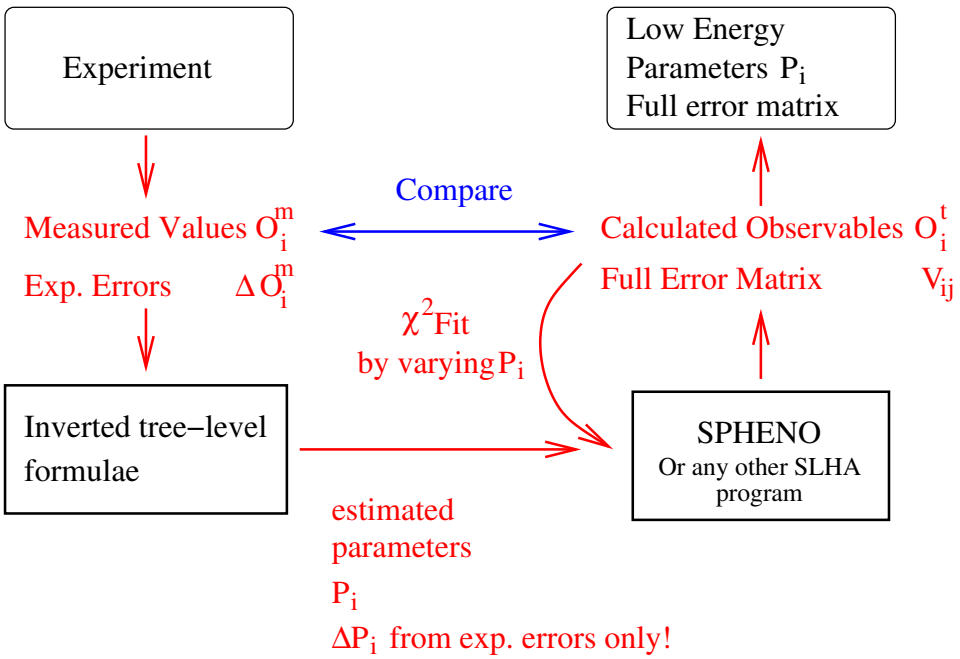

Figure 5.42: Iterative fit procedure

Correlations among observables and both experimental and theoretical errors can be supplied by the user. Both SM and MSSM observables can be used in the fit. Parametric uncertainties of SUSY observables can be taken into account by fitting the relevant SM parameters simultaneously with the MSSM parameters. The prediction of the MSSM observables for a given set of parameters is obtained from SPheno [441]. The communication with SPheno is realized via the SUSY Les Houches Accord [492] (SLHA). Other SUSY generators or spectrum calculators can be included via SLHA. MINUIT [503] is used for the fitting process.

In the following, we describe the principles of Fittino in more detail, followed by example fits based on SPS1a.

5.2.2.2 MSSM Parameter Determination

General Principles of Fits with Fittino

The full MSSM parameter space in Fittino, consisting of maximally 24 MSSM parameters plus SM parameters, cannot be scanned completely, neither in a fit nor in a grid approach. Therefore, in order to find the true parameters in a fit by minimizing a χ^2 function, it is essential to begin with reasonable start values, allowing for a smooth transition to the true minimum. As default, no *a priori* knowledge of the parameters can be used in a realistic attempt of a fit, since in a real measurement no information on true parameters will be available either.

The program Fittino uses an iterative procedure to determine the parameters. It is displayed in Fig. 5.42. In a first step, the SUSY parameters are estimated using tree-level relations as follows:

1. $\mu, m_A, \tan\beta, M_1, M_2, M_3$ are determined from gaugino and Higgs sector observ-

Measurement	Value	Uncertainty
m_{Z}	91.1187 GeV	0.0021 GeV
m_{W}	80.3382 GeV	0.039 GeV
m_{c}	1.2 GeV	0.2 GeV
m_{b}	4.2 GeV	0.5 GeV
m_{t}	174.3 GeV	0.3 GeV
m_{τ}	1.77699 GeV	0.00029 GeV
α_s	0.1172	0.0002
G_F	$1.16639{\cdot}10^{-5}$ GeV^{-2}	$1{\cdot}10^{-11}$ GeV^{-2}
$1/\alpha$	127.934	0.027
$\sin^2\theta_W$	0.23113	0.00015
m_{h^0}	110.2 GeV	0.5 GeV
m_{H^0}	400.8 GeV	1.3 GeV
m_{A^0}	399.8 GeV	1.3 GeV
$m_{\mathrm{H}^\pm}$	407.7 GeV	1.1 GeV
$m_{\tilde{\mathrm{u}}_L}$	583.5 GeV	9.8 GeV
$m_{\tilde{\mathrm{u}}_R}$	566.5 GeV	23.6 GeV
$m_{\tilde{\mathrm{d}}_L}$	586.7 GeV	9.8 GeV
$m_{\tilde{\mathrm{d}}_R}$	566.3 GeV	23.6 GeV
$m_{\tilde{\mathrm{c}}_L}$	583.6 GeV	9.8 GeV
$m_{\tilde{\mathrm{c}}_R}$	566.5 GeV	23.6 GeV
$m_{\tilde{\mathrm{s}}_L}$	586.7 GeV	9.8 GeV
$m_{\tilde{\mathrm{s}}_R}$	566.3 GeV	23.6 GeV
$m_{\tilde{\mathrm{t}}_R}$	417.5 GeV	2.0 GeV
$m_{\tilde{\mathrm{b}}_R}$	532.1 GeV	5.7 GeV
$m_{\tilde{\mathrm{b}}_L}$	565.6 GeV	6.2 GeV
$m_{\tilde{\nu}_{eL}}$	192.3 GeV	0.7 GeV
$m_{\tilde{\mathrm{e}}_L}$	208.0 GeV	0.2 GeV
$m_{\tilde{\mathrm{e}}_R}$	143.91 GeV	0.05 GeV
$m_{\tilde{\mu}_L}$	208.0 GeV	0.5 GeV
$m_{\tilde{\mu}_R}$	143.9 GeV	0.2 GeV
$m_{\tilde{\tau}_R}$	134.3 GeV	0.3 GeV
$m_{\tilde{\tau}_L}$	211.8 GeV	1.1 GeV
$m_{\tilde{\mathrm{g}}}$	630.4 GeV	6.4 GeV
$m_{\tilde{\chi}_1^0}$	95.74 GeV	0.05 GeV
$m_{\tilde{\chi}_2^0}$	182.40 GeV	0.08 GeV
$m_{\tilde{\chi}_1^\pm}$	180.46 GeV	0.55 GeV
$m_{\tilde{\chi}_2^\pm}$	380.0 GeV	3.0 GeV
σ ($\mathrm{e}^+\mathrm{e}^- \to \tilde{\chi}_1^0\tilde{\chi}_2^0$, $\sqrt{s} = 500$ GeV, $P_{\mathrm{e}^-} = 0.8$, $P_{\mathrm{e}^+} = 0.6$)	22.7 fb	2.0 fb
σ ($\mathrm{e}^+\mathrm{e}^- \to \tilde{\chi}_2^0\tilde{\chi}_2^0$, $\sqrt{s} = 500$ GeV, $P_{\mathrm{e}^-} = 0.8$, $P_{\mathrm{e}^+} = 0.6$)	19.5 fb	2.0 fb
σ ($\mathrm{e}^+\mathrm{e}^- \to \tilde{\mathrm{e}}_L\tilde{\mathrm{e}}_L$, $\sqrt{s} = 500$ GeV, $P_{\mathrm{e}^-} = 0.8$, $P_{\mathrm{e}^+} = 0.6$)	205.0 fb	4.0 fb
σ ($\mathrm{e}^+\mathrm{e}^- \to \tilde{\mu}_L\tilde{\mu}_L$, $\sqrt{s} = 500$ GeV, $P_{\mathrm{e}^-} = 0.8$, $P_{\mathrm{e}^+} = 0.6$)	36.8 fb	4.0 fb
σ ($\mathrm{e}^+\mathrm{e}^- \to \tilde{\tau}_1\tilde{\tau}_1$, $\sqrt{s} = 500$ GeV, $P_{\mathrm{e}^-} = 0.8$, $P_{\mathrm{e}^+} = 0.6$)	39.1 fb	4.0 fb
σ ($\mathrm{e}^+\mathrm{e}^- \to \tilde{\chi}_1^\pm\tilde{\chi}_1^\mp$, $\sqrt{s} = 500$ GeV, $P_{\mathrm{e}^-} = 0.8$, $P_{\mathrm{e}^+} = 0.6$)	46.7 fb	1.0 fb
σ ($\mathrm{e}^+\mathrm{e}^- \to \mathrm{Z}\,\mathrm{h}^0$, $\sqrt{s} = 500$ GeV, $P_{\mathrm{e}^-} = 0.8$, $P_{\mathrm{e}^+} = 0.6$)	11.13 fb	0.21 fb
σ ($\mathrm{e}^+\mathrm{e}^- \to \tilde{\chi}_1^\pm\tilde{\chi}_1^\mp$, $\sqrt{s} = 500$ GeV, $P_{\mathrm{e}^-} = -0.8$, $P_{\mathrm{e}^+} = -0.6$)	104.8 fb	3.5 fb
σ ($\mathrm{e}^+\mathrm{e}^- \to \tilde{\chi}_1^0\tilde{\chi}_2^0$, $\sqrt{s} = 500$ GeV, $P_{\mathrm{e}^-} = -0.8$, $P_{\mathrm{e}^+} = -0.6$)	43.9 fb	2.0 fb
σ ($\mathrm{e}^+\mathrm{e}^- \to \tilde{\chi}_2^0\tilde{\chi}_2^0$, $\sqrt{s} = 500$ GeV, $P_{\mathrm{e}^-} = -0.8$, $P_{\mathrm{e}^+} = -0.6$)	43.8 fb	2.0 fb
σ ($\mathrm{e}^+\mathrm{e}^- \to \tilde{\mathrm{e}}_L\tilde{\mathrm{e}}_L$, $\sqrt{s} = 500$ GeV, $P_{\mathrm{e}^-} = -0.8$, $P_{\mathrm{e}^+} = -0.6$)	97.4 fb	4.0 fb

Measurement	Value	Uncertainty
σ ($e^+e^- \to \tilde{e}_L\tilde{e}_R$, $\sqrt{s} = 500$ GeV, $P_{e^-} = -0.8$, $P_{e^+} = -0.6$)	223.7 fb	4.0 fb
σ ($e^+e^- \to \tilde{e}_R\tilde{e}_R$, $\sqrt{s} = 500$ GeV, $P_{e^-} = -0.8$, $P_{e^+} = -0.6$)	29.0 fb	2.0 fb
σ ($e^+e^- \to \tilde{\mu}_L\tilde{\mu}_L$, $\sqrt{s} = 500$ GeV, $P_{e^-} = -0.8$, $P_{e^+} = -0.6$)	22.7 fb	2.0 fb
σ ($e^+e^- \to \tilde{\tau}_1\tilde{\tau}_1$, $\sqrt{s} = 500$ GeV, $P_{e^-} = -0.8$, $P_{e^+} = -0.6$)	25.7 fb	2.0 fb
BR ($h^0 \to b\overline{b}$)	0.82	0.01
BR ($h^0 \to c\overline{c}$)	0.04	0.01
BR ($h^0 \to \tau^+\tau^-$)	0.14	0.01

Table 5.30: Simulated measurements at LHC and a 0.5 and 1 TeV LC. For the cross sections, the corresponding center-of-mass energy and the electron and positron polarization are given.

ables using formulae from [177]. In order to extract these parameters, information from chargino cross-sections is needed, which enters in form of the chargino mixing angles $\cos 2\phi_L$ and $\cos 2\phi_R$. These pseudo-observables are only used for the determination of the start values, no use is made of them for the fit.

2. A_t, A_b, M_Q, M_U, M_D are determined from the squark sector masses, using formulae from [504]. No mixing in the third generation is assumed to get the start values.

3. A_τ, M_L, M_E are determined from the slepton sector masses, using formulae from [504]. No mixing in the third generation is assumed to get the start values.

Instead of the trilinear couplings A_t, A_b and A_τ the following sfermion mixing parameters

$$\begin{aligned} X_t &= A_t - \mu/\tan\beta \\ X_b &= A_b - \mu \cdot \tan\beta \\ X_\tau &= A_\tau - \mu \cdot \tan\beta \end{aligned}$$

are used in the fit. This is done in order to reduce the correlations between the parameters μ, $\tan\beta$ and A_t, A_b and A_τ. The tree-level initialization is done such that $A_{t,b,\tau} = 0$.

Since the mixing in the third generation has not been taken correctly into account on tree-level, the parameters X_t, X_b, X_τ tend to be badly initialized. A global fit with these starting values would most likely not converge. Therefore next the estimates from the slepton sector are improved by fitting only the slepton parameters X_τ, M_L, M_E to the observables from the slepton sector, i. e. slepton masses and cross-sections. Observables not directly related to the slepton sector can degrade the fit result, since parameters of other sectors are likely to be still wrong. In such a case a parameter of the slepton sector will be pulled into a wrong direction, in order to compensate for the wrong parameters of other sectors. All parameters not from the slepton sector are fixed to their tree-level estimates obtained in the previous step. In this fit with reduced number of dimensions MINUIT can handle the correlations among the parameters better than in a global fit with all parameters free.

Then the third generation squark parameters are improved by only fitting X_t, X_b, M_Q, M_U, M_D to the observables of the squark sector, masses and cross-sections. All other parameters are fixed to their previous values.

No.	Parameter	Start Value (GeV)	Start Uncertainty (GeV)
1	$\tan\beta$	10.0	12.8
2	μ	354.4	2.6
3	$m_{\tilde{\mathrm{e}}_R}$	150.2	15.0
4	$m_{\tilde{\tau}_R}$	141.0	14.1
5	$m_{\tilde{\mathrm{e}}_L}$	202.7	20.3
6	$m_{\tilde{\tau}_L}$	206.6	20.7
7	X_{t}	-35	100
8	X_τ	-3558	100
9	$m_{\tilde{\mathrm{d}}_R}$	567	57
10	$m_{\tilde{\mathrm{b}}_R}$	566	57
11	$m_{\tilde{\mathrm{u}}_R}$	567	57
12	$m_{\tilde{\mathrm{t}}_R}$	381	38
13	$m_{\tilde{\mathrm{u}}_L}$	581	58
14	$m_{\tilde{\mathrm{t}}_L}$	575	58
15	M_1	99.08	0.58
16	M_2	195.08	0.73
17	M_3	630.5	6.4
18	m_{A^0}	399.8	1.3
19	m_{t}	174.3	0.3

Table 5.31: Estimates of the MSSM parameters, obtained from tree-level relations.

No.	Parameter	SPS1a Value (GeV)	Fit Value (GeV)	Uncertainty (GeV)
1	A_τ	-250.77	-250.82	65.81
2	A_{b}	-855.06	-854.66	1269.16
3	A_{t}	-506.39	-506.35	2.02

Table 5.32: Fit result for a fit where only the trilinear couplings $A_{\mathrm{t}}, A_{\mathrm{b}}, A_\tau$ are fitted, with all other parameters fixed to their SPS1a values. No sensitivity is obtained for A_{b}.

After this step still the correlations among $\tan\beta$ and the third generation slepton and squark parameters are not optimally modelled. Therefore another intermediate step ist introduced, where $\tan\beta, X_{\mathrm{t}}, X_{\mathrm{b}}, X_\tau$ and $m_{\tilde{\mathrm{t}}_{L,R}}$ are fitted to all observables and all other parameters are fixed to their present values.

After this, all MSSM parameters are released and a global fit is done, using the method MINIMIZE in MINUIT. During the MSSM parameter fit Standard Model parameters have been kept fixed. If requested by the user, an additional fit step can be done which also releases SM parameters. Provided the fit has converged, a subsequent MINOS error analysis is performed, yielding asymmetrical uncertainties, the full correlation matrix and 2D fit contours.

The SPS1a Fit

The approach described above has been tested for the scenario SPS1a [14]. For this scenario, a set of hypothetical measurements at LHC, a 500 GeV and a 1 TeV Linear

Collider has been collected in Table 5.30. In this example a theoretical error on the prediction of the lightest Higgs boson mass of 500 MeV is included. All observables from Table 5.30 were selected as input to fit the 24 parameters of the unconstrained MSSM and the top quark mass. In order to reduce the number of fit parameters and to simplify the fit procedure, unification of the first two generations has been assumed. Table 5.28 shows that this is a reasonable assumption which does not imply any loss of accurarcy.

The parameter X_b has been fixed to -4000 GeV. The reason for this is summarized in Table 5.32. It contains the fitted trilinear couplings A_τ, A_t and A_b from a fit where all other parameters from Table 5.33 are fixed to their SPS1a values. Evidently the selected observables have no sensitivity to A_b. Fixing X_b is a passable way to circumvent this insensitivity.

Taking these simplifications into account, 18 MSSM parameters and the top quark mass remain. All fitted parameters are listed in Table 5.33 including the predicted SPS1a values, the fitted values and the uncertainties from the fit. All fitted parameters except the third generation squark sector agree well with the generated values. The discrepancy in the third generation squark sector stems from the fact that X_b is fixed to an approximate value which does not coincide with its SPS1a value. The inclusion of a theoretical error of 500 MeV on the lightest Higgs mass increases the uncertainty on $\tan\beta$ by a factor of 2.

Albeit the fitted third generation squark parameters do not match their SPS1a values, the obtained χ^2 of the fit is only 0.043. This shows the importance to fit all parameters simultaneously, since parameters fixed to wrong values tend to distort the whole spectrum of the fitted parameters to compensate for the wrongly fixed parameters. As it is obvious from Table 5.33, the systematic distortion can be much larger than the 1σ uncertainties of the parameters.

Improving the determination of the trilinear couplings and a release of the $X_\mathrm{b} = -4000\,\mathrm{GeV}$ constraint requires the inclusion of additional, more sensitive observables. Good candidates are probably stop and stau polarization measurements. Unfortunately such predictions are not yet available in SPheno.

In addition the contribution of the various observables to the determination of a given parameter has been studied by looking at $\Delta\chi^2$ for the individual observables if the parameter is changed by $\pm1\sigma$. As an example, Table 5.34 summarizes the three most important contributions to $\tan\beta$, μ, M_1, M_2 and M_3.

It has also been tried to carry out fits using only a reduced set of measurements as input such as they are available in "LHC only" and "LC only" scenarios. The "LHC only" case shows a quite comprehensive particle spectrum but only poor information on the slepton sector is avaiable. In contrast to that the "LC only" scenario is characterized by an incomplete MSSM particle spectrum (no information from squark sector) but a very precise slepton and gaugino sector. Even when poorly determined parameters are fixed (as in Table 5.29), no converging fits are obtained. This fact shows the importance of combined LHC and LC data analyses.

5.2.2.3 Conclusions

Fittino is a program to determine the MSSM parameters from a global fit to measurements at the LHC and a future Linear Collider. No prior knowledge of any of

No.	Parameter	Generated Value	Fitted Value (GeV)	Uncertainty (GeV)
1	$\tan\beta$	10.0	9.92	1.43
2	μ	358.6	358.6	4.4
3	X_τ	-3836.8	-3769	648
4	$m_{\tilde{\mathrm{e}}_R} = m_{\tilde{\mu}_R}$	135.76	135.86	0.13
5	$m_{\tilde{\tau}_R}$	134.6	133.1	3.0
6	$m_{\tilde{\mathrm{e}}_L} = m_{\tilde{\mu}_L}$	195.2	195.19	0.20
7	$m_{\tilde{\tau}_L}$	194.4	194.5	1.9
8	X_t	-506.4	-508.7	35.8
9	$m_{\tilde{\mathrm{d}}_R} = m_{\tilde{\mathrm{s}}_R}$	528.1	528.2	15.9
10	$m_{\tilde{\mathrm{b}}_R}$	524.8	495.6	6.6
11	$m_{\tilde{\mathrm{u}}_R} = m_{\tilde{\mathrm{c}}_R}$	530.3	530.3	10.2
12	$m_{\tilde{\mathrm{t}}_R}$	424.3	412.8	8.0
13	$m_{\tilde{\mathrm{u}}_L} = m_{\tilde{\mathrm{c}}_L}$	548.7	548.7	5.2
14	$m_{\tilde{\mathrm{t}}_L}$	500.0	529.8	7.3
15	M_1	101.809	101.84	0.22
16	M_2	191.76	191.66	0.71
17	M_3	588.8	588.4	7.8
18	m_{A^0}	399.77	399.78	0.73
19	m_t	174.3	174.30	0.30
	X_b	-4441.1	-4000	fixed
	m_b	4.2	4.2	fixed
	m_c	1.2	1.2	fixed

Table 5.33: Fit result for a global fit of SM and MSSM parameters to the observables listed in Table 5.30. The obtained total χ^2 of the fit amounts to 0.043.

the parameters is needed. To get reasonable start values for the fit, tree-level formulae are used to relate the observables to the SUSY parameters. First results obtained with this powerful tool clearly reveal the benefit from combining the LHC and LC results. The comprehensive SUSY particle spectrum accessible at LHC and the precise measurements of the lightest SUSY particles at a Linear Collider are crucial to get a converging fit. Attempts to fit only individual sectors of the theory are unsuccessful, if no prior knowledge of any parameter is assumed. This fact shows the fruitfulness of combining measurements of both machines.

5.3 SUSY and Dark Matter

5.3.1 Reach of LHC and LC in Dark Matter allowed regions of the mSUGRA model

Recently, the WMAP collaboration has analyzed the anisotropies in the cosmic microwave background radiation. The analysis leads to a determination that the universe is comprised of $\sim 5\%$ baryons, $\sim 25\%$ cold dark matter, and $\sim 70\%$ dark energy. In particular, the cold dark matter density is determined to be $\Omega_{CDM}h^2 = 0.1126^{+0.0161}_{-0.0181}$

Parameter	$\Delta\chi^2_{\text{total}}$	Contributing Observable	Rel. Contrib. (%)
$\tan\beta$	75.4	$m_{\chi_2^0}$	71.4
		$m_{\chi_1^0}$	22.5
		$m_{\chi_1^\pm}$	1.6
μ	21.7	$m_{\chi_2^0}$	81.1
		$m_{\chi_1^0}$	9.0
		$m_{\chi_2^\pm}$	7.6
M_1	17.2	$m_{\chi_1^0}$	99.78
		σ ($e^+e^- \to \tilde{e}_L\tilde{e}_L$, 500 GeV, 0.8, 0.6)	0.13
		σ ($e^+e^- \to \tilde{e}_L\tilde{e}_L$, 500 GeV, -0.8, -0.6)	0.03
M_2	68.4	$m_{\chi_2^0}$	96.9
		$m_{\chi_1^\pm}$	2.1
		σ ($e^+e^- \to \tilde{\chi}_1^\pm\tilde{\chi}_1^\mp$, 500 GeV, 0.8, 0.6)	0.6
M_3	1.1	$m_{\tilde{g}}$	91.4
		$m_{\tilde{t}_R}$	6.0
		$m_{\tilde{b}_R}$	0.7

Table 5.34: The relative contribution of the three most important observables to the determination of the parameters $\tan\beta$, μ, M_1, M_2 and M_3 and the total $\Delta\chi^2_{\text{total}}$ obtained if the parameter is changed by $\pm 1\sigma$.

(at 2σ level), where $\Omega_{CDM} = \rho_{CDM}/\rho_c$ is the density of cold dark matter in the universe, scaled to the critical closure density ρ_c, and $h = 0.71^{+0.04}_{-0.03}$ is the scaled Hubble constant.

R-parity conserving supersymmetric models provide good candidates for CDM particles in the universe. In this section, we assume the lightest neutralino is the CDM particle. We work within the mSUGRA model, although our qualitative conclusions apply rather more broadly than this framework might suggest. Sparticle masses and mixings are determined within the mSUGRA model by specifying the parameter set

$$m_0,\ m_{1/2},\ A_0, \tan\beta \text{ and } sign(\mu). \tag{5.62}$$

We use the Isajet 7.69 program [505] for calculating sparticle masses and mixings.

The relic density of neutralinos can be calculated by solving the Boltzman equation for a Friedmann-Robertson-Walker universe. The IsaReD program determines the neutralino relic density via relativistic thermal averaging of all relevant neutralino annihilation and co-annihilation processes in the early universe [506]. We adopt the upper bound $\Omega_{CDM}h^2 < 0.129$ as a robust limit on neutralino dark matter; the lower limit from WMAP need not apply in the case of mixed dark matter scenarios. Several regions of mSUGRA parameter space have been found to be consistent with WMAP constraints.

- The bulk region at low m_0 and low $m_{1/2}$, where neutralino annihilation via t-channel slepton exchange is dominant.

- The stau co-annihilation region at low m_0 where $m_{\tilde{\tau}_1} \simeq m_{\tilde{\chi}_1^0}$.

- The hyperbolic branch/focus point region (HB/FP) at large m_0, where $|\mu|$ becomes small and the $\tilde{\chi}_1^0$ becomes partially higgsino-like.
- The A-annihilation funnel at large $\tan\beta$, where $2m_{\tilde{\chi}_1^0} \simeq m_A,\ m_H$, and neutralino annihilation takes place through the broad s-channel heavy higgs A and H resonances.

In addition, there is a narrow region at low $m_{1/2}$ where neutralino annihilation can occur through the light Higgs h resonance, and an additional stop-neutralino co-annihilation region exists for particular A_0 values.

The reach of the CERN LHC for SUSY in the mSUGRA model has been calculated in Ref. [507] assuming 100 fb^{-1} of integrated luminosity. Briefly, sparticle pair production events were generated for many mSUGRA model parameter choices in the $m_0\ vs.\ m_{1/2}$ plane for various $\tan\beta$ values. A fast LHC detector simulation (CMSJET) was used, and cuts were imposed to extract signal rates in a variety of multilepton plus multijet plus missing transverse energy channels. Backgrounds were also calculated from a variety of QCD and vector boson production processes. A large set of selection cuts were used to give some optimization over broad regions of parameter space. It was required to have at least a 5σ signal over background, with at least 10 signal events in the sample.

The reach of the CERN LHC is shown in Fig. 5.43 for the case of $\tan\beta = 10$, $\mu > 0$, $A_0 = 0$ and $m_t = 175$ GeV. The dark shaded (red) regions are disallowed by lack of radiative electroweak symmetry breaking (REWSB) (right hand side) or presence of a stau LSP (left hand side). The light gray (yellow) region is excluded by LEP2 chargino searches ($m_{\tilde{\chi}^+} > 103.5$ GeV), while the region below the yellow contour gives $m_h < 114.4$ GeV, in contradiction of LEP2 SM Higgs searches (here, the SUSY h Higgs boson is essentially SM-like). The medium gray (green) regions have $\Omega_{CDM}h^2 < 0.129$, and are *allowed* by WMAP. The broad HB/FP region is seen on the right-hand side, while the stau co-annihilation region is shown on the left-hand side. At the edge of the LEP2 excluded region is the light Higgs annihilation corridor. The reach of the Fermilab Tevatron via the trilepton channel is also shown [508], assuming a 5σ signal over background for 10 fb^{-1}. The reach of the CERN LHC for 100 fb^{-1} of integrated luminosity is shown by the contour labeled "LHC". It extends from $m_{1/2} \sim 1400$ GeV (corresponding to a value of $m_{\tilde{g}} \sim 3$ TeV) on the left-hand side, to $m_{1/2} \sim 700$ GeV (corresponding to $m_{\tilde{g}} \sim 1.8$ TeV) on the right-hand side. In particular, for this value of $\tan\beta$, the LHC reach covers the entire stau co-annihilation region, plus the low $m_{1/2}$ portion of the HB/FP region. The outer limit of the reach contour is mainly determined by events in the E_T^{miss}+ jets channel, which arises from gluino and squark pair production, followed by hadronic cascade decays.

We also show in the plot the reach of a $\sqrt{s} = 500$ and 1000 GeV LC, assuming 100 fb^{-1} of integrated luminosity [509]. Events were generated using Isajet 7.69, and compared against various SM backgrounds. The left-most portion of the reach contour arises where selectron and smuon pair production are visible, while the main portion (flat with $m_{1/2}$) arises due to chargino pair searches. An additional reach is gained between these two regions by searching for $e^+e^- \to \tilde{\chi}_2^0\tilde{\chi}_1^0$ production, followed by $\tilde{\chi}_2^0 \to \tilde{\chi}_1^0 b\overline{b}$ decay. In addition, in Ref. [510], additional reach can be gained by searching for stau pair events, although two photon backgrounds must be accounted for, due to the low energy release in the stau co-annihilation region.

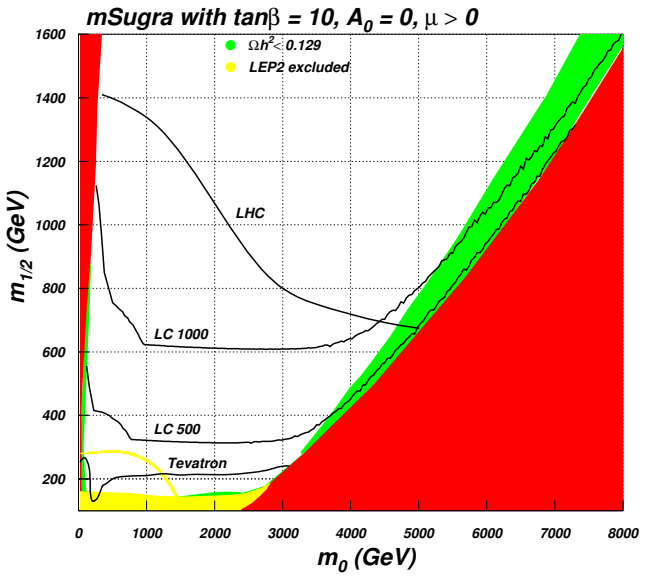

Figure 5.43: Parameter space of mSUGRA model for $\tan\beta = 10$, $A_0 = 0$ and $\mu > 0$, showing the reach of the Fermilab Tevatron, the CERN LHC and a 0.5 and 1 TeV linear e^+e^- collider for supersymmetry discovery.

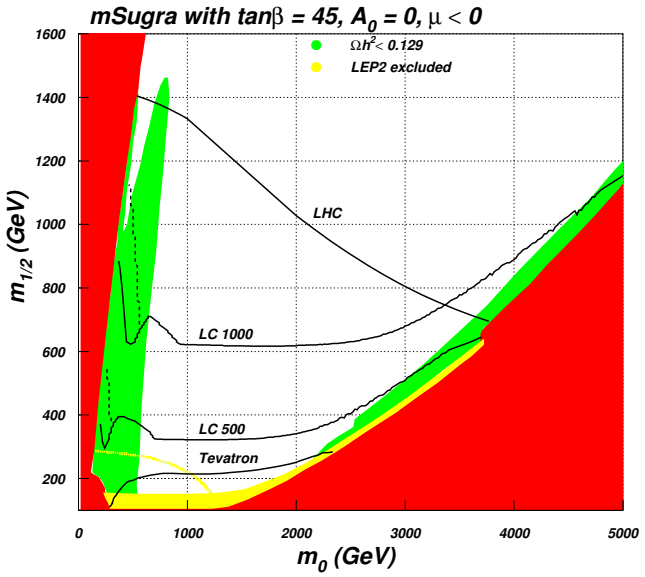

Figure 5.44: Parameter space of mSUGRA model for $\tan\beta = 45$, $A_0 = 0$ and $\mu < 0$, showing the reach of the Fermilab Tevatron, the CERN LHC and a 0.5 and 1 TeV linear e^+e^- collider for supersymmetry discovery.

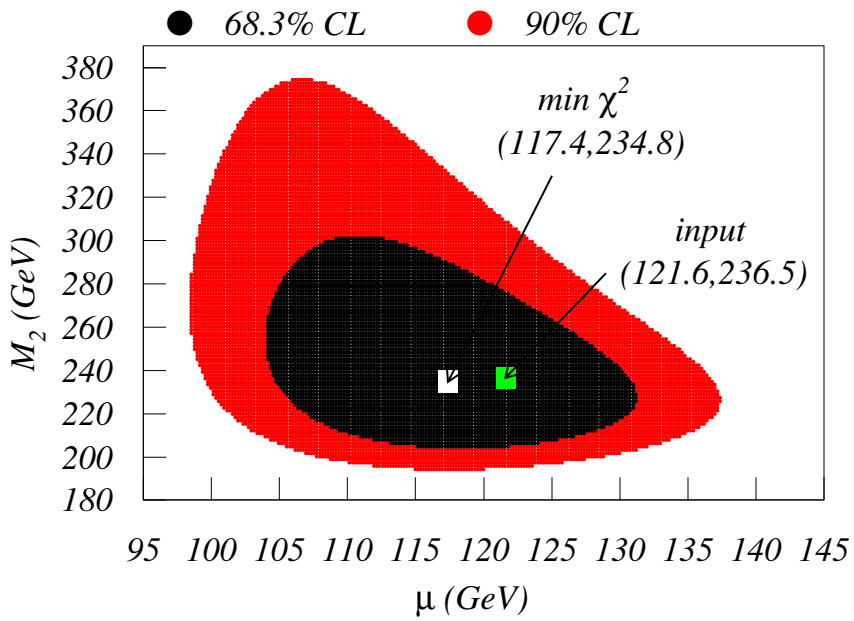

Figure 5.45: Determination of SUSY parameters from examining chargino pair production at a $\sqrt{s} = 0.5$ TeV LC, for the HB/FP mSUGRA point listed in the text.

While a 500 GeV LC can cover only a portion of the stau co-annihilation region, a 1 TeV LC can cover the entire region, at least for this value of $\tan\beta$. As one moves into the HB/FP region, the LC retains a significant reach for SUSY, which in fact extends *beyond* that of the CERN LHC! It is significant that this additional reach occurs in a DM allowed region of parameter space. In the HB/FP region, the superpotential μ parameter becomes small, and the lightest chargino and neutralino become increasingly light, with increased higgsino content. In fact, the decreasing mass gap between $\tilde{\chi}_1^+$ and $\tilde{\chi}_1^0$ makes chargino pair searches difficult at a LC using conventional cuts because there is so little visible energy release from the chargino decays. In Ref. [509,510], we advocated cuts that pick out low energy release signal events from SM background, and allow a LC reach for chargino pairs essentially up to the kinematic limit for their production. In this case, it is important to fully account for $\gamma\gamma \to f\overline{f}$ backgrounds, where f is a SM fermion.

In Fig. 5.44, we show a similar reach plot, but this time for $\tan\beta = 45$ and $\mu < 0$. In this case, the broad DM A-annihilation funnel has appeared on the left-hand side of parameter space. It can be seen that the LHC can cover most of the A annihilation funnel, although a somewhat higher integrated luminosity might be needed to cover it completely. Also, the stau co-annihilation region has increased to cover higher $m_{1/2}$ values, and now extends beyond the LC1000 reach. Still higher values of $\tan\beta$ push the allowed stau co-annihilation region somewhat beyond the reach of even the CERN LHC. Meanwhile, the HB/FP region is qualitatively insensitive to $\tan\beta$ values ranging from 10-50, and a 1 TeV LC can still probe much of this region, well beyond

what can be accessed at the LHC.

The study of Ref. [509] also examined a case study in the HB/FP region with parameters $m_0 = 2500$ GeV, $m_{1/2} = 300$ GeV, $A_0 = 0$, $\tan\beta = 30$, $\mu > 0$ and $m_t = 175$ GeV, *i.e.* in the HB/FP region. In this case, chargino pair events were selected from the 1ℓ+jets $+E_T^{miss}$ channel, and the dijet mass distribution was used to extract the value of $m_{\tilde{\chi}_1^+}$ and $m_{\tilde{\chi}_1^0}$ at the 10% level. The mass resolution is somewhat worse than previous case studies in the literature because the charginos undergo three-body rather than two-body decays, and no sharp edges in energy distributions are possible. Nonetheless, the measured value of chargino and neutralino mass, along with a measure of the total chargino pair cross section, was enough to determine the SUSY parameters M_2 and μ to 10-20% precision. The results, shown in Fig. 5.45, demonstrate that $\mu < M_2$, which points to a $\tilde{\chi}_1^+$ and $\tilde{\chi}_1^0$ which are higgsino/gaugino mixtures, as is characteristic of the HB/FP region.

In conclusion, we would like to stress that the CERN LHC and an e^+e^- LC are highly complementary to each other in exploring the dark matter allowed parameter space of the mSUGRA model. LHC covers the stau co-annihilation region (completely for $\tan\beta < 40$) as well as the $H,\ A$ funnel region (much of which is typically beyond the maximum reach of a LC). However only the lower part of the HB/FP region can be covered by the LHC. On the other hand, as we have demonstrated, LCs can probe much of the *upper* part of the HB/FP region with the new proposed cuts. Therefore, the combination of the LHC and a TeV scale LC can cover almost the entire parameter space of the mSUGRA scenario.

5.3.2 Impact of the LHC and LC on the accuracy of the predicted Dark Matter relic density

One of the attractive features of the minimal supersymmetric standard model (MSSM) is that it provides a natural candidate for cold dark matter, the neutralino, $\tilde{\chi}_1^0$. With cosmology entering the era of precision measurements and the next colliders aiming at discovering and constraining supersymmetry some crucial cross breeding is emerging. Already, assuming the standard cosmology, the measurement of the relic density of dark matter has been used to put strong constraints on the supersymmetric model [511]. For example, WMAP [20,21], which at 2σ constrains the relic density in the range $.094 < \Omega h^2 < .129$, effectively reduces the dimensionality of the MSSM parameter space by one. The accuracy of this constraint will increase with future data from the PLANCK satellite, which expects precision on Ωh^2 at the 2% level [512].

In this paper, we look at the problem from the inverse perspective and examine what is required from collider data in order to get a precise prediction for Ωh^2, which could then be used to test the cosmology. For this we assume that supersymmetric particles will be produced and measured at the LHC and the future linear collider (LC) and that enough information [513] will be present in order to discriminate between various models of supersymmetry breaking. When we have identified a successful model of SUSY breaking, an accurate prediction of Ωh^2 will allow us to test the cosmological assumptions that go into its prediction.

In order to predict Ωh^2 in the MSSM one generally needs to know all the underlying parameters of the model, since that determines the available annihilation channels for

neutralinos in the early universe. In the context of mSUGRA however, the scenarios allowed by WMAP are rather fine-tuned and one can concentrate only on a handful of relevant observables. The point is that in mSUGRA the neutralino LSP happens to be, for practically all cases, an almost pure bino. This bino annihilates mainly into leptons through the right-handed sleptons but this mechanism is not efficient enough to satisfy the newest WMAP data. Then only three acceptable scenarios remain: coannihilation, rapid annihilation through Higgs exchange or a Higgsino LSP. Our study will cover these three rather constrained regions in the mSUGRA parameter space.

We will investigate the accuracy required on a few of the most relevant collider observables in order to control the uncertainty on the predicted Ωh^2. These observables could be either physical masses or Lagrangian parameters such as the chargino mixing parameter μ or $\tan\beta$. We will refer throughout to two benchmarks on accuracy: those that produce a 10% change in Ωh^2 ("WMAP accuracy") and those which change Ωh^2 by 2% ("PLANCK accuracy"). We only quote precisions on input parameters obtained by varying only one parameter at a time.

Although we mention some results obtained with the mSUGRA scenario, we concentrate mainly on what we call the perturbed mSUGRA scenario (PmSUGRA). In this scenario we pick a parameter point in mSUGRA derived from the high-scale parameters $m_0, M_{1/2}, A_0$ then we examine the impact on Ωh^2 of a parameter change while *assuming the more general MSSM only*. In practice we use an iterative procedure to determine the fractional change $a = |\Delta p/p|$ in an input parameter p that will result in a fractional change $r = \Delta\Omega/\Omega = 10\%$ for WMAP accuracy. An estimate of the PLANCK accuracy can be obtained by dividing that of WMAP by a factor of 5, for the interesting range of accuracies not exceeding 50%, say. Here we do not address the feasibility of any measurements, but rather only identify which measurements are needed and with what precision. Preliminary investigations into the effects of uncertainties in the predictions of the sparticle mass spectrum on Ωh^2 were presented in Refs. [514] and more details can be found in Ref. [515]. The relic density is computed with `micrOMEGAs1.3` [516] with the supersymmetric spectrum provided by `SOFTSUSY1.8.7` [499] and the interface between the two by the *SUSY Les Houches Accord* [492].

5.3.2.1 Coannihilation

In mSUGRA at small M_0 there exists a region with almost degenerate $\tilde{\tau}_1 - \tilde{\chi}_1^0$. In this region the LSP is almost purely bino. The contribution of coannihilation channels is essential in bringing the relic density in the desired range. In computing the effective annihilation cross section, coannihilation processes are suppressed by a Boltzmann factor $\propto exp^{-\Delta M/T_f}$ where ΔM is the mass difference between the NLSP and the LSP and T_f the decoupling temperature. One expects Ωh^2 to be very sensitive to this mass difference. Following Ref. [517], we take a slope "S1" in parameter space with $\mu > 0, \tan\beta = 10$, $A_0 = 0$ and

$$M_0 = 5.84615 + 0.1764 * M_{1/2} + 1.9780 \times 10^{-5} * M_{1/2}^2 \tag{5.63}$$

Here masses are given in GeV units. Along this slope the relic density is in rough agreement with the WMAP range ($M_{1/2} = 350 - 950$ GeV). The coannihilation processes involving $\tilde{\chi}_1^0 - \tilde{\tau}_1$ dominate at low masses when $\Delta M \approx 10$ GeV. As one increases

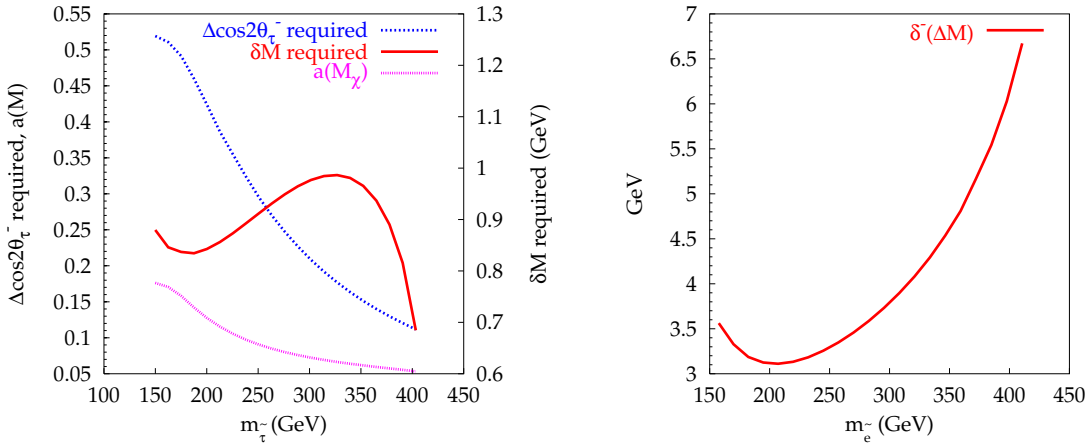

Figure 5.46: *(a) Required accuracy on the $\tilde{\tau}_1$-$\tilde{\chi}_1^0$ mass difference, $\cos 2\theta_\tau$ and $m_{\tilde{\chi}_1^0}$ in order to achieve WMAP precision. The latter is performed by keeping ΔM constant. (b) Required accuracy on $\Delta M = m_{\tilde{e}_R} - m_{\tilde{\chi}_1^0}$ assuming $m_{\tilde{e}_R} = m_{\tilde{\mu}_R}$. The abscissa range corresponds to $M_{1/2} = 350 - 950$ GeV.*

the LSP mass ΔM decreases to 300MeV, $\tilde{\tau}_1\tilde{\tau}_1$ channels as well as coannihilation with selectrons and smuons become important. In fact the latter contribute up to 40% of the effective annihilation cross section toward the upper end of the slope.

The physical parameters that need to be measured precisely then are those entering the dominant channels. The most relevant physical parameters include the masses of all the light sleptons, in particular the $\tilde{\tau}_1$, the mass of the neutralino LSP and the mixing in the $\tilde{\tau}_1$ sector. The latter enters the $\tilde{\tau}_1$ coupling to gauge bosons or to neutralinos. In addition one needs also the couplings of the LSP. These involve the mixing matrix of neutralinos. To estimate the sensitivity of Ωh^2 on a given parameter we keep all others fixed. For example, for the mass difference we have, for each point on the slope, varied the mass of the $\tilde{\tau}_1$ while keeping all other parameters fixed. Fig. 5.46 shows that the mass difference must be measured within slightly less than 1 GeV. This dependence can directly be related to the fact that the coannihilation channels crucially depend on the Boltzmann factor. The mixing angle $\cos 2\theta_\tau$ must be measured within 0.55 for light staus to about 0.1 for heavy staus when its value is almost 1. Finally we also compute the accuracy on the overall scale, defined as the accuracy required on $m_{\tilde{\chi}_1^0}$ once we keep ΔM constant. To determine the accuracy we have varied the parameter M_1 leaving all other parameters of the neutralino sector constant and have changed all slepton masses by the same amount that $m_{\tilde{\chi}_1^0}$ was shifted. We find that the required accuracy ranges from 15% for low masses to 5% for $m_{\tilde{\chi}_1^0} \approx 400GeV$. Although the overall scale is an important parameter, the precision required is not nearly as important as for the mass difference. Finally, the selectron and smuon masses need to be measured to 1.5% to achieve WMAP precision, see Fig.5.46b. This is obtained by varying the $m_{\tilde{e}_R} = m_{\tilde{\mu}_R}$ by the same amount while keeping all other parameters fixed. We have also checked that the relic density is not very sensitive to $\tan\beta$ and μ once we assume constant ΔM.

These results indicate that once the LHC has established compatibility with the coannihilation scenario one will need a linear collider to measure precisely both the

mass of the LSP as well as ΔM. Recent simulations of the coannihilation region indicate that the relevant parameters can be measured with the required accuracy to meet WMAP (and maybe even PLANCK) precision if one is in the region with large enough ΔM [518]. Note that this is the region relevant for LC500 . For increasingly smaller ΔM associated with higher masses the situation is more problematic. On the other hand if one assumes mSUGRA, that is that combined fits from the LHC data agree with the mSUGRA predictions, then $m_0, M_{1/2}$ and A_0 can be constrained from observables involving other particles than just those relevant for the co-annihilation region. If the theoretical predictions are all under control, this means that we could predict the relic density without having accurate information on the stau mass or on ΔM. However the precision required on m_0 and $M_{1/2}$ to match WMAP accuracy ranges from around $1-3\%$. It remains to be seen whether such an accuracy can be reached considering that from previous analyses mostly done in the bulk (low $M_0 - M_{1/2}$) region, the precision ranged from 1% to 10% depending on the point in parameter space [89].

5.3.2.2 Higgs funnel

Rapid and efficient annihilation can occur through the Higgs resonance, this is the funnel region. In fact because of the Majorana nature of the neutralino the resonant enhancement proceeds through a pseudoscalar Higgs boson. In this situation $A \to b\overline{b}$ is by far dominant at high $\tan\beta$, with some contribution from $\tau\tau$. In our discussion of the Higgs funnel we will take $\tan\beta = 50, A_0 = 0, \mu > 0$. We parameterise the funnel region through the slope S2, defined as a cubic:

$$m_0 = 814.88 - 2.20022 M_{1/2} + 3.30904 \times 10^{-3} M_{1/2}^2 - 1.05066 \times 10^{-6} M_{1/2}^3 \qquad (5.64)$$

where masses are in units of GeV. The important physical parameters are $M_A, \Gamma_A, m_{\tilde{\chi}_1^0}$ as well as the parameters that enter the vertices $Ab\overline{b}$ as well as $\tilde{\chi}_1^0\tilde{\chi}_1^0 A$. The latter is controlled by μ which for all purposes can be equated with $m_{\tilde{\chi}_3^0}$.

Fig. 5.47 shows that both the neutralino mass and the pseudoscalar mass must be measured very accurately, from $2-0.2\%$ depending upon the position on the slope. More precision is needed for the heavy spectrum. To compute the accuracy on the parameter $m_{\tilde{\chi}_1^0}$, we in fact vary the parameter M_1. These accuracies on the masses can also be expressed as an accuracy on the resonant parameter, $2m_{\tilde{\chi}_1^0} - M_A$ which is around 5%. To compute the accuracy on the parameter μ, we simply change the value of μ at the Lagrangian level given at the weak scale. This will directly change the LSP coupling to the pseudoscalar Higgs, the resulting change in the value of the LSP mass will be very small. We see in Fig. 5.47 that one needs an accuracy of about 5% on μ for a 10% WMAP precision which corresponds to the fact that $\Omega h^2 \propto \mu^2$. The accuracy on the total width is also around 10%. It is important to note that once we fix the following parameters from experiment, $M_A, \Gamma_A, m_{\tilde{\chi}_1^0}, \mu(m_{\tilde{\chi}_3^0})$, the $\tan\beta$ dependence is very mild.

An important remark is that the funnel region features a rather heavy spectrum, see Fig. 5.47b. In the lower part of the slope the pseudoscalar can be produced at a 500GeV machine. In this region, the LHC can also measure to the needed accuracy the mass of the pseudoscalar if the $A \to \mu^+\mu^-$ channel [89] can be used. At a linear collider, the most accessible process is the associated production of $\tilde{\chi}_2^0$, which could

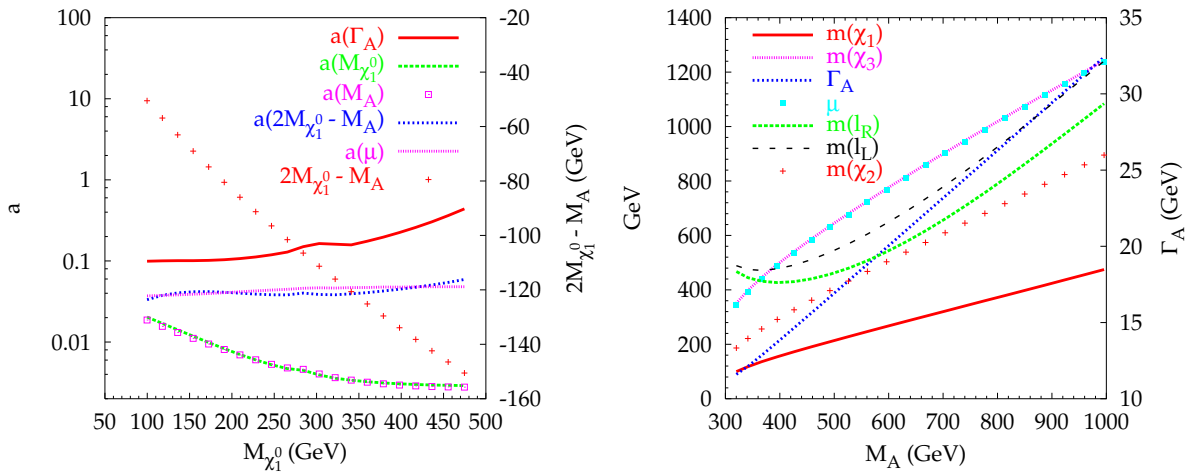

Figure 5.47: *(a) Mass spectrum of the relevant particles in the funnel region. (b) Accuracies a required to achieve WMAP precision along slope S2 in the PmSUGRA scenario. The scale for the quantity $2m_{\tilde{\chi}_1^0} - M_A$ is displayed on the right hand axis. The range of the abscissa corresponds to $M_{1/2} = 250 - 1100$ GeV.*

serve as a good measurement of $m_{\tilde{\chi}_1^0}$. The $\gamma\gamma$ option of a LC could bring important constraint upon the mass and couplings of the A as well as its width. Combined with a determination of μ from the LHC, through $m_{\tilde{\chi}_3^0}$ one could reconstruct the parameter space that defines the funnel region.

5.3.2.3 Focus point

The focus point region corresponds to high values of M_0, near the boundary of viable electroweak symmetry breaking and where the value of μ drops rapidly. The LSP has a significant Higgsino fraction which means enhanced couplings to the Z and the Higgses. Annihiliation into fermion or gauge boson pairs dominate. Although coannihilation with heavier neutralinos/charginos can occur these coannihilations should not be too efficient otherwise the relic density is less than what is measured by WMAP. We will take $\tan\beta = 50, \mu > 0, A_0 = 0$ and define a slope S3 where the relic density is compatible with WMAP:

$$m_0 = 3019.85 + 2.6928 M_{1/2} - 1.01648 \times 10^{-4} \left(M_{1/2}\right)^2 . \tag{5.65}$$

with $M_{1/2}$ in the range $440 - 1100$GeV. Along this slope, we have $M_1 < \mu < M_2$ and the Higgsino component of the LSP is about 25%. The relevant parameters for computing the relic density are the weak scale values of the neutralino mass matrix, in particular M_1 and μ since thes determines the Higgsino component. $\tan\beta$ enters in the contribution of the $b\bar{b}$ annihilation and in the neutralino couplings. Some dependence on M_2 and M_A is also expected.

Fig. 5.48 displays the required accuracies a for several parameters to match the WMAP accuracy. The sensitivities of μ, M_1 require fractional precisions of 1%. This rather demanding accuracy originates more from the couplings of the neutralinos to

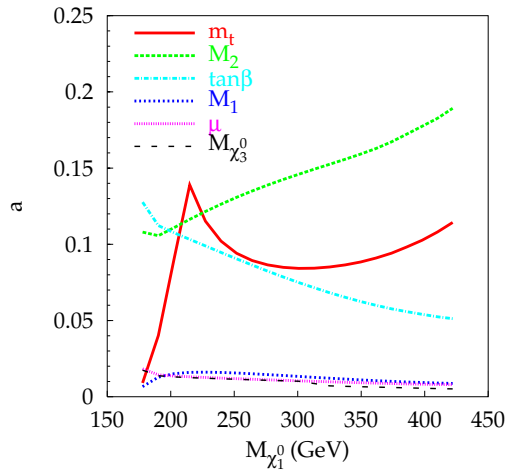

Figure 5.48: *Required fractional accuracy upon MSSM parameters in the PmSUGRA scenario along slope S3. The abscissas correspond to* $M_{1/2} = 440 - 1000$ *GeV.*

the Golsdtone and the A boson than from the neutralino mass dependence. As we show in Fig. 5.48 the accuracies on M_1 and μ can be converted into accuracies on $m_{\tilde{\chi}_1^0}$ and $m_{\tilde{\chi}_3^0}$. The needed accuracy on M_2 is an order of magnitude worse, though still relevant. Therefore we see that if one can reconstruct the neutralino mass matrix this scenario can be very much constrained. More problematic though is the needed accuracy on $\tan\beta$ which ranges from $5 - 10\%$. We also show in Fig. 5.48 the accuracy needed on m_t, which at the 10% level is very mild. A stronger dependence is found only near the top threshold. This is a major improvement over the mSUGRA case where to achieve WMAP precision requires knowing m_t to 20 MeV. The expected precision on m_t at a linear collider when combining theoretical and experimental uncertainties is only 100MeV, thus preventing a precise prediction of Ωh^2 in this scenario. Finally we do not need to know M_A very accurately, the accuracy needed varies from more than 100 may not be accessible at LHC, it would not be possible to get even a rough estimate of M_A.

This scenario is rather difficult to handle at the LHC because the sfermions and the pseudoscalar are too heavy to be accessible. Furthermore the charginos and neutralinos cannot be measured easily. On the other hand, a LC has the possibility to measure precisely the neutralino mass matrix provided there is enough energy to produce the neutralinos [519]. However a realistic study of the achievable accuracy in this scenario at a linear collider still needs to be performed as well as a study on how to benefit from a combination of LHC and LC data. In particular the value of $\tan\beta$ might be very difficult to pin down, although some information could be extracted from the light Higgs mass.

5.3.2.4 Conclusion

The relic density calculation often involves a large number of processes. The precise knowledge of the cross-sections necessary to make an accurate prediction of the relic density of dark matter rests on a precise knowledge of the physical parameters of the

MSSM. Nevertheless we have shown that within the scenarios that are favoured by WMAP, only a few parameters are needed to be measured with very high precision. Furthermore, using the collider data rather than relying on some theoretical prejudice, considerably improves the precision of the prediction of Ωh^2. Nevertheless the precision required from colliders to match the WMAP accuracy is rather demanding. The LHC will be able to determine roughly which scenario one is in as well as provide measurements of heavier particles (pseudoscalar, heavy neutralinos) that can be essential for an accurate prediction of the relic density, for example in the Higgs funnel or the focus point regions. However to make a prediction of Ωh^2 that matches the WMAP accuracy, or even more so the PLANCK accuracy, one absolutely needs the high precision achievable at a linear collider.

5.4 Further SUSY scenarios

5.4.1 Non-decoupling effect in sfermion-chargino/neutralino couplings

5.4.1.1 Introduction

The main aim of a high energy e^+e^- Linear Collider (LC) is to perform very high precision measurements of the elementary particles properties at a level better than 1%, in order to discriminate different models of particle interactions. In order to be able to compare these measurements with the underlying theory at this high level of accuracy, it is not sufficient to relate the different observables using lowest order in perturbation theory: the computation of radiative corrections (strong and electroweak) form a necessary ingredient of this program.

In this note we concentrate on the properties of supersymmetric (SUSY) particles [422–425]. It is known that the radiative corrections to some SUSY observables develop radiative corrections which do not decouple if one takes some of the SUSY masses to be large [426–433]. Furthermore, the observables which exhibit this non-decoupling behaviour are the ones that probe the SUSY nature of the particles under study. Therefore the following situation could happen: some new physics is observed at the LHC and LC, which is roughly consistent with the predictions from SUSY models, however at the LC only *some* of the new particles are visible, but, in order to predict their production cross-sections and branching ratios at a sufficient level of accuracy the properties of the heavy SUSY particles (visible at the LHC) are needed. This situation is, in fact, natural in SUSY models, where the strongly interacting SUSY particles usually are predicted to be much heavier than the weakly interacting ones (see e.g. [14]). In this note we want to address this issue, asking ourselves: how large could be the effects of the heavy particles; how much accuracy on their masses is needed in order to make sufficiently precise predictions for the light ones; and whether there is some way of avoiding the uncertainty introduced by the heavy particles.

For the sake of simplicity we will work in the following scenario: scalar-quarks (squarks) and the gluino are heavy, and beyond the reach of the LC, whereas scalar-leptons (sleptons) and some charginos/neutralinos are light, and can be studied at the LC. Then, we study the radiative effects of squarks in chargino/neutralino-lepton-

slepton interactions, computing the value of the radiative corrections induced by quarks/squarks, and comparing them with the corrections from other sectors of the model. We will analyze these effects in the partial decay widths of selectrons and the electron-sneutrino into charginos and neutralinos.

5.4.1.2 Theoretical introduction: non-decoupling effects and effective coupling matrices

We concentrate in the analysis of the sfermion decays as discussed thoroughly in Refs. [426, 427, 434, 435][5]. In the radiative corrections of the partial decay widths

$$\Gamma(\tilde{f} \to f' \chi) \ , \tag{5.66}$$

$\tilde{f}$ being a sfermion, f' a Standard Model (SM) fermion, and χ a chargino or neutralino, non-decoupling effects appear, and the radiative corrections grow as the logarithm of the largest SUSY mass of the model [426, 427]. These non-decoupling effects reflect the fact that SUSY is (softly) broken, and the Yukawa couplings of the charginos/neutralinos are no longer equal to the gauge bosons and Higgs bosons couplings beyond leading order.

A part of these corrections can be encoded in a set of counterterm expressions which appear in all observables. Concretely they can be written as a shift to the U, V and N matrices that diagonalize the chargino and neutralino mass matrices[6]:

$$\tilde{U} = U + \Delta U \ , \ \tilde{V} = V + \Delta V \ , \ \tilde{N} = N + \Delta N \ , \tag{5.67}$$

where ΔU, ΔV, and ΔN are a certain combination of counterterms, which can be computed using self-energies of gauge bosons, Higgs bosons, charginos and neutralinos.

Unfortunately the full contributions to the expressions (5.67) are divergent. The only consistent subset of corrections which makes all the expressions in (5.67) finite is the subset of fermion and sfermion loops contributing to the self-energies of the gauge bosons, Higgs bosons, charginos and neutralinos. With this restriction, we can define *effective coupling matrices*

$$U^{eff} = U + \Delta U^{(f)} \ , \ V^{eff} = V + \Delta V^{(f)} \ , \ N^{eff} = N + \Delta N^{(f)} \ , \tag{5.68}$$

where $\Delta U^{(f)}$, $\Delta V^{(f)}$, $\Delta N^{(f)}$ are given by the expressions (5.67) taking into account only loops of fermions and sfermions. We will refer to these corrections as *universal corrections*. They are the equivalent of the *super-oblique corrections* of Ref. [432].

As an example, we have computed analytically the electron-selectron contributions to the ΔU and ΔV matrices (5.67), assuming zero mixing angle in the selectron sector ($\theta_e = 0$), we have identified the leading terms in the approximation $m_{\tilde{e}_i}, m_{\tilde{\nu}} \gg (M_W, M_i) \gg m_e$, and analytically canceled the divergences and the renormalization scale dependent terms; finally, we have kept only the terms logarithmic in the slepton masses. The result reads as follows:

$$\Delta U^{(e)}_{i1} = \frac{\alpha}{4\,\pi\,s_W^2} \log\left(\frac{M^2_{\tilde{e}_L}}{M_X^2}\right) \left[\frac{U^3_{i1}}{6} - U_{i2} \frac{\sqrt{2}\,M_W\,(M\,c_\beta + \mu\,s_\beta)}{3\,(M^2-\mu^2)\,(M_1^2-M_2^2)^2} \left(M^4 - M^2\,\mu^2 + \right.\right.$$

[5] The corresponding FORTRAN codes are available from [436]

[6] In this note we follow the notation and conventions of Ref. [426]. Note, in particular, that $m_{\tilde{f}_1} > m_{\tilde{f}_2}$.

$$
\begin{aligned}
& +3\,M^2\,M_W^2+\mu^2\,M_W^2+M_W^4+M_W^4\,c_{4\beta}+(\mu^2-M^2)\,M_i^2+4\,M\,\mu\,M_W^2\,s_{2\beta}\big)\Big]\,,\\
\Delta U_{i2}^{(e)} &= \frac{\alpha}{4\,\pi\,s_W^2}\log\left(\frac{M_{\tilde{e}_L}^2}{M_X^2}\right)U_{i1}\,\frac{M_W\,(M\,c_\beta+\mu\,s_\beta)}{3\,\sqrt{2}\,(M^2-\mu^2)\,\left(M_1^2-M_2^2\right)^2}\times\\
&\times\ \big((M^2-\mu^2)^2+4\,M^2\,M_W^2+4\,\mu^2\,M_W^2+2\,M_W^4+2\,M_W^4\,c_{4\beta}+8\,M\,\mu\,M_W^2\,s_{2\beta}\big)\,,\\
\Delta V_{i1}^{(e)} &= \frac{\alpha}{4\,\pi\,s_W^2}\log\left(\frac{M_{\tilde{e}_L}^2}{M_X^2}\right)\left[\frac{V_{i1}^3}{6}-V_{i2}\frac{\sqrt{2}\,M_W\,(\mu\,c_\beta+M\,s_\beta)}{3\,(M^2-\mu^2)\,\left(M_1^2-M_2^2\right)^2}\left(M^4-M^2\,\mu^2+\right.\right.\\
& \left.\left.+3\,M^2\,M_W^2+\mu^2\,M_W^2+M_W^4+M_W^4\,c_{4\beta}+(\mu^2-M^2)\,M_i^2+4\,M\,\mu\,M_W^2\,s_{2\beta}\right)\right]\,,\\
\Delta V_{i2}^{(e)} &= \frac{\alpha}{4\,\pi\,s_W^2}\log\left(\frac{M_{\tilde{e}_L}^2}{M_X^2}\right)V_{i1}\,\frac{M_W\,(\mu\,c_\beta+M\,s_\beta)}{3\,\sqrt{2}\,(M^2-\mu^2)\,\left(M_1^2-M_2^2\right)^2}\times\\
&\times\ \big((M^2-\mu^2)^2+4\,M^2\,M_W^2+4\,\mu^2\,M_W^2+2\,M_W^4+2\,M_W^4\,c_{4\beta}+8\,M\,\mu\,M_W^2\,s_{2\beta}\big)\,,
\end{aligned}
\tag{5.69}
$$

$M_{\tilde{e}_L}^2$ being the soft-SUSY-breaking mass of the $(\tilde{e}_L,\tilde{\nu})$ doublet, whereas M_X is a SM mass.

In this way the effects of the (heavy) squarks can be encoded in the definition of *effective couplings* in the lepton-slepton-chargino/neutralino interactions.

In the following we will separate three kind of corrections: the universal corrections induced by the quark-squark particles $U^{eff(q)}$, $V^{eff(q)}$, $N^{eff(q)}$; the universal contributions induced by leptons-sleptons $U^{eff(l)}$, $V^{eff(l)}$, $N^{eff(l)}$, and the non-universal contributions.

5.4.1.3 Numerical Analysis

For the numerical analysis we choose some default *typical* set of input parameters. We will concentrate in the parameter set given by point 1a of the *Snowmass Points and Slopes* (SPS) [14][7]. For completeness we give here the soft-SUSY-breaking parameters:

$$
\begin{aligned}
&\tan\beta=10, M_{A^0}=393.6\,\text{GeV}, \mu=352.4\,\text{GeV}, M=192.7\,\text{GeV}, M'=99.1\,\text{GeV}\ ,\\
&M_{\{\tilde{d},\tilde{s}\}_L}=539.9\,\text{GeV}, M_{\tilde{b}_L}=495.9\,\text{GeV}, M_{\{\tilde{d},\tilde{s}\}_R}=519.5\,\text{GeV}, M_{\tilde{b}_R}=516.9\,\text{GeV},\\
&A_{\{d,s\}}=3524\,\text{GeV}, A_b=-772.7\,\text{GeV},\\
&M_{\{\tilde{u},\tilde{c}\}_R}=521.7\,\text{GeV}, M_{\tilde{t}_R}=424.8\,\text{GeV}, A_{u,c}=35.24\,\text{GeV}, A_t=-510\,\text{GeV},\\
&M_{\{\tilde{e},\tilde{\mu}\}_L}=196.6\,\text{GeV}, M_{\tilde{\tau}_L}=195.8\,\text{GeV}, M_{\{\tilde{e},\tilde{\mu}\}_R}=136.2\,\text{GeV}, M_{\tilde{\tau}_R}=133.6\,\text{GeV},\\
&A_{e,\mu}=3524\,\text{GeV}, A_\tau=-254.2\,\text{GeV},
\end{aligned}
\tag{5.70}
$$

where the soft-SUSY-breaking trilinear couplings of the first and second generation sfermions have been chosen such that the non-diagonal elements of the sfermion mass matrix are zero.

However, a note of caution should be given, our computation is performed in the On-shell renormalization scheme, whereas the SPS parameters are given in the $\overline{DR}$ renormalization scheme, and one should make a scheme conversion of the parameters, this conversion is beyond the scope of the present work. In this note we are interested only in establishing whether the effects of heavy particles are important,

[7] The spectrum and tree-level branching ratios for the several SPSs can be found e.g. in Ref. [369].

	Γ^{tree} [GeV]	$\delta\Gamma^{(q)}/\Gamma$	$\delta\Gamma^{(l)}/\Gamma$	$\delta\Gamma^{no-uni}/\Gamma$	$\delta\Gamma/\Gamma$
$\tilde{e}_1 \to e^-\chi_1^0$	0.110	0.043	0.032	-0.002	0.073
$\tilde{e}_1 \to e^-\chi_2^0$	0.047	0.030	0.034	-0.012	0.051
$\tilde{e}_1 \to \nu_e\chi_1^-$	0.081	0.026	0.033	0.006	0.065
$\tilde{e}_2 \to e^-\chi_1^0$	0.194	0.052	0.034	0.000	0.086
$\tilde{\nu}_e \to \nu_e\chi_1^0$	0.140	0.059	0.035	-0.005	0.089
$\tilde{\nu}_e \to \nu_e\chi_2^0$	0.006	0.018	0.033	-0.014	0.036
$\tilde{\nu}_e \to e^-\chi_1^+$	0.016	0.024	0.033	0.002	0.059

Table 5.35: Tree-level partial decay widths and relative corrections for the selectron and sneutrino decays into charginos and neutralinos for SPS 1a.

and therefore we are only interested in obtaining a suitable SUSY spectrum, therefore we treat the given numerical parameters of SPS 1a as On-shell SUSY parameters [8].

In Table 5.35 we show the partial decay widths of selectrons into charginos/neutralinos for SPS 1a. We show: the tree-level partial widths Γ^{tree}; the relative corrections induced by quarks-squarks $\delta\Gamma^{(q)}/\Gamma$; the relative corrections induced by the lepton-slepton universal contributions (5.68) $\delta\Gamma^{(l)}/\Gamma$; the process-dependent non-universal contributions $\delta\Gamma^{no-uni}/\Gamma$; and the total corrections $\delta\Gamma/\Gamma$.

The universal corrections $\delta\Gamma^{(q)}/\Gamma$ and $\delta\Gamma^{(l)}/\Gamma$ in Table 5.35 represent a correction that will be present whenever a fermion-sfermion-chargino/neutralino coupling enters a given observable. The correction $\delta\Gamma^{no-uni}/\Gamma$ represents the process-dependent part. For the presented observables the non-universal corrections turn out to be quite small, but this is not necessarily always the case. From the values of Table 5.35 it is clear that the corrections of the quark-squark sector are as large as the corrections from the (light) lepton-slepton sector, for the presented observables they amount to a $2-6\%$ relative correction, depending on the particular decay channel.

For SPS 1a the squark mass scale is around 500 GeV, however the corrections grow logarithmically with the squark mass scale. In Fig. 5.49 we show the relative corrections induced by the quark-squark sector ($\delta\Gamma^{(q)}/\Gamma$) in the observables of Table 5.35 as a function of a common value for all soft-SUSY-breaking squark mass parameters in (5.70), in a range where the squarks are accessible at the LHC. The several lines in Fig. 5.49 are neatly grouped together: the upper lines correspond to the lightest neutralino (χ_1^0) which is *bino*-like, whereas the lower lines correspond to the second neutralino and lightest chargino (χ_2^0, $\chi_1^\pm$), which are *wino*-like. Since the coefficient of the logarithm in the universal corrections (5.68) is proportional to the corresponding gauge coupling, the behaviour of the corrections is different between the two kinds of gauginos, but similar for different gauginos of the same kind. We see that for a *bino*-like neutralino the corrections undergo an absolute shift of less than 2% (from 4.5% to 6.5% in the channel $\tilde{e}_1 \to e^-\chi_1^0$) by changing the squark mass scale from 500 GeV to 3 TeV. For a *wino*-like gaugino the shift is much larger, being up to 4% in the case under study (from 2% to 6% in the $\tilde{\nu}_e \to \nu_e\chi_2^0$ channel). We conclude, therefore, that a certain knowledge of the squark masses is necessary in order to provide a theoretical

[8] Of course, once we will be analyzing the real LC data, the $\overline{DR}$-On-shell conversion will need to be made in order to extract the fundamental soft-SUSY-breaking parameters.

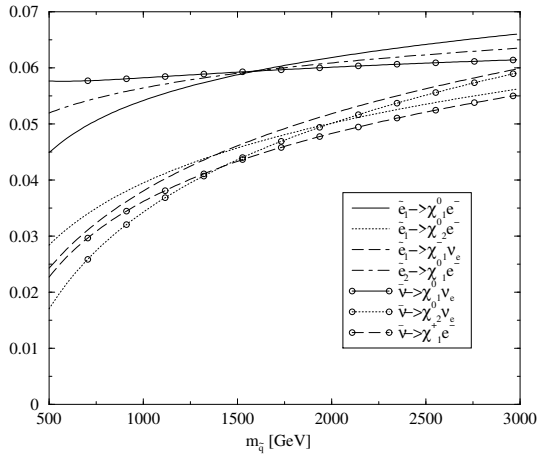

Figure 5.49: Squark contributions to the radiative corrections of the partial decay widths of sleptons ($\delta\Gamma^{(q)}/\Gamma$) for SPS 1a as a function of a common soft-SUSY-breaking mass parameter for all squarks.

prediction with an uncertainty below 1%, but only a rough knowledge of the scale is necessary.

As explained previously these corrections admit a description in terms of effective coupling matrices. In Fig. 5.50 we show the relative finite shifts induced by the quark-squark sector in the effective coupling matrices as a function of a common soft-SUSY-breaking squark mass parameter. The tree-level values for the mixing matrices are:

$$U = \begin{pmatrix} 0.91 & 0.41 \\ -0.41 & 0.91 \end{pmatrix}, \quad V = \begin{pmatrix} 0.97 & 0.24 \\ -0.24 & 0.97 \end{pmatrix}, \quad N = \begin{pmatrix} -0.99 & -0.10 & -0.06i & 0.11 \\ 0.06 & -0.94 & 0.09i & -0.32 \\ -0.15 & 0.28 & 0.69i & -0.64 \\ 0.05 & -0.16 & 0.71i & 0.68 \end{pmatrix}. \tag{5.71}$$

One can perform a one-to-one matching of Fig. 5.50 with Fig. 5.49. By neglecting the small electron-higgsino couplings we obtain:

$$\begin{aligned} \delta\Gamma^{(q)}(\tilde{e}_L \to e^-\chi^0_\alpha)/\Gamma &= 2\tfrac{\Delta N^{(q)}_{\alpha 2} - Y_L t_w \Delta N^{(q)}_{\alpha 1}}{N_{\alpha 2} - Y_L t_w N_{\alpha 1}}, \quad & \delta\Gamma^{(q)}(\tilde{\nu}_e \to e^-\chi^+_1)/\Gamma &= 2\Delta V^{(q)}_{11}/V_{11}, \\ \delta\Gamma^{(q)}(\tilde{e}_L \to \nu_e\chi^-_1)/\Gamma &= 2\Delta U^{(q)}_{11}/U_{11}, & \delta\Gamma^{(q)}(\tilde{\nu}_e \to \nu_e\chi^0_\alpha)/\Gamma &= 2\tfrac{\Delta N^{(q)}_{\alpha 2} + Y_L t_w \Delta N^{(q)}_{\alpha 1}}{N_{\alpha 2} + Y_L t_w N_{\alpha 1}}; \\ \delta\Gamma^{(q)}(\tilde{e}_R \to e^-\chi^0_\alpha)/\Gamma &= 2\Delta N^{(q)}_{\alpha 1}/N_{\alpha 1}, & & \end{aligned}$$

and $\tilde{e}_{\{L,R\}} = \tilde{e}_{\{1,2\}}$ for the case (5.70) under study. We see in Fig. 5.50 variations up to 5% in the coupling matrices, which would translate to variations up to 10% in the observables.

We are also interested in the variation with the soft-SUSY-breaking squark trilinear coupling A_q. For the first and second generation squarks the variation is negligible. The corrections show some variation with A_b, but it is well below the 1% level. In Fig. 5.51 we show the variation of the chargino effective couplings with A_t. In this figure we have chosen a squark mass scale of 1 TeV. Since A_t enters the computation of the physical top-squark masses, choosing a *light* squark mass scale ($\sim 500\,\text{GeV}$) would produce light physical top-squark masses ($\sim 100\,\text{GeV}$) for certain values of A_t. In that case one would find large variations in the corrections which are due to the presence of light top-squark particles, and not to the trilinear coupling *per se*.

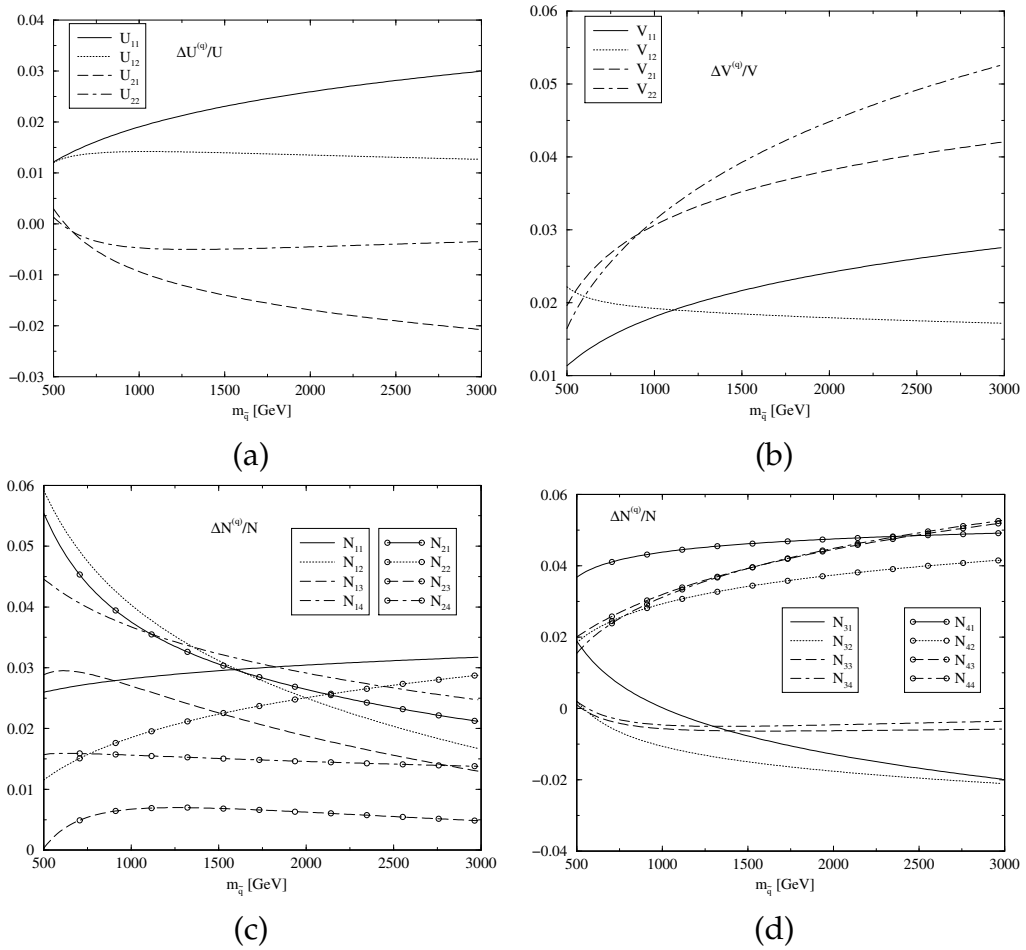

Figure 5.50: Quark-squark contributions to the effective chargino/neutralino mixing coupling matrices (5.68) as a function of a common squark mass parameter for SPS 1a.

Furthermore, these light top-squark particles could be produced at the LC, and their properties precisely measured. In this figure we see large variations of the corrections (up to 4%), mainly in the *higgsino* components of the charginos (U_{i2}, V_{i2}). Therefore these corrections are mainly relevant for the couplings of third generation sfermions ($\tilde{\tau}, \tilde{b}, \tilde{t}$). Again, a precise knowledge of A_t is not necessary to provide a prediction with sufficient precision, but a rough knowledge of the scale and sign is needed.

We have performed a study to gauge the importance of the knowledge of the squark mass scale. We have performed an analysis of the uncertainty in the prediction for the partial decay widths when only part of the spectrum is known, under two conditions:

- First, including data only from the LC, the slepton, chargino/neutralino and lightest stop spectrum is known. We perform a scan in the MSSM parameter space, for the squark spectrum between 500 GeVand 5 TeV.
- Second, using additionally data from the LHC, with a known squark mass spectrum.

The spectrum determination at the LC/LHC+LC is taken from Table 5.25. The results are shown in Table 5.36. Here we show the range of possible values in the squark

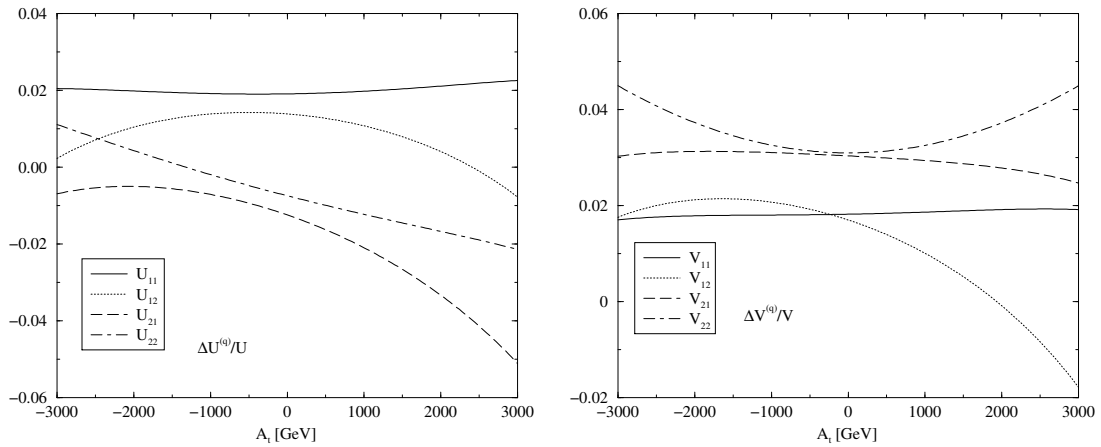

(a) (b)

Figure 5.51: Variation of the chargino effective coupling matrices (5.68) as a function of the top-squark soft-SUSY-breaking trilinear coupling A_t for SPS 1a, but with a squark mass scale of 1 TeV.

	LC		LHC+LC	
Process	$\delta\Gamma^{(q)}/\Gamma$	uncert (%)	$\delta\Gamma^{(q)}/\Gamma$	uncert (%)
$\tilde{e}_1 \to e^-\chi_1^0$	0.040 – 0.076	3.6	0.042 – 0.064	2.3
$\tilde{e}_1 \to e^-\chi_2^0$	0.029 – 0.075	4.6	0.028 – 0.030	0.3
$\tilde{e}_1 \to \nu_e\chi_1^-$	0.026 – 0.082	5.6	0.024 – 0.031	0.6
$\tilde{e}_2 \to e^-\chi_1^0$	0.052 – 0.063	1.1	0.052 – 0.054	0.2
$\tilde{\nu}_e \to \nu_e\chi_1^0$	0.041 – 0.075	3.4	0.045 – 0.060	1.5
$\tilde{\nu}_e \to \nu_e\chi_2^0$	0.016 – 0.080	6.4	0.015 – 0.032	1.7
$\tilde{\nu}_e \to e^-\chi_1^+$	0.023 – 0.067	4.4	0.022 – 0.027	0.5

Table 5.36: Uncertainty in the prediction of the partial decay widths of selectrons and sneutrinos assuming that only LC data is available, and combining LHC+LC data.

universal corrections ($\delta\Gamma^{(q)}/\Gamma$) due to the unknown spectrum, and the corresponding uncertainty in the prediction of the partial decay widths. Using only LC data the uncertainty in the partial decay widths prediction is at the percent level for all possible decays. When we restrict the squark spectrum to the values provided by the LHC, the uncertainty decreases significantly, in most of the channels by a factor five, or even a factor ten. However, in some special cases, namely $\Gamma(\tilde{e}_1 \to e^-\chi_1^0)$ and $\Gamma(\tilde{\nu}_e \to \nu_e\chi_1^0)$, the uncertainty decreases only a factor two.

5.4.1.4 Conclusions

In SUSY models non-decoupling effects appear. These effects are due to two kinds of splittings among the particle masses: a splitting between a particle and its SUSY partner (given by the soft-SUSY-breaking masses); and a splitting among the SUSY particles themselves. In this situation the radiative corrections grow with the logarithm of the largest SUSY particle of the model. In this scenario some of the particles (presumably strongly interacting particles) are heavy, and can only be produced at

the LHC, whereas another set of particles (selectrons, lightest charginos/neutralinos) can be studied at the LC, and their properties measured with a precision better than 1%.

In order to provide a prediction at the same level of accuracy, one needs a knowledge of the squark masses (and A_t) obtained from the LHC measurements, but a high precision measurement of the squark parameters is not necessary.

The effects of squarks can be taken into account by the use of effective coupling matrices in the chargino/neutralino sector. These effects can be extracted from LC data, by finding the finite difference between the mixing matrices obtained from the chargino/neutralino masses, and the mixing matrices obtained from the couplings analysis.

Of course, to reach the high level of accuracy needed at the LC the complete one-loop corrections to the observables under study is needed, but the effective coupling matrices form a necessary and universal subset of these corrections.

5.4.2 Correlations of flavour and collider physics within supersymmetry

5.4.2.1 Sources of Flavour Violation

Within the Minimal Supersymmetric Standard Model (MSSM) there are two new sources of flavour changing neutral currents, namely new contributions which are induced through the quark mixing like in the SM and generic supersymmetric contributions through the squark mixing. In contrast to the Standard Model (SM), the structure of the unconstrained MSSM does not explain the suppression of FCNC processes which is observed in experiments; this is the essence of the well-known supersymmetric flavour problem. Flavour changing neutral current (FCNC) processes therefore yield important (indirect) information on the construction of supersymmetric extensions of the SM and can contribute to the question of which mechanism ultimately breaks supersymmetry. The experimental measurements of the rates for these processes, or the upper limits set on them, impose in general a reduction of the size of parameters in the soft supersymmetry-breaking terms.

To understand the sources of flavour violation that may be present in supersymmetric models, in addition to those enclosed in the CKM matrix K, one has to consider the contributions to the squark mass matrices

$$\mathcal{M}_f^2 \equiv \begin{pmatrix} M_{f,\,LL}^2 + F_{f\,LL} + D_{f\,LL} & M_{f,\,LR}^2 + F_{f\,LR} \\ \left(M_{f,\,LR}^2\right)^\dagger + F_{f\,RL} & M_{f,\,RR}^2 + F_{f\,RR} + D_{f\,RR} \end{pmatrix}, \tag{5.72}$$

where f stands for up- or down-type squarks. The matrices $M_{u,LL}$ and $M_{d,LL}$ are related by $SU(2)_L$ gauge invariance. In the super-CKM basis, where the quark mass matrices are diagonal and the squarks are rotated in parallel to their superpartners, the relation reads as $K^\dagger M_{u,LL}^2 K = M_{d,LL}^2 = M_Q^2$. In this basis the F-terms $F_{f\,LL}$, $F_{f\,RL}$, $F_{f\,RR}$ as well as the D-terms $D_{f\,LL}$ and $D_{f\,RR}$ are diagonal. All the additional flavour structure of the squark sector is encoded in the soft SUSY breaking terms M_Q^2, $M_{f,\,RR}^2$ (=M_U^2 for $f = u$ and M_D^2 for $f = d$) and $M\,f,\,LR^2$ (=$v_u(A^u)^*$ for $f = u$ and $v_d(A^d)^*$ for $f = d$). Note, that the A-matrices are in general non-hermitian.

These additional flavour structures induce flavour violating couplings to the neutral gauginos and higgsinos in the mass eigenbasis which give rise to additional contributions to observables in the K and B meson sector. At present, new physics contributions to $s \to d$ and $b \to d$ transitions are strongly constrained. In particular, the transitions between first- and second-generation quarks, namely FCNC processes in the K system, are the most formidable tools to shape viable supersymmetric flavour models. As was recently emphasized again [437], most of the phenomena involving $b \to s$ transitions are still largely unexplored and leave open the possibility of large new physics effects in spite of the strong bound of the famous $B \to X_s\gamma$ decay which still gives the most stringent bounds in this sector. Nevertheless, additional experimental information from the $B \to X_s\ell^+\ell^-$ decay at the B factories and new results on the $B_s - \overline{B}_s$ mixing at the Tevatron might change this situation in the near future. Within the present analysis, we take the present phenomenological situation into account by setting the off-diagonal elements with an index 1 to zero. Regarding the $b \to s$ transitions, we restrict ourselves on the most powerful constraint from the decay $B \to X_s\gamma$ only.

Two further remarks are in order: Within a phenomenological analysis of the constraints on the flavour violating parameters in supersymmetric models with the most general soft terms in the squark mass matrices, we prefer to use the mass eigenstate formalism which remains valid (in contrast to the mass insertion approximation) when the intergenerational mixing elements are not small. Moreover, a consistent analysis of the bounds should also include interference effects between the various contributions, namely the interplay between the various sources of flavour violation and the interference effects of SM, gluino, chargino, neutralino and charged Higgs boson contributions. In [438] such an analysis was performed for the example of the rare decay $B \to X_s\gamma$ and new bounds on simple combinations of elements of the soft part of the squark mass matrices are found to be, in general, one order of magnitude weaker that the bound on the single off-diagonal elements $m_{LR,23}$ which was derived in previous work [439, 440], where any kind of interference effects were neglected.

5.4.2.2 Squark decays

Squarks can decay into quarks of all generations of quarks once the most general form the squark mass matrix is considered. The most important decays modes for the example under study are:

$$\tilde{u}_i \;\to\; u_j\tilde{\chi}^0_k\,,\; d_j\tilde{\chi}^+_l \tag{5.73}$$

$$\tilde{d}_i \;\to\; d_j\tilde{\chi}^0_k\,,\; u_j\tilde{\chi}^-_l \tag{5.74}$$

with $i = 1,..,6$, $j = 1,2,3$, $k = 1,..4$ and $l = 1,2$. These decays are controlled by the same mixing matrices as the contributions to $b \to s\gamma$. As this decay mode restricts the size of some of the elements, the questions arises to which extent flavour violating squark decays are also restricted. We will show below that flavour violating decay modes are hardly constrained by present days data.

We will take the so–called Snowmass point SPS#1a as a specific example which is specified by $m_0 = 100$ GeV, $m_{1/2} = 250$ GeV, $A_0 = -100$ GeV, $\tan\beta = 10$ and $\mathrm{sign}(\mu) = 1$. At the electroweak scale one gets the following data: $M_2 = 192$ GeV, $\mu = 351$ GeV, $m_{H^+} = 396$ GeV, $m_{\tilde{g}} = 594$ GeV, $m_{\tilde{t}_1} = 400$ GeV, $m_{\tilde{t}_2} = 590$ GeV, $m_{\tilde{q}_R} \simeq 550$ GeV,

$M^2_{Q,23}$	$M^2_{D,23}$	$M^2_{U,23}$	$v_u A^u_{23}$	$v_u A^u_{32}$	$v_d A^d_{23}$	$v_d A^d_{32}$
47066	9399	46465	23896	-44763	14470	15701

Table 5.37: Flavour violating parameters in GeV^2 which are added to the SPS#1a point. The corresponding BR($b \to s\gamma$) is $4 \cdot 10^{-4}$.

	$\tilde{\chi}^0_1 c$	$\tilde{\chi}^0_1 t$	$\tilde{\chi}^0_2 c$	$\tilde{\chi}^0_2 t$	$\tilde{\chi}^0_3 c$	$\tilde{\chi}^0_3 t$	$\tilde{\chi}^0_4 c$	$\tilde{\chi}^0_4 t$	$\tilde{\chi}^+_1 s$	$\tilde{\chi}^+_1 b$	$\tilde{\chi}^+_2 s$	$\tilde{\chi}^+_2 b$
$\tilde{u}_1$	4.7	18	5.2	9.6	$6\ 10^{-3}$	0	0.02	0	11.3	46.4	$2\ 10^{-3}$	4.7
$\tilde{u}_2$	19.6	1.1	0.4	17.5	$2\ 10^{-2}$	0	$6\ 10^{-2}$	0	0.5	57.5	$3\ 10^{-3}$	2.9
$\tilde{u}_3$	7.3	3.7	20	1.4	$6\ 10^{-2}$	0	0.6	0	40.3	3.1	1	18.5
$\tilde{u}_6$	5.7	0.4	11.1	5.3	$4\ 10^{-2}$	5.7	0.6	13.2	22.9	13.1	0.6	8.0

Table 5.38: Branching ratios (in %) of u-type squarks for the point specified in Table 5.37

and $m_{\tilde{q}_L} \simeq 570$ GeV. We have used the program SPheno [441] for the calculation. In the following we will concentrate on the mixing between the second and third generation. As a specific example we have added a set of flavour violating parameters given in Table 5.37; the resulting up-squark masses in GeV are in ascending order: 408, 510, 529, 542, 558 and 627. This point is a random one out of 1000 points fulfilling the $b \to s\gamma$ constraint. For the calculation of BR($b \to s\gamma$) we have used the formulas given in ref. [442]. Note, that for SPS#1a both, the chargino as well as the gluino loops, are important for the calculation of BR($b \to s\gamma$). Therefore, there is an interplay between the flavour structure of the down-type squarks and of the one of the up-type squarks.

In what follows we will concentrate on up-type squarks. However, we want to note that also down-type squarks as well the gluino large flavour violating decay modes[9]. The corresponding branching ratios into charginos and neutralinos are given in Table 5.38. In addition the following branching ratios are larger than 1%: BR($\tilde{u}_3 \to \tilde{u}_1 Z$)=2.6%, BR($\tilde{u}_3 \to \tilde{u}_1 h^0$)=1.2%, BR($\tilde{u}_6 \to \tilde{g}c$) = 4%, BR($\tilde{u}_6 \to \tilde{d}_1 W$)=2%, BR($\tilde{u}_6 \to \tilde{u}_1 h^0$)=4.9% and BR($\tilde{u}_6 \to \tilde{u}_2 Z$)=1.8%.

It is clear from Table 5.38 that all four particles have large flavour changing decay modes. This clearly has an impact on the edge variables, for example, the ones involving the second lightest neutralino: m^{max}_{llq}, m^{min}_{llq}, m^{low}_{lq}, and m^{high}_{lq} [443]. In the studies for SPS#1a it has been assumed up to now that the squarks under consideration have approximately the same mass within a few percent. In this example the masses of the squarks range from 408 GeV up to 627 GeV. In particular $\tilde{u}_1$ and $\tilde{u}_6$ will give rise to additional structures in the lepton and jet distributions. In such a case a refined analysis will be necessary to decide whether this additional structure are caused by background, new particles or flavour changing decay modes. Here it will be of clear advantage if a linear collider could measure the branching of the lightest squark(s) to see if there are sizable flavour violating decays in the squark sector.

In ref. [381] several variables have been proposed for extracting information on stops and sbottoms in gluino decays. One class of these variables considers final states containing $b\tilde{\chi}^+_1$. In our example, three u-type squarks contribute with branch-

[9]Strictly speaking one should use the expression 'generation violating decay modes' in this context.

ing ratios larger than 10%, in contrast to the assumption that only the two stops contribute. As a consequence we expect that additional structures will be present in the corresponding observables. Moreover, we expect also in this case that a combination of LHC and LC will be useful in the exploration of these structures.

In conclusion, we have seen, that large flavour changing decays of squarks are consistent with present days data from Tevatron and the B factories. In this note we have concentrated on the decays of up-type squark. These decays will lead to additional structures in the lepton and jet distributions which are used to determine the edge variables proposed for the LHC. A linear with sufficient energy can in principle measure the branching ratios of the lightest up- and/or down-type squark proving the hypothesis of large flavour violation in the squark sector. This information can then be put back in the analysis of the LHC data.

5.4.3 Supersymmetric lepton flavour violation at LHC and LC

5.4.3.1 Introduction

Neutrino oscillations imply the violation of individual lepton flavours and raise the interesting possibility of observing lepton flavour violation in processes with charged leptons, such as $\mu \to e\gamma$ or $\tau \to \mu\gamma$. In the Standard Model these processes are strongly suppressed due to small neutrino masses. In the supersymmetric extension of the Standard Model, however, the situation may be quite different. For example, the slepton mass matrices need not simultaneously be diagonalized with the lepton mass matrices. When sleptons are rotated to the mass eigenstate basis, the slepton mass diagonalization matrices $W_{i\alpha}$ enter the chargino and neutralino couplings

$$\tilde{e}_i (W^*_{\tilde{l}})_{i\alpha} \overline{e}_\alpha \tilde{\chi}^0 + \tilde{\nu}_i (W^*_{\tilde{\nu}})_{i\alpha} \overline{e}_\alpha \tilde{\chi}^- + \dots \tag{5.75}$$

and mix lepton flavour (Latin and Greek subscripts refer to the mass-eigenstate and flavour basis, respectively). Contributions from virtual slepton exchanges can therefore enhance the rates of rare decays like $\mu \to e\gamma$. Furthermore, once superpartners are discovered, the supersymmetric lepton flavour violation (SLFV) can also be searched for directly at future colliders where the signal will come from the production of real sleptons (either directly or from chain decays of other sparticles), followed by their subsequent decays. Searches for SLFV at colliders have a number of advantages: superpartners can be produced with large cross-sections, flavour violation in the production and decay of sleptons occurs at tree level and therefore is suppresed only by powers of $\Delta m_{\tilde{l}}/\Gamma_{\tilde{l}}$ [444] in contrast to the $\Delta m_{\tilde{l}}/m_{\tilde{l}}$ suppression in radiative lepton decays, where SLFV occurs at one-loop ([445] and references therein). Generally, respecting the present bounds on rare lepton decays, large SLFV signals are possible both at the LHC [446] and at e^+e^- colliders [444,447–451]. This suggests that in some cases the LHC and future e^+e^- colliders may provide competitive tools to search for and explore supersymmetric lepton flavour violation.

In this note we first discuss the sensitivity at future e^+e^- colliders to SLFV independently of the lepton flavour violating mechanism. The simulation has been performed assuming a simplified situation with a pure 2-3 intergeneration mixing between $\tilde{\nu}_\mu$ and $\tilde{\nu}_\tau$, and ignoring any mixings with $\tilde{\nu}_e$. In the analysis the mixing angle $\tilde{\theta}_{23}$ and $\Delta\tilde{m}_{23} = |m_{\tilde{\nu}_2} - m_{\tilde{\nu}_3}|$ have been taken as free, independent parameters [449].

In the second part, SLFV generated by the seesaw mechanism is considered. The heavy right-handed Majorana neutrinos give rise not only to light neutrino masses but also to mixing of different slepton flavours due to the effects of the heavy neutrinos on the renormalization-group running of the slepton masses. The implications of recent neutrino measurements on this mixing are investigated. Moreover we emphasize the complementarity of the radiative decays $l_\alpha \to l_\beta \gamma$ and the specific lepton flavour violating processes $e^\pm e^- \to l_\beta^\pm l_\alpha^- \tilde{\chi}_b^0 \tilde{\chi}_a^0$ involving slepton pair production and subsequent decay [451].

5.4.3.2 Sensitivity at future e^+e^- colliders to SLFV

In discussing the SLFV collider signals at future colliders, one has to distinguish two cases in which an oscillation of lepton flavour can occur: in processes with slepton pair production and in processes with single slepton production, which differ in the interference of the intermediate sleptons [444]. Slepton pair production is the dominant mechanism at lepton colliders, but it may also occur at hadron colliders via the Drell-Yan process. Single sleptons may be produced in cascade decays of heavier non-leptonic superparticles. Such processes are particularly important for hadron colliders, but they may also be relevant for lepton colliders where a single slepton can be the decay product of a chargino or neutralino.

The amplitudes for pair production, $\overline{f}\, f \to \tilde{l}_i^+ \tilde{l}_i^- \to l_\alpha^+ X\, l_\beta^- Y$, and single production, $f\, f' \to l_\alpha^+ X\, \tilde{l}_i^- \to l_\alpha^+ X\, l_\beta^- Y$, read, e.g.,

$$\mathcal{M}_{\alpha\beta}^{\text{pair}} = \sum_i \mathcal{M}_P^{\text{pair}} \frac{i}{q^2 - \tilde{m}_i^2 + i\tilde{m}_i\Gamma_i} W_{i\alpha} \mathcal{M}_D^+ \frac{i}{p^2 - \tilde{m}_i^2 + i\tilde{m}_i\Gamma_i} W_{i\beta}^* \mathcal{M}_D^- \quad \text{(s-channel)} \tag{5.76}$$

$$\mathcal{M}_{\alpha\beta}^{\text{sin}} = \sum_i \mathcal{M}_P^{\text{sin}} W_{i\alpha} \frac{i}{q^2 - \tilde{m}_i^2 + i\tilde{m}_i\Gamma_i} W_{i\beta}^* \mathcal{M}_D^- \tag{5.77}$$

where $\mathcal{M}_P$ and $\mathcal{M}_D$ are the respective production and decay amplitudes for sleptons in the absence of SLFV, and $W_{i\alpha}$ stands for the lepton flavour mixing matrix element.

For nearly degenerate in mass and narrow sleptons, $\Delta\tilde{m}_{ij} \ll \tilde{m}$ and $\tilde{m}\overline{\Gamma}_{ij} \simeq (\tilde{m}_i\Gamma_i + \tilde{m}_j\Gamma_j)/2 \ll \tilde{m}^2$, the products of slepton propagators can be simplified as follows

$$\frac{i}{q^2 - \tilde{m}_i^2 + i\tilde{m}_i\Gamma_i} \, \frac{-i}{q^2 - \tilde{m}_j^2 - i\tilde{m}_j\Gamma_j} \sim \frac{1}{1 + i\,\Delta\tilde{m}_{ij}/\overline{\Gamma}_{ij}} \, \frac{\pi}{\tilde{m}\overline{\Gamma}_{ij}} \, \delta(q^2 - \tilde{m}^2). \tag{5.78}$$

Then, in the case of 2-3 intergeneration mixing, the cross-sections for the above processes (5.76, 5.77), take a particularly simple form [452]:

$$\sigma_{\alpha\beta}^{\text{pair}} = \chi_{23}(3 - 4\chi_{23}) \sin^2 2\tilde{\theta}_{23}\, \sigma(\overline{f}\, f \to \tilde{l}_\alpha^+ \tilde{l}_\alpha^-) Br(\tilde{l}_\alpha^+ \to l_\alpha^+ X) Br(\tilde{l}_\alpha^- \to l_\alpha^- Y) \tag{5.79}$$

$$\sigma_{\alpha\beta}^{\text{sin}} = \chi_{23} \sin^2 2\tilde{\theta}_{23}\, \sigma(f\, f' \to l_\alpha^+ X\, \tilde{l}_\alpha^-) Br(\tilde{l}_\alpha^- \to l_\alpha^- Y) \tag{5.80}$$

where $\sigma(f\, f' \to l_\alpha^+ X\, \tilde{l}_\alpha^-)$, $\sigma(\overline{f}\, f \to \tilde{l}_\alpha^+ \tilde{l}_\alpha^-)$ and $Br(\tilde{l}_\alpha^\pm \to l_\alpha^\pm X)$ are the corresponding cross-sections and branching ratios in the absence of flavour violation. The slepton flavour violating mixing effects are encoded in

$$\chi_{23} = \frac{x_{23}^2}{2(1 + x_{23}^2)} \qquad \text{and} \qquad \sin^2 2\tilde{\theta}_{23} \tag{5.81}$$

where $x_{23} = \Delta\tilde{m}_{23}/\overline{\Gamma}_{23}$. In the limit $x_{23} \gg 1$, χ_{23} approaches 1/2, the interference can be neglected and the cross-sections behave as $\sigma \sim \sin^2 2\tilde{\theta}_{23}$. In the opposite case, the interference suppresses the flavour changing processes, and $\sigma \sim (\Delta\tilde{m}_{23} \sin 2\tilde{\theta}_{23})^2$.

To assess the sensitivity of a 500 GeV e^+e^- linear collider to the SLFV, the following processes have been analysed

$$e^+e^- \rightarrow \tilde{\nu}_i\tilde{\nu}_j^c \rightarrow \tau^\pm\mu^\mp\tilde{\chi}_1^+\tilde{\chi}_1^- \quad (5.82)$$

$$e^+e^- \rightarrow \tilde{\chi}_2^+\tilde{\chi}_1^- \rightarrow \tau^\pm\mu^\mp\tilde{\chi}_1^+\tilde{\chi}_1^- \quad (5.83)$$

$$e^+e^- \rightarrow \tilde{\chi}_2^0\tilde{\chi}_1^0 \rightarrow \tau^\pm\mu^\mp\tilde{\chi}_1^0\tilde{\chi}_1^0 \quad (5.84)$$

Here $\tilde{\chi}_1^\pm \rightarrow \tilde{\chi}_1^0 f\overline{f}'$, and $\tilde{\chi}_1^0$ escapes detection. The signature of SLFV would be $\tau^\pm\mu^\mp$ + 4 jets+$\not{E}_T$, $\tau^\pm\mu^\mp+\ell$+2 jets+$\not{E}_T$, or $\tau^\pm\mu^\mp+\not{E}_T$, depending on the hadronic or leptonic $\tilde{\chi}_1^\pm$ decay mode. The purely leptonic decay modes are overwhelmed by background. In particular, the neutralino pair production process (5.84), which could still be open if the second chargino and sleptons were too heavy for (5.82) and (5.83), is difficult to extract from background. On the other hand, with charginos decaying hadronically, the signal $\tau^\pm\mu^\mp + 4$ jets + $\not{E}_T$ comes from both processes (5.82) and (5.83) and is SM-background free. The flavour-conserving processes analogous to (5.82) and (5.83), but with two τ's in the final state where one of the τ's decays leptonically to μ, contribute to the background. On the other hand, if jets are allowed to overlap, an important SM background to the final states with $\tau^\pm\mu^\mp+ \geq 3$ jets + $\not{E}_T$ comes from $e^+e^- \rightarrow t\overline{t}g$.

The simulation of the signal and background has been performed for one of the MSSM representative points chosen for detailed case studies at the ECFA/DESY Workshop [57]: a mSUGRA scenario defined by $m_0 = 100$ GeV, $M_{1/2} = 200$ GeV, $A_0 = 0$ GeV, $\tan\beta = 3$ and $\mathrm{sgn}(\mu) = +$. A simple parton level simulation has been performed with a number of kinematic cuts listed in [449]. For the processes (5.82) and (5.83) we find after cuts the following cross-sections, $\chi_{23}(3 - 4\chi_{23}) \sin^2 2\tilde{\theta}_{23} \times 0.51$ fb and $\chi_{23} \sin^2 2\tilde{\theta}_{23} \times 0.13$ fb, respectively, while the background amounts to 0.28 fb.

In Fig. 5.52 the significance is given by $\sigma_d = \frac{S}{\sqrt{S+B}}$ where S and B are the numbers of signal and background events, respectively, for a given luminosity. Shown is the region (to the right of the curves) in the $\Delta\tilde{m}_{23} - \sin 2\tilde{\theta}_{23}$ plane that can be explored or ruled out at a 3σ level at a linear collider of energy 500 GeV for the given integrated luminosity. The contour A is for 500 fb^{-1} and B for 1000 fb^{-1}. For comparison, the boundary C shows the reach in the process $\tilde{\nu}_i\tilde{\nu}_i^c$ alone (previously studied in [444,448]) using our cuts and assuming a luminosity of 500 fb^{-1}. The chargino contribution increases the sensitivity range to $\sin 2\tilde{\theta}_{23}$ by 10-20%, while the sensitivity to $\Delta\tilde{m}_{23}$ does not change appreciably.

In the same figure, the contour lines for constant branching ratios of $\tau \rightarrow \mu\gamma$ are shown for comparison [453]. In the limit of small mass splitting, $Br(\tau \rightarrow \mu\gamma)$ can be calculated in the flavour basis using the mass insertion technique [454]. In our 2-3 intergeneration mixing scenario the radiative process $\tau \rightarrow \mu\gamma$ constrains the combination of parameters

$$\delta_{\mu\tau} = \sin 2\tilde{\theta}_{23}\Delta\tilde{m}_{23}/\tilde{m}. \quad (5.85)$$

The contours in Fig. 5.52 have been obtained from the approximate formula of Ref.

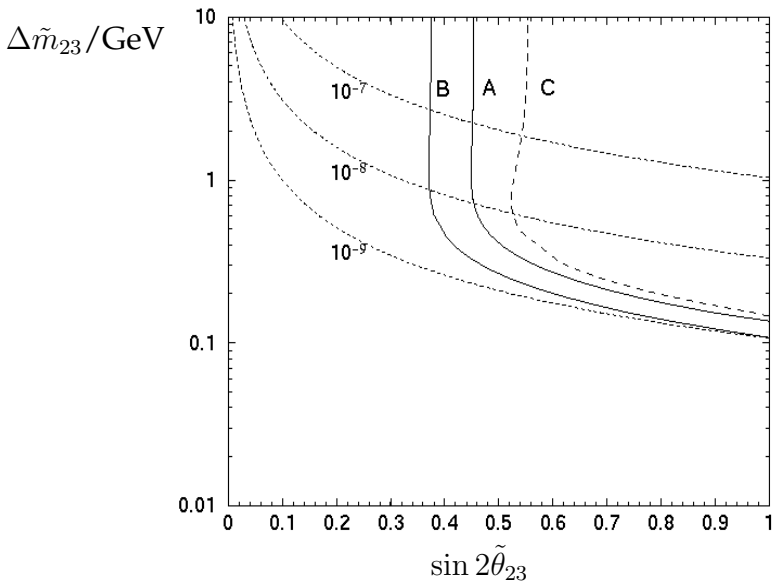

Figure 5.52: Various 3σ significance contours in the $\Delta\tilde{m}_{23} - \sin 2\tilde{\theta}_{23}$ plane, for the SUSY point mentioned in the text. The contours A and B show the integrated signals (5.82–5.83) at $\sqrt{s}$ =500 GeV and for 500 fb^{-1} and 1000 fb^{-1}, respectively. The contour C shows the $\tilde{\nu}\tilde{\nu}^c$ contribution separately for 500 fb^{-1} [449]. The dotted lines indicate contours for $Br(\tau \to \mu\gamma)$=10^{-7}, 10^{-8} and 10^{-9} [453].

[455], normalized to the current experimental limit,

$$Br(\tau \to \mu\gamma) \sim 1.1 \times 10^{-6} \left(\frac{\delta_{\mu\tau}}{1.4}\right)^2 \left(\frac{100\,\text{GeV}}{\tilde{m}}\right)^4 . \tag{5.86}$$

This approximation only provides an order of magnitude estimate of the upper limit for the supersymmetric contribution to the radiative lepton decay. The exact result, which is sensitive to the details of mass spectra and mixings, can in fact be much smaller due to cancellations among different contributions [445]. Fig. 5.52 demonstrates that information from slepton production and decay could be competitive to the radiative lepton decays. In particular a LC can help to explore the small $\Delta\tilde{m}_{23}$ region. It should be stressed, though, that in a given model for lepton flavour violation also the correlation with $\mu \to e\gamma$ has to be considered [451], which in many cases can yield a more severe bound, as discussed in the next section.

5.4.3.3 Case study for the supersymmetric seesaw model

As a definite and realistic example for SLFV we consider the seesaw mechanism in mSUGRA models. In supersymmetric theories with heavy right-handed Majorana neutrinos, the seesaw mechanism [456] can give rise to light neutrino masses at or below the sub-eV scale. Furthermore, the massive neutrinos affect the renormalization group running of the slepton masses, generating flavour off-diagonal terms in the mass matrix. These in turn lead to SLFV in scattering processes at high energies and in rare decays. For illustration of the potential and complementarity of such SLFV searches we focus on the LC processes $e^\pm e^- \to l^\pm_\beta l^-_\alpha \tilde{\chi}^0_b \tilde{\chi}^0_a$ involving slepton pair production and subsequent decay, and on the corresponding radiative decay $l_\alpha \to l_\beta \gamma$.

In particular, in an early ATLAS note [457] $\tau \to \mu\gamma$ is estimated to be observable at the LHC for a branching ratio of order 10^{-7}. However, the limit one can reasonably expect may be an order of magnitude better [458].

For our study we use the mSUGRA benchmark scenarios proposed in [459] for LC studies, concentrating on those which predict charged left-handed sleptons that are light enough to be pair-produced at the center-of-mass energy $\sqrt{s} = 500$ GeV. Furthermore, we implement the seesaw mechanism assuming degenerate Majorana masses for the right-handed neutrinos and constrain the neutrino Yukawa couplings by the measured masses and mixings of the light neutrinos. Further sources of SLFV exist in other models such as GUTs [460]. However, no realistic three generation case study of effects for collider processes has been performed so far, so that we restrict the discussion to the minimal seesaw model, here.

Supersymmetric seesaw mechanism

If three right-handed neutrino singlet fields ν_R are added to the MSSM particle content, one has the additional terms [461]

$$W_\nu = -\frac{1}{2}\nu_R^{cT} M \nu_R^c + \nu_R^{cT} Y_\nu L \cdot H_2 \tag{5.87}$$

in the superpotential. Here, Y_ν is the matrix of neutrino Yukawa couplings, M is the right-handed neutrino Majorana mass matrix, and L and H_2 denote the left-handed lepton and hypercharge +1/2 Higgs doublets, respectively. At energies much below the mass scale M_R of the right-handed neutrinos, W_ν leads to the following mass matrix for the light neutrinos:

$$M_\nu = Y_\nu^T M^{-1} Y_\nu (v \sin\beta)^2. \tag{5.88}$$

From that the light neutrino masses m_1, m_2, m_3 are obtained after diagonalization by the unitary MNS matrix U. The basis is chosen such that the matrices of the charged lepton Yukawa couplings and Majorana masses are diagonal, which is always possible.

Furthermore, the heavy neutrino mass eigenstates give rise to virtual corrections to the slepton mass matrix that are responsible for lepton flavour violating processes. More specifically, in the mSUGRA models considered, the mass matrix of the charged sleptons is given by

$$m_{\tilde{l}}^2 = \begin{pmatrix} m_{\tilde{l}_L}^2 & (m_{\tilde{l}_{LR}}^2)^\dagger \\ m_{\tilde{l}_{LR}}^2 & m_{\tilde{l}_R}^2 \end{pmatrix} \tag{5.89}$$

with

$$\begin{aligned}
(m_{\tilde{l}_L}^2)_{ij} &= (m_L^2)_{ij} + \delta_{ij}\left(m_{l_i}^2 + m_Z^2 \cos 2\beta \left(-\frac{1}{2} + \sin^2\theta_W\right)\right) \\
(m_{\tilde{l}_R}^2)_{ij} &= (m_R^2)_{ij} + \delta_{ij}(m_{l_i}^2 - m_Z^2 \cos 2\beta \sin^2\theta_W) \\
(m_{\tilde{l}_{LR}}^2)_{ij} &= A_{ij} v \cos\beta - \delta_{ij} m_{l_i} \mu \tan\beta.
\end{aligned}$$

When $m_{\tilde{l}}^2$ is evolved from the GUT scale M_X to the electroweak scale characteristic for the experiments, one obtains

$$m_L^2 = m_0^2 \mathbf{1} + (\delta m_L^2)_{\text{MSSM}} + \delta m_L^2 \tag{5.90}$$

$$m_R^2 = m_0^2 \mathbf{1} + (\delta m_R^2)_{\text{MSSM}} + \delta m_R^2 \tag{5.91}$$

$$A = A_0 Y_l + \delta A_{\text{MSSM}} + \delta A, \tag{5.92}$$

where m_0 is the common soft SUSY-breaking scalar mass and A_0 the common trilinear coupling. The terms $(\delta m_{L,R}^2)_{\text{MSSM}}$ and δA_{MSSM} are well-known flavour-diagonal MSSM corrections. In addition, the evolution generates the off-diagonal terms $\delta m_{L,R}^2$ and δA which, in leading-log approximation and for degenerate right-handed Majorana masses $M_i = M_R, i = 1, 2, 3$, are given by [462]

$$\delta m_L^2 = -\frac{1}{8\pi^2}(3m_0^2 + A_0^2)(Y_\nu^\dagger Y_\nu)\ell_{\text{n}}\left(\frac{M_X}{M_R}\right) \tag{5.93}$$

$$\delta m_R^2 = 0 \tag{5.94}$$

$$\delta A = -\frac{3A_0}{16\pi^2}(Y_l Y_\nu^\dagger Y_\nu)\ell_{\text{n}}\left(\frac{M_X}{M_R}\right). \tag{5.95}$$

In order to determine the product $Y_\nu^\dagger Y_\nu$ of the neutrino Yukawa coupling matrix entering these corrections, one uses the expression

$$Y_\nu = \frac{\sqrt{M_R}}{v \sin\beta} R \cdot \text{diag}(\sqrt{m_1}, \sqrt{m_2}, \sqrt{m_3}) \cdot U^\dagger, \tag{5.96}$$

which follows from $U^T M_\nu U = \text{diag}(m_1, m_2, m_3)$ and (5.88) [461]. Here, R is an unknown complex orthogonal matrix parametrizing the ambiguity in the relation of Yukawa coupling and mass matrices. In the following we will assume R to be real which suffices for the present purpose. In this case, R drops out from the product $Y_\nu^\dagger Y_\nu$,

$$Y_\nu^\dagger Y_\nu = \frac{M_R}{v^2 \sin^2\beta} U \cdot \text{diag}(m_1, m_2, m_3) \cdot U^\dagger. \tag{5.97}$$

Using existing neutrino data on the mass squared differences and the mixing matrix U together with bounds and assumptions on the absolute mass scale one can calculate $Y_\nu^\dagger Y_\nu$. The only free parameter is the Majorana mass scale M_R. The result is then evolved to the unification scale M_X and used as an input in the renormalization group corrections (5.93) to the slepton mass matrix. Finally, diagonalization of (5.89) yields the slepton mass eigenvalues $\tilde{m}_i$ and eigenstates $\tilde{l}_i$ $(i = 1, 2, ...6)$.

Lepton flavour violating processes

The flavour off-diagonal elements (5.93) in $m_{\tilde{l}}^2$ ($\delta A = 0$ in the mSUGRA scenarios of [459]) induce, among other SLFV effects, the processes $e^+e^- \to \tilde{l}_j^+ \tilde{l}_i^- \to l_\beta^+ l_\alpha^- \tilde{\chi}_b^0 \tilde{\chi}_a^0$, where SLFV can occur in the production and decay vertices. The helicity amplitudes for the pair production of $\tilde{l}_j^+$ and $\tilde{l}_i^-$, and the corresponding decay amplitudes are given explicitly in [451]. In the approximation (5.79) for $\sigma_{\alpha\beta}^{\text{pair}}$ one finds

$$\sigma_{\alpha\beta}^{\text{pair}} \propto \frac{|(\delta m_L)_{\alpha\beta}^2|^2}{\tilde{m}^2 \Gamma^2}\, \sigma(\overline{f}\, f \to \tilde{l}_\alpha^+ \tilde{l}_\alpha^-) Br(\tilde{l}_\alpha^+ \to l_\alpha^+ \tilde{\chi}_0) Br(\tilde{l}_\alpha^- \to l_\alpha^- \tilde{\chi}_0) \tag{5.98}$$

In the numerical evaluation no slepton degeneracy has been assumed as in (5.78), and the amplitude for the complete $2 \to 4$ processes is summed coherently over the intermediate slepton mass eigenstates.

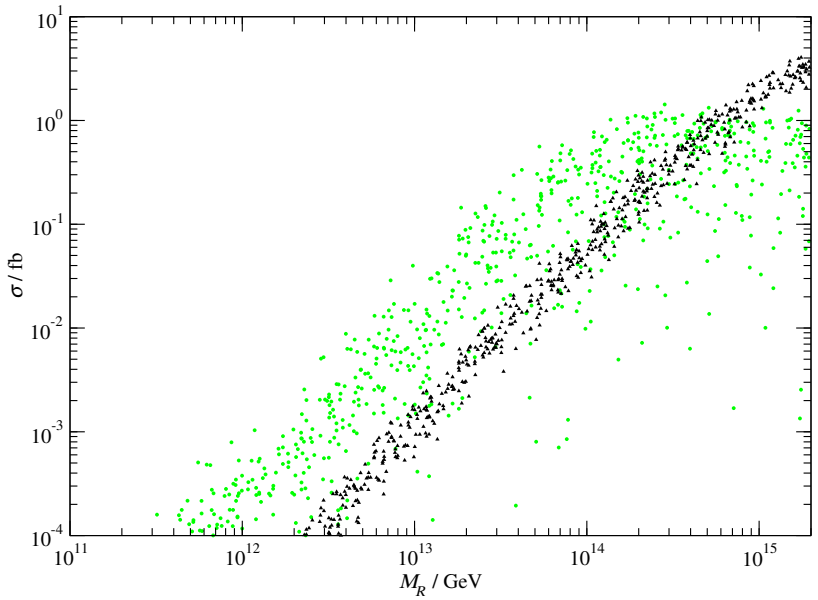

Figure 5.53: Cross-sections at $\sqrt{s} = 500$ GeV for $e^+e^- \to \mu^+e^- + 2\tilde{\chi}_1^0$ (circles) and $e^+e^- \to \tau^+\mu^- + 2\tilde{\chi}_1^0$ (triangles) in scenario B.

Similary, the terms (5.93) are responsible for SLFV radiative decays $l_\alpha \to l_\beta\gamma$ induced by photon-penguin type diagrams with charginos / sneutrinos or neutralinos / charged sleptons in the loop. Again schematically, the decay rates are given by [461,462]

$$\Gamma(l_\alpha \to l_\beta\gamma) \propto \alpha^3 m_{l_\alpha}^5 \frac{|(\delta m_L)^2_{\alpha\beta}|^2}{\tilde{m}^8} \tan^2\beta, \tag{5.99}$$

where $\tilde{m}$ stands for the relevant sparticle masses in the loop.

Scenario	$m_{1/2}$/GeV	m_0/GeV	$\tan\beta$	$\tilde{m}_6$/GeV	$\tilde{\Gamma}_6$/GeV	$m_{\tilde{\chi}_1^0}$/GeV
B	250	100	10	208	0.32	98
C	400	90	10	292	0.22	164
G	375	120	20	292	0.41	154
I	350	180	35	313	1.03	143

Table 5.39: Parameters of selected mSUGRA benchmark scenarios (from [459]). The sign of μ is chosen to be positive and A_0 is set to zero. Given are also the mass and total width of the heaviest charged slepton and the mass of the lightest neutralino.

Signals and background

Among the mSUGRA benchmark scenarios proposed in [459] for LC studies, the models B, C, G, and I (see Tab.5.39) predict left-handed sleptons which can be pair-produced at e^+e^- colliders $\sqrt{s} = 500 \div 800$ GeV cms energies. In the following we will confine ourselves to these models.

Most likely, at the time when a linear collider will be in operation, more precise measurements of the neutrino parameters will be available than today. In order to simulate the expected improvement, we take the central values of the mass squared

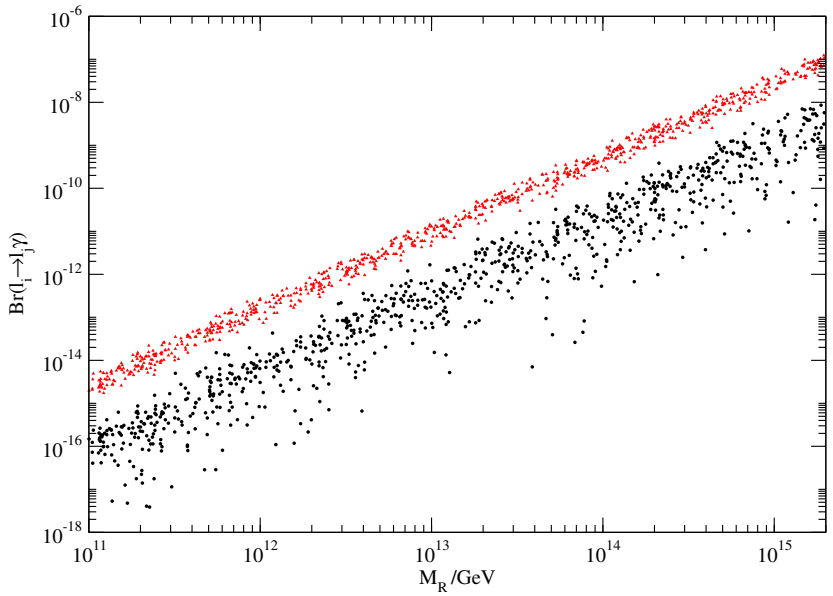

Figure 5.54: Branching ratios $Br(\tau \to \mu\gamma)$ (upper) and $Br(\mu \to e\gamma)$ (lower) in scenario B.

differences $\Delta m^2_{ij} = |m^2_i - m^2_j|$ and mixing angles θ_{ij} from a global fit to existing data [463] with errors that indicate the anticipated 90 % C.L. intervals of running and proposed experiments as further explained in [445]:

$$\tan^2\theta_{23} = 1.40^{+1.37}_{-0.66}, \quad \tan^2\theta_{13} = 0.005^{+0.001}_{-0.005}, \quad \tan^2\theta_{12} = 0.36^{+0.35}_{-0.16}, \tag{5.100}$$

$$\Delta m^2_{12} = 3.30^{+0.3}_{-0.3} \cdot 10^{-5}\ \text{eV}^2, \quad \Delta m^2_{23} = 3.10^{+1.0}_{-1.0} \cdot 10^{-3}\ \text{eV}^2. \tag{5.101}$$

Furthermore, for the lightest neutrino we assume the mass range $m_1 \approx 0 - 0.03$ eV, which at the lower end corresponds to the case of a hierarchical spectrum. Towards the upper end, it approaches the degenerate case.

In Fig. 5.53, the cross-sections for $e^+e^- \to \mu^+e^- + 2\tilde{\chi}^0_1$ and $e^+e^- \to \tau^+\mu^- + 2\tilde{\chi}^0_1$ are plotted for model B. The channel $\tau^+e^- + 2\tilde{\chi}^0_1$ is not shown since it is strongly suppressed by the small mixing angle θ_{13}, and therefore more difficult to observe. As can be seen, for a sufficiently large Majorana mass scale the SLFV cross-sections can reach several fb. The spread of the predictions reflects the uncertainties in the neutrino data.

The Standard Model background mainly comes from W-pair production, W production with t-channel photon exchange, and τ-pair production. A 10 degree beam pipe cut and cuts on the lepton energy and missing energy reduce the SM background cross-sections to less than 30 fb for (μe) final states and less than 10 fb for $(\tau\mu)$ final states. If one requires a signal to background ratio, $S/\sqrt{S+B} = 3$, and assumes a typical signal cross-section of 0.1 fb, one can afford a background of about 1 fb. Here an integrated luminosity of 1000 fb^{-1} has been assumed. Whether or not the background process estimate above can be further suppressed to this level by applying selectron selection cuts, for example, on the acoplanarity, lepton polar angle and missing transverse momentum has to be studied in dedicated simulations. For lepton flavour conserving processes it has been shown that the SM background to slepton pair production can be reduced to about 2-3 fb at $\sqrt{s} = 500$ GeV [464].

The MSSM background is dominated by chargino/slepton production with a total

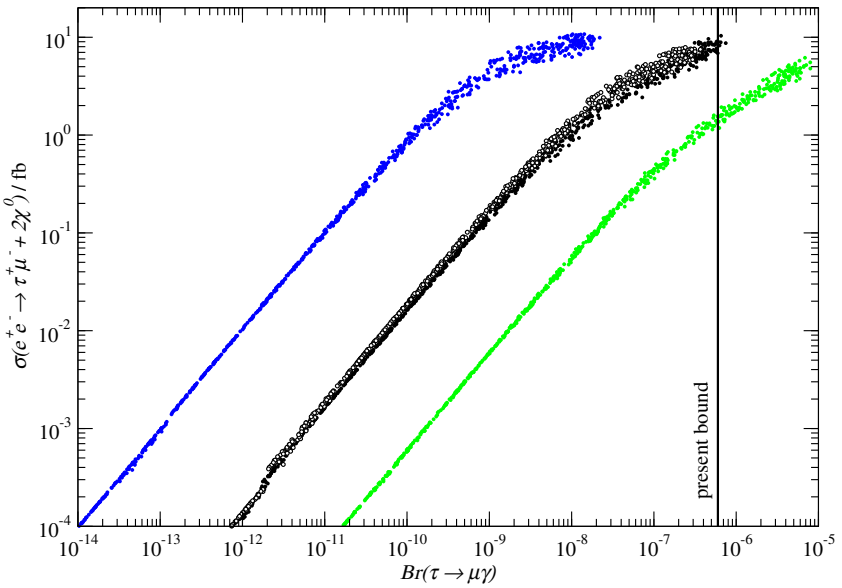

Figure 5.55: Correlation of $\sigma(e^+e^- \to \tau^+\mu^- + 2\tilde{\chi}_1^0)$ at $\sqrt{s} = 800$ GeV with $Br(\tau \to \mu\gamma)$ in scenario (from left to right) C, G (open circles), B and I.

cross-section of 0.2-5 fb and 2-7 fb for (μe) and $(\tau\mu)$ final states, respectively, depending on the SUSY scenario and the collider energy. The MSSM background in the (τe) channel can also contribute to the μe channel via the decay $\tau \to \mu\nu_\mu\nu_\tau$. If $\tilde{\tau}_1$ and $\tilde{\chi}_1^+$ are very light, like in scenarios B and I, this background can be as large as 20 fb. However, such events typically contain two neutrinos in addition to the two LSPs which are also present in the signal events. Thus, after τ decay one has altogether six invisible particles instead of two, which may allow to discriminate the signal in $\mu^+e^- + \not{E}$ also from this potentially dangerous MSSM background by cutting on various distributions. But also here one needs a dedicated simulation study, in order to make more definite statements.

The corresponding branching ratios, $Br(\mu \to e\gamma)$ and $Br(\tau \to \mu\gamma)$, in model B are displayed in Fig. 5.54 [445]. One sees that a positive signal for $\mu \to e\gamma$ at the minimum branching ratio observable in the new PSI experiment, $Br(\mu \to e\gamma) \simeq 10^{-13}$ [465] would imply a value of M_R between $2 \cdot 10^{12}$ GeV and $2 \cdot 10^{13}$ GeV. In comparison to $\mu \to e\gamma$ the channel $\tau \to \mu\gamma$ is less affected by the neutrino uncertainties. If the sensitivity goal $Br(\tau \to \mu\gamma) = 10^{-8}$ [458] at the LHC is reached one could probe $M_R = 10^{15}$ GeV.

Particularly interesting and useful are the correlations between SLFV in radiative decays and slepton pair production. Such a correlation is illustrated in Fig. 5.55 for $e^+e^- \to \tau^+\mu^- + 2\tilde{\chi}_1^0$ and $Br(\tau \to \mu\gamma)$. One sees that the neutrino uncertainties drop out, while the sensitivity to the mSUGRA parameters remains. An observation of $\tau \to \mu\gamma$ with the branching ratio 10^{-8} at the LHC would be compatible with a cross-section of order 10 fb for $e^+e^- \to \sum_{i,j} \tilde{l}_j^+\tilde{l}_i^- \to \tau^+\mu^- + 2\tilde{\chi}_1^0$, at least in model C. However, there are also correlations of different flavor channels. This is illustrated in Fig. 5.56, where the correlation of $e^+e^- \to \tau^+\mu^- + 2\tilde{\chi}_1^0$ and $\mu \to e\gamma$ is shown. Despite of the uncertainties from the neutrino sector, already the present experimental bound $Br(\mu \to e\gamma) < 1.2 \cdot 10^{-11}$ yields a stronger constraint on $\sigma(e^+e^- \to \tau^+\mu^- + 2\tilde{\chi}_1^0)$

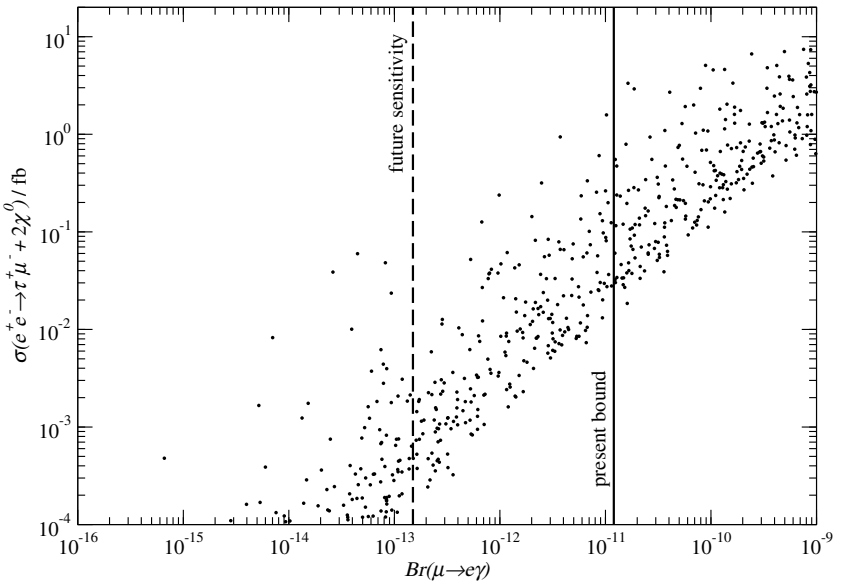

Figure 5.56: Correlation of $\sigma(e^+e^- \to \tau^+\mu^- + 2\tilde{\chi}_1^0)$ at $\sqrt{s} = 800$ GeV with $Br(\mu \to e\gamma)$ in scenario B.

than the one obtained from Fig. 5.55, making cross-sections larger than a few 10^{-1} fb at $\sqrt{s} = 800$ GeV very unlikely in model B. If this scenario is correct, non-observation of $\mu \to e\gamma$ at the new PSI experiment will exclude the observability of this channel at a LC. As a final remark we stress that in the channel $e^+e^- \to \mu^+e^- + 2\tilde{\chi}_1^0$ cross-sections of 1 fb are compatible with the present bounds, while no signal at the future PSI sensitivity would constrain this channel to less than 0.1 fb. However we want to emphasize again that these statements are very model dependent, and much bigger cross-sections are possible in general, as shown in section 5.4.3.2.

5.4.3.4 Summary and outlook

If superpartners are discovered at future colliders, we advocate the search for SUSY lepton flavour violation as a high priority topic of the experimental programme. At a LC, the most favourable signals are expected to come from the production and decay of sleptons and charginos. Considering only LFV in the $\mu - \tau$ sector, a case motivated by the large atmospheric neutrino mixing but more difficult to detect than LFV in the $e - \mu$ sector due to the presence of decaying taus, we have shown that the LC measurements may be complementary to searches for the radiative τ decay at the LHC. For example, a measurement of $Br(\tau \to \mu\gamma) = 10^{-8}$ at the LHC combined with the SLFV signal at a LC would point to $\sin 2\tilde{\theta}_{23} \geq 0.4$ and $\Delta\tilde{m}_{23} \simeq 0.3 - 1$ GeV.

In the context of the SUSY seesaw mechanism of neutrino mass generation, correlations between SLFV in radiative decays and slepton pair production have been found particularly interesting. For instance, in a given MSSM scenario the measurement of $\tau \to \mu\gamma$ at the LHC would imply a definite cross section for $e^+e^- \to \tau^+\mu^- + 2\tilde{\chi}_1^0$ at the LC. Assuming a reasonable set of MSSM benchmark scenarios and $Br(\tau \to \mu\gamma) = 10^{-8}$ and using the present neutrino data, one predicts $\sigma(e^+e^- \to \tau^+\mu^- + 2\tilde{\chi}_1^0)$ in the range 0.05 to 10 fb. However, the non-observation of $\mu \to e\gamma$ with a branching ratio of about 10^{-13} at the new PSI experiment would exclude the observability

of $\sigma(e^+e^- \to \tau^+\mu^- + 2\tilde{\chi}_1^0)$ at a linear collider. While the former correlation involving the same lepton flavours is insensitive to the uncertainties in the neutrino data (Fig. 5.55), the latter correlation is somewhat smeared out (Fig. 5.56). However, both types of correlations remain sensitive to the mSUGRA parameters and, hence, provide very useful tools for probing the origin of lepton flavour violation.

The complementarity of the LHC and LC (and of low-energy experiments) in the context of lepton flavour violation is far from being exhausted by the present study. Quantitative analyses of the impact of precise mass measurements at the LC on identifying the LFV decay chains at the LHC (and vice-versa) and other important features call for detailed Monte Carlo simulations which should be undertaken in the next round of the LHC/LC studies.

5.4.4 Detection difficulties for MSSM and other SUSY models for special boundary conditions

5.4.4.1 Anomaly-mediated boundary conditions — the degenerate wino-LSP scenario

One interesting limiting case of SUSY boundary conditions is loop-induced gaugino masses proportional to the respective renormalization group beta functions, as in Anomaly-Mediated SUSY breaking (AMSB) and the simplest moduli-dominated SUSY breaking models. In such models, the mass difference $\Delta m_{\tilde{\chi}_1} \equiv m_{\widetilde{\chi}_1^\pm} - m_{\widetilde{\chi}_1^0}$ is most typically very small. The phenomenology of $\widetilde{\chi}_1^\pm$ production and decay has been studied extensively in [466,467], and also in [468,469]. For $\Delta m_{\tilde{\chi}_1} < m_\pi$, as achievable in some models even after radiative corrections, the $\widetilde{\chi}_1^\pm$ may exit the detector, leading to an easily detected long-lived heavily-ionizing track (LHIT), or decay to a soft, but visible, e or μ track in the vertex detector and inner part of the tracker yielding a disappearing isolated track (DIT). For $\Delta m_{\tilde{\chi}_1}$ above, but close to m_π, the $\widetilde{\chi}_1^\pm$ decay to a soft $\pi^\pm$ may still have sufficient path length (including sufficient β) to leave a distinctive track in the vertex detector while also having low enough β (e.g. $\beta < 0.8$) to be highly-ionizing, yielding a "STUB" track; the decay π need not be visible. For somewhat larger $\Delta m_{\tilde{\chi}_1}$, the STUB is not visible, but the soft $\pi^\pm$ will be detected and may have a high impact parameter (HIP). For still larger $\Delta m_{\tilde{\chi}_1}$, the $\pi^\pm$ will simply be soft, but readily detected. Once $\Delta m_{\tilde{\chi}_1} \gtrsim 2-3$ GeV, the $\widetilde{\chi}_1^\pm$ decay products have significant energy. The most typical range for $\Delta m_{\tilde{\chi}_1}$ in the models studied is $\Delta m_{\tilde{\chi}_1} \in [200\ \mathrm{MeV}, 2\ \mathrm{GeV}]$.

Assuming that only the $\widetilde{\chi}_1^0$ and $\widetilde{\chi}_1^\pm$ are light, the primary LC SUSY processes are $\widetilde{\chi}_1^+\widetilde{\chi}_1^-$, $\gamma\widetilde{\chi}_1^+\widetilde{\chi}_1^-$, and $W^\mp\widetilde{\chi}_1^0\widetilde{\chi}_1^\pm$ production. Observable signatures are:

- $\Delta m_{\tilde{\chi}_1} < m_\pi$: the $\widetilde{\chi}_1^\pm$ yields a 'stable particle' LHIT and/or DIT track and is easily detected: $\widetilde{\chi}_1^+\widetilde{\chi}_1^-$ production will be easily seen.
- $m_\pi < \Delta m_{\tilde{\chi}_1} < 200$ MeV: the $\widetilde{\chi}_1^\pm$ decay yields a STUB track. Assuming small $\gamma\gamma$ background, no trigger would be needed; we denote such a signal by SNT.
- 200 MeV $< \Delta m_{\tilde{\chi}_1} < 2-3$ GeV: the $\widetilde{\chi}_1^\pm$ decay yields a soft, possibly HIP ($\Delta m_{\tilde{\chi}_1} <$ 1 GeV), π track. Backgrounds from $\gamma\gamma$-induced interactions are large. One must tag $\widetilde{\chi}_1^+\widetilde{\chi}_1^-$ production using $e^+e^- \to \gamma\widetilde{\chi}_1^+\widetilde{\chi}_1^-$ [470] or employ the more kinematically limited $W^\mp\widetilde{\chi}_1^0\widetilde{\chi}_1^\pm$ final state.
- $\Delta m_{\tilde{\chi}_1} > 2-3$ GeV: the $\widetilde{\chi}_1^\pm$ decay products are sufficiently energetic that $\gamma\gamma$ induced

backgrounds can be rejected to the extent necessary for mSUGRA-like mode detection of direct $e^+e^- \to \widetilde{\chi}_1^+\widetilde{\chi}_1^-$ production.
LEP experience suggests that these various signatures are all viable in their respective domains of validity for an appropriately designed detector. Current LEP2 ($\sqrt{s} \sim 200$ GeV) analyzes exclude $m_{\widetilde{\chi}_1^\pm} < \sqrt{s}/2$ in the 'stable' and 'standard' regions of $\Delta m_{\widetilde{\chi}_1}$ and $m_{\widetilde{\chi}_1^\pm} < 80$ GeV or so, assuming the $\widetilde{\nu}_e$ is relatively heavy, in the $m_\pi \leq \Delta m_{\widetilde{\chi}_1} \leq 2$ GeV region [471, 472]. The backgrounds to the 'stable' and γ-tag+soft-π signals are very small, and we assume they remain so at higher $\sqrt{s}$ with simple cuts. (For the γ-tag+soft-π signal, we require $p_T^\gamma > 10$ GeV, $10^\circ \leq \theta_\gamma \leq 170^\circ$.) The appropriate SUSY discovery mode(s) at a $\sqrt{s} = 600$ GeV LC are shown as a function of $\Delta m_{\widetilde{\chi}_1}$ and $m_{\widetilde{\chi}_1^\pm}$ in Fig. 5.57 [473]. We assume that 10 events are adequate to establish a signal. The rapid turn-on of $\widetilde{\chi}_1^+\widetilde{\chi}_1^-$ production allows one to probe almost to the kinematic limit [$m_{\widetilde{\chi}_1^\pm} \sim \sqrt{s}/2$ or $(\sqrt{s} - p_T^\gamma)/2$], although the totally iron-clad SNT and HIP signatures disappear at the largest $m_{\widetilde{\chi}_1^\pm}$ values due to inadequate boost. The SNT signature is somewhat suppressed at smaller $m_{\widetilde{\chi}_1^\pm}$ as more of the $\widetilde{\chi}_1^\pm$'s are boosted to $\beta > 0.8$. The discovery reach of the SNT and HIP channels is increased only slightly for $L = 50\text{fb}^{-1} \to 1\text{ab}^{-1}$. Since $\Delta m_{\widetilde{\chi}_1} \in [200\text{ MeV}, 2\text{ GeV}]$ is typical of models with loop-dominated gaugino masses, the γ-tag signals are of great importance.

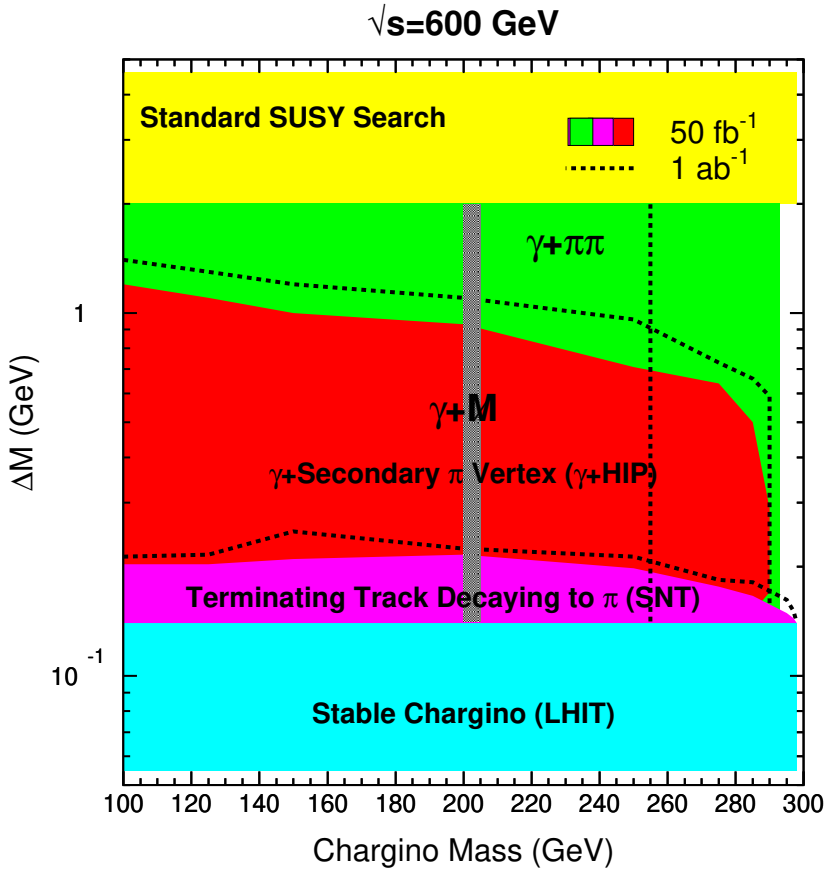

Figure 5.57: Discovery reach for the various modes described in the text as a function of $\Delta m_{\widetilde{\chi}_1}$ and $m_{\widetilde{\chi}_1^\pm}$ at a $\sqrt{s} = 600$ GeV LC; from [473].

Detector design is critical to observing the soft pion signatures. If the $\vec{B}$ field is too strong, soft pions will curl up before they can be detected/tracked. Then, the only signal $\gamma\widetilde{\chi}_1^+\widetilde{\chi}_1^-$ production yields $\gamma + \not{M}$, which has a large $\gamma\nu\overline{\nu}$ background. Fig. 5.57

illustrates the discovery reach. For $m_{\widetilde{\chi}_1^\pm} \lesssim 200$ GeV (260 GeV), $\not{M}$ cuts can give $S/B \geq 0.02$ and $S/\sqrt{B} \geq 5$ for $L = 50\text{fb}^{-1}$ ($\sim 1\text{ab}^{-1}$). The $\ell^\mp + \not{M}$ final state from $W^\mp \widetilde{\chi}_1^0 \widetilde{\chi}_1^\pm$ production will provide an alternative signal with similar reach in $m_{\widetilde{\chi}_1^\pm}$; the only SM background is single $W \to \ell\nu$ production with the ℓ lost down the beam pipe.

Let us now consider the prospects for exploring the degenerate wino-LSP scenario at the Tevatron and LHC. At hadron colliders, typical signatures of mSUGRA are tri–lepton events from neutralino–chargino production, like–sign di–leptons from gluino pair production, and multijets+$\not{E}_T$ from squark and gluino production. The tri–lepton signal from $\widetilde{\chi}_1^\pm \widetilde{\chi}_2^0$ production and the like–sign di–lepton signal from $\widetilde{g}\widetilde{g}$ production are both suppressed when $\Delta m_{\tilde{\chi}_1}$ is small by the softness of the leptons coming from the $\widetilde{\chi}_1^\pm$ decay(s). For the $M_2 < M_1 << |\mu|$ AMSB boundary conditions, the tri–lepton signal is further diminished by the suppression of the $\widetilde{\chi}_1^\pm \widetilde{\chi}_2^0$ cross section. For small enough $\Delta m_{\tilde{\chi}_1}$, the LHIT and DIT 'stable'-chargino signals will be viable [467, 473]. But, for larger $\Delta m_{\tilde{\chi}_1}$, direct observation of the $\widetilde{\chi}_1^\pm$ becomes more challenging. In this case, assuming that the $\widetilde{g}$ is light enough, the most obvious signal for SUSY in degenerate models is jet(s) plus missing energy. In one AMSB study, it was found that $\widetilde{g}\widetilde{g}$ production at the LHC will be sufficiently abundant that jets + $\not{E}_T$ will probe up to $m_{\widetilde{g}} \sim 1.7$ TeV (1 TeV) for $L = 300\text{fb}^{-1}$ ($L = 30\text{fb}^{-1}$), assuming that squarks and sleptons are too heavy to provide useful signals [474, 475]. Using $m_{\widetilde{g}} \sim 7 m_{\widetilde{\chi}_1^\pm}$, $m_{\widetilde{g}} \sim 1.7$ TeV is equivalent to $m_{\widetilde{\chi}_1^\pm} \sim 250$ GeV, the effective reach of a $\sqrt{s} = 500$ GeV LC. A more extensive reach for the jets + $\not{E}_T$ channel at the LHC, $m_{\widetilde{g}} \sim 2.1 \div 2.5$ TeV, was found in [476].

An important question is whether direct detection of the charginos at the LHC is possible when $\Delta m_{\tilde{\chi}_1}$ is large enough that the $\widetilde{\chi}_1^\pm$ decay is prompt, but small enough that the (single) charged particle from its decay (a charged pion or lepton) is quite soft. Direct detection might prove crucial to unambiguously showing that the model is truly AMSB in character. The most difficult backgrounds to the soft (but isolated) $\pi^\pm$ tracks in this case are those arising from events containing the baryons Σ^+, Σ^-, Ξ, and Ω, all of which have decays in which a single soft pion emerges [467]. One might hope to remove such backgrounds by requiring the soft pion track(s) to be sufficiently isolated due to the fact that the normal hadrons above are not produced in isolation. So even if they decay to an isolated soft pion, there will be hadrons that are nearby in ΔR that will be visible. In [476], this and the alternative possibility of detecting the soft isolated $\ell^\pm$ from the chargino decay are pursued. Aside from appropriate isolation requirements for the leptons, a critical ingredient is the use of the Cambridge m_{TX} variables [377] which provide sensitivity to $m_{\widetilde{\chi}_1^\pm}$ when a $\widetilde{\chi}_1^+ \widetilde{\chi}_1^-$ pair is produced through looking at distributions in $m_{TX} - m_{\widetilde{\chi}_1^0}$. For this technique, it is necessary that $m_{\widetilde{\chi}_1^0}$ be known (from kinematic endpoints) and that the bulk of the $\widetilde{\chi}_1^\pm$ come from the two-body decay chain sequence $\widetilde{q} \to q\widetilde{\chi}_1^\pm \to \widetilde{\chi}_1^0 e\nu_e q$ or similar. As noted, squarks are not guaranteed to be sufficiently light to be abundantly produced in the AMSB models. But, assuming they are, [476] concludes that the isolation + $m_{TX} - m_{\widetilde{\chi}_1^0}$ procedures can determine the presence and mass of the $\widetilde{\chi}_1^\pm$ for $\Delta m_{\tilde{\chi}_1} \gtrsim 700$ MeV. For $\Delta m_{\tilde{\chi}_1} < 200$ MeV, the HIT, DIT, STUB, HIP, ...signatures make it easy to detect the $\widetilde{\chi}_1^\pm$. In the $200 < \Delta m_{\tilde{\chi}_1} < 700$ GeV part of parameter space, which unfortunately is somewhat preferred, techniques for direct $\widetilde{\chi}_1^\pm$ detection have not yet been developed. In this part of parameter space, the LHC is needed to see the gluino and squark

signatures while the LC is needed to directly observed the $\widetilde{\chi}_1^\pm$ and determine its mass.

5.4.4.2 Baryonic R-parity violation coupled with the degenerate wino-LSP scenario

If one wishes to construct a "worst case" scenario for the hadron colliders, an obvious approach is to assume: (1) a small $\Delta m_{\tilde{\chi}_1}$ AMSB (or other) scenario with $200\ \mathrm{MeV} \lesssim \Delta m_{\tilde{\chi}_1} \lesssim 1\ \mathrm{GeV}$; and (2) baryonic R-parity violation in which the $\widetilde{\chi}_1^0$ decays to (semi-soft) jets. A very incomplete consideration of this kind of scenario was given for the Tevatron and the LC in [478] (see also the earlier discussion in [477]). The summary below is based on this reference.

First, because $200\ \mathrm{MeV} \lesssim \Delta m_{\tilde{\chi}_1}$, the $\widetilde{\chi}_1^\pm$ decay will be prompt and there will be no HIT, DIT, STUB, HIP, ... type signatures. Second, because $\Delta m_{\tilde{\chi}_1} \lesssim 1\ \mathrm{GeV}$, the leptons (if significant in the $\widetilde{\chi}_1^\pm$ decays at all) will be very soft, making it impossible to look for either the like-sign dilepton signal from gluino or squark pair production or the tri-lepton signal from $\widetilde{\chi}_1^\pm \widetilde{\chi}_2^0$ production.

Other opportunities for SUSY detection depend in detail upon the $\widetilde{\chi}_1^0 \to 3j$ decay scenario. The rather strong upper bound on the baryonic R-parity violating coupling λ''_{usd} means that one (or more) of the ubd, ubs, csd, cbd, cbs channels will most likely dominate $\widetilde{\chi}_1^0$ decay. All of these contain at least one heavy quark. Since SUSY pair production events contain at least two $\widetilde{\chi}_1^0$'s, we can then use double-tagging to reduce the background relative to the signal. For all but the cds decay channel, at least two of the jets in the final state will be b-jets. If cds decays dominate, we would have two c-jets. Since c-tagging will have lower efficiency than b-tagging, dominance of $\widetilde{\chi}_1^0$ decays by the cds channel results in the most difficult scenario for supersymmetry detection. An exception is the case in which all the λ'' are so small that the $\widetilde{\chi}_1^0$ decay is not prompt. If the $\widetilde{\chi}_1^0$ is long-lived, then one reverts to the R-parity conserving signals of the small $\Delta m_{\tilde{\chi}_1}$ case. If the $\widetilde{\chi}_1^0$ decays within the detector after a substantial path length, the sudden appearance of three jets inside the detector will provide a clear signature for SUSY. The most difficult case is when the $\widetilde{\chi}_1^0 \to cds$ decay is prompt.

In this case, since the $\widetilde{\chi}_1^0$ decays promptly to jets, there will also be no missing energy signal for gluino/squark production. In short, the only possible signal will be an excess of jets (some of which can be tagged with modest efficiency) due to the two $\widetilde{\chi}_1^0 \to cds$ decays. In addition, in the AMSB scenario (for which $m_{\widetilde{g}} \sim 3m_{\widetilde{\chi}_1^\pm} \sim m_{\widetilde{\chi}_1^0}$) each event will typically have a number of hard jets (from the $\widetilde{g} \to q'\overline{q}\widetilde{\chi}_1^\pm$ decays) accompanied by six jets from the $\widetilde{\chi}_1^0$ decays. However, since some of the jets from $\widetilde{\chi}_1^0$ decay will be quite soft (unless $m_{\widetilde{\chi}_1^0}$ is quite large) the excess of jets over standard QCD will not be that pronounced and c tagging will not be very efficient. To date, there is no convincing study indicating that SUSY detection at the Tevatron or LHC will be possible for this very difficult scenario when $m_{\widetilde{g}}$ is sufficiently large that the $\widetilde{g}\widetilde{g}$ production rate is not large. In other models with small $\Delta m_{\tilde{\chi}_1}$, $m_{\widetilde{g}}$ can be quite a bit smaller and even of order $m_{\widetilde{\chi}_1^\pm}$. In this case, one loses the extra jets from $\widetilde{g}$ decay, but the $\widetilde{g}\widetilde{g}$ production rate is quite large and its detection at the LHC is fairly likely after cuts requiring a large number of jets and several c tags.

Thus, depending upon the exact model, the LC could be absolutely crucial for SUSY detection. In fact, detection of $e^+e^- \to \widetilde{\chi}_1^0\widetilde{\chi}_1^0 \to 6j$ would be completely straightforward at the LC and would provide a dramatic confirmation of SUSY as well as bary-

onic R-parity violation. In addition, the $e^+e^- \to \widetilde{\chi}_1^+\widetilde{\chi}_1^- \to \ell^+\ell^- + 6j$ signal would almost certainly be observable and allow an accurate determination of $\Delta m_{\widetilde{\chi}_1}$. Once $m_{\widetilde{\chi}_1^0} \sim m_{\widetilde{\chi}_1^\pm}$ is known from the LC data, it might be possible to return to the LHC data and detect the gluino/squark signals that would have remained hidden without this knowledge.

If baryonic R-parity violation is present, a very important goal will be to measure the relevant λ''. There are two possibilities at a hadron collider for directly determining λ''. If λ'' is large, RPV-induced single squark production cross sections are also typically substantial, and, if a signal can be isolated, the cross section size gives a measure of λ''. If λ'' is small, the decay path length for the $\widetilde{\chi}_1^0$ might be observable and would again provide a measure of λ''. However, rough estimates indicate that there is a region of intermediate λ'' at higher $m_{\widetilde{q}_R}$ for which neither $c\tau(\widetilde{\chi}_1^0)$ nor $\sigma(\widetilde{q}_R)$ will be measurable. In this region, determination of λ'' would only be possible if an RPV decay mode of the $\widetilde{\chi}_1^\pm$ is competitive with its standard SUSY decay modes and these can be separated from one another. The relative size of the branching ratios would then provide a measure of λ''. At an e^+e^- collider, if λ'' is small it could again be measured via the $\widetilde{\chi}_1^0$ decay length or the relative branching ratio for RPV decays versus normal SUSY decays. If λ'' is large, these techniques would not be available and in addition there are no sources of quarks or antiquarks as needed for squark production via baryonic RPV couplings.

In short, there is a complicated model-dependent interplay between the abilities of the LHC and LC in models with small $\Delta m_{\widetilde{\chi}_1}$. If there is no sign of normal SUSY events at the LHC, models having baryonic R-parity violation and small $\Delta m_{\widetilde{\chi}_1}$ would provide a possible explanation that might only be tested at the LC.

5.4.4.3 The gluino-LSP scenario

It is possible to write down SUSY models in which the gluino is the LSP [466,479,480]. Other motivations for a light gluino include the ability to unify couplings for $\alpha_s \sim 0.12$ [481] and a decreased level of fine tuning [482].

For a gluino-LSP, the detection of SUSY is quite different than in the usual $\widetilde{\chi}_1^0$ LSP scenarios. Techniques have been developed [466, 483] for detecting $\widetilde{g}\widetilde{g}$ pair production at the Tevatron and LHC. They involve signatures related to a very heavy, possibly neutral, strongly interacting object moving through detectors composed of much lighter objects. By a careful examination of these signatures, it is possible to conclude [466, 483] (by combining Run I CDF/D0 data with Z pole data from LEP) that $m_{\widetilde{g}} \lesssim 130$ GeV is excluded except, possibly, for a small interval of $m_{\widetilde{g}} \sim 30$ GeV. The same studies indicate that the range of sensitivity to $m_{\widetilde{g}}$ will increase dramatically at the LHC, with detection being possible up to $m_{\widetilde{g}} \sim 1$ TeV.

In contrast, the discovery reach of the LC will be strictly limited by $\sqrt{s}$. By definition of the scenario, the absolutely minimal energy required is $\sqrt{s} > 2m_{\widetilde{g}}$. But, $e^+e^- \to \widetilde{g}\widetilde{g}$ is mediated by one-loop-induced $\gamma\widetilde{g}\widetilde{g}$ and $Z\widetilde{g}\widetilde{g}$ couplings where the loop contains one or two squarks. The virtual photon exchange diagrams vanish if (for any given flavor q) we have $m_{\widetilde{q}_L} = m_{\widetilde{q}_R}$. The virtual Z exchange diagrams vanish if there is mass degeneracy for each quark isospin doublet, i.e. if $m_d = m_u, \ldots$, and if there is mass degeneracy also in each squark isospin doublet, i.e. if $m_{\widetilde{d}_1} = m_{\widetilde{d}_2} = m_{\widetilde{u}_1} = m_{\widetilde{u}_2}$, ... Thus, given that for the first two families the quarks have small and not very

different masses while FCNC considerations require rather degenerate squarks, only loops involving top and bottom squarks and quarks contribute significantly. Still, despite the fact that $m_t >> m_b$, if there is only small splitting between the $\widetilde{t}_L$ and $\widetilde{t}_R$ and if the squark mixing is also small, gluino pair production in e^+e^- collisions will be hard to observe, even with $L = 1000\text{fb}^{-1}$ [484, 485].

It is also interesting to consider cross sections for $\widetilde{g}\widetilde{g}$ production at a γC [486]. The process $\gamma\gamma \to \widetilde{g}\widetilde{g}$ is mediated by box diagrams containing one, two or three squarks. Other contributions to $\widetilde{g}\widetilde{g}$ production arise from resolved photons. For a given value of $m_{\widetilde{g}}$, the optimum machine energy (giving the largest cross section) is typically $\sqrt{s} \sim 3m_{\widetilde{g}}$. For this optimal choice, $\sigma(e^-e^- \to \gamma\gamma \to \widetilde{g}\widetilde{g})$ falls rapidly with increasing squark mass and with decreasing $m_{\widetilde{g}}$. As an example, if $m_{\widetilde{g}} \sim 200$ GeV and $\sqrt{s_{ee}} \sim 600$ GeV one finds $\sigma(e^-e^- \to \gamma\gamma \to \widetilde{g}\widetilde{g}) \sim 0.1$fb (0.005fb) for a general squark mass scale of 800 GeV (1.5 TeV). For $m_{\widetilde{g}} \sim 150$ GeV and the optimal choice of $\sqrt{s_{ee}} \sim 500$ GeV, the cross sections for these two squark mass scales will be about a factor of three smaller. Thus, there is no guarantee that $\widetilde{g}\widetilde{g}$ production will be seen at a γC facility.

A final LC possibility is the tree-level process $e^+e^- \to q\overline{q}\widetilde{g}\widetilde{g}$ (see, for example, [466]). However, this has a very limited kinematic reach. For example, $\sum_q \sigma(e^+e^- \to q\overline{q}\widetilde{g}\widetilde{g}) < 0.01$fb for $m_{\widetilde{g}} > 140$ GeV at a $\sqrt{s} = 500$ GeV LC.

In short, while there are many scenarios for which an LC with $\sqrt{s} \lesssim 1$ TeV and/or the associated γC will allow $\widetilde{g}$ detection, there are also many scenarios for which they will not.

Thus, if the gluino is the LSP and if squarks are considerably heavier (as typical for existing models), it is conceivable that only the LHC would be capable of detecting SUSY until the $\sqrt{s}$ of the LC is increased well above the initial ~ 500 GeV first stage value.

5.5 Determination of mSUGRA parameters and discrimination between SUSY breaking scenarios

5.5.1 Complementarity of LHC and Linear Collider measurements of slepton and lighter neutralino masses

5.5.1.1 Introduction

It has recently become clear that measurements of the masses of supersymmetric particles (sparticles) carried out at the LHC and at a $\sqrt{s} \geq 500$ GeV linear collider will in many cases be complementary. The reason for this is that although the LHC will provide the greater search reach for SUSY particles, only the LC will be able to provide accurate ($\lesssim 1\%$) measurements of the absolute masses of produced sparticles. LHC experiments may be able to measure combinations of masses of heavier sparticles such as $\tilde{q}_L$ [89, 523], but these can only be used to derive accurate absolute mass values with LC input regarding absolute masses of lighter sparticles (lighter neutralinos or charged sleptons).

While this will be the case for many models, it is clear that there may also be models where kinematics will require that a combination of LC and LHC data be used to

measure even the masses of the lighter sparticles. This note seeks to identify and study such models occurring within the mSUGRA framework.

5.5.1.2 Parameter Space Scan

In this study we have chosen to work within the minimal Supergravity (mSUGRA) framework [524] used in many previous studies of LHC physics capabilities [89]. In order to map out representative regions of parameter space in which LC and LHC sparticle mass measurements are complementary a scan of $m_0 - m_{1/2}$ parameter space was performed using `isajet 7.51` [525] with $A_0 = 0$, $\tan(\beta) = 10$ and $\mu > 0$. At each point in parameter space the σ.BR for LHC events producing $\tilde{\chi}_2^0$ decaying to $\tilde{\chi}_1^0$ and two leptons was calculated for two-body decays proceeding through an intermediate $\tilde{l}_L$ or $\tilde{l}_R$:

$$\tilde{\chi}_2^0 \to \tilde{l}_L^{+(-)} l^{-(+)} \to \tilde{\chi}_1^0 l^+ l^-, \tag{5.102}$$

$$\tilde{\chi}_2^0 \to \tilde{l}_R^{+(-)} l^{-(+)} \to \tilde{\chi}_1^0 l^+ l^-, \tag{5.103}$$

and three-body direct (*i.e.* not through Z^0) decays:

$$\tilde{\chi}_2^0 \to \tilde{\chi}_1^0 l^+ l^-. \tag{5.104}$$

Fig. 5.58 shows a plot of the mSUGRA $m_0 - m_{1/2}$ plane with full contours indicating constant values of σ.BR = 0.02 pb for $\tilde{\chi}_2^0$ decays direct to $\tilde{\chi}_1^0$ (black), through an intermediate $\tilde{l}_R$ (blue) or an intermediate $\tilde{l}_L$ (red). Also shown (dashed) are contours of constant $m(\tilde{\chi}_2^0) + m(\tilde{\chi}_1^0)$ = 500 GeV (black), $m(\tilde{l}_R)$ = 250 GeV (blue) and $m(\tilde{l}_L)$ = 250 GeV (red). These dashed contours correspond to the kinematics limited sensitivities of a $\sqrt{s}$ = 500 GeV linear collider to the $e^+e^- \to \tilde{\chi}_2^0\tilde{\chi}_1^0$, $e^+e^- \to \tilde{l}_R^+\tilde{l}_R^-$ and $e^+e^- \to \tilde{l}_L^+\tilde{l}_L^-$ discovery channels respectively. It is expected that in the event of a SUSY signal being observed in the $e^+e^- \to \tilde{l}_R^+\tilde{l}_R^-$ or $e^+e^- \to \tilde{l}_L^+\tilde{l}_L^-$ channels at a LC then the masses of the produced sparticles will be measured to high accuracy [57]. In the case where $e^+e^- \to \tilde{\chi}_2^0\tilde{\chi}_1^0$ is kinematically accessible then accurate measurements of the $\tilde{\chi}_2^0$ and $\tilde{\chi}_1^0$ masses can be performed using threshold scans and dilepton invariant mass edges provided that slepton pair production (the dominant source of SUSY background) does not occur [526]. If slepton pair production does occur then only the threshold scan can be used, constraining $m(\tilde{\chi}_2^0) + m(\tilde{\chi}_1^0)$.

Given the extreme accuracy of LC measurements we may now ask whether there are any regions of the $m_0 - m_{1/2}$ plane in Fig. 5.58 where LHC data can be used *in conjunction* with LC data to give more precise mass bounds. Consider first the case where $\tilde{\chi}_2^0 \to \tilde{l}_R^{+(-)} l^{-(+)} \to \tilde{\chi}_1^0 l^+ l^-$ decays are observed at the LHC. In the majority of the parameter space in Fig. 5.58 where this occurs the LC will also observe $e^+e^- \to \tilde{l}_R^+\tilde{l}_R^-$ *and* $e^+e^- \to \tilde{\chi}_2^0\tilde{\chi}_1^0$ (labelled '3' in blue). In this case the LC will measure $m(\tilde{\chi}_1^0)$ and $m(\tilde{l}_R)$ from the dislepton channel and hence $m(\tilde{\chi}_2^0)$ from an $e^+e^- \to \tilde{\chi}_2^0\tilde{\chi}_1^0$ threshold scan, with no input from the LHC. There is also a region (labelled '4') where a LC will see nothing and here there can be no input from LC data. In regions '1' and '2' (hatched) however there is indeed complementarity between LHC and LC data. In region '1' the LC measures $m(\tilde{\chi}_2^0)$ and $m(\tilde{\chi}_1^0)$ which in turn allows the LHC to measure $m(\tilde{l}_R)$. In region '2' the LC measures $m(\tilde{l}_R)$ and $m(\tilde{\chi}_1^0)$ enabling the LHC to

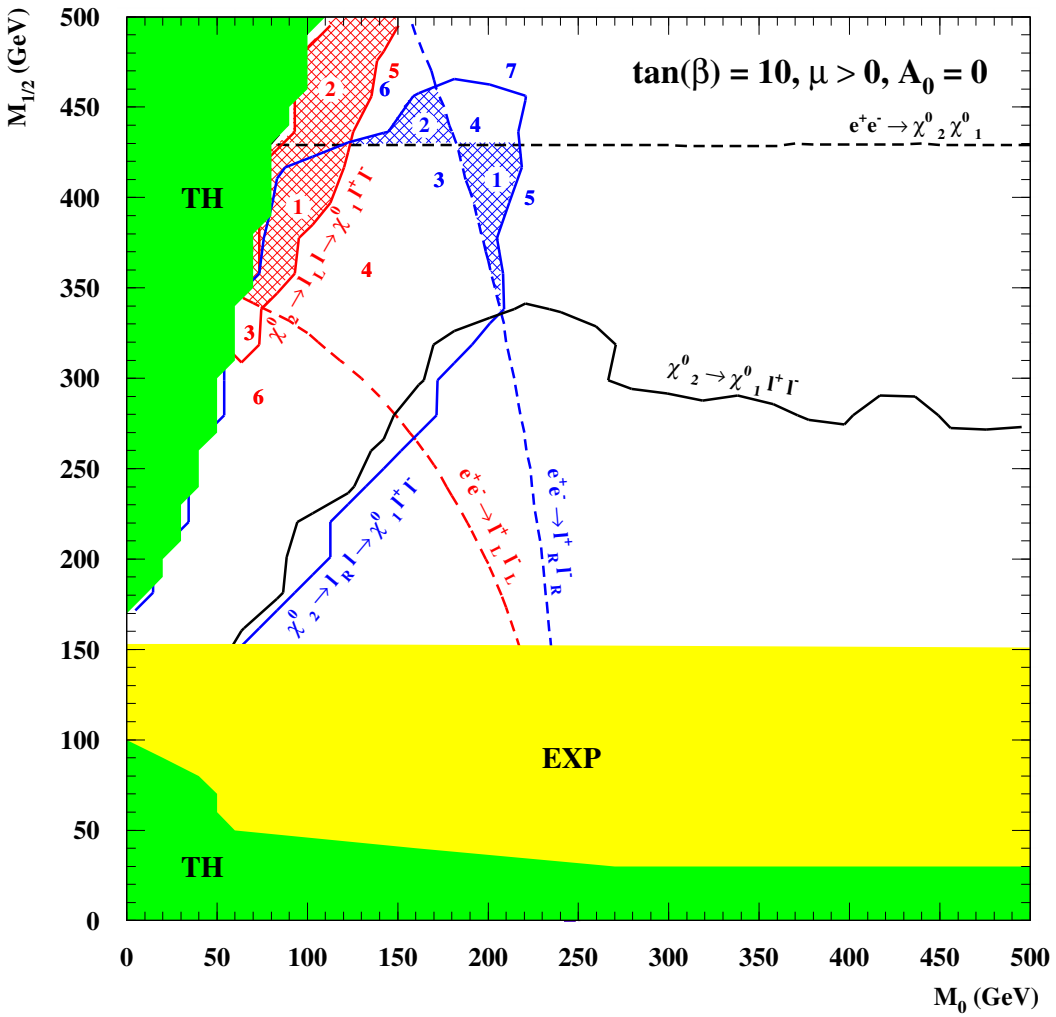

Figure 5.58: *Contours of σ.BR = 0.02 pb for $\tilde{\chi}_2^0$ decays in LHC events (full contours). Contours correspond to $\tilde{\chi}_2^0$ decays direct to $\tilde{\chi}_1^0$ (black), through an intermediate $\tilde{l}_R$ (blue) or an intermediate $\tilde{l}_L$ (red). Also shown (dashed) are contours of constant $m(\tilde{\chi}_2^0)$ = 250 GeV (black), $m(\tilde{l}_R)$ = 250 GeV (blue) and $m(\tilde{l}_L)$ = 250 GeV (red). The full green regions are excluded by theory, the full yellow region by experimental bounds from LEP and elsewhere. Small blue and red numbers refer to regions decribed in the text.*

measure $m(\tilde{\chi}_2^0)$. It should be noted that a LC could use the dilepton edge technique [89] to gain independent sensitivity to $m(\tilde{l}_R)$ in region '1', however in this case it is not clear that there would not still be an advantage to use of the high statistics LHC $\tilde{\chi}_2^0$ sample. In regions '5' and '6' the LHC can measure nothing as no dilepton signature is observed (assuming an arbitrary 0.02 pb observation threshold) and only one channel is observed in LC data. In region '7' no dilepton measurement channels are open either at LHC or LC (although the LHC will still discover SUSY [527]).

Consider next the case where $\tilde{\chi}_2^0 \to \tilde{l}_L^{+(-)} l^{-(+)} \to \tilde{\chi}_1^0 l^+ l^-$ decays are observed at the

LHC (red region). In region '1' (hatched red) LHC and LC data is complementary because the LC measures $m(\tilde{\chi}_2^0)+m(\tilde{\chi}_1^0)$ from an $e^+e^- \to \tilde{\chi}_2^0\tilde{\chi}_1^0$ threshold scan providing input to LHC measurements of $m(\tilde{l}_L)$, $m(\tilde{\chi}_2^0)$ and $m(\tilde{\chi}_1^0)$ combinations. Note that here constraints on $m(\tilde{l}_L)$ from LC dilepton edge measurements would be very difficult due to dislepton SUSY background. In region '2' (hatched red) the LC observes neither the $e^+e^- \to \tilde{l}_L^+\tilde{l}_L^-$ channel nor the $e^+e^- \to \tilde{\chi}_2^0\tilde{\chi}_1^0$ channel but can still help the LHC measure mass combinations involving $m(\tilde{l}_L)$ and $m(\tilde{\chi}_2^0)$ by measuring $m(\tilde{\chi}_1^0)$ using $e^+e^- \to \tilde{l}_R^+\tilde{l}_R^-$. In region '3' the LC can measure $m(\tilde{\chi}_1^0)$ and $m(\tilde{l}_L)$ from $e^+e^- \to \tilde{l}_L^+\tilde{l}_L^-$ and hence $m(\tilde{\chi}_2^0)$ from a $e^+e^- \to \tilde{\chi}_2^0\tilde{\chi}_1^0$ threshold scan, with no LHC input, giving no complementarity. In regions '4', '5' and '6' the LC observes two channels, one channel or three channels respectively but the LHC sees no $\tilde{l}_L$ mediated $\tilde{\chi}_2^0$ decay. Again, in a limited region of parameter space useful combined measurements significantly improving measurement accuracy can be carried out.

Consider finally the case where $\tilde{\chi}_2^0 \to \tilde{\chi}_1^0 l^+ l^-$ decays are observed at the LHC (black). This region lies entirely within the LC reach in the $e^+e^- \to \tilde{\chi}_2^0\tilde{\chi}_1^0$ channel and also the $e^+e^- \to \tilde{\chi}_2^0\tilde{\chi}_2^0$ and $e^+e^- \to \tilde{\chi}_1^+\tilde{\chi}_1^-$ channels (not shown). The LC will therefore be able to measure both $m(\tilde{\chi}_2^0)$ and $m(\tilde{\chi}_1^0)$ without reference to LHC data and no additional input from the LHC will be required.

These results illustrate the scope for combined LC + LHC sparticle mass measurements for charged sleptons and lighter neutralinos. The regions of parameter space where such an approach is applicable are admittedly rather limited but it must be remembered that these results were obtained using mSUGRA models with fixed values of tan(β), A_0 and sign(μ). While it is to be expected that similar behaviour will be exhibited for other values of these parameters (although possibly modified at high tan(β) to take into account the large branching ratios to $\tilde{\tau}_1$ and $\tilde{\tau}_2$) very different phenomenology may occur in less constrained SUSY models. In these models combination of results is still likely to be appropriate in regions where the LHC observes two-body $\tilde{\chi}_2^0$ decay processes and the LC observes only $e^+e^- \to \tilde{\chi}_2^0\tilde{\chi}_1^0$ or $e^+e^- \to \tilde{l}^+\tilde{l}^-$ (but not both) however the size of these regions may be considerably enlarged. Further regions of interest may also arise where the LHC observes three-body $\tilde{\chi}_2^0$ decays and the LC observes only $e^+e^- \to \tilde{l}^+\tilde{l}^-$ thereby providing input on $m(\tilde{\chi}_1^0)$. Finally, in less constrained models with different relationships between sparticle (*e.g.* gaugino) masses it may be advantageous to make use of LC $\tilde{\chi}_1^0$ mass measurements provided by *e.g.* chargino or sneutrino decays.

5.5.1.3 Conclusions

The mSUGRA $m_0 - m_{1/2}$ plane has been mapped to identify regions in which combination of LHC and linear collider data can significantly improve the accuracy of lighter neutralino and charged slepton mass measurements.

5.5.2 Discriminating SUSY breaking scenarios

5.5.2.1 Introduction

Supersymmetric (SUSY) phenomenology is notoriously complicated, and many studies of experimental measurement capabilities have focused on individual points in

the parameter space (see, for example, SUSY studies in this document). Here, we want to examine what is required to discriminate between different SUSY breaking scenarios, when the parameters within each are allowed to vary (as long as they agree with current experimental data). By this we hope to provide *guaranteed* discrimination, whatever the parameter point, provided measurement accuracies are low enough. The results we present here are updated versions of the ones in ref. [528], using a more up-to-date spectrum predictor: `SOFTSUSY1.71` [499].

Given that we need to scan over parameters in the scenarios we will consider, a detailed empirically-based analysis is unfeasible. The existence of SUSY backgrounds and signals depend crucially upon the part of MSSM parameter space one examines, thus it would be necessary to perform a separate study for each point in parameter space. A more tractable analysis is followed: we try to find simple functions of sparticle masses that may be used to discriminate between some test scenarios. In this initial study, we examine sparticle mass *ratios*.

The three scenarios we choose to study are inspired by type I string models [529]: (1) String scale at the GUT scale $M_{GUT} \sim O(10^{16})$ GeV, defined by the scale of electroweak gauge unification $g_1(M_{GUT}) = g_2(M_{GUT})$. (2) Intermediate string scale ($M_I = 10^{11}$ GeV) with extra leptons to achieve gauge coupling unification at M_I, which we will refer to as *early unification* (EU) and (3) intermediate string scale ($M_I = 10^{11}$ GeV) with *mirage unification* [530] at M_I. In scenarios (1) and (3), we assume that the low-energy effective field theory corresponds to the R-parity conserving MSSM. In order to keep the volume of SUSY breaking parameter space manageable, we will here look only at the dilaton dominated limit of scenarios (1)-(3).

5.5.2.2 Discriminators

As advertised above, we use sparticle mass ratios to discriminate between models. Ratios rather than absolute masses are used in order to factor out dependence upon the overall SUSY mass scale. Fig. 5.59a shows the idea: we expect each model to inhabit some closed 2-dimensional surface in the ratio space $\{R_1, R_2\}$. The "distance" vector between the two regions is defined as the vector $(\Delta R_1, \Delta R_2)$ where $\sqrt{\Delta R_1^2 + \Delta R_2^2}$, is minimised. It can only be defined when separation is achieved, ie where the regions do not overlap. The distance vector is therefore the measurement accuracy of the ratios $R_{1,2}$ required to discriminate between the two models *in all cases*. In practice, we populate the regions with a random scan over parameter space that satisfy experimental constraints and do not have sparticles heavier than a few TeV (see ref. [528] for details).

We achieve separation, as shown in figure 5.59b. The distance ratios here are shown to be $(\Delta[m_{\tilde{g}}/m_{\tilde{q}_{avq}}], \Delta[m_{\tilde{e}_L}/m_{\tilde{e}_R}]) = (0.03, 0.04)$ to discriminate EU and mirage scenarios, $(0.02, 0.07)$ to discriminate the EU and GUT scenarios and $(0.05, 0.03)$ to discriminate between the GUT and mirage scenarios, in their respective dilaton-dominated limits. $m_{\tilde{q}_{avg}}$ is an average over the first two generations' squark masses.

5.5.2.3 Conclusions

We have examined three test SUSY breaking scenarios in the MSSM, finding discriminating ratios of sparticle masses. Simple combinations of two ratios can discriminate

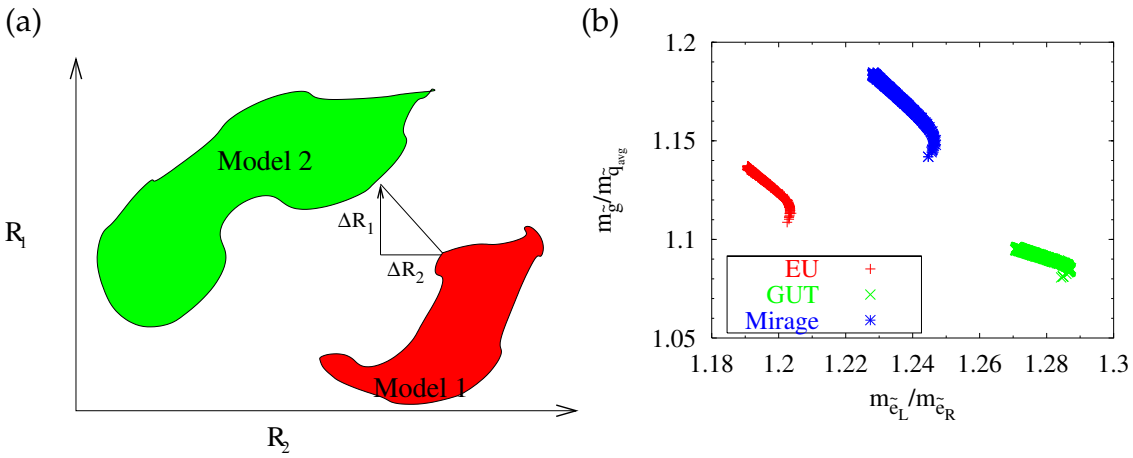

Figure 5.59: Discriminating ratios and parameter scans: (a) schematic, (b) results of the scans for the three scenarios considered.

all three scenarios. The percent-level accuracies required indicate a rough level for the desired accuracy upon sparticle masses. The combined experimental and theoretical [520] errors should therefore not be larger than the percent-level in order to achieve discrimination. 3% accuracies on the measurements of $m_{\tilde{e}_L}/m_{\tilde{e}_R}$ would be required in order to always discriminate between the scenarios. Such a precision should be readily available at a future LC facility that has polarised beams. We require maximum errors of 2% on $m_{\tilde{g}}/m_{\tilde{q}_{avq}}$ for discrimination. At the LHC, errors upon $m_{\tilde{g}}$ or $m_{\tilde{q}_{av}}$ are expected to be of order 10%, too high for our purposes. At a 500 GeV LC on the other hand, it is difficult to produce squarks and gluinos because they are typically kinematically inaccessible. However a few-percent uncertainty upon the ratio might be feasible if LC information on slepton and weak gaugino masses is fed into an LHC analysis. New techniques to study discrimination in models which depart from dilaton domination are currently underway [531].

5.5.3 Gravitino and goldstino at colliders

Introduction

The discovery of supersymmetry at the Tevatron, the LHC or a future Linear Collider would raise the question how supersymmetry is realized in nature. Clearly, supersymmetry is broken. Spontaneously broken global supersymmetry would predict the existence of a spin-1/2 goldstino (χ) whereas the theoretically favoured case of local supersymmetry requires a massive spin-3/2 gravitino ($\psi_{3/2}$).

In a recent paper [532] we have studied how a massive gravitino, if it is the lightest superparticle (LSP), may be discovered in decays of $\widetilde{\tau}$, the scalar τ lepton, which is naturally the next-to-lightest superparticle (NSP). The determination of gravitino mass and spin appears feasible for gravitino masses in the range from about $1\,\mathrm{GeV}$ to $100\,\mathrm{GeV}$. As we shall discuss in this note, evidence for the characteristic couplings of a pseudo-goldstino, which corresponds to the spin-1/2 part of the gravitino, can be obtained even for masses much smaller than $1\,\mathrm{GeV}$.

The gravitino mass depends on the mechanism of supersymmetry breaking. It can be of the same order as other superparticle masses, like in gaugino mediation [533]

or gravity mediation [534]. But it might also be much smaller as in gauge mediation scenarios [535]. As LSP, the gravitino is an attractive dark matter candidate [536].

The $\widetilde{\tau}$ NSP has generally a long lifetime because of the small, Planck scale suppressed coupling to the gravitino LSP. The production of charged long-lived heavy particles at colliders is an exciting possibility [537]. They can be directly produced in pairs or in cascade decays of heavier superparticles. In the context of models with gauge mediated supersymmetry breaking the production of slepton NSPs has previously studied for the Tevatron [538], for the LHC [539] and for a Linear Collider [540].

The dominant $\widetilde{\tau}$ NSP decay channel is $\widetilde{\tau} \to \tau +$ missing energy. In the following we shall study how to identify the gravitino or goldstino as carrier of the missing energy. First, one will measure the NSP lifetime. Since the gravitino couplings are fixed by symmetry, the NSP lifetime is predicted by supergravity given the gravitino mass, which can be inferred from kinematics. Second, one can make use of the 3-body NSP decay $\widetilde{\tau} \to \tau + \gamma + X$ where $X = \psi_{3/2}$ or $X = \chi$. The angular and energy distributions and the polarizations of the final state photon and lepton carry the information on the spin and couplings of gravitino or goldstino.

For gravitino masses in the range from about $10\,\mathrm{keV}$ to $100\,\mathrm{GeV}$, the NSP is essentially stable for collider experiments, and one has to accumulate the NSPs to study their decay. Sufficiently slow, strongly ionizing sleptons will be stopped within the detector. One may also be able to collect faster sleptons in a storage ring. For gravitino masses less than $\mathcal{O}(10\,\mathrm{keV})$ the $\widetilde{\tau}$ can decay inside the detector, which may be advantageous from the experimental point of view.

At LHC one expects $\mathcal{O}(10^6)$ NSPs per year which are mainly produced in cascade decays of squarks and gluinos [541]. The NSPs are mostly produced in the forward direction [542] which should make it easier to accumulate $\widetilde{\tau}$s in a storage ring. In a Linear Collider an integrated luminosity of $500\,\mathrm{fb}^{-1}$ will yield $\mathcal{O}(10^5)$ $\widetilde{\tau}$s [9]. Note that, in a Linear Collider, one can also tune the velocity of the produced $\widetilde{\tau}$s by adjusting the e^+e^- center-of-mass energy. A detailed study of the possibilities to accumulate $\widetilde{\tau}$ NSPs is beyond the scope of this note. In the following we shall assume that a sufficiently large number of $\widetilde{\tau}$s can be produced and collected.

This study is strongly based on Ref. [532]. Here, we discuss in more detail the case of a very light gravitino, or pseudo-goldstino, for which the $\widetilde{\tau}$ NSP can decay inside the detector. Although in this case it is difficult to determine mass and spin of the gravitino, one can still see the characteristic coupling of the gravitino, which is essentially the goldstino coupling, via the 3-body decay $\widetilde{\tau} \to \tau + \gamma + X$ with $X = \psi_{3/2}$ or $X = \chi$.

Planck mass from $\widetilde{\tau}$ decays

The $\widetilde{\tau}$ decay rate is dominated by the two-body decay into τ and gravitino,

$$\Gamma_{\widetilde{\tau}}^{2-\mathrm{body}} = \frac{\left(m_{\widetilde{\tau}}^2 - m_{3/2}^2 - m_\tau^2\right)^4}{48\pi\, m_{3/2}^2\, M_{\mathrm{P}}^2\, m_{\widetilde{\tau}}^3} \left[1 - \frac{4 m_{3/2}^2\, m_\tau^2}{\left(m_{\widetilde{\tau}}^2 - m_{3/2}^2 - m_\tau^2\right)^2}\right]^{3/2} , \qquad (5.105)$$

where $M_{\mathrm{P}} = (8\pi\, G_{\mathrm{N}})^{-1/2}$ denotes the reduced Planck mass, $m_\tau = 1.78\,\mathrm{GeV}$ is the τ mass, $m_{\widetilde{\tau}}$ is the $\widetilde{\tau}$ mass, and $m_{3/2}$ is the gravitino mass. For instance, $m_{\widetilde{\tau}} = 150\,\mathrm{GeV}$

and $m_{3/2} = 10\,\mathrm{keV}$ leads to a lifetime of $\Gamma_{\widetilde{\tau}}^{-1} \simeq 7.8 \times 10^{-7}\,\mathrm{s}$, and $m_{\widetilde{\tau}} = 150\,\mathrm{GeV}$ and $m_{3/2} = 75\,\mathrm{GeV}$ results in $\Gamma_{\widetilde{\tau}}^{-1} \simeq 4.4\,\mathrm{y}$.

Since the decay rate depends only on two unknown masses $m_{\widetilde{\tau}}$ and $m_{3/2}$, independently of other SUSY parameters, gauge and Yukawa couplings, it is possible to test the prediction of the supergravity if one can measure these masses. The mass $m_{\widetilde{\tau}}$ of the NSP will be measured in the process of accumulation. Although the outgoing gravitino is not directly measurable, its mass can also be inferred kinematically unless it is too small,

$$m_{3/2}^2 \;=\; m_{\widetilde{\tau}}^2 + m_\tau^2 - 2m_{\widetilde{\tau}}E_\tau \;. \tag{5.106}$$

The gravitino mass can be determined with the same accuracy as E_τ and $m_{\widetilde{\tau}}$, i.e. with an uncertainty of a few GeV.

Once the masses $m_{\widetilde{\tau}}$ and $m_{3/2}$ are measured, one can compare the predicted decay rate (5.105) with the observed decay rate, thereby testing an important supergravity prediction. In other words, one can determine the 'supergravity Planck scale' from the NSP decay rate which yields, up to $\mathcal{O}(\alpha)$ corrections,

$$M_{\mathrm{P}}^2(\text{supergravity}) \;=\; \frac{\left(m_{\widetilde{\tau}}^2 - m_{3/2}^2 - m_\tau^2\right)^4}{48\pi\, m_{3/2}^2\, m_{\widetilde{\tau}}^3\, \Gamma_{\widetilde{\tau}}} \left[1 - \frac{4m_{3/2}^2\, m_\tau^2}{\left(m_{\widetilde{\tau}}^2 - m_{3/2}^2 - m_\tau^2\right)^2}\right]^{3/2} \tag{5.107}$$

The result can be compared with the Planck scale of Einstein gravity, i.e. Newton's constant determined by macroscopic measurements, $G_{\mathrm{N}} = 6.707(10) \cdot 10^{-39}\,\mathrm{GeV}^{-2}$ [543],

$$M_{\mathrm{P}}^2(\text{gravity}) \;=\; (8\pi\, G_{\mathrm{N}})^{-1} \;=\; (2.436(2) \cdot 10^{18}\,\mathrm{GeV})^2 \;. \tag{5.108}$$

The consistency of the microscopic and macroscopic determinations of the Planck scale is an unequivocal test of supergravity.

Note that the measurement of the gravitino mass yields another important quantity in supergravity, the mass scale of spontaneous supersymmetry breaking $M_{\mathrm{SUSY}} = \sqrt{\sqrt{3} M_{\mathrm{P}}\, m_{3/2}}$. This is the analogue of the Higgs vacuum expectation value v in the electroweak theory, where $v = \sqrt{2} m_W/g = (2\sqrt{2} G_{\mathrm{F}})^{-1/2}$.

Gravitino and goldstino versus neutralino

If the measured decay rate and the kinematically determined mass of the invisible particle are consistent with Eq. (5.105), one already has strong evidence for supergravity and the gravitino LSP. To analyze the couplings of the invisible particle, one can study the 3-body decay $\widetilde{\tau} \to \tau + \gamma + X$ for the gravitino $X = \psi_{3/2}$ and compare it with the case where X is a hypothetical spin-1/2 neutralino. This is of particular importance if the mass of the invisible particle is so small that the supergravity prediction for the NSP lifetime, as described in the previous section, cannot be tested.

The NSP $\widetilde{\tau}$ is in general a linear combination of $\widetilde{\tau}_{\mathrm{R}}$ and $\widetilde{\tau}_{\mathrm{L}}$, the superpartners of the right-handed and left-handed τ leptons τ_{R} and τ_{L}, respectively. The interaction of the gravitino $\psi_{3/2}$ with scalar and fermionic τ leptons is described by the lagrangian [544],

$$L_{3/2} \;=\; -\frac{1}{\sqrt{2} M_{\mathrm{P}}} \left[(D_\nu\, \widetilde{\tau}_{\mathrm{R}})^* \overline{\psi^\mu}\, \gamma^\nu\, \gamma_\mu\, P_{\mathrm{R}} \tau + (D_\nu\, \widetilde{\tau}_{\mathrm{R}})\, \overline{\tau} P_{\mathrm{L}} \gamma_\mu\, \gamma^\nu\, \psi^\mu\right] \;, \tag{5.109}$$

where $D_\nu \widetilde{\tau}_\mathrm{R} = (\partial_\nu + \mathrm{i}e\, A_\nu)\widetilde{\tau}_\mathrm{R}$ and A_ν denotes the gauge boson. The interaction lagrangian of $\widetilde{\tau}_\mathrm{L}$ has an analogous form.

As an example for the coupling of a hypothetical spin-1/2 neutralino to $\widetilde{\tau}$ and τ, we consider the Yukawa interaction[10],

$$L_\mathrm{Yukawa} \;=\; h\left(\widetilde{\tau}_\mathrm{R}^*\,\overline{\lambda}\,P_\mathrm{R}\,\tau + \widetilde{\tau}_\mathrm{L}^*\,\overline{\lambda}\,P_\mathrm{L}\,\tau\right) + \mathrm{h.c.}\,. \tag{5.110}$$

Note that for very small coupling h, the $\widetilde{\tau}$ decay rate could accidentally be consistent with the supergravity prediction Eq. (5.105).

Also the goldstino χ has Yukawa couplings of the type given in Eq. (5.110). The full interaction lagrangian is obtained by performing the substitution $\psi_\mu \to \sqrt{\frac{2}{3}}\frac{1}{m_{3/2}}\partial_\mu\chi$ in the supergravity lagrangian. The non-derivative form of the effective lagrangian for χ is given by [545],

$$L_\mathrm{eff} \;=\; \frac{m_{\widetilde{\tau}}^2}{\sqrt{3}M_\mathrm{P}\,m_{3/2}}\,(\widetilde{\tau}_\mathrm{R}^*\,\overline{\chi}\,P_\mathrm{R}\,\tau + \widetilde{\tau}_\mathrm{R}\,\overline{\tau}\,P_\mathrm{L}\,\chi) - \frac{m_{\widetilde{\gamma}}}{4\sqrt{6}M_\mathrm{P}\,m_{3/2}}\overline{\chi}[\gamma^\mu,\gamma^\nu]\,\widetilde{\gamma}\,F_{\mu\nu}\;, \tag{5.111}$$

where we have neglected a quartic interaction term which is irrelevant for our discussion. In the following, we consider a massive pseudo-goldstino χ, in order to compare it with the massive gravitino and neutralino. Like a pseudo-Goldstone boson, the pseudo-goldstino has goldstino couplings and a mass which explicitly breaks global supersymmetry.

Note that the goldstino coupling to the photon supermultiplet is proportional to the photino mass $m_{\widetilde{\gamma}}$. As a consequence, the contribution to 3-body $\widetilde{\tau}$-decay with intermediate photino (cf. Fig. 5.60(c)) is not suppressed for very large photino masses. As we shall see, this leads to significant differences between the angular distributions for pure Yukawa and goldstino couplings, even when χ and λ are very light.

In $\widetilde{\tau}$ decays both, photon and τ lepton will mostly be very energetic. Hence the photon energy E_γ and the angle θ between τ and γ can be well measured (cf. Fig. 5.61(a)). We can then compare the differential decay rate

$$\Delta(E_\gamma,\cos\theta) \;=\; \frac{1}{\alpha\,\Gamma_{\widetilde{\tau}}}\frac{\mathrm{d}^2\Gamma(\widetilde{\tau}\to\tau+\gamma+X)}{\mathrm{d}E_\gamma\,\mathrm{d}\cos\theta}\;, \tag{5.112}$$

for the gravitino LSP ($X = \psi_{3/2}$), the pseudo-goldstino ($X = \chi$) and the hypothetical neutralino ($X = \lambda$). Details of the calculation are given in Ref. [532]. The differences between $\psi_{3/2}$, χ and λ become significant in the backward direction ($\cos\theta < 0$) as demonstrated by Fig. 5.61 (b)-(d), where $m_{\widetilde{\tau}} = 150\,\mathrm{GeV}$ and $m_X = 75\,\mathrm{GeV}$ ($X = \psi_{3/2},\chi,\lambda$). The three differential distributions are qualitatively different and should allow to distinguish experimentally gravitino, goldstino and neutralino.

Let us now consider the case of small m_X. Then the goldstino lagrangian (5.111) effectively describes the gravitino interactions. Therefore, one can no longer distinguish between gravitino and goldstino in this case. However, even for small m_X one can discriminate the gravitino or goldstino from the neutralino. The difference between goldstino χ and neutralino λ stems from the photino contribution (cf. Fig. 5.60(c))

[10] This interaction would arise from gauging the anomaly free U(1) symmetry $L_\tau - L_\mu$, the difference of τ- and μ-number, in the MSSM, with λ being the gaugino.

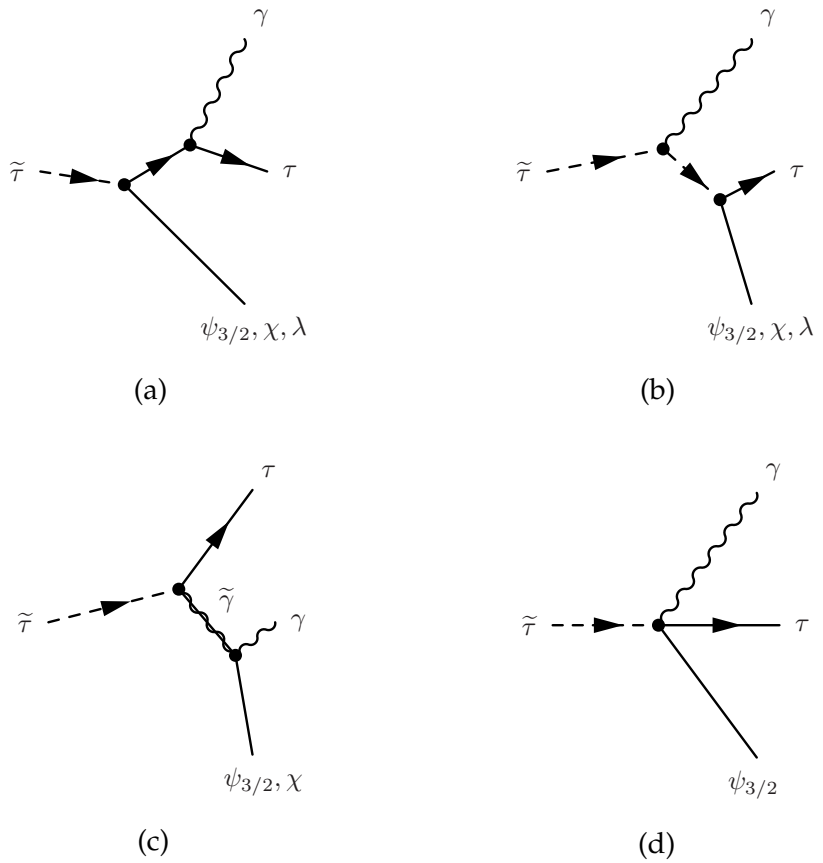

Figure 5.60: Diagrams contributing to the 3-body decay $\widetilde{\tau} \to \tau + \gamma + X$ where $X = \psi_{3/2}, \chi, \lambda$. In the limit of very large $m_{\widetilde{\gamma}}$, diagram (c) becomes irrelevant for the gravitino, but it always contributes for the goldstino where it leads effectively to a 4-point interaction.

which does not decouple for large photino mass $m_{\widetilde{\gamma}}$. This is different from the gravitino case where the analogous diagram becomes irrelevant in the limit $m_{\widetilde{\gamma}} \gg m_{\widetilde{\tau}}$ which is employed throughout this study.

The arising discrepancy between gravitino or goldstino and neutralino is demonstrated by Fig. 5.62. It clearly shows that even for very small masses $m_{3/2}$ and m_λ, the differential decay rates Δ for gravitino $\psi_{3/2}$ and neutralino λ are distinguishable. This makes it possible to discriminate gravitino and goldstino from a hypothetical neutralino even for very small masses. Note that the plots of Fig. 5.62 remain essentially the same as long as $r = m_X^2/m_{\widetilde{\tau}}^2 \ll 1$.

Let us finally comment on the experimental feasibility to determine gravitino or goldstino couplings. The angular distribution of the 3-body decay is peaked in forward direction ($\theta = 0$). Compared to the 2-body decay, backward ($\cos\theta < 0$) 3-body decays are suppressed by $\sim 10^{-1} \times \alpha \simeq 10^{-3}$. Requiring $10 \ldots 100$ events for a signal one therefore needs 10^4 to 10^5 $\widetilde{\tau}$s, which appears possible at the LHC and also at a Linear Collider according to the above discussion.

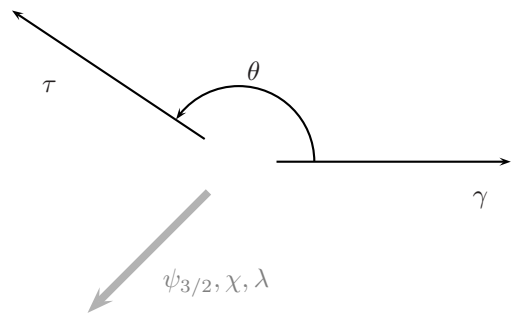

(a) Kinematical configuration. The arrows denote the momenta.

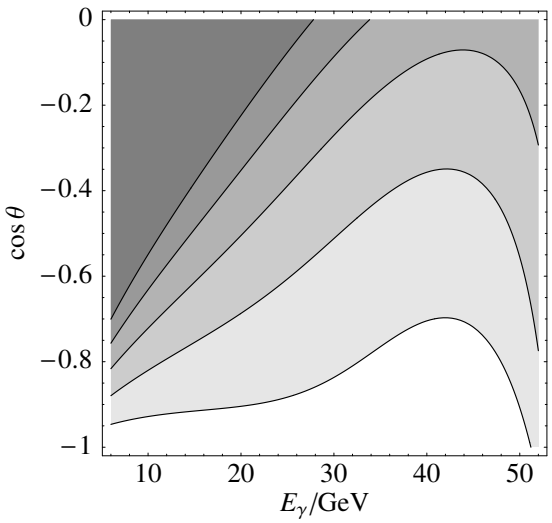

(b) Gravitino $\psi_{3/2}$

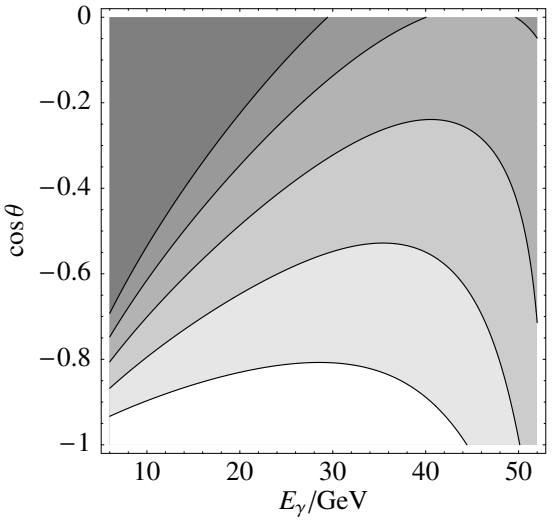

(c) Pseudo-goldstino χ

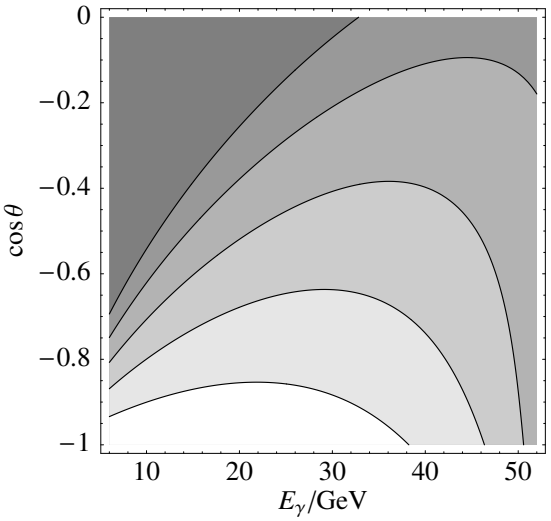

(d) Spin-1/2 neutralino λ

Figure 5.61: (a) shows the kinematical configuration of the 3-body decay. The others are contour plots of the differential decay rates for (b) gravitino $\psi_{3/2}$, (c) pseudo-goldstino χ and (d) neutralino λ. $m_{\tilde{\tau}} = 150\,\mathrm{GeV}$ and $m_X = 75\,\mathrm{GeV}$ ($X = \psi_{3/2}, \lambda, \chi$). The boundaries of the different gray shaded regions (from bottom to top) correspond to $\Delta(E_\gamma, \cos\theta)[\mathrm{GeV}^{-1}] = 10^{-3}, 2\times10^{-3}, 3\times10^{-3}, 4\times10^{-3}, 5\times10^{-3}$. Darker shading implies larger rate.

Gravitino spin

A third test of supergravity is intuitively more straightforward though experimentally even more challenging than the previous ones. It is again based on 3-body decays. We now take into account also the polarizations of the visible particles, γ and τ.

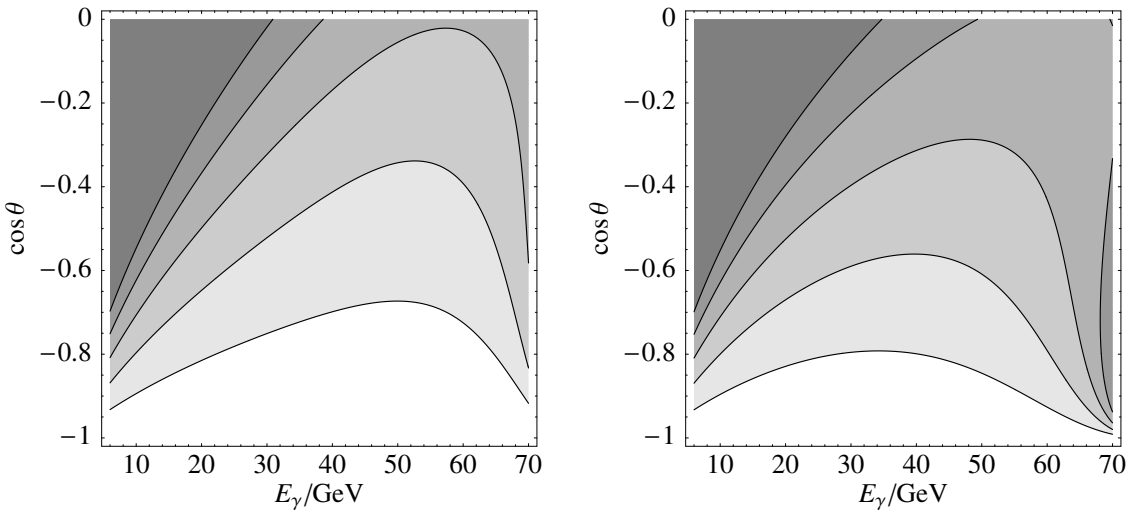

(a) Gravitino/goldstino (b) Neutralino

Figure 5.62: Contour plots of the differential decay rates for (a) gravitino $\psi_{3/2}$ and (b) neutralino λ. $m_{\widetilde{\tau}} = 150\,\mathrm{GeV}$, $m_X = 0.1$ GeV ($X = \psi_{3/2}, \lambda$). The figures remain essentially the same as long as $r = m_X^2/m_{\widetilde{\tau}}^2 \ll 1$. The contours have the same meaning as in Fig. 5.61.

The main point is obvious from Fig. 5.63(a) where a left-handed photon and a right-handed τ move in opposite directions.[11] Clearly, this configuration is allowed for an invisible spin-3/2 gravitino but it is forbidden for a spin-1/2 goldstino or neutralino. Unfortunately, measuring the polarizations is a difficult task.

As Fig. 5.63(a) illustrates, the spin of the invisible particle influences the angular distribution of final states with polarized photons and τ leptons. An appropriate observable is the angular asymmetry

$$A_{\mathrm{RL}}(\cos\theta) = \frac{\frac{\mathrm{d}\Gamma}{\mathrm{d}\cos\theta}(\widetilde{\tau}_{\mathrm{R}} \to \tau_{\mathrm{R}} + \gamma_{\mathrm{R}} + X) - \frac{\mathrm{d}\Gamma}{\mathrm{d}\cos\theta}(\widetilde{\tau}_{\mathrm{R}} \to \tau_{\mathrm{R}} + \gamma_{\mathrm{L}} + X)}{\frac{\mathrm{d}\Gamma}{\mathrm{d}\cos\theta}(\widetilde{\tau}_{\mathrm{R}} \to \tau_{\mathrm{R}} + \gamma_{\mathrm{R}} + X) + \frac{\mathrm{d}\Gamma}{\mathrm{d}\cos\theta}(\widetilde{\tau}_{\mathrm{L}} \to \tau_{\mathrm{R}} + \gamma_{\mathrm{L}} + X)}\,, \tag{5.113}$$

where X denotes gravitino ($X = \psi_{3/2}$), goldstino ($X = \chi$) or neutralino ($X = \lambda$). Note that, as discussed before, the photino does not decouple in the case $X = \chi$.

The three angular asymmetries are shown in Fig. 5.63 for $m_{\widetilde{\tau}} = 150\,\mathrm{GeV}$ and different masses of the invisible particle. As expected, the decay into right-handed τ and left-handed photon at $\theta = \pi$ is forbidden for spin-1/2 invisible particles (χ and λ), whereas it is allowed for the spin-3/2 gravitino. This is clearly visible in Figs. 5.63(c) and (d); for small gravitino masses the goldstino component dominates the gravitino interaction as illustrated by Fig. 5.63(b). The discrepancy between gravitino and goldstino compared to a hypothetical neutralino persists for arbitrarily small m_X, which is analogous to the double differential distribution discussed in the previous section.

[11] For simplicity, we here restrict ourselves to the case of a right-handed $\widetilde{\tau}$ LSP, leaving finite left-right mixing angles for future investigations.

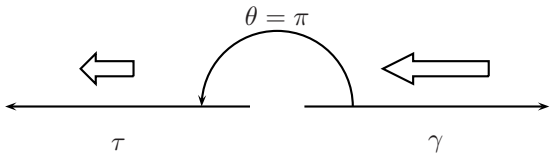

(a) Characteristic spin-3/2 process. The thick arrows represent the spins.

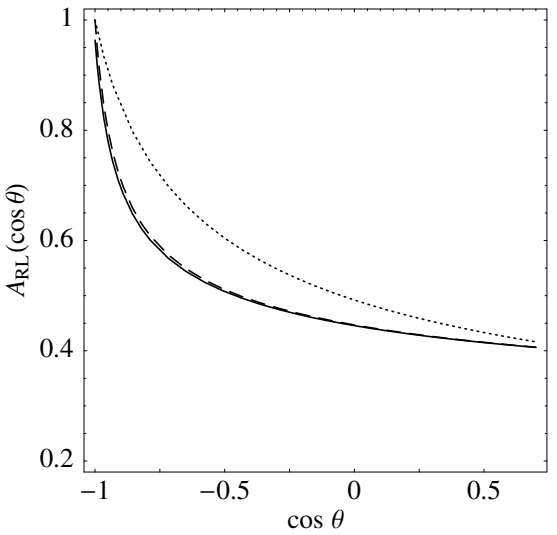

(b) $m_X = 10\,\mathrm{GeV}$.

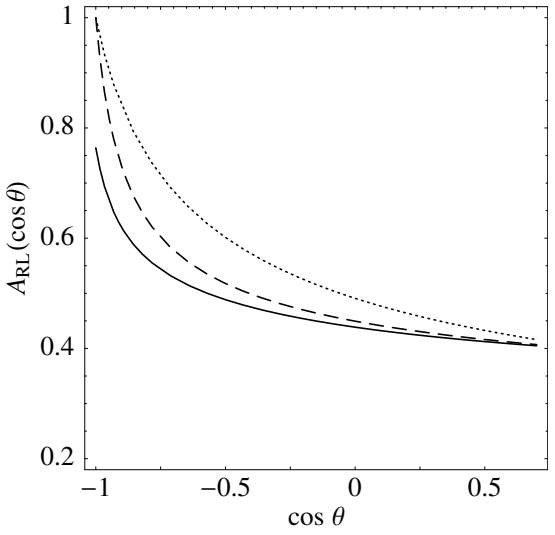

(c) $m_X = 30\,\mathrm{GeV}$.

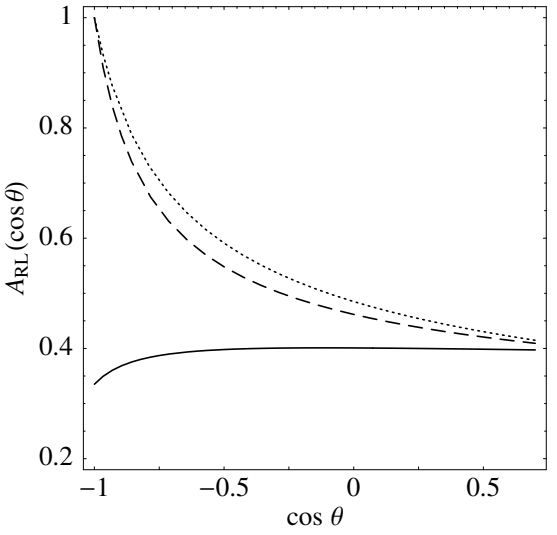

(d) $m_X = 75\,\mathrm{GeV}$.

Figure 5.63: (a) illustrates the characteristic spin-3/2 process: photon and τ lepton move in opposite directions and the spins add up to $3/2$, so the invisible particle also has spin $3/2$. The other figures show angular asymmetries for gravitino $\psi_{3/2}$ (solid curve), goldstino χ (dashed curve) and neutralino λ (dotted curve). $m_{\tilde{\tau}} = 150\,\mathrm{GeV}$. The photon energy is larger than 10% of the maximal kinematically allowed energy (cf. Ref. [532]). Note that the asymmetries only depend on the ratio $r = m_X^2/m_{\tilde{\tau}}^2$ ($X = \psi_{3/2}, \chi, \lambda$).

Conclusions

We have discussed how one may discover a massive gravitino, and thereby supergravity, at the LHC or a future Linear Collider, if the gravitino is the LSP and a

charged slepton is the NSP. With the gravitino mass inferred from kinematics, the measurement of the NSP lifetime will test an unequivocal prediction of supergravity. The analysis of 3-body NSP decays will reveal the couplings of the gravitino or the goldstino. For very small masses, one can distinguish the gravitino from the neutralino but not from the goldstino. For masses larger than about $1\,\mathrm{GeV}$, the determination of gravitino mass and spin appears feasible.

5.5.4 Reconstructing supersymmetric theories by coherent LHC / LC analyses

5.5.4.1 Physics Base

The roots of standard particle physics are expected to go as deep as the Planck length of 10^{-33} cm where gravity is intimately linked to the particle system. A stable bridge between the electroweak energy scale of 100 GeV and the vastly different Planck scale of $\Lambda_{\mathrm{PL}} \sim 10^{19}$ GeV, and the (nearby) grand unification scale $\Lambda_{\mathrm{GUT}} \sim 10^{16}$ GeV, is provided by supersymmetry. If this scenario is realized in nature, experimental methods must be developed to shed light on the physics phenomena near $\Lambda_{\mathrm{GUT}}/\Lambda_{\mathrm{PL}}$. Among other potential tools, the extrapolation of supersymmetry (SUSY) parameters measured at the LHC and an e^+e^- linear collider with high precision, can play a central rôle [546]. A rich ensemble of gauge and Yukawa couplings, and of gaugino/higgsino and scalar particle masses allows the detailed study of the supersymmetry breaking mechanism and the reconstruction of the physics scenario near the GUT/PL scale.

The reconstruction of physical structures at energies more than fourteen orders above the energies available through accelerators is a demanding task. Not only must a comprehensive picture be delineated near the electroweak scale, but the picture must be drawn, moreover, as precisely as possible to keep the errors small enough so that they do not blow up beyond control when the SUSY parameters are extrapolated over many orders of magnitude. The LHC [547] and a future e^+e^- linear collider (LC) [9] are a perfect tandem for solving such a problem: **(i)** While the colored supersymmetric particles, gluinos and squarks, can be generated with large rates for masses up to 2 to 3 TeV at the LHC, the strength of e^+e^- linear colliders is the comprehensive coverage of the non-colored particles, charginos/neutralinos and sleptons. If the extended Higgs spectrum is light, the Higgs particles can be discovered and investigated at both facilities; heavy Higgs bosons can be produced at the LHC in a major part of the parameter space; at an e^+e^- collider, without restriction, for masses up to the beam energy; **(ii)** If the analyses are performed coherently, the accuracies in measurements of cascade decays at LHC and in threshold production as well as decays of supersymmetric particles at LC complement and augment each other *mutually* so that a high-precision picture of the supersymmetric parameters at the electroweak scale can be drawn. Such a comprehensive and precise picture is necessary in order to carry out the evolution of the supersymmetric parameters to high scales, driven by perturbative loop effects that involve the entire supersymmetric particle spectrum.

Minimal supergravity (mSUGRA) provides us with a scenario within which these general ideas can be quantified. The form of this theory has been developed in great detail, creating a platform on which semi-realistic experimental studies can be per-

formed. Supersymmetry is broken in mSUGRA in a hidden sector and the breaking is transmitted to our eigenworld by gravity [548]. This mechanism suggests, yet does not enforce, the universality of the soft SUSY breaking parameters – gaugino and scalar masses, and trilinear couplings – at a scale that is generally identified with the unification scale. The (relatively) small number of parameters renders mSUGRA a well-constrained system that suggests itself in a natural way as a test ground for coherent experimental analyses at LHC and LC. The procedure will be exemplified for a specific set of parameters, defined as SPS1a among the Snowmass reference points [14, 369].

5.5.4.2 Minimal Supergravity: SPS1a

The mSUGRA Snowmass reference point SPS1a is characterised by the following values [14, 369]:

$$\begin{array}{ll} M_{1/2} = 250\ \mathrm{GeV} & M_0 = 100\ \mathrm{GeV} \\ A_0 = -100\ \mathrm{GeV} & \mathrm{sign}(\mu) = + \\ \tan\beta = 10 & \end{array} \tag{5.114}$$

for the universal gaugino mass $M_{1/2}$, the scalar mass M_0, the trilinear coupling A_0, the sign of the higgsino parameter μ, and $\tan\beta$, the ratio of the vacuum-expectation values of the two Higgs fields. As the modulus of the Higgsino parameter is fixed at the electroweak scale by requiring radiative electroweak symmetry breaking, μ is finally given by:

$$\mu = 357.4\ \mathrm{GeV} \tag{5.115}$$

This reference point is compatible with the constraints from low-energy precision data, predicting BR($b \to s\gamma$) $= 2.7 \cdot 10^{-4}$ and $\Delta[g_\mu - 2] = 17 \cdot 10^{-10}$. The amount of cold dark matter is, with $\Omega_\chi h^2 = 0.18$, on the high side but still compatible with recent WMAP data [21] if evaluated on their own without reference to other experimental results; moreover, only a slight shift in M_0 downwards drives the value to the central band of the data while such a shift does not alter any of the conclusions in this report in a significant way.

In the SPS1a scenario the squarks and gluinos can be studied very well at the LHC while the non-colored gauginos and sleptons can be analyzed partly at LHC and in comprehensive form at an e^+e^- linear collider operating at a total energy below 1 TeV with high integrated luminosity close to 1 ab^{-1}.

The masses can best be obtained at LHC by analyzing edge effects in the cascade decay spectra. The basic starting point is the identification of the a sequence of two-body decays: $\tilde{q}_L \to \tilde{\chi}_2^0 q \to \tilde{\ell}_R \ell q \to \tilde{\chi}_1^0 \ell\ell q$. This is effected through the detection of an edge structure of the invariant mass of opposite-sign same-flavour leptons from the χ_2^0 decay in events with multi-jets and E_T^{miss}. One can then measure the kinematic edges of the invariant mass distributions among the two leptons and the jet resulting from the above chain, and thus an approximately model-independent determination of the masses of the involved sparticles is obtained. This technique was developed in Refs. [371, 549] and is worked out in detail for point SPS1a in Ref. [550]. The four sparticle masses ($\tilde{q}_L$, $\tilde{\chi}_2^0$, $\tilde{\ell}_R$, and $\tilde{\chi}_1^0$) thus measured are used as an input to additional analyses which rely on the knowledge of the masses of the lighter gauginos in order

to extract masses from the observed kinematic structures. Examples are the studies of the decay $\tilde{g} \to \tilde{b}_1 b \to \tilde{\chi}_2^0 bb$, where the reconstruction of the gluino and sbottom mass peaks relies on an approximate full reconstruction of the $\tilde{\chi}_2^0$, and the shorter decay chains $\tilde{q}_R \to q\tilde{\chi}_1^0$ and $\tilde{\chi}_4^0 \to \tilde{\ell}\ell$, which require the knowledge of the sparticle masses downstream of the cascade. For SPS1a the heavy Higgs bosons can also be searched for in the decay chain: $A^0 \to \tilde{\chi}_2^0\tilde{\chi}_2^0 \to \tilde{\chi}_1^0\tilde{\chi}_1^0 l^+l^-l^+l^-$ [551]. The invariant four-lepton mass depends sensitively on m_{A^0} and $m_{\chi_1^0}$. The same holds true for H^0. Note however that the main source of the neutralino final states are A^0 decays, and that the two Higgs bosons A^0 and H^0 cannot be discriminated in this channel.

The mass measurements obtained at the LHC are thus very correlated among themselves, and this correlation must be taken into account in the fitting procedure. Another source of correlation comes from the fact that in most cases the uncertainty on the mass measurement is dominated by the systematic uncertainty on the hadronic energy scale of the experiment, which will affect all the measurements involving jets approximately by the same amount and in the same direction.

At linear colliders very precise mass values can be extracted from decay spectra and threshold scans [552–554]. The excitation curves for chargino production in S-waves [555] rise steeply with the velocity of the particles near the threshold and thus are very sensitive to their mass values; the same is true for mixed-chiral selectron pairs in $e^+e^- \to \tilde{e}_R^+\tilde{e}_L^-$ and for diagonal pairs in $e^-e^- \to \tilde{e}_R^-\tilde{e}_R^-,\ \tilde{e}_L^-\tilde{e}_L^-$ collisions [554]. Other scalar sfermions, as well as neutralinos, are produced generally in P-waves, with a somewhat less steep threshold behaviour proportional to the third power of the velocity [554,556]. Additional information, in particular on the lightest neutralino $\tilde{\chi}_1^0$, can be obtained from decay spectra.

Typical mass parameters and the related measurement errors are presented in Table 5.40. The column denoted "LHC" collects the errors from the LHC analysis, the column "LC" the errors expected from the LC operating at energies up to 1 TeV with an integrated luminosity of ~ 1 ab^{-1}. The error estimates are based on detector simulations for the production of the light sleptons, $\tilde{e}_R$, $\tilde{\mu}_R$ and $\tilde{\tau}_1$, in the continuum. For the light neutralinos and the light chargino threshold scans have been simulated. Details will be given elsewhere; see also Ref. [557]. The expected precision of the other particle masses is taken from Ref. [554], or it is obtained by scaling the LC errors from the previous analysis in Ref. [552], taking into account the fact that the $\tilde{\chi}^0/\tilde{\chi}^\pm$ cascade decays proceed dominantly via τ leptons in the reference point SPS1a, which is experimentally challenging. The third column of Tab. 5.40 denoted "LHC+LC" presents the corresponding errors if the experimental analyses are performed coherently, i.e. the light particle spectrum, studied at LC with very high precision, is used as an input set for the LHC analysis.

Mixing parameters must be obtained from measurements of cross sections and polarization asymmetries, in particular from the production of chargino pairs and neutralino pairs [555, 556], both in diagonal or mixed form: $e^+e^- \to \tilde{\chi}_i^+\tilde{\chi}_j^-$ [i,j = 1,2] and $\tilde{\chi}_i^0\tilde{\chi}_j^0$ [i,j = 1,...,4]. The production cross sections for charginos are binomials of $\cos 2\phi_{L,R}$, the mixing angles rotating current to mass eigenstates. Using polarized electron and positron beams, the cosines can be determined in a model-independent way. [In specified models like MSSM the analysis of the low-lying states is already sufficient for this purpose [559].]

Based on this high-precision information, the fundamental SUSY parameters can

	Mass, ideal	"LHC"	"LC"	"LHC+LC"
$\tilde{\chi}_1^\pm$	179.7		0.55	0.55
$\tilde{\chi}_2^\pm$	382.3	–	3.0	3.0
$\tilde{\chi}_1^0$	97.2	4.8	0.05	0.05
$\tilde{\chi}_2^0$	180.7	4.7	1.2	0.08
$\tilde{\chi}_3^0$	364.7		3-5	3-5
$\tilde{\chi}_4^0$	381.9	5.1	3-5	2.23
$\tilde{e}_R$	143.9	4.8	0.05	0.05
$\tilde{e}_L$	207.1	5.0	0.2	0.2
$\tilde{\nu}_e$	191.3	–	1.2	1.2
$\tilde{\mu}_R$	143.9	4.8	0.2	0.2
$\tilde{\mu}_L$	207.1	5.0	0.5	0.5
$\tilde{\nu}_\mu$	191.3	–		
$\tilde{\tau}_1$	134.8	5-8	0.3	0.3
$\tilde{\tau}_2$	210.7	–	1.1	1.1
$\tilde{\nu}_\tau$	190.4	–	–	–
$\tilde{q}_R$	547.6	7-12	–	5-11
$\tilde{q}_L$	570.6	8.7	–	4.9
$\tilde{t}_1$	399.5		2.0	2.0
$\tilde{t}_2$	586.3		–	
$\tilde{b}_1$	515.1	7.5	–	5.7
$\tilde{b}_2$	547.1	7.9	–	6.2
$\tilde{g}$	604.0	8.0	–	6.5
h^0	110.8	0.25	0.05	0.05
H^0	399.8		1.5	1.5
A^0	399.4		1.5	1.5
$H^\pm$	407.7	–	1.5	1.5

Table 5.40: *Accuracies for representative mass measurements at "LHC" and "LC", and in coherent "LHC+LC" analyses for the reference point SPS1a [masses in* GeV*]. $\tilde{q}_L$ and $\tilde{q}_R$ represent the flavours $q = u, d, c, s$ which cannot be distinguished at LHC. Positions marked by bars cannot be filled either due to kinematical restrictions or due to small signal rates; blank positions could eventually be filled after significantly more investments in experimental simulation efforts than performed until now. The "LHC" and "LC" errors have been derived in Ref. [550] and Ref. [558], respectively, in this document.*

	Parameter, ideal	"LHC+LC" errors
M_1	101.66	0.08
M_2	191.76	0.25
M_3	584.9	3.9
μ	357.4	1.3
$M^2_{L_1}$	$3.8191 \cdot 10^4$	82.
$M^2_{E_1}$	$1.8441 \cdot 10^4$	15.
$M^2_{Q_1}$	$29.67 \cdot 10^4$	$0.32 \cdot 10^4$
$M^2_{U_1}$	$27.67 \cdot 10^4$	$0.86 \cdot 10^4$
$M^2_{D_1}$	$27.45 \cdot 10^4$	$0.80 \cdot 10^4$
$M^2_{L_3}$	$3.7870 \cdot 10^4$	360.
$M^2_{E_3}$	$1.7788 \cdot 10^4$	95.
$M^2_{Q_3}$	$24.60 \cdot 10^4$	$0.16 \cdot 10^4$
$M^2_{U_3}$	$17.61 \cdot 10^4$	$0.12 \cdot 10^4$
$M^2_{D_3}$	$27.11 \cdot 10^4$	$0.66 \cdot 10^4$
$M^2_{H_1}$	$3.25 \cdot 10^4$	$0.12 \cdot 10^4$
$M^2_{H_2}$	$-12.78 \cdot 10^4$	$0.11 \cdot 10^4$
A_t	$-497.$	9.
$\tan\beta$	10.0	0.4

Table 5.41: *The extracted SUSY Lagrange mass and Higgs parameters at the electroweak scale in the reference point SPS1a [mass units in* GeV*].*

be extracted at low energy in analytic form. To lowest order:

$$\begin{aligned}
|\mu| &= M_W[\Sigma + \Delta[\cos 2\phi_R + \cos 2\phi_L]]^{1/2} \\
\text{sign}(\mu) &= [\Delta^2 - (M_2^2 - \mu^2)^2 - 4m_W^2(M_2^2 + \mu^2) \\
&\quad -4m_W^4 \cos^2 2\beta]/8m_W^2 M_2|\mu| \sin 2\beta \\
M_2 &= M_W[\Sigma - \Delta(\cos 2\phi_R + \cos 2\phi_L)]^{1/2} \\
|M_1| &= \left[\sum_i m^2_{\tilde{\chi}^0_i} - M_2^2 - \mu^2 - 2M_Z^2\right]^{1/2} \\
|M_3| &= m_{\tilde{g}} \\
\tan\beta &= \left[\frac{1 + \Delta(\cos 2\phi_R - \cos 2\phi_L)}{1 - \Delta(\cos 2\phi_R - \cos 2\phi_L)}\right]^{1/2}
\end{aligned} \tag{5.116}$$

where $\Delta = (m^2_{\tilde{\chi}^\pm_2} - m^2_{\tilde{\chi}^\pm_1})/(4M_W^2)$ and $\Sigma = (m^2_{\tilde{\chi}^\pm_2} + m^2_{\tilde{\chi}^\pm_1})/(2M_W^2) - 1$. The signs of $M_{1,3}$ with respect to M_2 follow from measurements of the cross sections for $\tilde{\chi}\tilde{\chi}$ production and gluino processes. In practice one-loop corrections to the mass relations have been used to improve on the accuracy.

The mass parameters of the sfermions are directly related to the physical masses if mixing effects are negligible:

$$m^2_{\tilde{f}_{L,R}} = M^2_{L,R} + m^2_f + D_{L,R} \tag{5.117}$$

with $D_L = (T_3 - e_f \sin^2\theta_W)\cos 2\beta\, m_Z^2$ and $D_R = e_f \sin^2\theta_W \cos 2\beta\, m_Z^2$ denoting the D-terms. The non-trivial mixing angles in the sfermion sector of the third generation can be measured in a way similar to the charginos and neutralinos. The sfermion production cross sections for longitudinally polarized e^+/e^- beams are bilinear in $\cos/\sin 2\theta_{\tilde{f}}$. The mixing angles and the two physical sfermion masses are related to the tri-linear couplings A_f, the higgsino mass parameter μ and $\tan\beta(\cot\beta)$ for down(up) type sfermions by:

$$A_f - \mu \tan\beta(\cot\beta) = \frac{m^2_{\tilde{f}_1} - m^2_{\tilde{f}_2}}{2m_f} \sin 2\theta_{\tilde{f}} \quad [f : \text{down(up) type}] \tag{5.118}$$

This relation gives us the opportunity to measure A_f if μ has been determined in the chargino sector.

Accuracies expected for the SUSY Lagrange parameters at the electroweak scale for the reference point SPS1a are shown in Table 5.41. The errors are presented for the coherent "LHC+LC" analysis. They have been obtained by fitting the LHC observables and the masses of SUSY particles and Higgs bosons accessible at a 1 TeV Linear Collider. For the fit the programs SPheno2.2.0 [441] and MINUIT96.03 [496] have been used. The electroweak gaugino and higgs/higgsino parameters cannot be determined individually through mass measurements at the LHC as the limited number of observable masses leaves this sector in the SPS1a system under-constrained. Moreover, the Lagrange mass parameters in the squark sector can be determined from the physical squark masses with sufficient accuracy only after the LHC mass measurements are complemented by LC measurements in the chargino/neutralino sector; this information is necessary as the relation between the mass parameters is affected by large loop corrections.

5.5.4.3 Reconstruction of the Fundamental SUSY Theory

As summarized in the previous section, the minimal supergravity scenario mSUGRA is characterized by the universal gaugino parameter $M_{1/2}$, the scalar mass parameter M_0 and the trilinear coupling A_0, all defined at the grand unification scale. These parameters are complemented by the sign of the higgs/higgsino mixing parameter μ, with the modulus determined by radiative symmetry breaking, and the mixing angle, $\tan\beta$, in the Higgs sector.

The fundamental mSUGRA parameters at the GUT scale are related to the low-energy parameters at the electroweak scale by supersymmetric renormalization group transformations (RG) [560, 561] which to leading order generate the evolution for

gauge couplings	:	$\alpha_i = Z_i\, \alpha_U$	(5)
gaugino mass parameters	:	$M_i = Z_i\, M_{1/2}$	(6)
scalar mass parameters	:	$M^2_{\tilde{j}} = M_0^2 + c_j M^2_{1/2} + \sum_{\beta=1}^{2} c'_{j\beta} \Delta M^2_\beta$	(7)
trilinear couplings	:	$A_k = d_k A_0 + d'_k M_{1/2}$	(8)

The index i runs over the gauge groups $i = SU(3)$, $SU(2)$, $U(1)$. To leading order, the gauge couplings, and the gaugino and scalar mass parameters of soft–supersymmetry breaking depend on the Z transporters with

$$Z_i^{-1} = 1 + b_i \frac{\alpha_U}{4\pi} \log \left(\frac{M_U}{M_Z} \right)^2 \tag{5.123}$$

and $b[SU_3, SU_2, U_1] = -3,\ 1,\ 33/5$; the scalar mass parameters depend also on the Yukawa couplings h_t, h_b, h_τ of the top quark, bottom quark and τ lepton. The coefficients c_j [$j = L_l, E_l, Q_l, U_l, D_l, H_{1,2}$; $l = 1, 2, 3$] for the slepton and squark doublets/singlets of generation l, and for the two Higgs doublets are linear combinations of the evolution coefficients Z; the coefficients $c'_{j\beta}$ are of order unity. The shifts ΔM_β^2 are nearly zero for the first two families of sfermions but they can be rather large for the third family and for the Higgs mass parameters, depending on the coefficients Z, the universal parameters M_0^2, $M_{1/2}$ and A_0, and on the Yukawa couplings h_t, h_b, h_τ. The coefficients d_k of the trilinear couplings A_k [$k = t, b, \tau$] depend on the corresponding Yukawa couplings and they are approximately unity for the first two generations while being O(10^{-1}) and smaller if the Yukawa couplings are large; the coefficients d'_k, depending on gauge and Yukawa couplings, are of order unity. Beyond the approximate solutions shown explicitly, the evolution equations have been solved numerically in the present analysis to two–loop order [561] and threshold effects have been incorporated at the low scale [562]. The 2-loop effects as given in Ref. [563] have been included for the neutral Higgs bosons and the μ parameter.

Gauge Coupling Unification

Measurements of the gauge couplings at the electroweak scale support very strongly the unification of the couplings at a scale $M_U \simeq 2 \times 10^{16}$ GeV [564]. The precision, being at the per–cent level, is surprisingly high after extrapolations over fourteen orders of magnitude in the energy from the electroweak scale to the grand unification scale M_U. Conversely, the electroweak mixing angle has been predicted in this approach at the per–mille level. The evolution of the gauge couplings from low energy to the GUT scale M_U is carried out at two–loop accuracy. The gauge couplings g_1, g_2, g_3 and the Yukawa couplings are calculated in the $\overline{DR}$ scheme by adopting the shifts given in Ref. [562]. These parameters are evolved to M_U using 2–loop RGEs [561]. At 2-loop order the gauge couplings do not meet exactly [565], the differences attributed to threshold effects at the unification scale M_U which leave us with an ambiguity in the definition of M_U. In this report we define M_U as the scale, *ad libitum*, where $\alpha_1 = \alpha_2$, denoted α_U, in the RG evolution. The non–zero difference $\alpha_3 - \alpha_U$ at this scale is then accounted for by threshold effects of particles with masses of order M_U. The quantitative evolution implies important constraints on the particle content at M_U [566].

Based on the set of low–energy gauge and Yukawa parameters $\{\alpha(m_Z),\ \sin^2\theta_W,\ \alpha_s(m_Z), Y_t(m_Z), Y_b(m_Z), Y_\tau(m_Z)\}$ the evolution of the inverse couplings α_i^{-1} [$i = U(1)$, $SU(2)$, $SU(3)$] is depicted in Fig 5.64. The evolution is performed for the mSUGRA reference point defined above. Unlike earlier analyses, the low–energy thresholds of supersymmetric particles can be calculated in this framework exactly without reference to effective SUSY scales. The outer lines in Fig. 5.64b correspond to the present experimental accuracy of the gauge couplings [567]: $\Delta\{\alpha^{-1}(m_Z),\ \sin^2\theta_W,\ \alpha_s(m_Z)\} =$

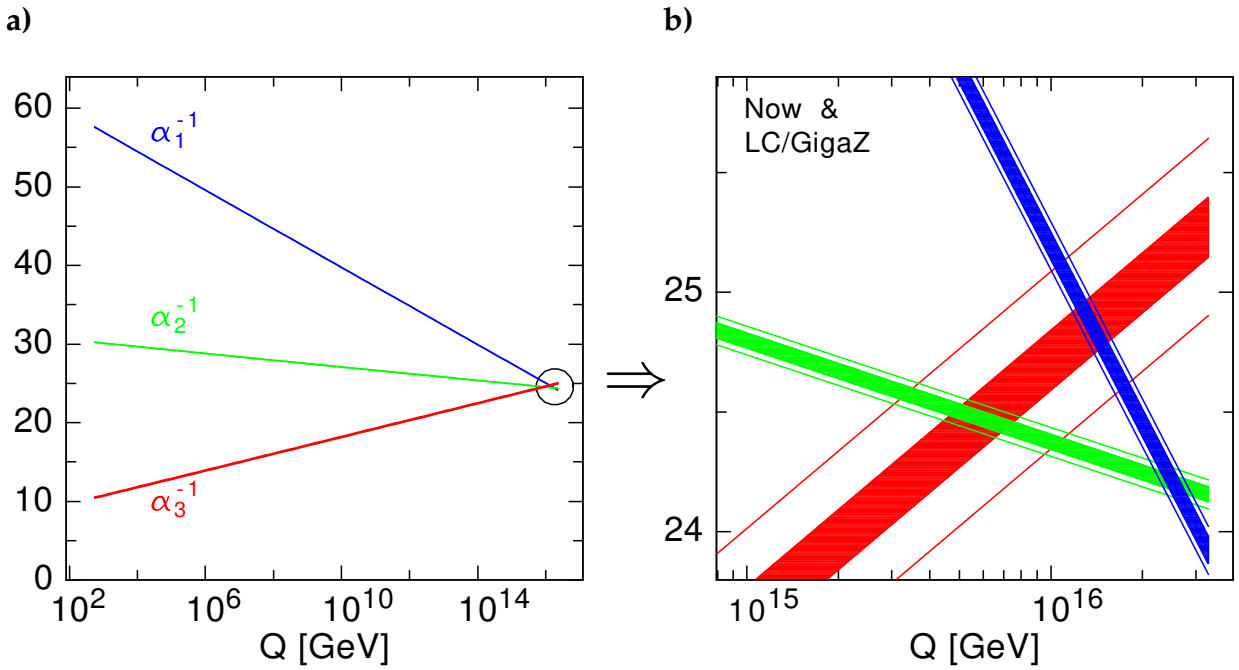

Figure 5.64: *(a) Running of the inverse gauge couplings from low to high energies. (b) Expansion of the area around the unification point M_U defined by the meeting point of α_1 with α_2. The wide error bands are based on present data, and the spectrum of superymmetric particles from LHC measurementes within mSUGRA. The narrow bands demonstrate the improvement expected by future GigaZ analyses and the measurement of the complete spectrum at "LHC+LC".*

$\{0.03, 1.7{\cdot}10^{-4}, 3{\cdot}10^{-3}\}$, and the spectrum of supersymmetric particles from LHC measurements complemented in the top-down approach for mSUGRA. The full bands demonstrate the improvement for the absolute errors $\{8 \cdot 10^{-3}, 10^{-5}, 10^{-3}\}$ after operating GigaZ [568, 569] and inserting the complete spectrum from "LHC+LC" measurements. The expected accuracies in M_U and α_U are summarized in the values given in Tab. 5.42. The gap between α_U and α_3 is bridged by contributions from high scale physics. Thus, for a typical set of SUSY parameters, the evolution of the gauge couplings from low to high scales leads to a precision of 1.5 per–cent for the Grand Unification picture.

Gaugino and Scalar Mass Parameters: Top-down Approach

The structure of the fundamental supersymmetric theory is assumed, in the top-down approach, to be defined uniquely at a high scale. In mSUGRA the set of parameters characterizing the specific form of the theory includes, among others, the scalar masses M_0 and the gaugino masses $M_{1/2}$. These universal parameters are realized at the grand unification point M_U. Evolving the parameters from the high scale down to the electroweak scale leads to a comprehensive set of predictions for the masses, mixings and couplings of the physical particles. Precision measurements of these observables can be exploited to determine the high-scale parameters M_0, $M_{1/2}$, etc., and to perform consistency tests of the underlying form of the theory. The small number of fundamental parameters, altogether five in mSUGRA, gives rise to many correlations between a large number of experimental observables. They define a set

	Present/"LHC"	GigaZ/"LHC+LC"
M_U	$(2.53 \pm 0.06) \cdot 10^{16}$ GeV	$(2.532 \pm 0.016) \cdot 10^{16}$ GeV
α_U^{-1}	24.12 ± 0.10	24.12 ± 0.05
$\alpha_3^{-1} - \alpha_U^{-1}$	0.96 ± 0.45	0.95 ± 0.12

Table 5.42: *Expected errors on M_U and α_U for the mSUGRA reference point, derived for the present level of accuracy and compared with expectations from GigaZ [supersymmetric spectrum as discussed in the text]. Also shown is the difference between α_3^{-1} and α_U^{-1} at the unification point M_U.*

Particle	Δ_{th} [GeV]	Particle	Δ_{th} [GeV]
$\tilde{\chi}_1^+$	1.2	$\tilde{q}_R$	8.4
$\tilde{\chi}_2^+$	2.8	$\tilde{q}_L$	9.1
$\tilde{\chi}_1^0$	0.34	$\tilde{t}_1$	4.4
$\tilde{\chi}_2^0$	1.1	$\tilde{t}_2$	8.3
$\tilde{\chi}_3^0$	0.6	$\tilde{b}_1$	7.4
$\tilde{\chi}_4^0$	0.3	$\tilde{b}_2$	8.2
$\tilde{e}_R$	0.82	$\tilde{g}$	1.2
$\tilde{e}_L$	0.31	h^0	1.2
$\tilde{\nu}_e$	0.24	H^0	0.7
$\tilde{\tau}_1$	0.59	A^0	0.7
$\tilde{\tau}_2$	0.30	H^+	1.0
$\tilde{\nu}_\tau$	0.25		

Table 5.43: *Theoretical errors of the SPS1a mass spectrum, calculated as difference between the minimal and the maximal value of the masses if the scale $\tilde{M}$ is varied between 100 GeV and 1 TeV.*

of *necessary consistency conditions* for the realization of the specific fundamental theory in nature.

Interludium: In addition to the experimental errors, theoretical uncertainties must be taken into account. They are generated by truncating the perturbation series for the evolution of the fundamental parameters in the $\overline{DR}$ scheme from the GUT scale to a low SUSY scale $\tilde{M}$ near the electroweak scale, and for the relation between the parameters at this point to the on-shell physical mass parameters, for instance. Truncating these series in one- to two-loop approximations leads to a residual $\tilde{M}$ dependence that would be absent from the exact solutions and may therefore be interpreted as an estimate of the neglected higher-order effects.

We estimate these effects by varying $\tilde{M}$ between the electroweak scale and 1 TeV. The theoretical uncertainties of the physical masses and LHC observables derived in

	m_{ll}^{max}	m_{llq}^{max}	m_{llq}^{min}	m_{lq}^{high}	m_{lq}^{low}	$m_{\tau\tau}^{max}$	$m_{ll}^{max}(\tilde{\chi}_4^0)$	m_{llb}^{min}
SPheno 2.2.0	80.64	454.0	216.8	397.2	325.6	83.4	283.4	195.9
Δ_{exp}	0.08	4.5	2.6	3.9	3.1	5.1	2.3	4.1
Δ_{th}	0.72	8.1	3.6	7.7	5.5	0.8	0.7	2.9

	$m_{\tilde{q}_R} - m_{\tilde{\chi}_1^0}$	$m_{\tilde{l}_L} - m_{\tilde{\chi}_1^0}$	$m_{\tilde{g}} - m_{\tilde{b}_1}$	$m_{\tilde{g}} - m_{\tilde{b}_2}$	$m_{\tilde{g}} - 0.99\, m_{\tilde{\chi}_1^0}$	m_{h^0}
SPheno 2.2.0	450.3	110.0	88.9	56.9	507.8	110.8
Δ_{exp}	10.9	1.6	1.8	2.6	6.4	0.25
Δ_{th}	8.1	0.23	6.8	7.6	1.3	1.2

Table 5.44: *LHC observables assumed for SPS1a and their experimental (Δ_{exp}) and present theoretical (Δ_{th}) uncertainties. [All quantities in GeV].*

this way are listed in Tables 5.43 and 5.44, respectively. They are of similar size as the differences found by comparing the observables with different state-of-the-art codes for the spectra [520]. The comparison of the present theoretical uncertainties with the experimental errors at LHC demonstrates that the two quantities do match *cum grano salis* at the same size. Since LC experiments will reduce the experimental errors roughly by an order of magnitude, considerable theoretical efforts are needed in the future to reduce Δ_{th} to a level that matches the expected experimental precision at LC. Only then we can deepen our understanding of the underlying supersymmetric theory by tapping the full experimental potential of "LC" and of the combined "LHC+LC" analyses.

In the top-down approach, models of SUSY-breaking are tested by fitting their high-scale parameters to experimental data. The minimum χ^2 of the fit gives a measure of the probability that the model is wrong. The results of such a fit of mSUGRA to anticipated "LHC", "LC", and "LHC+LC" measurements are shown in Table 5.45 and Fig. 5.65. For the "LHC" case the observables in Table 5.44 have been used, for the LC the masses in Table 5.40 and for "LHC+LC" the complete information have been used. If mSUGRA is assumed to be the underlying supersymmetric theory, the universal parameters $M_{1/2}$ and M_0 can be determined at the LHC at the per–cent level. LC experiments and coherent "LHC+LC" analyzes improve the accuracy by an order of magnitude, thus allowing for much more powerful tests of the underlying supersymmetric theory. Table 5.45 takes only experimental errors into account. The accuracy of the present theoretical calculations matches the errors of the "LHC" analysis and can thus be included in a meaningful way in a combined experimental plus theoretical error analysis. Adding Δ_{th} and Δ_{exp} quadratically the errors of the "LHC" analysis increases to: $\Delta M_{1/2} = 2.7$ GeV, $\Delta M_0 = 2.9$ GeV, $\Delta A_0 = 51$ GeV, and $\Delta \tan\beta = 5$. As argued above, significant theoretical improvements by an order of magnitude, i.e. "the next loop", are necessary to exploit fully the "LC" and "LHC+LC" potential.

The minimum χ^2 of the fit to mSUGRA as in Table 5.45 is indeed small, $\chi^2_{min}/n.d.o.f. \leq 0.34$ for "LHC", "LC", as well as "LHC+LC". When fitting instead mGMSB model pa-

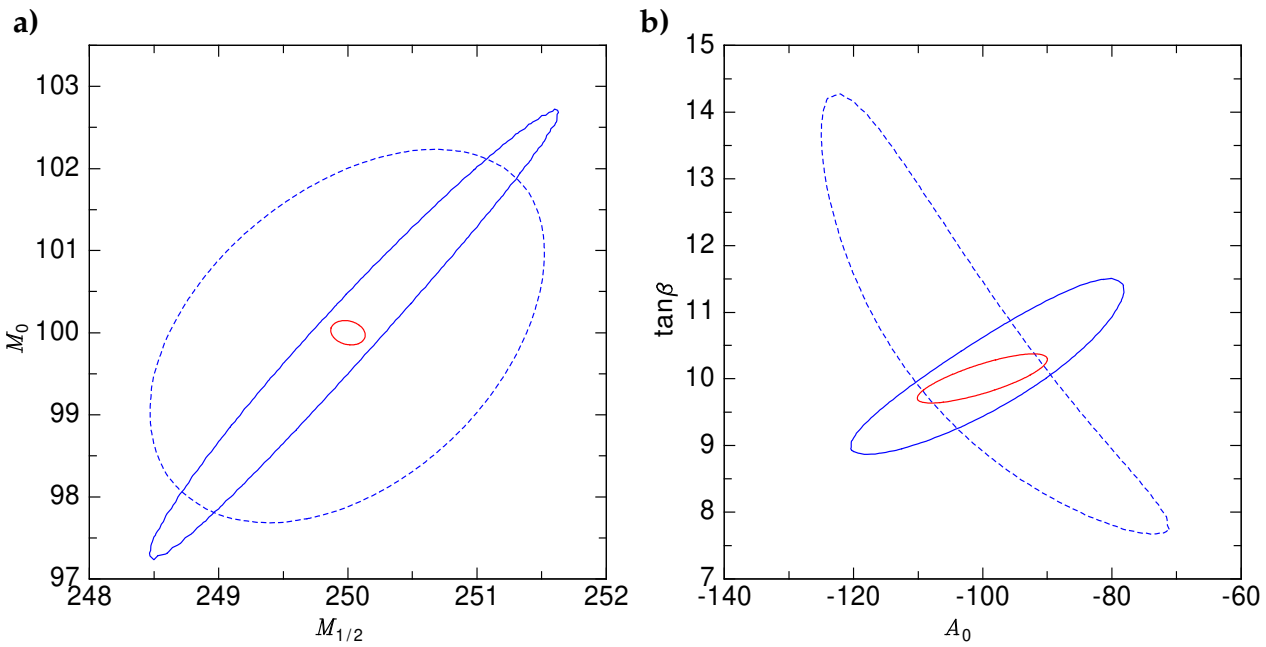

Figure 5.65: *1-σ error ellipses for the mSUGRA parameters in the top-down approach [i.e. the contours of $\Delta\chi^2 = 4.7$ in the $M_0 - M_{1/2}$ and $\tan\beta - A_0$ planes with the respective other parameters fixed to their best fit values, c.f. Table 5.45]. The full blue ellipses are the results obtained from LHC measurements alone while the red ones are for the combined "LHC+LC" analyses. The dashed blue lines show the results for the "LHC" case including today's theoretical uncertainties.*

rameters as an alternative to the same data, we would obtain $\chi^2_{min}/14\,d.o.f. = 68$ from LHC data alone. Such a result would clearly disfavour this model.

Gaugino and Scalar Mass Parameters: Bottom-up Approach

In the bottom-up approach the fundamental supersymmetric theory is reconstructed at the high scale from the available *corpus* of experimental data without any theoretical prejudice. This approach exploits the experimental information to the maximum extent possible and reflects an undistorted picture of our understanding of the basic theory.

At the present level of preparation in the "LHC" and "LC" sectors, such a program can only be carried out in coherent "LHC+LC" analyses while the separate informa-

	"LHC"	"LC"	"LHC+LC"
$M_{1/2}$	250.0 ± 2.1	250.0 ± 0.4	250.0 ± 0.2
M_0	100.0 ± 2.8	100.0 ± 0.2	100.0 ± 0.2
A_0	-100.0 ± 34	-100.0 ± 27	-100.0 ± 14
$\tan\beta$	10.0 ± 1.8	10.0 ± 0.6	10.0 ± 0.4

Table 5.45: *Results for the high scale parameters in the top-down approach including the experimental errors.*

tion from either machine proves insufficient. The results for the evolution of the mass parameters from the electroweak scale to the GUT scale M_U are shown in Fig. 5.66.

On the left of Fig. 5.66a the evolution is presented for the gaugino parameters M_i^{-1}, which clearly is under excellent control for the coherent "LHC+LC" analyses, while "LHC" [and "LC"] measurements alone are insufficient for the model-independent reconstruction of the parameters and the test of universality in the $SU(3) \times SU(2) \times U(1)$ group space. The error ellipse for the unification of the gaugino masses in the final analysis is depicted on the right of Fig. 5.66a. Technical details of the "LHC+LC" analysis can be found in Ref. [546].

In the same way the evolution of the scalar mass parameters can be studied, presented in Figs. 5.66b separately for the first/second and the third generation in "LHC+LC" analyses. Compared with the slepton parameters, the accuracy deteriorates for the squark parameters, and for the Higgs mass parameter $M_{H_2}^2$. The origin of the differences between the errors for slepton and squark/Higgs mass parameters can be traced back to the numerical size of the coefficients in Eqs. (5.121). Typical examples, evaluated at $Q = 500$ GeV, read as follows [546]:

$$M_{\tilde{L}_1}^2 \simeq M_0^2 + 0.47 M_{1/2}^2 \tag{5.124}$$

$$M_{\tilde{Q}_1}^2 \simeq M_0^2 + 5.0 M_{1/2}^2 \tag{5.125}$$

$$M_{\tilde{H}_2}^2 \simeq -0.03 M_0^2 - 1.34 M_{1/2}^2 + 1.5 A_0 M_{1/2} + 0.6 A_0^2 \tag{5.126}$$

$$|\mu|^2 \simeq 0.03 M_0^2 + 1.17 M_{1/2}^2 - 2.0 A_0 M_{1/2} - 0.9 A_0^2 \tag{5.127}$$

While the coefficients for the sleptons are of order unity, the coefficients c_j for the squarks grow very large, $c_j \simeq 5.0$, so that small errors in $M_{1/2}^2$ are magnified by nearly an order of magnitude in the solution for M_0. By close inspection of Eqs.(5.121) for the Higgs mass parameter it turns out that the formally leading M_0^2 part is nearly cancelled by the M_0^2 part of $c'_{j,\beta} \Delta M_\beta^2$. Inverting Eqs.(5.121) for M_0^2 therefore gives rise to large errors in the Higgs case. Extracting the trilinear parameters A_k is difficult and more refined analyses based on sfermion cross sections and Higgs and/or sfermion decays are necessary to determine these parameters accurately.

A representative set of the final mass values and the associated errors, after evolution from the electroweak scale to M_U, are presented in Table 5.46. It appears that the joint "LHC+LC"analysis generates a comprehensive and detailed picture of the fundamental SUSY parameters at the GUT/PL scale. Significant improvements however would be welcome in the squark sector where reduced experimental errors would refine the picture greatly.

5.5.4.4 Summary

We have shown in this brief report that in supersymmetric theories stable extrapolations can be performed from the electroweak scale to the grand unification scale, close to the Planck scale. This feature has been demonstrated compellingly in the evolution of the three gauge couplings and of the soft supersymmetry breaking parameters, which approach universal values at the GUT scale in minimal supergravity. As a detailed scenario we have adopted the Snowmass reference point SPS1a. It turns out that the information on the mSUGRA parameters at the GUT scale from pure "LHC"

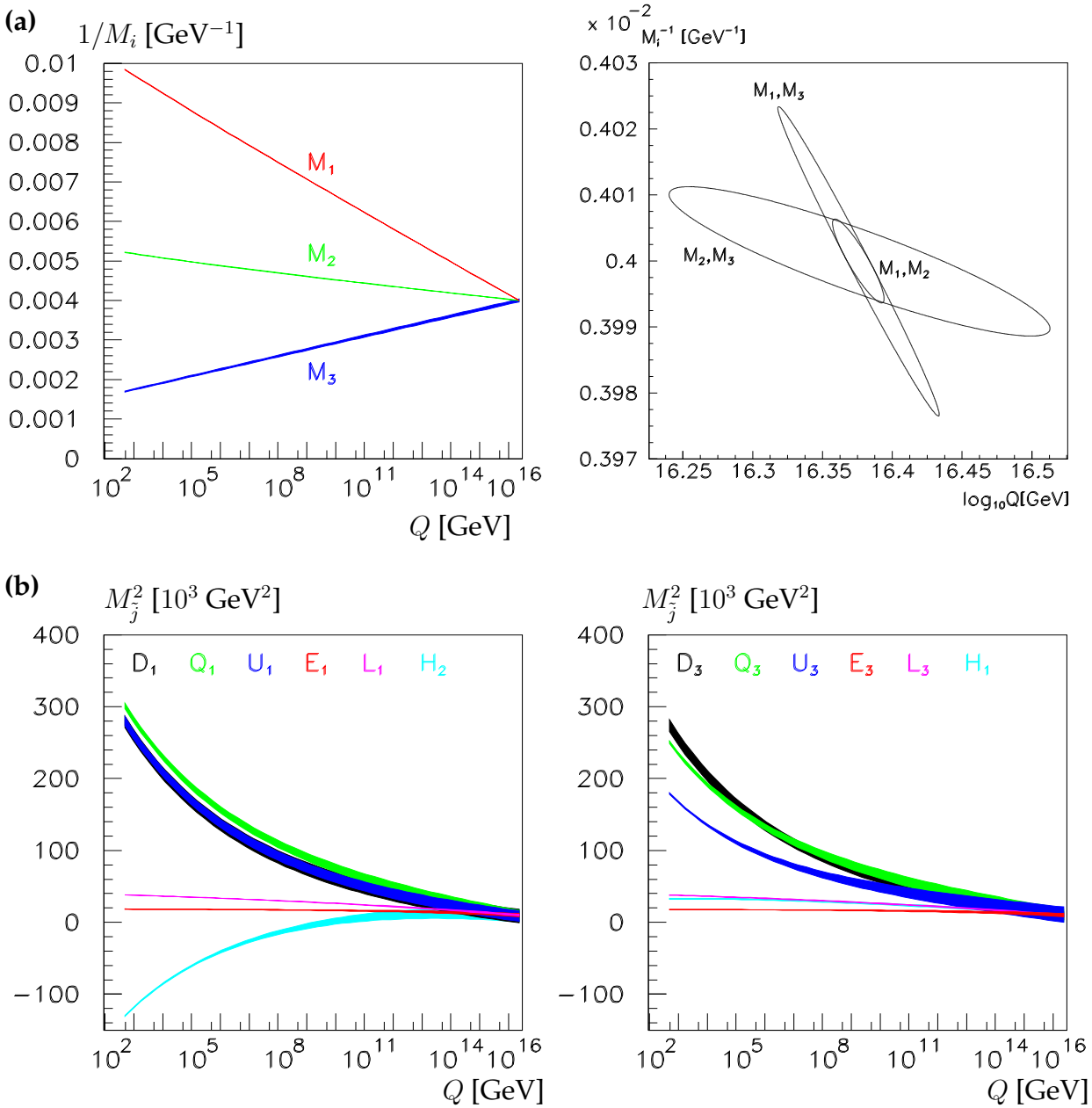

Figure 5.66: *Evolution, from low to high scales, (a) of the gaugino mass parameters for "LHC+LC" analyses and the corresponding error ellipses of the universal GUT values; (b) left: of the first–generation sfermion mass parameters (second generation, dito) and the Higgs mass parameter $M^2_{H_2}$; right: of the third–generation sfermion mass parameters and the Higgs mass parameter $M^1_{H_2}$.*

	Parameter, ideal	"LHC+LC" errors
M_1	250.	0.15
M_2	*ditto*	0.25
M_3		2.3
M_{L_1}	100.	6.
M_{E_1}	*ditto*	12.
M_{Q_1}		23.
M_{U_1}		48.
M_{L_3}		7.
M_{E_3}		14.
M_{Q_3}		37.
M_{U_3}		58.
M_{H_1}	*ditto*	8.
M_{H_2}		41.
A_t	$-100.$	40.

Table 5.46: *Values of the SUSY Lagrange mass parameters after extrapolation to the unification scale where gaugino and scalar mass parameters are universal in mSUGRA [mass units in* GeV*].*

	Parameter, ideal	Experimental error
M_U	$2.53 \cdot 10^{16}$	$2.2 \cdot 10^{14}$
α_U^{-1}	24.12	0.05
$M_{\frac{1}{2}}$	250.	0.2
M_0	100.	0.2
A_0	-100.	14
μ	357.4	0.4
$\tan\beta$	10.	0.4

Table 5.47: *Comparison of the ideal parameters with the experimental expectations in the combined "LHC+LC" analyses for the particular mSUGRA reference point adopted in this report [units in* GeV*].*

analyses is too limited to allow for the reconstruction of the high-scale theory in a model-independent way. The coherent "LHC+LC" analyses however in which the measurements of SUSY particle properties at LHC and LC mutually improve each other, result in a comprehensive and detailed picture of the supersymmetric particle system. In particular, the gaugino sector and the non-colored scalar sector are under excellent control.

Though mSUGRA has been chosen as a specific example, the methodology can equally well be applied to left-right symmetric theories and to superstring theories. The analyses offer the exciting opportunity to determine intermediate scales in left-right symmetric theories and to measure effective string-theory parameters near the Planck scale.

Thus, a thorough analysis of the mechanism of supersymmetry breaking and the reconstruction of the fundamental supersymmetric theory at the grand unification scale has been shown possible in the high-precision high-energy experiments at LHC and LC. This point has been highlighted by performing a global mSUGRA fit of the universal parameters, c.f. Tab. 5.47 Accuracies at the level of per-cent to per-mille can be reached, allowing us to reconstruct the structure of nature at scales where gravity is linked with particle physics.

6 Electroweak and QCD Precision Physics

6.1 Top physics

The top quark, with the mass slightly less than the mass of the gold nucleus, is the heaviest elementary particle found. The direct top-quark mass (pole mass) measurement by the CDF [570] and D0 [571] collaborations in Run I at the Tevatron gives $M_t = 174.3 \pm 5.1$ GeV [292], which is in spectacular agreement with the result from the electroweak (EW) data analysis by LEP and SLC [572]. This is a well known historical example of important influence of lepton collider results on physics analyses at hadron colliders.

The Standard Model (SM) top quark couplings are uniquely fixed by the principle of gauge invariance, the structure of the quark generations, and a requirement of including the lowest dimension interaction Lagrangian. Within the SM the top quark is considered as a point-like particle, albeit its heavy mass. The mass of the top quark is close to the electroweak breaking scale, and the top Yukawa coupling $\lambda_t = (2\sqrt{2}G_F)^{1/2}m_t$ is numerically very close to unity. This suggests that a study of the properties of the top quark might also reveal details of the electroweak symmetry breaking mechanism. In particular, it has been argued that new physics might lead to measurable deviations from the Standard Model values.

The top quark decay width, $\Gamma_t/|V_{tb}|^2 = 1.39$ GeV for the pole mass, was calculated in the SM to second order in QCD [573] and to first order in EW [574] corrections including the W-boson and b-quark masses. Since the CKM matrix element V_{tb} is close to one, in the SM the top-quark lifetime $\tau_t \approx 0.4 \times 10^{-24}$s is much smaller then the typical time for a formation of QCD bound states $\tau_{QCD} \approx 1/\Lambda \approx 3 \times 10^{-24}$s. Therefore, the top quark decays long before it can hadronize [575] and it provides a very clean source for fundamental information on the constituents of matter.

The physics of the top quark at the LHC [576] and LC [57] has been studied in great detail, including in many cases a realistic simulation of the detectors. We summarize here only the basic predictions.

6.1.1 Top-quark production

At hadron and lepton colliders, top quarks may be produced either in pairs or singly. The pair-production cross section, about 850 pb, is known at the LHC to NLO level [577] including the re-summation of the Sudakov logarithms (NLL) [578]. About 90% of the rate is due to gluon-gluon collisions, while quark-antiquark collisions give the remaining 10%. The estimated overall theoretical systematic uncertainty is about 12%, which would lead to about 4% accuracy in the determination of the top-quark mass. However, combining various top-quark decay channels and using

Table 6.1: NLO cross sections for t and $\bar{t}$ production at the LHC, $\sqrt{s} = 14$ TeV.

	s-channel	t-channel
$\sigma_{NLO}(t)$, pb	6.55	152.6
$\sigma_{NLO}(\bar{t})$, pb	4.07	90.0

various methods, the error on the top-quark mass (dominated by systematics) is expected to reach $\sim 0.5\%$, beyond which more data offers no obvious improvement.

A precise knowledge of the top-quark mass is necessary for many precision observables. The better the top-quark mass from the LHC is known, the more appropriate the energy interval for the threshold scan at the LC can be chosen for $t\bar{t}$-pair production. Several NNLO calculations have been performed for various definitions of the threshold top-quark mass parameter [579]. A delicate comparison of different calculations leads to the conclusion that a scan at the threshold is expected to reduce the error on the top mass down to $\delta m_t \simeq 100\,\text{MeV}$ [57], a value not achievable at hadron machines.

The total top-quark pair production cross section at the LC in the continuum has been calculated to the NLO QCD [580] and 1-loop EW [581] level. The cross section is about 10^3 times smaller than at the LHC approaching about 0.85 pb at maximum around 390 GeV and falling down with the energy as $1/s$. However, a very clean environment of the LC experiment and a possibility to use beam polarization allow access to unique information on various couplings, as we discuss later. In particular, an important aspect related to $t\bar{t}$-production is the top-Higgs Yukawa coupling. This subject is considered in details in the section 3.

Single-top-quark production provides many new avenues to physics that cannot be observed in $t\bar{t}$ production. Single-top-quark production allows a direct measurement of the CKM matrix element V_{tb}, and can provide a verification of the unitarity of the CKM matrix. The top quark is produced through a left-handed interaction and is highly polarized. Since no hadronization occurs, spin correlations survive in the final decay products. Hence, single-top-quark production offers an opportunity to observe the polarization of the top-quark at production. Finally, measurement of the charged-current couplings of the top quark may probe non-standard couplings that would provide hints about new physics. A survey of all new-physics-scenarios which have been studied is beyond the scope of this document and we refer the reader to the review article [582] and the references therein.

The single-top-quark production rate at the LHC is known to the NLO level for all tree production mechanisms which are classified by the virtuality of the W-boson involved: t-channel ($q^2_W < 0$) [583], s-channel ($q^2_W > 0$) [584], and associated tW ($q^2_W = M^2_W$) [585]. The representative diagrams for the three production mechanisms [586] are shown in Fig. 6.1. Note that the LHC is a pp-collider and therefore the cross sections for t and $\bar{t}$ production are not equal for the t and s- channel mechanisms as shown in the Table 6.1. For the associated W production channel, the cross section for t and $\bar{t}$ production are the same, giving a $W^-t + W^+\bar{t}$ cross section of about 60 pb.

It was demonstrated that single-top-quark production at the LHC could be ex-

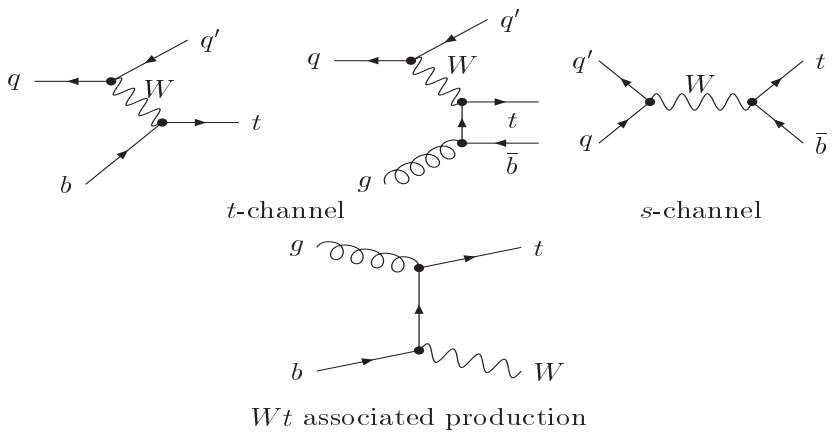

Figure 6.1: Representative Feynman diagrams for single-top-quark production at hadron colliders.

tracted from the backgrounds, see [89, 586–589] for details. In order to do that correctly, fully differential Monte Carlo programs which include the decay of the top quark and the complete irreducible non-resonant background have been used.

At the LC the single-top-quark production cross section was calculated to LO at e^+e^-, $\gamma\gamma$ and γe collision modes including various beam polarizations [590]. The recently calculated NLO corrections to the single-top-quark production in γe are well under control and rather small [591].

The single-top-quark production rate at LHC energies is about $1/3$ of the top-pair rate, while at a 500–800 GeV LC it is smaller by a factor of 1/80 than the corresponding pair-production rate. Single-top-quark production in γe collisions is of special interest; the rate is smaller than the top-pair rate in e^+e^- only by a factor of 1/8 at 500–800 GeV energies, and it becomes the dominant LC processes for top production at a multi-TeV LC like CLIC as demonstrated in Fig. 6.2.

Since single-top-quark production allows a direct measurement of the CKM matrix element V_{tb} it is worth examining the measurement of the CKM matrix element V_{tb} in more detail. V_{tb} is known indirectly from unitarity of the CKM matrix to a very high precision [292]:

$$|V_{tb}| \;=\; 0.9990 - 0.9993\ . \tag{6.1}$$

In the near future there will be no way to measure $|V_{tb}|$ directly to this precision. Without an assumption of unitarity the $|V_{tb}|$ element becomes virtually unconstrained [292]:

$$|V_{tb}| \;=\; 0.08 - 0.9993\ . \tag{6.2}$$

A direct measurement of V_{tb} without any assumptions on the number of generations is possible through two processes. In single-top-quark production the cross section at both LHC and LC is proportional to $|V_{tb}|^2$, and hence is a direct measure of $|V_{tb}|^2$. The partial width of the top-quark decaying into bW is also proportional to $|V_{tb}|^2$, and at a linear collider one can measure indirectly the partial width by extracting the total top quark width from the $t\bar{t}$ threshold and by measuring the branching of

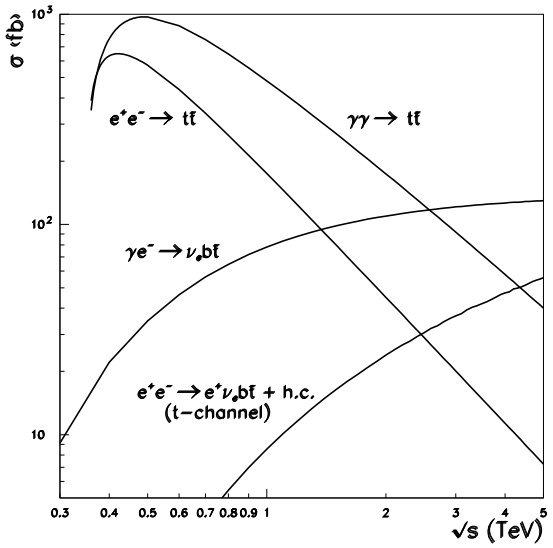

Figure 6.2: Top-quark cross sections at the LC

$t \to Wb$. The anticipated accuracy of a direct measurement of $|V_{tb}|$ is about 7% at the LHC [89] and in the e^+e^- option of a linear collider [576, 587, 590], and can possibly reach 1% for a polarized γe^- collider [590].

Note, the $|V_{tb}|$ matrix element can be measured at a LC significantly more accurately as compared to the LHC. Therefore, its value could be used at LHC in single-top analysis of the process t-channel $qb \to q't$ to measure the b-quark distribution function in the proton. Such a measurement is of a great importance in order to get correctly the MSSM Higgs production rate, especially at large values of $\tan\beta$, and gives a nice example of the potential LHC&LC interplay.

6.1.2 Spin correlations in top production and decays

Since the top quark decays before hadronization, its spin properties are not spoiled. Therefore spin correlations in top production and decays is an interesting issue in top-quark physics. As well known from the polarized top decays [593] the down type fermions are the best top-quark spin analyzers. Such a unique property of polarized top-quark decay is a consequence of the pure (V-A) structure of the charged currents in the Standard Model. NLO corrections do not change this property drastically: to the leptonic K_l they are very small $-0.0015\alpha_s$ [594], and to quarks $K_{d,s}$ they are about -6% [595].

The (V-A) structure of the top quark interaction leads to simple top-quark spin properties for the single-top-quark production at the LHC. It was shown [596] that the top-quark spin in each event should follow the direction of the down-type quark momentum in the top-quark rest frame. This is the direction of the initial $\bar{d}$-quark for the s-channel, and the dominant direction of the final d-quark for the t-channel single-top-quark production processes. This follows from the above results on polarized top decays, because these two production modes could be considered as top-quark

decays "backward in time" [597]. Further, the best variable to observe maximal top-quark spin correlations in single-top-quark s-channel or t-channel production and the subsequent decay of the top-quark is the angle between this down-type quark direction in the production processes and the charged lepton (or d, s-quark) direction from the top-quark decay in the top-quark rest frame. Since the u-quark density is the largest among the quark densities, the observed light-quark jet in the t-channel is predominately initiated by $\overline{d}$-quarks. It is useful to define the quantity [598]

$$a \;=\; \frac{1}{2}\left(1+\cos\theta_{q\bar{l}}\right)\;, \tag{6.3}$$

where $\theta_{q\bar{l}}$ is the angle between the light-quark jet and the charged lepton. In the rest frame of the top quark the differential cross section with respect to this variable is given by

$$\frac{d\sigma}{da} \;=\; \sigma\left(2Pa+(1-P)\right), \tag{6.4}$$

where P is the polarization of the top quark. As an example, a plot for the spin correlation is shown in Fig. 6.3, based on the complete LO matrix elements (cf. [587] for a method to extract this signal from the backgrounds). It was demonstrated that the top spin correlation properties for the single top production and decay are preserved at next-to-leading order [599, 600].

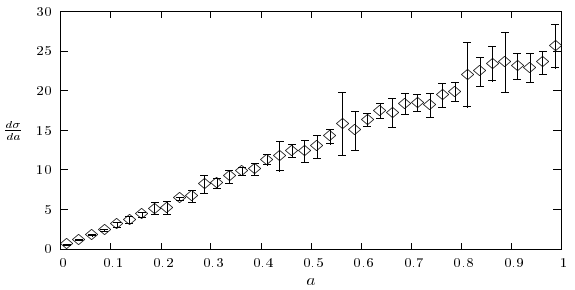

Figure 6.3: The distribution for the angular correlation a for t-channel production at the LHC.

Spin properties of the t-quark in the tW production process follows from the analogy of the tW production mode to radiative polarized top decay. Here one can find a kinematic region in which top quarks are produced with the polarization vector preferentially close to the direction of the charged lepton or the d, s-quark momentum from the associated W decay. In this kinematic region the direction of the produced charged lepton or the d, s-quark should be as close as possible to the direction of the initial gluon beam in the top-quark rest frame [597] as demonstrated in Fig. 6.4.

The latter result of the LHC process is an additional nice example of "theoretical" LHC&LC interplay. Indeed it has an immediate implication for single-top-quark production in γe collisions in the process $\gamma e \to \nu_e \bar{t} b$. Here the directions of the initial photon and the electrons play the role of the gluon and lepton direction in the tW process at a hadron collider. The directions of γ and electron beams are close to the top-quark rest frame since the top is moving slowly here. So one would expect the that the top-quark is strongly polarized in the direction of the initial electron beam.

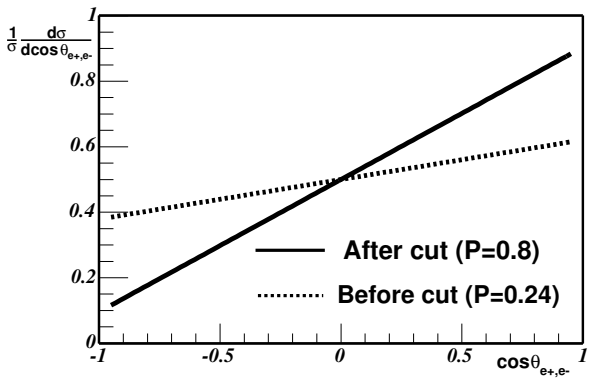

Figure 6.4: The angular distribution for the associated tW production before and after cuts.

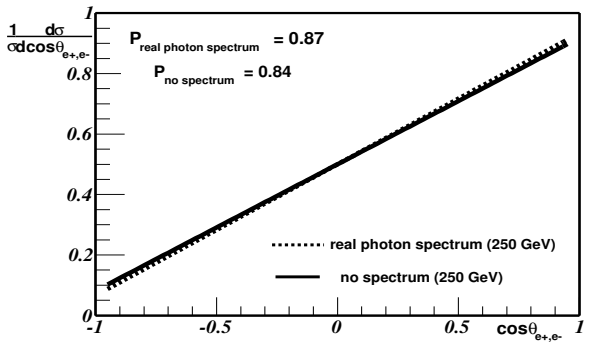

Figure 6.5: Angular distribution for the angle between the electron beam and muon from the top decay in single-antitop-quark production at γe^- 500 GeV collider.

Indeed, the angular distribution for the angle between the lepton from the top decay and the initial electron beam shows about 90% correlation [601] (see Fig. 6.5).

For top-quark-pair production at Linear Colliders, and in the quark-antiquark production part at hadron colliders, specifically important at the Tevatron, one can find a top-quark spin-quantization axis, or in other words, a top-spin basis (so called "off-diagonal" basis), in which there will be very strong spin correlations for produced top and anti-top quarks [602].

For the case of e^+e^- collisions one can show [604] the QCD corrections lead to the known K-factors for the dominant Up-Down spin configuration and to a very small appearing Down-Up configuration in the "off-diagonal basis." So, one may conclude that, in contrast to the helicity basis, the QCD corrections in the "off-diagonal" basis affect very little the top-antitop spin configuration. Therefore, it provides an interesting possibility to search for anomalous top-quark interactions by looking for deviations from the predicted SM $t\bar{t}$ spin correlations in the "off-diagonal" basis. However, detailed studies in that direction, both at the $t\bar{t}$ threshold and in the continuum regions, still remain to be done.

The situation with $t\bar{t}$ spin correlations at the LHC is more complex. Here the $q\bar{q}$ collisions give the only about 10% of the rate. Unfortunately, for the dominating gg collision mode there is no optimal spin basis [605]. As a result one needs to analyze the top-antitop spin correlation matrix in this case. Since there is no optimal basis for the case of top pair production at the LHC one can compute, for example, double-angle distributions for the top and antitop decay products: e.g. charged leptons

$$\frac{1}{\sigma}\frac{d^2\sigma(pp \to t\bar{t}X \to l^+l^-X)}{d\cos\theta_+ \cos\theta_-} = \frac{1}{4}(1 + B_1\cos\theta_+ + B_2\cos\theta_- + C\cos\theta_+\cos\theta_-), \quad (6.5)$$

where θ_+, θ_- are the angles of charged leptons with respect to the top-quark spin-quantization axis in the $t(\bar{t})$ rest frame. It was shown [605] that the QCD corrections are smaller for the helicity basis, and this choice of the basis allows for about 30% spin correlations. The first analysis for the LHC including detector response was performed by both ATLAS [606] and CMS [607] collaborations for di-lepton and semileptonic final states. It was shown that at the LHC the coefficient C in eq. (6.5) could be measured with about (10-15)% accuracy. Further LHC studies are ongoing.

6.1.3 Anomalous couplings

The search for *anomalous (i.e. non-SM) interactions* is one of the main motivations for studying top-quark physics. New physics can manifest itself in two ways. Firstly, we may expect a modification of the SM couplings ($gt\bar{t}$, $\gamma t\bar{t}$, $Zt\bar{t}$, and tWb vertexes). Secondly, the new physics may lead to the appearance (or huge increase) of new types of interactions (like tH^+b or anomalous Flavor Changing Neutral Current (FCNC) – tgc, $t\gamma c$, and tZc interactions). We do not know which type of new physics will be responsible for a future deviation from the SM predictions. However, top-quark couplings can be parametrized in a model independent way by an effective Lagrangian (cf. [576]).

In practice, any tVq coupling (with V being any gauge boson: the gluon, photon,

or $W^{\pm}$, Z-bosons) could be parametrized with four (complex, in general) parameters:

$$t\,V\,q \;=\; \frac{g}{\sqrt{2}}\kappa(V - A\gamma^5)\gamma^\mu V^\mu \;+\; \frac{g}{\sqrt{2}}\frac{\eta}{\Lambda}\sigma^{\mu\nu}(f + ih\gamma^5)G_{\mu\nu}, \tag{6.6}$$

where Λ is a new physics scale (we set $\Lambda = 1$ TeV); $G_{\mu\nu} = \partial_\mu V_\nu - \partial_\nu V_\mu$ and V_μ is a gauge boson, $|V|^2 + |A|^2 = |f|^2 + |h|^2 = 1$. New physics in the top-quark sector will be probed through anomalous top decays as well as through anomalous production rates or channels.

Both types of couplings (the "vector-like" $\propto \gamma^\mu$ and "tensor-like" $\propto \sigma^{\mu\nu}$, see Eq. (6.6)) could be investigated by means of rare top decays. On the other hand these two types of anomalous interactions have different behavior with respect to the energy of the subprocess of t-quark production. Indeed, near the threshold region the "vector-like" coupling gives the main contribution, while the "tensor-like" coupling becomes essential at high values of $\sqrt{\hat{s}} \gg m_t$. Note, that in hadronic collisions the production of a system with the high values of $\sqrt{\hat{s}}$ is suppressed due to parton luminosities. Therefore, we may conclude very roughly that in the production processes the "vector-like" couplings will be better investigated in hadronic collisions, while a linear collider provides the better potential to probe the "tensor-like" interactions. So, one expects the only combine analysis of the LHC and LC data could provide tiny constraints on the both types of couplings. Obviously that can not be achieved by analyzing the data from the only one type of a collider.

6.1.3.1 Probes of anomalous $gt\bar{t}$ coupling

Due to gauge invariance, only "tensor-like" interaction (top quark anomalous chromoelectric and chromomagnetic moments) ($\propto \sigma^{\mu\nu}$) could contribute to anomalous $gt\bar{t}$ couplings [576]. Such an anomalous coupling could be probed via the t-quark production at both LHC and LC machines. In hadronic collisions as it was shown in Ref. [608] the high-end tail of the top-quark p_T and $M_{t\bar{t}}$ distributions are the observables most sensitive to non-zero values of $\eta^g f$, with a reach for the combination $\frac{4m_t}{\Lambda}\eta^g f$ as small as $\simeq 0.03$. For these values only a minor change in the total $t\bar{t}$ rate is expected. The information on $\eta^g h$ could be obtained also by studying the correlation observables between $\ell^+\ell^-$ lepton pairs produced in the dilepton decays of $t\bar{t}$ pair [610]. In e^+e^- collisions such a coupling could be investigated by a measurement of the energy spectrum of the additional light (gluon) jet radiated off the top quark in the process $e^+e^- \to t\bar{t}g$ [608].

From the LHC collider alone one can achieve sensitivities to $\frac{4m_t}{\Lambda}\eta^g$ of order 0.03 with 100 fb^{-1} of integrated luminosity. This is similar in magnitude to what can be obtained at a 500 GeV LC with an integrated luminosity of 50 fb^{-1}. One should point out that at the LHC and at LC different kinematic characteristics are mostly sensitive to the anomalous moments. Therefore one expects that the combining analysis of the LHC and LC data will allow to get better accuracy in measurement of top-gluon anomalous couplings and possibly to distinguish chromoelectric and chromomagnetic moments by using polarized options of LC including photon collisions. The polarized electron-positron and photon-photon collisions are also allow to measure uniquely the $\gamma t\bar{t}$ and $Zt\bar{t}$ anomalous couplings [609].

6.1.3.2 Search for anomalous Wtb couplings

The Wtb vertex structure can be probed and measured using either top-quark-pair or single-top-quark production processes. The total $t\bar{t}$ rate depends very weakly on the Wtb vertex structure, as top quarks are dominantly produced on-shell [611]. However, more sensitive observables, like C and P asymmetries, top-quark polarization, and spin correlations provide interesting information. The single-top-quark production rate is directly proportional to the square of the Wtb coupling, and therefore it is potentially very sensitive to the Wtb structure [612]. The potential to measure anomalous Wtb couplings at the LHC via the production rate of single top quarks and from kinematic distributions has been studied in several papers [89, 613–616].

The potential of the hadron colliders can be compared to the potential of a next generation e^+e^- linear collider (LC) where the best sensitivity could be obtained in high energy γe-collisions [611, 617]. The results of this comparison are shown in Table 6.2 [in this table we present the constraints on the following combinations of anomalous couplings: $F_{L2} = \frac{2M_W}{\Lambda}\eta^W(-f^W - ih^W)$ and $F_{R2} = \frac{2M_W}{\Lambda}\eta^W(-f^W + ih^W)$]. One may conclude that the upgraded Tevatron will be able to perform the first direct measurements of the structure of the Wtb coupling. The LHC with 5% systematic uncertainties will improve the Tevatron limits considerably, rivaling the reach of a high-luminosity (500 fb^{-1}) 500 GeV LC option. A very high energy LC with 500 fb^{-1} luminosity will eventually improve the LHC limits by a factor of three to eight, depending on the coupling under consideration.

Table 6.2: Uncorrelated limits on anomalous couplings from measurements at different machines.

	F_{L2}			F_{R2}		
Tevatron ($\Delta_{\text{sys.}} \approx 10\%$)	-0.18	...	$+0.55$	-0.24	...	$+0.25$
LHC ($\Delta_{\text{sys.}} \approx 5\%$)	-0.052	...	$+0.097$	-0.12	...	$+0.13$
γe ($\sqrt{s_{e^+e^-}} = 0.5\,\text{TeV}$)	-0.1	...	$+0.1$	-0.1	...	$+0.1$
γe ($\sqrt{s_{e^+e^-}} = 2.0\,\text{TeV}$)	-0.008	...	$+0.035$	-0.016	...	$+0.016$

6.1.4 FCNC in top quark physics

While most of the rare decays expected in the SM are beyond any possible reach, there is a large class of theories beyond the SM where branching fractions for decays of top quarks induced by flavor-changing neutral currents (FCNC) could be as large as $10^{-5} - 10^{-6}$. Present constraints on top anomalous couplings are derived from low-energy data, direct searches of top rare decays [618], deviations from the SM prediction for $t\bar{t}$ production and searches for single-top-quark production at LEP 2 [619] and HERA [620]. A short summary of the present constraints on FCNC couplings, recalculated in terms of "branching ratio" (BR) is given in Table 6.3.

At present only a few cases (like-sign top-pair production, $t \to qZ$ and $t \to q\gamma$ decays, see [89, 207, 621]) have been investigated with a more or less realistic detector

Table 6.3: Current constraints on top-quark FCNC anomalous interactions presented in terms of "branching ratios" (here the symbol q stands for an up or charm quark).

	CDF	LEP-2	HERA
BR($t \to gq$)	$\leq 29\%$	–	–
BR($t \to \gamma q$)	$\leq 3.2\%$	–	$\leq 0.7\%$
BR($t \to Zq$)	$\leq 32\%$	$\leq 7.0\%$	–

simulation (ATLFAST [622] or CMSJET [390]). Other investigations were done at the parton level (the final quarks were considered as jets and a simple smearing of lepton, jet and photon energies was applied, cf. [623–626]).

For the LHC case all three possible FCNC decays have been investigated [89, 207]:

$$t \to qV, \quad \text{where } V = \gamma, Z, g \quad \text{and} \quad q = u \text{ or } c \tag{6.7}$$

The most important background processes include the production of $t\bar{t}$ pairs, $W+$ jets, $WW + WZ + ZZ$, $W + \gamma$, and single-top-quark production. The achievable branching ratios are summarized in Table 6.4.

The anomalous FCNC top-quark interaction can be probed also in the processes of single-top-quark production. There are four different subprocesses which lead to anomalous top-quark production in the final state together with one associated jet (see Fig. 6.6):

$$q\overline{q} \to t\overline{q}, \quad gg \to t\overline{q}, \quad qq \to tq, \quad qg \to tg\,. \tag{6.8}$$

The major background comes from $W + 2$ jets and $W + b\overline{b}$ production, as well as from single-top-quark production within SM approach [576].

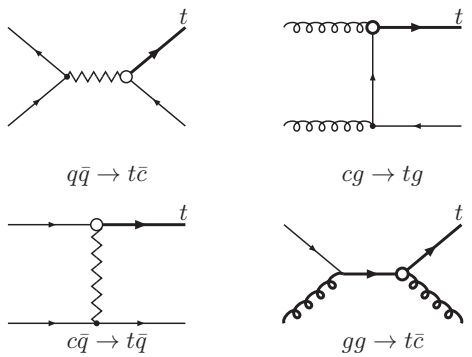

Figure 6.6: $2 \to 2$ single-top-quark production.

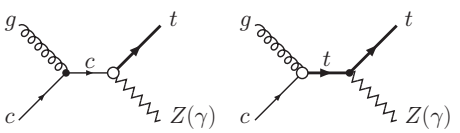

Figure 6.7: s-channel diagrams for tV ($V = Z, \gamma$) production

All anomalous FCNC couplings may contribute to the processes of single-top-quark production with an associated hard photon or Z-boson [625]:

$$qg \to \gamma t, \quad qg \to Zt.$$

The left diagram in Fig. 6.7 corresponds to the $Z(\gamma)tq$ coupling, while the right one shows the top-gluon anomalous coupling (the corresponding t-channel diagrams are not shown). It has been shown that the best limits on the top-quark FCNC couplings can be obtained from the decay channels $Zt \to \ell^+\ell^-\,\ell\nu b$ and $\gamma t \to \gamma\,\ell\nu b$. The most promising way to measure the anomalous FCNC top-gluon coupling seems to be the investigation of single-top-quark production processes, as the search for $t \to gq$ decays would be overwhelmed by background from QCD multi-jet events. At the same time, both top-quark production and decay would provide comparable limits on top-quark anomalous FCNC interactions with a photon or a Z-boson. In general, the studies shown above indicate that the LHC will improve by a factor of at least 10 the Tevatron sensitivity to top-quark FCNC couplings [207].

At a linear e^+e^- collider both methods of searching for FCNC interactions were considered (see [626, 627]): $t\bar{t}$-pair production via SM γ/Z-exchange with following FCNC decays $t \to q\gamma\,(Z)$:

$$e^+e^- \to t\bar{t}, \quad \text{with} \quad t \to q\gamma\,(Z), \tag{6.9}$$

and single-top-quark production due to FCNC anomalous interactions with the SM decay channel $t \to bW$:

$$e^+e^- \to tu(\bar{c}), \quad \text{with} \quad t \to bW. \tag{6.10}$$

It was shown in [626], that the top-quark decay signal from the process (6.9) is cleaner than ($t\bar{q}$) production (6.10). On the other hand, the cross sections for $t\bar{q}$-processes is larger than for $t\bar{t}$-production. At the same time the processes with FCNC top-quark decays (6.9) could help to determine the nature of the couplings involved, $t\gamma q$ or tZq. Also, it was shown that beam polarization will be very useful to improve the limits from $t\bar{q}$ production due to a substantial background decrease (see [626] for details).

Table 6.4: Future expectations on FCNC interactions from Run II of the Tevatron, LHC(CMS), and linear e^+e^- collider.

	Tevatron	LHC		e^+e^-
$t \to$	Run II	decay	production	$\sqrt{s} > 500$ GeV
$g\,q$	0.06%	1.6×10^{-3}	1×10^{-5}	–
$\gamma\,q$	0.28%	2.5×10^{-5}	3×10^{-6}	4×10^{-6}
$Z\,q$	1.3%	1.6×10^{-4}	1×10^{-4}	2×10^{-4}

Table 6.4 presents a short comparison of LHC and LC potentials to investigate FCNC couplings. Branching ratios of order 10^{-6} are achievable, which are of interest for some theories beyond the Standard Model, as discussed in Ref. [576]. Note that, due to the limited statistics which could be gathered in a future linear collider in the reaction $e^+e^- \to t\bar{t}$, the LHC has an advantage in the searches for rare top-quark decays. On the other hand, the future LC has a much smaller background. Therefore, both the LHC and a future LC have great potential to discover top-quark production

due to anomalous interactions. Only for anomalous interactions with a gluon (tgc or tgu) will the LHC have an evident advantage. There are many studies devoted to top-quark rare decays, like $t \to bWZ$, $t \to bH^+$, etc. However, almost all these investigations were performed for the LHC option only. We refer the reader to the most comprehensive review [576].

It has to be stressed that different types of new interactions may manifest itself in different ways at different colliders even for the same observables. So, only mutual LHC&LC analysis will provide more definite conclusions about a type of possible new interactions.

6.2 Electroweak precision physics

In this section the electroweak precision measurements, triple gauge boson couplings (TGC), and contact interactions are analyzed. Electroweak precision observables can play a role in various models. In many physics scenarios they can provide information about new physics scales that are too heavy to be detected directly. Several possible applications of precision observables are discussed in different parts of this report. Examples of the application of electroweak precision observables are

- the search for new gauge bosons, see Sect. 7.3.3,
- limits for new physics scales in little Higgs models, see Sect. 3.6,
- investigations on strong electroweak symmetry breaking, see Sect. 4,
- the search for heavy scales in supersymmetric theories, which will be covered in this section.

For the electroweak precision measurements (in the context of Supersymmetry) three example studies are presented. Physics scenarios which are dominated by LHC measurements can be probed much better if in addition the information from electroweak precision observables, obtained at the LC, is used. The triple gauge couplings are analyzed in view of a possible combination of the results of the LHC and the LC. In the case that both colliders can obtain independently about the same uncertainty, the combination of the two experiments can result in an even higher precision.

Concerning the physics of contact interactions a possible LHC/LC interplay could arise as follows. Precision measurements of $e^+e^- \to f\overline{f}$ at the LC and of Drell-Yan production at the LHC might exhibit deviations that could be interpreted in terms of contact interactions. While the LHC is sensitive to $u\overline{u} \to \ell^+\ell^-$ and to a somewhat lesser extend to $u\overline{d} \to \ell^+\ell^-$ the linear collider measures $e^+e^- \to q\overline{q}$ with unidentified quarks, $e^+e^- \to b\overline{b}$ and $e^+e^- \to \ell^+\ell^-$ with identified leptons. The combination of the two machines can thus disentangle the flavour structure of the new interactions in case a signal is seen.

6.2.1 Electroweak precision measurements at the LHC and the LC

The precision that can be achieved for electroweak precision observables (EWPO), including m_t and m_h has been analyzed in detail in Ref. [629] and is reviewed in

Table 6.5. The numbers listed there represent the sensitivities that can be reached by each individual collider. The reach of the LC is seen to exceed that of the LHC (due to its cleaner environment) for all relevant observables. It is therefore difficult to find a case of positive LHC/LC interplay by just looking at EWPO's. This, however, changes if SUSY scenarios are analyzed. It is conceivable that part of the SUSY spectrum, due to the large masses of some of the SUSY partners, can only be determined by the LHC [14]. This may especially be relevant in the case of scalar top quarks which play an important role for the SUSY interpretation of EWPO's, see e.g. Refs. [569, 630]. In this case, the measurement of the SUSY mass spectrum at the LHC and the LC can be combined with precision measurements of the EWPO's to derive constraints on the remaining unknown parameters or to perform stringent consistency checks of the underlying model. This will be shown for some representative scenarios in the following subsections.

	now	Tev. Run IIA	Run IIB	LHC	LC	GigaZ
$\delta \sin^2\theta_{\rm eff}(\times 10^5)$	17	78	29	14–20	(6)	1.3
δM_W [MeV]	34	27	16	15	10	7
δm_t [GeV]	5.1	2.7	1.4	1.0	0.2–0.1	0.1
δm_h [MeV]	—	—	$\mathcal{O}(2000)$	200	50	50

Table 6.5: Current and anticipated future experimental uncertainties for the effective leptonic mixing angle, $\sin^2\theta_{\rm eff}$, the W boson mass, M_W, the top quark mass, m_t, and the Higgs boson mass, m_h. See Ref. [629] for a detailed discussion and further references.

6.2.2 Constraints on the parameters of the scalar top sector

Once a Higgs boson compatible with the MSSM predictions has been discovered, the dependence of m_h on the top and scalar top [32, 630] sector can be utilized to determine unknown parameters of the $\tilde{t}$ sector [170, 631].

The mass matrix relating the interaction eigenstates $\tilde{t}_L$ and $\tilde{t}_R$ to the mass eigenstates is given by

$$\mathcal{M}^2_{\tilde{t}} = \begin{pmatrix} M^2_{\tilde{t}_L} + m_t^2 + \cos 2\beta\,(\frac{1}{2} - \frac{2}{3}s^2_W)M^2_Z & m_t X_t \\ m_t X_t & M^2_{\tilde{t}_R} + m_t^2 + \frac{2}{3}\cos 2\beta\, s^2_W M^2_Z \end{pmatrix}, \quad (6.11)$$

where X_t can be decomposed as $X_t = A_t - \mu/\tan\beta$. A_t denotes the trilinear Higgs–$\tilde{t}$ coupling. Assuming that $\tan\beta$ and μ can be determined from other sectors, there are three new parameters in the mass matrix, the soft SUSY-breaking parameters $M_{\tilde{t}_L}$, $M_{\tilde{t}_R}$, and A_t. The mass eigenvalues of the scalar top states are obtained after a rotation with the angle $\theta_{\tilde{t}}$,

$$\mathcal{M}^2_{\tilde{t}} \quad \xrightarrow{\theta_{\tilde{t}}} \quad \begin{pmatrix} m^2_{\tilde{t}_1} & 0 \\ 0 & m^2_{\tilde{t}_2} \end{pmatrix}. \quad (6.12)$$

Scenario I: the two masses $m_{\tilde{t}_1}$, $m_{\tilde{t}_2}$ are determined at the LHC, but $\tilde{t}_1$ and $\tilde{t}_2$ are too heavy for direct production at the LC. In this case the direct measurement of the off-diagonal entry in the $\tilde{t}$ mass matrix Eq. (6.11), i.e. a measurement of $\theta_{\tilde{t}}$, is not possible and the trilinear coupling A_t cannot be determined. However, measurement of m_h would allow an indirect determination of A_t [170]. This is shown for the benchmark scenario SPS1b [14] in Fig. 6.8 (evaluated with *FeynHiggs* [632–634]). In this scenario, a measurement of M_A and $\tan\beta$ at the LHC is possible [114]. In Fig. 6.8 the experimental error of m_h is indicated, whereas the theoretical error due to unknown higher order corrections has been neglected; see Ref. [170] for details. Fig. 6.8 demonstrates that A_t can be determined with LHC measurements alone; the allowed range is indicated by the green (light shaded) area. However, the precise determination of m_t at the LC improves the accuracy for A_t by about a factor of three over that which can be achieved with the LHC m_t measurement. Concerning resolving the sign ambiguity of A_t, see Sect. 3.3.1.

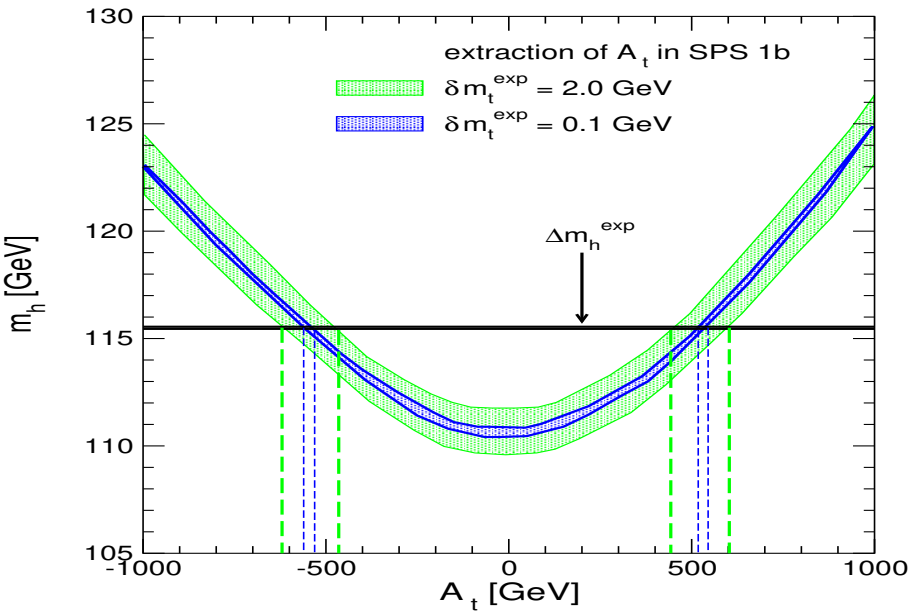

Figure 6.8: Indirect determination of A_t in the SPS1b scenario for $\tan\beta = 30$, $\delta m_t^{\rm exp} = 2$ GeV (LHC) and $\delta m_t^{\rm exp} = 0.1$ GeV (LC). The statistical uncertainty of the Higgs boson mass, $\Delta m_h^{\rm exp}$, is indicated. The SUSY parameters $m_{\tilde{t}_1}, m_{\tilde{t}_2}, m_{\tilde{b}_1}, m_{\tilde{b}_2}$ are assumed to be given by the values predicted by SPS1b with an uncertainty of 5%. M_A and $\tan\beta$ are assumed to be determined with a precision of 10% and 15%, respectively.

Scenario II: in this example [57, 170], the lighter scalar top quark and M_A are accessible at the LC, whereas only a lower bound can be established for $\tan\beta$. The LC will provide precise measurements of its mass, $m_{\tilde{t}_1}$, and the $\tilde{t}$ mixing angle, $\theta_{\tilde{t}}$ [635, 636]. On the other hand, the heavier scalar top, $\tilde{t}_2$, can only be detected at the LHC. The measurement of m_h can then be used to obtain indirect limits on $m_{\tilde{t}_2}$. Comparison of the indirectly determined $m_{\tilde{t}_2}$ with the value obtained from a direct measurement at the LHC will provide a stringent consistency test of the MSSM. In Fig. 6.9 we show the allowed region in the $m_{\tilde{t}_2} - m_h$-plane for this scenario. Assuming that the top

quark mass can be determined with a precision of $\delta m_t = 0.1$ GeV at the LC, one finds $680 \text{ GeV} \lesssim m_{\tilde{t}_2} \lesssim 695 \text{ GeV}$. For comparison, for $\delta m_t = 2$ GeV, as expected from LHC experiments, one obtains $670 \text{ GeV} \lesssim m_{\tilde{t}_2} \lesssim 705 \text{ GeV}$, i.e. the precise determination of m_t at the LC reduces the uncertainty of $m_{\tilde{t}_2}$ by about a factor 3. Again the theoretical error due to unknown higher order corrections to m_h has been neglected; see Ref. [170] for details.

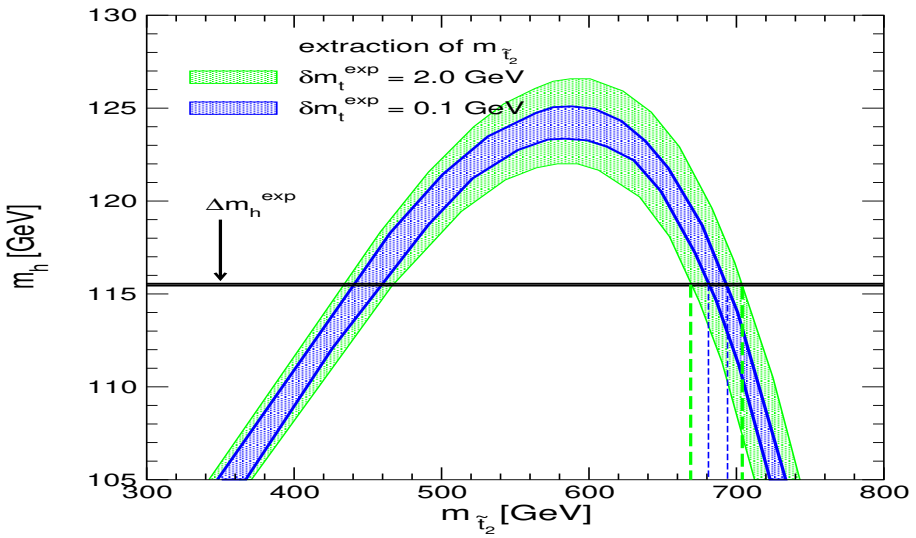

Figure 6.9: Indirect determination of $m_{\tilde{t}_2}$ from the measurement of m_h for $\delta m_t^{\text{exp}} = 2$ GeV (LHC) and $\delta m_t^{\text{exp}} = 0.1$ GeV (LC). The experimental error of the Higgs boson mass, δm_h^{exp}, is indicated. The other parameters are given by $m_{\tilde{t}_1} = 180 \pm 1.25$ GeV, $\cos\theta_{\tilde{t}} = 0.57 \pm 0.01$, $M_A = 257 \pm 10$ GeV, $\tan\beta > 10$, $\mu = 263 \pm 1$ GeV, $m_{\tilde{g}} = 496 \pm 10$ GeV, $A_b = A_t \pm 30\%$, and a lower bound of 200 GeV has been imposed on the lighter sbottom mass.

6.2.3 Constraints on the parameters of the MSSM Higgs boson sector

In the previous scenarios the parameters of the Higgs sector were assumed to be known. However, it may also be possible to use SUSY mass measurements at the LHC in combination with the EWPO measurement (especially M_W and $\sin^2\theta_{\text{eff}}$) at the LC to obtain information on the (unknown) parameters of the Higgs sector [569].

Scenario III: In Fig. 6.10 we show the parameter space of a scenario where the MSSM Higgs mass scale, the mass of the CP-odd Higgs boson M_A, cannot be measured directly at the LHC nor the LC (for most of the shown parameter space). However, the combination of LHC and LC mass measurements together with the M_W, $\sin^2\theta_{\text{eff}}$ from GigaZ and the m_h determination at the LC (see the plot for further details) can set an upper bound of $M_A \lesssim 1200$ GeV.

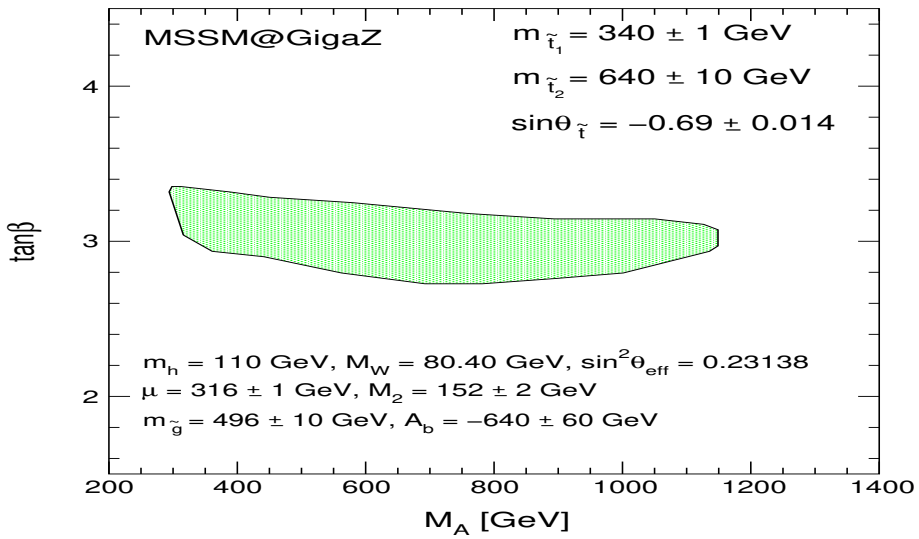

Figure 6.10: The region in the $M_A - \tan\beta$ -plane allowed by the measurements of the SUSY spectrum at the LHC and the LC and by the measurements of M_W, $\sin^2\theta_{\text{eff}}$ and m_h at the LC.

6.2.4 Triple gauge boson couplings

The LHC will significantly improve the precision of the measurements of the triple gauge boson couplings (TGC) compared to the LEP and Tevatron results [637]. In the SM, the TGC's are uniquely fixed by gauge invariance. Extensions to the SM, in particular models in which the W and Z bosons are composite objects, often lead to deviations from the SM predictions for the TGC's.

Assuming electromagnetic gauge invariance, Lorentz invariance, and C-and P-conservation, five parameters can be used to describe the three gauge boson vertices [637]:

$$\Delta g_1^Z = g_1^Z - 1\,, \qquad \Delta\kappa_V = \kappa_V - 1\,, \qquad \lambda_V \qquad\qquad (V = \gamma,\, Z)\,. \tag{6.13}$$

In the SM, at tree level, all five parameters vanish.

At the LHC, $W\gamma$ and WZ production can be used to constrain TGC's. WW production, which is also sensitive to the weak boson self-couplings, suffers from a large $t\bar{t}$ background, and, therefore, is not considered. $W\gamma$ production probes the $WW\gamma$ couplings $\Delta\kappa_\gamma$ and λ_γ. WZ production is sensitive to the WWZ couplings Δg_1^Z, $\Delta\kappa_Z$ and λ_Z.

The experimental sensitivity to anomalous TGC's arises from the growth of the non-standard contributions to the helicity amplitudes with energy, and from modifications to angular distributions. In hadronic collisions, one usually exploits the former by measuring the transverse momentum distribution of the photon or Z boson [637]. The energy dependence is most pronounced for λ_V and Δg_1^Z. Figure 6.11 shows the expected 95% confidence level constraints on TGC's in ATLAS, resulting from two-parameter fits [207]. There are strong correlations between Δg_1^Z and the other WWZ couplings, $\Delta\kappa_Z$ and λ_Z. At the LHC, the limits for λ_V and Δg_1^Z are of $\mathcal{O}(10^{-3})$, while the precision of $\Delta\kappa_V$ is $\mathcal{O}(10^{-2})$. An increase in the integrated luminosity by a factor 10 improves the limits by a factor 1.3 to 2. A similar improvement

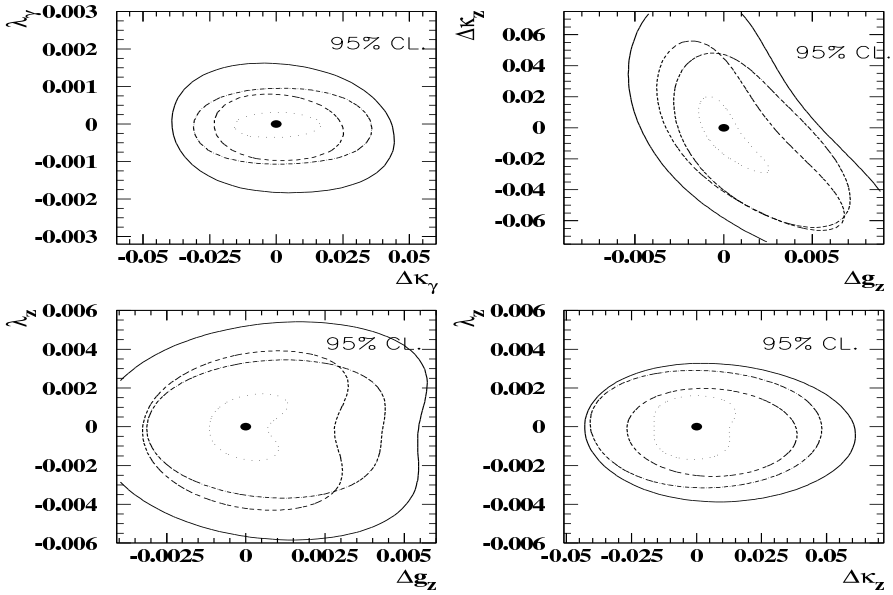

Figure 6.11: Expected 95% CL constraints on TGC's in ATLAS resulting from two-parameter fits. Shown are results for $\sqrt{s} = 14$ TeV and 100 fb^{-1} (solid), $\sqrt{s} = 28$ TeV and 100 fb^{-1} (dot-dash), $\sqrt{s} = 14$ TeV and 1000 fb^{-1} (dash), and $\sqrt{s} = 28$ TeV and 1000 fb^{-1} (dotted). The figure has been taken from Ref. [207].

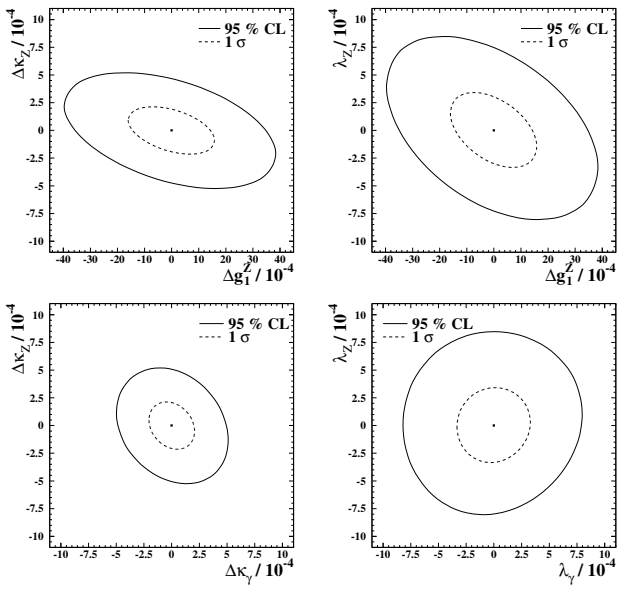

Figure 6.12: 1σ and 95% CL (2D) contours for TGC's in the 5-parameter fit of $e^+e^- \to W^+W^-$ ($\sqrt{s} = 800$ GeV, $\mathcal{L} = 1000\,\text{fb}^{-1}$, $\mathcal{P}_{e^-} = 0.8$, $\mathcal{P}_{e^+} = 0.6$). The figure is taken from Ref. [57].

is observed if the machine energy is doubled. Doubling the energy and increasing the luminosity yields bounds which are up to a factor 7 more stringent than those obtained for $\sqrt{s} = 14$ TeV and 100 fb^{-1}.

At the LC, the most stringent bounds are obtained from angular distributions in

W pair production. Sensitivity bounds for $\sqrt{s} = 800$ GeV and an integrated luminosity of 1 ab^{-1} are shown in Fig. 6.12 [57]. For these bounds electron and positron polarization has been assumed, $\mathcal{P}_{e^-} = 0.8$, $\mathcal{P}_{e^+} = 0.6$. If positron polarizaation would not be available, the bounds would be weakened by about a factor 2. For e^+e^- collisions at $\sqrt{s} = 500$ GeV, but both beams polarized, one finds bounds which are a factor 1.2 to 2 less stringent than those shown in Fig. 6.12. All bounds, with the exception of those for Δg_1^Z, are of $\mathcal{O}(10^{-4})$ and thus are significantly better than those obtained at the LHC, even with an energy and/or luminosity upgrade. The results for the anticipated precision of all TGC's for LEP, the Tevatron assuming 1 fb^{-1} for each experiment [638], the LHC assuming 30 fb^{-1} for each experiment [639] and for the LC assuming either 500 fb^{-1} at $\sqrt{s} = 500$ GeV or 1000 fb^{-1} at $\sqrt{s} = 800$ GeV [57] is summarized in Fig. 6.13. Both, LEP and Tevatron analyses employ the relations $\Delta\kappa_\gamma = -\cot^2\theta_W(\Delta\kappa_Z - \Delta g_1^Z)$ and $\lambda_\gamma = \lambda_Z$ (with $\cos\theta_W = M_W/M_Z$).

Only for Δg_1^Z would a combined measurement from LHC and LC experiments result in a noticeable improvement of our knowledge of gauge boson self-interactions: from Figs. 6.11 and 6.12 one observes that Δg_1^Z can be measured with similar precision independently at the LHC and a LC. Combining LHC and LC limits for Δg_1^Z may thus result in significantly improved constraints by up to a factor of two for this parameter.

Electroweak radiative corrections within the SM to the TGC's are of order $\sim 10^{-3}$ [640] and thus significantly larger than the expected sensitivities at the LC. Similar corrections can be expected in the MSSM. No detailed study exists yet, but it can be expected that LHC/LC analyses similar to the one presented in Sect 6.2.3 are possible.

Although (with the above exception) TGC's can in general be determined much more precisely at a LC, a positive interplay with the LHC may arise in specific models. For example, in models where the electroweak symmetry is broken dynamically, TGC's may be related to the masses of heavy vector resonances which appear in these models. These resonances have masses which typically are of $\mathcal{O}(1 - 2$ TeV$)$. A precise measurement of the TGC's at a 500–800 GeV LC may thus allow for an indirect determination of the masses of such resonances, and provide specific information for a search for such particles at the LHC (see Sect. 4 for more details).

One can also probe the self-couplings of the neutral gauge bosons ($ZZ\gamma$,¿ $Z\gamma\gamma$ and ZZZ couplings) at the LHC [641, 642] and LC [643]. In the SM, at tree level, these couplings all vanish. The sensitivity limits which can be achieved for these couplings at the LHC strongly depend on the form factor scale assumed. For a form factor scale in the range of $2 - 3$ TeV, the bounds which can be achieved at the LHC and LC are similar. They are about one order of magnitude larger than what the SM predicts at the one-loop level [641].

6.2.5 Conclusions

In this section the electroweak precision measurements (in the context of supersymmetry) and triple gauge boson couplings (TGC) have been analyzed. Other applications of electroweak precision observables can be found in Sects. 7.3.3, 3.6, 4.

For the electroweak precision measurements within Supersymmetry three example studies have been performed. Often SUSY scenarios possess scales that cannot be

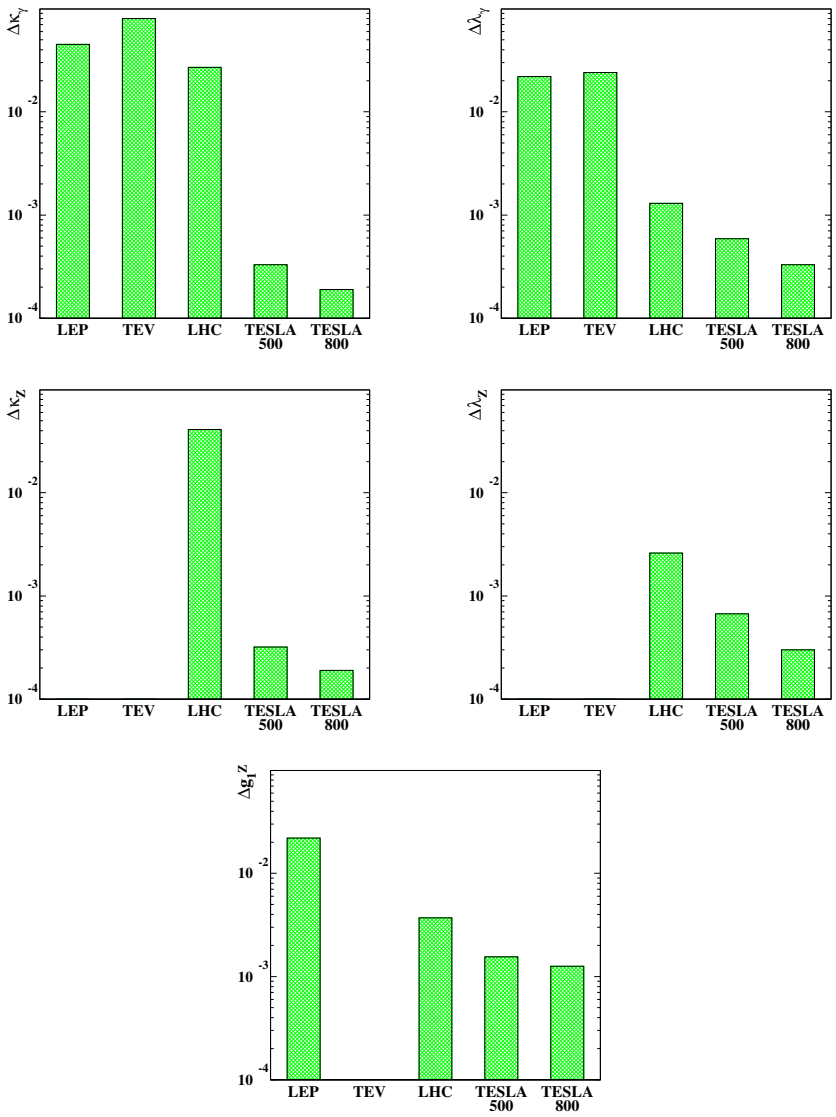

Figure 6.13: Anticipated precisions for the TGC's at the Tevatron [638] (assuming 1 fb^{-1} for each experiment), the LHC [639] (assuming 30 fb^{-1} for each experiment) and a LC [57] (assuming either 500 fb^{-1} at $\sqrt{s} = 500$ GeV or 1000 fb^{-1} at $\sqrt{s} = 800$ GeV). Both, LEP and Tevatron analyses employ the relations $\Delta\kappa_\gamma = -\cot^2\theta_W(\Delta\kappa_Z - \Delta g_1^Z)$ and $\lambda_\gamma = \lambda_Z$.

detected at the LHC and LC. The three examples have shown how in this case electroweak precision observables (e.g. M_W, $\sin^2\theta_{\text{eff}}$ and m_t), measured most accuratly at the LC, can help to determine these heavy scales. The interplay of observables measured at the LHC and at the LC, together with the precision observables can be crucial.

The triple gauge couplings have been analyzed in view of a possible combination of the results of the LHC and the LC. In the case of Δg_1^Z both colliders can obtain independently about the same uncertainty. Thus the combination of the two experiments

can result in an higher precision by up to a factor of 2.

Concerning the physics of contact interactions the LHC/LC interplay could help to disentangle the flavour structure of the new interactions in case a signal is seen.

6.3 QCD studies

Both the Large Hadron Collider and the Linear Collider are ideal machines for testing Quantum Chromodynamics, and in particular for making precision measurements related to the strong interaction. As has already been clearly demonstrated by past and present machines (for example LEP and the CERN and Tevatron $p\overline{p}$ colliders), the two colliders are complementary in what they can measure and with what precision. The benchmark QCD measurements for each machine are:

Linear Collider [9]

- precision determination of α_S through event shape observables, multijet final states, etc.
- Q^2 evolution of α_S and "higher-twist" (i.e. Q^{-n}) contributions to hadronic observables
- QCD effects in $t\bar{t}$ production, both at threshold and in the continuum
- fragmentation functions
- $\gamma\gamma$ physics
  - unpolarised and polarised photon structure functions $F_2^\gamma(x,Q^2)$ ($g_1^\gamma(x,Q^2)$) at low x or high Q^2
  - $\gamma\gamma$ and $\gamma^*\gamma^*$ total cross sections as a test of non-perturbative and perturbative QCD (BFKL dynamics) respectively

LHC [644]

- production of high E_T jets, to determine α_S and pin down parton distribution functions (pdfs) and to calibrate backgrounds to new-physics processes
- W and Z total cross sections, as a test of precision NNLO QCD predictions
- W and Z transverse momentum distributions, as a test of Sudakov resummation
- heavy flavour (c, b and t) cross sections, as a test of QCD dynamics, for example threshold resummations, production mechanisms for quarkonia, etc.
- prompt photon and diphoton production, to measure the gluon distribution and to calibrate backgrounds to Higgs production
- forward jet, $W+$ jet, heavy quark, .. production as a test of BFKL dynamics

- diffractive processes, both 'hard' and 'soft'

In terms of the *complementarity* of the QCD measurements at the two machines, one can note the following:

- There is a strong correlation between the gluon distribution and the strong coupling α_S in the theoretical prediction for the large E_T jet cross section at hadron colliders. A precision measurement of α_S at high Q^2 at the LC can be fed back into the LHC analysis to extract the gluon pdf from large E_T jet and prompt photon data with greater precision, see Section 6.3.1 below.

- Among the backgrounds to Higgs $\rightarrow \gamma\gamma$ production at the LHC, one of the most important arises from the fragmentation of a quark or gluon into a photon, $q, g \rightarrow \gamma + X$. A precise knowledge of these fragmentation functions is required to control the SM background. The LC can provide such information, particularly in the large z region. This is discussed in more detail in Section 6.3.3 below.

- The tests of (small-x) BFKL dynamics at the two machines centre on the exchange of a 'perturbative pomeron' between two softly scattered hadronic systems, but utilise different initial and final states ($\gamma^*\gamma^* \rightarrow q\overline{q}q\overline{q}$ for the LC and $gg \rightarrow gg, b\overline{b}b\overline{b}$, ... for the LHC) and therefore have different systematics. The phenomenology of such processes is not straightforward at either machine, and therefore information from both will probably be necessary to provide firm evidence for BFKL effects. This is discussed in more detail in Section 6.3.2 below.

- If supplemented with forward detectors to measure the scattered protons, the LHC could also study $\gamma\gamma$ interactions. Centre-of-mass energy values, $\sqrt{s_{\gamma\gamma}}$, above 1 TeV could be reached. If total $\gamma\gamma$ cross sections can be measured at these high energies, with sufficiently small systematic errors, these measurements can be used to estimate more accurately the expected background at a LC, particularly for a multi-TeV collider such as CLIC. Conversely, the measurement of total $\gamma\gamma$ cross sections at a LC, in particular at its derived photon collider, with much better precision than at the LHC will give improved understanding of the LHC results in the $\sqrt{s_{\gamma\gamma}}$ region of overlap, i.e. below 500 GeV.

6.3.1 Measurements of α_S

The strong coupling α_S can in principle be measured at hadron colliders through processes involving jets, either from 'pure QCD' multijet final states or from processes like $W+$ jet production. Difficulties arise, however, from the need for an accurate measurement of the jet (i.e. parton) energies, which requires detailed knowledge of calorimeter response, fragmentation effects, the underlying event, etc.

A further problem is that α_S is inevitably correlated with the parton distribution functions. For example, in the combination $\alpha_S f(x, Q^2)$, where $f = q, g$, at high x increasing the value of α_S will, via the DGLAP evolution equations, cause a decrease in f, thus compensating the effect due to the explicit factor of the coupling. In fact for this reason the $W+$ jet cross section at the Tevatron is relatively insensitive to the value of the coupling constant, see for example [645].

The inclusive high E_T jet cross section offers high statistics and more sensitivity to the coupling. For example, a recent measurement by the CDF collaboration at the Tevatron $p\overline{p}$ collider [646] gives

$$\alpha_S(M_Z^2)_{\rm NLO} = 0.1178 \pm 0.0001 \text{ (stat)} \; {}^{+0.0081}_{-0.0095} \text{ (expt. syst.)} \tag{6.14}$$

There are many contributions to the experimental systematic error, the largest being due to the calorimeter response to jets.

The above result does not include any additional theoretical error from factorisation and renormalisation scale dependence — the standard variation of these scales is estimated to give rise to an additional (theoretical) error of approximately ± 0.005 [648]. There is also a systematic error from the dependence on the input parton distribution functions.[1] Because of the strong correlation between these and α_S, it is difficult to estimate this accurately in isolation from the global pdf fit. Note that Tevatron large E_T jet data are included in both the latest MRST [650] and CTEQ [651] global analyses, and have some influence on the α_S value that is a by-product of such studies.[2] Combining errors in quadrature would give $\alpha_S(M_Z^2) = 0.118 \pm 0.011$ from the CDF jet data, to be compared to the world average (PDG, 2002) value of $\alpha_S(M_Z^2) = 0.1172 \pm 0.002$ [647].

When considering how such a measurement would extrapolate to the LHC, one can assume that the NNLO corrections will be known (for a recent review of progress in this area, see for example [652]), and therefore that the theoretical systematic error will be much reduced. The statistical error will also be small, and the systematic errors associated with the jet measurement may improve by a factor two or so, using the channel $W \to$ jets, in tagged $t\bar{t}$ events. However, the problem with the α_S – pdf correlation will persist, indeed the jet cross section data will be used to pin down the gluon distribution at medium and high x. Note that even though the measurements of α_S will be made at a very high scale $Q \sim E_T^{\rm jet} \sim \mathcal{O}(\text{TeV})$, this does not help improve the precision on the derived value of $\alpha_S(M_Z^2)$.

At the e^+e^- colliders LEP and SLC, α_S was measured in a number of ways, including (i) from the Z^0 hadronic width via a global precision electroweak fit ($\alpha_S(M_Z^2) = 0.1200 \pm 0.0028 \pm 0.002$ (scale), [647]) (LEP1 and SLC) and (ii) from various hadronic final state jet and event shapes measures (Thrust, C parameter, R_3 etc, ...) at LEP1, LEP2 and SLC. These latter measurements are all based on the basic $\mathcal{O}(\alpha_S)$ $e^+e^- \to q\overline{q}g$ process, with NLO $\mathcal{O}(\alpha_S^2)$ perturbative QCD corrections included. An average value based on many such measurements from all the collaborations at LEP and SLC is $\alpha_S(M_Z^2) = 0.122 \pm 0.007$, where the error is totally dominated by the theoretical uncertainties associated with the choice of scale, and the effect of hadronisation on the different quantities fitted [647].

Extrapolation of the hadronic final state α_S measurement to a LC is reasonably straightforward, assuming of course similar or even improved detector capabilities.[3]

[1] A study of the impact of the pdf uncertainty on the production cross sections for Drell-Yan lepton pairs and Higgs bosons at the LHC has been performed by Bourilkov as part of this workshop, see Ref. [649].

[2] For example, the most recent MRST value is $\alpha_S(M_Z^2) = 0.1165 \pm 0.002$ (expt.) ± 0.003 (theory).

[3] The results for the estimated errors on α_S at a LC in this section are taken from [57].

With luminosities of order $10^{34}\ \mathrm{cm}^{-2}\mathrm{s}^{-1}$ or greater, and centre-of-mass energies $\sqrt{s} = 500 - 1000$ TeV, a LC should produce enough $e^+e^- \to q\overline{q}(g)$ events to achieve a statistical error of order $\Delta\alpha_S(M_Z^2) \simeq 0.001$ or better. Assuming hermetic detectors with good calorimetry and tracking, the systematic uncertainties from detector effects should also be controllable to this level of accuracy. The uncertainties associated with hadronisation depend quite sensitively on the observable, but in every case are expected to decrease with increasing energy at least as fast as $1/Q$. An order of magnitude improvement can therefore be expected at a LC compared with LEP1/SLC, and once again the associated uncertainty should be well below the $\Delta\alpha_S(M_Z^2) = 0.001$ level. This leaves the theoretical systematic error from unknown higher-order corrections as the dominant source of uncertainty on α_S, as at LEP/SLC. However, it will certainly be the case that the NNLO corrections to all the relevant jet rates and event shape variables will be known by the time a LC comes into operation [652]. The current error on α_S from this source, $\Delta\alpha_S(M_Z^2) \simeq 0.006$, is therefore likely to decrease significantly, and could well be at the 0.001 level. Putting everything together, a reasonable expectation is

$$\Delta\alpha_S(M_Z^2)\ |_{\mathrm{LC}} = \ \pm 0.001\ \text{(expt.)}\ \pm 0.001\ \text{(theory)} \tag{6.15}$$

which is (a) comparable with the current world average error, and (b) much smaller than the likely error from any measurement at the LHC.

Of course by running a linear collider in a GigaZ mode at the Z resonance, precision α_S measurements can be made using the same techniques as at LEP1 and SLC. For example, the ratio of leptonic to hadronic Z decay widths could be measured with a precision of order $\delta R_l/R_l = \pm 0.05\%$, or maybe even slightly better, which provides a very clean determination of the strong coupling (via the perturbative QCD corrections $[1 + \alpha_S/\pi + ...]$ to the hadronic decay widths) with an estimated error of $\Delta\alpha_S(M_Z^2) \approx \pm 0.001$. For a more complete discussion see Refs. [569, 653].

In terms of the synergy between the two machines, therefore, precision measurements of α_S at a LC, made at comparable Q scales, can be input into QCD analyses at the LHC, thus improving the precision on the pdf measurements for example. To see the possible quantitative effect of this, consider the contribution to the theoretical systematic error on the Higgs ($gg \to H$) total cross section at LHC from the uncertainty on the input gluon distribution. From Fig. 6.14, taken from Ref. [650], we see that this is currently $\pm 3\%$ when α_S is allowed to vary in the fit, but reduces to $\pm 2\%$ when α_S is fixed, for example by a high-precision external measurement such as could be made at the LC.

6.3.2 BFKL physics

6.3.2.1 Introduction

Many processes in QCD can be described by a fixed order expansion in the strong coupling constant α_S. In some kinematic regimes, however, each power of α_S gets multiplied by a large logarithm (of some ratio of relevant scales), and fixed-order calculations must give way to leading-log calculations in which such terms are resummed. The BFKL equation [654] resums these large logarithms when they arise

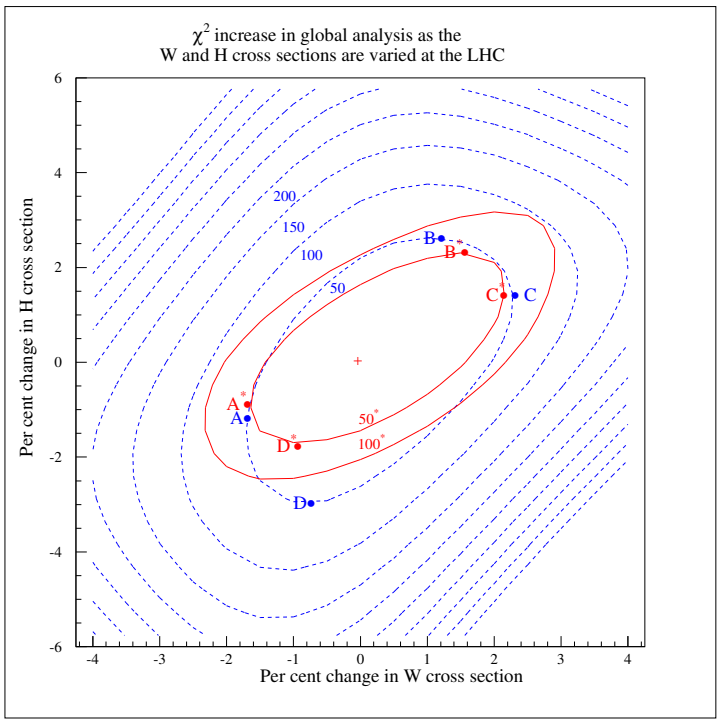

Figure 6.14: Contours with $\Delta\chi^2 = 50, 100\ldots$ obtained by performing global pdf fits with the values of σ_W and σ_H, at the LHC energy, fixed in the neighbourhood of their values predicted by the unconstrained MRST2001 fit. The $\Delta\chi^2 = 50$ contour is taken to represent the errors on σ_W and σ_H (arising from the experimental errors on the data used in the global pdf fit). The dashed contours are obtained if $\alpha_S(M_Z^2)$ is allowed to vary. The superimposed solid $\Delta\chi^2 = 50, 100$ contours are obtained if $\alpha_S(M_Z^2)$ is fixed at 0.119.

from multiple (real and virtual) gluon emissions for scattering processes in the so called high-energy limit, for example $gg \to gg$ for $s \to \infty$, $|t|$ fixed. In the BFKL regime, the transverse momenta of the contributing gluons are comparable but they are strongly ordered in rapidity.

The leading-order BFKL equation can be solved analytically, and its solutions usually result in (parton-level) cross sections that increase as the power λ, where $\lambda = 4C_A\ell_n 2\,\alpha_s/\pi \approx 0.5$.[4] For example, in dijet production at large rapidity separation Δ in hadron colliders [655], BFKL predicts for the (qq, qg or gg) parton-level cross section $\hat{\sigma} \sim e^{\lambda\Delta}$. In virtual photon - virtual photon scattering into hadrons, as measured for example in e^+e^- collisions, BFKL becomes relevant when the electron and positron emerge with a small scattering angle and hadrons are produced centrally [656, 657]. In that case BFKL predicts $\sigma_{\gamma^*\gamma^*} \sim (W^2/Q^2)^\lambda$, where W^2 is the invariant mass of the hadronic system (equivalently, the photon-photon centre-of-mass energy) and Q^2 is the invariant mass of either photon.

[4] λ is also known as $\alpha_P - 1$.

6.3.2.2 Experimental status and improved predictions

The experimental status of BFKL is ambiguous at best, with existing results being far from definitive. The data tend to lie between the predictions of fixed-order QCD and analytic solutions to the BFKL equation. This happens, for example, for the azimuthal decorrelation in dijet production at the Fermilab Tevatron [658] and for the virtual photon cross section at LEP [659]. Similar results are found for forward jet production in deep inelastic ep collisions at HERA [660, 661].

It is not so surprising that analytic BFKL predicts stronger effects than seen in data. Analytic BFKL solutions implicitly contain sums over arbitrary numbers of gluons with arbitrary energies, but the kinematics are leading-order only. As a result there is no kinematic cost to emit gluons, and energy and momentum are not conserved, and BFKL effects are artificially enhanced.

This situation can be remedied by a Monte Carlo implementation of solutions to the BFKL equation [662,663]. In such an implementation the BFKL equation is solved by iteration, making the sum over gluons explicit. Then kinematic constraints can be implemented directly, and conservation of energy and momentum is restored. This tends to lead to a suppression of BFKL-type effects. The Monte Carlo approach has been applied to dijet production at hadron colliders [662–665] leading to better (though still not perfect) agreement with the dijet azimuthal decorrelation data at the Tevatron [662]. Predictions for the azimuthal angle decorrelation in dijet production at the Tevatron and the LHC, as a function of the dijet rapidity difference Δy, are shown in Fig. 6.15 [664]. The normalisation is such that $\langle \cos \Delta\phi \rangle = 1$ corresponds to jets which are back-to-back in the transverse plane, while completely uncorrelated jets have $\langle \cos \Delta\phi \rangle = 0$. Kinematic suppression of gluon emission accounts for a substantial part of the difference between analytic (asympototic) and Monte Carlo BFKL predictions. This kinematic suppression is however not as dramatic at the LHC, because of its relatively higher centre-of-mass energy compared to the jet transverse momentum threshold. As a result, improved BFKL MC predictions tend to retain more BFKL-type behaviour because of the greater phase space for emitting gluons [664]. Studies of dijet production in BFKL physics therefore look promising at the LHC, and such studies will benefit from jet detection capabilities that extend far into the forward region and allow for p_T thresholds as low as possible.

Other similar studies have considered forward $W+$ jet production at hadron colliders [666], and the associated jet production in dijet production [667]. Applications to forward jet production at HERA and to virtual photon scattering in e^+e^- collisions are underway; an update on the latter appears in the next section.

6.3.2.3 $\gamma^*\gamma^*$ scattering at the Linear Collider: a closer look

BFKL effects can arise in e^+e^- collisions via the scattering of virtual photons emitted from the initial e^+ and e^-. The scattered electron and positron appear in the forward and backward regions ("double-tagged" events) with hadrons in between. With total centre-of-mass energy s, photon virtuality $-Q^2$, and photon-photon invariant mass (= invariant mass of the final hadronic system) W^2, BFKL effects are expected in the kinematic regime where W^2 is large and

$$s \gg Q^2 \gg \Lambda^2_{QCD}.$$

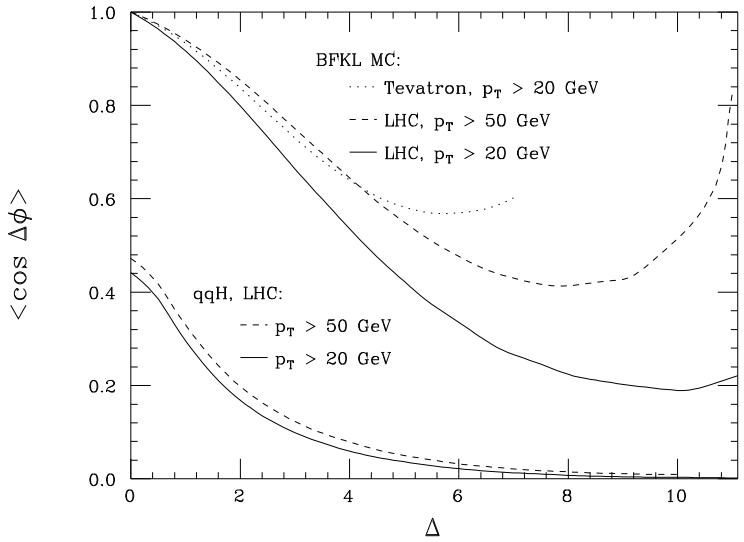

Figure 6.15: The azimuthal angle decorrelation in dijet production at the Tevatron ($\sqrt{s} = 1.8$ GeV) and LHC ($\sqrt{s} = 14$ TeV) as a function of dijet rapidity difference $\Delta = \Delta y$. The upper curves are computed using the improved BFKL MC with running α_s; they are: (i) Tevatron, $p_T > 20$ GeV (dotted curve), (ii) LHC, $p_T > 20$ GeV (solid curve), and (iii) LHC, $p_T > 50$ GeV (dashed curve). The lower curves are for dijet production in the process $qq \to qqH$ for $p_T > 20$ GeV (solid curve) and $p_T > 50$ GeV (dashed curve).

At fixed order in QCD, the dominant process is four-quark production with t-channel gluon exchange (each photon couples to a quark box; the quark boxes are connected via the gluon). The corresponding BFKL contribution arises from diagrams with a gluon ladder attached to the exchanged t-channel gluon.

The relative contributions of fixed-order QCD and BFKL are most easily understood by looking at

$$W^2 Q_1^2 Q_2^2 \, \frac{d^3\sigma}{dW^2 dQ_1^2 dQ_2^2} \tag{6.16}$$

as a function of W^2/Q^2 for fixed $\sqrt{s}/W$. The asymptotic regime then corresponds to large W^2/Q^2. This quantity is shown in Figure 6.16 for $Q_1^2 = Q_2^2 = Q^2 = 10$ GeV^2 and $\sqrt{s} = 2W$. The solid points are the QCD calculations of two-quark ('qq') and four-quark production ('qqqq'); we see that the latter dominates for large W^2/Q^2 and approaches a constant asymptotic value. In contrast, the analytic BFKL result, shown with open circles, rises well above that of fixed-order QCD. The diamonds show analytic BFKL with energy conservation imposed, but not exact kinematics; it can be interpreted as an upper limit for the Monte Carlo prediction, the calculation of which is in progress.

It is important to note in Figure 6.16 that although BFKL makes a definite leading-order prediction for the behavior of the cross section as a function of W^2/Q^2, the origin in W^2/Q^2 (i.e., where BFKL meets asymptotic QCD) is *not* determined in leading order. We have chosen $W^2/Q^2 = 10^3$ GeV^2 as a reasonable value where the QCD behavior is sufficiently asymptotic for BFKL to become relevant, but another choice

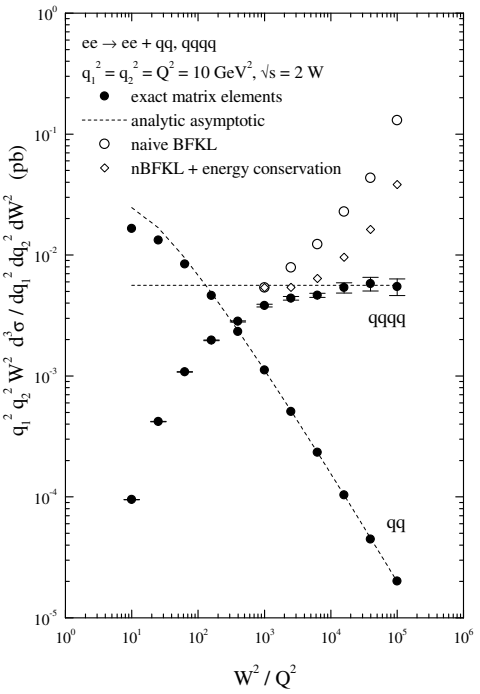

Figure 6.16: Exact (closed data points) and analytic asymptotic (dashed line) $e^+e^- \to e^+e^- q\overline{q}$ and $e^+e^- \to e^+e^- q\overline{q}q\overline{q}$ cross sections versus W^2/Q^2 at fixed $W^2/s = 1/4$. Also shown: analytic BFKL without (open circles) and with (open diamonds) energy conservation imposed.

might be just as reasonable. Only when higher order corrections are computed can the BFKL prediction be considered unique.

From an experimental point of view, the cross section at fixed $\sqrt{s}$ is more directly relevant. Figure 6.17 shows $W^2Q_1^2Q_2^2 \ \frac{d^3\sigma}{dW^2 dQ_1^2 dQ_2^2}$ for a linear collider energy $\sqrt{s} = 500\ \mathrm{GeV}$. The solid lines show the exact fixed-order QCD prediction. The dashed line is the asymptotic four-quark production cross section, and the dotted line is the analytic BFKL prediction. Now we see that all of the curves fall off at large W, but the BFKL cross section lies well above the others.

6.3.2.4 Status of NLO Corrections

It is apparent that, although it is not yet clear whether BFKL is necessary to describe the data in hand, leading-order analytic BFKL is not sufficient. In view of the experimental precision that is likely to be achieved for the above processes at the LHC and the LC, a next-to-leading order (strictly speaking, next-to-leading log order) analysis will be required. The calculation of the NLO BFKL kernel was completed several years ago [669, 670], but it is only very recently that the formalism has been implemented [671] in a Monte Carlo framework appropriate for phenomenology at the LHC and the LC. Although in principle the NLO contributions should affect the relevant hadron collider and e^+e^- collider cross section in a similar way, only detailed numerical studies will show whether this is in fact true. The convergence of the per-

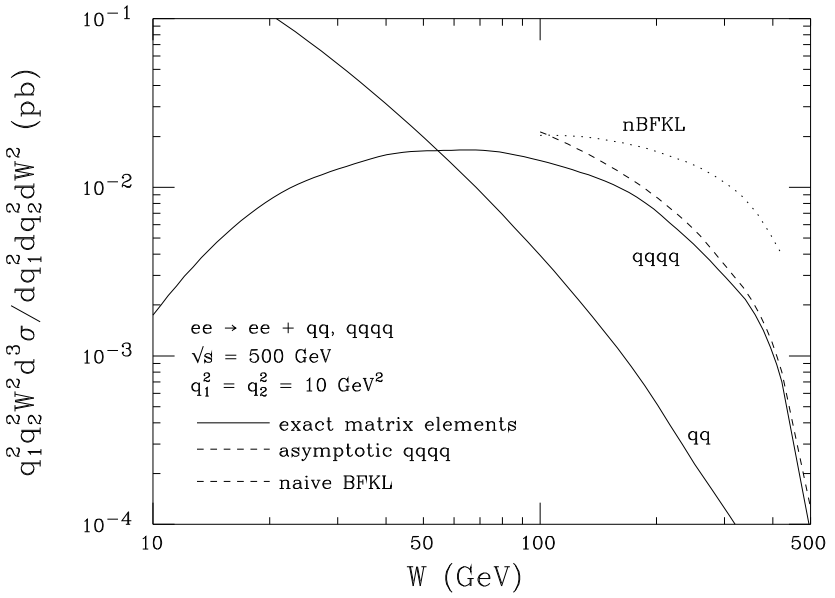

Figure 6.17: Exact (solid lines) and analytic asymptotic (dashed line) $e^+e^- \to e^+e^- q\overline{q}$ and $e^+e^- \to e^+e^- q\overline{q}q\overline{q}$ cross sections versus W^2/Q^2 at fixed $\sqrt{s} = 500$ GeV. Also shown: analytic BFKL (dotted line).

turbation series is likely to depend sensitively on the kinematics of the intial and final states that can be accessed experimentally.

6.3.2.5 Other BFKL processes at a Linear Collider

There are a number of related processes in $\gamma\gamma$ collisions at high energy which also provide a test of BFKL dynamics. These include $\gamma\gamma \to J/\psi J/\psi$ [668], where the J/ψ mass plays the role of the γ^* virtuality in $\sigma_{\gamma^*\gamma^*}$, and $\gamma\gamma \to \rho\rho$ at fixed momentum transfer $|t|$.

Inclusive polarised structure function measurements may show BFKL effects: the most singular terms in the small x resummation on $g_1(x, Q^2)$ behave like $\alpha_s^n \ell_{\rm n}^{2n} 1/x$, compared to $\alpha_s^n \ell_{\rm n}^n 1/x$ in the unpolarised case. Thus large $\ell_{\rm n} 1/x$ effects are expected to set in much more rapidly for polarised than for unpolarised structure measurements. For leading order calculations, including consistency constraints, the differences in predictions for g_1 with and without these large logarithms can be as large as a factor 2 to 3 for $x = 10^{-4}$ and could thus be easily measured with a few years of data taking at a photon collider [672].

Further candidate measurements are the processes $e^+e^- \to e^+e^-\gamma X$ and $\gamma\gamma \to \gamma X$ [673] and a process similar to the 'forward jets' at HERA: $e\gamma$ scattering with a forward jet produced in the direction of the real photon [674].

6.3.2.6 Conclusions

In summary, BFKL physics is a complicated business. Tests have so far been performed in a variety of present experiments (Tevatron, HERA, LEP) and there is potential for the future as well (LHC, LC). The advantage of these latter machines is that they provided a better access to the asymptotic (high-energy) regime where the formalism most naturally applies. At present energies, however, comparisons between theory and experiment are not straightforward; leading-order BFKL is apparently insufficient, and subleading corrections such as kinematic constraints can be very important. The recent availability of the next-to-leading order corrections to the BFKL kernel (and their implementation in a Monte Carlo framework suitable for studying the processes described above) provides a way of gauging the convergence of the perturbative approach at present and future colliders. Much detailed phenomenology remains to be done.

6.3.3 Improving the $H \to \gamma\gamma$ background prediction by using combined collider data

6.3.3.1 Introduction

Particle searches at future colliders rely on a precise understanding of Standard Model backgrounds. In prominent cases like Higgs boson search in the two-photon channel at the LHC, the background is dominated by fragmentation processes where photons and mesons are produced in the hadronisation of a jet. To reduce these backgrounds severe isolation cuts are imposed which lead to the situation that fragmentation models are tested at large z, where z is the ratio between the transverse energy of the photon or meson and the jet. Fragmentation functions are up to now experimentally well constrained only for not too large z ($\sim z < 0.7$). On the other hand predictions of the two photon background are very sensitive to the large z region. By measuring high p_t mesons and photons at the Tevatron and the LC, these uncertainties can be pinned down considerably. The study is aimed to quantify the present uncertainties of fragmentation functions by comparing recent parametrizations.

6.3.3.2 Sensitivity of the $H \to \gamma\gamma$ background on fragmentation functions

The LEP data favour a light Higgs boson above 114 GeV and below about 200 GeV [675]. In the mass window between 80 and 140 GeV one of the most promising search channels at the LHC is the Higgs decay into two photons, as the hadronic decays are swamped by huge QCD backgrounds. The corresponding background is constituted out of direct photons, photons from fragmentation and neutral mesons, the latter being misidentified as a single photon in the detector.

Recently a dedicated calculation was completed which treated all three contributions in next–to–leading order (NLO) in α_s [676,679]. Comparison of NLO QCD with existing di-photon [677] and di-pion [678] data shows an excellent agreement between theory and experiment. In Fig. 6.18 the $\gamma\gamma$, $\gamma\pi^0$, $\pi^0\pi^0$ NLO predictions are plotted for the invariant mass distribution of the photon/pion pairs at the LHC. In [680]

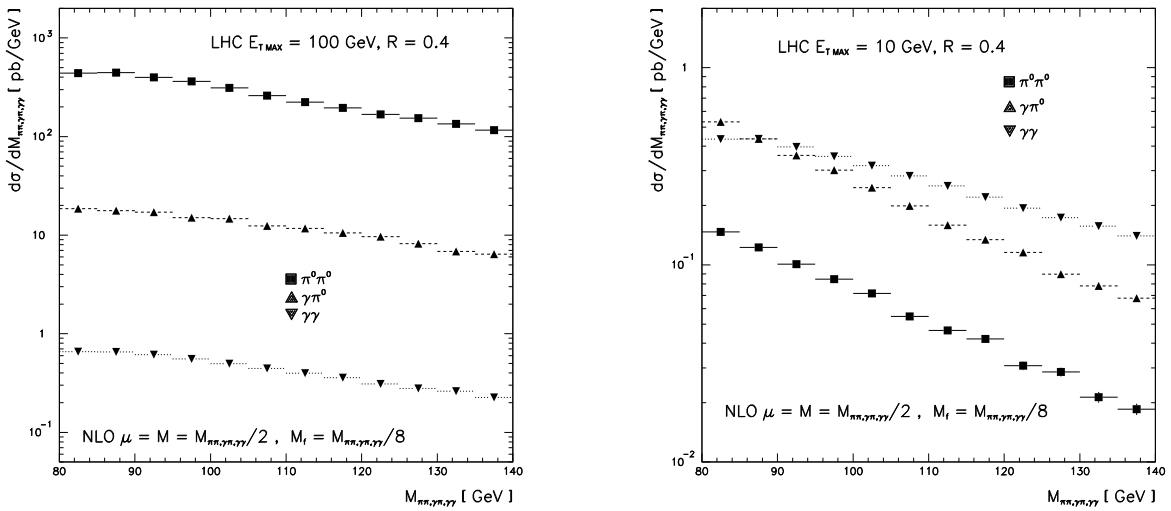

Figure 6.18: NLO predictions for $\gamma\gamma$, $\gamma\pi^0$, $\pi^0\pi^0$ rates at the LHC. Severe isolation (right) is needed to suppress the pion contributions.

it was shown that the inclusion of NLO corrections generally increases the discovery potential for the Higgs boson in the two photon channel.

To isolate a Higgs signal of the order 100 fb/GeV from this distribution, severe isolation cuts have to be applied to reduce the background from fragmentation processes. Applying isolation criteria around the photon/pion means that only a certain amount of transverse hadronic energy, $E_{T\,max}$, is allowed in a cone in rapidity and azimuthal angle space around the photon/pion, $R = \sqrt{(\Delta\eta)^2 + (\Delta\phi)^2}$. As the minimal p_T values at the LHC are 25 and 40 GeV for the detected particles one finds for example for the energy fraction of the pion with respect to the jet:

$$z = \frac{E_{T\,\pi^0}}{E_{T\,jet}} > \frac{p_{T\,min}}{p_{T\,min} + E_{T\,max}} = 0.7 \tag{6.17}$$

when typical values for $E_{T\,max} = 10$ GeV and $p_{T\,min} = 25$ GeV are used. This means that fragmentation functions are tested in a regime where they are not restricted by experimental data. In Fig. 6.18 (right) one sees that the pion contributions are still sizable, but photons from fragmentation are less important. Although additional photon/pion selection cuts will help to reduce the pions further it has to be stressed that the uncertainties for the pion contributions are large.

To quantify the uncertainty from fragmentation functions in the given prediction three recent NLO parametrizations of the parton–to–pion fragmentation functions were compared to each other. In Fig. 6.19 (right) one sees that the $\gamma\pi^0$ invariant mass spectrum scales by a factor of about 1.5 when switching from the BKK [681] to the KKP [683] parametrization. The parametrization of Kretzer [682] is almost indistinguishable to the one of BKK and is not plotted separately. The difference in the predicted rates is easily understood by looking at the ratio of the respective fragmentation functions $D_{q\to\pi^0}(z, Q^2)$ Fig. 6.19 (left). As only the tails of the distributions are probed the prediction is sensitive to the experimentally unconstrained tails. For the $\pi^0\pi^0$ component of the background the situation is even more dramatic as one pion

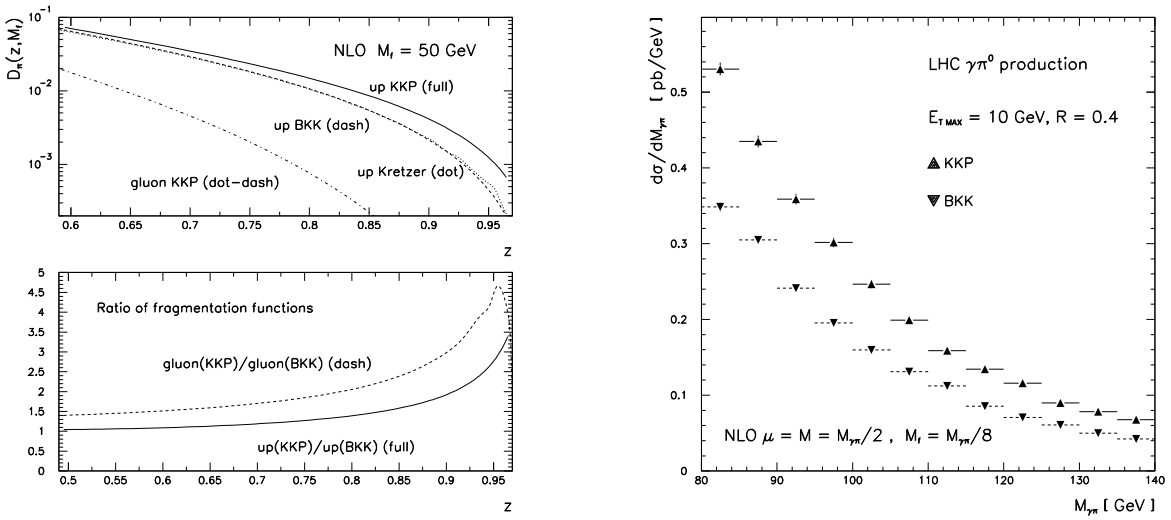

Figure 6.19: Differences of the tails of fragmentation functions (left) lead to large uncertainties in the predictions for $\gamma\pi^0$ rates. Only the quark to pion fragmentation matters here.

has to have a $p_{T\,min} = 40$ GeV leading to $z_{min} = 0.8$. Taking into account also usual theoretical scale uncertainties one can not claim that the $\gamma\pi^0$, $\pi^0\pi^0$ contribution of the $H \to \gamma\gamma$ background is quantitatively well under control.

6.3.3.3 Conclusion

The Run 2 at the Tevatron will provide large data samples of multi-jet events which will enhance the experimental handles to constrain the fragmentation functions. However, in particular the clean data expected at a forthcoming LC will provide very important measurements for these studies. By analyzing mesons/photons with high p_t in the jets fragmentation functions can be determined with an unprecedented accuracy. Especially the region $z > 0.7$ where data from LEP and SLD is becoming insufficient will be probed much more precisely. This in turn will lead to an improvement of our understanding of two-photon events at the LHC. This is not only relevant for Higgs searches but also for other non-standard particles coupled to photons. Apart from that, as the di-photon spectrum will be measured very precisely at the LHC, it also amounts to a good test of perturbative QCD in general.

7 New Gauge Theories

7.1 Scenarios with extra gauge bosons

New massive gauge bosons are suggested by most extensions of the Standard Model gauge group; neutral heavy gauge bosons Z′ as well as charged bosons, W′. Within a variety of models the new bosons sit just below the Planck scale or near the weak scale or they originate in certain classes of theories with extra dimensions. Another recent example for a theory beyond the Standard Model is the 'Little Higgs' model.

For the physics program of near future colliders those predictions with gauge bosons of a few hundred GeV or few TeV are of interest. Some of the models also include the existence of an extended fermion sector.

Here, the following models will be considered:

- The popular scenario for extra gauge bosons is based on the symmetry breaking schemes: SO(10)→SU(2)$_L$×SU(2)$_R$×U(1) predicts new neutral and charged gauge bosons, Z′ and W′, and E$_6$ →SU(3)×SU(2)×U(1)×U(1)$_{Y'}$ anticipates neutral Z′ bosons. Details about the models can be found in [684].

- The 'Little Higgs' scenario [685–688] is proposed as an alternative to SUSY and extra dimensions to provide a solution to the hierarchy problem. In these models new symmetries imply the existence of a rich spectrum of new particles, in particular new gauge bosons that could be light. The Higgs boson appears as a pseudo-Goldstone boson and is protected by the global symmetry from 1-loop quadratic divergences.

- KK excitations of the Standard Model gauge bosons are a natural prediction of models with additional dimensions [689]. The details of such models are described in chapter 8.

- In the so called Universal Extra Dimension scenario (UED) [690] all SM fields propagate in extra dimensions, there is no direct vertex involving one non-zero Kaluza-Klein (KK) mode.

7.1.1 Sensitivity to new physics models

New interactions beyond the Standard Model can be parametrized in terms of effective four-fermion contact interactions [691],

$$\mathcal{L}_{CI} = \sum_{i,j=\mathrm{L,R}} \eta_{ij} \frac{g^2}{\Lambda_{ij}^2} (\overline{\mathrm{u}}_{F,i} \gamma^\mu \mathrm{u}_{F,i})(\overline{u}_{f,j} \gamma^\mu u_{f,j}). \tag{7.1}$$

with the helicity coefficients η_{ij} and the couplings g (by convention $g^2 = 4\pi$). Λ can be interpreted as the compositeness scale, or it approximates the effects of exchanged

new particles, $M_X \approx \Lambda$. Contact interactions preserve the chiral symmetry and the Standard Model matrix element is extended by an additional contact term.

The new interactions could arise in hadron-hadron collisions producing lepton or quark pairs at the LHC by means of the Drell-Yan mechanism or in fermion-pair production processes at lepton colliders. The parton cross section or the differential cross section, respectively, have the form

$$\frac{d\sigma}{d\cos\Omega} \propto \sum_{i,j=L,R} \rho_{ij}|A_{ij}|^2, \tag{7.2}$$

with

$$\begin{aligned} A_{ij} &\sim A_{ij}^{SM} + \frac{\eta_{ij} \cdot s}{\Lambda^2} \\ \rho_{LL,RR} &= (1+\cos\theta)^2 \\ \rho_{LR,RL} &= (1-\cos\theta)^2. \end{aligned} \tag{7.3}$$

The angular distribution functions, ρ_{ij}, describe the exchange of the spin-1 particles. The sensitivity reaches for the new interactions can be tested by searching for deviations from the Standard Model expectations.

7.1.1.1 Sensitivity to Contact Interactions at the LHC and LC

The sensitivity reaches for various models of four-fermion contact interactions expected for the LHC and LC have been determined [692–696]. Some main results are summarized in Table 7.1 for qqee interactions at the LHC as well as for eeqq and eell interactions at the LC (for $\Lambda_{eeqq}(LC)$ the same strength of contact interaction to all quark flavors is assumed). New studies [696] show that these conservative bounds for the LHC can be improved by a factor roughly 1.5. The sensitivity regions for $e^+e^- \rightarrow e^+e^-$ are related to an optimistic scenario for systematic uncertainties; with the high statistics the systematic effects can be better controlled. A 'safe' realistic scenario lowers the Λ_{eeee} bounds by a factor ≈ 2 [696]. With the LHC new interactions between quarks and leptons can be examined whereas a LC opens the window to new interactions between leptons only or leptons and quarks. In Ref. [697] also the sensitivity of LHC measurements to quark compositeness is derived by analysing the dijet angular distributions and the transverse energy distribution of jets. With an integrated luminosity of 30 (300) fb^{-1} a sensitivity to compositeness of quarks up to a scale of 25 (40) TeV can be achieved.

This complementarity demonstrates the need to have both colliders to be sensitive to the full spectrum of new physics.

7.1.1.2 Distinction of new physics models

Contact terms describe the effective new contributions in model-independent manner. If hints to new effects are found the quest for their source could be answered with the exchange of new particles, $M_X \approx \Lambda$. Well known examples of these interpretations are the exchange of extra gauge bosons, leptoquarks, supersymmetric

		LHC Λ [TeV]				LC Λ [TeV]			
model		LL	RR	LR	RL	LL	RR	LR	RL
eeqq:	Λ_+	20.1	20.2	22.1	21.8	64	24	92	22
	Λ_-	33.8	33.7	29.2	29.7	63	35	92	24
ee$\mu\mu$:	Λ_+					90	88	72	72
	Λ_-					90	88	72	72
eeee:	Λ_+					44.9	43.4	52.4	52.4
	Λ_-					43.5	42.1	50.7	50.7

Table 7.1: The 95% sensitivity reaches for a basic choice of contact interactions expected for the LHC [692] ($L_{int} = 100\ fb^{-1}$ at 14 TeV and δL=5%) and the LC [694, 696] ($L_{int} = 1\ ab^{-1}$ at 0.5 TeV and P_{e^-}=0.8, P_{e^+}=0.6).

particles, gravitons etc. It will be a puzzle to deduce from bounds on effective interactions back to special models and phenomena. An important step is the check of the angular distribution: If new spin-1 particles are exchanged the typical $(1 \pm \cos\theta)^2$ (Eq. 7.3) behaviour will be observed and can be distinguished from an exchange of other particles (spin-0, spin-2). In case of an exchange of spin-2 particles like gravitons the additional contribution to the helicity amplitudes depend on the scattering angle [698, 699] (see also chapter 8) and Equations (7.2, 7.3) are modified:

$$\begin{aligned} A_{LL,RR} &= A^{SM}_{LL,RR} - \frac{\lambda \cdot s^2}{4\pi\alpha M_S^4}(2\cos\theta - 1) \\ A_{LR,RL} &= A^{SM}_{LR,RL} - \frac{\lambda \cdot s^2}{4\pi\alpha M_S^4}(2\cos\theta + 1) \end{aligned} \tag{7.4}$$

M_S is the cut-off scale ([700]) and $|\lambda|$ is of the order 1. Details about the identification of this kind of new physics will be discussed in the next chapter.

7.1.1.3 Z′ in the context of Contact Interactions

Let's assume that the angular distributions indicates the exchange of a new spin-1 particle but the available energy is to low to produce it directly. This particle could be a Z′: Then a simultaneous analysis of the contact terms η^{ef}_{LL}/Λ^2, η^{ef}_{RR}/Λ^2, η^{ef}_{LR}/Λ^2 and η^{ef}_{RL}/Λ^2 will show that the condition

$$\frac{\eta^{ef}_{LL}}{\Lambda^2}\frac{\eta^{ef}_{RR}}{\Lambda^2} = \frac{\eta^{ef}_{LR}}{\Lambda^2}\frac{\eta^{ef}_{RL}}{\Lambda^2} \sim \frac{g^e_L}{M_{Z'}}\frac{g^f_L}{M_{Z'}}\frac{g^e_R}{M_{Z'}}\frac{g^f_R}{M_{Z'}}$$

is fulfilled. The helicity amplitudes in Equ. (7.3) can be replaced by amplitudes including γ, Z and Z′ exchange:

$$A_{ij} = Q^e Q^f + \frac{g^Z_i g^Z_j}{s^2_W c^2_W}\frac{s}{s - M^2_Z + iM_Z\Gamma_Z} + \frac{g^{Z'}_i g^{Z'}_j}{c^2_W}\frac{s}{s - M^2_{Z'} + iM_{Z'}\Gamma_{Z'}} \tag{7.5}$$

Exploring the expected search reaches in terms of contact interactions shown in Table 7.1 it is evident that the sensitivity to a Z′ could be higher with a LC. But it is widely assumed that new heavy vector bosons are 'light' enough to be directly produced at the LHC by means of the Drell-Yan mechanism [8], $pp \rightarrow q\overline{q} \rightarrow W_R^+W_R^-,\ Z_R, Z'$ and discovered through fermionic or bosonic decay modes. Most likely the energy of a LC - at least in the first phase of operation - will not be not sufficient to run a Z′ factory and to measure all characteristics. But below a Z′ production threshold new gauge bosons appear virtually and cause significant deviations from the Standard Model expectations that allow to determine Z′ parameters or bounds on them.

With a GigaZ option the propagator term in Eq. (7.5) becomes negligible but the sensitivity of loop corrections to new bosons can be explored: Precision measurements of g_i^Z, g_j^Z, $\sin^2\theta_{eff}$ and the ρ-parameter will allow to deduce the effects beyond the Standard Model and a potential Z-Z′ mixing can be measured.

Recent direct measurements from the Tevatron by CDF and D0 exclude Z′ masses in conventional models below ≈700 GeV [701], corresponding indirect limits from LEP vary between 330 GeV and 670 GeV for E_6 models and between 470 GeV and 900 GeV for left-right symmetric models [702]. Extra charged bosons, W′, are excluded below 785 GeV [703]. Hence, with a linear collider operating at energies of 0.5 TeV up to about 1 TeV it is expected to observe the virtual effects of new gauge bosons.

7.2 Z′ studies at the LHC

7.2.1 Z′mass reaches at the LHC

Detailed studies have been performed on sensitivity reaches for new gauge bosons at the LHC and LC [8, 694, 704–706, 708].

The Z′ production cross section at LHC, $\sigma(pp \rightarrow Z')$, is measured via the leptonic cross section $\sigma(pp \rightarrow Z')Br(Z' \rightarrow l^+l^-)$. Depending on the underlying model new particles can influence the total Z′ width. Therefore, it is assumed that all Z′ decay modes are known. In a recent paper [709] the potential of a Z′ search at the LHC is updated. Based on a more realistic simulation the signals of Z′ bosons originating in various theoretical models are analyzed and the discovery potential up to $m_{Z'} = 5$ TeV for $\mathcal{L}$=100fb^{-1} is reconfirmed. In [89] the ability of the process $Z' \rightarrow jj$ for Z′ detection is studied: Depending on the model a Z′ observation up to $m_{Z'} \leq 3 - 4$ TeV will be possible. The discovery power of this channel does not reach that of the leptonic channel but it comes closer for high Z′ masses where the statistics in the leptonic channels is low.

7.2.2 Distinction of models at the LHC

The measurement of the production cross section, well suited for Z' detection by observing a mass bump, is not sufficient to distinguish models. In [704] the authors demonstrate the determination of Z′ couplings with LHC measurements. They introduce a new parameter set of normalized Z′ couplings resolving the left- and right-handed coupling contributions that are characteristic of the particular model. Al-

though they neglect all systematic errors and assume 100% efficiency in data reconstruction it is accepted that a distinction of Z′ models will be possible by measuring the cross section, the asymmetry and the rapidity distribution [709, 712]. Besides ambiguities this will of course work better for light Z′ bosons.

7.2.2.1 Forward-Backward Asymmetry measurement at LHC

The more realistic study of the Z′ search potential in [709] devotes special attention to the discrimination between models. Due to the model-dependent values of the Z′ couplings to quarks and leptons the foward-backward asymmetry, A^l_{FB}, is a sensitive measure to distinguish models. The asymmetry cannot be measured directly in the symmetric collisions of LHC. However, from the rapidity distribution of the dilepton system the quark direction can be obtained by assuming to be the boost direction of the ll system with respect to the beam axis (see [710]). The probability to assign the correct quark direction increases for larger rapidities of the dilepton system. With a cut on the rapidity distribution, $Y_{ll} > 0.8$, a cleaner but smaller signal sample can be observed and the asymmetry obtained, see Figure 7.1(a).

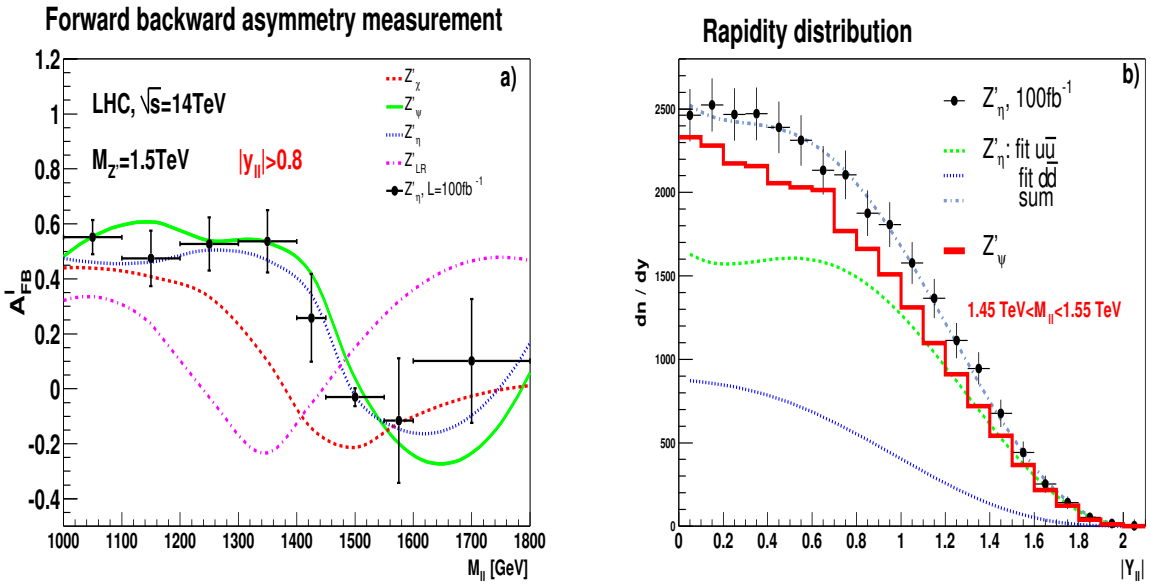

Figure 7.1: A^l_{FB} (a) as a function of M_{ll} for several Z′ models. The observable rapidity distribution for two Z′ models is shown in (b), including the fit results which determine the types of $q\overline{q}$fractions. A simulation of the statistical errors, including random fluctuations of the Z'_η model and with errors corresponding to a luminosity of 100 fb^{-1} has been included in both plots. For details see [709].

7.2.2.2 Rapidity Distribution

To complete the Z′ analysis, one can obtain some information about the fraction of Z′'s produced from $u\overline{u}$ and $d\overline{d}$ by analyzing the Z' rapidity distribution. Assuming

that the $W^{\pm}$ and Z rapidity distribution has been measured in detail, following the ideas given in [711], relative parton distribution functions for u and d quarks as well as for the corresponding sea quarks and antiquarks are well known. Thus, the rapidity spectra can be calculated separately for $u\overline{u}$ and $d\overline{d}$ as well as for sea quark anti-quark annihilation and for the mass region of interest to analyze the Z' rapidity distribution [712]. Using these distributions a fit can be performed to the Z' rapidity distribution which allows to obtain the corresponding fractions of Z''s produced from $u\overline{u}$, $d\overline{d}$ as well as for sea quark anti-quark annihilation. This will thus reveal how the Z' couples to different quark flavors in a particular model.

7.2.2.3 Extracting the Z′ couplings

Due to the significant shape of A_{FB}^{l} in the vicinity of a Z′ peak, the Z′ peak region as well as the 'interference' region provide complentary information for the analysis. Furthermore, the analysis of the rapidity distribution gives additional Z′ information. Figure 7.1(b) shows the expected rapidity distribution for the Z'_{η} model. A particular Z' rapidity distribution is fitted using a combination of the three pure quark-antiquark rapidity distributions. The fit output gives the $u\overline{u}$, $d\overline{d}$ and sea quarks fraction in the sample. In order to demonstrate the analysis power of this method we also show the Z'_{ψ} rapidity distribution which has equal couplings to $u\overline{u}$ and $d\overline{d}$ quarks.

7.2.3 Summary: Z′ search at the LHC

Z′ signals like mass bumps will be observed up to $M_{Z'} = 5$ TeV. The statistical significance of A_{FB}^{l} measurements will allow a distinction of 'usual' models with the LHC if $m_{Z'} < 2 - 2.5$ TeV.

However, if nothing is detected at the LHC the indirect searches at the LC are strongly required to check whether heavier gauge bosons could exist or whether they have couplings that make them invisible at the LHC.

7.3 Z′ studies at the LC

7.3.1 Z′ mass reaches at the LC

Most likely, at the LC new bosons will be detected via Z-Z′ interference effects. Then the significance of deviations from the Standard Model expectations is determined by the ratio of Z′$f\overline{f}$ couplings and Z′ mass.

Usually, the sensitivity reach of indirect searches is given at the 95% C.L. assuming special models, e.g. E_6 or left-right symmetric models. To compare these 2σ deviations from the Standard Model expectations with the direct search reaches one has to consider at least a 5σ deviation. Figure 7.2 illustrates the discovery and sensitivity reaches of the LHC and LC. The sensitivity limits at LC would improve up to roughly 12% if all systematic errors could be reduced to zero.

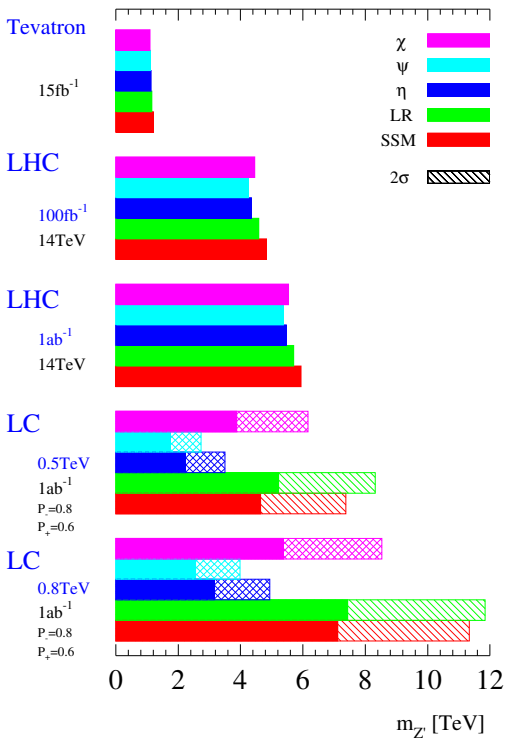

Figure 7.2: Comparison of the Z′ discovery reaches at LHC [706] and the 2σ and 5σ sensitivity bounds at LC [694].

7.3.2 Distinction of models with the LC

To learn about the Z′ properties the measurement of the couplings is essential. The couplings and also the behaviour of the angular distribution of the observables measured with polarized beams allow the study of the nature of new gauge bosons. First, the usual scenario is considered where the extra gauge bosons carry vector and axial vector couplings.

In the ideal case the new gauge bosons are light enough to be found with the LHC. Then both colliders provide the feasibility to determine the Z′ couplings.

At the LC at high energies, fermion pair production is a process with high statistics and clear topologies. Moreover with the expected integrated luminosity of 1 ab^{-1} and with the possibility of polarisation of at least the electron beam. If the mass of a potential Z′ is known from LHC the Z′ model can be resolved with a good accuracy. Figure 7.3 demonstrates the powerful interplay of LHC and LC measurements: Leptonic final states obtained at a LC are analyzed with the knowledge of the mass of a potential Z′.

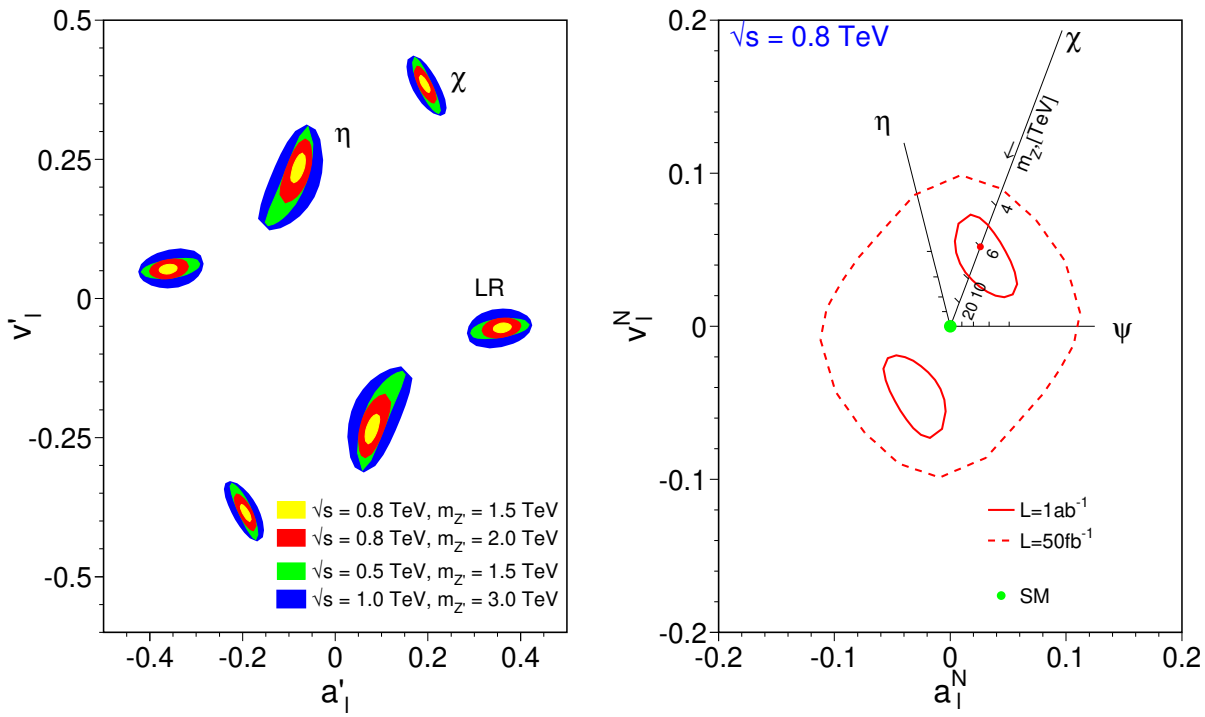

Figure 7.3: Left figure: The 95% C.L. contours on leptonic Z′ couplings, assuming the mass of the Z′ is measured at LHC. Right figure: The 95% C.L. contours on normalized leptonic Z′ couplings. The LC parameters are $\mathcal{L}_{int} = 1ab^{-1}$, $\Delta\mathcal{L}_{int} = 0.2\%$, $P_- = 0.8$, $P_+ = 0.6$, $\Delta P_- = \Delta P_+ = 0.5\%$, Δsys(lept)=0.2%.

7.3.2.1 Sensitivity to Z′ models beyond the LHC reach

An interesting situation arises if the Z′ is too heavy to be detected at the LHC, e.g. $m_{Z'} > 5$ TeV, or if the Z′ couplings to quarks are unexpectedly negligable. If the

Z′ is not too heavy (approximately 6 TeV for the usual Z′ models) there is still the possibility of measuring significant deviations from the Standard Model predictions. Instead of a direct implementation of the Z′ parameters normalized couplings have to be considered:

$$a_f^N = a'_f \sqrt{\frac{s}{m_{Z'}^2 - s}}; \qquad v_f^N = v'_f \sqrt{\frac{s}{m_{Z'}^2 - s}}. \tag{7.6}$$

It should be remarked that these normalized couplings correspond to contact interactions, $\eta_{ij}^{ef}/\Lambda^2 \approx g_i^e g_j^f / M_{Z'}^2$.

An example is given in Figure 7.3: A Z′ with $m_{Z'} = 6$ TeV realised in the χ model cannot be seen at the LHC but can just be detected at the LC. The Z′ models are characterized by the lines $v_l^N = f(a_l^N)$, the distance of a special reconstructed point on this line allows the determination of the model and the mass of the Z′ boson. It should be remarked that the lines, $v_l^N = f(a_l^N)$, correspond to the observables P_V^l introduced in [704,712]. By measuring the normalized couplings at two different c.m.s. energies, the Z′ mass and the Z′ couplings, a'_f and v'_f, can possibly be determined. The success of this procedure depends on the c.m.s. energies of the measurements, the luminosity distributed among these energies and, of course, on the Z′ mass (see [713,714]).

Similar studies were also performed for the process $e^+e^- \to q\overline{q}$ [707,708,715]. The expected resolution power, based on Z′$q\overline{q}$ couplings, is less significant than that derived from Z′l^+l^- couplings. It depends on the uncertainty of the measurement of leptonic Z′ couplings and on systematic errors due to quark flavour tagging and charge reconstruction. Although the performance of the detector and the high luminosity will provide an excellent and efficient reconstruction of the b- and c-quarks, the resulting Z-Z′ interference effects for leptonic initial and quark final states provide less stringent constraints on Z′ parameters. A global analysis of the measurements of all final states at and above the Z resonance will enhance the resolution sensitivity. But a numerical evaluation of the expected improvement is rather model-dependent. The combination of LHC and LC measurements allows a comprehensive analysis of the new gauge boson parameters, and becomes even more important for higher Z′ masses approaching the discovery limit of the LHC.

7.3.3 Z′ search at GigaZ

The new gauge bosons can mix with the standard model Z^0 and therefore modify electroweak parameters. Precision measurements on the Z peak are sensitive to these modifications. Measurements at LEP/SLD result in a Z-Z′ mixing angle which is presently consistent with zero (see for example [716]). Hence, all Z′ studies at energies off the Z or Z′ resonances based on Z-Z′ and γ-Z′ interference effects are less sensitive to the Z-Z′ mixing and can be performed with the assumption of zero Z-Z′ mixing.

In general, it should be remarked that the majority of studies with new gauge bosons assume a scenario with the weak parameter $\rho = 1$ at tree level. Other models would require new loop calculations and will lead to largely modified electroweak corrections and their relations to the Standard Model parameters. In [717] this is demonstrated in detail for the $\Delta r(m_{top})$ behaviour considering Z′ bosons in a specific Left-Right model without the restriction $\rho = 1$. A similar procedure has to be executed in the case of UED.

Z-Z′ mixing modifies electroweak parameters, e.g. M_W, $\sin^2\theta_{eff}^{lept}$, Z total and partial widths. This results in a very high sensitivity of precision measurements performed at the Z resonance to the Z-Z′ mixing. With accuracies available at GigaZ it will become possible to elucidate the origin of new gauge bosons and the symmetry breaking mechanism responsible for the mixing. Even in the 'zero coupling' limit there could remain an observable contribution to the ρ parameter, e.g. in the case of UED the effect of t-b mass splitting leading to weak isospin violation in the KK spectrum.

Although the precision data from LEP/SLD [718] constrain the Standard Model Higgs to be light, the contribution of a heavy Higgs could be compensated by a Z′. In [719] it is shown that such scenarios are not very likely for the popular E_6 and LR models and they are already excluded by recent precision measurements. Nevertheless, the discovery of Higgs bosons at the LHC gives a strong restriction for the extremely precise measurements with the GigaZ option at a LC. It is obvious that GigaZ results have to be compatible with LHC results, LC results at high energies and with the existing LEP/SLD/APV data. Only the consideration of all results will allow the extraction of the physics of symmetry breaking. Disagreements between direct measurements (including non-observation of hypothetical particles) and precision measurements will improve the search strategies at least at the LHC. Examples of the resolution power for new physics with GigaZ are given in Figures 7.4 and 7.5 by demonstrating the (mis)matching of electroweak observables and new physics depending on the Standard Model Higgs mass.

Finally, in Figure 7.6 the mass regions covered by the LHC, LC and a GigaZ option at the LC for various Z′ models are compared and summarized [719], the limits for the LC are given at the 95% C.L.

7.4 Z′ in Little Higgs models

In 'Little Higgs' models (LHM) new symmetries imply the existence of a rich spectrum of new particles, in particular new gauge bosons that could be light. In the minimal version of LHM only a triplet and a singlet of gauge bosons, a triplet of Higgs bosons and a vector-like quark, T, are generated. This leads to two Z′: B_H, the U(1) singlet, and and the triplet Z_H. For calculations the 'Little Higgs' formalism includes 3 new parameters: the mass scale f and the two coupling ratios, $x = g_t'/g'$ and $y = g_t/g$ [686]. Only with $t - T$ mixing significant contributions from the T to pseudoobservables at the Z resonance will be expected.

7.4.1 Studies at LC

In [719] it is discussed in detail how Z′ bosons arising from LHM influence measurements on the Z resonance and at high energies. It is still quite difficult to puzzle the existing precision measurements from LEP/SLD and the search limits from the Tevatron with future results from GigaZ, LC high energies and the LHC. A crucial point is the mass of the Higgs boson which is presently restricted to values below 200 GeV. Performing a fine-tuning one can find bounds on the mass scale f as shown in Figure 7.7. (It should be remarked that here the scale f corresponds to the definition in [686] and therefore it is a factor $1/\sqrt{2}$ smaller than the f used in section 3.6.)

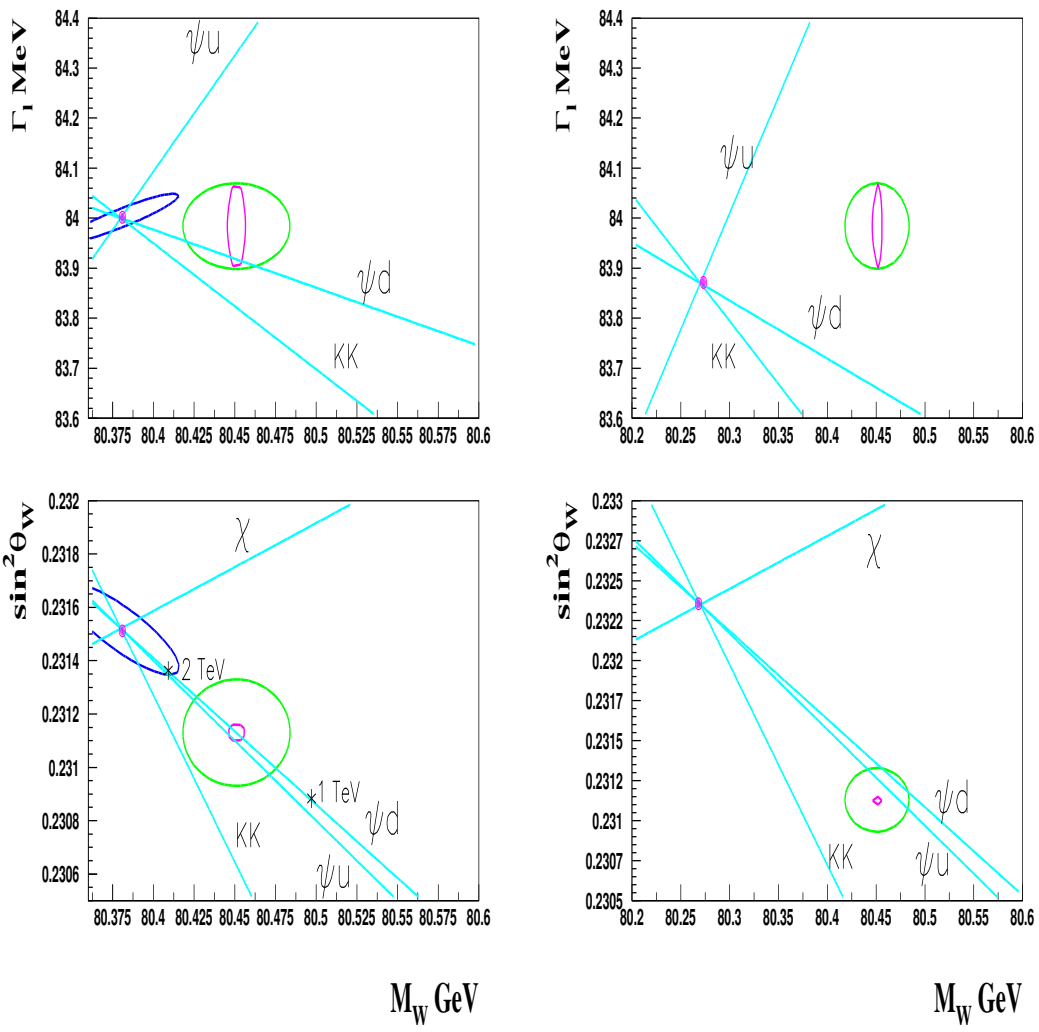

Figure 7.4: SM prediction, LEP/SLD and GigaZ expected precision compared with Z′ models (m_H=115 GeV). On the left parts of the upper plots are indicated the SM prediction ellipses (dark blue) taking into account uncertainties coming from the top mass and from $\alpha(M_Z)$ and assuming a 115 GeV (500 GeV) SM Higgs boson in the upper (lower) part of the figure. The experimental measurements from LEP/SLD/Tevatron appear on the second ellipse (right, green at each plot) while inside these ellipses are the anticipated ellipses (purple) from GigaZ. For details see [719].

In [720] the sensitivities of various observables to Z′ bosons in the LH and KK models are examined. Figure 7.8 shows how the modified observables influence the χ^2 distribution and therefore it illustrates the discrimination potential of the LC. For example, the LH model gives rise to large LR asymmetries while the Kaluza-Klein Z' does not. The χ^2 contributions are given for 50 fb^{-1} but they reflect the relations in general; a scaling to other luminosities and c.m.s. energies can be done following the well known scaling law $\sim (s \cdot L_{int})^{1/4}$.

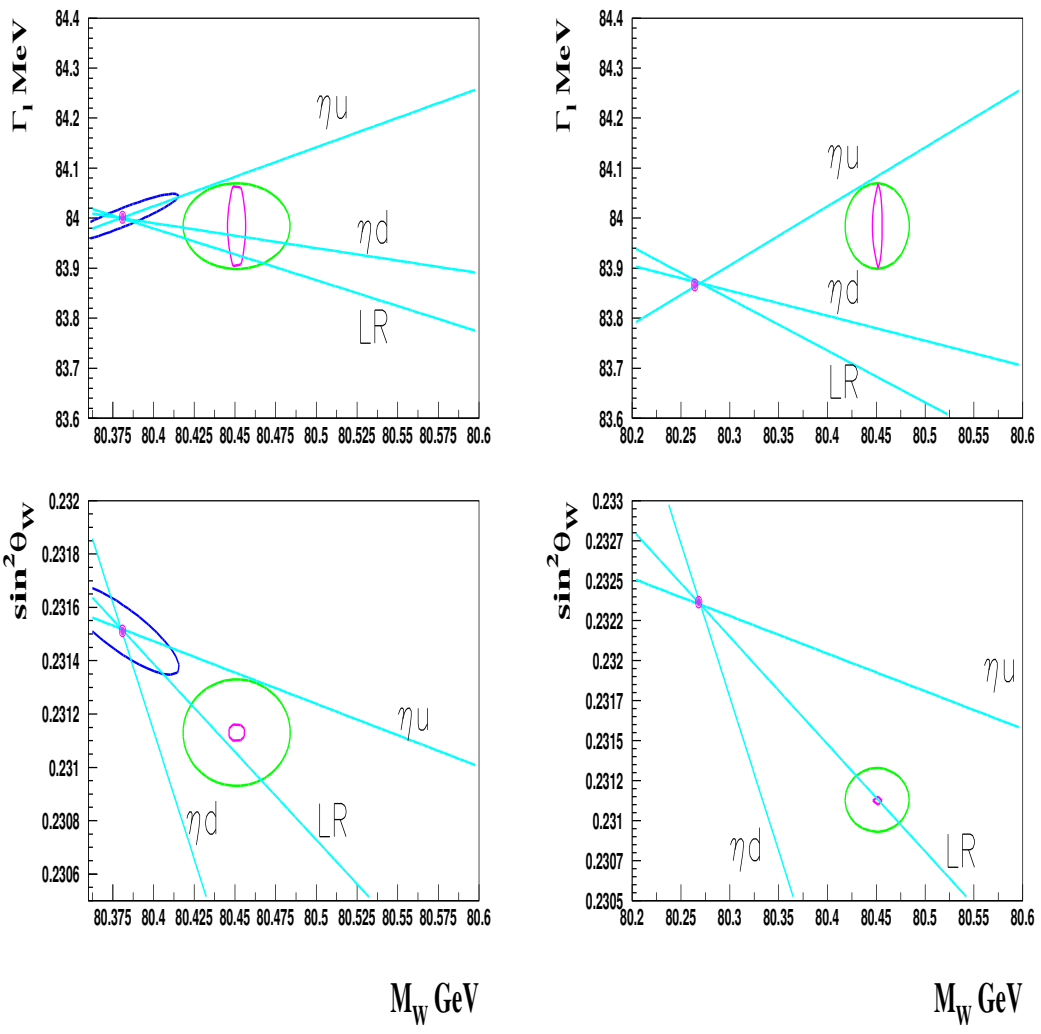

Figure 7.5: Corresponding to Figure 7.4, three Z′ models are tested against the LEP/SLD/Tevatron data assuming a 115 GeV (500 GeV) SM Higgs boson in the upper (lower) part of the figure. For details see [719].

7.4.2 Studies at LHC

Studies of Little Higgs Models at the LHC are described in detail in section 3.6. It includes the heavy SU(2) gauge bosons Z_H and W_H that can be produced via Drell-Yan at the LHC. The cross section for the Z_H production will be about 1 fb^{-1} for $M_H \approx 5$ TeV and $\cot\theta = 1$. The $W_H^{\pm}$ cross section is expected to be about 1.5 times that of Z_H due to the larger $W_H^{\pm}$ couplings to fermion doublets.

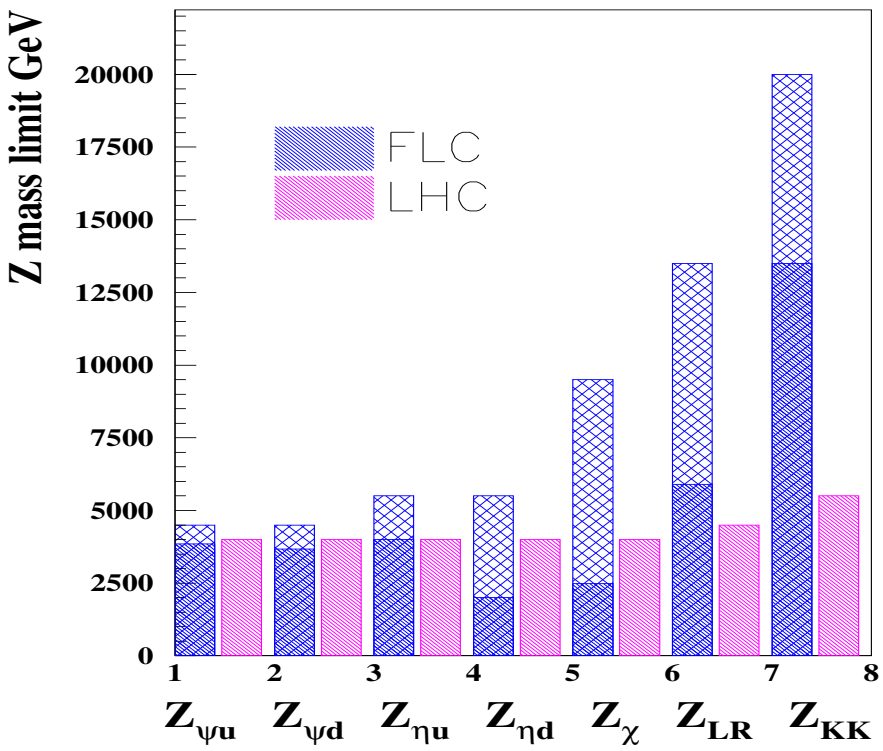

Figure 7.6: Mass regions covered by LHC and future LC (FLC) for a Z′ in various scenarios. For the FLC (the left tower, in blue) the heavy hatched region is covered by exploiting the GigaZ option (sensitive to the Z-Z′ mixing) and the high energy region (sensitive to Z-Z′ interference effects) [719].

7.5 Charged new gauge bosons

Limits have been placed on the existence of new charged gauge bosons based on indirect searches for deviations of electroweak measurements from the Standard Model predictions. Limits from μ decay constrain the mass of a righthanded extra W boson, W′, to m_{W_R} >550 GeV [721]. More stringent are the results derived from $K_L - K_S$ mass splitting with m_{W_R} >1.6 TeV [722].

A W′ search at hadron colliders considers the direct production via the Drell-Yan process and the subsequent decay. Present bounds from measurements at the Tevatron collider exclude low W′ masses, m_{W_R} >720 GeV [703]. Former studies show that the LHC is expected to be able to detect extra charged gauge bosons up to masses of ≈ 5.9 TeV [723]. In [724] the resolution power of experiments at the LHC is considered and the possible approaches for disentangling the source of the new bosons are illustrated.

Complementary, the search for a W′ at e^+e^- colliders is studied in [725]. Based on the assumption that a W′ will be found at the LHC the process $e^+e^- \to W' \to \nu\nu\gamma$ is used to reconstruct the W′ couplings; ad-hoc systematic errors are taken into account. The results demonstrate the necessary combination of LHC and LC results to cover

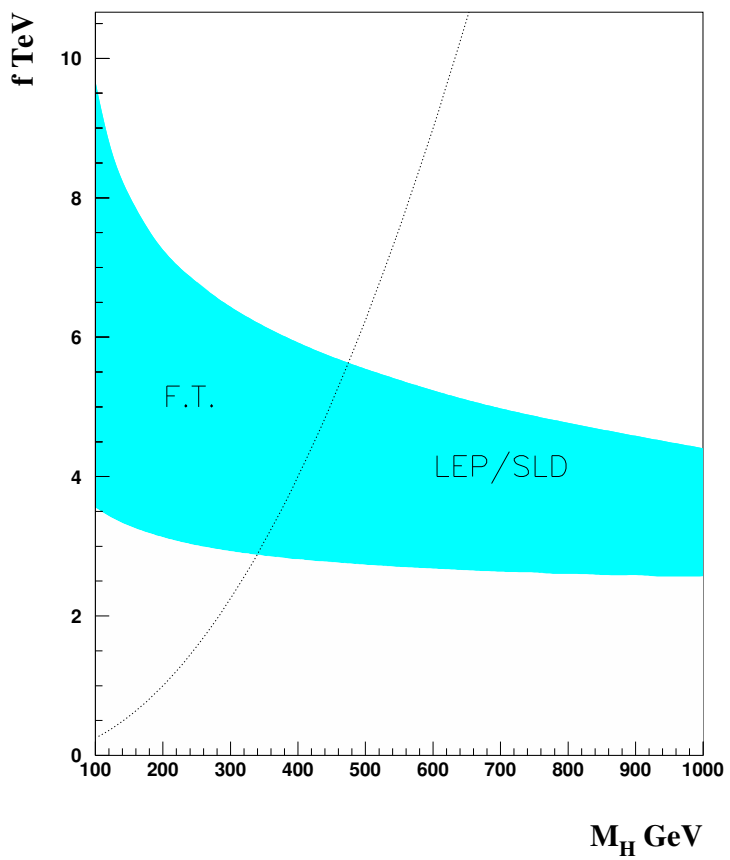

Figure 7.7: Allowed regions for the mass scale parameter f in the 'Little Higgs' scenario versus the Higgs mass in the low x approximation [719]. The blue (dark) band is allowed by the measurements from LEP/SLD. The dotted curve indicates the fine-tuning limit and cuts away the LEP/SLD solution in the region marked F.T. The mass of B_H is of the same order as f if one takes $x = 0.1$. It scales like $1/x$.

all possible sources of a W′.

7.6 Z′ from a Kaluza-Klein excitation

7.6.1 Discovery reach for a Z′ from a Kaluza-Klein excitation

KK excitations of the Standard Model gauge bosons are a natural prediction of models with additional dimensions. In [720] the discovery limits for a Kaluza-Klein Z′ are derived and compared for the LC and LHC. The discovery limits for the LHC are based on 10 events in the Drell-Yan $e^+e^- + \mu^+\mu^-$ channels using the EHLQ quark distribution functions [691] set 1, taking $\alpha = 1/128.5$, $\sin^2\theta_w = 0.23$, and including a 1-loop K-factor in the Z' production [726]. The 2-loop QCD radiative corrections and 1-loop QED radiative corrections are included in calculating the Z' width. Using

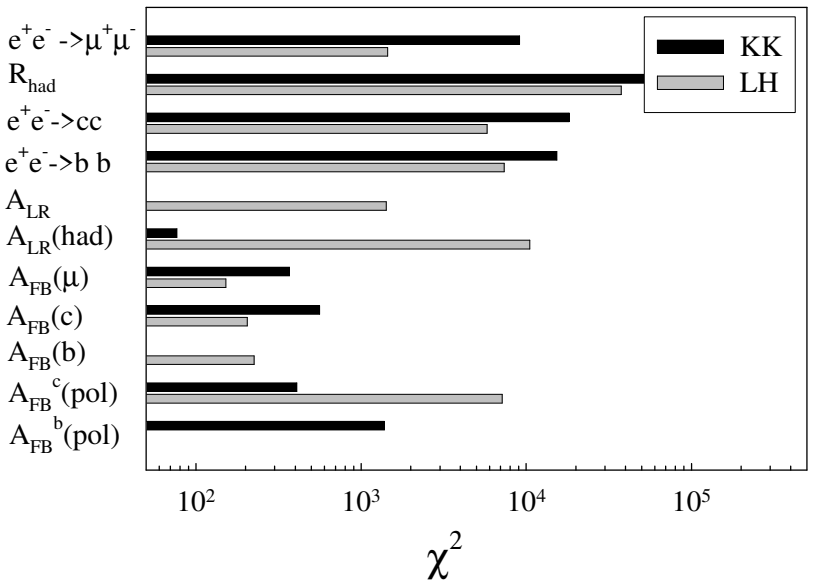

Figure 7.8: The contributions to χ^2 for the observables $\sigma(e^+e^- \to \mu^+\mu^-)$, R^{had}, $\sigma(e^+e^- \to c\overline{c})$, $\sigma(e^+e^- \to b\overline{b})$, A^{μ}_{LR}, A^{had}_{LR}, A^{c}_{FB}, A^{b}_{FB}, $A^{c}_{FB}(pol)$, and $A^{b}_{FB}(pol)$ for the Kaluza-Klein and Little Higgs models (see [720]). These are based on $\sqrt{s} = 500$ GeV, L=50 fb^{-1}, and $M_{Z'} = 2$ TeV. The χ^2 is based solely on the statistical error. We assume 100% polarization and do not include finite c and b-quark detection efficiencies.

different quark distribution functions results in a roughly 10% variation in the Z' cross sections [727] with the subsequent change in discovery limits. The discovery limit for the Little Higgs Z′ given in Table 7.6.1 is consistent with other calculations [687,728].

At e^+e^- collider searches the process $e^+e^-_\lambda \to f\overline{f}$ is used, λ denotes the e^- polarization; here 90% is assumed. There are numerous observables that can be used to search for the effects of Z' bosons. Table 7.6.1 presents the 95% C.L. exclusion limits and a comparison with the LHC.

Collider	$\sqrt{s}$	L	KK (TeV)	LHM (TeV)
LHC pp	14 TeV	100 fb^{-1}	6.3	5.1
LC (e^+e^-)	0.5 TeV	1 ab^{-1}	15	13
	1 TeV	1 ab^{-1}	25	23

Table 7.2: Discovery limits for the extra gauge bosons arising in theories with finite size extra dimensions and in the Little Higgs Model at the LHC and the LC ([720]).

7.6.2 Distinguishing a 'conventional' and KK Z′

In the simplest schemes, the lightest KK states is assumed to be produced at the LHC yet sufficiently heavy that any higher KK excitation are not observable. In [727] the capabilities of the LHC (directly) and the LC (indirectly) are explored to distinguish these types of states from the more conventional GUT-type Z′ discussed above. It is shown that such a separation is straightforward at the LC while only possible under certain circumstances at the LHC even with a luminosity upgrade.

The model studied (see also chapter 8) assumes one flat extra dimension where all the fermions are constrained to lie at one of the two orbifold fixed points, $y = 0, \pi R$, associated with the compactification on S^1/Z_2 [729], where R is the compactification radius. Two specific cases are considered: All fermions are placed at $y = 0$ $(D = 0)$ or quarks and leptons are localized at opposite fixed points $(D = \pi R)$. Here, D is the distance between leptons and quarks in one extra dimension.

Up to $M_c \leq 7$ TeV, KK excitations are directly accessible at the LHC by observing a single bump in the l^+l^- channel. Figure 7.9 shows the invariant mass spectrum and the forward-backward asymmetries for $M_{Z'} = 4$ TeV in 'conventional' models and the forward-backward asymmetries for $M_c = 4$ TeV for the two cases, $D = 0,\ D = \pi R$. For $D = 0$ a narrow dip (destructive interference) below the KK resonance will be obtained at $M \approx 0.55 M_c$ in the asymmetry an the invariant mass spectrum (see chapter 8). This structure with a dip position sensitive to the model is missing in the case $D = \pi R$ due to the constructive interference. For either D choice the cross section and asymmetry excitations are qualitatively different from that expected with a typical Z′. Nevertheless, it could happen that a special Z′ model mimics the KK cases. Therefore, the ability to distinguish between Z′ and KK scenarios is an interesting problem. The probabilities to identify at the LHC and at the LC a KK excitation as a Z′ for the two scenarios D=0 and D=πR are summarized in Table 7.3. The separation of a Z′ and KK should be possible up to $M_c \approx 5$ TeV for sufficiently high luminosities at the LHC. The Z′-KK separation for larger values of M_c is slightly better at a 500 GeV LC. With increasing c.m.s. energy the resolution power of the LC increases substantially compared to the LHC.

7.7 Summary

With the LHC and the LC new interactions between and quarks and leptons will be studied. In addition, the LC is sensitive to new phenomena in 'pure' electron-lepton interactions and the LHC to quark compositeness. Depending on the model assumed and the type of fermions involved in the new interaction a sensitivity is given up to ≈30 TeV at the LHC and roughly $100 \cdot \sqrt{s}$ at the LC. The full picture of new physics demands investigations at both colliders.

If a Z′ exists it will be seen with the LHC up to c.m.s. energies of 5 TeV. The reconstruction of the Z′ model will be possible only if $M_{Z'} < 2$ TeV-2.5 TeV.

With a linear collider operating at 0.5 TeV to 1 TeV – most likely below the production threshold of new gauge bosons – these particles will be observed indirectly. A very good resolution of the Z′ models will be possible for Z′ bosons with masses below $\approx 3 \cdot \sqrt{s}$. But there is also a reasonable sensitivity to Z′ effects up to masses of

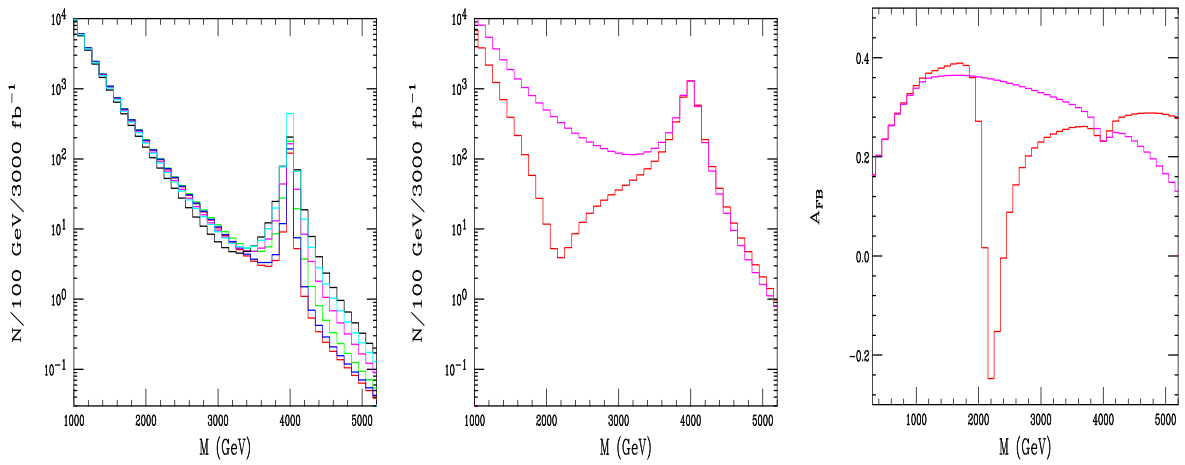

Figure 7.9: The lepton pair invariant mass spectrum (left) and the forward-backward lepton asymmetry for the production of a 4 TeV Z′ in various models (middle). The red(green, blue, magenta, cyan, black) histograms correspond to E_6 model $\psi(\chi,\ \eta)$, the Left Right Symmetric Model with $\kappa = g_R/g_L = 1$, the Alternative Left Right Model and the Sequential Standard Model, respectively. For descriptions of these models and original references see References [693], [705]. On the right: Forward-backward lepton asymmetry for the production of a 4 TeV KK resonance (right) for $D = 0$ (red) and $D = \pi R$ (magenta).

$\approx 7 \cdot \sqrt{s} - 8 \cdot \sqrt{s}$ that allows to conclude the Z′ models. This search reach extends that of a LHC substantially.

With both together, LHC and LC, the model resolution is substantially improved: The knowledge of the new particle mass from LHC can be used for more precise distinctions of the possible new physics sources.

Without a LC it is more than challenging to find out the properties of new physics. To enlighten a Confusion between models as for example in the case of KK excitations and Z′ bosons the LC is essential.

The clean topologies and the high luminosity at a LC allow precison measurements at high energies, completed by highest precision measurements on the Z peak. The accuracy of these measurements extends the sensitivity widely over the direct search ranges of a linear collider.

probability of confusion	M_c [TeV]	required luminosity [fb^{-1}]			
		LHC		LC	
		$D = 0$	$D = \pi R$	$\sqrt{s} = 0.5$ TeV	$\sqrt{s} = 1.0$ TeV
$5 \cdot 10^{-1}$	4	30	800	190	<50
	5	220	2500	500	130
	6	>3000		1200	260
	7			>3000	480
	8				820
	9				1300
10^{-5}	4	65	1800	300	100
	5	450		720	200
	6			2400	400
	7				730
	8				1250
	9				>2000

Table 7.3: The probability for the Z′ hypothesis in fits to KK generated data. Depending on the mass of the generated KK excitation, M_c, the luminosity required at LHC and LC to reach a confusion probability of $5 \cdot 10^{-1}$ and of 10^{-5} is given. For the LC the cases $D = 0$ and $D = \pi R$ are here identical.

8 Models with Extra Dimensions

It has been proposed that the hierarchy between the electroweak and Planck scales may be related to the geometry of extra spatial dimensions. This idea makes use of the fact that gravity has yet to be probed at energy scales much above 10^{-3} eV in laboratory experiments, admitting for the possibility that gravity behaves differently than expected at higher energies. If new dimensions are indeed related to the source of the hierarchy, then they should provide detectable signatures in experiments at the electroweak scale.

Theoretical frameworks with extra dimensions have some general features. In most scenarios, our observed 3-dimensional space is a 3-brane and is embedded in a higher D-dimensional spacetime, $D = 3 + \delta + 1$, which is known as the 'bulk.' The δ extra spatial dimensions are orthogonal to our 3-brane. If the additional dimensions are small enough, the Standard Model gauge and matter fields are phenomenologically allowed to propagate in the bulk; otherwise they are stuck to the 3-brane. Gravity, however, propagates throughout the full higher dimensional volume. Conventional wisdom dictates that if the additional dimensions are too large then deviations from Newtonian gravity would result and hence the extra dimensional space must be compactified. As a result of compactification, fields propagating in the bulk expand into a series of states known as a Kaluza-Klein (KK) tower, with the individual KK excitations being labeled by mode numbers. The collider signature for the existence of additional dimensions is the observation of a KK tower of states. The detailed properties of the KK states are determined by the geometry of the compactified space and their measurement would reveal the underlying geometry of the bulk. A review of extra dimensional models and their experimental signatures can be found in Ref. [730].

8.1 Large extra dimensions

In this scenario [731] the apparent gauge hierarchy is generated by a large volume of the extra dimensions. The Standard Model gauge and matter fields are confined to the 3-brane, while gravity propagates and becomes strong in the bulk. The Planck scale of the effective 4-dimensional theory is related to the Fundamental scale where gravity becomes strong in the full higher dimensional spacetime, M_D, via Gauss' Law,

$$M_{\rm Pl}^2 = V_\delta M_D^{2+\delta} \,, \tag{8.1}$$

where $V_\delta \sim (2\pi R_c)^\delta$ is the volume of the compactified space and R_c represents the radius of the compactified dimensions. Taking $M_D \sim 1$ TeV eliminates the gauge hierarchy and results in extra dimensions of size ~ 0.1 mm to 1 fm for $\delta = 2$ to 6. The states in the resulting KK tower of gravitons are evenly spaced with masses $m_{\vec{n}} = \sqrt{\vec{n}^2/R_c^2}$, where $\vec{n}$ represents the KK level number, and couple to the wall fields with inverse Planck strength. The details of the KK decomposition for the bulk gravitons

and the derivation of their Feynman rules can be found in [732, 733]. We note that both gravitensor and graviscalar fields result from the KK decomposition.

8.1.1 Indirect effects: graviton exchange

One collider signature for this scenario is that of virtual exchange of the graviton KK excitation states in all $2 \to 2$ scattering processes. This results in deviations in cross sections and asymmetries in SM processes as well as giving rise to new reactions which are not present at tree-level in the SM, such as $gg \to G_n \to \ell^+\ell^-$. In particular, as discussed in [732–737], the exchange of spin-2 graviton KK states modifies the differential cross section for fermion pair production in e^+e^- and pp collisions in a unique way, providing clear signatures for the existence of large extra dimensions. The exchange process is governed by the effective Lagrangian

$$\mathcal{L} = i\frac{4\lambda}{\Lambda_H^2} T^{\mu\nu} T_{\mu\nu} \,, \tag{8.2}$$

employing the notation of [734], and is similar to a dimension-8 contact interaction. $T^{\mu\nu}$ is the conserved stress-energy tensor. The sum over the propagators for the full graviton KK tower is divergent for $\delta \geq 1$ and thus introduces a sensitivity to the unknown ultraviolet physics. Several approaches for regulating this sum may be employed. The most model independent is the introduction of a naive cut-off, with the cut-off being set to Λ_H which is of order the fundamental scale M_D. In addition, the parameter $\lambda = \pm 1$ is usually incorporated.

• e^+e^- **and** $\mu^+\mu^-$ **Production at a Linear Collider**

The effects of graviton exchange at a LC with $\sqrt{s} = 500$ GeV are computed here [737] with a semi-analytical program in the improved Born approximation, using effective couplings. QED effects in the initial and final states are taken into account. Events without substantial energy loss due to initial state radiation are selected by a cut on the "effective" energy: $\sqrt{s'}/\sqrt{s} > 0.85$. With this cut, the interactions occur close to the nominal machine energy and offer the best sensitivity for manifestations of new physics. The virtual graviton effects are computed using the calculations from [732, 734, 736]. The sensitivity to graviton KK exchange is determined by a log likelihood fit. Two cases are distinguished:

1. **Realistic**: a cross section error is composed of the statistical error and a systematic error of 0.5% coming from the experiment, 0.2% from the luminosity determination, and a theoretical uncertainty of 0.5%. The forward-backward asymmetry error consists of the statistical error and a systematic uncertainty of 0.002 (absolute) for e^+e^- and 0.001 (absolute) for $\mu^+\mu^-$ final states. The main origins of the latter are from charge confusion of the leptons and uncertainties in the acceptance edge determination. Both of these effects are more important for electrons due to the forward peak in the differential cross section and the longer lever arm for measuring the muon momenta. One should stress that the forward-backward asymmetry systematics is lower than what was achieved at LEP, and requires a substantially improved detector.

2. **Optimistic**: a cross section error is composed just of the statistical error and a 0.2% contribution from the luminosity determination. The forward-backward asymmetry error consists of the statistical error and a systematic uncertainty which is given

Table 8.1: Sensitivity reach for extra dimensions at 95% CL at a $\sqrt{s} = 0.5$ TeV linear collider, taking $\lambda = +1$, as a function of the accumulated luminosity. From [737].

$e^+e^- \to e^+e^-$		
	"Realistic"	Optimistic
Luminosity $[fb^{-1}]$	Λ_H [TeV]	Λ_H [TeV]
1	2.6	2.6
10	3.1	3.5
100	3.3	4.2
1000	3.3	4.6
$e^+e^- \to \mu^+\mu^-$		
	"Realistic"	Optimistic
Luminosity $[fb^{-1}]$	Λ_H [TeV]	Λ_H [TeV]
1	1.6	1.6
10	2.1	2.1
100	2.8	2.8
1000	3.5	3.5

by the minimum of the systematic uncertainty for the 'Realistic' case and the statistical error. The rationale behind this is the hope that with increasing statistics one can better control the systematic effects. In practice, this turns out to play a role only for e^+e^-, as for muon pairs the statistical error of the forward-backward asymmetry is always larger than 0.001.

The optimization of the acceptance range is an important experimental question. The strong forward peak of Bhabha scattering is less sensitive to new physics as the SM amplitudes dominate the interference terms. We have investigated two regions:

(i) barrel: from 44° to 136°, where the polar angle is with respect to the electron beamline.

(ii) barrel+backward endcap: from 44° to 170°, so the region of the backward scattering is added.

The sensitivity reach from our fits [737] for electron and muon pair production are summarized in Table 8.1. They evolve from 2.6 (1.6) TeV for electrons (muons) at nominal luminosity to 3.3 (2.8) TeV for 100 fb^{-1}. Here, the electron channel is saturated by the systematic uncertainties, while the muon channel is still statistically dominated and continues to yield an improved sensitivity for the highest luminosi-

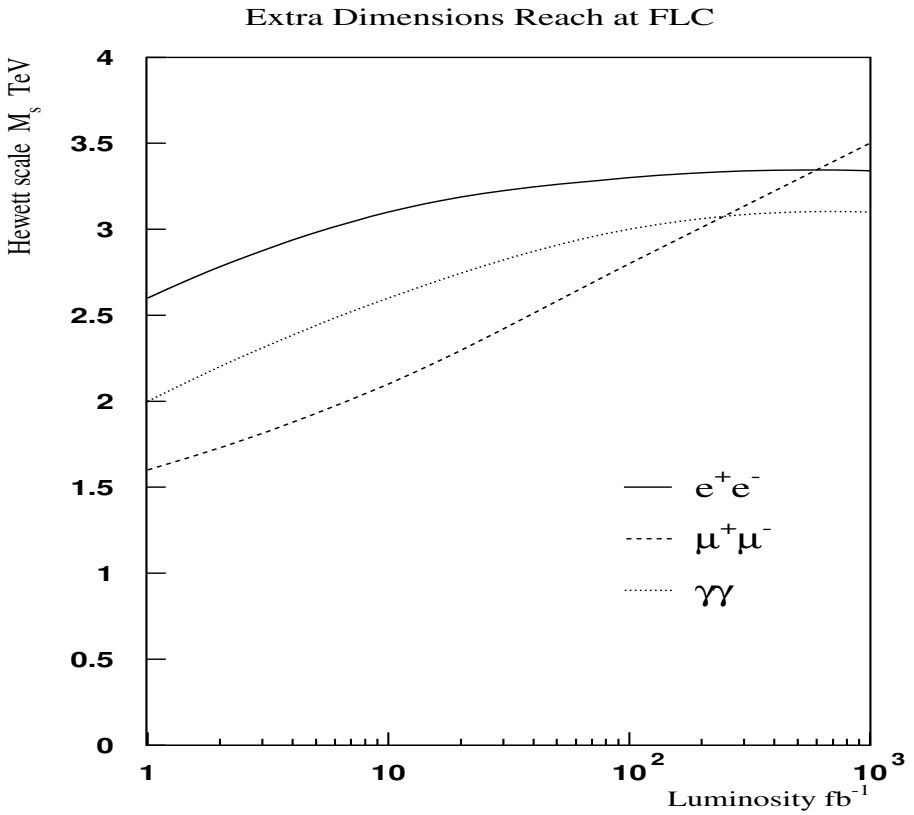

Figure 8.1: *Evolution of the sensitivity reach for extra dimensions at a linear collider with* $\sqrt{s} = 0.5$ *TeV in different final states with the accumulated luminosity.* $M_S = \Lambda_H$*. From [737].*

ties. In the Table, only the numbers for the positive interference case ($\lambda = +1$) are shown, as the sensitivity reach for negative interference is practically the same. The results are also displayed in Fig. 8.1 and agree with estimates from [734,736,738].

It is interesting to note the large difference between the "Realistic" and the Optimistic scenarios for the two channels: while the systematic errors for the electrons start to saturate above 10 fb^{-1}, the muons do not show any saturation at all. This is explained by the fact that for Bhabhas the sensitivity comes mainly from the cross section measurement, while for muons it is dominated completely by the forward-backward asymmetry.

We also investigate the optimal acceptance region for this process. For final state electrons, the gain in sensitivity is below 1% from including the backward endcap, so the measurement may as well be restricted to the barrel region. For muons, the sensitivity comes from the asymmetry which is best measured at lower angles, hence the results in the Table are derived under the assumption that both the barrel and the two endcaps are used *i.e.*, from 10° to 170°.

• $\gamma\gamma$ Production at a Linear Collider

The production of photon pairs in $\mathrm{e}^+\mathrm{e}^-$ collisions is described by t- and u-channel QED diagrams. The differential cross section has the following simple form

$$\frac{d\sigma}{d\Omega} = |e_t + e_u + New\ Physics|^2 \tag{8.3}$$

with

$$\left(\frac{d\sigma}{d\Omega}\right)_{QED} = \frac{\alpha^2}{2s}\left[\frac{t}{u} + \frac{u}{t}\right] = \frac{\alpha^2}{s}\left[\frac{1+\cos^2\theta}{1-\cos^2\theta}\right] . \tag{8.4}$$

Deviations from QED typically have the form:

$$\frac{d\sigma}{d\Omega} = \left(\frac{d\sigma}{d\Omega}\right)_{QED}\left(1 \pm \frac{s^2\sin^2\theta}{2(\mathcal{L}_{\pm}^{QED})^4}\right) , \tag{8.5}$$

$$\frac{d\sigma}{d\Omega} = \left(\frac{d\sigma}{d\Omega}\right)_{QED}\left(1 \pm \frac{\lambda s^2\sin^2\theta}{2\pi\alpha(\Lambda_H)^4} + ...\right) . \tag{8.6}$$

The QED cut-off in Equation (8.5) represents the basic form of possible modifications to quantum electrodynamics. Equation (8.6) displays the deviations specifically due to graviton KK exchange as calculated in [732, 739]. If we ignore the contributions from higher order graviton terms (denoted as ...), the two equations predict the same angular form of modifications to the differential cross section. Thus, it is particularly simple to compare the results from different searches by transforming the relevant parameters; the relation is

$$\Lambda_H = 2.57\ \mathcal{L}^{QED}.$$

The sensitivity reach from our fits [737] is summarized in Table 8.2 and Fig. 8.1. The sensitivity evolves from 2 TeV at nominal luminosities to 3 TeV for 100 fb^{-1}, where the process becomes saturated by systematic effects. As in the case of Bhabha scattering, there is no gain in sensitivity from going outside of the barrel region; in this case, the differential cross section is symmetric, exhibiting both a forward and a backward peak.

Table 8.2: Sensitivity reach for extra dimensions at 95% CL at a linear collider with $\sqrt{s} = 0.5$ TeV for the case $\lambda = +1$. From [737].

$e^+e^- \to \gamma\gamma$		
	"Realistic"	Optimistic
Luminosity $[fb^{-1}]$	Λ_H [TeV]	Λ_H [TeV]
1	2.0	2.0
10	2.6	2.6
100	3.0	3.4
1000	3.1	4.1
$\mathcal{L}^{QED}$ 1000	1.2	1.6

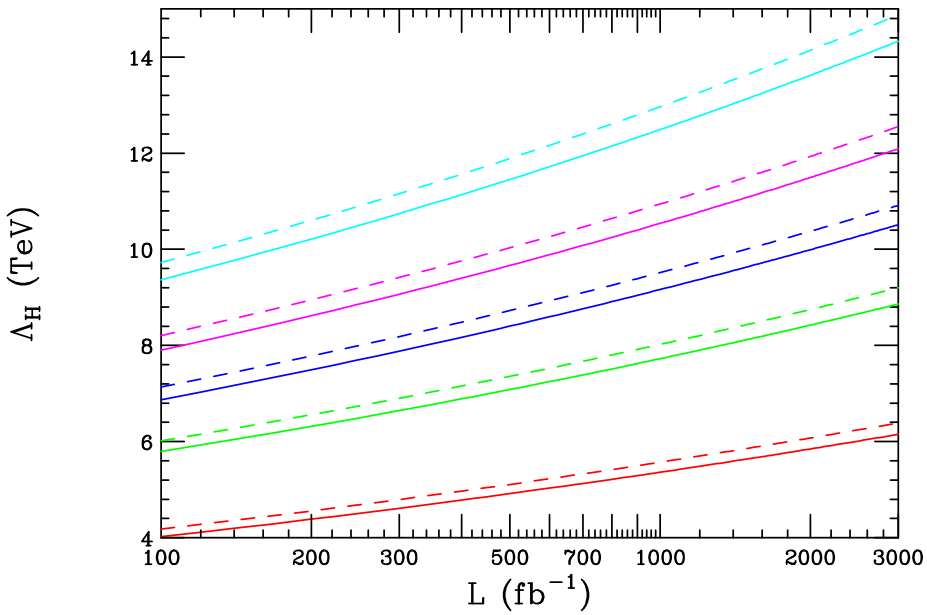

Figure 8.2: 95% CL search reach for the scale associated with the exchange of graviton KK states in $e^+e^- \to f\overline{f}$. The solid (dashed) curves correspond to a initial state positron polarization of 0 (60)%. Each pair of curves is for $\sqrt{s} = 0.5\,, 0.8\,, 1.0\,, 1.2\,,$ and 1.5 TeV, from bottom to top, respectively. From [740].

Summing over all fermion final states ($e\,, \mu\,, \tau\,, c\,, b$, and t) and examining the deviations in the total cross section, forward-backward asymmetry, and left-right asymmetry in each case, as well as the tau polarization asymmetry, yields the search reach [740] for Λ_H shown in Fig. 8.2 as a function of integrated luminosity. We see that for a 1 TeV LC, scales of order $\Lambda_H \sim 8.4$ TeV can be observed with 500 fb^{-1}.

The sensitivities for virtual graviton exchange at the LHC have been evaluated in [741] and are found to be $\Lambda_H \leq 7.5, 7.1$ TeV for Drell-Yan and di-photon production, respectively. We see that this search region is comparable to that of a TeV-class LC. In addition, the spin-2 exchange also modifies the forward-backward asymmetry in Drell-Yan production; however, the utility of this asymmetry in extending the search reach or for identifying the spin-2 nature of the exchange has yet to be analyzed.

If deviations are observed at the LC or LHC from the virtual exchange of new particles, then it will be necessary to have techniques available to differentiate between the possible scenarios giving rise to the effect. One such method is the use of transverse polarization at the LC. If longitudinal positron polarization is available at the LC, then spin rotators may be used to convert these to transversely polarized beams. This allows for new asymmetries to be constructed which are associated with the azimuthal angle formed by the directions of the $e^\pm$ polarization and the plane of the momenta of the outgoing fermions in $e^+e^- \to f\overline{f}$. The spin-averaged matrix element for this process can be written as

$$\begin{aligned} |\mathcal{M}|^2 &= \frac{1}{4}(1 - P_L^- P_L^+)(|T_+|^2 + |T_-|^2) + (P_L^- - P_L^+)(|T_+|^2 - |T_-|^2) \\ &\quad + (2P_T^- P_T^+)[\cos 2\phi \mathcal{R}e\,(T_+ T_-^*) - \sin 2\phi \mathcal{I}m\,(T_+ T_-^*)]\,, \end{aligned} \tag{8.7}$$

where ϕ is the azimuthal angle defined on an event-by-event basis described above,

$\sqrt{s}$ (GeV)	Search Reach Λ_H (TeV)	ID Reach (TeV)
500	10.2	5.4
800	17.0	8.8
1000	21.5	11.1
1200	26.0	13.3
1500	32.7	16.7

Table 8.3: 95% CL search reach and identification of spin-2 exchange from the azimuthal asymmetries discussed in the text. From [742].

$P^{-}_{L,T}(P^{+}_{L,T})$ represent the polarizations of the electron(positron), and $T_{+,-}$ correspond to the relevant helicity amplitudes. Note that the ϕ dependence in this expression is only accessible if both beams are transversely polarized. Spin-2 exchange does not introduce any new helicity amplitudes over those present for spin-1 exchange, but does yield an asymmetric distribution in $\cos\theta$ unlike the case of spin-1 exchange. Asymmetries in the differential cross section $d\sigma/d\cos\theta d\phi$ extend the search reach for graviton KK exchange by more than a factor of two, and provide an additional tool for isolating the signatures for spin-2 exchange up to mass scale in excess of $10\sqrt{s}$. These results [742] are shown in Table 8.3. If deviations due to virtual graviton exchange were observed in, *e.g.*, Drell-Yan production at the LHC, we see that a LC with positron polarization and $\sqrt{s} \geq 800$ GeV can identify the spin-2 nature of the exchange for the entire LHC search region.

If positron polarization is not available at the LC, then the spin-2 nature of virtual graviton exchange can be identified by expanding the fermion pair production cross section into multipole moments. Studies indicate [743] that this technique can uniquely identify spin-2 exchange at the 5σ level for fundamental scales M_D up to $6\sqrt{s}$.

8.1.2 Direct production: graviton emission

A second class of collider signals for large extra dimensions is that of real emission of graviton states in the scattering processes $e^+e^- \rightarrow \gamma(Z) + G_n$ and $pp \rightarrow$jet$+G_n$ [732, 744]. The produced graviton behaves as if it were a massive, non-interacting stable particle and thus appears as missing energy in the detector. The emission processes probe the fundamental scale M_D directly. The cross section is computed for the production of a single massive KK excitation and then summed over the full tower of KK states. Since the mass splittings in the KK tower are so small, this sum may be replaced by an integral weighted by the density of KK states. Due to this integration, the radiated graviton appears to have a continuous mass distribution; this corresponds to the probability of emitting gravitons with different extra dimensional momenta. The observables for graviton production are then distinct from those of other physics processes with a missing energy signature involving fixed masses for the undetectable particles. The expected discovery reach from this process has been computed in [57] at a 800 GeV LC with 1000 fb^{-1} of integrated luminosity and vari-

$e^+e^- \to \gamma + G_n$		2	4	6
LC	$P_{-,+} = 0$	5.9	3.5	2.5
LC	$P_- = 0.8$	8.3	4.4	2.9
LC	$P_- = 0.8$, $P_+ = 0.6$	10.4	5.1	3.3
$pp \to g + G_n$		2	3	4
LHC		$4 - 8.9$	$4.5 - 6.8$	$5.0 - 5.8$

Table 8.4: 95% CL sensitivity to the fundamental scale M_D in TeV for different values of δ, from the emission process for various polarization configurations and different colliders as discussed in the text. $\sqrt{s} = 800$ GeV and 1 ab^{-1} has been assumed for the LC and 100 fb^{-1} for the LHC. Note that the LHC only probes M_D within the stated range. From [57,745].

ous configurations for the beam polarization. These results are displayed in Table 8.4 and include kinematic acceptance cuts, initial state radiation, and beamsstrahlung. In hadronic collisions, the effective theory breaks down for some regions of the parameter space as the parton-level center of mass energy can exceed the value of M_D. Experiments are then sensitive to the new physics appearing above the fundamental scale that is associated with the low-scale UV theory of quantum gravity. An ATLAS simulation [745] of the missing transverse energy in signal and background events at the LHC with 100 fb^{-1} is presented in Fig. 8.3 for various values of M_D and δ. This study results in the discovery range displayed in Table 8.4. The lower end of the range corresponds to where the ultraviolet physics sets in and the effective 4-dimensional theory fails, while the upper end represents the boundary where the signal is observable above background. Note that the search regions for a polarized LC are comparable to that of the LHC.

If an emission signal is observed, one would like to determine the values of the fundamental parameters M_D and δ. The evolution of the emission cross section with center of mass energy in e^+e^- annihilation depends quite strongly on the values of these parameters. This is displayed in Fig. 8.4, where the cross section is normalized at 500 GeV for $M_D = 5$ TeV and $\delta = 2$. The dashed curves in the bottom panel also include the effects of including a finite value for the brane tension. A finite brane tension takes into account the effects of a non-rigid brane and introduces the additional parameter Δ. Measurement of this cross section at different values of $\sqrt{s}$ thus determines the values of the fundamental parameters of the theory. We see that a long lever arm (corresponding to measurements at high values of $\sqrt{s}$) are necessary to disentangle the effects of a finite brane tension.

Looking at the LHC missing energy distributions displayed in Fig. 8.3, we see that the shape and normalizations of the curves also vary for different values of M_D and δ. However, there are uncertainties, *e.g.*, due to the parton densities, associated with determining the overall normalization at the LHC. Input from the cross section measurement at the LC for a single value of $\sqrt{s}$ would help to determine the overall normalization at the LHC. With this information from the LC, the determination of the fundamental parameters from LHC data would be improved [747]. This will be quantified below.

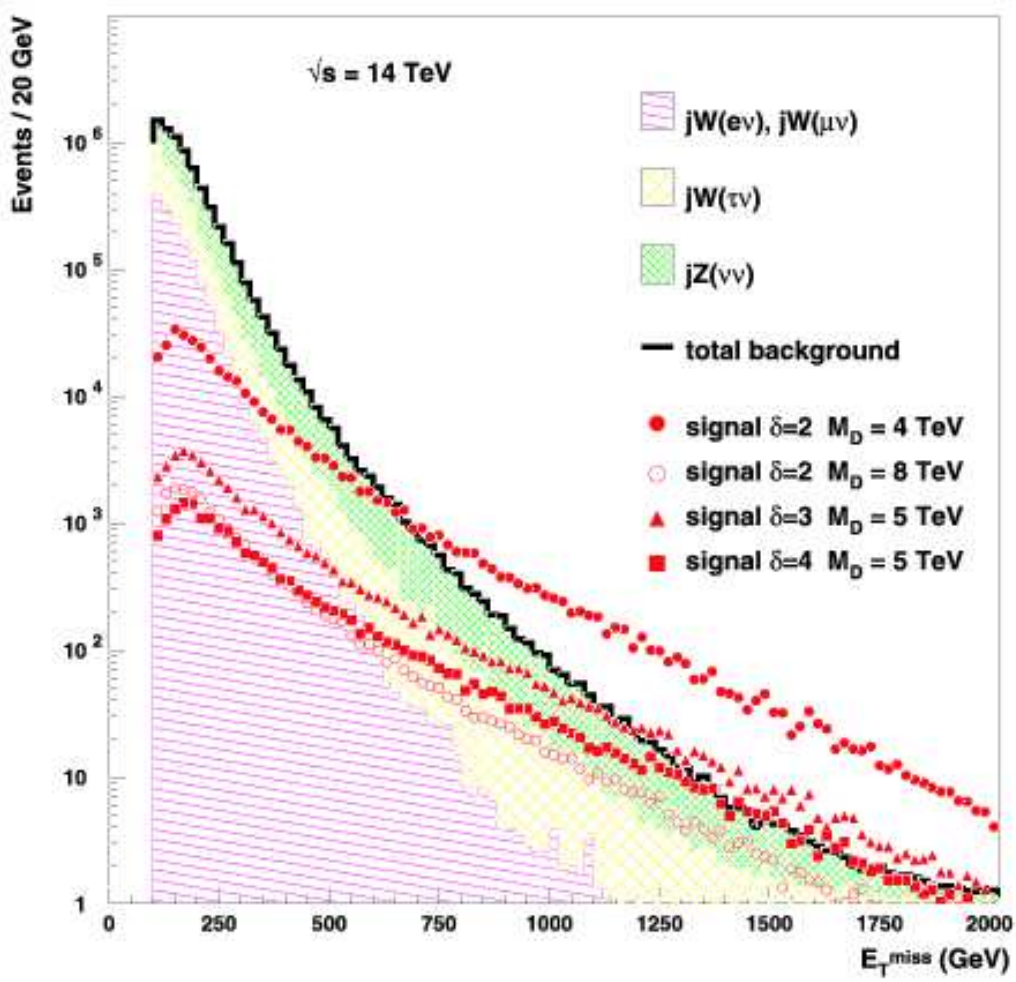

Figure 8.3: Distribution of the missing transverse energy in background events and signal events for 100 fb^{-1}. The contribution of the three principal Standard Model background processes is shown as well as the distribution of the signal for several values of δ and M_D. From [745].

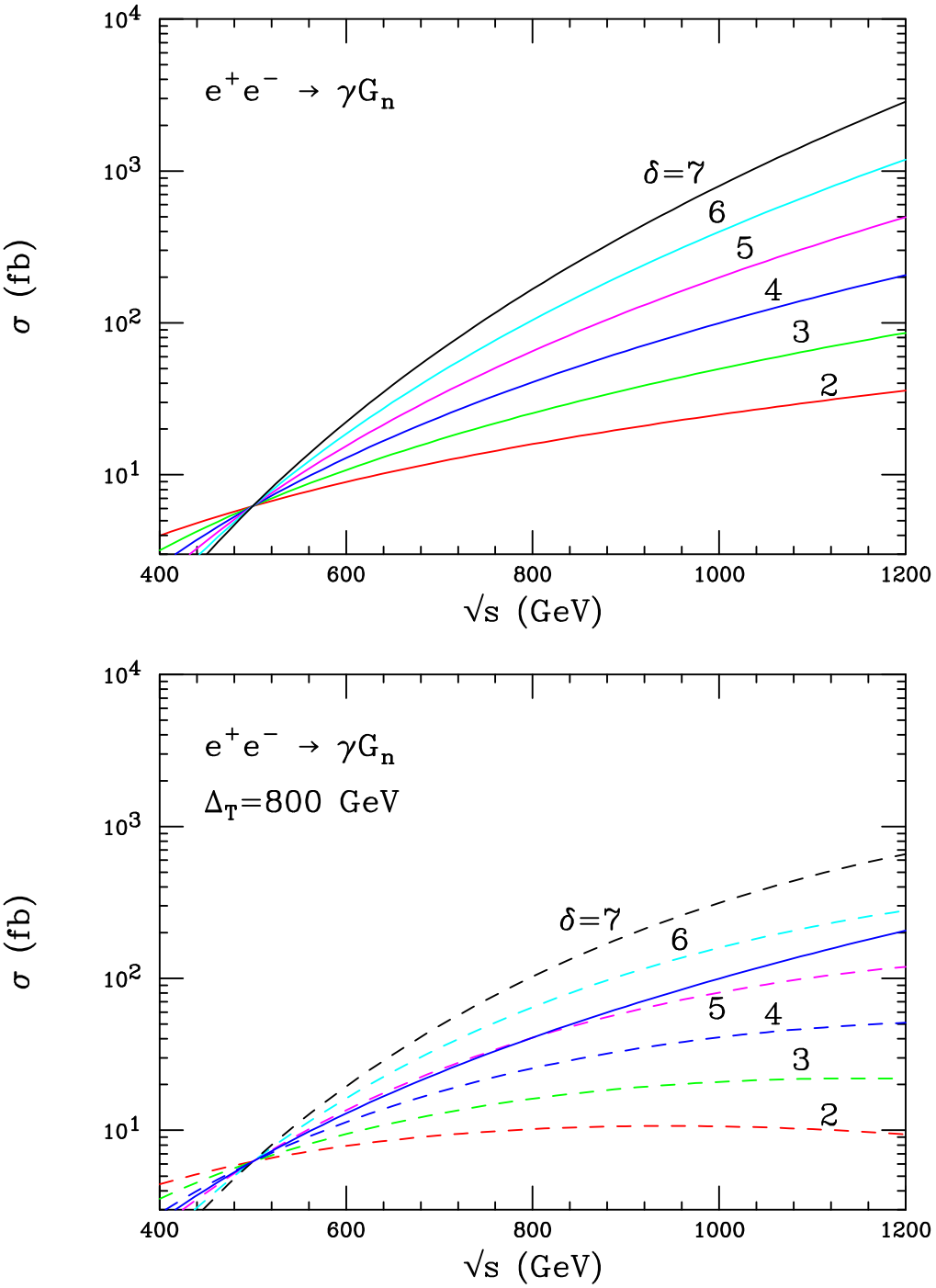

Figure 8.4: Emission cross section in e^+e^- annihilation as a function of $\sqrt{s}$ for $\delta = 2 - 7$ from top to bottom on the right-hand side. The cross sections are normalized to $M_D = 5$ TeV and $\delta = 2$ at $\sqrt{s}$ = 500 GeV. Top: Brane terms are not included. Bottom: The effects of finite brane tension are included, taking the relevant tension parameter to be $\Delta = 800$ GeV. Here, the lone solid curve represents the case without brane term effects for $\delta = 5$. From [746].

8.1.3 Graviscalar effects in Higgs production

Another class of signals that can arise in models with large extra dimensions is associated with the allowed mixing between the Higgs boson and the graviscalar states. Such mixing is discussed in Sec 3.5 in this Report in the case of warped extra dimensions. The present scenario differs from the warped case in that there is a KK tower of densely-packed graviscalar states rather than a single radion. The graviscalar KK states have masses $m_{\vec{n}} = \sqrt{\vec{n}^2/R_c^2}$ and couple to the trace of the stress-energy tensor with inverse Planck strength. The presence of this graviscalar KK tower alters the phenomenology of the Higgs boson. For example, instead of computing the production of a single Higgs boson, one must now consider the production of the full set of densely spaced mass eigenstates, all of which are mixing with one another. Due to this mixing, the Higgs will effectively acquire a potentially large branching ratio to invisible final states which are composed primarily of the graviscalars.

The interaction between the complex doublet Higgs field H and the Ricci scalar curvature R of the induced 4-dimensional metric g_{ind} is given by the action

$$S = -\xi \int d^4x \sqrt{g_{ind}} R(g_{ind}) H^\dagger H \,. \tag{8.8}$$

After the usual shift $H = (\frac{v+h}{\sqrt{2}}, 0)$, this interaction leads to the mixing term [748]

$$\mathcal{L}_{\rm mix} = -\frac{2\sqrt{2}}{\overline{M}_{Pl}} \xi v m_h^2 \sqrt{\frac{3(\delta-1)}{\delta+2}}\, h \sum_{\vec{n}>0} s_{\vec{n}} \,. \tag{8.9}$$

Here, ξ is a dimensionless parameter which is naturally of order unity and $s_{\vec{n}}$ represents the graviscalar KK excitations.

At colliders, one should consider the production and decay of the coherent state $h_{eff} = h' + \sum_{\vec{n}>0} s'_{\vec{n}}$, which is the sum of the physical eigenstates h' and $s'_{\vec{n}}$ that are obtained after diagonalizing the Hamiltonian. For a SM initial state I (*e.g.*, think of $WW \to h_{eff}$ fusion at the LHC or $Z + h_{eff}$ at the LC) and a SM final state F, the net production cross section is given by

$$\sigma(I \to h_{eff} \to F) \simeq \sigma_{SM}(I \to h \to F) \left[\frac{\Gamma^{SM}_{h\to F}}{\Gamma^{SM}_h + \Gamma_{h_{eff}\to graviscalar}} \right] . \tag{8.10}$$

Here,

$$\begin{aligned} \Gamma_{h_{eff}\to graviscalar} &= 2\pi\xi^2 v^2 \frac{3(\delta-1)}{\delta+2} \frac{m_h^{1+\delta}}{M_D^{2+\delta}} S_{\delta-1} \\ &\sim (16\,\mathrm{MeV}) 20^{2-\delta} \xi^2 S_{\delta-1} \frac{3(\delta-1)}{\delta+2} \left(\frac{m_h}{150\,\mathrm{GeV}}\right)^{1+\delta} \left(\frac{3\,TeV}{M_D}\right)^{2+\delta} \end{aligned} \tag{8.11}$$

and can be thought of an invisible width for the coherent h_{eff} state. $S_{\delta-1}$ is the surface of a unit-radius sphere in δ dimensions. The net result is that the coherently summed amplitude gives the SM Higgs cross section multiplied by a branching ratio to the final state that must be computed with the inclusion of the invisible $h_{eff} \to graviscalar$ width. For graviscalar final states, the production rate $\sigma(I \to h_{eff} \to graviscalar)$ is

obtained by replacing $\Gamma^{SM}_{h\to F}$ with $\Gamma_{h_{eff}\to graviscalar}$. The branching ratio into invisible final states, including contributions from mixing as well as from the direct decay into graviscalars, is

$$BR(h_{eff} \to invisible) = \frac{\Gamma_{h_{eff}\to graviscalar}}{\Gamma^{SM}_{h} + \Gamma_{h_{eff}\to graviscalar}} \,. \tag{8.12}$$

The rates for the usual SM Higgs decay channels are then reduced by $1 - BR(h_{eff} \to invisible)$. The importance of the invisible decay width is illustrated in Figs. 8.5 and 8.6 in the M_D, ξ parameter space for $m_h = 120$ GeV with $\delta = 2$ and $\delta = 4$, respectively. One should keep in mind that the SM Higgs boson with mass of 120 GeV would have a width of about 3.6 MeV. We thus see that the graviscalar mixing results in substantial corrections to the expected Higgs width and a significant invisible branching fraction.

Detailed studies of the SM Higgs boson signal significance, with inclusive production, have been carried out by the ATLAS [89] and CMS [750] collaborations. Here, the results of Fig. 25 in [750], obtained for $L = 30$ fb^{-1}, are employed by reducing the SM Higgs boson signal rates in the usual visible channels by $1 - BR(h_{eff} \to invisible)$. For $L = 100$ fb^{-1}, the statistical significance in each channel is simply rescaled by $\sqrt{100/30}$. To understand the impact of the invisible branching ratio, we focus on $m_h = 120$ GeV and perform a full scan of the parameter space by varying M_D and ξ for different values of the number of extra dimensions δ. It is found [749] that there are regions at high ξ where the significance of the Higgs boson signal in the canonical channels drops below the 5 σ threshold. However, the LHC experiments will also be sensitive to an invisibly decaying Higgs boson produced via WW-fusion, with tagged forward jets. In Ref. [750] the results of a detailed CMS study for this mode are given in Fig. 25 for integrated luminosity of 10 fb^{-1}. These results assume a 100% invisible branching ratio; they are rescaled here by multiplying the signal rate by $BR(h_{eff} \to invisible)$ and are adjusted for different luminosities by scaling statistical significances according to $\sqrt{L(\text{fb}^{-1})/10}$. (The latter is probably somewhat inaccurate for high-luminosity operation because of effects from pile-up.) The portion of the (M_D, ξ) parameter space where the h_{eff} signal can be recovered at the 5σ level through invisible decays for $L = 30$ fb^{-1} and $L = 100$ fb^{-1} is summarized in Fig. 8.7. It is important to observe that whenever the Higgs boson sensitivity is lost due to the suppression of the canonical decay modes the invisible rate from WW fusion is large enough to still ensure detection through a dedicated analysis.

As discussed in the previous section, the production of $jets/\gamma+$ missing energy from graviton emission is also sensitive to the values of M_D and δ. For comparison, the 5σ search range given in Table 8.4 for M_D is also displayed in Fig. 8.7. Also shown is the 95% CL lower limit on M_D coming from the combination of LEP, LEP2 and Tevatron data, as summarized in [751]. From Fig. 8.7 we observe that the invisible Higgs decay width is predicted to probe (at 5 σ) parts of parameter space where the $jets/\gamma$ + missing energy signature either falls below this level or is not reliably computable.

A TeV-class e^+e^- linear collider will be able to see the h_{eff} Higgs signal regardless of the magnitude of the invisible branching ratio simply by looking for a peak in the M_X mass spectrum in $e^+e^- \to ZX$ events. As shown in [752], a substantial signal for the case where X is an invisible final state is possible down to fairly low values of $BR(h_{eff} \to invisible)$. We have employed the $\sqrt{s} = 350$ GeV, $L = 500$ fb^{-1} results

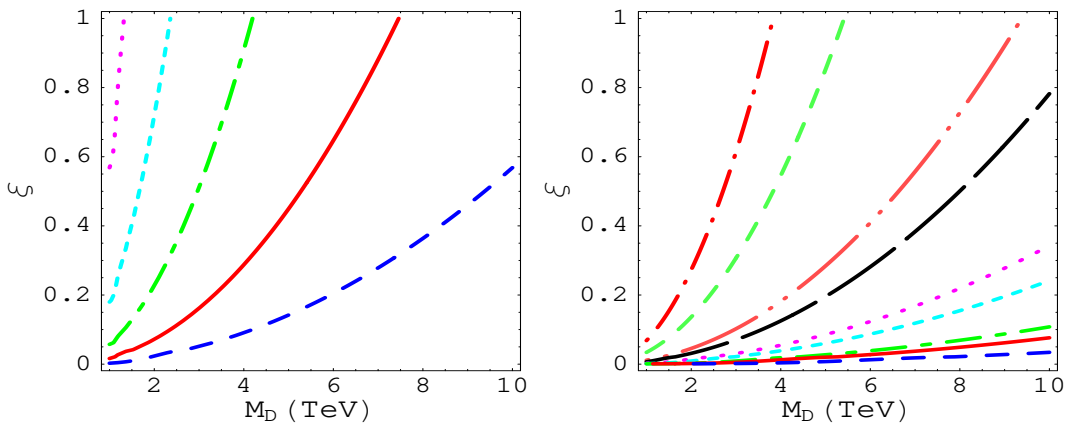

Figure 8.5: Contours of fixed $\Gamma_{h_{eff} \to graviscalar}$ (left) and fixed $BR(h_{eff} \to invisible)$ (right) in the $M_D - \xi$ parameter space for $m_h = 120$ GeV, taking $\delta = 2$. The width contours correspond to: 0.0001 GeV (large blue dashes), 0.001 GeV (solid red line), 0.01 GeV (green long dash – short dash line), 0.1 GeV (short cyan dashes), and 1 GeV (purple dots). The BR contours correspond to: 0.0001 (large blue dashes), 0.0005 (solid red line), 0.001 (green long dash – short dash line), 0.005 (short cyan dashes), $.01$ (purple dots), $.05$ (long black dashes), 0.1 (chartreuse long dashes with double dots), 0.5 (green dashes), and 0.85 (red long dash, short dot line at high ξ and low M_D). From [749].

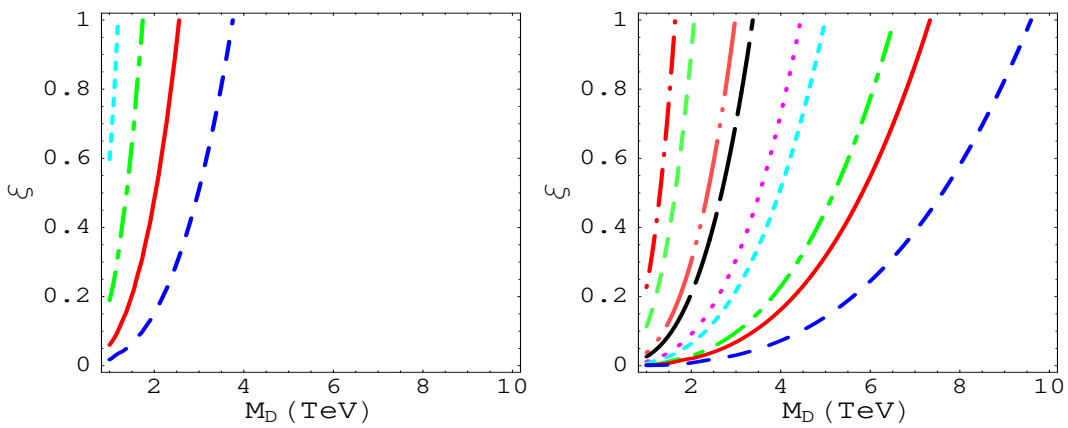

Figure 8.6: As in Fig. 8.5 but for $\delta = 4$.

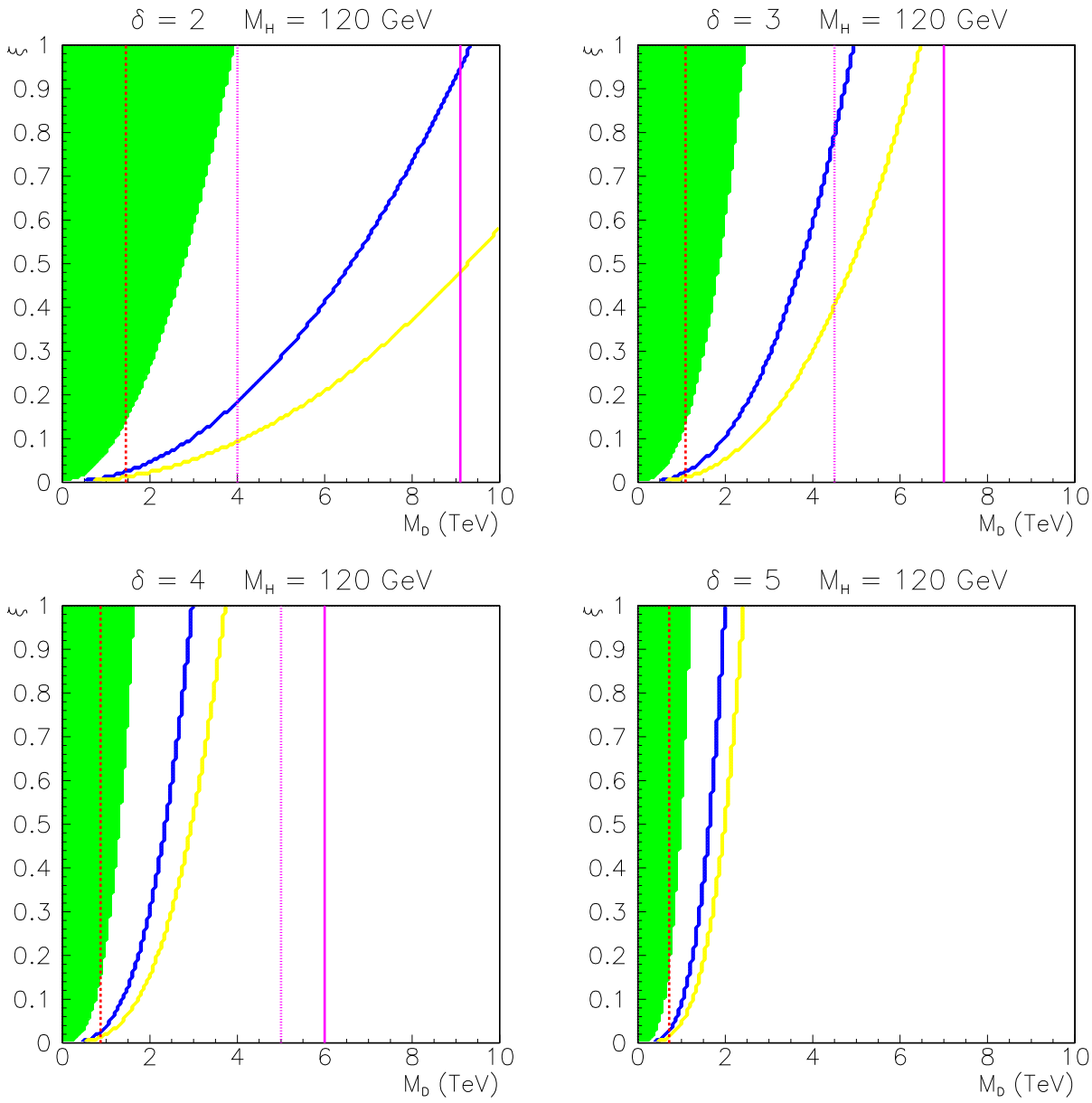

Figure 8.7: Invisible decay width effects in the ξ - M_D plane for m_h = 120 GeV. The figures are for different values of δ as labeled. The shaded regions indicate where the Higgs signal at the LHC drops below the 5σ threshold in the canonical channels for 100 fb^{-1} of data. The regions above the blue (bold) line are the parts of the parameter space where the LHC invisible Higgs signal in the WW-fusion channel exceeds 5σ significance. The regions above the yellow (light gray) line are the parts of the parameter space where the LC invisible Higgs signal will exceed 5σ assuming $\sqrt{s} = 350$ GeV and $L = 500$ fb^{-1}. The solid vertical line at the largest M_D value in each panel shows the upper limit on M_D which can be probed at the 5σ level by the analysis of $jets/\gamma$ with missing energy at the LHC. The middle dotted vertical line shows the value of M_D below which the theoretical computation at the LHC is unreliable (For $\delta = 5$, there is no value of M_D for which the LHC computation is reliable.) The dashed vertical line at the lowest M_D value is the 95% CL lower limit coming from combining Tevatron and LEP/LEP2 limits. From [749].

of [752] to determine the portion of (M_D, ξ) parameter space for which the invisible Higgs signal will be observable at the LC at the 5σ or better level. This is the region above the light gray (yellow) curves in Fig. 8.7. The LC will be able to detect this signal over a larger part of the parameter space than can the LHC.

8.1.4 Determination of the model parameters

In principle, the graviton emission signature at the LHC and LC can be used to provide information on M_D and δ and then, as discussed above, the Higgs signals in visible and invisible channels can be used to further constrain these parameters and to determine ξ. However, as discussed in section 8.1.2, the LHC has two difficulties regarding the use of the $jets/\gamma+$ missing energy signal. First, it is not possible to measure the cross section at different center of mass energies in a controlled fashion, and second, the effective theory breaks down when the parton center of mass energy exceeds the value of M_D. Thus, although the LHC may well see an excess in this channel from graviton emission, its interpretation in terms of M_D and δ will be highly ambiguous. The situation at the LC for the $\gamma/Z+$ missing energy signal is completely different. There, the machine energy can be controlled to probe several fixed energies (below M_D), and as discussed previously (see Fig. 8.4) the ratio of the cross sections at two different energies can determine δ and the absolute normalization of the cross sections can determine M_D.

With regard to the Higgs sector, a crucial first test for this model will be to determine if the $e^+e^- \to ZX$ events at the LC exhibit a resonance structure with the predicted rate for a SM Higgs with an observed peak mass. This can be done at about the 3% level. If such a peak is observed with SM normalization, then a determination of the parameters for large extra dimensions can be performed. Without the LC, there will be no decay-mode-independent means for checking that the Higgs is produced with a SM-like rate. This can only be accomplished by checking for consistency of the rates for visible and invisible final states in various production modes with the prediction from large extra dimensions that the standard visible states are reduced in rate from the SM prediction by the uniform factor of $[1 - BR(h_{eff} \to invisible)]$.

The parameter determination at the LHC is computed [749] assuming that the production cross section for the Higgs signal in each of the many production modes studied by ATLAS and CMS is SM-like. The errors on the parameter determination will be somewhat increased if one allows for the possibility of non-SM production rates. Thus, the results presented here for LHC operation alone are somewhat optimistic. The procedure is as follows:

- The $jets/\gamma+$ missing energy signal from graviton emission is not included in the determination of M_D and δ due to the ambiguities discussed above.
- For the Higgs signal in visible channels, the SM ATLAS and CMS results are rescaled according to $1 - BR(h_{eff} \to invisible)$.
- For the Higgs signal in the invisible final state, the detailed results of [753] (used in the CMS analysis [750]) are employed. In this reference, the Higgs signal and background event rates are given for the $WW \to Higgs \to invisible$ channel

assuming SM production rate and 100% invisible branching ratio. Here, the signal rate is rescaled using $S_{inv}^{h_{eff}} = BR(h_{eff} \to invisible) S_{inv}^{SM}$ and the error in the signal rate is computed as $[\Delta S_{inv}^{h_{eff}}]^2 = S_{inv}^{h_{eff}} + B_{inv}$.

The LC will be able to improve the determination of the model parameters considerably with respect to the LHC alone. In the present analysis [749], the Higgs signals in both visible and invisible final states as well as the $\gamma+$ missing energy signal for graviton production have been employed.

- For the process of graviton emission, the results from the TESLA study [57] (see Table 8.4) have been used. The $e^+e^- \to \nu_e\overline{\nu}_e + \gamma$ background has been computed using the KK [754] and nunugpv [755] simulation programs. Results from the two programs agree well. It is assumed that measurements are performed at both $\sqrt{s} = 500\,, 1000$ GeV with integrated luminosities of 1000 fb^{-1} and 2000 fb^{-1}, respectively. (Results obtained for 500 fb^{-1} and 1000 fb^{-1}, respectively, are not very different.)

- For the invisible Higgs signal, the results of [752] are employed from which the fractional error for the measurement of any given $BR(h_{eff} \to invisible)$ can be extracted.

- For the visible Higgs signal, the best available LC errors for the $b\overline{b}$ final state are used, assuming operation at an energy of $\sqrt{s} = 500$ GeV with luminosity of 1000 fb^{-1} and with polarization. The corresponding SM fractional error for this channel at $m_h = 120$ GeV is 0.02. This SM result is adjusted assuming signal rate reduction by the factor $1 - BR(h_{eff} \to invisible)$.

To determine how well the M_D, ξ, δ parameters can be determined, specific input values, M_D^0, ξ^0, δ^0, are chosen. The expected experimental errors are then computed for each of the above observables assuming this input parameter set. The expected $\Delta\chi^2$ for each of the above observables is then computed for different values of M_D, ξ, δ.

The $BR(h_{eff} \to visible)$ measurement turns out to be important in discriminating between different models when the invisible branching fraction is large (requiring small to moderate m_h, small M_D, $\delta = 2$ or 3, and substantial ξ). In such a case, the visible branching fraction can be quite small and typically varies rapidly as a function of the model parameters (in particular ξ), whereas the invisible branching fraction, although large, will vary more slowly and will not provide as good a discrimination between different parameter values. Of course, if $BR(h_{eff} \to visible)$ is so small that the background is dominant, our ability to determine ξ, M_D and δ from this measurement deteriorates. Complementary statements apply to the case when $BR(h_{eff} \to invisible)$ is small and $BR(h_{eff} \to visible)$ is slowly varying.

Given the $\Delta\chi^2$ for the five measurements outlined above, we will characterize the net discrimination between models by using LHC data alone, $\Delta\chi^2(LHC)$, and LHC+LC data, $\Delta\chi^2(LHC + LC)$ (the latter being completely dominated by the LC information), where

$$\Delta\chi^2(LHC) \;=\; \Delta\chi^2(LHC,\, H_{vis}) + \Delta\chi^2(LHC,\, H_{inv})$$

$$\begin{aligned} \Delta\chi^2(LC) &= \Delta\chi^2(LC,\ \gamma + \text{missing energy}) + \Delta\chi^2(LC,\ H_{inv}) + \Delta\chi^2(LC,\ H_{vis}) \\ \Delta\chi^2(LHC + LC) &= \Delta\chi^2(LHC) + \Delta\chi^2(LC)\,. \end{aligned} \tag{8.13}$$

Note that since m_h will be very precisely measured, one can concentrate on the ability to determine the parameters M_D, δ and ξ. Regions of parameter space corresponding to a 95% CL determination, which for three parameters corresponds to $\Delta\chi^2 = 7.82$ are presented in Figs. 8.8–8.9. Here, $m_h = 120$ GeV and the fixed input value $\xi^0 = 0.5$ are assumed.

The most important point of these figures is that the ability of the LHC alone to determine the input parameters is **very** limited, whereas by including the LC data, a quite precise δ, ξ and M_D determination is possible when M_D and δ are not too large. Similar results are also found (see [749]) for the case $m_h > 2M_W$.

8.2 TeV^{-1} extra dimensions

The possibility of TeV^{-1}-sized extra dimensions naturally arises in braneworld theories [756]. By themselves, they do not allow for a reformulation of the hierarchy problem, but they may be incorporated into a larger structure in which this problem is solved. In these scenarios, the SM fields are phenomenologically allowed to propagate in the bulk. This presents a wide variety of choices for model building: (i) all, or only some, of the SM gauge fields exist in the bulk; (ii) the Higgs field may lie on the brane or in the bulk; (iii) the SM fermions may be confined to the brane or to specific locales in the extra dimensions, or they may freely reside in the bulk. The phenomenological consequences of this scenario strongly depend on the location of the fermion fields.

8.2.1 Gauge fields in the bulk

We first discuss the case where the SM matter fields are rigidly fixed to the brane and do not feel the effects of the additional dimensions. The simplest model of this class is the case of only one extra TeV^{-1}-sized dimension, where the fermions are constrained to lie at one of the two orbifold fixed points, $y = 0, \pi R$, associated with the compactification on the orbifold S^1/Z_2, where R is the radius of the compactified TeV^{-1} dimension. Two specific cases will be considered below: either all of the fermions are placed at $y = 0$ ($D = 0$), or the quarks and leptons are localized at opposite fixed points ($D = \pi R$). Here D is the distance between the quarks and leptons in the single extra TeV^{-1} dimension. The latter scenario may assist in the suppression of proton decay.

In this framework, the fermionic couplings of the KK excitations of a given gauge field are identical to those of the SM, apart from a possible sign if the fermion lives at the $y = \pi R$ fixed point, and an overall factor of $\sqrt{2}$. The gauge boson KK excitation masses are given to lowest order in $(M_0/M_c)^2$ by the relationship

$$M_n^2 = (nM_c)^2 + M_0^2\,, \tag{8.14}$$

where n labels the KK level as usual, $M_c = 1/R \sim 1$ TeV is the compactification scale, and M_0 is the zero-mode mass. M_0 is obtained via spontaneous symmetry breaking

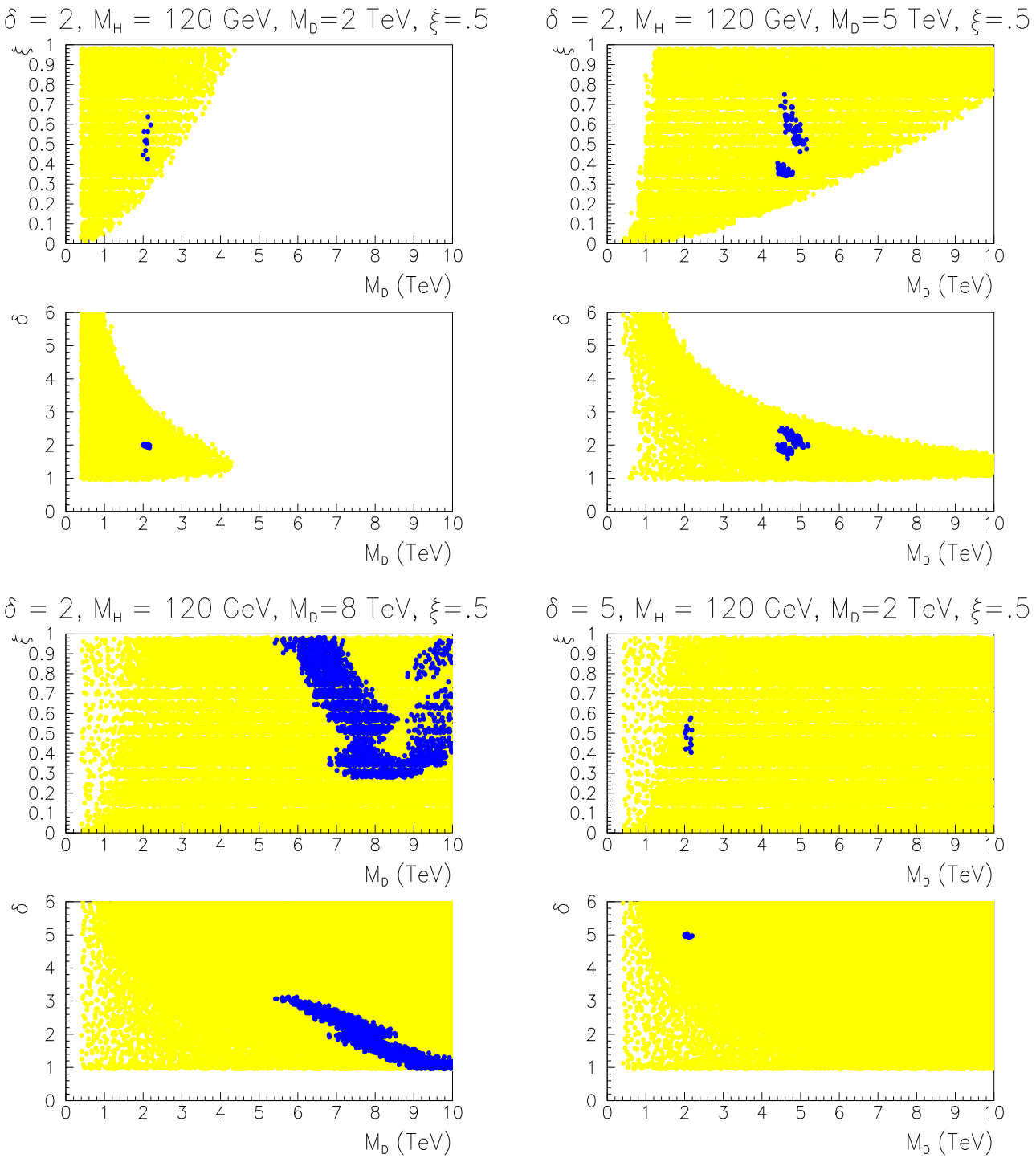

Figure 8.8: 95% CL contours for determination of M_D, ξ and δ assuming $m_h = 120$ GeV, input $\xi^0 = 0.5$ and input δ^0 and M_D^0 values as indicated above each pair of figures. All results are obtained assuming $L = 100$ fb^{-1} Higgs measurements at the LHC, $\sqrt{s} = 350$ GeV (500 GeV) invisible (visible) mode Higgs measurements at the LC, and $\sqrt{s} = 500$ GeV and $\sqrt{s} = 1000$ GeV $\gamma+$ missing energy measurements at the LC with $L = 1000$ fb^{-1} and $L = 2000$ fb^{-1} at the two respective energies. The larger light gray (yellow) regions are the 95% CL regions in the ξ, M_D and δ, M_D planes using only $\Delta\chi^2(LHC)$. The smaller dark gray (blue) regions or points are the 95% CL regions in the ξ, M_D and δ, M_D planes using $\Delta\chi^2(LHC + LC)$. From [749].

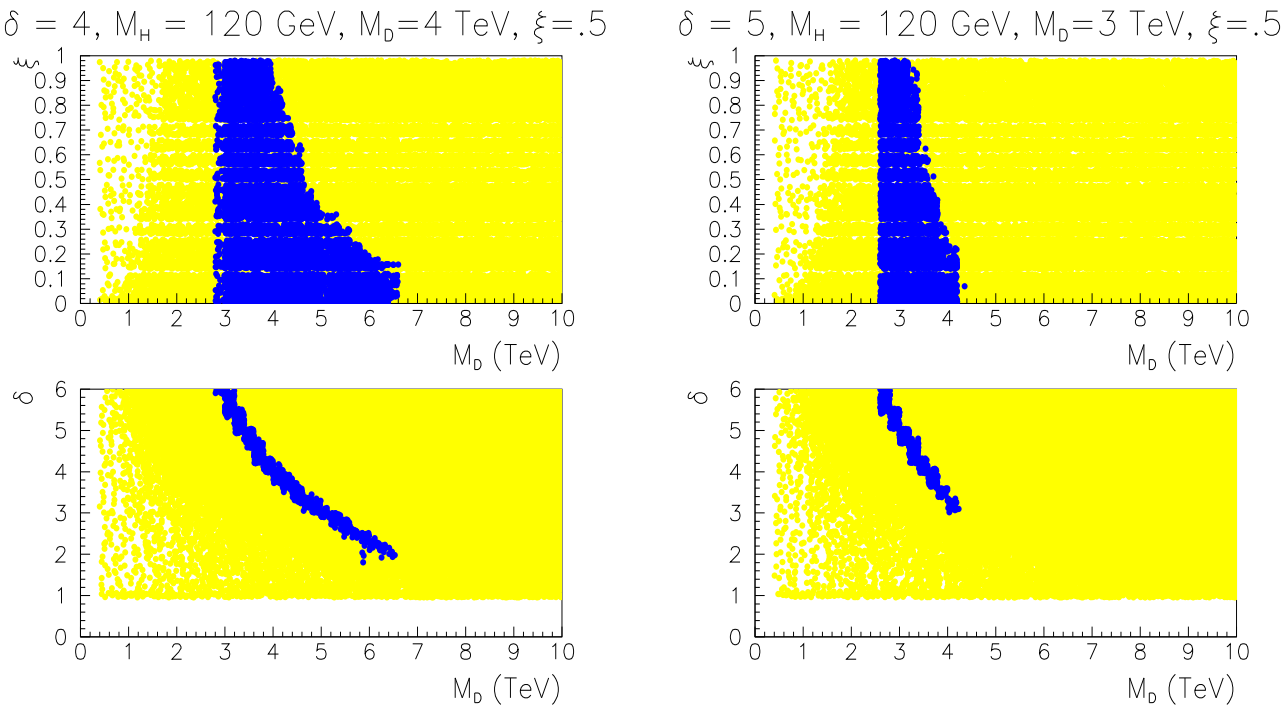

Figure 8.9: As in Fig. 8.8, but for different values of δ^0 and M_D^0 as indicated.

for the cases of the W and Z and vanishes for the γ and gluon. Note that the KK excitations of all the gauge states will be highly degenerate. For example, if $M_c = 4$ TeV, the splitting between the first Z and γ KK states is less than ~ 1 GeV, which is too small to be observed at the LHC; the two states then appear as a single resonance in the Drell-Yan channel.

An updated analysis [757] of precision electroweak data constrains $M_c \gtrsim 4 - 5$ TeV, independently (i) of whether the Higgs field vev is mostly in the bulk or on the brane, or (ii) of which orbifold fixed points the SM fermions are located. At a LC with $\sqrt{s} = 500 - 1000$ GeV the effects of gauge KK exchanges with masses well in excess of the $M_c \sim 4 - 5$ TeV range are easily observable via their virtual exchange as shown in Fig. 8.10. This implies that there will be sufficient 'resolving power' at the LC to determine the properties of the exchange state in analogy with the case of extra gauge bosons discussed in the previous chapter.

The large constraint from precision data on M_c implies that the LHC experiments will at best observe only a single resonance in the $\ell^+\ell^-$ channel. The next set of KK states, which are essentially twice as heavy with $M_2 \gtrsim 8 - 10$ TeV, are too massive to be seen even with an integrated luminosity of order $1 - 3\ ab^{-1}$ [758]. This can be seen from Fig. 8.11. As mentioned above, these apparently isolated single resonance structures are, of course, superpositions of the individual KK excitations of both the SM γ and Z. This double excitation plus the existence of the heavier KK tower states lead to the very unique resonance shapes displayed in the figure. This figure shows that KK states up to masses somewhat in excess of $\simeq 7$ TeV or so should be directly observable at the LHC (or at the LHC with a luminosity upgrade) in a single lepton pair channel (See also [759]). In addition, gluon KK states may be observable in the

dijet channel at the LHC for $M_c < 15$ TeV [760].

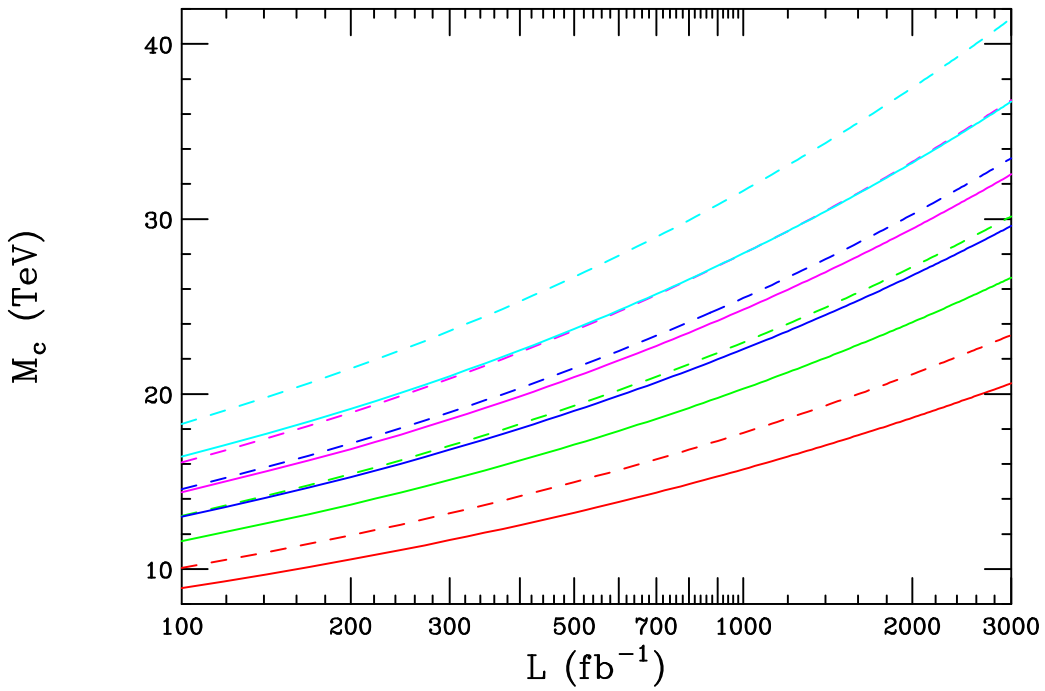

Figure 8.10: 95% CL bound on the scale M_c from the reaction $e^+e^- \to f\overline{f}$, where $f = \mu, \tau, c, b, t$ have been summed over, as a function of the LC integrated luminosity . The solid (dashed) curves assume a positron polarization $P_+ = 0(0.6)$; an electron polarization of 80% has been assumed in all cases. From bottom to top the center of mass energy of the LC is taken to be 0.5, 0.8, 1, 1.2 and 1.5 TeV, respectively. From [740].

Next we examine [761] the identification of gauge KK states at both the LHC and LC. Here we consider a time line where the LC turns on after several years of data taking by the LHC, at roughly the time of an LHC luminosity upgrade, and assume that the LHC discovers a resonance peak in the Drell-Yan invariant mass distribution. Measurement of the lepton pair angular distribution at the LHC will determine that the resonance is spin-1, provided sufficient statistics are available. Perhaps the most straightforward interpretation of such a resonance would be that of an extended gauge model [762], *e.g.*, a GUT scenario, which predicts the existence of a degenerate W' and Z'; many such models have been explored in the literature [763]. Here we address whether such a scenario with a degenerate Z'/W' can be distinguished from KK excitations without the observation of any of the higher KK excitations. This issue has been previously discussed to a limited extent by several authors [759].

Fig. 8.12 shows a closeup of the excitation spectra and forward-backward asymmetries, A_{FB}, for KK production near the first resonance region assuming $M_c = 4$ TeV and with $D = 0, \pi R$. Note the strong destructive interference minimum in the cross section for the $D = 0$ case near $M \simeq 0.55 M_c$ which is also reflected in the corresponding narrow dip in the asymmetry. This dip structure is a common feature in higher dimensional models ($\delta > 1$) and in models with warped extra dimensions, with the precise location of the dip being sensitive to model details. In addition, while the overall behaviour of the $D = 0$ and $D = \pi R$ cases is completely different below the

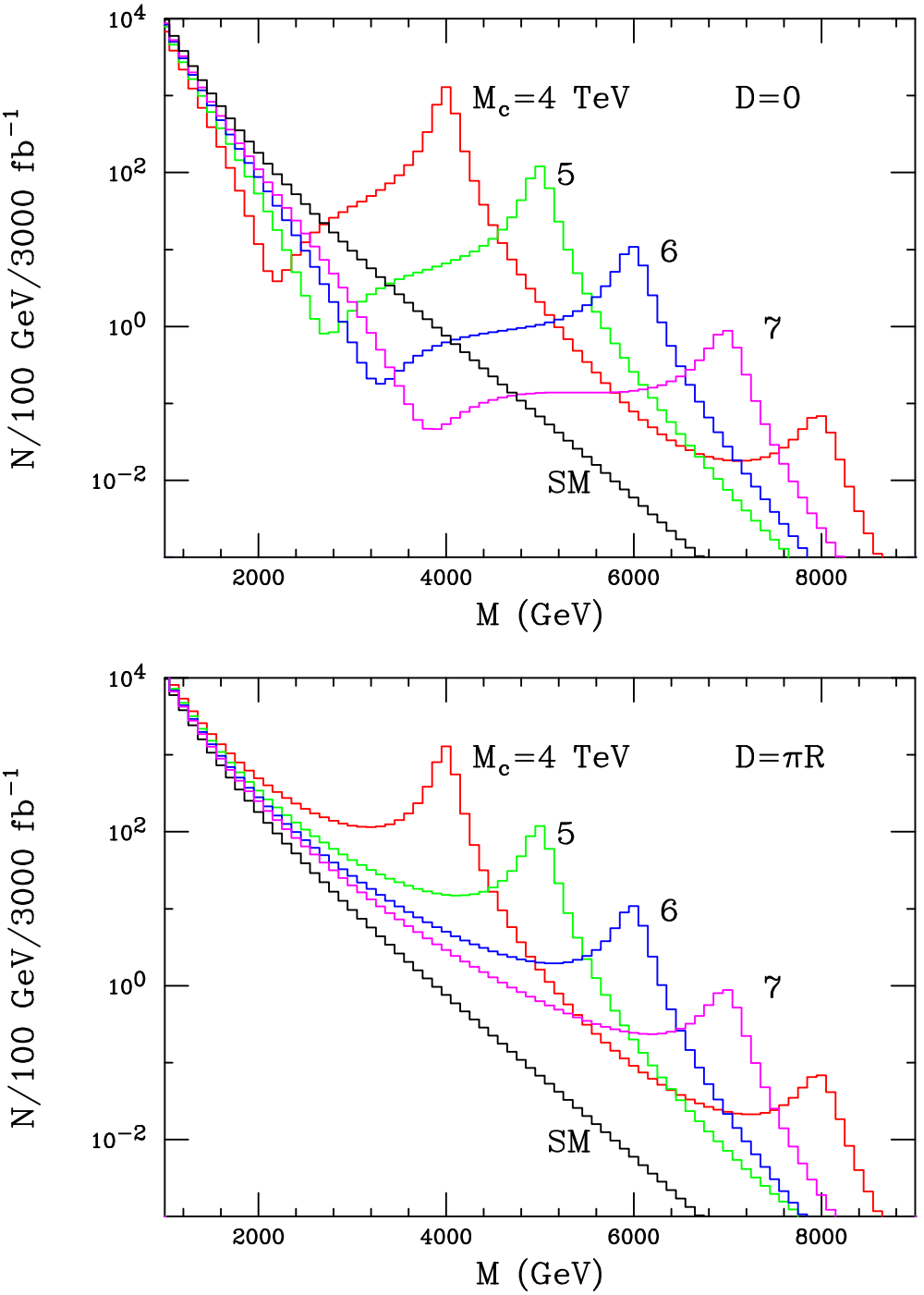

Figure 8.11: Production rate in the Drell-Yan channel $pp \to e^+e^-X$ for γ/Z KK resonances as a function of dilepton invariant mass assuming a very high luminosity LHC. A rapidity cut $|\eta_l| \leq 2.5$ has been applied to the final state leptons. The red(green, blue, magenta) histogram corresponds M_c=4(5, 6, 7) TeV, respectively. The black histogram is the SM background. In the top panel all fermions are assumed to lie at the $y = 0$ fixed point, $D = 0$, while the quarks and leptons are split, $D = \pi R$, in the lower panel. From [761].

peak, it is almost identical above it. This difference in the two spectra is due solely to an additional factor of $(-1)^n$ appearing in the KK sum; this arises from the placement of the quarks and leptons at opposite fixed points. Lastly, note also that the peak cross section and peak A_{FB} values are nearly identical in the two cases.

For either choice of the fermion placement, the excitation curve and A_{FB} for KK production appear to be qualitatively different than that for typical Z' models [762] as discussed in the previous chapter. None of the various Z' models produces resonance structures similar to those for KK excitations. The resonance structure for the KK case is significantly wider and has a larger peak cross section than does the typical Z' model, and the latter does not have the strong destructive interference below the resonance. (Recall, however, that the height and width of the Z' or KK resonance also depends on the set of allowed decay modes.) In addition, the dip in the value of A_{FB} occurs much closer to the resonance region for the typical Z' model than it does in the KK case. Clearly, while the KK resonance structure does not resemble that of a conventional Z', without further study, one could not simply claim that some unusual Z' model could not mimic KK production.

Next, the differences between the KK and Z' scenarios are quantified [761]. For $M_c = 4(5,\ 6)$ TeV cross section 'data' at the LHC is generated corresponding to dilepton masses in the range 250-1850 (2150, 2450) GeV in 100 GeV bins for both the $D = 0$ and πR cases. Lower invariant dilepton masses are not useful due to the presence of the Z peak and the photon pole. We next try to fit these cross section distributions by making the assumption that the data is due to the presence of a single Z'. For simplicity, we restrict our attention to the class of Z' models with generation-independent couplings and where the associated a new gauge group generator commutes with weak isospin. These conditions are satisfied, *e.g.*, by GUT-inspired Z' models as well as by many others [762]. If these constraints hold then the Z' couplings to SM fermions can be described by only 5 independent parameters: the couplings to the left-handed quark and lepton doublets and the corresponding ones to the right-handed quarks and leptons. These couplings are all varied independently in order to obtain the fit to the dilepton mass distribution with the best χ^2 per degree of freedom, and the relevant probability (confidence level) of the fit is obtained using statistical errors only. The overall normalization of the cross section is determined at the Z-pole which is outside of the fit region and is governed solely by SM physics.

The results [761] of performing these fits for different values of M_c and the two choices $D = 0, \pi R$ are displayed in Fig. 8.13. Explicitly, this shows the best fit probability for the Z' hypothesis to the KK generated data. For example, taking the case $D = 0$ with $M_c = 4$ TeV we see that with an integrated luminosity of order 60 fb^{-1} the best fit probability is near a few $\times 10^{-5}$. For such low probabilities one could certainly claim that the KK generated 'data' is not well fit by the Z' hypothesis. As the mass of the KK state increases, the difference in the production cross section from the SM expectation is reduced and greater statistics are needed; for $M_c = 5$ TeV an integrated luminosity of order 400 fb^{-1} is required to get to the same level of rejection of the Z' hypothesis. For the $D = \pi R$ case, we see that the level of confusion between KK states and Z' scenarios is potentially greater. Even for $M_c = 4$ TeV we see that only at very high integrated luminosities, of order $\sim 1.5\ ab^{-1}$, can the KK and Z' scenarios be distinguished at the level discussed above. For larger KK masses this separation becomes essentially impossible at the LHC.

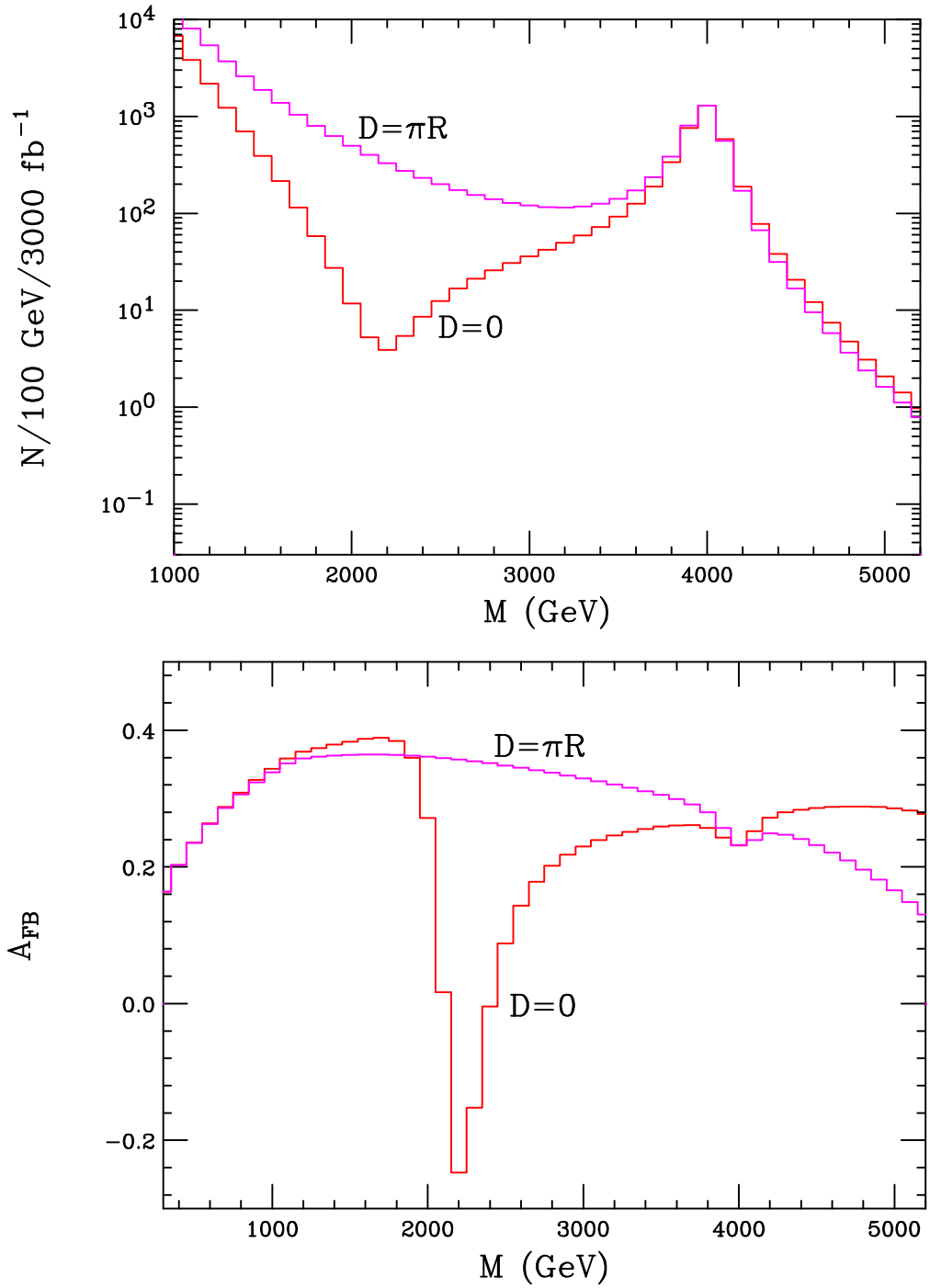

Figure 8.12: A comparison of the lepton pair invariant mass spectrum and forward-backward lepton asymmetry for the production of a 4 TeV KK resonance for the two choices of D. The red(magenta) histograms are for the case $D = 0(\pi R)$. From [761].

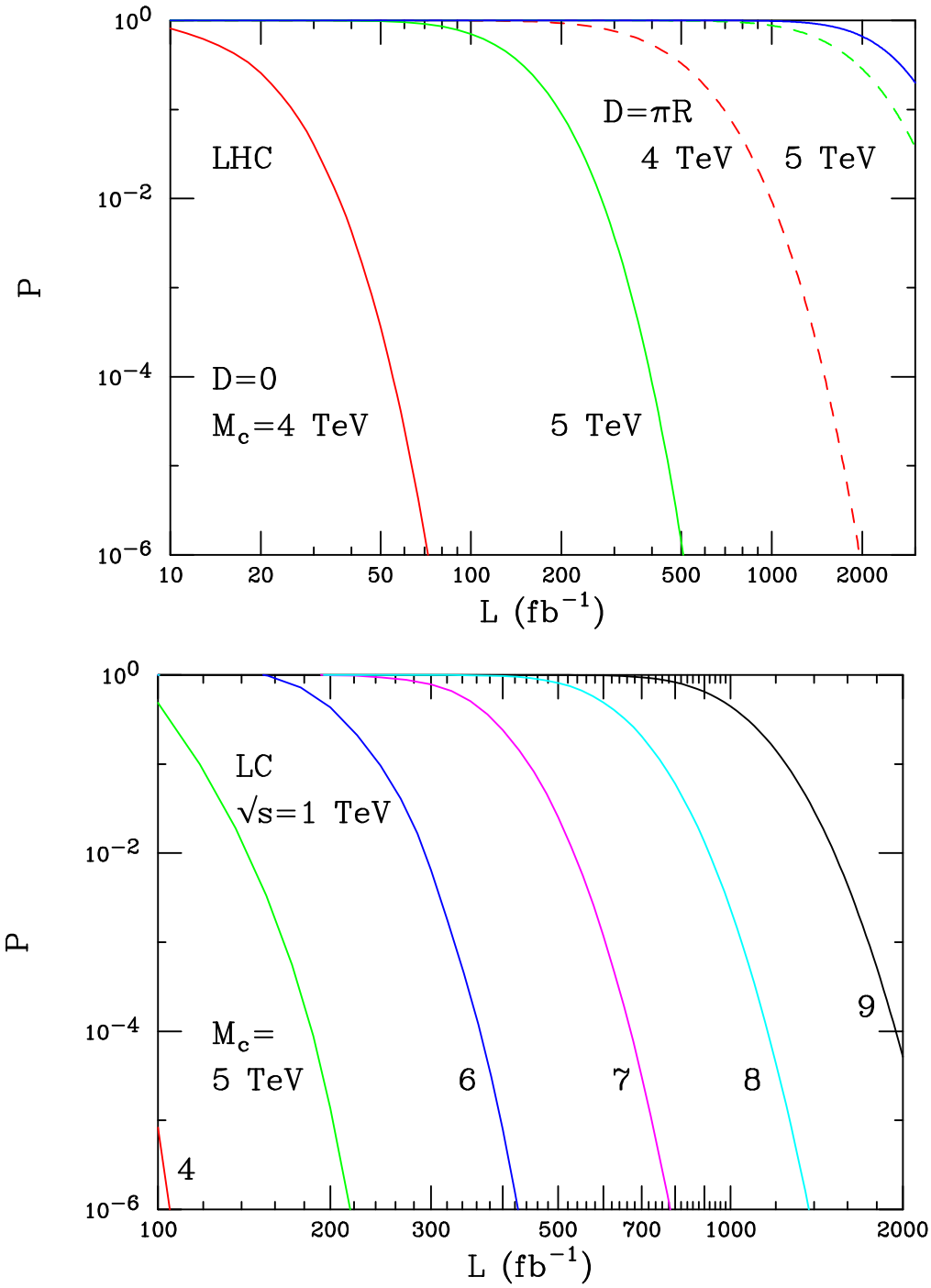

Figure 8.13: Top Panel: Probability associated with the best Z' fit hypothesis as a function of the LHC integrated luminosity for the cases $D = 0$ (solid) and $D = \pi R$ (dashed). Bottom Panel: Same as the above but now for a 1 TeV LC using leptonic data only. In this case, the $D = 0$ and $D = \pi R$ cases are identical. The value of M_c is assumed to be determined at the LHC. From [761].

The corresponding analysis [761] for the LC is different since actual resonances are not observed. It is assumed that data is taken at a single value of $\sqrt{s}$ so that the mass of the KK or Z' resonance obtained from the LHC must be used as input to the analysis. Without such input an analysis can still be performed provided data from at least two distinct values of $\sqrt{s}$ are available [764]. In that case M_c becomes an additional fit parameter.

At the LC, a tower of gauge KK states with fixed M_c are exchanged in the process $e^+e^- \to f\overline{f}$. 'Data' is generated for both the differential cross section and the Left-Right polarization asymmetry, A_{LR} as functions of the scattering angle $\cos\theta$ in 20 (essentially) equal sized bins, and including the effects of ISR. The electron beam is assumed to be 80% polarized and angular acceptance cuts are applied. Other detailed assumptions in performing this analysis are the same as those employed in Ref. [740]. A fit is performed to this 'data' making the assumption that the deviations from the SM are due to the exchange of a single Z'. For simplicity, we concentrate on the processes $e^+e^- \to \mu^+\mu^-, \tau^+\tau^-$ as only the two leptonic couplings are then involved in performing the fits. In this case, the $D = 0$ and $D = \pi R$ scenarios lead to identical results for the shifts in all observables at the LC. Adding new final states, such as $b\overline{b}$ or $c\overline{c}$, may lead to potential improvements in the fit although additional parameters must now be introduced and the $D = 0$ and $D = \pi R$ cases would be distinct as at the LHC.

As in the above analysis for the LHC, the two assumed Z' couplings to leptons are varied and the best χ^2/df is obtained for the fit. For the case of a $\sqrt{s}$ = 500 GeV LC, we find that an integrated luminosity of 300 fb^{-1} is roughly equivalent to 60 fb^{-1} at the LHC for the case of $M_c = 4$ TeV assuming $D = 0$. For larger values of M_c, 800 (2200) fb^{-1} at a 500 GeV LC gives equivalent discrimination power as 400 (7500) fb^{-1} at the LHC assuming $M_c = 5\ (6)$ TeV. The results [761] for a 1 TeV LC are displayed in Fig. 8.13. Here, we see that once the LC center-of-mass energy increases, it is superior to the LHC in resolving power, but the analysis still relies upon the LHC for the input value of M_c. This figure shows results for values of M_c beyond the range which is directly observable at the LHC $M_c \geq 7-8$ TeV (although still assuming that the value of M_c is an input). This would seem to imply that by extending the present analysis to include data from at least two values of $\sqrt{s}$, KK/Z' separation may be feasible out to very large masses at the LC.

In summary, the power of the LC to discriminate between models is shown to be better than that of the LHC, however, the LC analysis depends upon the LHC determination of the resonance mass as an input.

8.2.2 Universal extra dimensions

In the scenario known as universal extra dimensions, all SM fields propagate in the bulk and branes need not be present. The simplest model of this type contains a single extra dimension compactified on an S_1/Z_2 orbifold. Translational invariance in the higher dimensional space is preserved. This leads to the tree-level conservation of the δ-dimensional momentum of the bulk fields, which in turn implies that KK number is conserved at tree-level while KK parity, $(-1)^n$, is conserved to all orders. Two immediate consequences of KK number and parity conservation are that (i) at tree-level, KK excitations can no longer be produced as s-channel resonances and can

only be produced in pairs, and (ii) the lightest KK particle (LKP) is stable and is thus a dark matter candidate [765]. The former results in a substantial reduction of the sensitivity to such states in precision electroweak and collider data with the present bound on the mass of the first KK excitation being of order a few hundred GeV for $\delta = 1$ [766].

Due to the conservation of KK parity, the phenomenology of universal extra dimensions resembles that of supersymmetric theories with R-parity conservation. Every SM field has KK partners. These KK partners carry a conserved quantum number, KK parity, which guarantees that the LKP is stable. Heavier KK modes decay via cascades to the LKP, which escapes detection resulting in a missing energy signature. The Lagrangian of the model includes both bulk terms and interactions which are localized at the orbifold fixed points. The bulk interactions yield masses for the KK states as given in Eq. (8.14); these are highly degenerate within each KK level. The boundary interactions take the form of loop induced localized kinetic terms [767] and are not universal for the different SM fields. The low scale boundary terms are determined via high energy parameters which are evolved through the renormalization group. In addition, non-local radiative corrections [768] also affect the KK mass spectrum. Combined, this has the effect of removing the degeneracy between the modes in a KK level and also affects their decay chains. A typical KK spectrum [770] is displayed in Fig. 8.14. The KK modes with strong interactions receive larger corrections than those with only electroweak interactions. This spectrum resembles that of the superpartners in a Minimal Supersymmetric Standard Model where the sparticles all lie relatively close together.

Once the KK mass degeneracy is lifted, the states decay promptly. The resulting collider phenomenology is strikingly similar to that of supersymmetry [770]. Indeed, if such a scenario were observed at the LHC, it is reasonable to expect that it would be mis-identified as the discovery of supersymmetry! Superpartner status would most likely be assigned to the various KK states. Hence, techniques to distinguish the two scenarios need to be developed.

The cleanest way to identify Universal Extra Dimensions would be the observation of the second KK level. However, due to the conservation of KK parity, second level KK states must be pair produced with each other (or singly at loop-level) and will likely be out of kinematic reach of the LHC. The distinguishing factor for this scenario is then that the KK states have the same spin as their SM partners, unlike the case of supersymmetry. It is thus imperative to measure the spin of the particles in the spectrum. In principle, particle spins can be determined at the LHC from examination of their decay distributions. However, given the cascade decay chains and the size of the pair production cross sections, this is expected to be problematic at the LHC. At a LC, threshold cross sections can be easily measured and their S-wave versus P-wave behaviour can be cleanly determined. The cross sections for 300 GeV muon KK state as well as smuon pair production [769] as a function of the $\mathrm{e^+e^-}$ center of mass energy are displayed in Fig. 8.15. The S- and P-wave behaviour is clearly observable and distinguishes between the two spins. If the LC determined that KK states were being produced at the LHC, then dedicated searches for the second KK level would be well-motivated. Since the mass scale and signatures would be known, the $n = 2$ modes may be detectable with the LHC luminosity upgrades.

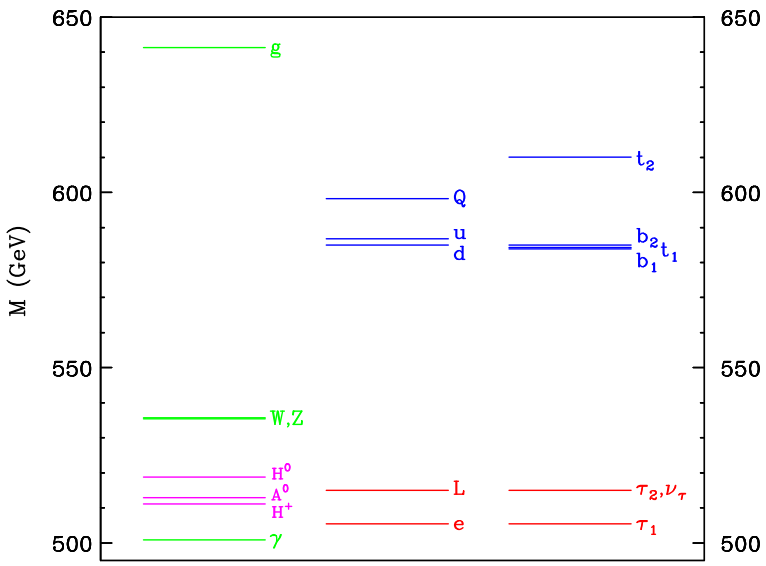

Figure 8.14: Mass spectrum, including radiative corrections, of the first level KK states in the Universal Extra Dimensions scenario, taking $R^{-1} = 500$ GeV. From [770].

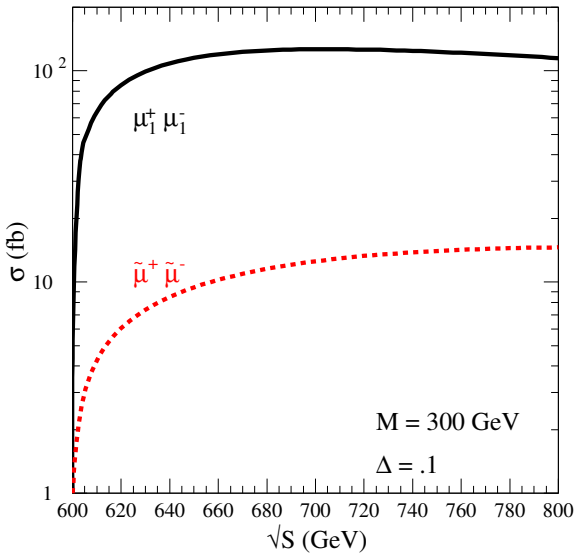

Figure 8.15: Pair production of 300 GeV smuons and muon KK states at an e^+e^- collider as a function of center of mass energy. Δ represents the mass splitting between the smuon and LSP as well as of the muon KK and LKP. From [769].

8.3 Warped extra dimensions

In this scenario, known as the Randall-Sundrum (RS) model [771], the hierarchy is explained in the context of a 5-dimensional nonfactorizable background geometry with large curvature. This background manifold is a slice of anti-de Sitter (AdS_5) spacetime where two 3-branes of equal and opposite tension sit at orbifold fixed points at the boundaries of the AdS_5 slice. The 5-d warped geometry induces a 4-d effective scale $\Lambda_\pi = e^{-kr_c\pi}\overline{M}_{Pl} \sim$ TeV on one of the branes, denoted as the TeV-brane. Here, k represents the 5-d curvature scale, which together with M_5 is assumed to be of order $\overline{M}_{Pl}$ (where $\overline{M}_{Pl} = M_{Pl}/\sqrt{8\pi}$), and πr_c is the length of the fifth dimension. Consistency of the low-energy description requires that the curvature be bounded by $k/\overline{M}_{Pl} \lesssim 0.1$. TeV scales are naturally realized and stablized [772] on the TeV-brane provided that $kr_c \sim 10$.

8.3.1 Conventional RS model

In the simplest version of this scenario, the SM fields reside on the TeV-brane and gravity propagates throughout the 5-d spacetime. The 4-d phenomenology of the graviton KK tower is governed by two parameters, Λ_π and $k/\overline{M}_{Pl}$. The masses of the 4-d graviton states are given by $m_n = x_n\Lambda_\pi k/\overline{M}_{Pl}$, with x_n being the roots of the first-order Bessel function J_1, *i.e.*, $J_1(x_n) = 0$, and their interactions with the SM fields on the TeV-brane are [773]

$$\mathcal{L} = -\frac{1}{\overline{M}_{Pl}}T^{\mu\nu}(x)h^0_{\mu\nu}(x) - \frac{1}{\Lambda_\pi}T^{\mu\nu}(x)\sum_{n=1}^{\infty}h^{(n)}_{\mu\nu}(x)\,, \tag{8.15}$$

where $T^{\mu\nu}$ is the conserved stress-energy tensor. Note that in this scenario, the coupling strength of the graviton KK tower interactions and the mass of the first excitation are of order of the weak scale. The hallmark signature for this scenario is the presence of TeV-scale spin-2 graviton resonances at colliders. The KK spectrum in $e^+e^- \to \mu^+\mu^-$, taking $m_1 = 500$ GeV, is shown in Fig. 8.16. Note that the curvature parameter controls the width of the resonance. The LHC can discover these resonances in the Drell-Yan channel if $\Lambda_\pi < 10$ TeV [773], provided that the resonance width is not too narrow, and determine their spin-2 nature via the angular distributions of the final-state lepton pairs [774] if enough statistics are available. An accurate determination of the branching fractions for the graviton KK decays to various final states will probe the universal $T^{\mu\nu}$ structure of the couplings and verify the production of gravity. Numerical studies of such coupling determinations have yet to be performed, but are likely to demonstrate the benefits of the LC even if the graviton KK states are kinematically inaccessible at the LC and are produced indirectly; this is in analogy to the Z' studies discussed in the previous chapter.

If the KK gravitons are too massive to be produced directly, their contributions to fermion pair production may still be felt via virtual exchange. In this case, the uncertainties associated with a cut-off (as present in the large extra dimensions scenario) are avoided, since there is only one additional dimension and thus the KK states may be neatly summed. The resulting sensitivity to the scale Λ_π at the LHC and LC is displayed in Table 8.5. We see that the reach of the 500 GeV LC is complementary to that

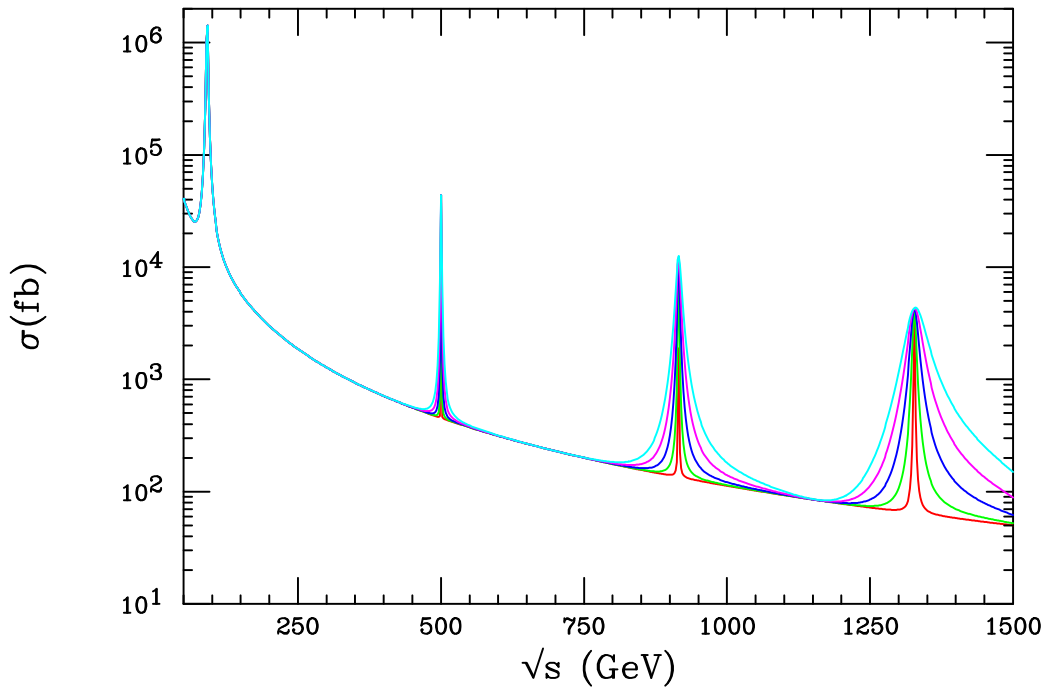

Figure 8.16: The cross section for $e^+e^- \to \mu^+\mu^-$ including the exchange of a KK tower of gravitons in the RS model with $m_1 = 500$ GeV. The various curves correspond to $k/\overline{M}_{Pl}$ in the range $0.01 - 0.1$. From [773].

of the LHC and that a 1 TeV LC extends the discovery reach of the LHC. This degree of sensitivity to virtual graviton KK exchange at the LC implies that the KK coupling measurements discussed above should be viable.

8.3.2 Extensions of the RS model

• Extended Manifolds

From a theoretical perspective, the RS model may be viewed as an effective theory whose low energy features originate from a full theory of quantum gravity, such as string theory. One may thus expect that a more complete version of this scenario admits the presence of additional dimensions compactified on a manifold $\mathcal{M}^\delta$ of dimen-

	$k/\overline{M}_{Pl}$		
	0.01	0.1	1.0
LC $\sqrt{s} = 0.5$ TeV	20.0	5.0	1.5
LC $\sqrt{s} = 1.0$ TeV	40.0	10.0	3.0
LHC	20.0	7.0	3.0

Table 8.5: 95% CL search reach for Λ_π (in TeV) in the contact interaction regime taking 500 fb^{-1} and 100 fb^{-1} of integrated luminosity at the LC and LHC, respectively. From [773].

sion δ. From a model-building point of view, it can also be advantageous to place at least some of the SM fields in the higher δ-dimensional space to *e.g.*, suppress proton decay or address gauge coupling unification and the flavor problem. The presence of an additional manifold may reconcile string theory and several model-building features with the RS scenario.

The existence of an extra manifold modifies the conventional RS phenomenology and collider signatures. As a first step, the additional manifolds S^δ with $\delta \geq 1$, representing both flat and curved geometries, have been considered [775]. In this case, additional graviton KK states appear, corresponding to orbital excitations of the S^δ manifold. For the simplest scenario of S^1, the RS metric is expanded to

$$ds^2 = e^{-2kr_c\phi}\eta_{\mu\nu}dx^\mu dx^\nu + r_c^2 d\phi^2 + R^2 d\theta^2 \,, \tag{8.16}$$

where θ parameterizes the S^1, and R represents its radius. The masses of the KK states are now given by $m_{n\ell} = x_{n\ell}\Lambda_\pi k/\overline{M}_{Pl}$, where the $x_{n\ell}$ are solutions of the equation

$$2J_\nu(x_{n\ell}) + x_{n\ell}J'_\nu(x_{n\ell}) = 0 \,, \tag{8.17}$$

with $\nu \equiv \sqrt{4+(\ell/kR)^2}$. The KK mode number ℓ corresponds to the orbital excitations, while n denotes the usual RS AdS_5 mode levels. The couplings of the $m_{n\ell}$ graviton KK states are then given by

$$\mathcal{L} = -\frac{1}{\overline{M}_{Pl}}T^{\mu\nu}(x)h^0_{\mu\nu}(x) - \frac{1}{\Lambda_\pi}T^{\mu\nu}(x)\sum_{n=1}^{\infty}\xi(n\ell)h^{(n,\ell)}_{\mu\nu}(x) \,, \tag{8.18}$$

where $\xi(n\ell)$ depends on k , R, and $x_{n\ell}$ [775]. The KK spectrum and couplings are thus modified due to the presence of the new manifold.

In particular, the addition of the S^δ background to the RS setup results in the emergence of a forest of graviton KK resonances. These originate from the orbital excitations on the S^δ and occur in between the original RS resonances. A representative KK spectrum is depicted as a histogram in Drell-Yan production in the electron channel at the LHC in Fig 8.17. Here, $kR = 1.0$ and $m_{10} = 1$ TeV is assumed and detector smearing [89] is included. In this case, the individual peaks at smaller masses are well separated due to this choice of model parameters. At larger masses there is increased overlap among the KK states and individual resonances may be difficult to isolate. A detailed detector study of this KK forest is required to determine what separation between the states is necessary in order to isolate the resonances. The separation between the states decreases as the model parameters are varied. This is displayed in Fig. 8.18 which shows the cross section in $e^+e^- \to \mu^+\mu^-$ for $kR = 2.0$ and $m_{10} = 600$ GeV. Note that the density of the KK spectrum is substantially increased; in particular, both n and ℓ KK excitations are present in the same kinematic region and the peaks are not well separated. In the case shown here, the spacing between the $n = 1\,, \ell = 0$ and $n = 1\,, \ell = 1$ states is only 425 MeV, which is comparable to the individual KK widths of $\simeq 525$ MeV. The μ pair resolution at a LC should be sufficient to resolve these two states if they are within kinematic reach. However, the separation of these states may prove problematic at the LHC; in this case, the LC would be needed to observe the distinct states.

• Brane Localized Kinetic Terms

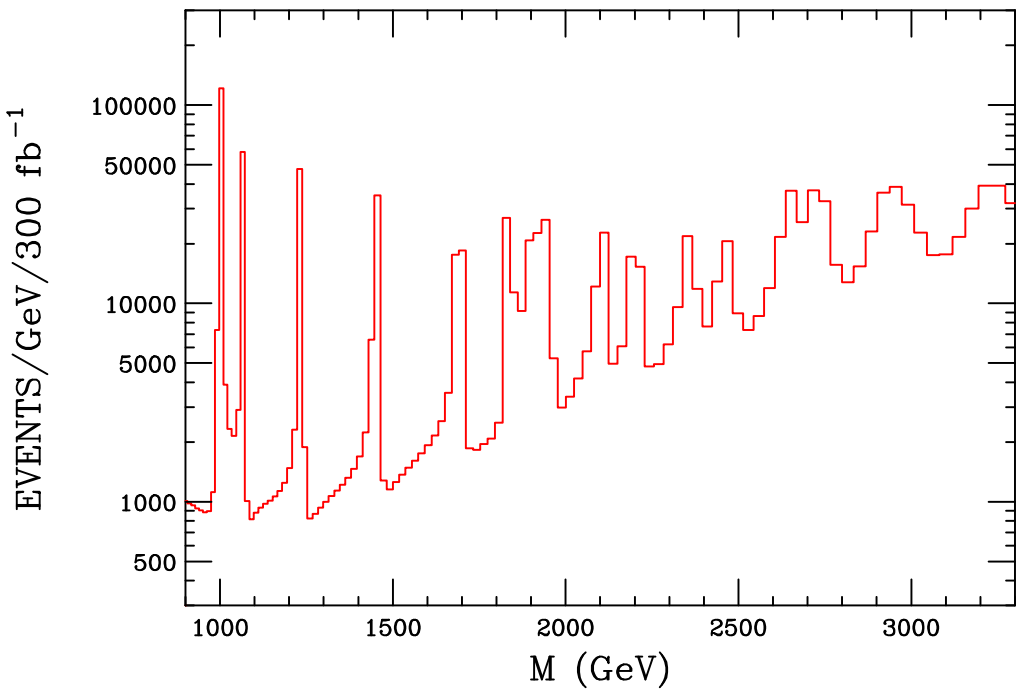

Figure 8.17: Binned Drell-Yan cross section for e^+e^- production at the LHC assuming $m_{10} = 1$ TeV, $k/\overline{M}_{Pl} = 0.03$, and $kR = 1.0$. The cross section has been smeared by an electron pair mass resolution of 0.6% as might be expected at ATLAS [89]. From [775].

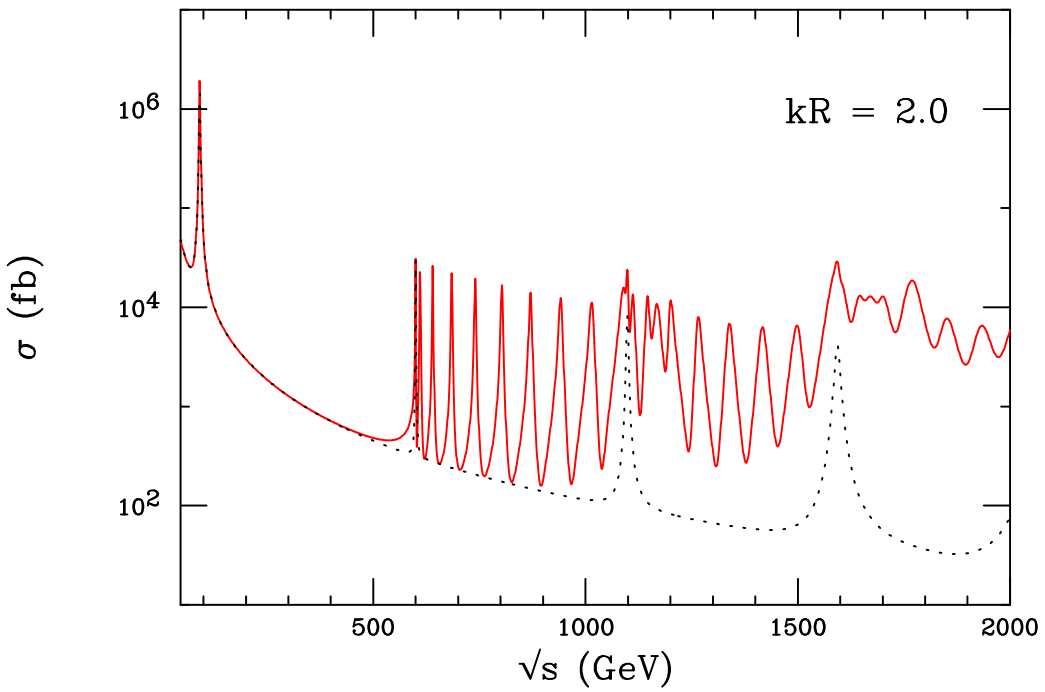

Figure 8.18: The solid (red) curve corresponds to the cross section for $e^+e^- \to \mu^+\mu^-$ when the additional dimension is orbifolded, *i.e.*, for S^1/Z_2, with $m_{10} = 600$ GeV, $k/\overline{M}_{Pl} = 0.03$ and $kR = 2.0$. The result for the conventional RS model is also displayed, corresponding to the dotted curve. From [775].

An additional well-motivated extension to the conventional RS model is the inclusion of brane curvature terms for the graviton. These terms respect all 4-d symmetries, and are expected to be present in a 4-d theory, leading to brane localized kinetic terms for the graviton. In fact, it has been demonstrated [776] that brane quantum effects can generate such brane kinetic terms, and that these terms are required as brane counter terms for bulk quantum effects. In addition, a tree-level Higgs-curvature term is allowed in the brane action and can also induce brane kinetic terms for the graviton. There are thus many good theoretical reasons for assuming the presence of such terms for gravitons.

The existence of boundary kinetic terms results in novel features and can substantially modify the KK phenomenology of both gravitons and bulk gauge fields [776]. In the presence of these terms, the graviton KK spectrum and couplings is again modified and alters the low-energy 4-d phenomenology of the RS model [776]. In this case, the graviton action is now augmented by brane localized curvature terms on both branes. The graviton KK masses are again given by $m_n = x_n \Lambda_\pi k/\overline{M}_{Pl}$, where the x_n are now roots of the equation

$$J_1(x_n) - \gamma_\pi x_n J_2(x_n) = 0\,. \tag{8.19}$$

Here, γ_π represents the coefficient of the boundary term for the TeV-brane and is naturally of order unity. The couplings are modified to be

$$\mathcal{L} = -\frac{1}{\overline{M}_{Pl}} T^{\mu\nu}(x) h^0_{\mu\nu}(x) - \frac{1}{\Lambda_\pi} T^{\mu\nu}(x) \sum_{n=1}^{\infty} \lambda_n h^{(n)}_{\mu\nu}(x)\,, \tag{8.20}$$

where λ_n depends on the coefficient of the boundary terms on both branes. This results in a dramatic reduction of the graviton KK couplings to SM fields on the TeV-brane, even for small values of the brane kinetic term coefficients. For coefficients of order ~ 10, the graviton KK couplings are reduced by a factor of $\sim 1/100$ of their value in the conventional RS model. This clearly results in a substantial decrease in the cross section for spin-2 graviton KK resonance production, which is the hallmark collider signature of the RS scenario, due to their extremely narrow width in this scenario. The resulting degradation in the graviton search reach at the LHC is displayed in Fig 8.19 for 100 fb^{-1} of integrated luminosity. From this figure, it is clear that the LHC can no longer cover all of the interesting parameter space for this model. For example, a first graviton KK excitation of mass 600 GeV with $k/\overline{M}_{Pl} = 0.01$ may still miss detection. Very light KK gravitons may thus escape direct detection at the Tevatron and LHC.

However, it is possible that such narrow resonances may be observed at the LC via radiative return. The differential cross section for radiative return in $e^+e^- \to mu^+\mu^-\gamma$ [777] including a 750 GeV KK state with $\gamma_\pi = -8$ and $k/\overline{M}_{Pl} = 0.025$, a resonance which is invisible at the LHC, is displayed in Fig. 8.19. From the figure we see that there is a sharply defined peak; the narrrow width approximation yields a ~ 1 fb^{-1} cross section under the peak. Hence, the radiative return search technique at the LC is very powerful and may guide dedicated analyses at the LHC in the search for narrow resonances.

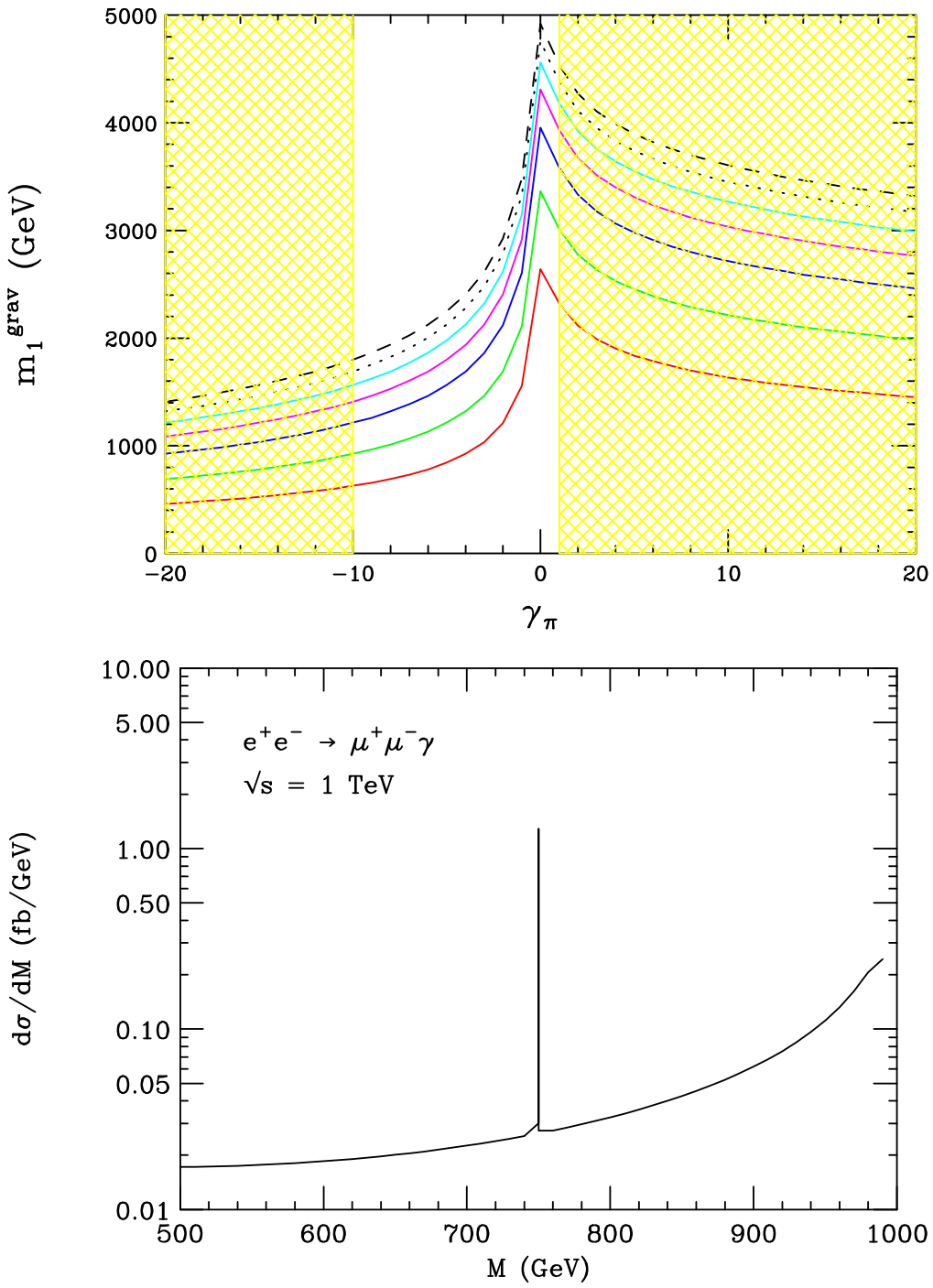

Figure 8.19: Top: Search reach for the first graviton KK resonance employing the Drell-Yan channel at the LHC with an integrated luminosity of 100 fb^{-1} as a function of the boundary term coefficient γ_π assuming $\gamma_0 = 0$. From bottom to top on the RHS of the plot, the curves correspond to $k/\overline{M}_{Pl} = 0.01, 0.025, 0.05, 0.075, 0.10, 0.125$ and 0.15, respectively. The unshaded region is that allowed by naturalness considerations and the requirement of a ghost-free radion sector. From [776] Bottom: Differential cross section for $e^+e^- \to \mu^+\mu^-\gamma$ including a 750 GeV graviton excitation with $k/\overline{M}_{Pl} = 0.025$ and boundary term $\gamma_\pi = -8$. From [778].

8.3.3 Conclusions

Collider signatures for the presence of extra spatial dimensions are wide and varied, depending on the geometry of the additional dimensions. The basic signal is the observation of a Kaluza-Klein (KK) tower of states corresponding to a particle propagating in the higher dimensional space-time. The measurement of the properties of the KK states determines the size and geometry of the extra dimensions.

In the scenario of large extra dimensions, where gravity alone can propagate in the bulk, the indirect effects and direct production of KK gravitons are both available at the LHC and at the LC. For the indirect exchange of KK gravitons, the search reach of the LC exceeds that of the LHC for $\sqrt{s} \gtrsim 800$ GeV. Measurement of the moments of the resulting angular distributions at the LC can identify the spin-2 nature of the graviton exchange for roughly half of the search reach range. If positron polarization is available, then azimuthal asymmetries can (i) extend the search for graviton exchange by a factor of 2, probing fundamental scales of gravity up to 21 TeV for $\sqrt{s} = 1$ TeV with 500 fb^{-1} of integrated luminosity, and (ii) identify the spin-2 exchange for the entire LHC search region. In the case of direct KK graviton production, the LHC and LC have comparable search reaches. However, the LHC is hampered by theoretical ambiguities due to a break-down of the effective theory when the parton-level center of mass energy exceeds the fundamental scale of gravity; in this case the LHC may directly detect effects of quantum gravity. Measurement of direct graviton production at two different center of mass energies at the LC can determine the number of extra dimensions and the absolute normalization of the cross section can determine the fundamental scale. Simultaneous determination of all the model parameters has been examined in a quantitative fashion with the result that data from the LC and LHC analyzed together substantially improves the accuracy of this determination over the LHC data taken alone.

Standard Model fields are allowed to propagate in extra dimensions with size less than TeV^{-1}. Signatures for the KK states of the SM gauge fields mimic those for new heavy gauge bosons in extended gauge theories. The LHC may discover electroweak gauge KK states via direct production in the mass range $M_c \simeq 4 - 6$ TeV (lower masses are excluded by LEP/SLC data), while indirect detection at the LC is possible for $M_c \lesssim 20$ TeV for $\sqrt{s} = 1$ TeV. Indirect detection of electroweak gauge KK states is also possible at the LHC for $M_c \lesssim 12$ TeV via a detailed study of the shape of the Drell-Yan lepton-pair invariant mass distribution. If discovered, a quantitative analyses shows that the determination of the mass of the first gauge KK excitation at the LHC, together with indirect effects at the LC can be used to distinguish the production of a KK gauge state from a new gauge field in extended gauge sectors.

The possibility of universal extra dimensions, where all SM fields are in the bulk, can cause confusion with the production of supersymmetric states, since the KK spectrum and phenomenology resembles that of supersymmetry. In fact, the lightest KK state is a Dark Matter candidate. In this case, threshold production of the new (s)particle at the LC can easily determine its spin and distinguish universal extra dimensions from supersymmetry. Spin determination analyses are on-going for the LHC.

Lastly, the presence of warped extra dimensions results in the resonance production of spin-2 gravitons. This produces a spectacular signature at the LHC for the

conventional construction of the Randall-Sundrum model. However, extensions to this model, such as the embedding in a higher dimension manifold, or the inclusion of kinetic brane terms, result in reduced coupling strengths and extremely narrow-width graviton KK states. Such states may be difficult to observe at the LHC and even very light KK states may escape detection. In this case, radiative return at the LC may pinpoint the existence of these states, which can then be confirmed by a dedicated search at the LHC.

9 Conclusions and Outlook

The Large Hadron Collider and the Linear Collider will explore physics at the TeV scale, opening a new territory where ground-breaking discoveries are expected. There is a huge variety of possible manifestations of new physics in this domain that have been advocated in the literature, and even more possibilities surely exist beyond our present imagination. The physics programme of both the LHC and the LC in exploring this territory will be very rich. The different characteristics of the two machines give rise to different virtues and capabilities. The high collision energy of the LHC leads to a large mass reach for the discovery of heavy new particles. The clean experimental environment of the LC allows detailed studies of directly accessible new particles and gives rise to a high sensitivity to indirect effects of new physics.

Thus, physics at LHC and LC is complementary in many respects. While qualitatively this is obvious, a more quantitative investigation of the interplay between LHC and LC requires detailed information about the quantities that can be measured at the two colliders and the prospective experimental accuracies. Based on this input, case studies employing realistic estimates for the achievable accuracy of both the experimental measurements and the theory predictions are necessary for different physics scenarios in order to assess the synergy from the interplay of LHC and LC. The LHC / ILC Study Group was formed in order to tackle this task. The present report is the first step on this way, and summarises the initial results obtained within the LHC / ILC Study Group. The results are based on a close collaboration between the LHC and LC experimental communities and many theorists.

A large variety of possible scenarios has been investigated, including different manifestations of physics of weak and strong electroweak symmetry breaking, supersymmetric models, new gauge theories, models with extra dimensions and possible implications of gravity at the TeV scale. For scenarios where detailed experimental simulations of the possible measurements and the achievable accuracies are available both for LHC and LC, the LHC / LC interplay has been investigated in a quantitative manner. In other scenarios many promising possibilities have been pointed out where the interaction between LHC and LC can be foreseen to have a large impact.

Based on the results in this report important synergy from a concurrent running of LHC and LC has been established. The intimate interplay of the results of the two collider facilities will allow one to probe, much more effectively and more conclusively than each machine separately, the fundamental interactions of nature and the structure of matter, space and time.

Experience from the past shows that the gain of knowledge often proceeds in iterative steps. Once experimental data from both LHC and LC will be available, it is very likely that new questions to the LHC will arise which weren't apparent before. The synergy between LHC and LC will extend the physics potential of both machines. Results from both colliders will be crucial in order to decipher the underlying physics in the new territory that lies ahead of us and to draw the correct conclusions about

its nature. This information will be decisive for guiding the way towards effective experimental strategies and dedicated searches. It will not only sharpen the goals for a subsequent phase of running of both LHC and LC, but will also be crucial for the future roadmap of particle physics.

The interplay between LHC and LC is a very rich field, of which only very little has been explored so far. The ongoing effort of the LHC and LC physics groups in performing thorough experimental simulations for different scenarios will enable further quantitative assessments of the synergy between LHC and LC. The exploratory work collected in the present report is aimed to serve as a starting point for future studies.

Acknowledgements

This research was supported in part by the Alfred P. Sloan Foundation, by the Benoziyo center for high energy physics, by the Bundesministerium für Bildung und Forschung (BMBF, Bonn, Germany) under the contract numbers 05HT1WWA2, 05HT4WWA2, by the Davis Institute for High Energy Physics, by the Department of Science and Technology, India, under project number SP/S2/K-01/2000-II, by the 'Erwin Schrödinger fellowship No. J2272' of the 'Fonds zur Förderung der wissenschaftlichen Forschung' of Austria by the European Community's Human Potential Programme under contract HPRN-CT-2000-00149 Physics at Colliders and contracts HPRN-CT-2000-00131, HPRN-CT-2000-00148, HPRN-CT-2000-00152, by the France-Berkeley fund, by the German Federal Ministry of Education and Research (BMBF) within the Framework of the German-Israeli Project Cooperation (DIP), by the Grant-in-Aid for Science Research, Ministry of Education, Science and Culture, Japan, No. 11207101, 13135297, 14046210, 14046225 and 14540260, by the KBN Grant 2 P03B 040 24 (2003-2005) and 115/E-343/SPB/DESY/P-03/DWM517/2003-2005, by MECYT and FEDER under project FPA2001-3598, by the Polish Committee for Scientific Research, grant no. 1 P03B 040 26 and project no. 115/E-343/SPB/DESY/P-03/DWM517/2003-2005, by the RFBR grants 04-02-16476 and 04-02-17448, by the Swiss Nationalfonds, by UK-PPARC, by the grant of the Program "Universities of Russia" UR.02.03.028, by the U.S. National Science Foundation under grants No. ITR-0086044, PHY-0122557, PHY-0139953, PHY-0239817, PHY-9600155, PHY-9970703, by the U.S. Department of Energy under grants DE-AC02-76CH02000, DE-AC02-76SF00515, DE-AC03-76SF00515, DE-FG02-91ER40674, DE-FG02-95ER40542, DE-FG02-91ER40685, DE-FG02-95ER40896, and by the Wisconsin Alumni Research Foundation.

Bibliography

[1] R. Barate *et al.* [ALEPH, DELPHI, L3, OPAL Collaborations and LEP Working Group for Higgs boson searches], Phys. Lett. B **565** (2003) 61 [arXiv:hep-ex/0306033].

[2] P. Renton, talk given at the 32nd International Conference on High Energy Physics (ICHEP04), Beijing, China, August 2004, see `http://lepewwg.web.cern.ch/LEPEWWG`.

[3] D. L. Wark, Nucl. Phys. Proc. Suppl. **117** (2003) 164 and references therein.

[4] M. Kamionkowski, Nucl. Phys. Proc. Suppl. **117** (2003) 335 and references therein.

[5] S. K. Choi *et al.* [Belle Collaboration], Phys. Rev. Lett. **91** (2003) 262001 [arXiv:hep-ex/0309032].

[6] D. Acosta *et al.* [CDF II Collaboration], arXiv:hep-ex/0312021.

[7] J. Stark [D0 Collaboration], arXiv:hep-ex/0407002.

[8] ATLAS Coll., Technical Design Report, CERN/LHCC/99-15 (1999);
CMS Coll., Technical Proposal, CERN/LHCC/94-38 (1994);
J. G. Branson, D. Denegri, I. Hinchliffe, F. Gianotti, F. E. Paige and P. Sphicas [ATLAS and CMS Collaborations], Eur. Phys. J. directC **4** (2002) N1.

[9] J. A. Aguilar-Saavedra *et al.* [ECFA/DESY LC Physics Working Group Collaboration], arXiv:hep-ph/0106315;
T. Abe *et al.* [American Linear Collider Working Group Collaboration], in *Proc. of Snowmass 2001*, ed. N. Graf, arXiv:hep-ex/0106055;
K. Abe *et al.* [ACFA Linear Collider Working Group Coll.], arXiv:hep-ph/0109166; see: `lcdev.kek.jp/RMdraft/`.

[10] J.-E. Augustin *et al.* [International Technology Recommendation Panel], see `http://www.interactions.org/linearcollider`;
J. Dorfan, talk given at the 32nd International Conference on High Energy Physics (ICHEP04), Beijing, China, August 2004.

[11] S. Heinemeyer, W. Hollik and G. Weiglein, Eur. Phys. J. C **9** (1999) 343 [arXiv:hep-ph/9812472];
G. Degrassi, S. Heinemeyer, W. Hollik, P. Slavich and G. Weiglein, Eur. Phys. J. C **28** (2003) 133 [arXiv:hep-ph/0212020];
B. C. Allanach, A. Djouadi, J. L. Kneur, W. Porod and P. Slavich, arXiv:hep-ph/0406166.

[12] M. Beneke *et al.*, arXiv:hep-ph/0003033, in: Standard Model Physics (and more) at the LHC, eds. G. Altarelli and M. Mangano, CERN, Geneva, 1999 [CERN-2000-004].

[13] A. H. Hoang *et al.*, Eur. Phys. J. directC **2** (2000) 3 [arXiv:hep-ph/0001286]; M. Martinez and R. Miquel, Eur. Phys. J. C **27** (2003) 49 [arXiv:hep-ph/0207315].

[14] B. C. Allanach *et al.*, Eur. Phys. J. C **25** (2002) 113, arXiv:hep-ph/0202233, see: `www.ippp.dur.ac.uk/~georg/sps`.

[15] G. Bertone, D. Hooper and J. Silk, arXiv:hep-ph/0404175.

[16] G. Polesello and D. R. Tovey, JHEP **0405** (2004) 071 [arXiv:hep-ph/0403047].

[17] P. Bambade, M. Berggren, F. Richard and Z. Zhang, arXiv:hep-ph/0406010.

[18] M. Battaglia, I. Hinchliffe and D. Tovey, arXiv:hep-ph/0406147.

[19] P. Janot [CMS Collaboration], arXiv:hep-ph/0406275.

[20] C. L. Bennett *et al.*, Astrophys. J. Suppl. **148** (2003) 1 [arXiv:astro-ph/0302207].

[21] D. N. Spergel *et al.* [WMAP Collaboration], Astrophys. J. Suppl. **148** (2003) 175 [arXiv:astro-ph/0302209].

[22] see `astro.estec.esa.nl/Planck`.

[23] B. C. Allanach, G. Belanger, F. Boudjema and A. Pukhov, arXiv:hep-ph/0410091.

[24] H. Baer, A. Belyaev, T. Krupovnickas and X. Tata, JHEP **0402** (2004) 007 [arXiv:hep-ph/0311351].

[25] J.F. Gunion, H.E. Haber, G. Kane and S. Dawson, *The Higgs Hunter's Guide* (Perseus Publishing, Cambridge, MA, 1990).

[26] D. Abbaneo *et al.* [LEP Electroweak Working Group] and N. de Groot *et al.* [SLD Electroweak and Heavy Flavor Groups], hep-ex/0312023 (December 2003), and additional updates at `http://lepewwg.web.cern.ch/LEPEWWG/`; see also P. Renton, talk given at the 32nd International Conference on High Energy Physics (ICHEP04), Beijing, China, August 2004.

[27] R. Barate *et al.* [ALEPH, DELPHI, L3 and OPAL Collaborations, and the LEP working group for Higgs boson searches, Phys. Lett. **B565** (2003) 61 [hep-ex/0306033].

[28] H.P. Nilles, Phys. Rep. **110** (1984) 1; H.E. Haber and G.L. Kane, Phys. Rep. **117** (1985) 75; S.P. Martin, hep-ph/9709356;

[29] For a review, see *e.g.*, L. Susskind, Phys. Rep. **104** (1984) 181.

[30] K. Inoue, A. Kakuto, H. Komatsu, and S. Takeshita, Prog. Theor. Phys. **68** (1982) 927 [E: **70** (1983) 330]; **71** (1984) 413; R. Flores and M. Sher, Ann. Phys. (NY) **148** (1983) 95; J.F. Gunion and H.E. Haber, Nucl. Phys. **B272** (1986) 1 [E: **B402** (1993) 567].

[31] J.R. Espinosa and M. Quiros, Phys. Rev. Lett. **81** (1998) 516 [hep-ph/9804235].

[32] G. Degrassi, S. Heinemeyer, W. Hollik, P. Slavich and G. Weiglein, Eur. Phys. J. **C28**, 133 (2003) [hep-ph/0212020].

[33] For a comprehensive review, see C.T. Hill and E.H. Simmons, Phys. Rep. **381** (2003) 235 [E: **390** (2004) 553] [hep-ph/0203079].

[34] E. Farhi and L. Susskind, Phys. Rep.**74** (1981) 277; R.K. Kaul, Rev. Mod. Phys. **55** (1983) 449.

[35] For a brief review, see M. Schmaltz, Nucl. Phys. Proc. Suppl. **117** (2003) 40 [hep-ph/0210415].

[36] N. Arkani-Hamed, S. Dimopoulos and G.R. Dvali, Phys. Lett. **B429** (1998) 263; L. Randall and R. Sundrum, Phys. Rev. Lett. **83** (1999) 3370. For a recent review, see V.A. Rubakov, *Phys. Usp.* **44** (2001) 871.

[37] M. Quiros, "New ideas in symmetry breaking," hep-ph/0302189.

[38] G.F. Giudice, R. Rattazzi and J.D. Wells, Nucl. Phys. **B595** (2001) 250 [hep-ph/0002178]; F.J. Petriello, JHEP **0205** (2002) 003 [hep-ph/0204067]; A. Datta, K. Huitu, J. Laamanen and B. Mukhopadhyaya, hep-ph/0404056.

[39] C. Csaki, C. Grojean, L. Pilo and J. Terning, Phys. Rev. Lett. **92** (2004) 101802 [hep-ph/0308038]; Y. Nomura, JHEP **0311** (2003) 050 [hep-ph/0309189]; H. Davoudiasl, J.L. Hewett, B. Lillie and T.G. Rizzo, JHEP **0405** (2004) 015 [hep-ph/0403300].

[40] M.E. Peskin and T. Takeuchi, Phys. Rev. Lett. **65** (1990) 964, Phys. Rev. **D46** (1992) 381.

[41] M. Carena and H.E. Haber, Prog. Part. Nucl. Phys. **50** (2003) 63 [hep-ph/0208209].

[42] M. Duhrssen, S. Heinemeyer, H. Logan, D. Rainwater, G. Weiglein and D. Zeppenfeld, arXiv:hep-ph/0406323.

[43] H.E. Haber and Y. Nir, Nucl. Phys. **B335** (1990) 363; J.F. Gunion and H.E. Haber, Phys. Rev. **D67** (2003) 075019 [hep-ph/0207010].

[44] ALEPH, DELPHI, L3 and OPAL Collaborations, The LEP Working Group for Higgs Boson Searches, LHWG Note 2001-04 (July 2001) [hep-ex/0107030].

[45] D. Zeppenfeld, R. Kinnunen, A. Nikitenko and E. Richter-Wąs, Phys. Rev. **D62** (2000) 013009 [hep-ph/0002036]; D. Zeppenfeld, "Higgs Couplings at the LHC," in *Proceedings of the APS/DPF/DPB Summer Study on the Future of Particle Physics* (Snowmass 2001), edited by R. Davidson and C. Quigg, SNOWMASS-2001-P123 [hep-ph/0203123].

[46] A. Belyaev and L. Reina, JHEP **0208** (2002) 041 [hep-ph/0205270].

[47] M. Dührssen, "Prospects for the measurement of Higgs boson coupling parameters in the mass range from 110–190 Gev/c^2," ATL/PHYS-2003-030.

[48] See, *e.g.* J.F. Gunion, H.E. Haber and R. Van Kooten, " Higgs Physics at the Linear Collider," SCIPP-02-37 and UCD-02-18 [hep-ph/0301023], to appear in *Linear Collider Physics in the New Millennium*, edited by K. Fujii, D. Miller and A. Soni and references contained therein.

[49] J. Cammin, M. Schumacher, "THE ATLAS discovery potential for the channel $t\bar{t}h_0$, $h_0 \to b\bar{b}$", ATL-PHYS-2003-024.

[50] J. Dai, J.F. Gunion and R. Vega, Phys. Rev. Lett. **71** (1993) 2699.

[51] M. Beneke *et. al.*, "Top Quark Physics," hep-ph/0003033.

[52] V. Drollinger, Th. Müller and D. Denegri, CMS Note 2001/054 [hep-ph/0111312].

[53] J. Leveque *et al.*, "Search for the Standard Model Higgs boson in the channel $t\bar{t}h_0$, $h_0 \to WW$ channel", ATL-PHYS-2002-19.

[54] F. Maltoni, D. Rainwater, and S. Willenbrock, Phys. Rev. **D66** (2002) 034033 [hep-ph/0202205].

[55] L. Zivkovic and E. Gross, ATLAS Higgs working group (February, 19 2001).

[56] A. Ito, ATLAS Higgs working group (April, 10 2003).

[57] J.A. Aguilar-Saavedra *et al.* [ECFA/DESY LC Physics Working Group Collaboration], "TESLA Technical Design Report Part III: Physics at an e^+e^- Linear Collider," arXiv:hep-ph/0106315.

[58] D. Bourilkov, this report and references therein.

[59] A. Djouadi and S. Ferrag, Phys. Lett. **B586** (2004) 345 [hep-ph/0310209].

[60] W. Beenakker, S. Dittmaier, M. Krämer, B. Plümper, M. Spira and P.M. Zerwas, Phys. Rev. Lett. **87** (2001) 201805 [hep-ph/0107081].

[61] W. Beenakker, S. Dittmaier, M. Krämer,B. Plümper, M. Spira and P. M. Zerwas, Nucl. Phys. **B653** (2003) 151 [hep-ph/0211352].

[62] L. Reina and S. Dawson, Phys. Rev. Lett. **87** (2001) 201804 [hep-ph/0107101]; L. Reina, S. Dawson and D. Wackeroth, Phys. Rev. **D65** (2002) 053017 [hep-ph/0109066].

[63] S. Dawson, L.H. Orr, L. Reina, and D. Wackeroth, Phys. Rev. **D67** (2003) 071503 [hep-ph/0211438]; S. Dawson, C. Jackson, L.H. Orr, L. Reina and D. Wackeroth, Phys. Rev. **D68** (2003) 034022 [hep-ph/0305087].

[64] A. Gay, results presented at the 2nd ECFA/DESY Workshop, Saint Malo, France, 12-15 April 2002, http://www.desy.de/~desch/higgs/stmalo/gay.ps.

[65] M. Battaglia and K. Desch, in *Physics and experiments with future linear e^+e^- colliders*, Proceedings of the 5th International Linear Collider Workshop, Batavia, IL, USA, 2000, edited by A. Para and H.E. Fisk (American Institute of Physics, New York, 2001), pp. 163–182 [hep-ph/0101165].

[66] C.T. Potter, J.E. Brau and M. Iwasaki, "Standard Model Higgs Boson Branching Ratio Measurements at a Linear Collider," in *Proceedings of the APS/DPF/DPB Summer Study on the Future of Particle Physics* (Snowmass 2001), edited by R. Davidson and C. Quigg, SNOWMASS-2001-P118; and "Standard Model Higgs boson branching ratio measurements at a linear collider," to appear in the Proceedings of the International Workshop on Linear Colliders, *Workshop on Physics and Experiments with Future Electron-Positron Linear Colliders*, 26–30 August, 2002, Jeju Island, Korea.

[67] K.J.F. Gaemers and G.J. Gounaris, Phys. Lett. **B77** (1978) 379; A. Djouadi, J. Kalinowski and P.M. Zerwas, Z. Phys. **C54** (1992) 255.

[68] S. Dawson and L. Reina, Phys. Rev. **D59** (1999) 054012 [hep-ph/9808443].

[69] A. Juste and G. Merino, hep-ph/9910301.

[70] A. Juste, results presented at Chicago linear collider workshop, January, 2002, http://www.pas.rochester.edu/˜orr/justelc.pdf.

[71] S. Dittmaier, M. Krämer, Y. Liao, M. Spira, and P.M. Zerwas, Phys. Lett. **B441** (1998) 383 [hep-ph/9808433].

[72] G. Bélanger, preliminary results of the GRACE collaboration presented at Loopfest II, May 14, 2003; G. Bélanger, F. Boudjema, J. Fujimoto, T. Ishikawa, T. Kaneko, K. Kato, Y. Shimizu, and Y. Yasui, *Phy. Lett.* **B571** (2003) 163 [hep-ph/0307029].

[73] Y. Yu, M. Wen-Gan, C. Hui, Z. Ren-You, S. Y-Bin, and H. Hong-Sheng, *Phys. Lett.* **B51** (2003) 85, hep-ph/0306036.

[74] A. Denner, S. Dittmaier, M. Roth and M. Weber, Phys. Lett. B **575** (2003) 290 [arXiv:hep-ph/0307193]; Nucl. Phys. B **680** (2004) 85 [arXiv:hep-ph/0309274].

[75] S. Moretti, 2nd ECFA/DESY Study, hep-ph/9911501, Phys. Lett. **B452** (1999) 338 [hep-ph/9902214].

[76] H. Baer, S. Dawson, and L. Reina, Phys. Rev. **D61** (2000) 013002 [hep-ph/9906419].

[77] H. Baer, F.E. Paige, S.D. Protopopescu and X. Tata, hep-ph/0001086; http://paige.home.cern.ch/paige.

[78] A. Gay, results presented at the 3rd ECFA/DESY Workshop, Prague, Czech Republic, 15-18 November 2002, http://ireswww.in2p3.fr/ires/recherche/capteurs/ed/prague/prague_ag.html.

[79] A. Gay, results presented at the 4th ECFA DESY Workshop, Amsterdam, Netherlands, 1-4 April 2003, http://www.nikhef.nl/ecfa-desy/ECspecific/Program/Presentations/April-2/Par-1/1A/gay-a.ps.

[80] Y. Sumino, K. Fujii, K. Hagiwara, H. Murayama, and C. Ng, Phys. Rev. **D47** (1993) 56; A. Hoang and T. Teubner, Phys. Rev. **D60** (1999) 114027 [hep-ph/9904468].

[81] K. Fujii, T. Matsui and Y. Sumino, Phys. Rev. **D50** (1994) 4341.

[82] M. Martinez and R. Miquel, Eur. Phys. J. **C27** (2003) 49 [hep-ph/0207315].

[83] A.H. Hoang *et al.*, Eur. Phys. J. **C2** (2000) 3 [hep-ph/0001286].

[84] A.H. Hoang, A.V. Manohar, I.W. Stewart and T. Teubner, Phys. Rev. **D65** (2002) 014014 [hep-ph/0107144].

[85] R. Harlander, M. Jezabek, J.H. Kühn and T. Teubner, Phys. Lett. **B346** (1995) 137 [hep-ph/9411395]; M. Jezabek and T. Teubner, Z. Phys. **C59** (1993) 669; M. Jezabek and J.H. Kühn, Phys. Lett. **B316** (1993) 360; M. Jezabek, J.H. Kühn and T. Teubner, Z. Phys. **C56** (1992) 653.

[86] B. Grzadkowski, J.H. Kühn, P. Krawczyk, and R. Stuart, *Nucl. Phys.* **B282** (1987) 18; R. Guth and J.H. Kühn, *Nucl. Phys.* **B368** (1992) 38.

[87] J. Goldstein, C. S. Hill, J. Incandela, S. Parke, and D. Stuart, *Phys. Rev. Lett.* **86** (2001) 1694 [hep-ph/0006311].

[88] E. Richter-Wąs and M. Sapinski, Acta Phys. Polon. **B30** (1999) 1001.

[89] ATLAS Collaboration, Technical Design Report, CERN/LHCC/99-15 (1999).

[90] S. Dittmaier, M. Krämer, Y. Liao, M. Spira and P.M. Zerwas, Phys. Lett. **B478** (2000) 247 [hep-ph/0002035].

[91] S. Dawson and L. Reina, Phys. Rev. **D60** (1999) 015003 [hep-ph/9812488].

[92] A. Dedes, S. Heinemeyer, S. Su and G. Weiglein, Nucl. Phys. B **674** (2003) 271, arXiv:hep-ph/0302174.

[93] B. Kniehl, F. Madricardo and M. Steinhauser, Phys. Rev. **D66** (2002) 054016 [hep-ph/0205312].

[94] M. Dittmar and H.K. Dreiner, Phys. Rev. **D55** (1997) 167 [hep-ph/9608317]; D. Rainwater and D. Zeppenfeld, Phys. Rev. **D60** (1999) 113004 [Erratum: **D61** (2000) 099901] [hep-ph/9906218]; N. Kauer, T. Plehn, D. Rainwater and D. Zeppenfeld, Phys. Lett. **B503** (2001) 113 [hep-ph/0012351].

[95] D. Rainwater, D. Zeppenfeld and K. Hagiwara, Phys. Rev. **D59** (1999) 014037 [hep-ph/9808468]; T. Plehn, D. Rainwater and D. Zeppenfeld, Phys. Lett. **B454** (1999) 297 [hep-ph/9902434]; Phys. Rev. **D61** (2000) 093005 [hep-ph/9911385].

[96] D. Rainwater, Phys. Lett. **B503** (2001) 320 [hep-ph/0004119]; V. Drollinger, T. Müller and D. Denegri, hep-ph/0201249.

[97] B.W. Lee, C. Quigg and H.B. Thacker, Phys. Rev. Lett. **38** (1977) 883; Phys. Rev. **D16** (1977) 1519.

[98] M. Battaglia, E. Boos and W.M. Yao, hep-ph/0111276.

[99] A. Djouadi, W. Kilian, M. Mühlleitner and P.M. Zerwas, Eur. Phys. J. **C10** (1999) 27; D.J. Miller and S. Moretti, Eur. Phys. J. **C13** (2000) 459.

[100] C. Castanier, P. Gay, P. Lutz and J. Orloff, hep-ex/0101028.

[101] F. Gianotti *et al.*, hep-ph/0204087.

[102] U. Baur, T. Plehn and D. Rainwater, Phys. Rev. Lett. **89** (2000) 151801; Phys. Rev. **D67** (2003) 033003.

[103] U. Baur, T. Plehn and D. Rainwater, Phys. Rev. **D 69**, 053004 (2004).

[104] U. Baur, T. Plehn and D. Rainwater, Phys. Rev. **D68** (2003) 033001 [hep-ph/0304015].

[105] K. A. Assamagan *et al.* [Higgs Working Group Collaboration], arXiv:hep-ph/0406152.

[106] M. Battaglia and A. DeRoeck, in preparation.

[107] E.L. Berger, C.W. Chiang, J. Jiang, T.M.P. Tait and C.E.M. Wagner, Phys. Rev. **D66** (2002) 095001 [hep-ph/0205342].

[108] B.A. Dobrescu, G. Landsberg and K.T. Matchev, Phys. Rev. **D63** (2001) 075003 [hep-ph/0005308].

[109] M. Carena, J.R. Ellis, S. Mrenna, A. Pilaftsis and C.E.M. Wagner, Nucl. Phys. **B659** (2003) 145 [hep-ph/0211467].

[110] E.L. Berger, B.W. Harris, D.E. Kaplan, Z. Sullivan, T.M.P. Tait and C.E.M. Wagner, Phys. Rev. Lett. **86** (2001) 4231 [hep-ph/0012001].

[111] E.L. Berger, Int. J. Mod. Phys. **A18** (2003) 1263 [hep-ph/0201229]; E.L. Berger, hep-ph/0209374.

[112] M. Carena, S. Heinemeyer, C.E.M. Wagner and G. Weiglein, Phys. Rev. Lett. **86** (2001) 4463 [hep-ph/0008023].

[113] CMS Collaboration, Technical Proposal, CERN/LHCC/94-38 (1994).

[114] D. Cavalli *et al.*, "The Higgs working group: Summary report", to appear in the proceedings of Workshop on Physics at TeV Colliders, Les Houches, France, 21 May—1 June 2001, hep-ph/0203056.

[115] T. Abe *et al.* [American Linear Collider Working Group], "Linear Collider Physics Resource Book for Snowmass 2001," SLAC-R-570; TESLA Technical Design Report, Ed. by R. Heuer, D. Miller, F. Richard, A. Wagner, and P.M. Zerwas, www.desy.de/~lcnotes/tdr.

[116] R. Kinnunen, "Higgs physics at the LHC," in: *Proceedings of the 10th International Conference on Supersymmetry and Unification of Fundamental Interactions (SUSY02)*, Eds. P. Nath, P. M. Zerwas, and C. Grosche, DESY, Hamburg, Germany, 2002.

[117] B. Badelek *et al.* [ECFA/DESY Photon Collider Working Group Collaboration], "TESLA Technical Design Report, Part VI, Chapter 1: Photon collider at TESLA," arXiv:hep-ex/0108012; Proc. of Int. Workshop on High Photon Colliders Nucl. Instrum. Meth. A **472** (2001)

[118] S. Weinberg, Phys. Rev. Lett. **37** (1976) 657.

[119] For a review, see e.g. M. Dine and A. Kusenko, arXiv:hep-ph/0303065.

[120] J. F. Gunion, H. E. Haber and J. Wudka, Phys. Rev. D **43** (1991) 904.

[121] J. F. Gunion, B. Grzadkowski, H. E. Haber and J. Kalinowski, Phys. Rev. Lett. **79** (1997) 982 [arXiv:hep-ph/9704410].

[122] I. F. Ginzburg, M. Krawczyk and P. Osland, arXiv:hep-ph/0211371.

[123] OPAL Collaboration, OPAL Physics Note PN524 (2003).

[124] M. N. Dubinin and A. V. Semenov, Eur. Phys. J. C **28**, 223 (2003) [arXiv:hep-ph/0206205].

[125] A. Dedes and S. Moretti, Phys. Rev. Lett. **84** (2000) 22 [arXiv:hep-ph/9908516]; Nucl. Phys. B **576** (2000) 29 [arXiv:hep-ph/9909418].

[126] A. Pilaftsis and C. E. Wagner, Nucl. Phys. B **553**, 3 (1999) [arXiv:hep-ph/9902371].

[127] S. Y. Choi, M. Drees and J. S. Lee, Phys. Lett. B **481**, 57 (2000) [arXiv:hep-ph/0002287].

[128] S. Heinemeyer, Eur. Phys. J. C **22**, 521 (2001) [arXiv:hep-ph/0108059].

[129] J. S. Lee, A. Pilaftsis, M. Carena, S. Y. Choi, M. Drees, J. Ellis and C. E. Wagner, [arXiv:hep-ph/0307377].

[130] W. Bernreuther, M. Flesch and P. Haberl, Phys. Rev. D **58** (1998) 114031 [arXiv:hep-ph/9709284]; W. Bernreuther, A. Brandenburg and M. Flesch, arXiv:hep-ph/9812387.

[131] W. Khater and P. Osland, Nucl. Phys. B **661**, 209 (2003) [arXiv:hep-ph/0302004].

[132] J. F. Gunion and X. G. He, Phys. Rev. Lett. **76** (1996) 4468 [arXiv:hep-ph/9602226].

[133] B. Field, Phys. Rev. D **66** (2002) 114007 [arXiv:hep-ph/0208262].

[134] S. Y. Choi, D. J. Miller, M. M. Muhlleitner and P. M. Zerwas, Phys. Lett. B **553** (2003) 61 [arXiv:hep-ph/0210077].

[135] C. P. Buszello, I. Fleck, P. Marquard and J. J. van der Bij, Eur. Phys. J. C **32** (2004) 209 [arXiv:hep-ph/0212396].

[136] T. Plehn, D. Rainwater and D. Zeppenfeld, Phys. Rev. Lett. **88** (2002) 051801 [arXiv:hep-ph/0105325].

[137] V. Del Duca, W. Kilgore, C. Oleari, C. R. Schmidt and D. Zeppenfeld, [arXiv:hep-ph/0109147].

[138] K. Odagiri, JHEP **0303**, 009 (2003) [arXiv:hep-ph/0212215].

[139] V. A. Khoze, A. D. Martin and M. G. Ryskin, Eur. Phys. J. C **23** (2002) 311 [arXiv:hep-ph/0111078].

[140] B. E. Cox, J. R. Forshaw, J. S. Lee, J. Monk and A. Pilaftsis, Phys. Rev. D **68** (2003) 075004 [arXiv:hep-ph/0303206].

[141] V. A. Khoze, A. D. Martin and M. G. Ryskin, arXiv:hep-ph/0401078.

[142] A. Mendez and A. Pomarol, Phys. Lett. B **272** (1991) 313.

[143] B. Grzadkowski, J. F. Gunion and J. Kalinowski, Phys. Rev. D **60** (1999) 075011 [arXiv:hep-ph/9902308].

[144] A. G. Akeroyd and A. Arhrib, Phys. Rev. D **64** (2001) 095018 [arXiv:hep-ph/0107040].

[145] V. D. Barger, K. m. Cheung, A. Djouadi, B. A. Kniehl and P. M. Zerwas, Phys. Rev. D **49** (1994) 79 [arXiv:hep-ph/9306270].

[146] K. Hagiwara and M. L. Stong, Z. Phys. C **62** (1994) 99 [arXiv:hep-ph/9309248].

[147] D. J. Miller, S. Y. Choi, B. Eberle, M. M. Muhlleitner and P. M. Zerwas, Phys. Lett. B **505** (2001) 149 [arXiv:hep-ph/0102023].

[148] M. T. Dova, P. Garcia-Abia and W. Lohmann, arXiv:hep-ph/0302113.

[149] M. Kramer, J. H. Kuhn, M. L. Stong and P. M. Zerwas, Z. Phys. C **64** (1994) 21 [arXiv:hep-ph/9404280].

[150] B. Grzadkowski and J. F. Gunion, Phys. Lett. B **350** (1995) 218 [arXiv:hep-ph/9501339].

[151] J. F. Gunion, B. Grzadkowski and X. G. He, Phys. Rev. Lett. **77** (1996) 5172 [arXiv:hep-ph/9605326].

[152] G. R. Bower, T. Pierzchala, Z. Was and M. Worek, Phys. Lett. B **543** (2002) 227 [arXiv:hep-ph/0204292].

[153] K. Desch, Z. Was and M. Worek, Eur. Phys. J. C **29** (2003) 491 [arXiv:hep-ph/0302046].

[154] M. Worek, Acta Phys. Polon. B **34** (2003) 4549 [arXiv:hep-ph/0305082].

[155] K. Desch, A. Imhof, Z. Was and M. Worek, arXiv:hep-ph/0307331.

[156] K. Hagiwara, Nucl. Instrum. Meth. A **472** (2001) 12 [arXiv:hep-ph/0011360].

[157] B. Grzadkowski and J. F. Gunion, Phys. Lett. B **294** (1992) 361 [arXiv:hep-ph/9206262].

[158] M. M. Muhlleitner, M. Kramer, M. Spira and P. M. Zerwas, Phys. Lett. B **508**, 311 (2001) [arXiv:hep-ph/0101083].

[159] P. Niezurawski, A. F. Zarnecki and M. Krawczyk, arXiv:hep-ph/0307180.

[160] E. Asakawa, J. i. Kamoshita, A. Sugamoto and I. Watanabe, Eur. Phys. J. C **14** (2000) 335 [arXiv:hep-ph/9912373].

[161] P. Niezurawski, A. F. Zarnecki and M. Krawczyk, arXiv:hep-ph/0307175; arXiv:hep-ph/0403138;

[162] E. Asakawa, S. Y. Choi, K. Hagiwara and J. S. Lee, Phys. Rev. D **62** (2000) 115005 [arXiv:hep-ph/0005313].

[163] R. M. Godbole, S. D. Rindani and R. K. Singh, Phys. Rev. D **67** (2003) 095009 [arXiv:hep-ph/0211136].

[164] I. F. Ginzburg, M. Krawczyk and P. Osland, *Nucl. Instrum. Meth.* A472:149, 2001 [arXiv:hep-ph/0101229]; arXiv:hep-ph/0101331; arXiv:hep-ph/0101208.

[165] D. Bomestar, D. Denegri, R. Kinnunen, A. Nikitenko, FIZIKA B 4 (1995) 3, 273-286; CMS TN/95-018.

[166] R. Kinnunen, CMS CR-2002/020.

[167] N.Meyer, LC-PHSM-2003-066.

[168] P.Nieżurawski, A.F.Żarnecki, M.Krawczyk, JHEP 0211 (2002) 034 [arXiv:hep-ph/0207294]

[169] A. Hoang et al., Eur. Phys. J. C **3** (2000) 1, arXiv:hep-ph/0001286.

[170] S. Heinemeyer, S. Kraml, W. Porod and G. Weiglein, JHEP **0309** (2003) 075 [arXiv:hep-ph/0306181].

[171] K. Desch, E. Gross, S. Heinemeyer, G. Weiglein and L. Živković, arXiv:hep-ph/0406322.

[172] R. Lafaye, T. Plehn and D. Zerwas, arXiv:hep-ph/0404282;
P. Wienemann, talk given at the LCWS Paris, April 2004, see:
`agenda.cern.ch/fullAgenda.php?ida=a04172#s15`.

[173] J. R. Ellis, S. Heinemeyer, K. A. Olive and G. Weiglein, JHEP **0301** (2003) 006, arXiv:hep-ph/0211206.

[174] J. Guasch, W. Hollik and S. Peñaranda, Phys. Lett. B **515** (2001) 367, arXiv:hep-ph/0106027;
M. Carena, H. Haber, H. Logan and S. Mrenna, Phys. Rev. D **65** (2002) 055005, E: *ibid* **D 65** (2002) 099902, arXiv:hep-ph/0106116;
D. Asner et al., Eur. Phys. J. C **28** (2003) 27, arXiv:hep-ex/0111056.

[175] J.-C. Brient, LC-PHSM-2004-002, see: `www-flc.desy.de/lcnotes`.

[176] J. Erler, S. Heinemeyer, W. Hollik, G. Weiglein and P.M. Zerwas, Phys. Lett. B **486** (2000) 125, arXiv:hep-ph/0005024;
J. Erler and S. Heinemeyer, in *Proc. of the 5th International Symposium on Radiative Corrections (RADCOR 2000)* ed. Howard E. Haber, arXiv:hep-ph/0102083.

[177] K. Desch, J. Kalinowski, G. Moortgat-Pick, M. M. Nojiri and G. Polesello, JHEP **0402** (2004) 035 [arXiv:hep-ph/0312069].

[178] S. Heinemeyer, W. Hollik and G. Weiglein, Eur. Phys. J. C **16** (2000) 139, arXiv:hep-ph/0003022; Comp. Phys. Comm. **124** (2000) 76, arXiv:hep-ph/9812320, see: `www.feynhiggs.de`.

[179] H. E. Haber, M. J. Herrero, H. E. Logan, S. Penaranda, S. Rigolin and D. Temes, Phys. Rev. D **63** (2001) 055004, arXiv:hep-ph/0007006.

[180] T. L. Barklow, arXiv:hep-ph/0312268.

[181] F. Moortgat, S. Abdullin and D. Denegri, hep-ph/0112046.

[182] M. Bisset, F. Moortgat, S. Moretti, hep-ph/0303093, Eur.Phys.J.C **30**, 419-434 (2003).

[183] G. Weiglein *et al.*, in *Proc. of the APS/DPF/DPB Summer Study on the Future of Particle Physics (Snowmass 2001)* ed. N. Graf, hep-ph/0202233, Eur. Phys. J.C **25**, 113 (2002).

[184] F. Moortgat, M. Nojiri and W. Porod, private discussions during the 2003 Les Houches Workshop on Physics with TeV Colliders; M. Nojiri, G. Polesello and D. Tovey, hep-ph/0312317.

[185] E. Boos, A. Djouadi, M. Mühlleitner and A. Vologdin, Phys. Rev. D66 (2002) 055004.

[186] E. Boos, A. Djouadi and A. Nikitenko, Phys. Lett. B **578** (2004) 384

[187] A. Djouadi, J. Kalinowski and M. Spira, Comput. Phys. Commun. 108 (1998) 56.

[188] A. Pukhov et al., Report INP-MSU 98-41/542, hep-ph/9908288.

[189] A.S. Belyaev et al., hep-ph/0101232.

[190] T. Sjostrand, L. Lonnblad and S. Mrenna, hep-ph/0108264.

[191] M. Pohl and H. J. Schreiber, hep-ex/0206009.

[192] A. Andreazza and C. Troncon, Report DESY–123–E, p. 417.

[193] G. Blair and H.U. Martyn, Note LC–TH-2000–023 and hep-ph/0002290.

[194] E. Boos, V. Bounichev, A. Djouadi and J. Schreiber, in preparation.

[195] S. Lehti, Prospects for the Detection of the MSSM Higgs Bosons Decaying into Tau Leptons in the CMS Detector, *Dissertation, University of Helsinki, Report Series in Physics, HU-P-D93* (2001); S. Lehti, Study of $gg \to b\bar{b}H_{SUSY}$, $H_{SUSY} \to \tau\tau \to \ell\ell + X$, CMS NOTE 2002/035.

[196] R. Kinnunen and A. Nikitenko, *CMS NOTE 1997/106*.

[197] R. Kinnunen and A. Nikitenko, *CMS NOTE 2003/006*.

[198] M. Carena and H. Haber, *Prog. Part. Nucl. Phys.* **50** (2003) 63 and references therein.

[199] CMS Collaboration, *CERN/LHCC 2002-26, CMS TDR 6.2*.

[200] K. Hagiwara *et. al.*, *Phys. Rev.* **D66** (2002) 010001.

[201] S. Dittmaier, M. Spira, and M. Krämer, hep-ph/0309204.

[202] S. Dawson, C. Jackson, L. Reina and D. Wackeroth, hep-ph/0311067.

[203] J. Campbell, R. K. Ellis, F. Maltoni and S. Willenbrock, *Phys. Rev.* **D67** (2003) 093005.

[204] S.Y. Choi, J. Kalinowski, J.S. Lee, M. Mühlleitner, M. Spira and P.M. Zerwas, arXiv:hep-ph/0404119 and arXiv:hep-ph/0407048.

[205] K. Desch, private communication.

[206] J. Gunion, T. Han, J. Jiang, A. Sopczak, Phys. Lett. B **565**, 42 (2003).

[207] F. Gianotti *et al.*, arXiv:hep-ph/0204087.

[208] LEP Higgs Working Group, July 2002.

[209] J.F. Gunion, L. Poggioli, R. Van Kooten, C. Kao and P. Rowson, arXiv:hep-ph/9703330.

[210] S. Dawson, D. Dicus and C. Kao, Phys. Lett. B **545**, 132 (2002).

[211] K.A. Assamagan, Y. Coadou and A. Deandrea, Eur. Phys. J. direct C **4**, 9 (2002).

[212] A. Djouadi, J. Kalinowski and M. Spira, Comput. Phys. Commun. **108**, 56 (1998).

[213] M. Carena, S. Mrenna and C.E. Wagner, Phys. Rev. D **60**, 075010 (1999).

[214] J. R. Ellis, J. F. Gunion, H. E. Haber, L. Roszkowski and F. Zwirner, Phys. Rev. D **39** (1989) 844.

[215] J. F. Gunion, H. E. Haber and T. Moroi, eConf **C960625**, LTH095 (1996) [arXiv:hep-ph/9610337].

[216] U. Ellwanger, J. F. Gunion and C. Hugonie, arXiv:hep-ph/0111179.

[217] LEP Higgs Working Group, Notes 2002/01 (Zh) and 2001/04 (ha).

[218] CMS Collaboration, "Expected Observability of Standard Model Higgs in CMS with $100\ \mathrm{fb}^{-1}$", CMS NOTE 1997/057. ATLAS Collaboration, "Detector and Physics Performance Technical Design Report Vol. II (1999)", CERN/LHCC/99-15 p. 675–811. D. Zeppenfeld, R. Kinnunen, A. Nikitenko and E. Richter-Was, *Phys. Rev.* **D 62** (2000) 013009.D. Zeppenfeld, in *Proc. of the APS/DPF/DPB Summer Study on the Future of Particle Physics (Snowmass 2001)* ed. N. Graf, eConf **C010630**, P123 (2001).

[219] U. Ellwanger and C. Hugonie, Eur. Phys. J. C **25** (2002) 297.

[220] S. Moretti, K. Odagiri, P. Richardson, M. H. Seymour and B. R. Webber, JHEP **0204** (2002) 028 [arXiv:hep-ph/0204123].

[221] G. Corcella *et al.*, arXiv:hep-ph/0201201.

[222] G. Corcella *et al.*, JHEP **0101** (2001) 010 [arXiv:hep-ph/0011363].

[223] S. Moretti, private program.

[224] U. Ellwanger, J. F. Gunion, C. Hugonie and S. Moretti, "Towards a no-lose theorem for NMSSM Higgs discovery at the LHC," arXiv:hep-ph/0305109.

[225] See, for example, the summary of J. F. Gunion, H. E. Haber and R. Van Kooten, "Higgs physics at the linear collider," arXiv:hep-ph/0301023.

[226] U. Ellwanger, J.F. Gunion, C. Hugonie and S. Moretti, in progress.

[227] U. Ellwanger, J. F. Gunion, C. Hugonie and S. Moretti, arXiv:hep-ph/0305109, and this report.

[228] R. D. Peccei and H. R. Quinn, Phys. Rev. Lett. **38** (1977) 1440; Phys. Rev. D **16** (1977) 1791.

[229] D. J. Miller and R. Nevzorov, arXiv:hep-ph/0309143.

[230] D. J. Miller, R. Nevzorov and P. M. Zerwas, arXiv:hep-ph/0304049.

[231] P. A. Kovalenko, R. B. Nevzorov and K. A. Ter-Martirosian, Phys. Atom. Nucl. **61** (1998) 812 [Yad. Fiz. **61** (1998) 898].

[232] Searches for Higgs Bosons Decaying into Photons: Combined Results from the LEP Experiments LHWG Note/2002-02, 12 July '02

[233] G. Abbiendi *et al.* [OPAL Collaboration], Eur. Phys. J. C **27** (2003) 311 [arXiv:hep-ex/0206022].

[234] G. Jikia and S. Soldner-Rembold, Nucl. Phys. Proc. Suppl. **82** (2000) 373 [arXiv:hep-ph/9910366]; M. Melles, W. J. Stirling and V. A. Khoze, Phys. Rev. D **61** (2000) 054015 [arXiv:hep-ph/9907238]; P. Nieżurawski, A. F. Żarnecki and M. Krawczyk, hep-ph/0307183.

[235] J. L. Diaz-Cruz and A. Mendez, Nucl. Phys. B**380** (1992) 39,
J. L. Diaz-Cruz and G. Lopez Castro, Phys. Lett. B**301** (1993) 405.

[236] H. E. Haber, hep-ph/9501320; J. F. Gunion and H. E. Haber, Phys. Rev. D **67**, 075019 (2003) [hep-ph/0207010].

[237] G. C. Branco, L. Lavoura, J. P. Silva, "CP Violation" (Oxford Univ. Press, 1999)

[238] I. F. Ginzburg, M. Krawczyk and P. Osland, Linear Collider Note LC-TH-2001-026, in *2nd ECFA/DESY Study 1998–2001*, 1705 [hep-ph/0101208]; Nucl. Instrum. Meth. A**472** (2001) 149 [hep-ph/0101229]; hep-ph/0101331.

[239] I.F. Ginzburg, M.V. Vychugin. Phys. At. Nucl. **66** (2003) 5, [hep-ph/0201117]

[240] T. J. Weiler, UH-511-644-88 *Proceedings of the 8th Vanderbilt Int. Conf. on High Energy Physics, Nashville, TN, Oct 8-10, 1987*; Edited by J. Brau and R. Panvini (World Scientific, Singapore, 1988), p219; V. D. Barger, N. G. Deshpande, J. L. Hewett and T. G. Rizzo, arXiv:hep-ph/9211234. H. Pois, T. J. Weiler and T. C. Yuan, Phys. Rev. D **47** (1993) 3886; A. G. Akeroyd, Phys. Lett. B **368** (1996) 89; L. Brucher and R. Santos, Eur. Phys. J. C **12**, 87 (2000).

[241] A. Stange, W. J. Marciano and S. Willenbrock, Phys. Rev. D **49** (1994) 1354; M. A. Diaz and T. J. Weiler, arXiv:hep-ph/9401259.

[242] M. Dubinin, V. Ilyin and V. Savrin, CMS note 1997/101

[243] D. Rainwater and D. Zeppenfeld, JHEP **9712** (1997) 005

[244] E. Boos, J. C. Brient, D. W. Reid, H. J. Schreiber and R. Shanidze, Eur. Phys. J. C **19** (2001) 455

[245] D. Asner, B. Grzadkowski, arXiv:hep-ph/0208219; D. Asner *et al.*, arXiv:hep-ex/0111056.

[246] A. G. Akeroyd, J. Phys. G **24** (1998) 1983

[247] S. Mrenna and J. Wells, Phys. Rev. D **63** (2001) 015006

[248] A. G. Akeroyd, M. A. Diaz and F. J. Pacheco, arXiv:hep-ph/0312231.

[249] A. G. Akeroyd and M. A. Diaz, arXiv:hep-ph/0301203.

[250] A. Djouadi, Phys. Lett. B **435**, 101 (1998) [arXiv:hep-ph/9806315].

[251] G. Bélanger, F. Boudjema and K. Sridhar, Nucl. Phys. B **568**, 3 (2000) [arXiv:hep-ph/9904348].

[252] G. Bélanger, F. Boudjema, F. Donato, R. Godbole and S. Rosier-Lees, Nucl. Phys. B **581**, 3 (2000) [arXiv:hep-ph/0002039].

[253] G. Bélanger, F. Boudjema, A. Cottrant, R. M. Godbole and A. Semenov, Phys. Lett. B **519**, 93 (2001) [arXiv:hep-ph/0106275].

[254] A. Djouadi, J. L. Kneur and G. Moultaka, PM-99-57 *Prepared for 5th Workshop of the 2nd ECFA - DESY Study on Physics and Detectors for a Linear Electron - Positron Collider, Obernai, France, 16-19 Oct 1999* arXiv:hep-ph/9910269.

[255] O. J. Eboli and D. Zeppenfeld, Phys. Lett. B **495**, 147 (2000) [arXiv:hep-ph/0009158].

[256] B. Di Girolamo, A. Nikitenko, L. Neukermans, K. Mazumdar and D. Zeppenfeld, *Prepared for Workshop on Physics at TeV Colliders, Les Houches, France, 21 May - 1 Jun 2001*, L. Neukermans and B. Di Girolamo, ATL-COM-PHYS-2002-039.

[257] R. M. Godbole, M. Guchait, K. Mazumdar, S. Moretti and D. P. Roy, Phys. Lett. B **571**, 184 (2003) [arXiv:hep-ph/0304137].

[258] P. Gagnon, Presentation at the ATLAS Higgs WG meeting, December 2002, `http://agenda.cern.ch/fullAgenda.php?ida=a022046`, ATLAS note ATL-COM-PHYS-2003-011.

[259] J. F. Gunion, Phys. Rev. Lett. **72**, 199 (1994) [arXiv:hep-ph/9309216].

[260] B. P. Kersevan, M. Malawski and E. Richter-Was, arXiv:hep-ph/0207014.

[261] F. Boudjema, G. Bélanger and R. M. Godbole, arXiv:hep-ph/0206311.

[262] G. Bélanger, F. Boudjema, A. Pukhov and A. Semenov, Comput. Phys. Commun. **149**, 103 (2002) [arXiv:hep-ph/0112278].

[263] G. Bélanger, F. Boudjema, A. Cottrant, A. Pukhov and S. Rosier-Lees, arXiv:hep-ph/0310037.

[264] L. Randall, R. Sundrum, Phys. Rev. Lett. **83** (1999) 3370, [arXiv:hep-ph/9905221];
L. Randall, R. Sundrum, Phys. Rev. Lett. **83** (1999) 4690, [arXiv:hep-th/9906064].

[265] S. B. Bae, P. Ko, H. S. Lee and J. Lee, Phys. Lett. B **487** (2000) 299 [arXiv:hep-ph/0002224].

[266] H. Davoudiasl, J. L. Hewett and T. G. Rizzo, Phys. Rev. Lett. **84** (2000) 2080 [arXiv:hep-ph/9909255].

[267] K. Cheung, Phys. Rev. D **63** (2001) 056007 [arXiv:hep-ph/0009232].

[268] H. Davoudiasl, J. L. Hewett and T. G. Rizzo, Phys. Rev. D **63** (2001) 075004 [arXiv:hep-ph/0006041].

[269] S. C. Park, H. S. Song and J. Song, Phys. Rev. D **63** (2001) 077701 [arXiv:hep-ph/0009245].

[270] G. Giudice, R. Rattazzi, J. Wells, Nucl. Phys. B **595** (2001) 250 [arXiv:hep-ph/0002178].

[271] C. Csaki, M.L. Graesser, G.D. Kribs, Phys. Rev. D **63** (2001) 065002-1 [arXiv:hep-th/0008151].

[272] T. Han, G. D. Kribs and B. McElrath, Phys. Rev. D **64** (2001) 076003 [arXiv:hep-ph/0104074].

[273] M. Chaichian, A. Datta, K. Huitu and Z. h. Yu, Phys. Lett. B **524** (2002) 161 [arXiv:hep-ph/0110035].

[274] G. Azuelos, D. Cavalli, H. Przysiezniak and L. Vacavant, Eur. Phys. J. direct C **4** (2002) 16.

[275] J. L. Hewett and T. G. Rizzo, arXiv:hep-ph/0202155.

[276] D. Dominici, B. Grzadkowski, J. F. Gunion and M. Toharia, arXiv:hep-ph/0206192.

[277] M. Battaglia, S. De Curtis, A. De Roeck, D. Dominici, J.F. Gunion, hep-ph/0304245.

[278] A. Djouadi, J. Kalinowski and M. Spira, Comput. Phys. Commun. **108** (1998) 56, [arXiv:hep-ph/9704448].

[279] D. Zeppenfeld, R. Kinnunen, A. Nikitenko and E. Richter-Was, Phys. Rev. D **62** (2000) 013009, [arXiv:hep-ph/0002036].

[280] D. Zeppenfeld, Int. J. Mod. Phys. A **16S1B** (2001) 831.

[281] T. G. Rizzo, arXiv:hep-ph/0209076.

[282] J.F. Gunion, M. Toharia and J. Wells, in preparation.

[283] D. Asner *et al.*, Eur. Phys. J. C **28** (2003) 27 [arXiv:hep-ex/0111056].

[284] N. Arkani-Hamed, S. Dimopoulos and G. R. Dvali, Phys. Lett. B **429**, 263 (1998); I. Antoniadis, N. Arkani-Hamed, S. Dimopoulos and G. R. Dvali, Phys. Lett. B **436**, 257 (1998); N. Arkani-Hamed, S. Dimopoulos and J. March-Russell, Phys. Rev. D **63**, 064020 (2001).

[285] A. Aranda, J.L. Díaz-Cruz, C. Balázs, [arXiv:hep-ph/0212133].

[286] M. Masip and A. Pomarol, Phys. Rev. D **60**, 096005 (1999).

[287] R. W. Assmann *et al.*, SLAC-REPRINT-2000-096

[288] W. D. Goldberger and M. B. Wise, Phys. Rev. Lett. **83** (1999) 4922 [arXiv:hep-ph/9907447].

[289] B. Grzadkowski and J. F. Gunion, Phys. Rev. D **68** (2003) 055002 [arXiv:hep-ph/0304241].

[290] T. Appelquist and H. U. Yee, Phys. Rev. D **67** (2003) 055002 [arXiv:hep-ph/0211023].

[291] F. J. Petriello, JHEP **0205** (2002) 003 [arXiv:hep-ph/0204067].

[292] K. Hagiwara *et al.* [Particle Data Group Collaboration], Phys. Rev. D **66** (2002) 010001.

[293] R. Barbieri and A. Strumia, Phys. Lett. B **462** (1999) 144 [arXiv:hep-ph/9905281]; arXiv:hep-ph/0007265.

[294] N. Arkani-Hamed, A. G. Cohen and H. Georgi, Phys. Lett. B **513** (2001) 232 [arXiv:hep-ph/0105239].

[295] N. Arkani-Hamed, A. G. Cohen, E. Katz, A. E. Nelson, T. Gregoire and J. G. Wacker, JHEP **0208** (2002) 021 [arXiv:hep-ph/0206020].

[296] N. Arkani-Hamed, A. G. Cohen, E. Katz and A. E. Nelson, JHEP **0207** (2002) 034 [arXiv:hep-ph/0206021].

[297] I. Low, W. Skiba and D. Smith, Phys. Rev. D **66** (2002) 072001 [arXiv:hep-ph/0207243].

[298] D. E. Kaplan and M. Schmaltz, arXiv:hep-ph/0302049.

[299] S. Chang and J. G. Wacker, arXiv:hep-ph/0303001.

[300] W. Skiba and J. Terning, arXiv:hep-ph/0305302.

[301] S. Chang, arXiv:hep-ph/0306034.

[302] S. Dimopoulos and J. Preskill, Nucl. Phys. B **199** (1982) 206; D. B. Kaplan and H. Georgi, Phys. Lett. B **136** (1984) 183; D. B. Kaplan, H. Georgi and S. Dimopoulos, Phys. Lett. B **136** (1984) 187; H. Georgi, D. B. Kaplan and P. Galison, Phys. Lett. B **143** (1984) 152; H. Georgi and D. B. Kaplan, Phys. Lett. B **145** (1984) 216; T. Banks, Nucl. Phys. B **243** (1984) 125; M. J. Dugan, H. Georgi and D. B. Kaplan, Nucl. Phys. B **254** (1985) 299.

[303] S. R. Coleman and E. Weinberg, Phys. Rev. D **7** (1973) 1888.

[304] T. Han, H. E. Logan, B. McElrath and L. T. Wang, Phys. Rev. D **67** (2003) 095004 [arXiv:hep-ph/0301040].

[305] T. Han, H. E. Logan, B. McElrath and L. T. Wang, Phys. Lett. B **563** (2003) 191 [arXiv:hep-ph/0302188].

[306] C. Csaki, J. Hubisz, G. D. Kribs, P. Meade and J. Terning, Phys. Rev. D **68** (2003) 035009 [arXiv:hep-ph/0303236].

[307] G. Burdman, M. Perelstein and A. Pierce, Phys. Rev. Lett. **90** (2003) 241802 [arXiv:hep-ph/0212228].

[308] C. Csaki, J. Hubisz, G. D. Kribs, P. Meade and J. Terning, Phys. Rev. D **67** (2003) 115002 [arXiv:hep-ph/0211124].

[309] J. L. Hewett, F. J. Petriello and T. G. Rizzo, arXiv:hep-ph/0211218.

[310] A. E. Nelson, arXiv:hep-ph/0304036.

[311] K. Hagiwara, R. D. Peccei, D. Zeppenfeld and K. Hikasa, Nucl. Phys. B **282** (1987) 253.

[312] R. V. Harlander and W. Kilgore, Phys. Rev. Lett. **88** (2002) 201801 [arXiv:hep-ph/0201206]; C. Anastasiou and K. Melnikov, Nucl. Phys. B **646** (2002) 220 [arXiv:hep-ph/0207004].

[313] D. Zeppenfeld, in *Proc. of the APS/DPF/DPB Summer Study on the Future of Particle Physics (Snowmass 2001)* ed. N. Graf, eConf **C010630** (2001) P123 [arXiv:hep-ph/0203123]; D. Zeppenfeld, R. Kinnunen, A. Nikitenko and E. Richter-Was, Phys. Rev. D **62** (2000) 013009 [arXiv:hep-ph/0002036]; A. Belyaev and L. Reina, JHEP **0208** (2002) 041 [arXiv:hep-ph/0205270].

[314] T. Abe *et al.* [American Linear Collider Working Group Collaboration], "Linear collider physics resource book for Snowmass 2001. 2: Higgs and supersymmetry studies," in *Proc. of the APS/DPF/DPB Summer Study on the Future of Particle Physics (Snowmass 2001)* ed. N. Graf, arXiv:hep-ex/0106056.

[315] E. Boos, J. C. Brient, D. W. Reid, H. J. Schreiber and R. Shanidze, Eur. Phys. J. C **19** (2001) 455 [arXiv:hep-ph/0011366].

[316] G. Jikia and S. Soldner-Rembold, Nucl. Phys. Proc. Suppl. **82** (2000) 373 [arXiv:hep-ph/9910366]; Nucl. Instrum. Meth. A **472** (2001) 133 [arXiv:hep-ex/0101056]; M. M. Velasco *et al.*, in *Proc. of the APS/DPF/DPB Summer Study on the Future of Particle Physics (Snowmass 2001)* ed. N. Graf, eConf **C010630** (2001) E3005 [arXiv:hep-ex/0111055]; D. Asner *et al.*, Eur. Phys. J. C **28** (2003) 27 [arXiv:hep-ex/0111056].

[317] K. Abe *et al.* [ACFA Linear Collider Working Group Collaboration], "Particle physics experiments at JLC," arXiv:hep-ph/0109166.

[318] B. Grzadkowski, J. F. Gunion and J. Kalinowski, Phys. Lett. B **480**, 287 (2000) [arXiv:hep-ph/0001093].

[319] D. M. Asner, J. B. Gronberg and J. F. Gunion, Phys. Rev. D **67**, 035009 (2003) [arXiv:hep-ph/0110320].

[320] D. Asner *et al.*, arXiv:hep-ph/0308103.

[321] P. Chankowski, T. Farris, B. Grzadkowski, J. F. Gunion, J. Kalinowski and M. Krawczyk, Phys. Lett. B **496**, 195 (2000) [arXiv:hep-ph/0009271].

[322] J. F. Gunion, arXiv:hep-ph/0012199; and in *Proc. of the APS/DPF/DPB Summer Study on the Future of Particle Physics (Snowmass 2001)* ed. N. Graf, eConf **C010630**, P116 (2001) [arXiv:hep-ph/0110362].

[323] J. F. Gunion and H. E. Haber, Phys. Rev. D **67**, 075019 (2003) [arXiv:hep-ph/0207010].

[324] J. R. Espinosa and J. F. Gunion, Phys. Rev. Lett. **82**, 1084 (1999) [arXiv:hep-ph/9807275].

[325] A. Alves, O. Eboli, T. Plehn and D. Rainwater, arXiv:hep-ph/0309042.

[326] C. Csaki, C. Grojean, L. Pilo and J. Terning, arXiv:hep-ph/0308038; G. Cacciapaglia, C, Csaki, C. Grojean, J. Terning, arXiv: hep-ph/0401160; C. Csaki, C. Grojean, J. Hubisz, Y. Shirman, J. Terning, arXiv: hep-ph/0310355.

[327] P.W. Higgs, Phys. Rev. Lett. 12 (1964) 132; Phys. Rev. Lett. 13 (1964) 508; Phys. Rev. 145 (1966) 1156; F. Englert and R. Brout, Phys. Rev. Lett. 13 (1964) 321; G.S. Guralnik, C.R. Hagen, and T.W. Kibble, Phys. Rev. Lett. 13 (1964) 585; T.W. Kibble, Phys. Rev. 155 (1967) 1554.

[328] S.L. Glashow, Nucl. Phys. 22 (1961) 579; A. Salam, in: N. Svartholm (ed.), *Elementary Particle Theory*, Almqvist and Wiksells, Stockholm, 1968; S. Weinberg, Phys. Rev. Lett. 19 (1967) 1264.

[329] K. Hagiwara et al. (Particle Data Group), Phys. Rev. D. 66 (2002) 010001.

[330] see, e.g.: M.S. Chanowitz, LBNL-52452, hep-ph/0304199.

[331] B. Lee, C. Quigg and H. Thacker, Phys. Rev. Lett. 38 (1977) 883; Phys. Rev. D16 (1977) 1519; D. Dicus and V. Mathur, Phys. Rev. D7 (1973) 3111.

[332] S. Weinberg, Phys. Rev. D13 (1976) 974; Phys. Rev. D19 (1979) 1277; L. Susskind, Phys. Rev. D20 (1979) 2619.

[333] For reviews of models of dynamical symmetry breaking, see: R. Sekhar Chivukula, A. Cohen, and K. Lane, Nucl. Phys. B343 (1990) 554; G. Cvetic, Rev. Mod. Phys. 71 (1999) 513; C.T. Hill and E.H. Simmons, *Strong Dynamics and Electroweak Symmetry Breaking*, hep-ph/0203079, to appear in Phys. Rept.

[334] T. Appelquist and C. Bernard, Phys. Rev. D22 (1980) 200; A. Longhitano, Phys. Rev. D22 (1980) 1166; Nucl. Phys. B188 (1981) 118.

[335] S. Weinberg, Phys. Rev. Lett. 17 (1966) 616; M.S. Chanowitz, M. Golden, and H. Georgi, Phys. Rev. D36 (1987) 1490.

[336] S. Weinberg, Physica 96A (1979) 327.

[337] M. Peskin and T. Takeuchi, Phys. Rev. Lett. 65 (1990) 964; Phys. Rev. D46 (1992) 381.

[338] K.J.F. Gaemers and G.J. Gounaris, Z. Phys. C1 (1979) 259; K. Hagiwara, K. Hikasa, R.D. Peccei, and D. Zeppenfeld, Nucl. Phys. B282 (1987) 253.

[339] A. Dobado and J.R. Pelaez, Phys. Rev. D56 (1997) 3057.

[340] S.N. Gupta, *Quantum Electrodynamics*, Gordon and Breach, 1981; M.S. Chanowitz, Phys. Rept. 320 (1999) 139.

[341] M. Diehl, O. Nachtmann, and F. Nagel, Eur. Phys. J. C27 (2003) 375.

[342] C.E. Vayonakis, Lett. Nuovo Cim. 17 (1976) 383; M.S. Chanowitz and M.K. Gaillard, Nucl. Phys. B261 (1985) 379; G.J. Gounaris, R. Kögerler, and H. Neufeld, Phys. Rev. D34 (1986) 3257; Y.-P. Yao and C.-P. Yuan, Phys. Rev. D38 (1988) 2237; J. Bagger and C. Schmidt, Phys. Rev. D34 (1990) 264.

[343] M.S. Chanowitz and M.K. Gaillard, Phys. Lett. B142 (1984) 85; G.L. Kane, W.W. Repko, and W.R. Rolnick, Phys. Lett. B148 (1984) 367; S. Dawson, Nucl. Phys. B249 (1985) 42; J. Lindfors, Z. Phys. C28 (1985) 427; J.F. Gunion, J. Kalinowski, and A. Tofighi-Niaki, Phys. Rev. Lett. 57 (1986) 2351.

[344] A. Denner and T. Hahn, Nucl. Phys. **B525** (1998) 27.

[345] V. Barger, K. Cheung, and R.J.N. Phillips, Phys. Rev. **D52** (1995) 3815.

[346] E.E. Boos, H.-J. He, W. Kilian, A. Pukhov, and P.M. Zerwas, Phys. Rev. **D57** (1997) 1553.

[347] E.E. Boos, H.-J. He, W. Kilian, A. Pukhov, and P.M. Zerwas, Phys. Rev. **D61** (2000) 077901.

[348] W. Kilian, in: *Proceedings of the APS / DPF / DPB Summer Study on the Future of Particle Physics (Snowmass 2001)*, eConf C010630 (2001) P106.

[349] R. Chierici, S. Rosati, and M. Kobel, LC-PHSM-2001-038, and in: J.A. Aguilar-Saavedra et al. (ECFA/DESY LC Physics Working Group), *TESLA: Technical design report. Part III: Physics at an e^+e^- Linear Collider*, DESY-2001-011, hep-ph/0106315.

[350] W. Menges, *A Study of Charged Current Triple Gauge Couplings at TESLA*, LC-PHSM-2001-022.

[351] J. Bagger, V. Barger, K. Cheung, J. Gunion, T. Han, G.A. Ladinsky, R. Rosenfeld, and C.-P. Yuan, Phys. Rev. **D49** (1994) 1246.

[352] J. Bagger, V. Barger, K. Cheung, J. Gunion, T. Han, G.A. Ladinsky, R. Rosenfeld, and C.-P. Yuan, Phys. Rev. **D52** (1995) 3878.

[353] A. Dobado, M.J. Herrero, J.R. Pelaez, E. Ruiz Morales, and M.T. Urdiales, Phys. Lett. **B352** (1995) 400; A. Dobado and M.T. Urdiales, Z. Phys. **C71** (1996) 659.

[354] A.S. Belyaev, O.J.P. Éboli, M.C. Gonzalez-Garcia, J.K. Mizukoshi, S.F. Novaes, and I. Zacharov, Phys. Rev. **D59** (1998) 015022.

[355] J.M. Butterworth, B.E. Cox, and J.R. Forshaw, Phys. Rev. **D65** (2002) 096014.

[356] N. Amapane, M. Arneodo, G. Cerminara, A. Krokhotin, C. Mariotti, and P. Zych, work in progress.

[357] E. Accomando, A. Ballestrero, and E. Maina, work in progress.

[358] T. Sjöstrand, Comput. Phys. Commun. **82** (1994) 74.

[359] A. Pukhov, E. Boos, M. Dubinin, V. Edneral, V. Ilyin, D. Kovalenko, A. Kryukov, V. Savrin, S. Shichanin, and A. Semenov, INP-MSU 98-41/542, hep-ph/9908288.

[360] S. Abdullin, A. Khanov and N. Stepanov, CMS TN/94-180.

[361] S. Boogert, B. Cox, I. Duerdoth, and A. Osorio, work in progress.

[362] P. Krstonosic et al., work in progress.

[363] M. Beyer et al., work in progress.

[364] W. Kilian, LC-TOOL-2000-039.

[365] The American Linear Collider Working Group, T. Abe *et al.*, *Proc. of the APS/DPF/DPB Summer Study on the Future of Particle Physics (Snowmass 2001)* ed. N. Graf, hep-ex/0106057.

[366] T. L. Barklow, *Proc. of the APS/DPF/DPB Summer Study on the Future of Particle Physics (Snowmass 2001)* ed. N. Graf, eConf **C010630** (2001) E3067, hep-ph/0112286.

[367] T. L. Barklow *et al.*, hep-ph/9704217.

[368] G. Weiglein, arXiv:hep-ph/0301111.

[369] N. Ghodbane and H. U. Martyn, arXiv:hep-ph/0201233.

[370] [LEP Higgs Working Group Collaboration], arXiv:hep-ex/0107030.

[371] B. C. Allanach, C. G. Lester, M. A. Parker and B. R. Webber, JHEP **0009** (2000) 004 [arXiv:hep-ph/0007009].

[372] T. Sjöstrand, P. Edén, C. Friberg, L. Lönnblad, G. Miu, S. Mrenna, E. Norrbin, Comput.Phys.Commun. 135 (2001) 238; T. Sjostrand, L. Lonnblad and S. Mrenna, "PYTHIA 6.2: Physics and manual", arXiv:hep-ph/0108264.

[373] E. Richter-Was, D. Froidevaux and L. Poggioli, "ATLFAST 2.0: a fast simulation package for ATLAS", Tech. Rep. ATL-PHYS-98-131 (1998)

[374] G. Polesello, J. Phys. G **30** (2004) 1185.

[375] H. Baer, F. E. Paige, S. D. Protopopescu, X. Tata, hep-ph/9305342; hep-ph/980432; hep-ph/0001086.

[376] G. Marchesini, B.R. Webber, G. Abbiendi, I.G. Knowles, M.H. Seymour and L. Stanco, Comput. Phys. Commun. 67 (1992) 465;
G. Corcella, I.G. Knowles, G. Marchesini, S. Moretti, K. Odagiri, P. Richardson, M.H. Seymour and B.R. Webber, JHEP **0101** (2001) 010 [hep-ph/9912396].

[377] C.G.Lester, D.J.Summers, Phys.Lett. B463 (1999) 99.

[378] G. Moortgat-Pick *et al.*, these proceedings.

[379] I. Hinchliffe, F. E. Paige, M. D. Shapiro, J. Soderqvist and W. Yao, Phys. Rev. D **55**, 5520 (1997).

[380] J. Hisano, K. Kawagoe, R. Kitano and M. M. Nojiri, Phys. Rev. D **66**, 115004 (2002).

[381] J. Hisano, K. Kawagoe and M. M. Nojiri, Phys. Rev. D **68**, 035007 (2003).

[382] H.P. Nilles, *Phys. Rev.* **110**, (1984) 1

[383] H. Baer, C.H. Chen, F. Paige and X. Tata, *Phys. Rev.* D **52**, (1995) 2746; *Phys. Rev.* D **53**, (1996) 6241.

[384] S. Abdullin and F. Charles, *Nucl. Phys.* B **547**, (1999) 60; S. Abdullin, Ž. Antunović and M. Dželalija, *Mod. Phys. Lett.* A **15**, (2000) 465.

[385] H. Baer, C.H. Chen, F. Munroe, F. Paige and X. Tata, *Phys. Rev.* D **51**, (1995) 1046.

[386] M. Battaglia *et al.*, hep-ph/0106204 (2001); hep-ph/0112013 (2001).

[387] B.C. Allanach *et al.*, hep-ph/0202233 (2002).

[388] T. Sjostrand, Computer Phys. Comm. **82**, (1994) 74.

[389] F. Paige and S. Protopopescu, in *Supercollider Physics*, p. 41, ed. D. Soper (World Scientific, 1986); H. Baer, F. Paige, S. Protopopescu and X. Tata, in *Proceedings of the Workshop on Physics at Current Accelerators and Supercolliders*, ed. J. Hewett, A. White and D. Zeppenfeld (Argonne National Laboratory, 1993).

[390] S. Abdullin, A. Khanov and N. Stepanov, CMS TN/94-180 (1994).

[391] M. Chiorboli, A. Tricomi, *Squark and gluino reconstruction methods with the CMS detector*, CMS Note in preparation.

[392] M. Chiorboli, *Supersymmetric Particle Reconstructions with the CMS detector at LHC*, Ph.D. Thesis, Catania (2003),
`http://cmsdoc.cern.ch/documents/03/doc2003_002.pdf`.

[393] I. Hincliffe *et al.*, "*Precision SUSY measurements at LHC: Point 3.*", ATLAS Internal Note, 1997, ATLAS-NOTE-Phys-109; F. Gianotti, "*Precision SUSY measurements with ATLAS for SUGRA Point 4*", ATLAS Internal Note, 1997, PHYS-No-110; G. Polesello *et al.*, Precision SUSY measurements with ATLAS fro SUGRA point 5", ATLAS Internal Note, 1997, PHYS-No-111.

[394] P. Grannis, hep-ex/0211002; M. Battaglia et al., hep-ph/0201177.

[395] J. Kalinowski, hep-ph/0309235.

[396] H.-U. Martyn, Linear Collider Note LC-PHSM-2003-071 and talk at ECFA/DESY LC workshop Prague, November 2002,
http://www-hep2.fzu.cz/ecfadesy/Talks/SUSY/

[397] U. Nauenberg, talk at ECFA/DESY LC workshop Prague, November 2002, http://www-hep2.fzu.cz/ecfadesy/Talks/SUSY/

[398] M. Dima et al, Phys. Rev. D 65 (2002) 71701.

[399] A. Freitas, A. v. Manteuffel, P.M. Zerwas, hep-ph/0310112.

[400] J. Feng, D. Finell, Phys. Rev. D 49 (1994) 2369.

[401] Y. Kato et al, APPI Winter Institute, February 2003.

[402] K. Desch, talk at ECFA/DESY LC workshop Prague, November 2002, http://www-hep2.fzu.cz/ecfadesy/Talks/SUSY/

[403] B.K. Gjelsten, J. Hisano, K. Kawagoe, E. Lytken, D. Miller, M. Nojiri, P. Osland, G. Polesello, contribution to this report.

[404] M. Chiorboli, A. Tricomi, contribution to this report.

[405] B. Allanach et al, contribution to this report.

[406] SPA Project (SUSY PARAMETER ANALYSIS), SUSY working group of the ECFA LC STUDY, http://www-flc.desy.de/spa/

[407] A summary of current LHC and LC studies can be found e.g. in F.E. Paige, arXiv:hep-ph/0211017; J. Kalinowski, arXiv:hep-ph/0309235, and references therein.

[408] T. Tsukamoto, K. Fujii, H. Murayama, M. Yamaguchi and Y. Okada, Phys. Rev. D **51** (1995) 3153. J. L. Feng, M. E. Peskin, H. Murayama and X. Tata, Phys. Rev. D **52** (1995) 1418 [arXiv:hep-ph/9502260].

[409] S. Y. Choi, J. Kalinowski, G. Moortgat-Pick and P. M. Zerwas, Eur. Phys. J. C **22** (2001) 563 [arXiv:hep-ph/0108117]; S. Y. Choi, J. Kalinowski, G. Moortgat-Pick and P. M. Zerwas, Eur. Phys. J. C **23** (2002) 769 [arXiv:hep-ph/0202039].

[410] K. Desch, J. Kalinowski, G. Moortgat-Pick, M. M. Nojiri and G. Polesello, JHEP **0402** (2004) 035 [arXiv:hep-ph/0312069].

[411] H. E. Haber and G. L. Kane, Phys. Rep. **117** (1985) 75.

[412] S. Y. Choi, A. Djouadi, M. Guchait, J. Kalinowski, H. S. Song and P. M. Zerwas, Eur. Phys. J. C **14** (2000) 535 [arXiv:hep-ph/0002033]; S. Y. Choi, A. Djouadi, H. K. Dreiner, J. Kalinowski and P. M. Zerwas, Eur. Phys. J. C **7** (1999) 123 [arXiv:hep-ph/9806279].

[413] G. Moortgat-Pick, A. Bartl, H. Fraas and W. Majerotto, arXiv:hep-ph/0002253.

[414] S. Ambrosanio, B. Mele, G. Montagna, O. Nicrosini and F. Piccinini, Nucl. Phys. B **478** (1996) 46 [arXiv:hep-ph/9601292].

[415] T. Blank and W. Hollik, hep-ph/0011092; H. Eberl, M. Kincel, W. Majerotto and Y. Yamada, hep-ph/0104109. T. Fritzsche and W. Hollik, Eur. Phys. J. C **24** (2002) 619 [arXiv:hep-ph/0203159].

[416] E. Boos, G. Moortgat-Pick, H. U. Martyn, M. Sachwitz and A. Vologdin, arXiv:hep-ph/0211040; E. Boos, H. U. Martyn, G. Moortgat-Pick, M. Sachwitz, A. Sherstnev and P. M. Zerwas, Eur. Phys. J. C **30** (2003) 395 [arXiv:hep-ph/0303110].

[417] H.U. Martyn, talk given at the ECFA/DESY Linear Collider workshop, Prague, November 2002, http://www-hep2.fzu.cz/ecfadesy/Talks/SUSY/, and LC-note LC-PHSM-2003-071. M. Dima *et al.*, Phys. Rev. D 65 (2002) 071701.

[418] M. Ball, diploma thesis, University of Hamburg, January 2003, http://www-flc.desy.de/thesis/diplom.2002.ball.ps.gz; see also talk by K. Desch at the ECFA/DESY Linear Collider workshop, Prague, November 2002, http://www-hep2.fzu.cz/ecfadesy/Talks/SUSY/.

[419] 'Polarisation Write-Up: Beam Polarisation at a future Linear Collider', working group document by the polarisation 'POWER working group', G. Moortgat-Pick et al., in preparation, further details: http://www.ippp.durham.ac.uk/ gudrid/power.

[420] H. Baer, C. H. Chen, M. Drees, F. Paige and X. Tata, Phys. Rev. D **59** (1999) 055014 [arXiv:hep-ph/9809223]; J. L. Feng and T. Moroi, Nucl. Phys. Proc. Suppl. **62** (1998) 108 [arXiv:hep-ph/9707494]; V. D. Barger, T. Han and J. Jiang, Phys. Rev. D **63** (2001) 075002 [arXiv:hep-ph/0006223]; J. F. Gunion, T. Han, J. Jiang and A. Sopczak, hep-ph/0212151.

[421] G. Polesello, contribution to this report.

[422] H. P. Nilles, Phys. Rept. **110** (1984) 1.

[423] H. E. Haber, G. L. Kane, *Phys. Rept.* **117** (1985) 75.

[424] A. B. Lahanas, D. V. Nanopoulos, *Phys. Rept.* **145** (1987) 1.

[425] S. Ferrara, ed., *Supersymmetry*, vol. 1-2. North Holland/World Scientific, Singapore, 1987.

[426] J. Guasch, W. Hollik, J. Solà, JHEP **0210** (2002) 040 [arXiv:hep-ph/0207364].

[427] J. Guasch, W. Hollik, J. Solà, Nucl. Phys. Proc. Suppl. **116**, 301 (2003) [arXiv:hep-ph/0210118].

[428] A. Djouadi, W. Hollik and C. Junger, Phys. Rev. D **55** (1997) 6975 [arXiv:hep-ph/9609419].

[429] M. M. Nojiri, K. Fujii and T. Tsukamoto, Phys. Rev. D **54**, 6756 (1996) [arXiv:hep-ph/9606370].

[430] H. C. Cheng, J. L. Feng and N. Polonsky, Phys. Rev. D **56**, 6875 (1997) [arXiv:hep-ph/9706438].

[431] H. C. Cheng, J. L. Feng and N. Polonsky, Phys. Rev. D **57**, 152 (1998) [arXiv:hep-ph/9706476].

[432] E. Katz, L. Randall and S. f. Su, Nucl. Phys. B **536** (1998) 3 [arXiv:hep-ph/9801416].

[433] K. i. Hikasa and Y. Nakamura, Z. Phys. C **70** (1996) 139 [Erratum-ibid. C **71** (1996) 356] [arXiv:hep-ph/9501382].

[434] J. Guasch, J. Solà and W. Hollik, Phys. Lett. B **437** (1998) 88 [arXiv:hep-ph/9802329].

[435] J. Guasch, W. Hollik and J. Solà, Phys. Lett. B **510** (2001) 211 [arXiv:hep-ph/0101086].

[436] *Programs to compute the one-loop corrected partial decay width:* Γ*(sfermion → fermion chargino/neutralino)* available from `http://www-itp.physik.uni-karlsruhe.de/~guasch/progs`

[437] M. Ciuchini, E. Franco, A. Masiero and L. Silvestrini, Phys. Rev. D **67** (2003) 075016 [arXiv:hep-ph/0212397].

[438] T. Besmer, C. Greub and T. Hurth, Nucl. Phys. B **609** (2001) 359 [arXiv:hep-ph/0105292].

[439] F. Gabbiani, E. Gabrielli, A. Masiero and L. Silvestrini, Nucl. Phys. B **477** (1996) 321 [arXiv:hep-ph/9604387].

[440] J. S. Hagelin, S. Kelley and T. Tanaka, Nucl. Phys. B **415** (1994) 293.

[441] W. Porod, Comput. Phys. Commun. **153** (2003) 275 [arXiv:hep-ph/0301101].

[442] F. Borzumati, C. Greub, T. Hurth and D. Wyler, Phys. Rev. D **62** (2000) 075005 [arXiv:hep-ph/9911245].

[443] M. Chiorboli et al., these proceedings.

[444] N. Arkani-Hamed, J. L. Feng, L. J. Hall and H. Cheng, Phys. Rev. Lett. **77** (1996) 1937 [hep-ph/9603431].

[445] F. Deppisch, H. Päs, A. Redelbach, R. Rückl and Y. Shimizu, Eur. Phys. J. C **28** (2003) 365 [arXiv:hep-ph/0206122].

[446] N. V. Krasnikov, JETP Lett. **65** (1997) 148 [arXiv:hep-ph/9611282]. S. I. Bityukov and N. V. Krasnikov, arXiv:hep-ph/9806504. K. Agashe and M. Graesser, Phys. Rev. D **61** (2000) 075008 [arXiv:hep-ph/9904422]; I. Hinchliffe and F. E. Paige, Phys. Rev. D **63** (2001) 115006 [arXiv:hep-ph/0010086]; J. Hisano, R. Kitano and M. M. Nojiri, Phys. Rev. D **65** (2002) 116002; D.F. Carvalho *et al.*, hep-ph/0206148.

[447] N. Arkani-Hamed, J. L. Feng, L. J. Hall and H. Cheng, Nucl. Phys. B **505** (1997) 3 [hep-ph/9704205].

[448] J. Hisano, M. M. Nojiri, Y. Shimizu and M. Tanaka, Phys. Rev. D **60** (1999) 055008 [hep-ph/9808410].

[449] M. Guchait, J. Kalinowski and P. Roy, Eur. Phys. J. C **21** (2001) 163 [arXiv:hep-ph/0103161].

[450] W. Porod and W. Majerotto, Phys. Rev. D **66** (2002) 015003 [arXiv:hep-ph/0201284].

[451] F. Deppisch, H. Päs, A. Redelbach, R. Rückl and Y. Shimizu, accepted for publication in Phys. Rev. D, arXiv:hep-ph/0310053.

[452] J. Kalinowski, Acta Phys. Polon. B **32** (2001) 3755.

[453] J. Kalinowski, Acta Phys. Polon. B **33** (2002) 2613 [arXiv:hep-ph/0207051].

[454] F. Gabbiani, E. Gabrielli, A. Masiero and L. Silvestrini, Nucl. Phys. B **477** (1996) 321 [arXiv:hep-ph/9604387].

[455] J. L. Feng, Y. Nir and Y. Shadmi, Phys. Rev. D **61** (2000) 113005 [arXiv:hep-ph/9911370].

[456] M. Gell-Mann, P. Ramond and R. Slansky, Print-80-0576 (CERN). T. Yanagida, Prog. Theor. Phys. **64** (1980) 1103; R. N. Mohapatra and G. Senjanovic, Phys. Rev. Lett. **44** (1980) 912; Phys. Rev. D **23** (1981) 165.

[457] L. Serin and R. Stroynowski, ATLAS Internal Note (1997).

[458] D. Denegri, priv. comm.

[459] M. Battaglia *et al.*, Eur. Phys. J. C **22** (2001) 535 [arXiv:hep-ph/0106204].

[460] J. Hisano, T. Moroi, K. Tobe and M. Yamaguchi, Phys. Rev. D **53** (1996) 2442 [arXiv:hep-ph/9510309]; Y. Okada, K. I. Okumura and Y. Shimizu, Phys. Rev. D **61**, 094001 (2000) [arXiv:hep-ph/9906446]; T. Fukuyama, T. Kikuchi and N. Okada, Phys. Rev. D **68** (2003) 033012 [arXiv:hep-ph/0304190]; E. Jankowski and D. W. Maybury, arXiv:hep-ph/0401132; M. Hirouchi and M. Tanaka, Phys. Rev. D **58** (1998) 032004 [arXiv:hep-ph/9712532].

[461] J. A. Casas and A. Ibarra, Nucl. Phys. B **618** (2001) 171 [arXiv:hep-ph/0103065].

[462] J. Hisano and D. Nomura, Phys. Rev. D **59** (1999) 116005 [arXiv:hep-ph/9810479].

[463] M. C. Gonzalez-Garcia, M. Maltoni, C. Pena-Garay and J. W. F. Valle, Phys. Rev. D **63** (2001) 033005 [arXiv:hep-ph/0009350].

[464] R. Becker and C. Vander Velde, IIHE-93-08 *Prepared for Working Group on e+ e- Collisions at 500-GeV: The Physics Potential, Munich, Germany, 20 Nov 1992*.

[465] T. Mori, for the MEG Collab., EXP PSI-R-99-05, *Prepared for 31st Int. Conference on High Energy Physics (ICHEP 2002), Amsterdam, The Netherlands, 24-31 Jul 2002*. See also http://meg.web.psi.ch/docs/calculator/index.html.

[466] C. H. Chen, M. Drees and J. F. Gunion, Phys. Rev. Lett. **76**, 2002 (1996) [hep-ph/9512230]. Phys. Rev. **D55**, 330 (1997) [hep-ph/9607421]. and errata [hep-ph/9902309].

[467] J. F. Gunion and S. Mrenna, Phys. Rev. **D62**, 015002 (2000) [hep-ph/9906270].

[468] J. L. Feng, T. Moroi, L. Randall, M. Strassler and S. Su, Phys. Rev. Lett. **83**, 1731 (1999) [hep-ph/9904250].

[469] T. Gherghetta, G. F. Giudice and J. D. Wells, Nucl. Phys. **B559**, 27 (1999) [hep-ph/9904378].

[470] D.K. Ghosh, A. Kundu, P. Roy and S. Roy, Phys. Rev. **D64** 115001 (2001) [hep-ph/0104217]; D.K. Ghosh, P. Roy and S. Roy, JHEP **08**, 031 (2000) [hep-ph/0004127]; D. Choudhury, D.K. Ghosh and S. Roy, Nucl. Phys. **B646**, 3 (2002) [hep-ph/0208240].

[471] P. Abreu *et al.* [DELPHI Collaboration], Eur. Phys. J. **C11**, 1 (1999) [hep-ex/9903071] and CERN-EP-2000-033.

[472] M. Acciarri *et al.* [L3 Collaboration], Phys. Lett. **B482**, 31 (2000) [hep-ex/0002043].

[473] J.F. Gunion and S. Mrenna, Phys. Rev. **D64**, 075002 (2001) [hep-ph/0103167].

[474] F.E. Paige and J. Wells, hep-ph/0001249.

[475] H. Baer, J. K. Mizukoshi and X. Tata, Phys. Lett. **B488**, 367 (2000) [hep-ph/0007073].

[476] A. J. Barr, C. G. Lester, M. A. Parker, B. C. Allanach and P. Richardson, JHEP **0303**, 045 (2003) [arXiv:hep-ph/0208214].

[477] J. Amundson *et al.*, arXiv:hep-ph/9609374.

[478] See the contribution by H. Baer, C. Chen and J.Gunion in B. Allanach *et al.* [R parity Working Group Collaboration], "Searching for R-parity violation at Run-II of the Tevatron," arXiv:hep-ph/9906224.

[479] V.S. Kaplunovsky and J. Louis, Phys. Lett. **B306**, 269 (1993); A. Brignole, L.E. Ibanez and C. Munoz, Nucl. Phys. **B422** , 125 (1994), [E: **B436**, 747 (1995)]; CERN-TH/97-143 [hep-ph/9707209].

[480] S. Raby, Phys. Rev. **D56**, 2852 (1997); S. Raby, Phys. Lett. B **422**, 158 (1998) [arXiv:hep-ph/9712254].

[481] L.R. Roszkowski and M. Shifman, Phys. Rev. **D53**, 404 (1996).

[482] G. L. Kane and S. F. King, Phys. Lett. B **451**, 113 (1999) [arXiv:hep-ph/9810374].

[483] S. Raby and K. Tobe, Nucl. Phys. B **539**, 3 (1999) [arXiv:hep-ph/9807281].

[484] S. Berge and M. Klasen, arXiv:hep-ph/0303058.

[485] S. Berge and M. Klasen, Phys. Rev. D **66**, 115014 (2002) [arXiv:hep-ph/0208212].

[486] S. Berge and M. Klasen, Eur. Phys. J. C **30**, 123 (2003) [arXiv:hep-ph/0303032].

[487] J. Wess and B. Zumino, Nucl. Phys. B **70** (1974) 39.

[488] G. A. Blair, W. Porod and P. M. Zerwas, Eur. Phys. J. C **27** (2003) 263 [arXiv:hep-ph/0210058].

[489] S. Y. Choi, A. Djouadi, M. Guchait, J. Kalinowski, H.S. Song and P. M. Zerwas, Eur. Phys. J. C **14** (2000) 535 [arXiv:hep-ph/0002033]; V. D. Barger, T. Han, T. J. Li and T. Plehn, Phys. Lett. B **475** (2000) 342 [arXiv:hep-ph/9907425]; S. Y. Choi, J. Kalinowski, G. Moortgat-Pick and P. M. Zerwas, Eur. Phys. J. C **22** (2001) 563 [Addendum-ibid. C **23** (2002) 769] [arXiv:hep-ph/0108117]; K. Desch, J. Kalinowski, G. Moortgat-Pick, M. M. Nojiri and G. Polesello, arXiv:hep-ph/0312069.

[490] P. Fayet and J. Iliopoulos, Phys. Lett. B **51** (1974) 461.

[491] A. Djouadi, J. L. Kneur and G. Moultaka, arXiv:hep-ph/0211331.

[492] P. Skands *et al.*, arXiv:hep-ph/0311123.

[493] G. Ganis, MSMlib (unpublished)

[494] V. D. Barger, T. Falk, T. Han, J. Jiang, T. Li and T. Plehn, Phys. Rev. D **64** (2001) 056007 [arXiv:hep-ph/0101106].

[495] W. Beenakker, R. Hopker, M. Spira and P. M. Zerwas, Nucl. Phys. B **492** (1997) 51 [arXiv:hep-ph/9610490]; W. Beenakker, M. Kramer, T. Plehn, M. Spira and P. M. Zerwas, Nucl. Phys. B **515** (1998) 3 [arXiv:hep-ph/9710451]; W. Beenakker, M. Klasen, M. Kramer, T. Plehn, M. Spira and P. M. Zerwas, Phys. Rev. Lett. **83** (1999) 3780 [arXiv:hep-ph/9906298].

[496] F. James and M. Roos, Comput. Phys. Commun. **10** (1975) 343.

[497] M. Muhlleitner, A. Djouadi and Y. Mambrini, arXiv:hep-ph/0311167.

[498] R. Lafaye, T. Plehn and D. Zerwas, *Prepared for Workshop on Physics at TeV Colliders, Les Houches, France, 2003, LAPP-EXP-2003-27, CERN-TH/2003-312, LAL 04/06*

[499] B. C. Allanach, Comput. Phys. Commun. **143** (2002) 305 [arXiv:hep-ph/0104145].

[500] H. Baer, F. E. Paige, S. D. Protopescu and X. Tata, arXiv:hep-ph/0312045.

[501] B. K. Gjelsten *et al.*, H.-U. Martyn, M. Chiorboli *et al.*, all in this report.

[502] M. Drees and S. P. Martin, arXiv:hep-ph/9504324.

[503] F. James and M. Roos, "'Minuit' A System For Function Minimization And Analysis Of The Parameter Errors And Correlations," Comput. Phys. Commun. **10** (1975) 343.

[504] W. Porod, "Phenomenology of stops, sbottoms, staus and tau-sneutrino", arXiv:hep-ph/9804208.

[505] Isajet 7.69, by F. Paige, S. Protopopescu, H. Baer and X. Tata, hep-ph/0312045 (2003).

[506] H. Baer, C. Balazs and A. Belyaev, JHEP**0203** (2002) 042.

[507] H. Baer, C. Balazs, A. Belyaev, T. Krupovnickas and X. Tata, JHEP**0306** (2003) 054.

[508] H. Baer, T. Krupovnickas and X. Tata, JHEP**0307** (2003) 020.

[509] H. Baer, A. Belyaev, T. Krupovnickas and X. Tata, JHEP**0402** (2004) 007.

[510] H. Baer, T. Krupovnickas and X. Tata, JHEP**0406** (2004) 061.

[511] H. Baer, C. Balazs, *JCAP*, 0305:006, 2003; J. Ellis, K. Olive, Y. Santoso, V. Spanos, *Phys. Lett.*, B565:176–182, 2003; U. Chattopadhyay, A. Corsetti, P. Nath, *Phys. Rev.*, D68:035005, 2003. A. B. Lahanas, D. V. Nanopoulos, *Phys. Lett.*, B568:55–62, 2003; G. Bélanger, F. Boudjema, A. Cottrant, A. Pukhov, A. Semenov, hep-ph/0407218.

[512] A. Balbi, *et al.*, *Astrophys. J.*, 588:L5–L8, 2003.

[513] B. C. Allanach, D. Grellscheid, and F. Quevedo, *JHEP*, 05:048, 2002; B. C. Allanach, D. Grellscheid, and F. Quevedo, *JHEP*, 07:069, 2004.

[514] B. C. Allanach, G. Bélanger, F. Boudjema, A. Pukhov, and W. Porod, hep-ph/0402161.

[515] B. C. Allanach, G. Bélanger, F. Boudjema, A. Pukhov, in preparation.

[516] G. Bélanger, F. Boudjema, A. Pukhov, and A. Semenov, hep-ph/0405253; G. Bélanger, F. Boudjema, A. Pukhov, and A. Semenov, *Comput. Phys. Commun.*, 149:103, 2002.

[517] M. Battaglia *et. al.*, *Eur. Phys. J.* **C33** (2004) 273.

[518] P. Bambade, M. Berggren, F. Richard, and Z. Zhang, hep-ph/0406010; H.-U. Martyn, hep-ph/0408226.

[519] S. Y. Choi, J. Kalinowski, G. Moortgat-Pick, and P. M. Zerwas, *Eur. Phys. J.*, C22:563–579, 2001; S. Y. Choi et al., *Eur. Phys. J.*, C14:535–546, 2000.

[520] B. C. Allanach, S. Kraml and W. Porod, JHEP **0303** (2003) 016 [arXiv:hep-ph/0302102].

[521] J. Hisano, K. Kawagoe and M. M. Nojiri, arXiv:hep-ph/0304214.

[522] G. A. Blair et al., these proceedings.

[523] C.G. Lester *et al*, JHEP **0009** (2000) 004.

[524] L. Alvarez-Gaume, J. Polchinski and M.B. Wise, Nucl. Phys. **B221** (1983) 495; L. Ibanez, Phys. Lett. **B118** (1982) 73; J. Ellis, D.V. Nanopoulos and K. Tamvakis, Phys. Lett. **B121** (1983) 123; K. Inoue *et al.*, Prog. Theor. Phys. **68** (1982) 927; A.H. Chamseddine, R. Arnowitt and P. Nath, Phys. Rev. Lett. **49** (1982) 970.

[525] F. Paige and S. Protopopescu, in Supercollider Physics, ed. D. Soper (World Scientific, 1986); H. Baer, F. Paige, S. Protopopescu and X. Tata, in Proc. Workshop on Physics at Current Accelerators and Supercolliders, ed. J. Hewett, A. White and D. Zeppenfeld (Argonne National Laboratory, 1993).

[526] H.-U. Martyn, Private Communication.

[527] D.R. Tovey, Eur. Phys. J. directC **4**, N4 (2002) 1-24 (Atlas Scientific Note SN-ATLAS-2002-020).

[528] B. C. Allanach, D. Grellscheid and F. Quevedo, JHEP **0205** (2002) 048 [arXiv:hep-ph/0111057].

[529] K. Benakli, Phys. Rev. D **60** (1999) 104002 [arXiv:hep-ph/9809582]; C. P. Burgess, L. E. Ibanez and F. Quevedo, Phys. Lett. B **447** (1999) 257 [arXiv:hep-ph/9810535].

[530] L. E. Ibanez, arXiv:hep-ph/9905349.

[531] B.C. Allanach, D. Grellscheid and F. Quevedo, JHEP **0407** (2004) 069.

[532] W. Buchmüller, K. Hamaguchi, M. Ratz, T. Yanagida, hep-ph/0402179.

[533] D. E. Kaplan, G. D. Kribs, M. Schmaltz, Phys. Rev. **D62** (2000) 035010;
Z. Chacko, M. A. Luty, A. E. Nelson, E. Pontón, JHEP **01** (2000) 003;
K. Inoue, M. Kawasaki, M. Yamaguchi, T. Yanagida, Phys. Rev. **D45** (1992) 328.

[534] H. P. Nilles, Phys. Rept. **110** (1984) 1.

[535] G. F. Giudice, R. Rattazzi, Phys. Rept. **322** (1999) 419.

[536] M. Bolz, W. Buchmüller, M. Plümacher, Phys. Lett. **B443** (1998) 209;
M. Fujii, T. Yanagida, Phys. Lett. **B549** (2002) 273;
J. L. Feng, A. Rajaraman, F. Takayama, Phys. Rev. **D68** (2003) 063504;
W. Buchmüller, K. Hamaguchi, M. Ratz, Phys. Lett. **B574** (2003) 156;
M. Fujii, M. Ibe, T. Yanagida, Phys. Rev. **D69** (2004) 015006;
J. Ellis, K. A. Olive, Y. Santoso, V. C. Spanos, hep-ph/0312262.

[537] M. Drees, X. Tata, Phys. Lett. **B252** (1990) 695.

[538] J. L. Feng, T. Moroi, Phys. Rev. **D58** (1998) 035001;
S. P. Martin, J. D. Wells, Phys. Rev. **D59** (1999) 035008.

[539] S. Ambrosanio, B. Mele, S. Petrarca, G. Polesello, A. Rimoldi, JHEP **01** (2001) 014.

[540] S. Ambrosanio, G. A. Blair, Eur. Phys. J. **C12** (2000) 287;
P. G. Mercadante, J. K. Mizukoshi, H. Yamamoto, Phys. Rev. **D64** (2001) 015005.

[541] W. Beenakker, R. Hopker, M. Spira, P. M. Zerwas, Nucl. Phys. **B492** (1997) 51.

[542] K. Maki, S. Orito, Phys. Rev. **D57** (1998) 554.

[543] Particle Data Group, K. Hagiwara et al., Phys. Rev. **D66** (2002) 010001.

[544] J. Wess, J. Bagger, *Supersymmetry and Supergravity*, Princeton University Press, Princeton, New Jersey, 1992.

[545] T. Lee, G.-H. Wu, Phys. Lett. **B447** (1999) 83.

[546] G. A. Blair, W. Porod and P. M. Zerwas, Phys. Rev. **D63** (2001) 017703 and Eur. Phys. J. **C27** (2003) 263; P. M. Zerwas *et al.*, Proceedings, Int. Conference on High Energy Physics ICHEP.2002, Amsterdam 2002.

[547] I. Hinchliffe et al., Phys. Rev. **D 55**, 5520 (1997); Atlas Collaboration, Technical Design Report 1999, Vol. II, CERN/LHC/99-15, ATLAS TDR 15.

[548] A. H. Chamseddine, R. Arnowitt and P. Nath, Phys. Rev. Lett. **49** (1982) 970; H. P. Nilles, Phys. Rept. **110** (1984) 1.

[549] H. Bachacou, I. Hinchliffe and F. E. Paige Phys.Rev. **D62** (2000) 015009.

[550] M. Chiorboli et al., these proceedings.

[551] F. Moortgat, these proceedings.

[552] H.-U. Martyn and G. A. Blair, hep-ph/9910416.

[553] A. Freitas, D. J. Miller and P. M. Zerwas, Eur. Phys. J. **C21** (2001) 361; A. Freitas, A. von Manteuffel and P. M. Zerwas, arXiv:hep-ph/0310182, Eur. Phys. J. in press.

[554] A. Freitas *et al*, Proceedings, Int. Conference on High Energy Physics ICHEP.2002, Amsterdam 2002.

[555] S.Y. Choi, A. Djouadi, M. Guchait, J. Kalinowski, H.S. Song and P.M. Zerwas, Eur. Phys. J. **C14** (2000) 535.

[556] S.Y. Choi, J. Kalinowski, G. Moortgat-Pick and P.M. Zerwas, Eur. Phys. J. **C22** (2001) 563 and Eur. Phys. J. **C23** (2002) 769.

[557] H.-U. Martyn, Talk at the Prague Session of the ECFA/DESY Workshop, 2002 and Linear Collider Note LC-PHSM-2003-071.

[558] H.-U. Martyn, these proceedings.

[559] A detailed discussion for SPS1a can also be found in the contribution by K.Desch, J.Kalinowski, G.Moortgat-Pick, M.Nojiri, and G.Polesello, these proceedings.

[560] K. Inoue, A. Kakuto, H. Komatsu, and S. Takeshita, Prog. Theor. Phys. **68**, 927 (1982); Erratum, *ibid.* **70**, 330 (1983).

[561] S. Martin and M. Vaughn, Phys. Rev. **D50**, 2282 (1994); Y. Yamada, Phys. Rev. **D50**, 3537 (1994); I. Jack, D.R.T. Jones, Phys. Lett. **B333** (1994) 372.

[562] J. Bagger, K. Matchev, D. Pierce, and R. Zhang, Nucl. Phys. **B491** (1997) 3.

[563] G. Degrassi, P. Slavich and F. Zwirner, Nucl. Phys. **B611** (2001) 403; A. Brignole, G. Degrassi, P. Slavich and F. Zwirner, Nucl. Phys. **B631** (2002) 195; Nucl. Phys. **B643** (2002) 79; A. Dedes and P. Slavich, Nucl. Phys. **B657** (2003) 333; A. Dedes, G. Degrassi and P. Slavich, hep-ph/0305127.

[564] S. Dimopoulos, S. Raby and F. Wilczek, Phys. Rev. **D24** (1981) 1681; L. E. Ibanez, G. G. Ross, Phys. Lett. **B105** (1981) 439; U. Amaldi, W. de Boer and H. Fürstenau, Phys. Lett. **B260** (191) 447; P. Langacker and M. Luo, Phys. Rev. **D44** (1991) 817; J. Ellis, S. Kelley, D. V. Nanopoulos, Phys. Lett. **B260** (1991) 161.

[565] S. Weinberg, Phys. Lett. **B91** (1980) 51; L.J. Hall, Nucl. Phys. **B178** (1981) 75.

[566] G.G. Ross and R.G. Roberts, Nucl. Phys. **B377** (1992) 571; H. Murayama and A. Pierce, Phys. Rev. **D65** (2002) 055009.

[567] H. Hagiwara *et al.* [Particle Data Group Collaboration], Phys. Rev. **D66** (2002) 010001-1.

[568] K. Mönig, in "Physics and Experiments with Future Linear e^+e^- Colliders", *eds.* A. Para, H.E. Fisk, Melville 2001, hep-ex/0101005.

[569] J. Erler, S. Heinemeyer, W. Hollik, G. Weiglein and P.M. Zerwas, Phys. Lett. **B486** (2000) 125.

[570] F. Abe *et al.* [CDF Collaboration], Phys. Rev. Lett. **74** (1995) 2626 [arXiv:hep-ex/9503002].

[571] S. Abachi *et al.* [D0 Collaboration], Phys. Rev. Lett. **74** (1995) 2632 [arXiv:hep-ex/9503003].

[572] D. E. Groom *et al.* [Particle Data Group Collaboration], Eur. Phys. J. C **15** (2000) 1.

[573] K. G. Chetyrkin, R. Harlander, T. Seidensticker and M. Steinhauser, Phys. Rev. D **60** (1999) 114015 [arXiv:hep-ph/9906273].

[574] A. Denner and T. Sack, Nucl. Phys. B **358** (1991) 46.

[575] I. I. Bigi, Y. L. Dokshitzer, V. A. Khoze, J. H. Kuhn and P. M. Zerwas, Phys. Lett. B **181** (1986) 157.

[576] M. Beneke *et al.*, arXiv:hep-ph/0003033, in "Standard model physics (and more) at the LHC" G. Altarelli and M. L. Mangano eds., *Geneva, Switzerland: CERN (2000) 529 p*.

[577] P. Nason, S. Dawson and R. K. Ellis, Nucl. Phys. B **303** (1988) 607;
W. Beenakker, H. Kuijf, W. L. van Neerven and J. Smith, Phys. Rev. D **40** (1989) 54;
M. L. Mangano, P. Nason and G. Ridolfi, Nucl. Phys. B **373** (1992) 295.

[578] S. Catani, M. L. Mangano, P. Nason and L. Trentadue, Nucl. Phys. B **478** (1996) 273 [arXiv:hep-ph/9604351].

[579] A. H. Hoang and T. Teubner, Phys. Rev. D **58** (1998) 114023 [arXiv:hep-ph/9801397]; A. H. Hoang and T. Teubner, Phys. Rev. D **60** (1999) 114027 [arXiv:hep-ph/9904468];
K. Melnikov and A. Yelkhovsky, Nucl. Phys. B **528** (1998) 59 [arXiv:hep-ph/9802379];
O. I. Yakovlev, Phys. Lett. B **457** (1999) 170 [arXiv:hep-ph/9808463];
M. Beneke, A. Signer and V. A. Smirnov, Phys. Lett. B **454** (1999) 137 [arXiv:hep-ph/9903260];
T. Nagano, A. Ota and Y. Sumino, Phys. Rev. D **60** (1999) 114014 [arXiv:hep-ph/9903498].

[580] K. G. Chetyrkin, J. H. Kuhn and M. Steinhauser, Nucl. Phys. B **482** (1996) 213 [arXiv:hep-ph/9606230];
R. Harlander and M. Steinhauser, Eur. Phys. J. C **2** (1998) 151 [arXiv:hep-ph/9710413].

[581] W. Beenakker, S. C. van der Marck and W. Hollik, Nucl. Phys. B **365** (1991) 24;
W. Beenakker, A. Denner and A. Kraft, Nucl. Phys. B **410** (1993) 219.

[582] D. Chakraborty, J. Konigsberg and D. Rainwater, arXiv:hep-ph/0303092.

[583] T. Stelzer, Z. Sullivan and S. Willenbrock, Phys. Rev. D **56** (1997) 5919 [arXiv:hep-ph/9705398];
B. W. Harris, E. Laenen, L. Phaf, Z. Sullivan and S. Weinzierl, Phys. Rev. D **66** (2002) 054024 [arXiv:hep-ph/0207055].

[584] M. C. Smith and S. Willenbrock, Phys. Rev. D **54** (1996) 6696 [arXiv:hep-ph/9604223].

[585] T. M. Tait, Phys. Rev. D **61** (2000) 034001 [arXiv:hep-ph/9909352];
A. Belyaev and E. Boos, Phys. Rev. D **63** (2001) 034012 [arXiv:hep-ph/0003260];
S. Zhu, Phys. Lett. B **524** (2002) 283 [Erratum-ibid. B **537** (2002) 351].

[586] A. S. Belyaev, E. E. Boos and L. V. Dudko, Phys. Rev. D **59** (1999) 075001 [arXiv:hep-ph/9806332].

[587] T. Stelzer, Z. Sullivan and S. Willenbrock, Phys. Rev. D **58** (1998) 094021 [arXiv:hep-ph/9807340].

[588] E. Boos, L. Dudko, V. Savrin, CMS NOTE-2000/065, 2000;
D. Green, K. Maeshima, R. Vidal, J. Womersley, W. Wu, CMS NOTE-1999/048, 1999.

[589] B. W. Harris, E. Laenen, L. Phaf, Z. Sullivan and S. Weinzierl, Phys. Rev. D **66** (2002) 054024 [arXiv:hep-ph/0207055].

[590] E. Boos, M. Dubinin, A. Pukhov, M. Sachwitz and H. J. Schreiber, Eur. Phys. J. C **21** (2001) 81 [arXiv:hep-ph/0104279].

[591] J. H. Kuhn, C. Sturm and P. Uwer, arXiv:hep-ph/0303233.

[592] T. Affolder *et al.* [CDF Collaboration], Phys. Rev. Lett. **86** (2001) 3233 [arXiv:hep-ex/0012029].

[593] A. Czarnecki and M. Jezabek, Nucl. Phys. B **427** (1994) 3 [arXiv:hep-ph/9402326].

[594] A. Czarnecki, M. Jezabek and J. H. Kuhn, Nucl. Phys. B **351** (1991) 70.

[595] A. Brandenburg, Z. G. Si and P. Uwer, Phys. Lett. B **539** (2002) 235 [arXiv:hep-ph/0205023].

[596] G. Mahlon and S. Parke, Phys. Rev. D **55** (1997) 7249 [arXiv:hep-ph/9611367]; Phys. Lett. B **476** (2000) 323 [arXiv:hep-ph/9912458].

[597] E. E. Boos and A. V. Sherstnev, Phys. Lett. B **534** (2002) 97 [arXiv:hep-ph/0201271].

[598] J. van der Heide, E. Laenen, L. Phaf and S. Weinzierl, Phys. Rev. D **62** (2000) 074025 [arXiv:hep-ph/0003318].

[599] J. Campbell, R. K. Ellis and F. Tramontano, arXiv:hep-ph/0408158.

[600] Q. H. Cao and C. P. Yuan, arXiv:hep-ph/0408180.

[601] E.Boos and A.Sherstnev, in preparation

[602] S. Parke and Y. Shadmi, Phys. Lett. B **387** (1996) 199 [arXiv:hep-ph/9606419].

[603] G. Mahlon and S. Parke, Phys. Rev. D **53** (1996) 4886 [arXiv:hep-ph/9512264]; Phys. Lett. B **411** (1997) 173 [arXiv:hep-ph/9706304].

[604] Y. Kiyo, J. Kodaira, K. Morii, T. Nasuno and S. Parke, Nucl. Phys. Proc. Suppl. **89** (2000) 37 [arXiv:hep-ph/0006021];
A. Brandenburg, M. Flesch and P. Uwer, Phys. Rev. D **59**, 014001 (1999) [arXiv:hep-ph/9806306].

[605] W. Bernreuther, A. Brandenburg, Z. G. Si and P. Uwer, Phys. Rev. Lett. **87**, 242002 (2001) [arXiv:hep-ph/0107086]; Acta Phys. Polon. B **34**, 4477 (2003) [arXiv:hep-ph/0304244]; Nucl. Phys. B **690**, 81 (2004) [arXiv:hep-ph/0403035].

[606] C. Benchouk, L. Hinz, and E. Monnier, ATL-PHYS-2002-024, 2002;
K. Smolek and V. Simak, ATL-Phys-2003-012, 2003.

[607] S. Slabospitsky and L. Sonnenschein, Comput. Phys. Commun. **148**, 87 (2002), [arXiv:hep-ph/0201292].

[608] T. G. Rizzo, in *1996 DPF/DPB Summer Study on New Directions for High Energy Physics*, Snowmass, CO, July 1996, eds. D.G. Cassel, L.Trindle Gennari and R.H. Siemann, hep-ph/9609311.

[609] W. Bernreuther, J. P. Ma and B. H. J. McKellar, Phys. Rev. D **51** (1995) 2475 [arXiv:hep-ph/9404235];
A. Brandenburg, Eur. Phys. J. C **11**, 127 (1999) [arXiv:hep-ph/9904251].

[610] J. Lee, S. Y. Choi and C. S. Kim, hep-ph/9801236; S. Y. Choi, C. S. Kim and J. Lee, Phys. Lett. B **415**, 67 (1997) [arXiv:hep-ph/9706379].

[611] E. Boos, A. Pukhov, M. Sachwitz and H. J. Schreiber, Z. Phys. C **75**, 237 (1997) hep-ph/9610424;

[612] S. Parke, Proc. of the 1994 Meeting of the APS, (DPF 94), Albuquerque, NM, 2-6 Aug 1994, DPF Conf.1994:0726-730 (QCD161:A6:1994), hep-ph/9409312.

[613] K. Whisnant, J. Yang, B. Young and X. Zhang, Phys. Rev. D **56**, 467 (1997) [arXiv:hep-ph/9702305].

[614] F. Larios, E. Malkawi and C.-P. Yuan, Lectures given by C.-P. Yuan at the CCAST Workshop on 'Physics at TeV Energy Scale ' July 15-26, 1996, Beijing, China, hep-ph/9704288.

[615] E. Boos, L. Dudko and T. Ohl, Eur. Phys. J. C **11**, 473 (1999) [arXiv:hep-ph/9903215].

[616] T. Tait and C. P. Yuan, Phys. Rev. D **63**, 014018 (2001) [arXiv:hep-ph/0007298].

[617] J. Cao, J. Wang, J. M. Yang, B. Young and X. Zhang, Phys. Rev. D **58**, 094004 (1998) [arXiv:hep-ph/9804343].

[618] F. Abe *et al.* [CDF Collaboration], Phys. Rev. Lett. **80** (1998) 2525.

[619] Obraztsov V.F., Slabospitsky S.R., and Yushchenko O.P., Phys. Lett. B **426**, 393 (1998) [arXiv:hep-ph/9712394];
Abreu P. *et al.* [DELPHI Collaboration], Phys. Lett. B **446**, 62 (1999) [arXiv:hep-ex/9903072];
Abbiendi G. *et al.* [OPAL Collaboration], Phys. Lett. B **521**, 181 (2001) [arXiv:hep-ex/0110009]. Achard P. *et al.* [L3 Collaboration], Phys. Lett. B **549**, 290 (2002) [arXiv:hep-ex/0210041];
A. Heister A. *et al.* [ALEPH Collaboration], Phys. Lett. B **543**, 173 (2002) [arXiv:hep-ex/0206070].

[620] Wolf G., arXiv:hep-ex/0105055;
Alan A.T. and Senol A., Europhys. Lett. **59**, 669 (2002) [arXiv:hep-ph/0202119];
Dannheim H. [H1 Collaboration], arXiv:hep-ex/0212004.

[621] Y. P. Gouz and S. R. Slabospitsky, Phys. Lett. B **457** (1999) 177 [arXiv:hep-ph/9811330].

[622] Richter-Was E., Froidevaux D. and Poggioli L., *"ATLFAST 2.0 a fast simulation package for ATLAS"*, ATL-PHYS-98-131 (1998).

[623] E. Malkawi and T. Tait, Phys. Rev. D **54**, 5758 (1996) [arXiv:hep-ph/9511337].

[624] T. Tait and C. P. Yuan, Phys. Rev. D **55**, 7300 (1997) [arXiv:hep-ph/9611244].

[625] F. del Aguila, J.A. Aguilar-Saavedra and R. Miquel, Phys. Rev. Lett. **82**, 1628 (1999) [arXiv:hep-ph/9808400].

[626] Aguilar-Saavedra J.A. and Riemann T., arXiv:hep-ph/0102197;
Aguilar-Saavedra J.A., Phys. Lett. B **502**, 115 (2001) [arXiv:hep-ph/0012305].

[627] S. Bar-Shalom and J. Wudka, Phys. Rev. D **60** (1999) 094016 [arXiv:hep-ph/9905407];
T. Han and J. L. Hewett, Phys. Rev. D **60** (1999) 074015 [arXiv:hep-ph/9811237].

[628] T. G. Rizzo, hep-ph/9910255.

[629] U. Baur, R. Clare, J. Erler, S. Heinemeyer, D. Wackeroth, G. Weiglein and D. R. Wood, in *Proc. of the APS/DPF/DPB Summer Study on the Future of Particle Physics (Snowmass 2001)* ed. N. Graf, eConf **C010630** (2001) P122 [arXiv:hep-ph/0111314].

[630] S. Heinemeyer, W. Hollik and G. Weiglein, Eur. Phys. J. C **9** (1999) 343 [arXiv:hep-ph/9812472].

[631] S. Heinemeyer and G. Weiglein, arXiv:hep-ph/0012364.

[632] S. Heinemeyer, W. Hollik and G. Weiglein, Comput. Phys. Commun. **124** (2000) 76 [arXiv:hep-ph/9812320].

[633] M. Frank, S. Heinemeyer, W. Hollik and G. Weiglein, arXiv:hep-ph/0212037;
T. Hahn, S. Heinemeyer, W. Hollik and G. Weiglein, *in preparation*.

[634] The *FeynHiggs* code can be obtained from `www.feynhiggs.de`.

[635] M. Berggren, R. Keranen, H. Nowak and A. Sopczak, arXiv:hep-ph/9911345.

[636] A. Bartl, H. Eberl, S. Kraml, W. Majerotto and W. Porod, Eur. Phys. J. directC **2** (2000) 6 [arXiv:hep-ph/0002115].

[637] S. Haywood *et al.*, arXiv:hep-ph/0003275.

[638] R. M. Thurman-Keup, A. V. Kotwal, M. Tecchio and A. Byon-Wagner, Rev. Mod. Phys. **73** (2001) 267.

[639] M. Dobbs and L. Lefebvre, ATL-PHYS-2002-022 and ATL-PHYS-2002-023.

[640] E. N. Argyres, G. Katsilieris, A. B. Lahanas, C. G. Papadopoulos and V. C. Spanos, Nucl. Phys. B **391** (1993) 23.

[641] U. Baur and E.L. Berger, Phys. Rev. **D47**, 4889 (1992).

[642] U. Baur and D. L. Rainwater, Phys. Rev. **D62**, 113011 (2000).

[643] J. Alcaraz, *Neutral Gauge Boson Pair Production in e^+e^- Linear colliders*, Proceedings of the Worldwide Study on Physics and Experiments with Future Linear e^+e^- Colliders, Sitges 1999, Vol. 1, 431, Universitat Autonoma de Barcelone, Servei de Piblicacions.

[644] S. Catai et al., in Report on the Workshop on Standard Model Physics (And More) at the LHC, eds. G. Altarelli and M.L. Mangano, CERN-2000-004 (2000)

[645] S. Abachi *et al.* [D0 Collaboration], FERMILAB-CONF-96-172-E *Contributed to 28th International Conference on High-energy Physics (ICHEP 96), Warsaw, Poland, 25-31 Jul 1996*.

[646] T. Affolder *et al.* [CDF Collaboration], Phys. Rev. Lett. **88** (2002) 042001 [arXiv:hep-ex/0108034].

[647] K. Hagiwara *et al.* [Particle Data Group Collaboration], Phys. Rev. D **66** (2002) 010001.

[648] W. T. Giele, E. W. Glover and J. Yu, Phys. Rev. D **53** (1996) 120.

[649] D. Bourilkov, arXiv:hep-ph/0305126.

[650] A. D. Martin, R. G. Roberts, W. J. Stirling and R. S. Thorne, Eur. Phys. J. C **28** (2003) 455 [arXiv:hep-ph/0211080]; arXiv:hep-ph/0308087.

[651] J. Pumplin, D. R. Stump, J. Huston, H. L. Lai, P. Nadolsky and W. K. Tung, JHEP **0207** (2002) 012 [arXiv:hep-ph/0201195].

[652] E. W. Glover, Nucl. Phys. Proc. Suppl. **116** (2003) 3 [arXiv:hep-ph/0211412].

[653] M. Winter, LC Note LC-PHSM-2001-016, available at `www.desy.de/~lcnotes/notes.html`; talk given at the LHC/LC study group meeting, CERN, July 2002, see: `www.ippp.dur.ac.uk/~georg/lhclc/`.

[654] L.N. Lipatov, Sov. J. Nucl. Phys. **23** (1976) 338; E.A. Kuraev, L.N. Lipatov and V.S. Fadin, Sov. Phys. JETP **45** (1977) 199; Ya.Ya. Balitsky and L.N. Lipatov, Sov. J. Nucl. Phys. **28** (1978) 822.

[655] A.H. Mueller and H. Navelet, Nucl. Phys. B **282**, 727 (1987).

[656] J. Bartels, A. De Roeck and H. Lotter, Phys. Lett. B **389** (1996) 742.

[657] S.J. Brodsky, F. Hautmann and D.E. Soper, Phys. Rev. D **56**, 6957 (1997).

[658] S. Abachi *et al.* [D0 Collaboration], Phys. Rev. Lett. **77**, 595 (1996).

[659] M. Wadhwa for the L3 collaboration, these proceedings.

[660] C. Adloff *et al.* [H1 Collaboration], Nucl. Phys. B **538** (1999) 3.

[661] J. Breitweg *et al.* [ZEUS Collaboration], Eur. Phys. J. C **6** (1999) 239.

[662] L.H. Orr and W.J. Stirling, Phys. Rev. D **56** (1997) 5875.

[663] C.R. Schmidt, Phys. Rev. Lett. **78** (1997) 4531.

[664] L.H. Orr and W.J. Stirling, Phys. Lett. B **429** (1998) 135; Phys. Lett. B **436** (1998) 372.

[665] J. R. Andersen, V. Del Duca, S. Frixione, C. R. Schmidt and W. J. Stirling, JHEP **0102** (2001) 007.

[666] J. R. Andersen, V. Del Duca, F. Maltoni and W. J. Stirling, JHEP **0105** (2001) 048.

[667] J. R. Andersen and W. J. Stirling, JHEP **0302** (2003) 018.

[668] J. Kwiecinski, L. Motyka and A. De Roeck, arXiv:hep-ph/0001180.

[669] V. S. Fadin and L. N. Lipatov, Phys. Lett. B **429** (1998) 127 [arXiv:hep-ph/9802290].

[670] M. Ciafaloni and G. Camici, Phys. Lett. B **430** (1998) 349 [arXiv:hep-ph/9803389].

[671] J. R. Andersen and A. Sabio Vera, Phys. Lett. B **567** (2003) 116 [arXiv:hep-ph/0305236].

[672] J. Kwiecinski and B. Ziaja, Phys. Rev. D **63**, 054022 (2001) [arXiv:hep-ph/0006292].

[673] N. G. Evanson and J. R. Forshaw, [arXiv:hep-ph/9912487].

[674] J. G. Contreras and A. De Roeck, LC-TH-2001-031

[675] LEP Higgs working group, Phys. Lett. B **565** (2003) 61 [arXiv:hep-ex/0306033]. M. Grünewald, talk given at the workshop on "Electroweak precision data and the Higgs mass", DESY Zeuthen, February 2003, see: `lepewwg.web.cern.ch/LEPEWWG/`.

[676] T. Binoth, J. P. Guillet, E. Pilon and M. Werlen, Eur. Phys. J. C **16** (2000) 311 [arXiv:hep-ph/9911340].

[677] T. Binoth, J. P. Guillet, E. Pilon and M. Werlen, Phys. Rev. D **63** (2001) 114016 [arXiv:hep-ph/0012191].

[678] T. Binoth, J. P. Guillet, E. Pilon and M. Werlen, Eur. Phys. J. C **24** (2002) 245.

[679] T. Binoth, J. P. Guillet, E. Pilon and M. Werlen, arXiv:hep-ph/0203064.

[680] Z. Bern, L. Dixon and C. Schmidt, Phys. Rev. D **66** (2002) 074018 [arXiv:hep-ph/0206194].

[681] J. Binnewies, B. A. Kniehl and G. Kramer, Phys. Rev. D **53** (1996) 6110 [arXiv:hep-ph/9601278].

[682] S. Kretzer, Phys. Rev. D **62** (2000) 054001 [arXiv:hep-ph/0003177].

[683] B. A. Kniehl, G. Kramer and B. Potter, Nucl. Phys. B **582** (2000) 514 [arXiv:hep-ph/0010289].

[684] P. Langacker, R. W. Robinett and J. L. Rosner, Phys. Rev. D **30** (1984) 1470;
D. London and J. L. Rosner, Phys. Rev. D **34** (1986) 1530;
R. W. Robinett, Phys. Rev. D **26** (1982) 2388;
R. W. Robinett and J. L. Rosner, Phys. Rev. D **26** (1982) 2396;
J. C. Pati and A. Salam, Phys. Rev. D **10** (1974) 275;
R. N. Mohapatra and J. C. Pati, Phys. Rev. D **11** (1975) 566;
L. S. Durkin and P. Langacker, Phys. Lett. B **166** (1986) 436.

[685] C. Csaki, J. Hubisz, G. D. Kribs, P. Meade and J. Terning, Phys. Rev. D **67** (2003) 115002 [arXiv:hep-ph/0211124].

[686] J. L. Hewett, F. J. Petriello and T. G. Rizzo, JHEP **0310** (2003) 062 [arXiv:hep-ph/0211218].

[687] T. Han, H. E. Logan, B. McElrath and L. T. Wang, Phys. Rev. D **67** (2003) 095004 [arXiv:hep-ph/0301040].

[688] T. Han, H. E. Logan, B. McElrath and L. T. Wang, Phys. Rev. D **67** (2003) 095004 [arXiv:hep-ph/0301040].

[689] see for example: I. Antoniadis, Phys. Lett. B **246** (1990) 377;
I. Antoniadis, C. Munoz and M. Quiros, Nucl. Phys. B **397** (1993) 515 [arXiv:hep-ph/9211309];
I. Antoniadis and K. Benakli, Phys. Lett. B **326** (1994) 69 [arXiv:hep-th/9310151];
I. Antoniadis and K. Benakli, Int. J. Mod. Phys. A **15** (2000) 4237 [arXiv:hep-ph/0007226];
I. Antoniadis, K. Benakli and M. Quiros, Phys. Lett. B **331** (1994) 313 [arXiv:hep-ph/9403290].

[690] T. Appelquist, H. C. Cheng and B. A. Dobrescu, Phys. Rev. D **64** (2001) 035002 [arXiv:hep-ph/0012100]; H. C. Cheng, K. T. Matchev and M. Schmaltz, Phys. Rev. D **66**, 056006 (2002) [arXiv:hep-ph/0205314] and Phys. Rev. D **66**, 036005 (2002) [arXiv:hep-ph/0204342]; T. G. Rizzo, Phys. Rev. D **64**, 095010 (2001) [arXiv:hep-ph/0106336].

[691] E. Eichten, I. Hinchliffe, K. D. Lane and C. Quigg, Rev. Mod. Phys. **56** (1984) 579 [Addendum-ibid. **58** (1986) 1065].

[692] S. Jain, A. K. Gupta and N. K. Mondal, Phys. Rev. D **62** (2000) 095003 [arXiv:hep-ex/0005025].

[693] For a review of new gauge boson physics at colliders and details of the various models, see J. L. Hewett and T. G. Rizzo, Phys. Rept. **183** (1989) 193;
M. Cvetic and S. Godfrey, arXiv:hep-ph/9504216, and T. G. Rizzo, arXiv:hep-ph/9612440.

[694] S. Riemann, PREL-LCPHSM-2003-24;
S. Riemann, LC-TH-2001-007.

[695] A. A. Pankov and N. Paver, Eur. Phys. J. C **29** (2003) 313 [arXiv:hep-ph/0209058];
A. A. Babich, P. Osland, A. A. Pankov and N. Paver, Phys. Lett. B **518** (2001) 128 [arXiv:hep-ph/0107159].

[696] D. Bourilkov, arXiv:hep-ph/0305125.

[697] Z. U. Usubov and O. B. Abdinov, Phys. Atom. Nucl. **64** (2001) 1288 [Yad. Fiz. **64** (2001) 1364].

[698] G. F. Giudice, R. Rattazzi and J. D. Wells, Nucl. Phys. B **544** (1999) 3 [arXiv:hep-ph/9811291];
S. Cullen, M. Perelstein and M. E. Peskin, Phys. Rev. D **62** (2000) 055012 [arXiv:hep-ph/0001166].

[699] T. G. Rizzo, Phys. Rev. D **60** (1999) 115010 [arXiv:hep-ph/9904380].

[700] J. L. Hewett, Phys. Rev. Lett. **82** (1999) 4765 [arXiv:hep-ph/9811356].

[701] F. Abe *et al.* [CDF Collaboration], Phys. Rev. Lett. **79** (1997) 2198;
B. Abbott *et al.* [D0 Collaboration], Phys. Rev. Lett. **82** (1999) 4769 [arXiv:hep-ex/9812010];
A. Meyer [CDF Collaboration], Mod. Phys. Lett. A **18** (2003) 1643 [arXiv:hep-ex/0306046].

[702] [ALEPH Collaboration], arXiv:hep-ex/0212036.

[703] T. Affolder *et al.* [CDF Collaboration], Phys. Rev. Lett. **87** (2001) 231803 [arXiv:hep-ex/0107008].

[704] M. Cvetic and P. Langacker, Phys. Rev. D **46** (1992) 4943 [Erratum-ibid. D **48** (1993) 4484] [arXiv:hep-ph/9207216];
F. Del Aguila and M. Cvetic, Phys. Rev. D **50** (1994) 3158 [arXiv:hep-ph/9312329].

[705] A. Leike, Phys. Rept. **317** (1999) 143 [arXiv:hep-ph/9805494].

[706] S. Godfrey, Phys. Rev. D **51** (1995) 1402 [arXiv:hep-ph/9411237];
S. Godfrey, arXiv:hep-ph/9612384;
S. Godfrey, in *Proc. of the APS/DPF/DPB Summer Study on the Future of Particle Physics (Snowmass 2001)* ed. N. Graf, eConf **C010630** (2001) P344 [arXiv:hep-ph/0201093].

[707] A. Leike and S. Riemann, Z. Phys. C **75** (1997) 341 [arXiv:hep-ph/9607306].

[708] S. Riemann, arXiv:hep-ph/9610513.

[709] M. Dittmar, A. S. Nicollerat and A. Djouadi, Phys. Lett. B **583** (2004) 111 [arXiv:hep-ph/0307020].

[710] M. Dittmar, Phys. Rev. D **55** (1997) 161 [arXiv:hep-ex/9606002].

[711] M. Dittmar, F. Pauss and D. Zurcher, Phys. Rev. D **56** (1997) 7284 [arXiv:hep-ex/9705004].

[712] F. del Aguila, M. Cvetic and P. Langacker, Phys. Rev. D **48** (1993) 969 [arXiv:hep-ph/9303299].

[713] S. Riemann, arXiv:hep-ph/9710564.

[714] T. G. Rizzo, Phys. Rev. D **55** (1997) 5483 [arXiv:hep-ph/9612304].

[715] R. Casalbuoni, S. De Curtis, D. Dominici, R. Gatto and S. Riemann, arXiv:hep-ph/0001215.

[716] P. Abreu *et al.* [DELPHI Collaboration], Z. Phys. C **65** (1995) 603.

[717] M. Czakon, J. Gluza, F. Jegerlehner and M. Zralek, Eur. Phys. J. C **13** (2000) 275 [arXiv:hep-ph/9909242].

[718] LEP Electroweak Working Group and SLD Heavy Flavor and Electroweak Groups, D. Abbaneo et al., LEPEWWG-2001-02, hep-ex/0112021.

[719] F. Richard, arXiv:hep-ph/0303107.

[720] S. Godfrey, Contribution to this report.

[721] G. Barenboim, J. Bernabeu, J. Prades and M. Raidal, Phys. Rev. D **55** (1997) 4213 [arXiv:hep-ph/9611347].

[722] K. Hagiwara *et al.* [Particle Data Group Collaboration], Phys. Rev. D **66** (2002) 010001 and 2003 off-year partial update for the 2004 edition available on the PDG WWW pages (URL: http://pdg.lbl.gov/).

[723] T. G. Rizzo, arXiv:hep-ph/9612440.

[724] M. Cvetic, P. Langacker and J. Liu, Phys. Rev. D **49** (1994) 2405 [arXiv:hep-ph/9308251].

[725] S. Godfrey, P. Kalyniak, B. Kamal and A. Leike, Phys. Rev. D **61** (2000) 113009 [arXiv:hep-ph/0001074];
S. Godfrey, P. Kalyniak, B. Kamal, M. A. Doncheski and A. Leike, Phys. Rev. D **63** (2001) 053005 [arXiv:hep-ph/0008157].

[726] J. Kubar-Andre and F. E. Paige, Phys. Rev. D **19** (1979) 221;
G. Altarelli, R. K. Ellis and G. Martinelli, Nucl. Phys. B **143** (1978) 521 [Erratum-ibid. B **146** (1978) 544].

[727] T. G. Rizzo, arXiv:hep-ph/9612440;
T. G. Rizzo, arXiv:hep-ph/9609248;
J. L. Hewett and T. G. Rizzo, Phys. Rev. D **45** (1992) 161.

[728] G. Burdman, M. Perelstein and A. Pierce, Phys. Rev. Lett. **90** (2003) 241802 [Erratum-ibid. **92** (2004) 049903] [arXiv:hep-ph/0212228].

[729] See, for example, T.G. Rizzo and J.D. Wells, Phys. Rev. **D61** (2000) 016007;
P. Nath and M. Yamaguchi, Phys. Rev. **D60** (1999) 116006;
M. Masip and A. Pomarol, Phys. Rev. **D60** (1999) 096005;
L. Hall and C. Kolda, Phys. Lett. **B459** (1999) 213;
R. Casalbuoni, S. DeCurtis, D. Dominici and R. Gatto, Phys. Lett. **B462** (1999) 48;
A. Strumia, Phys. Lett. **B466** (1999) 107;
F. Cornet, M. Relano and J. Rico, Phys. Rev. **D61** (2000) 037701;
C.D. Carone, Phys. Rev. **D61** (2000) 015008.

[730] J. Hewett and M. Spiropulu, Ann. Rev. Nucl. Part. Sci. **52**, 397 (2002) [arXiv:hep-ph/0205106].

[731] N. Arkani-Hamed, S. Dimopoulos and G. R. Dvali, Phys. Lett. B **429**, 263 (1998) [arXiv:hep-ph/9803315]; Phys. Rev. D **59**, 086004 (1999) [arXiv:hep-ph/9807344].

[732] G. F. Giudice, R. Rattazzi and J. D. Wells, Nucl. Phys. B **544**, 3 (1999) [arXiv:hep-ph/9811291].

[733] T. Han, J. D. Lykken and R. J. Zhang, Phys. Rev. D **59**, 105006 (1999) [arXiv:hep-ph/9811350].

[734] J. L. Hewett, Phys. Rev. Lett. **82**, 4765 (1999) [arXiv:hep-ph/9811356].

[735] S. Nussinov and R. Shrock, Phys. Rev. D **59**, 105002 (1999) [arXiv:hep-ph/9811323].

[736] T. G. Rizzo, Phys. Rev. D **59**, 115010 (1999) [arXiv:hep-ph/9901209].

[737] D. Bourilkov, arXiv:hep-ph/0305125.

[738] S. Riemann, LC-TH-2001-007.

[739] K. Agashe and N. G. Deshpande, Phys. Lett. B **456**, 60 (1999) [arXiv:hep-ph/9902263].

[740] T. G. Rizzo, arXiv:hep-ph/0303056.

[741] F. Gianotti *et al.*, arXiv:hep-ph/0204087; V. Kabachenko, A. Miagkov, and A. Zenin, ATLAS Physics Note, ATL-PHYS-2001-012 (2001).

[742] T. G. Rizzo, JHEP **0302**, 008 (2003) [arXiv:hep-ph/0211374].

[743] T. G. Rizzo, JHEP **0210**, 013 (2002) [arXiv:hep-ph/0208027].

[744] E. A. Mirabelli, M. Perelstein and M. E. Peskin, Phys. Rev. Lett. **82**, 2236 (1999) [arXiv:hep-ph/9811337].

[745] L. Vacavant and I. Hinchliffe, J. Phys. G **27**, 1839 (2001).

[746] T.G. Rizzo, contribution to this report.

[747] A. deRoeck, J. Lykken, and M. Spiropulu, in progress.

[748] G. F. Giudice, R. Rattazzi and J. D. Wells, Nucl. Phys. B **595**, 250 (2001) [arXiv:hep-ph/0002178].

[749] M. Battaglia, D. Dominici, and J. Gunion, contribution to this report.

[750] S. Abdullin *et al.*, CMS Collaboration, CMS-NOTE-2003/033 (2003).

[751] G. F. Giudice and A. Strumia, Nucl. Phys. B **663**, 377 (2003) [arXiv:hep-ph/0301232].

[752] M. Schumacher, LC note LC-PHSM-2003-096 (2003).

[753] O. J. P. Eboli and D. Zeppenfeld, Phys. Lett. B **495**, 147 (2000) [arXiv:hep-ph/0009158].

[754] B. F. L. Ward, S. Jadach and Z. Was, Nucl. Phys. Proc. Suppl. **116**, 73 (2003) [arXiv:hep-ph/0211132].

[755] G. Montagna, O. Nicrosini and F. Piccinini, Comput. Phys. Commun. **98** (1996) 206.

[756] I. Antoniadis, Phys. Lett. B **246**, 377 (1990); J. D. Lykken, Phys. Rev. D **54**, 3693 (1996) [arXiv:hep-th/9603133]; I. Antoniadis and M. Quiros, Phys. Lett. B **392**, 61 (1997) [arXiv:hep-th/9609209].

[757] See, for example, T. G. Rizzo and J. D. Wells, Phys. Rev. D **61**, 016007 (2000) [arXiv:hep-ph/9906234]; P. Nath and M. Yamaguchi, Phys. Rev. D **60**, 116004 (1999) [arXiv:hep-ph/9902323]; M. Masip and A. Pomarol, Phys. Rev. D **60**, 096005 (1999) [arXiv:hep-ph/9902467]; L. J. Hall and C. F. Kolda, Phys. Lett. B **459**, 213 (1999) [arXiv:hep-ph/9904236]; R. Casalbuoni, S. De Curtis, D. Dominici and R. Gatto, Phys. Lett. B **462**, 48 (1999) [arXiv:hep-ph/9907355]; A. Strumia, Phys. Lett. B **466**, 107 (1999) [arXiv:hep-ph/9906266]; F. Cornet, M. Relano and J. Rico, Phys. Rev. D **61**, 037701 (2000) [arXiv:hep-ph/9908299]; C. D. Carone, Phys. Rev. D **61**, 015008 (2000) [arXiv:hep-ph/9907362].

[758] T. G. Rizzo, Phys. Rev. D **61**, 055005 (2000) [arXiv:hep-ph/9909232]; Phys. Rev. D **64**, 015003 (2001) [arXiv:hep-ph/0101278].

[759] See, for example, the analysis by G. Azuelos and G. Polesello in, G. Azuelos *et al.*, "The beyond the standard model working group: Summary report," Proceedings of Workshop on Physics at TeV Colliders, Les Houches, France, 21 May - 1 Jun 2001, arXiv:hep-ph/0204031; G. Azuelos and G. Polesello, EPJ Direct (2003), ATLAS note SN-ATLAS-2003-023. T. G. Rizzo, in *Proc. of the APS/DPF/DPB Summer Study on the Future of Particle Physics (Snowmass 2001)* ed. N. Graf, eConf **C010630**, P304 (2001) [arXiv:hep-ph/0109179].

[760] B. C. Allanach *et al.* [Beyond the Standard Model Working Group Collaboration], arXiv:hep-ph/0402295.

[761] T. G. Rizzo, JHEP **0306**, 021 (2003) [arXiv:hep-ph/0305077], and contribution to this report.

[762] For a review of new gauge boson physics at colliders and details of the various models, see J. L. Hewett and T. G. Rizzo, Phys. Rept. **183**, 193 (1989); M. Cvetic and S. Godfrey, in *Electroweak Symmetry Breaking and Beyond the Standard Model*, ed. T. Barklow *et al.*, (World Scientific, Singapore, 1995), hep-ph/9504216; T.G. Rizzo in *New Directions for High Energy Physics: Snowmass 1996*, ed. D.G. Cassel, L. Trindle Gennari and R.H. Siemann, (SLAC, 1997), hep-ph/9612440; A. Leike, Phys. Rept. **317**, 143 (1999) [arXiv:hep-ph/9805494].

[763] This is a common feature of the class of models wherein the usual $SU(2)_L$ of the SM is the result of a diagonal breaking of a product of two or more $SU(2)$'s. For a discussion of a few of these models, see H. Georgi, E. Jenkins and E. H. Simmons, Phys. Rev. Lett. **62**, 2789 (1989) [Erratum-ibid. **63**, 1540 (1989)]; V. D. Barger and T. Rizzo, Phys. Rev. D **41**, 946 (1990); T.G. Rizzo, Int. J. Mod. Phys. **A7**, 91 (1992); R. S. Chivukula, E. H. Simmons and J. Terning, Phys. Lett. B **346**, 284 (1995) [arXiv:hep-ph/9412309]; V. D. Barger, N. G. Deshpande, T. Kuo, A. Bagneid, S. Pakvasa and K. Whisnant, Int. J. Mod. Phys. A **2**, 1327 (1987); A. Bagneid, T. K. Kuo and N. Nakagawa, Int. J. Mod. Phys. A **2**, 1351 (1987); D. J. Muller and S. Nandi, Phys. Lett. B **383**, 345 (1996) [arXiv:hep-ph/9602390]; X. Li and E. Ma, Phys. Rev. Lett. **47**, 1788 (1981); Phys. Rev. D **46**, 1905 (1992); E. Malkawi, T. Tait and C. P. Yuan, Phys. Lett. B **385**, 304 (1996) [arXiv:hep-ph/9603349].

[764] T. G. Rizzo, Phys. Rev. D **55**, 5483 (1997) [arXiv:hep-ph/9612304].

[765] G. Servant and T. M. P. Tait, Nucl. Phys. B **650**, 391 (2003) [arXiv:hep-ph/0206071], New J. Phys. **4**, 99 (2002) [arXiv:hep-ph/0209262]; H. C. Cheng, J. L. Feng and K. T. Matchev, Phys. Rev. Lett. **89**, 211301 (2002) [arXiv:hep-ph/0207125].

[766] T. Appelquist, H. C. Cheng and B. A. Dobrescu, Phys. Rev. D **64**, 035002 (2001) [arXiv:hep-ph/0012100]; T. G. Rizzo, Phys. Rev. D **64**, 095010 (2001) [arXiv:hep-ph/0106336]; T. Appelquist and B. A. Dobrescu, Phys. Lett. B **516**, 85 (2001) [arXiv:hep-ph/0106140].

[767] H. Georgi, A. K. Grant and G. Hailu, Phys. Lett. B **506**, 207 (2001) [arXiv:hep-ph/0012379]; M. Carena, T. M. Tait and C. E. Wagner, Acta Phys. Polon. B **33**, 2355 (2002) [arXiv:hep-ph/0207056].

[768] H. C. Cheng, K. T. Matchev and M. Schmaltz, Phys. Rev. D **66**, 036005 (2002) [arXiv:hep-ph/0204342];

[769] J.L. Hewett and T. Tait, contribution to this report.

[770] H. C. Cheng, K. T. Matchev and M. Schmaltz, Phys. Rev. D **66**, 056006 (2002) [arXiv:hep-ph/0205314].

[771] L. Randall and R. Sundrum, Phys. Rev. Lett. **83**, 3370 (1999) [arXiv:hep-ph/9905221].

[772] W. D. Goldberger and M. B. Wise, Phys. Rev. Lett. **83**, 4922 (1999) [arXiv:hep-ph/9907447].

[773] H. Davoudiasl, J. L. Hewett and T. G. Rizzo, Phys. Rev. Lett. **84**, 2080 (2000) [arXiv:hep-ph/9909255]; Phys. Rev. D **63**, 075004 (2001) [arXiv:hep-ph/0006041].

[774] B. C. Allanach, K. Odagiri, M. A. Parker and B. R. Webber, JHEP **0009**, 019 (2000) [arXiv:hep-ph/0006114].

[775] H. Davoudiasl, J. L. Hewett and T. G. Rizzo, JHEP **0304**, 001 (2003) [arXiv:hep-ph/0211377].

[776] H. Davoudiasl, J. L. Hewett and T. G. Rizzo, Phys. Rev. D **68**, 045002 (2003) [arXiv:hep-ph/0212279]; JHEP **0308**, 034 (2003) [arXiv:hep-ph/0305086], M. Carena, E. Ponton, T. M. P. Tait and C. E. M. Wagner, Phys. Rev. D **67**, 096006 (2003) [arXiv:hep-ph/0212307].

[777] T. Buanes, E. W. Dvergsnes and P. Osland, Eur. Phys. J. C **35**, 555 (2004) [arXiv:hep-ph/0403267].

[778] J.L. Hewett, contribution to this report.